

Q.690

K33b

no.95-102

1982-83













Q.690  
K33b

ISSN 0453 - 4972  
BRI Research paper No. 95

CHARACTERIZATION OF THE INTERMITTENT  
FLAMING REGION OF THE UPWARD CURRENT  
ABOVE DIFFUSION FLAMES

THE LIBRARY OF THE

JUN 9 1983

UNIVERSITY OF ILLINOIS  
AT URBANA-CHAMPAIGN

by  
Yuji HASEMI

Building Research Institute  
Ministry of Construction

March 1982







## FOREWORD

This report presents a part of the results of research studies entitled "Analysis of Fire Spread for the Improvement of Fire Test Methods", which is being conducted as a continual project of BRI for 1979-1983.

The development of engineering design method of firesafety in buildings based on the quantitative prediction of fire phenomena is one of the significant aims of modern fire research. This approach has been successful in the fields of fire protection design of structural members and smoke control in high rise buildings, and it is now being applied to the development of firesafety design for preflashover fires. However, preflashover fires involve so many physical/chemical processes that a number of processes consisting fire growth are still left unformulated.

Fire plume, the process which supplies smoke and heat from fire source to ceiling layer and sometimes accelerates fire spread along wall if fire source is located near wall, is counted among the processes that have the most significant influences on firesafety in early stages of compartment fires. Though considerable studies have been made on fire plumes, they are almost limited to those far from fire source in semi-infinite space. This report has focused on the behavior of plume near to fire source, which has significant role in the transfer of energy and mass from fire source and lower air layer to the ceiling smoke layer. In this report, a mathematical model of the plume near to fire source was derived on the basis of recent experimental works, and some diagrams to calculate practical properties are prepared. The results induced herein should contribute to improve the engineering design method of firesafety for preflashover fires.

March, 1982

K. Kamimura, Director General  
Building Research Institute





CHARACTERIZATION OF THE INTERMITTENT FLAMING REGION OF THE UPWARD CURRENT  
ABOVE DIFFUSION FLAMES

by

Yuji Hasemi\*

Building Research Institute, Ministry of Construction, Tsukuba, Ibaraki.  
(BRI Research Paper, No. )

ABSTRACT

The study herein aims at characterizing the intermittent flaming region of upward current above diffusion flames, and consists of the similarity analysis of the region, derivation of the analytical solution of the basic equations for axisymmetric upward current due to buoyancy with respect to the experimental facts on the region and the determination of experimental constants which are involved in the solution by dimensional analysis and experiments.

As the growth of fire and spread of smoke depend significantly on the behavior of the upward current above fire source in early stages of compartment fire, the characterization of the upward current above fire source is a problem of increasing importance. However, though considerable informations are available on axisymmetric upward current, most of them are almost limited to the region far from fire source. This report analyzes the intermittent flaming region among the near regions to fire source, and derived a mathematical model of this region which enables it to predict the properties of the region at the comparable accuracy to that for the region far from fire source. The report also presents some diagrams for the practical calculation of the useful properties such as mass flow rate in the current and entrainment coefficient at every height in the intermittent region.

\* Research Member, Testing & Evaluation Department.





CHARACTERIZATION OF THE INTERMITTENT FLAMING REGION OF THE UPWARD CURRENT  
ABOVE DIFFUSION FLAMES

by  
Yuji HASEMI\*

CONTENTS

1. Introduction .....	1
2. Experimental Relationships .....	2
2-1. Flame Height .....	2
2-2. Centerline Properties .....	3
2-3. Transverse Characteristics .....	3
3. Estimation of the Eddy Coefficient in the Intermittent Flaming Region ....	6
3-1. Estimation Method of the Eddy Coefficient in an Axisymmetric Flow ...	6
3-2. Quantification of the Eddy Coefficient in the Intermittent Flaming Region .....	7
3-3. Dimensional Structure and Simplification of the Eddy Coefficient Formulae .....	8
4. Solution of the Equations for Axisymmetric Upward Current with the Uni- form Eddy Coefficient Hypothesis .....	9
5. Correlation between the Model and the Experimental Relationships .....	12
5-1. Centerline and Transverse Characteristics .....	13
5-2. Determination of $K/Q^{3/5}$ .....	14
6. Mass Flux, Energy Flux and Entrainment in the Upward Current .....	15
6-1. Mass and Bulk Flux .....	16
6-2. Energy Flux .....	17
6-3. Calculation Diagrams of Mass and Bulk Flux, Entrainment Coefficient and Energy Flux .....	17
7. Conclusions .....	18
Acknowledgements .....	18
Terminology .....	19
References .....	20

---

\* Research Member, Testing & Evaluation Department, Building Research Institute,  
Ministry of Construction.





## I. INTRODUCTION

In the early stages of a compartment fire, the growth of fire and spread of smoke depend significantly on the behaviour of the upward current above fire source. However, though considerable information is available to the upward current, the systematic studies have been almost concentrated to the region far from fire source<sup>1),2)</sup>. Recognizing that the region far from fire source is usually involved in the hot gas layer accumulated underneath ceiling, it is presumed quite naturally that the most meaningful regions of upward current in enclosure are those close to the fire source.

The first systematic measurement of the deterministic properties, such as mean vertical velocity and mean excess temperature, in the regions near fire source was made by Terai and Nitta<sup>3),4)</sup>. They have used methanol pool fires as heat source, and have found that the upward current in the lower regions is almost columnar shaped and the centerline velocity is almost constant with height. The measurement of the deterministic properties in the regions close to the flame or within it was followed by McCaffrey<sup>5)</sup> and Cox and Chitty<sup>6)</sup>. They both have used the diffusion flame by natural gas on a porous refractory burner, and have clarified quantitatively how the deterministic properties depend on height and heat release rate. According to their works, the upward current above diffusion flames appears to divide into three regions, which are distinguished by the normalized height,  $z/Q^{2/5}$ . The lowest region,  $z/Q^{2/5} < 0.08$ , corresponds to the continuous flame, where the centerline excess temperature is constant with height and the current is accelerated. The middle region,  $0.08 < z/Q^{2/5} < 0.20$ , corresponds to the intermittent flaming region, where the centerline excess temperature is in proportional to the inverse of height and the centerline velocity is constant with height. The centerline properties in the highest region,  $z/Q^{2/5} > 0.20$ , satisfies the dimensional relationships of the conventional models of thermal plume. McCaffrey and Cox-Chitty also found the dimensional relationship between the centerline properties, height and the heat release rate at fire source as described below.

$$w_a/Q^{1/5} = A(z/Q^{2/5})^n, \quad \theta_a = B(z/Q^{2/5})^{2n-1} \quad (1)$$

where  $n=1/2$  for the flaming region,  $n=0$  for the intermittent flaming region and  $n=-1/3$  for the plume. The features of the highest region coincide well with the classical model of the plume by Yokoi<sup>1)</sup> etc, and those of the lower regions can explain the results of Terai-Nitta qualitatively.

Independently from the works of McCaffrey and Cox-Chitty, the author

has analyzed Terai-Nitta's results, and has estimated that the eddy coefficient in their upward current be uniform<sup>7)</sup>. He has also derived a solution of the equations of the axially symmetric plume with the uniform-eddy-coefficient hypothesis and a few dimensional assumptions derived from Terai-Nitta's data. Though this solution explains the most features of the data of McCaffrey and Cox-Chitty for the intermittent flaming region, it has not been clarified how the eddy coefficient is formulated with the known parameters. Recently, the author has compared this solution with the experimental relationships of the upward current in this region, and has formulated an equation to predict the eddy coefficient<sup>8)</sup>.

This paper reviews the experimental relationships on the upward current above diffusion flames, and then summarizes the derivation process of the solution of the plume equations for the intermittent flaming region. The derivation process of the solution is modified from that shown in Ref.7), because the dimensional relationships derived by McCaffrey and Cox-Chitty are here considered.

## 2. EXPERIMENTAL RELATIONSHIPS

In order to find a clue to modeling the upward current in the intermittent flaming region, we will here review the empirical relationships from previous experimental works. Tab.1 outlines the works here studied, two of which use natural gas diffusion flame as heat source. Terai-Nitta and we both have used the methanol pool fire; the former settled metal screens around the fire source for cutting of the draft, whilst the latter has conducted test in a 30x20x15m calm space without obstacles against air movement.

### 2-1. Flame Height

According to the experiments of McCaffrey and Cox-Chitty on natural gas fires, the flame height is proportional to  $Q^{2/5}$ , and the centerline properties are normalized with  $z/Q^{2/5}$ . This suggests that the behaviour of the upward current above diffusion flames is essentially dependent on the flame height. Though the flame height depends on fuel types, we can demonstrate that the diffusion flame by natural gas and that by methanol pool fires are alike in the relationship between the flame height and the heat release rate.

McCaffrey has correlated the flame height with heat release rate as

$$\begin{aligned} L &= 0.08Q^{2/5} && \text{(continuous flame)} \\ L &= 0.20Q^{2/5} && \text{(including intermittent flaming region)} \end{aligned} \quad (2)$$



As the intensity of the fire source in the early stages of fire is the order of  $Q \approx 10^0 \sim 10^2$  kW, the above formula means that the upper limit of the intermittent flaming region may reach 1.0~1.5m in the preflashover stages of fire. This height is comparable with that of the neutral zone of a fire compartment installed with popular openings.

The height at the middle of the intermittent flaming region above methanol pool fire is formulated as a function of pan diameter by Terai-Nitta as<sup>3)</sup>

$$L_m = 3.5d^{4/5} \quad (3)$$

As it is expected quite naturally that  $Q$  is proportional to the square of the radius of the tray of burning methanol, the above relationship leads to

$$L_m = 0.10Q^{2/5} \quad (4)$$

In connection with this, the mean visible flame height in our case is correlated with the heat release rate as

$$L_m = 0.13Q^{2/5} \quad (5)$$

Comparing these data with those on natural gas fires, we find that the methanol pool fires and the natural gas fires are alike in the relationship between the flame height and the energy input.

## 2-2. Centerline Properties

As mentioned in the Introduction, McCaffrey and Cox-Chitty have correlated the centerline properties with the height from fire source and the heat release rate as

$$w_a/Q^{1/5} = A(z/Q^{2/5})^n, \quad \theta_a = B(z/Q^{2/5})^{2n-1} \quad (6)$$

where  $A$  and  $B$  are constant in the respective regions. McCaffrey and Cox-Chitty have further pointed out that  $w_a^2/g\beta\theta_a z (= A^2/g\beta B)$ , which is clearly constant in each region, takes the almost constant value irrespective of the regions. The experimental relationships concerning to the centerline properties are summarized in Tab.2.

## 2-3. Transverse Characteristics

The function characterizing the horizontal distribution of excess temperature and vertical velocity have been approximated conventionally by Gaussian distribution. The horizontal spread of the upward current has been usually characterized by the radial distance  $r_w^*$  or  $r_\theta^*$  at which velocity or excess

temperature takes the value of  $1/e$  of that at the centerline. Here, we investigate into the relationships between the transverse characteristics and the centerline properties referring to the other experiments on thermal plumes.

Tab.3 summarizes the ratio of  $r_\theta^*/r_w^*$  for the previous experimental works on both of the intermittent flaming region and the conventional plume region. According to these data, it is clear that the width for velocity is always wider than that for excess temperature in the intermittent flaming region. In contradistinction to this, the relationship between the two widths is rather disordered in the plume; that is, the temperature profile is wider than that of velocity in the experiments of Rouse-Yih-Humphreys<sup>2)</sup> and Yokoi<sup>1)</sup>, whilst the velocity profile is wider than that of excess temperature in the works of George-Tamanini-Alpert<sup>9)</sup> and McCaffrey<sup>5)</sup>. However, a certain order should hold between the centerline properties and the plume width ratio,  $r_\theta^*/r_w^*$ , if the similarity condition is satisfied in each region.

Approximating the horizontal distribution of velocity and excess temperature by Gaussian distribution as

$$w = az^n \cdot \exp(-\sigma_w^2 r^2 / z^{1-3n}), \quad \theta = b \cdot z^{2n-1} \cdot \exp(-\sigma_\theta^2 r^2 / z^{1-3n}) \quad (7)$$

then, the integrated form of the momentum equation for the axisymmetric plume becomes

$$\frac{d}{dz} \int_0^\infty r w^2 dr = \frac{(1-n) A^2 z^{-n}}{4\sigma_w} = \frac{(1-n) w_a^2 z^{-3n}}{4\sigma_w} = \frac{g\beta B z^{-n}}{2\sigma_\theta} = \frac{g\beta \theta_a z^{1-3n}}{2\sigma_\theta} \quad (8)$$

From the above relationship, we obtain the relationship between  $r_\theta^*/r_w^*$  and  $w_a^2/g\beta\theta_a z$ , which characterizes the axial characteristics, as follows.

$$\frac{w_a^2}{g\beta\theta_a z} = \frac{2\sigma_w}{(1-n)\sigma_\theta} = \frac{2}{1-n} (r_\theta^*/r_w^*)^2 \quad (9)$$

For the intermittent flaming region, we substitute  $n=0$  into (9), and obtain

$$w_a^2/g\beta\theta_a z = 2(r_\theta^*/r_w^*)^2 \quad (10)$$

and for the plume region, substituting  $n=-1/3$  to (9), we obtain

$$w_a^2/g\beta\theta_a z = 1.5(r_\theta^*/r_w^*)^2 \quad (11)$$

Consequently, if the similarity condition and Gaussian distribution are both assumed, it is expected that  $r_\theta^* \geq r_w^*$  holds for  $w_a^2/g\beta\theta_a z \geq 2$  in the intermittent flaming region and  $r_\theta^* \geq r_w^*$  holds for  $w_a^2/g\beta\theta_a z \geq 1.5$  in the plume region. Fig.2 compares these relationships and experimental results, where is seen that McCaffrey's data on the plume region does not satisfy the above relationship.



Inferring from the above considerations, it is expected that the temperature profile will become wider than that of velocity in the region higher than the area McCaffrey has observed, if  $w_a^2/g\beta\theta_a z > 1.5$  holds always. Fig.2 also demonstrates that  $w_a^2/g\beta\theta_a z$  is larger than  $2(r_\theta^*/r_w^*)$  in the many of the experiments on the intermittent flaming region. This suggests that Gaussian distribution may not be the most likely function to characterize the horizontal distribution of the properties in this region.

In connection with the scaling of the transverse characteristics, Cox-Chitty have shown that the width of the upward current can be also normalized with  $Q^{2/5}$ . That is, the observed values of the width at every height can be represented by the functions in the following forms.

$$r_w^*/Q^{2/5} = f_1(z/Q^{2/5}) \quad (12)$$

$$r_\theta^*/Q^{2/5} = f_2(z/Q^{2/5}) \quad (13)$$

Here, we will show that (12) and (13) can be derived from the conservation of heat flux, the similarity requirement and the hypothesis that the axial properties are represented in the form of (1). First, we assume that velocity and excess temperature are represented as  $w = A \cdot (z/Q^{2/5})^n \cdot Q^{1/5} \cdot W(r^2/x^{1+3n} z^{1-3n})$  and  $\theta = B \cdot (z/Q^{2/5})^{2n-1} \cdot \Theta(r^2/x^{1+3n} z^{1-3n})$  from the second and the third conditions above mentioned. Then, the conservation condition of heat flux is given by

$$\begin{aligned} Q &= 2\pi C_p \rho Q^{3(1-2n)/5} \cdot x^{1+3n} \int_0^\infty A \cdot B \cdot W(r^2/x^{1+3n} z^{1-3n}) \cdot \Theta(r^2/x^{1+3n} z^{1-3n}) \frac{r dr}{x^{1+3n} z^{1-3n}} \\ &= \pi C_p \rho Q^{3(1-2n)/5} \cdot x^{1+3n} \int_0^\infty A \cdot B \cdot W(\eta) \cdot \Theta(\eta) d\eta \end{aligned} \quad (14)$$

For this equation to hold, the power of  $Q$  in the right hand side should be equal to that in the left. Recognizing that the underlined part is constant, we can clarify how the parameter,  $x$ , depends on  $Q$ . Now, let  $x$  be proportional to  $Q^\ell$ . Then, the condition for (14) to hold is

$$3(1-2n)/5 + \ell(1+3n) = 1 \quad (15)$$

The value of  $\ell$  satisfying (15) for  $n=0$  is  $2/5$ . On the other hand,  $\ell$  is not necessary for  $n=-1/3$ . Substituting  $x \propto Q^{2/5}$  and (6) to the functions representing the horizontal distribution of excess temperature and velocity, we obtain

$$W(r^2/x^{1+3n} z^{1-3n}) = W(r^2/x^{1+3n} z^{1-3n} Q^{4/5}) = W(r'^2/x'^{1+3n} z'^{1-3n}) \quad (16)$$

$$\Theta(r^2/x^{1+3n} z^{1-3n}) = \Theta(r'^2/x'^{1+3n} z'^{1-3n}) \quad (17)$$

where  $x' \equiv x/Q^{2/5}$ ,  $z' \equiv z/Q^{2/5}$ ,  $r' \equiv r/Q^{2/5}$ . (12) and (13) are immediately obtained from (16) and (17).

### 3. ESTIMATION OF THE EDDY COEFFICIENT IN THE INTERMITTENT FLAMING REGION

Here, we will derive a mathematical model of the eddy coefficient in the intermittent flaming region. This procedure will employ not the statistical properties but only the deterministic ones, because it is difficult to measure the statistical properties in a flow with extreme gradient of temperature at present. The model of the eddy coefficient developed here involves one unknown parameter in common with the parameter,  $c$ , for the plume formulated with the concept of mixing length hypothesis by Yokoi<sup>1)</sup>. This parameter will be quantified in the following chapters by comparing the solution of the basic equations of the upward current with the experimental data.

#### 3-1. Estimation Method of the Eddy Coefficient in an Axisymmetric Flow

In order to quantify the eddy coefficient in an axisymmetric flow using the measured deterministic properties, we will first derive an explicit calculation method of the eddy coefficient,  $K_\xi$ , for one property  $\xi$ , whose conservation is described by (18).

$$u \frac{\partial \xi}{\partial r} + w \frac{\partial \xi}{\partial z} = \frac{1}{r} \frac{\partial}{\partial r} (K_\xi r \frac{\partial \xi}{\partial r}) + G_\xi \quad (18)$$

We consider the balance of  $\xi$  in the region as seen in Fig.3. The region "V" is a space lying between the axis and one stream line. It is evident that the transfer of  $\xi$  through the lines AD and BC is caused by convection and the transfer through CD is caused by turbulence. Now, taking the limit of the balance of  $\xi$  at  $\Delta z \rightarrow 0$ , we obtain the balance equation of  $\xi$  in the thin plate lying between the axis and the stream line for the stream function  $\psi^*$  at each height as follows.

$$\frac{d}{dz} \int_0^{r(\psi^*)} r w \xi dr = K_\xi \cdot r(\psi^*) \frac{\partial \xi}{\partial r} \Big|_{r=r(\psi^*)} + \int_0^{r(\psi^*)} G_\xi r dr \quad (19)$$

Then, the explicit equation to calculate  $K_\xi$  will be

$$K_\xi = \frac{\frac{d}{dz} \int_0^{r(\psi^*)} r w \xi dr - \int_0^{r(\psi^*)} G_\xi r dr}{r(\xi^*) \cdot \partial \xi / \partial r} \quad (20)$$

Applying (20) to the equations of momentum and energy for an axisymmetric plume, we obtain



$$K_w(r, z) = \frac{\frac{d}{dz} \int_0^{r(\psi^*)} r w^2 dr - \int_0^{r(\psi^*)} g \beta \theta r dr}{r(\psi^*) \cdot \partial w / \partial r} \quad (21)$$

$$K_\theta(r, z) = \frac{\frac{d}{dz} \int_0^{r(\psi^*)} w \theta r dr}{r(\psi^*) \cdot \partial \theta / \partial r} \quad (22)$$

where  $r(\psi^*)$  in (20), (21) and (22) means that  $r$  should be replaced with  $\psi$  after  $rw^2$  and  $rw\theta$  are integrated on  $r$ .

### 3-2. Quantification of the Eddy Coefficient in the Intermittent Flaming Region

To estimate the distribution of the eddy coefficient by the approach above described, it is necessary to assume the distribution of  $w$ ,  $\xi$  and  $G_\xi$  from the experimental data. Considering the dimensional relationships discussed in the previous chapter, (7) can be modified as

$$w = A \cdot Q^{1/5} \exp(-\zeta_w r^2 / Q^{2/5} z) \quad (23)$$

$$\theta = B(z / Q^{2/5})^{-1} \exp(-\zeta_\theta r^2 / Q^{2/5} z) \quad (24)$$

The stream function is then given by

$$\psi = \int_0^r r w dr = \int_0^r A \cdot Q^{1/5} \exp(-\zeta_w r^2 / Q^{2/5} z) r dr = \frac{Q^{3/5} A z}{2 \zeta_w} \{1 - \exp(-\zeta_w r^2 / Q^{2/5} z)\} \quad (25)$$

#### (1) Eddy Viscosity, $K_w$

Eddy viscosity in the intermittent flaming region can be quantified by substituting (23) and (24) to (21). The first term in the numerator of (21) can be quantified as follows.

$$\int_0^r r w^2 dr = \int_0^r A^2 Q^{2/5} \exp(-2\zeta_w r^2 / Q^{2/5} z) r dr = \frac{A^2 Q^{4/5} z}{4 \zeta_w} \{1 - \exp(-2\zeta_w r^2 / Q^{2/5} z)\} \quad (26)$$

Replacing  $r$  with  $\xi$  using (25),

$$\int_0^r r w^2 dr = \frac{A^2 Q^{4/5} z}{4 \zeta_w} \left\{1 - \left(1 - \frac{2 \zeta_w \psi}{A Q^{3/5} z}\right)^2\right\} = A \cdot Q^{1/5} \psi \left(1 - \frac{2 \zeta_w \psi}{A Q^{3/5} z}\right) \quad (27)$$

Then, differentiating (27) by  $z$ ,

$$\frac{d}{dz} \int_0^{r(\psi)} r w^2 dr = \frac{\zeta_w \psi^2}{Q^{2/5} z^2} \quad (28)$$

The other terms in (21) will be quantified by using (23) and (24) as

$$\int_0^r g \beta \theta r dr = \int_0^r g \beta B(z / Q^{2/5})^{-1} \exp(-\zeta_\theta r^2 / Q^{2/5} z) r dr = \frac{g \beta B Q^{4/5}}{2 \zeta_\theta} \{1 - \exp(-\zeta_\theta r^2 / Q^{2/5} z)\} \quad (29)$$

$$r \cdot \partial w / \partial r = \frac{-2A\zeta_w r^2}{Q^{1/5} z} \cdot \exp(-\zeta_w r^2 / Q^{2/5} z) \quad (30)$$

The eddy viscosity is then

$$K_w = \frac{g\beta B Q^{4/5} \{1 - \exp(-\zeta_\theta r^2 / Q^{2/5} z)\} / 2\zeta_\theta - \zeta_w \psi^2 / Q^{2/5} z^2}{2A\zeta_w r^2 \exp(-\zeta_w r^2 / Q^{2/5} z) / Q^{1/5} z} \quad (31)$$

(2) Eddy Diffusivity of Temperature,  $K_\theta$

In the common way as the derivation of the eddy viscosity, the eddy coefficient for the energy conservation equation is quantified by substituting (23) and (24) to (22). The first term in the numerator of (22) is transformed as follows.

$$\begin{aligned} \int_0^r r w \theta dr &= \int_0^r \frac{A \cdot B \cdot Q^{3/5} r}{z} \cdot \exp\{-(\zeta_w + \zeta_\theta) r^2 / Q^{2/5} z\} dr = \frac{A \cdot B \cdot Q^{3/5}}{2(\zeta_w + \zeta_\theta)} [1 - \exp\{-(\zeta_w + \zeta_\theta) r^2 / Q^{2/5} z\}] \\ &= \frac{A \cdot B \cdot Q^{3/5}}{2(\zeta_w + \zeta_\theta)} \left\{ 1 - \left( 1 - \frac{2\zeta_w \psi}{A Q^{3/5} z} \right)^{(\zeta_w + \zeta_\theta) / \zeta_w} \right\} \end{aligned} \quad (32)$$

$$\frac{d}{dz} \int_0^r r(\psi) w \theta dr = - \frac{B \cdot Q^{2/5} \psi}{z^2} \exp(-\zeta_\theta r^2 / Q^{2/5} z) \quad (33)$$

The denominator is quantified as

$$r \cdot \partial \theta / \partial r = -2B\zeta_\theta r^2 \cdot \exp(-\zeta_\theta r^2 / Q^{2/5} z) / Q^{1/5} z^2 \quad (34)$$

Then substituting (33) and (34) to (22), we obtain

$$K_\theta = \frac{Q^{2/5} \psi}{2\zeta_\theta r^2} = \frac{Q \cdot A z}{4\zeta_w \zeta_\theta r^2} \{1 - \exp(-\zeta_w r^2 / Q^{2/5} z)\} \quad (35)$$

### 3-3. Dimensional Structure and Simplification of the Eddy Coefficient Formulae

The central problem in modeling the eddy coefficient is to clarify how it depends on the heat release rate at fire source and to find a formula describing its spatial distribution. To study this problem, we here separate the formulae of the eddy viscosity and the eddy coefficient for temperature, (31) and (35), into two parts; the one representing its dependence on the heat release rate and the other representing its spatial distribution. Normalizing  $r$  and  $z$  in (31) and (35) by  $Q^{2/5}$ , then we obtain

$$K_w = Q^{3/5} \cdot \frac{g\beta B \{1 - \exp(-\zeta_\theta r'^2 / z')\} / 2\zeta_\theta - A^2 \{1 - \exp(-\zeta_w r'^2 / z')\}^2 / 4\zeta_w}{2A\zeta_w r'^2 \exp(-\zeta_w r'^2 / z') / z'} \quad (36)$$

$$K_\theta = Q^{3/5} \cdot \frac{A \cdot z'}{4\zeta_w \zeta_\theta r'^2} \{1 - \exp(-\zeta_w r'^2 / z')\} \quad (37)$$



The above equations means that  $K_w$  and  $K_\theta$  are proportional to  $Q^{3/5}$ . The underlined part, representing the spatial distribution of  $K_w$  and  $K_\theta$ , may be too complicated. Recognizing here that the functions characterizing the horizontal distribution of  $w$  and  $\theta$  are no more than practical approximations, an approximation with a simpler expression is desirable for the more essential modeling of the eddy coefficients for solving the basic equations of an axisymmetric upward current. According to Fig.4, representing the calculated results of  $K_w/Q^{3/5}$  and  $K_\theta/Q^{3/5}$ ,  $K_\theta$  is almost uniform in the intermittent flaming region.  $K_w$  is not so uniform, but it is not so different from  $K_\theta$  in the same region. Thus, the eddy coefficient in the intermittent flaming region will be approximated again by

$$K_w \approx K_\theta \approx k \cdot Q^{3/5} \quad (38)$$

where  $k$  is about  $0.003 \sim 0.004 [m^2/s \cdot kW^{3/5}]$  in Terai-Nitta's data. The value of  $k \equiv K/Q^{3/5}$  will be quantified again in Chapter 5 by comparing the solution of the equations for the upward current, which will be derived with the condition (38), and the experimental data shown in Chapter 2.

#### 4. SOLUTION OF THE EQUATIONS FOR AXISYMMETRIC UPWARD CURRENT WITH THE UNIFORM EDDY COEFFICIENT HYPOTHESIS

This chapter derives a solution of the basic equations of the axisymmetric upward current with respect to the experimental relationships shown in Chapter 2 and 3. The principal problem here is to derive the formulae representing the horizontal distribution of  $w$  and  $\theta$ , because the dependence of the centerline properties on the height and heat release rate at fire source has been already clarified. The basic approach is to derive the ordinary differential equations of  $W(\eta)$  and  $\Theta(\eta)$ , where  $\eta \equiv r^2/xz$ , from the basic equations of the upward current and then to solve them.

First, we rewrite the momentum equation using stream function instead of  $u$  and  $w$ , and decrease the number of variables.

$$\frac{\partial \psi}{\partial r} \left( r \frac{\partial \psi}{\partial r} - r^2 \frac{\partial^2 \psi}{\partial r^2} \right) + r^2 \frac{\partial \psi}{\partial r} \cdot \frac{\partial^2 \psi}{\partial r \partial z} = K_w \left( r^3 \frac{\partial^3 \psi}{\partial r^3} + r \frac{\partial \psi}{\partial r} - r^2 \frac{\partial^2 \psi}{\partial r^2} \right) + g\beta\theta r^4 \quad (39)$$

As the centerline velocity in the intermittent flaming region is constant with height, the form of  $\psi$  becomes

$$\psi = \int_0^r r w dr = \int_0^\eta r a W(\eta) d\eta = a z \int_0^\eta x W(\eta) d\eta / 2 = a z \Phi(\eta), \quad \Phi(\eta) \equiv \int_0^\eta x W(\eta) d\eta / 2 \quad (40)$$

Using  $\Phi(\eta)$  above defined, (39) will become

$$a^2(\Phi + z \frac{\partial \Phi}{\partial z})(rz \frac{\partial \Phi}{\partial r} - r^2 z \frac{\partial^2 \Phi}{\partial r^2}) + a^2 z r^2 \frac{\partial \Phi}{\partial r} (\frac{\partial \Phi}{\partial r} + z \frac{\partial^2 \Phi}{\partial r \partial z}) = a K_w z (r^3 \frac{\partial^3 \Phi}{\partial r^3} + r \frac{\partial \Phi}{\partial r} - r^2 \frac{\partial^2 \Phi}{\partial r^2}) + r^4 g \beta \theta \quad (41)$$

Furthermore, applying the following transforms for obtaining the ordinary differential equations of  $\Phi(\eta)$ ,

$$\begin{aligned} \frac{\partial \Phi}{\partial r} &= \frac{d\Phi}{d\eta} \frac{\partial \eta}{\partial r} = \frac{2r}{xz} \frac{d\Phi}{d\eta} = \frac{2\eta}{r} \frac{d\Phi}{d\eta} \\ \frac{\partial^2 \Phi}{\partial r^2} &= \frac{d^2 \Phi}{d\eta^2} (\frac{\partial \eta}{\partial r})^2 + \frac{d\Phi}{d\eta} \frac{\partial^2 \eta}{\partial r^2} = \frac{2\eta}{r^2} (2\eta \frac{d^2 \Phi}{d\eta^2} + \eta \frac{d\Phi}{d\eta}) \\ \frac{\partial^3 \Phi}{\partial r^3} &= \frac{d^3 \Phi}{d\eta^3} (\frac{\partial \eta}{\partial r})^3 + 3 \frac{d^2 \Phi}{d\eta^2} \frac{\partial^2 \eta}{\partial r^2} \frac{\partial \eta}{\partial r} + \frac{d\Phi}{d\eta} \frac{\partial^3 \eta}{\partial r^3} = \frac{8\eta^3}{r^3} \frac{d^3 \Phi}{d\eta^3} + \frac{12\eta^2}{r^3} \frac{d^2 \Phi}{d\eta^2} \\ \frac{\partial \Phi}{\partial z} &= \frac{d\Phi}{d\eta} \frac{\partial \eta}{\partial z} = - \frac{r^2}{xz^2} \frac{d\Phi}{d\eta} = - \frac{\eta}{z} \frac{d\Phi}{d\eta} \\ \frac{\partial^2 \Phi}{\partial r \partial z} &= \frac{d^2 \Phi}{d\eta^2} \frac{\partial \eta}{\partial r} \frac{\partial \eta}{\partial z} + \frac{d\Phi}{d\eta} \frac{\partial^2 \eta}{\partial r \partial z} = - \frac{2\eta^2}{rz} \frac{d^2 \Phi}{d\eta^2} - \frac{2\eta}{rz} \frac{d\Phi}{d\eta} \end{aligned} \quad (42)$$

then, we have

$$4a^2 \eta^2 z \frac{d^2 \Phi}{d\eta^2} + 8a K_w \eta^2 z \frac{d}{d\eta} (\frac{d^2 \Phi}{d\eta^2}) + r^4 g \beta \theta = 0 \quad (43)$$

For solving (43), it is necessary to derive the ordinary differential equation of  $\theta(\eta)$ . The energy conservation equation is rewritten with stream function as

$$\frac{a}{r} (\eta \frac{d\Phi}{d\eta} - \Phi) \frac{\partial \theta}{\partial r} + \frac{2a\eta z}{r^2} \frac{d\Phi}{d\eta} \frac{\partial \theta}{\partial z} = \frac{K_\theta}{r} \frac{\partial}{\partial r} (r \frac{\partial \theta}{\partial r}) \quad (44)$$

Considering that the axial temperature is propotional to the inverse of  $z$ , we can derive the following ordinary differential equation of  $\theta(\eta)$  from (44).

$$a (\eta \frac{d\Phi}{d\eta} - \Phi) \frac{d\theta}{d\eta} - a \frac{d}{d\eta} (\eta \theta) \frac{d\Phi}{d\eta} = 2K_\theta \frac{d}{d\eta} (\eta \frac{d\theta}{d\eta}) \quad (45)$$

where is applied the following transforms.

$$\begin{aligned} \frac{\partial \theta}{\partial r} &= \frac{b}{z} \frac{d\theta}{d\eta} \frac{\partial \eta}{\partial r} = \frac{2b\eta}{rz} \frac{d\theta}{d\eta} \\ \frac{\partial \theta}{\partial z} &= - \frac{b}{z^2} \theta + \frac{b}{z} \frac{d\theta}{d\eta} \frac{\partial \eta}{\partial z} = - \frac{b}{z^2} (\theta + \eta \frac{d\theta}{d\eta}) = - \frac{b}{z^2} \frac{d}{d\eta} (\eta \theta) \\ \frac{\partial}{\partial r} (r \frac{\partial \theta}{\partial r}) &= \frac{4b\eta}{rz} (\frac{d\theta}{d\eta} + \eta \frac{d^2 \theta}{d\eta^2}) = \frac{4b\eta}{rz} \frac{d}{d\eta} (\eta \frac{d\theta}{d\eta}) \end{aligned} \quad (46)$$

(45) can be transformed further into

$$\frac{d}{d\eta} (2K_\theta \eta \frac{d\theta}{d\eta} + a\Phi\theta) = 0 \quad (47)$$

(47) means that the value in ( ) is constant at every height. Considering that  $d\theta/d\eta=0$  and  $\Phi=0$  at  $\eta=0$ , the integration of (47) on  $\eta$  gives



$$2K_{\theta}\eta d\theta/d\eta + a\phi\theta = 0 \quad (48)$$

Then, the relationship between  $\theta$  and  $\phi$  will be

$$\phi = - \frac{2K_{\theta}\eta}{a\theta} \frac{d\theta}{d\eta} \quad (49)$$

Substituting (49) into (43), then we obtain

$$K \frac{d}{d\eta} \left( \frac{\eta}{\theta} \frac{d^2\phi}{d\eta^2} \right) = - \frac{g\beta b r^4}{8a\eta^2 z^2} = - \frac{g\beta b x^2}{8a} \quad (50)$$

where  $K \equiv K_w \approx K_{\theta}$ . As the right hand side of (50) is constant, we find the another relationship between  $\theta$  and  $\phi$  as follows.

$$\theta = - \frac{8aK}{g\beta b x^2} \frac{d^2\phi}{d\eta^2} \quad (51)$$

Substituting it into (49), we can eliminate  $\theta$  from (49).

$$\eta \frac{d^3\phi}{d\eta^3} + \mu \phi \frac{d^2\phi}{d\eta^2} = 0, \quad \mu \equiv a/2K \quad (52)$$

Recognizing that the  $n$ -th derivative of  $f(x) \equiv \delta x/(x+\sigma)$  is given by

$$\frac{d^n f}{dx^n} = (-1)^{n+1} \frac{n! \delta \sigma}{(x+\sigma)^{n+1}} \quad (53)$$

we find the solution of (52) in the form of

$$\phi = \frac{3\eta}{\mu(\eta+\sigma)} \quad (54)$$

Then, the stream function is quantified by substituting this into (40) as follows.

$$\psi = az\phi = 2K \cdot \mu z \frac{3\eta}{\mu(\eta+\sigma)} = \frac{6Kz\eta}{\eta+\sigma} \quad (55)$$

$\theta(\eta)$  is also formulated explicitly by substituting (54) into (51) as

$$\theta = - \frac{8aK}{g\beta b x^2} \frac{d^2\phi}{d\eta^2} = - \frac{8aK}{g\beta b x^2} \left\{ - \frac{6\sigma}{\mu(\eta+\sigma)^3} \right\} = \frac{96\sigma K^2}{g\beta b x^2 (\eta+\sigma)^3} \quad (56)$$

From the above results,  $w$  and  $\theta$  are formulated as

$$\theta = \frac{b}{z} \Theta = \frac{96\sigma K^2}{g\beta x^2 (\eta+\sigma)^3 z} \quad (57)$$

$$w = \frac{1}{r} \frac{\partial \psi}{\partial r} = \frac{12\sigma K}{x(\eta+\sigma)^2} \quad (58)$$

In order to quantify the parameter  $x$ , we apply  $w$  and  $\theta$  above obtained to the conservation condition of the vertical energy flux.

$$\begin{aligned}
2\pi C_p \rho \int_0^\infty r w \theta dr &= 2\pi C_p \rho \int_0^\infty \frac{1152 \sigma^2 K^3 r}{g \beta x^3 (\eta + \sigma)^5 z} dr = \frac{1152 \sigma^2 \pi C_p \rho K^3}{g \beta x^2} \int_0^\infty \frac{d\eta}{(\eta + \sigma)^5} \\
&= \frac{288 \pi C_p \rho K^3}{g \beta \sigma^2 x^2} = Q
\end{aligned} \tag{59}$$

Then,

$$x = \frac{12}{\sigma} \sqrt{\frac{2\pi C_p \rho K^3}{g \beta Q}} \tag{60}$$

Substituting this into (57) and (58),

$$w = \frac{g \beta Q}{2\pi C_p \rho K} \frac{\sigma^2}{(\eta + \sigma)^2} \tag{61}$$

$$\theta = \frac{\sigma^3 Q}{3\pi C_p \rho K z (\eta + \sigma)^3} \tag{62}$$

Recognizing the conditions,  $\eta = r^2/xz$  and  $x \propto \sigma^{-1}$ , it is evident that  $w$  and  $\theta$  as calculated results of (61) and (62) are independent from the value of  $\sigma$ . Applying  $\sigma=1$  for the simplicity, then the main results will become

$$w = \frac{g \beta Q}{2\pi C_p \rho K z} \frac{1}{(\eta + 1)^2} \tag{63}$$

$$\theta = \frac{Q}{3\pi C_p \rho K z (\eta + 1)^3} \tag{64}$$

$$\psi = 6Kz\eta/(\eta + 1) \tag{65}$$

$$x = 12\sqrt{2\pi C_p \rho K^3/g\beta Q} \tag{66}$$

Further substituting  $K=k \cdot Q^{3/5}$ , we have the following equations, only one unknown parameter " $k$ " will be quantified in the following chapter.

$$w = \frac{g \beta}{2\pi C_p \rho k} \frac{Q^{1/5}}{(\eta + 1)^2} \tag{67}$$

$$\theta = \frac{Q^{2/5}}{3\pi C_p \rho k z (\eta + 1)^3} \tag{68}$$

$$\psi = 6kQ^{3/5}z \cdot \eta/(\eta + 1) \tag{69}$$

$$x = 12Q^{2/5}\sqrt{2\pi C_p \rho k^3/g\beta} \tag{70}$$

## 5. CORRELATION BETWEEN THE MODEL AND THE EXPERIMENTAL RELATIONSHIPS

Though it is evident that the model represented as (67)~(70) satisfies some qualitative features of the intermittent flaming region of the upward



current above diffusion flames, we have to study, at least, the following two aspects for the further verification of the model. One problem is to clarify how the model agrees with the quantitative features of the experimental upward current, and the other one is to quantify the model of the eddy coefficient. In this chapter, we compare the model formulated as (67)~(70) with the experimental results on some centerline and transverse characteristics, and then we estimate  $K/Q^{3/5}$  by several approaches.

### 5-1. Centerline and Transverse Characteristics

Here, we derive some centerline and transverse properties which do not involve the eddy coefficient from the model, and compare them with those estimated from the experimental data.

#### (1) Rate of the Width of Excess Temperature Profile and that of Velocity Profile

Defining the width of excess temperature profile or velocity profile by the radial distance  $r^*$  where  $\theta/\theta_a$  or  $w/w_a$  takes one certain value  $\epsilon$  ( $0 < \epsilon < 1$ ,  $\epsilon = 1/e$  in the analyses of Terai-Nitta, McCaffrey and Cox-Chitty), the curve giving the width becomes

$$r_w^* = \sqrt{x(\epsilon^{-1/2} - 1)z} \quad (71)$$

$$r_\theta^* = \sqrt{x(\epsilon^{-1/3} - 1)z} \quad (72)$$

The rate of  $r_\theta^*/r_w^*$  is then

$$r_\theta^*/r_w^* = \sqrt{(\epsilon^{-1/3} - 1)/(\epsilon^{-1/2} - 1)} \quad (73)$$

From (73), it is evident that this rate is not dependent on the heat release rate nor the eddy coefficient.  $r_\theta^*/r_w^*$  calculated for the various values of  $\epsilon$ , seen in Fig.5, demonstrates that it is almost constant for  $\epsilon < 0.2$  and  $r_\theta^*/r_w^*$  is about 0.78 for  $\epsilon = 1/e$ . This value agrees well with the experimental values shown in Tab.3.

#### (2) Transverse Velocity and Excess Temperature Distribution

The experiments show that the transverse velocity and excess temperature distribution can be approximated practically by Gaussian distribution. We here compare the functions characterizing the transverse distribution in the model (67)~(70) with Gaussian distribution.

According to (63) and (64), the transverse velocity and excess temperature distribution is given by

$$W(\eta) = 1/(\eta+1)^2 \quad (74)$$

$$\theta(\eta) = 1/(\eta+1)^3 \quad (75)$$

The comparison of (74),(75) with Gaussian distribution is shown in Fig.6. The rate of  $\sigma_w$  to  $\sigma_\theta$  which is correlated with  $r_\theta^*/r_w^*$  by  $\sigma_w/\sigma_\theta \approx (r_\theta^*/r_w^*)^2$  is about 9/16 in this figure. This expresses well the experimental rate of profile widths.

$$(3) w_a^2/g\beta\theta_a z$$

According to the model, one parameter characterizing the force of buoyancy,  $w_a^2/g\beta\theta_a z$  is 1.5. Comparing this with those listed in Tab.2, we find that this is a little larger than the results of Terai-Nitta, Cox-Chitty and the present experiments, but it is a little smaller than McCaffrey's data.

## 5-2. Determination of $K/Q^{3/5}$

As the dimensional structure of  $K$  for the intermittent flaming region has been determined as  $K=k \cdot Q^{3/5}$  in Chapter 3, the principal problem in formulating  $K$  is to determine the parameter  $k$ . Before discussing for formulating  $K$ , we have to note something on the difference between  $Q$  in the model and that in experimental data.

The energy flux appearing in the model (67)~(70) arises from the conservation condition of energy flux and means the energy flux dissipating by convection, whilst the energy generated by combustion of methanol or natural gas dissipates not only by convection but also by radiation and thermal transfer through the methanol pan or the burner wall. Considering this, the dimensional relationship on  $K$  above mentioned should become

$$K = k \cdot Q^{3/5} = k(Q_c/c)^{3/5} = k/c^{3/5} \cdot Q_c^{3/5} \quad (76)$$

where  $Q_b$  is the heat release rate by combustion and  $Q_c$  is the energy dissipated by convection. The parameter,  $c$ , is then defined as  $c \equiv Q_c/Q_b$ . Of course, this parameter depends on the type of fuel. Considering only the flow characteristics, it should be more essential to estimate  $k' = k/c^{3/5}$  than to estimate  $k$  itself. However, as it is difficult to measure  $Q_c$  and the other heat losses independently, the heat release rate estimated from the consumption rate of fuel has been conventionally used as the characteristic heat release rate or heat flux in many analyses of plume experiments. Also we estimate only  $k$  in this section.

The value of  $k$  can be estimated with the measured excess temperature and velocity by transforming the equations on the profile or centerline properties to the explicit form on  $k$  and then substituting the measured properties into it. To estimate  $k$  from the centerline velocity or excess temperature, for example, the explicit formula to get  $k$  is derived from (67) or (68) as follows.



$$k = \frac{g\beta Q^{2/5}}{2\pi C_p \rho w_a^2} = \frac{g\beta}{2\pi C_p \rho} \left( \frac{w_a}{Q^{1/5}} \right)^{-2} = \frac{g\beta}{2\pi C_p \rho A^2} \quad (77)$$

$$k = \frac{Q^{2/5}}{3\pi C_p \rho \theta_a z} = \frac{1}{3\pi C_p \rho} \left( \frac{\theta_a z}{Q^{1/5}} \right)^{-1} = \frac{1}{3\pi C_p \rho B} \quad (78)$$

The formulae to estimate  $k$  are also derived from the formulae of the width of the profile of velocity and excess temperature as follows.

$$k = \left\{ \frac{(r_w^*/Q^{2/5})^4 g\beta}{288\pi C_p \rho (e^{1/2}-1)^2 (z/Q^{2/5})^2} \right\}^{1/3} \quad (79)$$

$$k = \left\{ \frac{(r_\theta^*/Q^{2/5})^4 g\beta}{288\pi C_p \rho (e^{1/3}-1)^2 (z/Q^{2/5})^2} \right\}^{1/3} \quad (80)$$

The values of  $k=K/Q^{3/5}$  estimated by the above four methods from the data of Terai-Nitta, McCaffrey, Cox-Chitty and our experiments are summarized in Tab. 4. The table shows that the difference of  $k$  due to the estimation methods or fuel species is very small except for the case of Terai-Nitta. Taking  $k=0.0025$  for the simplicity, the model (67)~(70) can be rewritten as

$$w \approx \sqrt{\frac{g\beta}{0.005\pi C_p \rho}} \frac{Q^{1/5}}{(\eta+1)^2} \quad (81)$$

$$\theta \approx \frac{Q^{2/5}}{0.0075\pi C_p \rho z (\eta+1)^3} \quad (82)$$

$$\eta = r^2/xz, \quad x \approx 0.00212Q^{2/5}\sqrt{\pi C_p \rho/g\beta} \quad (83)$$

Fig.7 shows the correlation between the widths estimated from the model and those estimated from experiments. The agreement between the model and the experiments is good for  $r_\theta^*$ , whilst the experimental data of  $r_w^*$  are somewhat scattering around the theoretical curve. Fig.8 shows the comparison between the calculated isotherms and those generated from McCaffrey's experiments. The calculated isotherms are more swelled than those by the experiments in the high temperature region; the reason for this is thought as a result of the ignorance of the compressibility in the derivation of the model.

## 6. MASS FLUX, ENERGY FLUX AND ENTRAINMENT IN THE UPWARD CURRENT

The practical quantities other than the centerline properties are such integral quantities as mass and energy flux. In this chapter, the model (67)~(70) are employed to calculate them with respect to the compressibility of the flow. As the consideration of compressibility makes it impossible to cal-

culate some integral properties, we will prepare the calculation diagrams of the integral properties as a practical result of this report.

#### 6-1. Mass and Bulk Flux

The mass flux between the axis and the radial distance,  $r$ , at the height,  $z$ , is defined as

$$M(z, r) = 2\pi \int_0^r \rho_w r dr \quad (84)$$

Employing the model (67)~(70), and considering also the compressibility due to the rise of temperature,  $M(z, r)$  will be formulated as

$$M(z, r) = 2\pi \rho_0 \int_0^r \frac{wr}{1+\beta\theta} dr = 0.03\pi \rho_0 Q^{3/5} z \int_0^\eta \frac{d\eta}{\{1+133\beta Q^{2/5}/\pi C_p \rho_m z (\eta+1)^3\} (\eta+1)^2} \quad (85)$$

The right hand side of the above equation may not be obtained analytically. To derive a practical calculation method of  $M(z, r)$ , we divide the both sides of (85) by  $Q$ . Then,  $M(z, r)/Q$  is written as a function of the normalized height,  $z' = z/Q^{2/5}$  as follows.

$$\frac{M(z, r)}{Q} = 0.03\pi \rho_0 z' \int_0^\eta \frac{d\eta}{\{1+133\beta/\pi C_p \rho_m z' (\eta+1)^3\} (\eta+1)^2} \quad (86)$$

The bulk flux in the upward current is also defined and formulated as

$$\begin{aligned} F(z, r) &= 2\pi \int_0^r wr dr = \pi x z \int_0^r \frac{2rw}{xz} dr = 0.03\pi Q^{3/5} z \int_0^\eta \frac{d\eta}{(\eta+1)^2} \\ &= \frac{0.03\pi Q^{3/5} r^2 z}{r^2 + 0.00212 Q^{2/5} z \sqrt{\pi C_p \rho_m / g \beta}} \end{aligned} \quad (87)$$

Dividing the both sides of (87) again by  $Q$ , we obtain the relationship between  $F(z, r)/Q$  and  $z'$  and  $r'$ .

$$\frac{F(z, r)}{Q} = \frac{0.03\pi r'^2 z'}{r'^2 + 0.00212 z' \sqrt{\pi C_p \rho_m / g \beta}} \quad (88)$$

The entrainment coefficient,  $\alpha$ , which is conventionally defined as  $dF(z, \infty)/dz = 2\alpha F(z, \infty)/r_w^*$  (3), (10), is then quantified as

$$\alpha = \frac{r_w^* \cdot dF(z, \infty)/dz}{2F(z, \infty)} = 0.0185 \left( \frac{\pi C_p \rho_m}{g \beta z'^2} \right)^{1/4} \quad (89)$$

While the entrainment coefficient has been assumed as constant in the conventional analyses of turbulent plumes, (89) means that it decreases with height in the intermittent flaming region.



## 6-2. Energy Flux

The energy flux between the axis and the radial distance,  $r$ , is formulated as (90), if the compressibility due to temperature change is considered.

$$\begin{aligned} H(z, r) &= 2\pi C \int_0^r \rho w \theta r dr = 2\pi C_p \rho_0 \int_0^r \frac{w \theta r}{1 + \beta \theta} dr \\ &= \frac{4\rho_0 Q}{\rho_m} \int_0^\eta \frac{d\eta}{\{1 + 133\beta Q^{2/5} / \pi C_p \rho_m z' (\eta + 1)^3\} (\eta + 1)^5} \end{aligned} \quad (90)$$

Dividing the both sides by  $Q$ , we obtain

$$\frac{H(z, r)}{Q} = \frac{\rho_0}{\rho_m} \int_0^\eta \frac{d\eta}{\{1 + 133\beta / \pi C_p \rho_m z' (\eta + 1)^3\} (\eta + 1)^2} \quad (91)$$

## 6-3. Calculation Diagrams of Mass and Bulk Flux, Entrainment Coefficient and Energy Flux

As  $M(z, r)/Q$ ,  $F(z, r)/Q$ ,  $\alpha$  and  $H(z, r)/Q$  are decisively determined for one set of the physical properties of air, we can here prepare the diagrams for the practical calculation of these properties. Recognizing that  $r = r_w^*$  and  $r \rightarrow \infty$  are usually taken as the characteristic radial distance of axisymmetric upward current, we show the diagrams of  $M(z, r_w^*)/Q$ ,  $M(z, \infty)/Q$ ,  $F(z, r_w^*)/Q$ ,  $F(z, \infty)/Q$ ,  $H(z, r_w^*)/Q$ ,  $H(z, \infty)/Q$  and  $\alpha$ .

As it seems impossible to calculate  $M/Q$  and  $H/Q$  by an analytical approach, we have to apply a numerical approach to get them. For the practical calculation with reasonable precision, we divide the integration interval into two parts; the one is the part where excess temperature is considerably high and the other is the one where excess temperature is not so high that the following approximation is reasonably assumed.

$$\rho = \rho_0 / (1 + \beta \theta) \approx \rho_0 (1 - \beta \theta) \quad (92)$$

Then, we can obtain  $M/Q$  and  $H/Q$  by integrating the first part numerically and integrating the latter part analytically.  $M(z, \infty)/Q$ , for example, can be calculated as follows.

$$\begin{aligned} \frac{M(z, \infty)}{Q} &= 0.03\pi\rho_0 z' \left[ \int_0^{\eta_\alpha} \frac{d\eta}{\{1 + 133\beta / \pi C_p \rho_m z' (\eta + 1)^3\} (\eta + 1)^2} \right. \\ &\quad \left. + \int_{\eta_\alpha}^\infty \frac{d\eta}{\{1 + 133\beta / \pi C_p \rho_m z' (\eta + 1)^3\} (\eta + 1)^2} \right] \\ &\approx 0.03\pi\rho_0 z' \left[ \int_0^{\eta_\alpha} \frac{d\eta}{\{1 + 133\beta / \pi C_p \rho_m z' (\eta + 1)^3\} (\eta + 1)^2} + \int_{\eta_\alpha}^\infty \left\{ 1 - \frac{133\beta}{\pi C_p \rho_m z' (\eta + 1)^3} \right\} \frac{d\eta}{(\eta + 1)^2} \right] \\ &= 0.03\pi\rho_0 z' \left[ \int_0^{\eta_\alpha} \frac{d\eta}{\{1 + 133\beta / \pi C_p \rho_m z' (\eta + 1)^3\} (\eta + 1)^2} + \frac{1}{\eta_\alpha + 1} - \frac{133\beta}{4\pi C_p \rho_m z' (\eta_\alpha + 1)} \right] \end{aligned} \quad (93)$$

The part where we employ the numerical calculation is underlined in (93). The integral properties calculated with the assumption,  $\rho_m = \rho_0 / (1 + \beta_m \theta_m)$  and  $\rho_m \theta_m = Q / C_p F(z, \infty)$  are shown in Fig.9 Fig.11.  $M/Q$  is almost proportional to  $z/Q^{2/5}$  and it is practically estimated by the following simple equation.

$$M(z, \infty)/Q \approx 1.17(z/Q^{2/5}) - 0.022 \quad (94)$$

The agreement between the estimated entrainment coefficient and Terai-Nitta's data is not good, but our result coincides well with the estimate of McCaffrey.

## 7. CONCLUSIONS

The behavior of the intermittent flaming region of the upward current above diffusion flames can be predicted practically by the model represented by (67)~(70), which is based on one solution of the equations of axisymmetric buoyant flow. Practical integral properties, such as mass and energy flux or entrainment coefficient can be also obtained diagrammatically from Fig.9 ~ Fig.11. Though it is an interesting problem why the eddy coefficient in this region depends on  $Q^{3/5}$ , it is not necessary to investigate further into the structure of the turbulence in this region as far as we are concerned in the engineering deterministic properties. The results of this report hold for methanol pool fire and diffusion flame above natural gas burner, but it may not be applicable to the fuels which are much different in the shape or height of the flame generating from them.

## ACKNOWLEDGEMENTS

The author wish to thank Prof.T. Sekine for his helpful suggestions on the derivation of the solution of the equations of upward current, and the students of the Science University of Tokyo for their assistance in the experiments. The author is also indepted to Dr.B.J. McCaffrey at National Bureau of Standards, USA, and Dr.G. Cox at Fire Research Station, UK, for providing useful informations.



## TERMINOLOGY

$C_p$	:specific heat[kW s/kgK]
$F$	:bulk flux in upward current[m <sup>3</sup> /s]
$H$	:heat flux in upward current[kW]
$K$	:eddy coefficient[m <sup>2</sup> /s]
$L$	:flame height[m]
$M$	:mass flux in upward current[kg/s]
$Q$	:heat release rate at fire source[kW]
$W(\eta)$	:characterizing function of the transverse distribution of vertical velocity[-]
$d$	:diameter of methanol fire source[m]
$g$	:acceleration of gravity[m/s <sup>2</sup> ]
$r$	:radial coordinate[m]
$r'$	:radial coordinate normalized with $Q^{2/5}$ [m/kW <sup>2/5</sup> ]
$r^*$	:width of upward current[m]
$u$	:radial velocity[m/s]
$u'$	:turbulent fluctuation of radial velocity[m/s]
$w$	:vertical velocity[m/s]
$w'$	:turbulent fluctuation of vertical velocity[m/s]
$x$	:characteristic scale length of plume width[m]
$z$	:vertical coordinate[m]
$z'$	:vertical coordinate normalized with $Q^{2/5}$ [m/kW <sup>2/5</sup> ]
$\Theta(\eta)$	:characterizing function of the transverse distribution of excess temperature[-]
$\Phi(\eta)$	:characterizing function of the transverse distribution of stream function[-]
$\alpha$	:entrainment coefficient[-]
$\beta$	:expansion coefficient[K <sup>-1</sup> ]
$\rho$	:densidy[kg/m <sup>3</sup> ]
$\eta$	:nondimensional parameter on the horizontal distribution of physical properties
$\theta$	:excess temperature

### subscripts

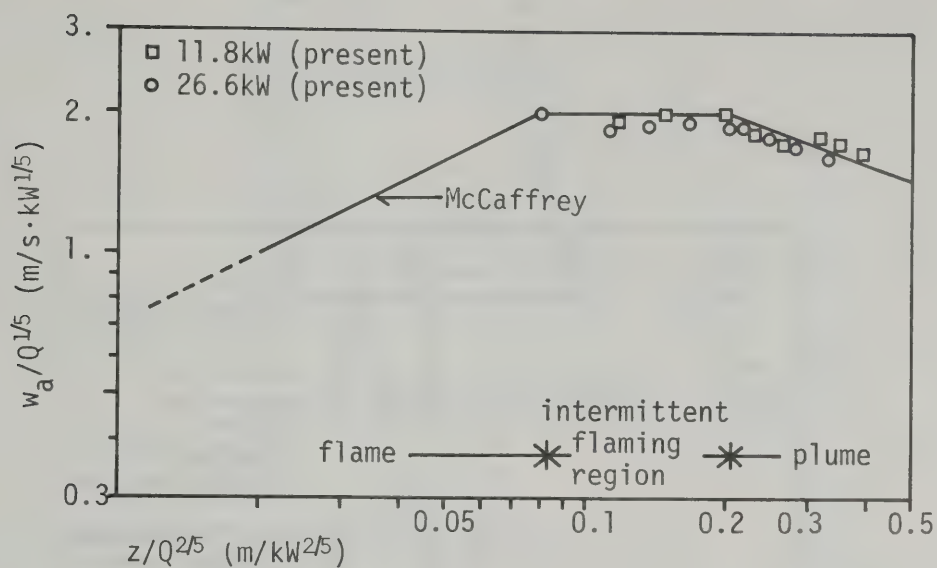
$a$	:axis
$m, \bar{m}$	:mean
$w$	:vertical velocity
$\theta$	:excess temperature

## REFERENCES

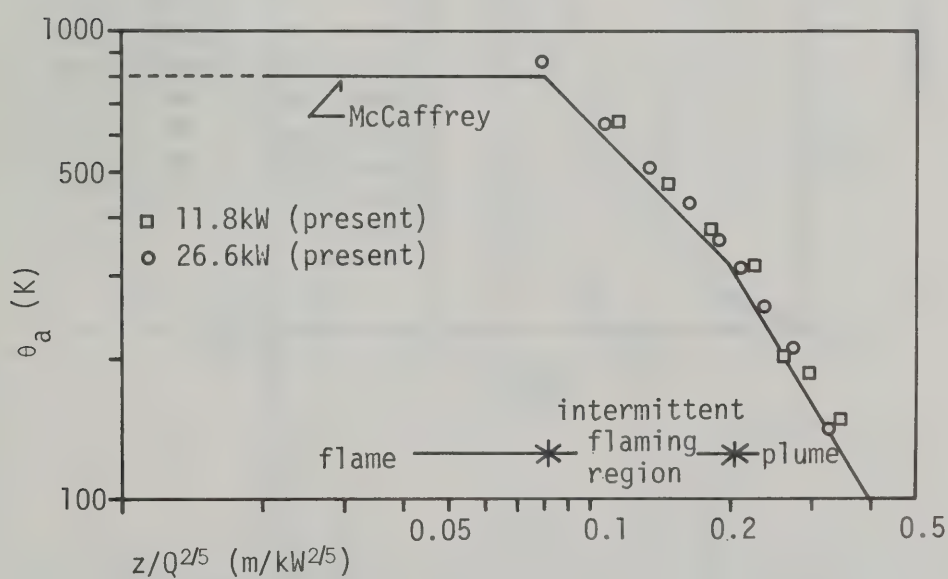
- 1) Yokoi, S., Report of B.R.I., No.34, 1960.
- 2) Rouse, H., Yih, C.S. and Humphreys, Tellus, 4, 201, 1952.
- 3)\* Terai, T. and Nitta, K., Annual Meeting of A.I.J., Nagoya, 1976.
- 4)\* Terai, T. and Nitta, K., Annual Meeting of A.I.J., Sapporo, 1978.
- 5) McCaffrey, B.J., NBSIR-79-1910, 1979.
- 6) Cox, G. and Chitty, R., Combustion and Flame, 39:191-209, 1980.
- 7)<sup>#</sup> Hasemi, Y., Bulletin of J.A.F.S.E., Vol.29, No.1, 1979.
- 8)<sup>#</sup> Hasemi, Y., Bulletin of J.A.F.S.E., Vol.31, No.2, 1981.
- 9) George, W.K., Alpert, R.L. and Tamanini, F., Int. J. Heat Mass Transfer, 20, 1145-1154, 1977.
- 10) Turner, J.S., "Buoyancy Effects in Fluids", Cambridge Univ. Press, 1973.
- 11) McCaffrey, B.J. and Heskestad, G., Combustion and Flame, 26:125-127, 1976.

—— The references with symbol \* are written in Japanese. Those with symbol <sup>#</sup> are written in Japanese with English abstract. The other references are written in English.





(a) Vertical Velocity along Centerline



(b) Excess Temperature along Centerline

Fig.1 Centerline Properties in Upward Current above Diffusion Flames

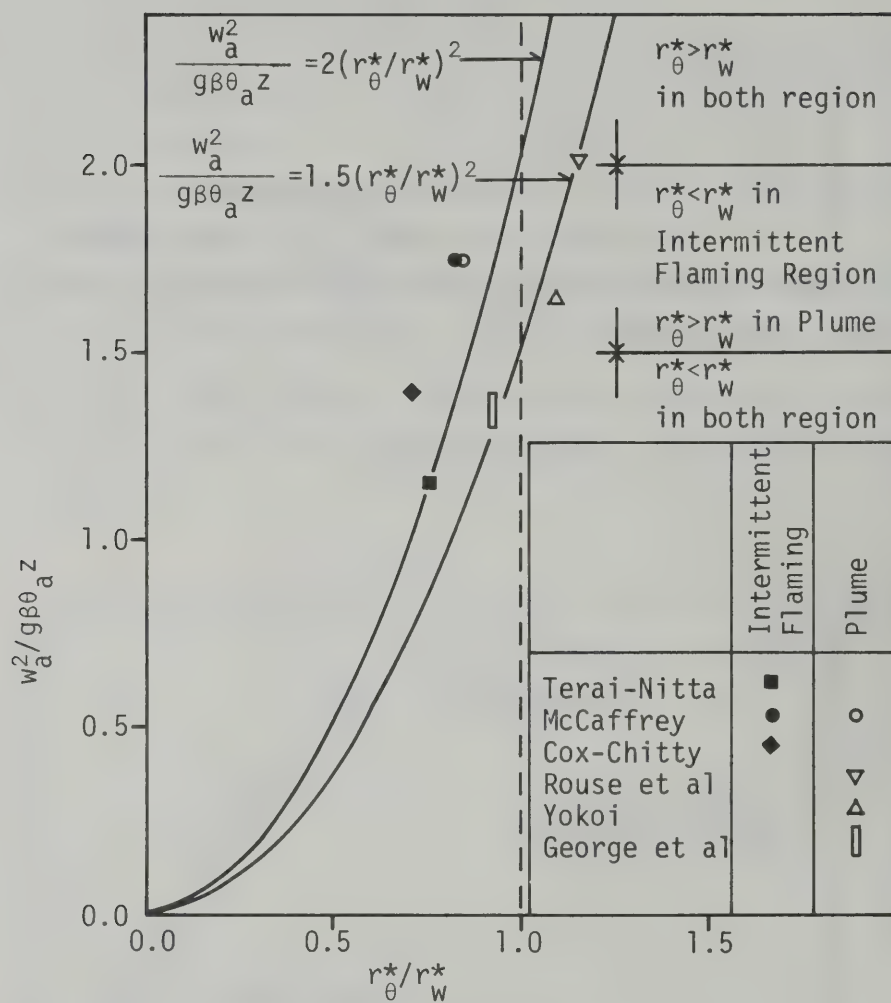


Fig.2 Relationship between Axial Properties and Plume-width Ratio in Upper Regions of Upward Current



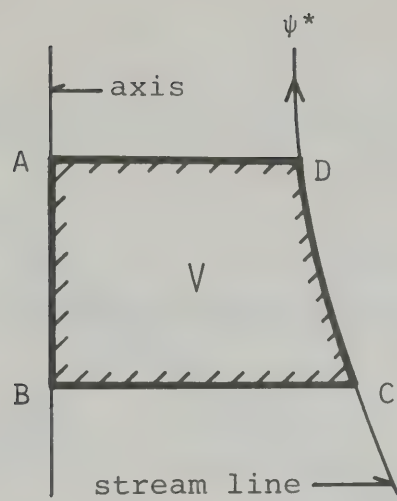


Fig.3 Schematic View of Region V

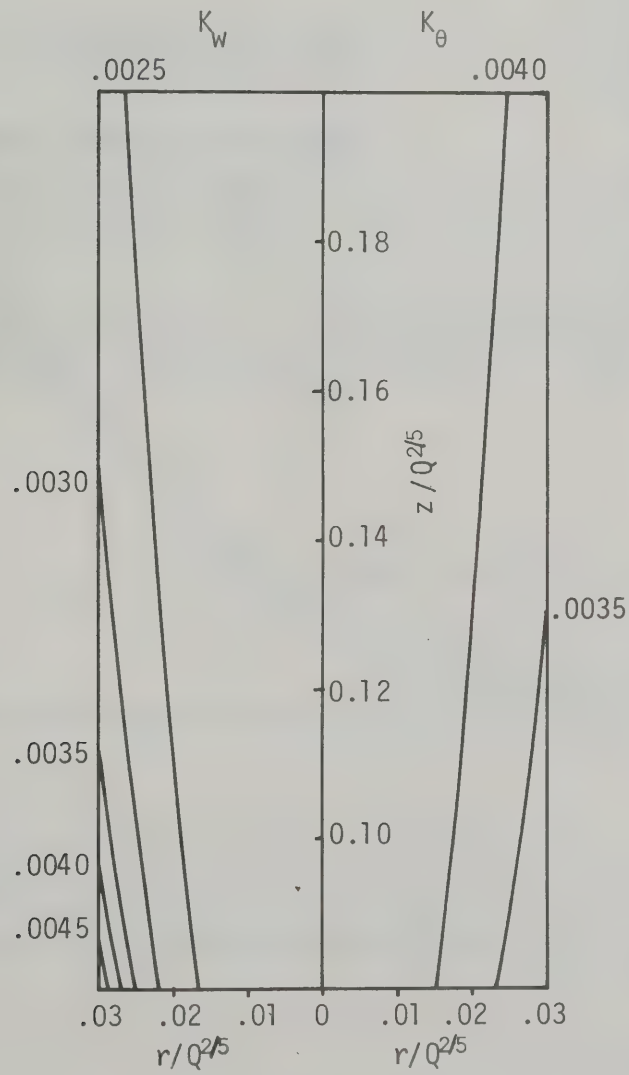


Fig.4 Estimated Distribution of  $K_{\theta}/Q^{3/5}$  and  $K_w/Q^{3/5}$  from Terai-Nitta's Experiment

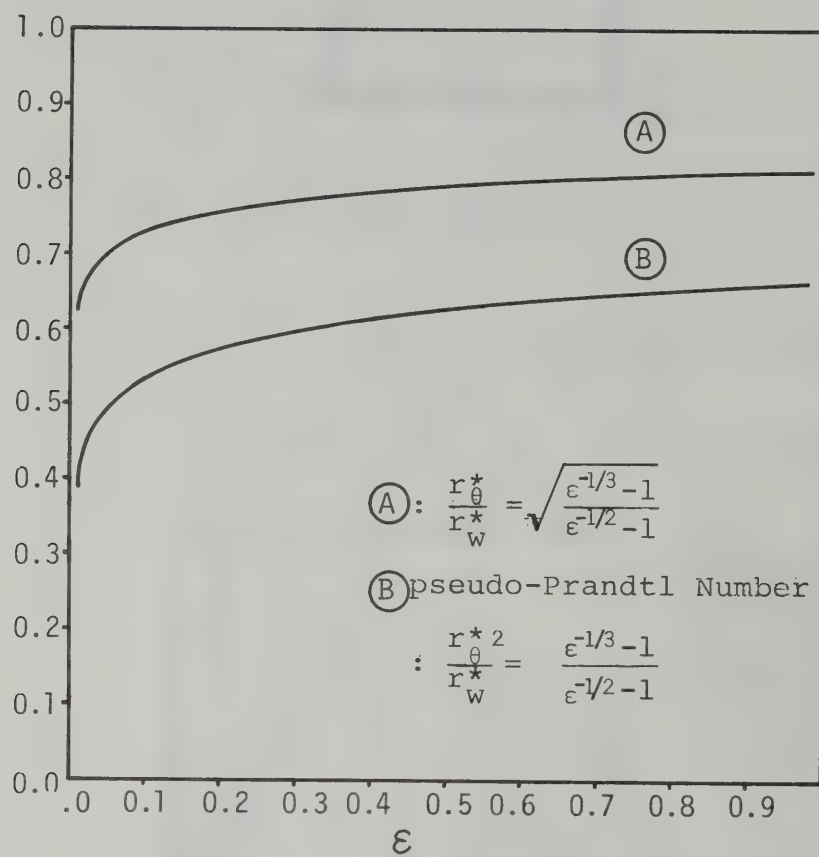
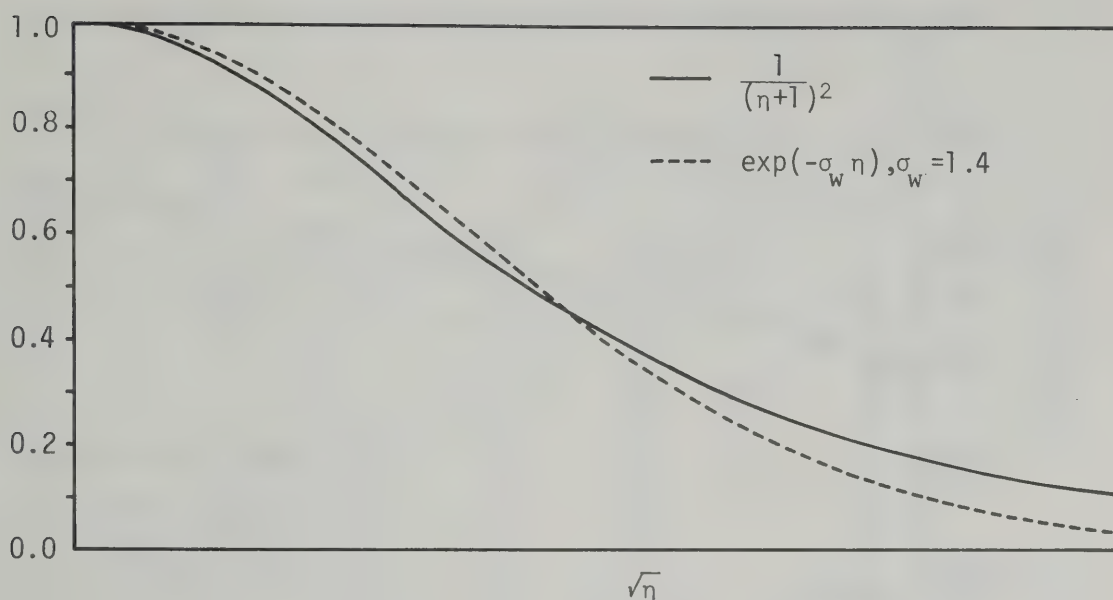
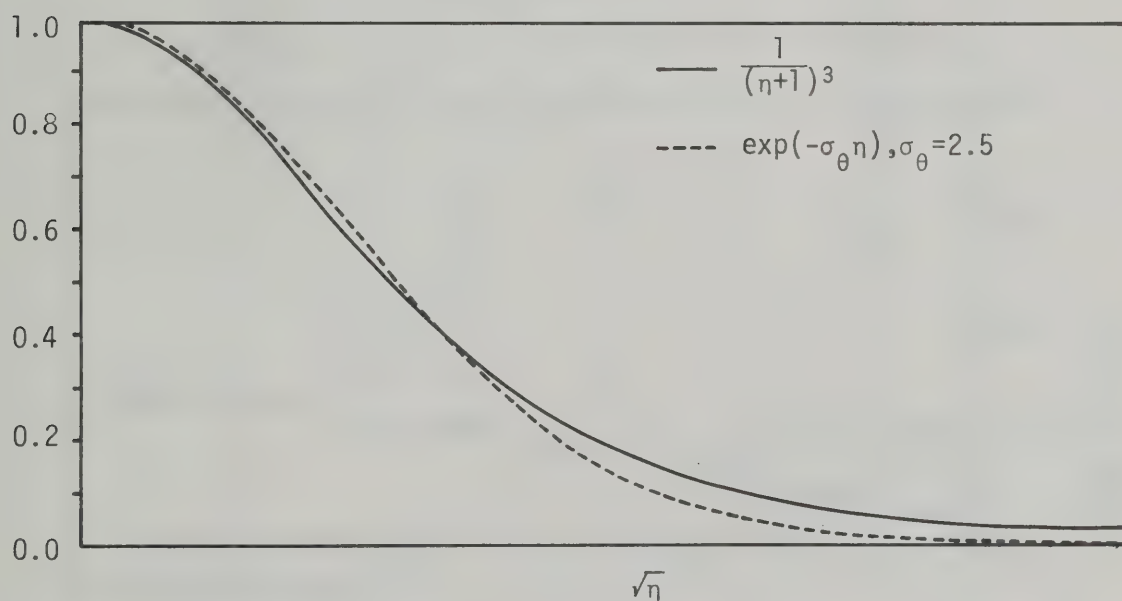


Fig.5  $r_{\theta}^*/r_w^*$  as a Function of  $\epsilon$



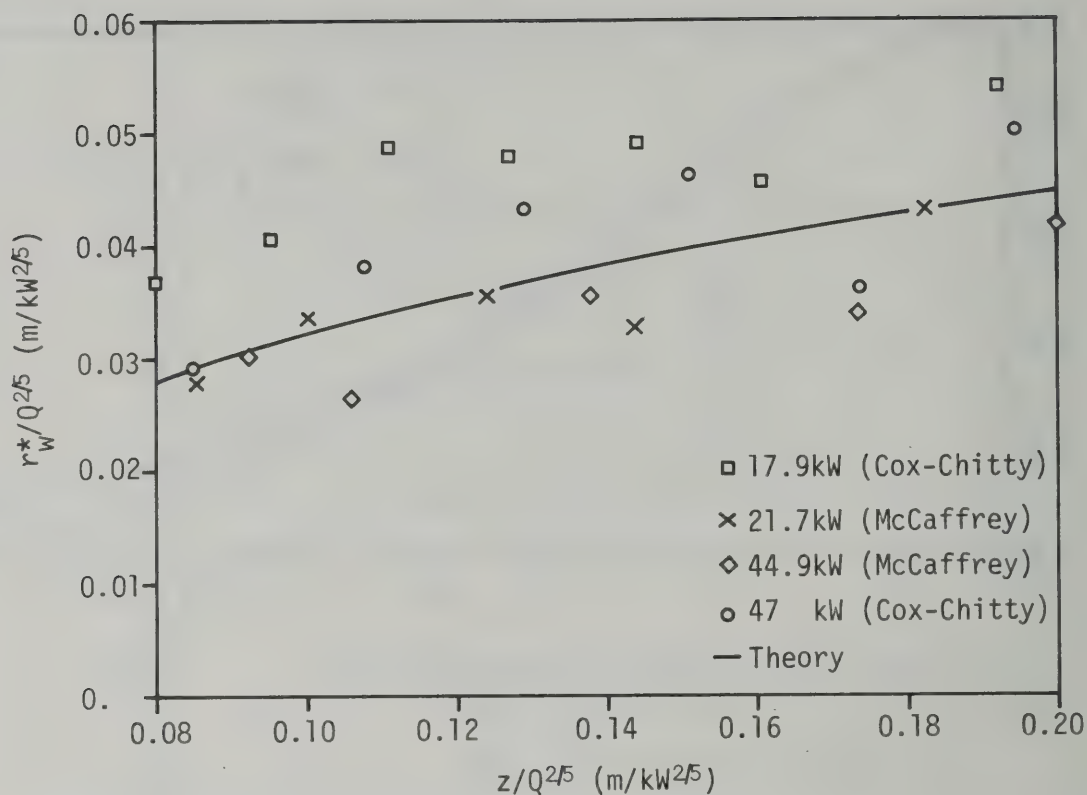


(a) Comparison of  $W(\eta) = (\eta+1)^{-2}$  with  $\exp(-1.4\eta)$

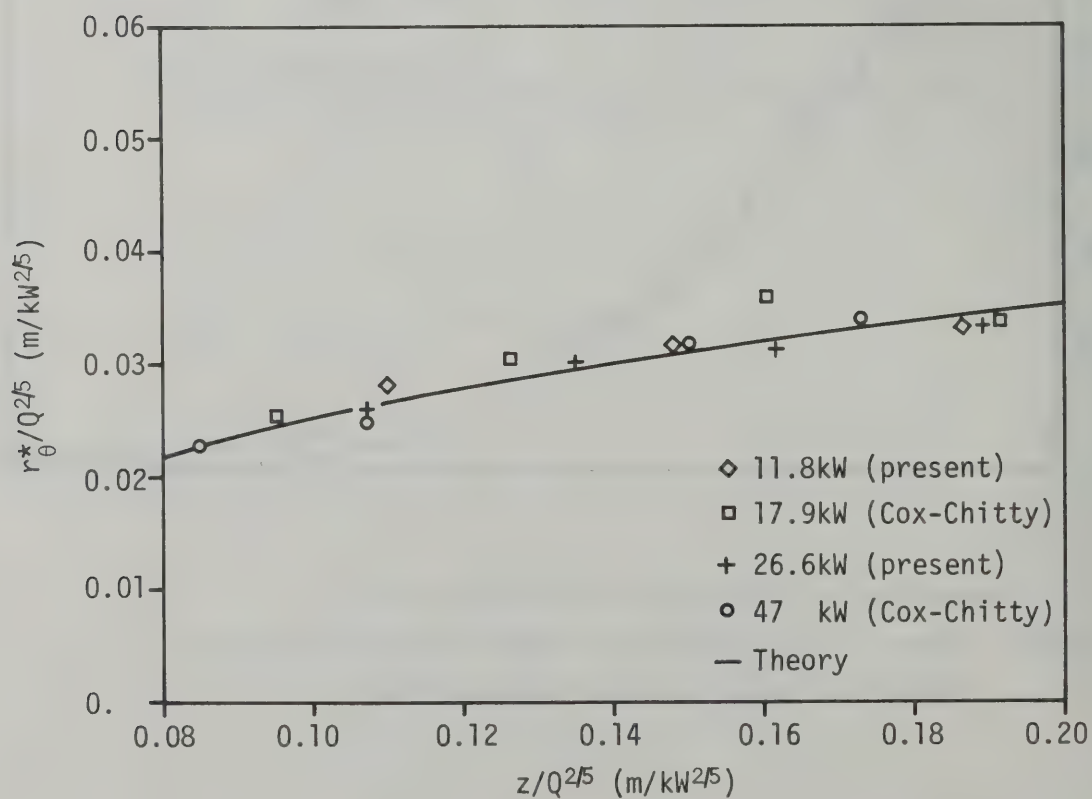


(b) Comparison of  $\Theta(\eta) = (\eta+1)^{-3}$  with  $\exp(-2.5\eta)$

Fig.6 Comparison of Analytical Transverse Distribution of Properties with Gaussian Distribution



(a) Width for Velocity Profile



(b) Width for Excess Temperature Profile

Fig.7 Comparison of Theoretical and Experimental Plume Width



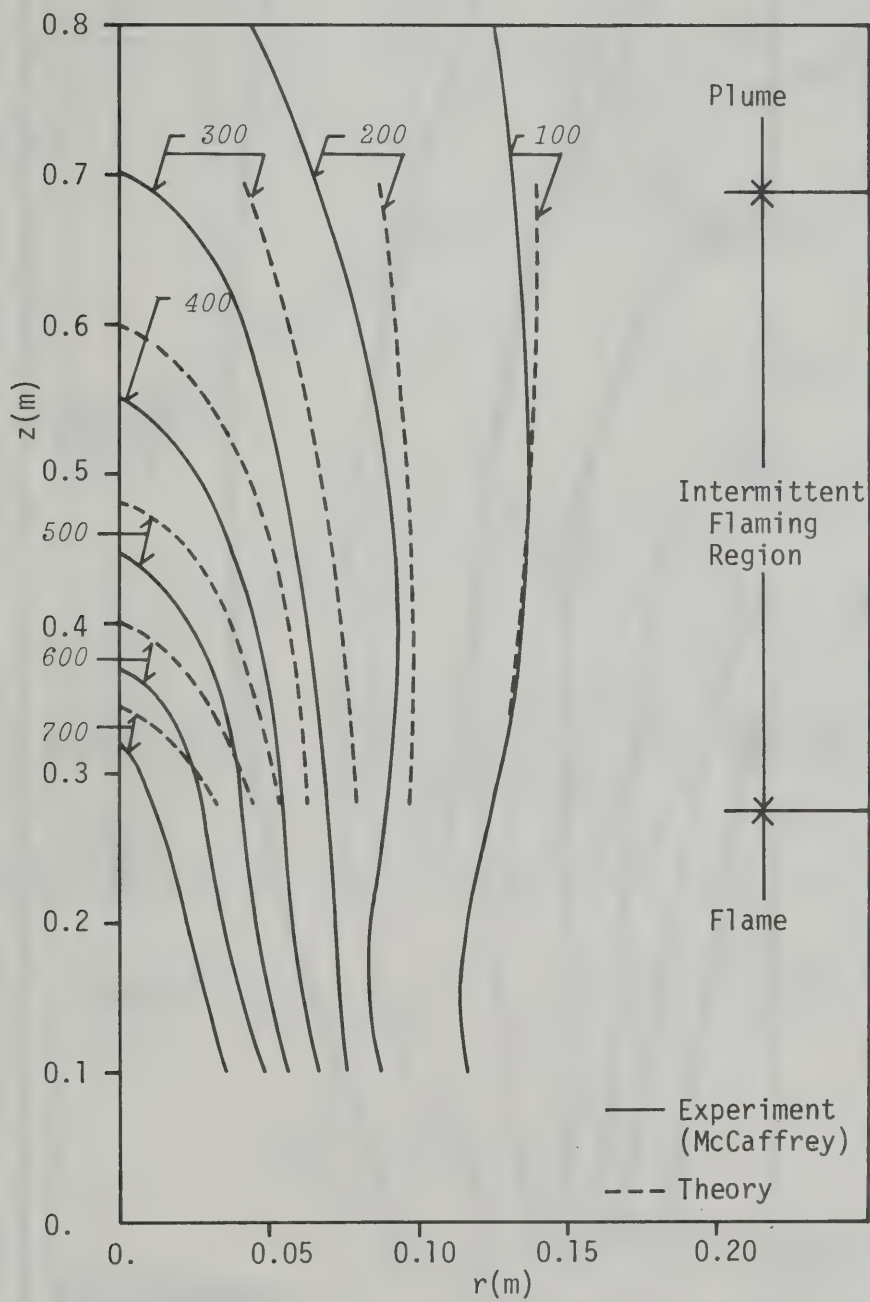


Fig.8(a) Theoretical and Experimental Isotherms( $Q=21.7\text{kW}$ )

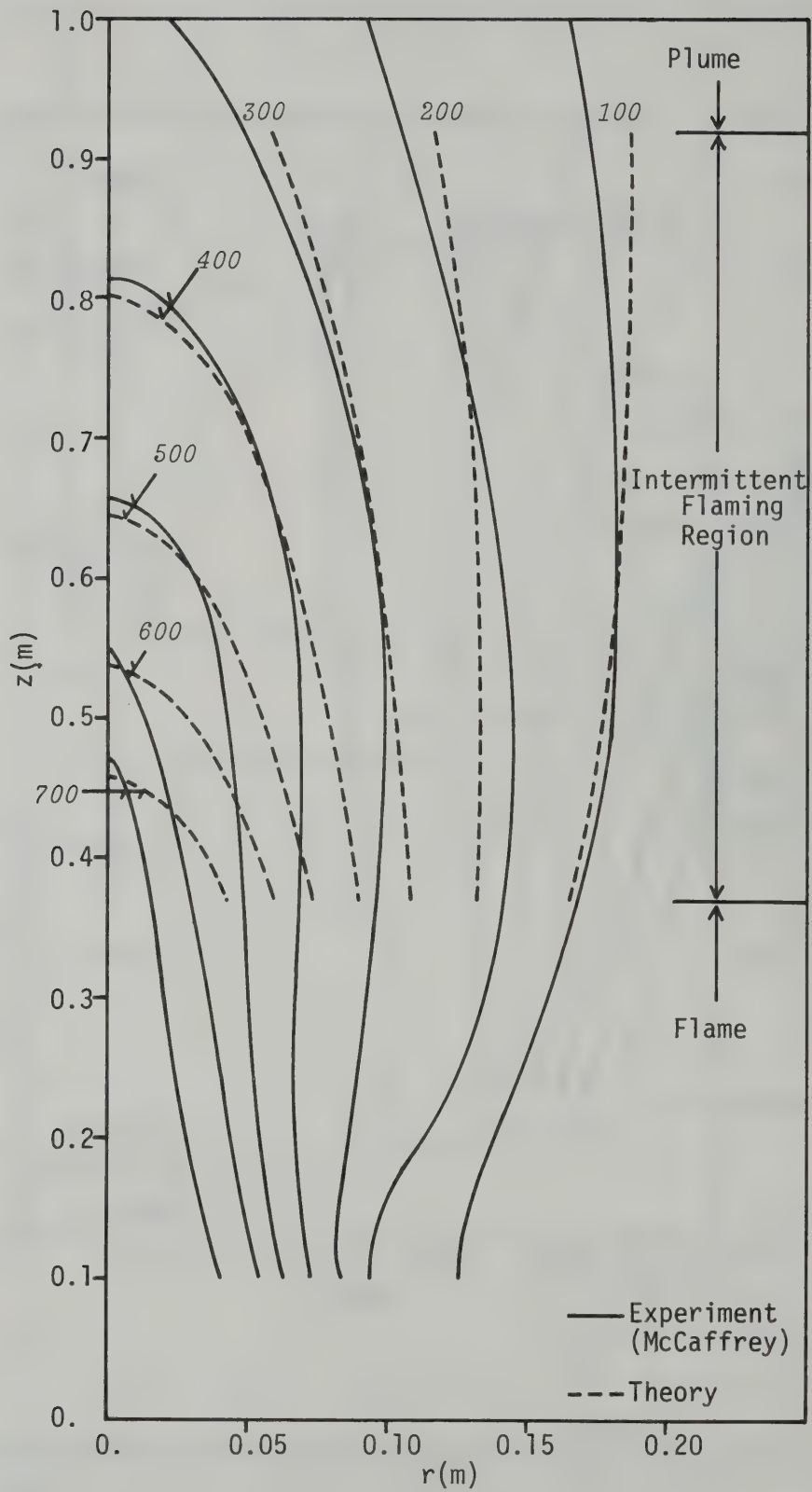


Fig.8(b) Theoretical and Experimental Isotherms ( $Q=44.9\text{kW}$ )

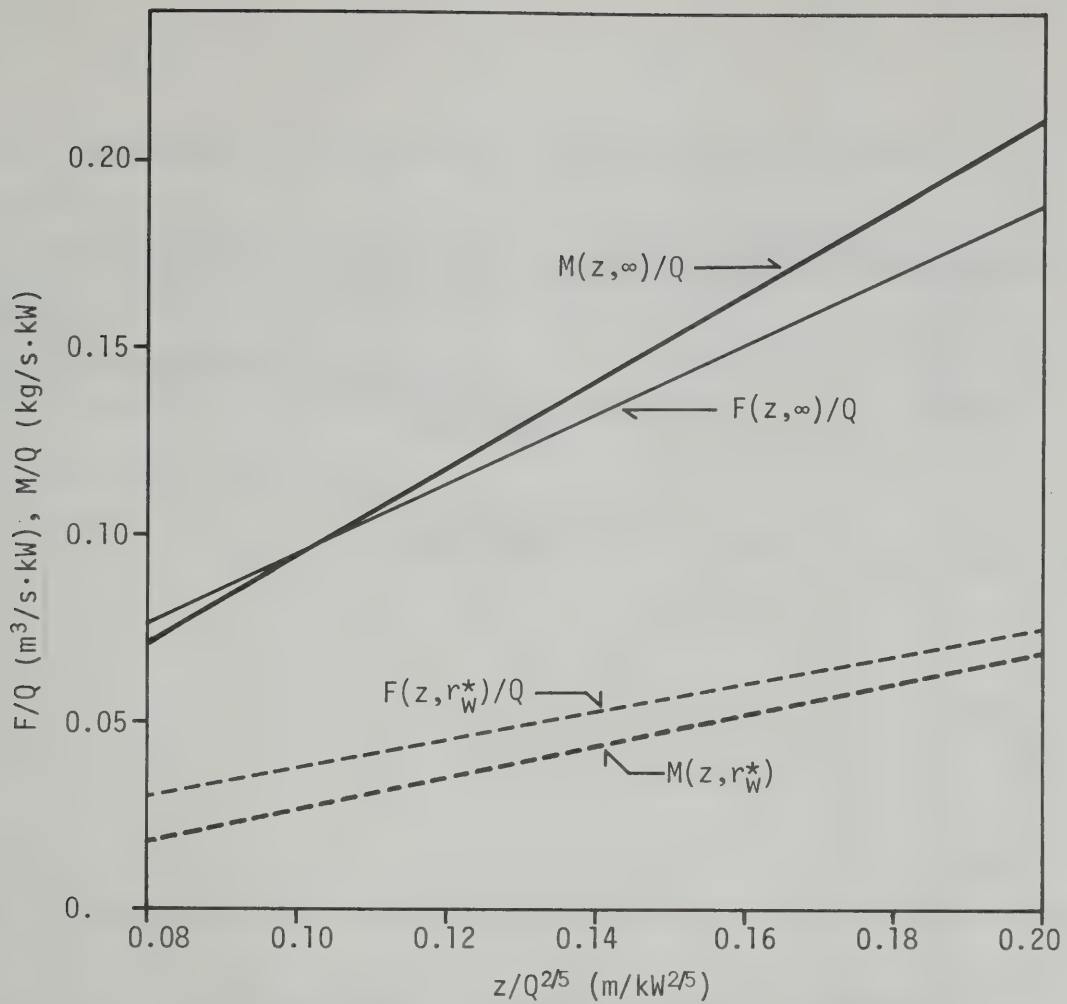


Fig.9 Normalized Mass and Bulk Flux vs Normalized Height from Fire Source

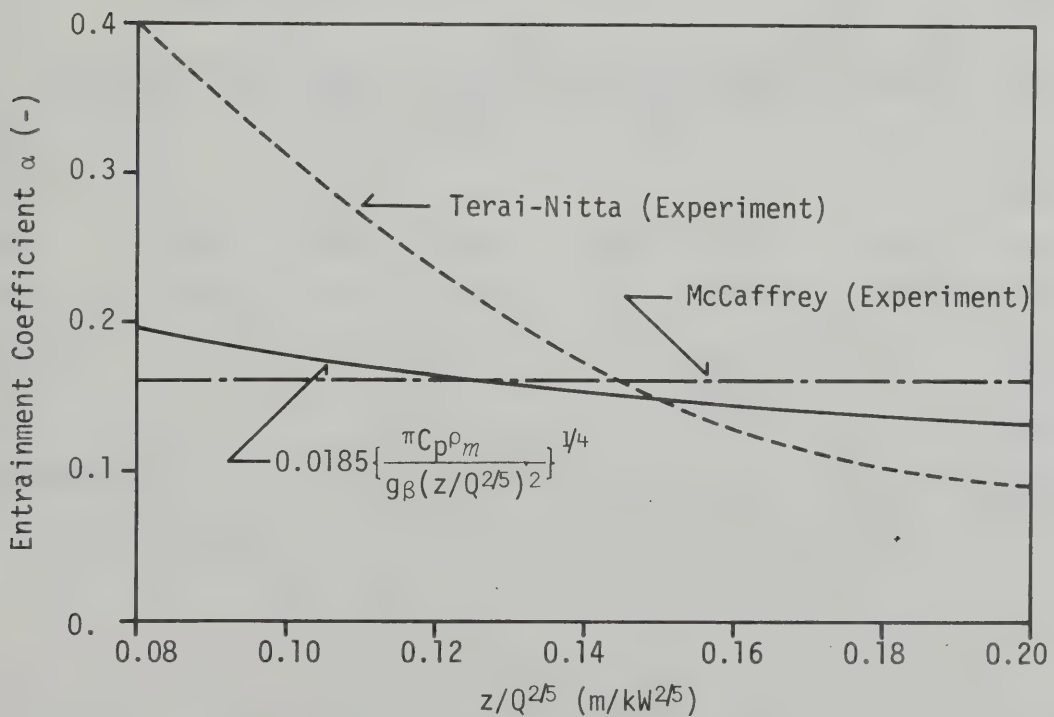


Fig.10 Entrainment Coefficient vs Normalized Height from Fire Source



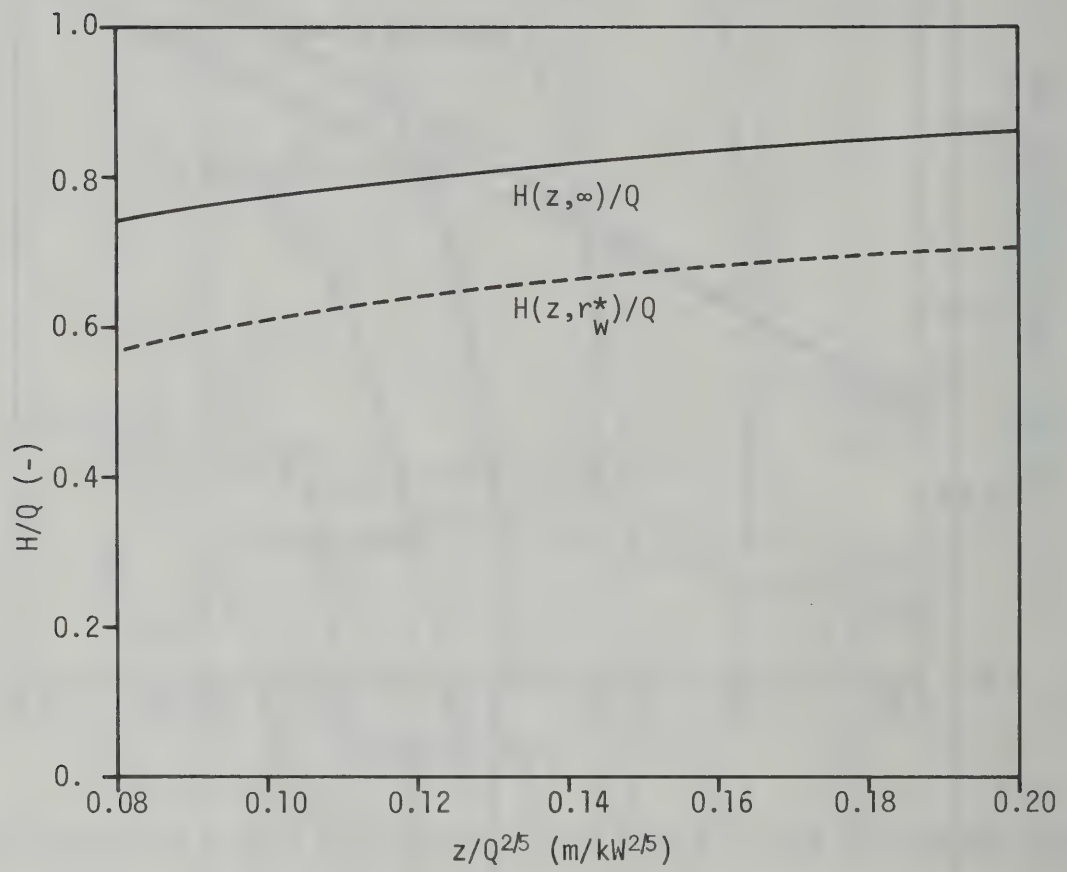


Fig.11 Normalized Heat Flux vs Normalized Height from Fire Source

Table.1 Experiments on the Upward Current above Diffusion Flames

	Heat Source, Intensity	Measurement	
		velocity	excess temperature
Present	pool fire of methanol, 11.8kW & 26.6kW	Bidirectional <sup>11)</sup>	C-A thermocouple
Terai-Nitta <sup>3),4)</sup>	pool fire of methanol	Correlation Method	C-A thermocouple
McCaffrey <sup>5)</sup>	natural gas, 21.7kW & 44.9kW	Bidirectional <sup>11)</sup>	C-A thermocouple
Cox-Chitty <sup>6)</sup>	natural gas, 17.9kW & 47kW	Correlation Method	thermocouple

Table.2 Summary of Axial Characteristics of Three Regions in Upward Current

	$w_a/Q^{1/5}=A \cdot z'^n, \quad \theta_a=B \cdot z'^{2n-1}, \quad z'=z/Q^{2/5}$						$\frac{w_a^2}{2g\theta_a z}$
	Flame		Intermittent Flaming		Plume		
	$0.03 < z' < 0.08$ $n = 1/2$		$0.08 < z' < 0.20$ $n = 0$		$0.20 < z'$ $n = -1/3$		
	A	B	A	B	A	B	
Present	-	-	1.90	70	-	-	0.72
Terai-Nitta	-	700~800	1.5	56	-	-	0.56
McCaffrey	6.84	797	1.93	63	1.12	21.6	0.86
Cox-Chitty	6.83	880	1.85	70	1.08	23.6	0.69
Rouse-Yih- Humphreys <sup>2)</sup>	-	-	-	-	1.42	29.7	1.00
Yokoi <sup>1)</sup>	-	-	-	-	1.17	24.6	0.81
George-Tamanini <sup>9)</sup> Alpert	-	-	-	-	1.24	24.6	0.64~0.69

Table.3 Plume-width Ratio for Upper Regions of Upward Current

	$r_{\theta}^*/r_w^*$	
	Intermittent Flaming	Plume
Terai-Nitta	0.75	-
McCaffrey	0.83	0.83
Cox-Chitty	0.71	-
Rouse-Yih- Humphreys	-	1.16
Yokoi	-	1.1
George-Tamanini- Alpert	-	0.92

Table.4 Estimation of  $K/Q^{3/5}$  from Previous Experimental Works

	Terai-Nitta	McCaffrey	Cox-Chitty	Present
$\frac{g\beta}{2\pi C_p \rho A}$	0.0042	0.0025	0.0028	0.0026
$\frac{1}{3\pi C_p \rho B}$	0.0031	0.0028	0.0025	0.0025
$\frac{(r_w^*/Q^{2/5})^4 g\beta}{\{288\pi C_p \rho (e^{1/2}-1)^2 (z/Q^{2/5})\}}^{1/3}$	-	0.0023	0.0027 ~0.0033	-
$\frac{(r_{\theta}^*/Q^{2/5})^4 g\beta}{\{288\pi C_p \rho (e^{1/3}-1)^2 (z/Q^{2/5})\}}^{1/3}$	-	-	0.0025	0.0024



# 火災における上昇気流の間歇火炎域の特性化

長谷見 雄 二 \*

リサーチ・ペーパーNo.95

March, 1982 建設省建築研究所

本報告は、火災時に火源上に形成される上昇気流の間歇火炎域の性状を相似理論的手法を用いて解析し、この領域に関する実験的知見を満足する軸対称上昇気流の基礎方程式の解を誘導するとともに、次元解析および実験により、解に含まれる経験的諸定数の値を決定したものである。

火源上の上昇気流については、火源から遠く離れた領域（plume域）が以前から研究され、その性状は実用的にはほぼ解明されているが、上昇気流の研究分野が、自由空間内の気流から火災室内の問題に移行した結果、plume域より火源に近い間歇火炎域、火炎域が主たる研究対象になるに至った。本研究は、このうち間歇火炎域について、著者および国内外の実験にもとずいて、plume域に関する数学モデルと同程度の精度で性状を予測できるモデルを誘導している。

本報告では、上昇気流に関する実用的な諸量、即ち気流中の空気流量、巻き込み率などを求める計算図表も整備している。







## Research Papers-Recent Issues

- No.70 T. Tanaka: A Mathematical Model of a Compartment Fire, February 1977, 38 pp.
- No.71 K. Hayakawa: The Consideration of Use Values and Prices of City Space in Japan, March, 1977, 18 pp.
- No.72 K. Hayakawa: Study on the Utilization of Space in the Management of Multi-Story Apartments ("Mansions") by Private Enterprises, March, 1977, 24 pp.
- No.73 Y. Kitagawa: Observation System for Underground Earthquake Motions in Japan, March, 1977, 12 pp.
- No.74 K. Imaizumi: Recent Progress in Research and Development Wood Frame Construction, May, 1977, 61 pp.
- No.75 S. Hattori, Y. Kitagawa, M. Ohtsuka: Regional Coefficients of Earthquakes for Aseismatic Designs, July, 1977, 26 pp.
- No.76 Y. Matsushima: Random Response of Single-degree-of-freedom System with Bilinear Hysteresis, September, 1977, 28 pp.
- No.77 A. Baba: Drying Shrinkage Mechanism of Building Materials, March, 1978, 79 pp.
- No.78 K. Hayakawa: The Management of Land as an Environmental Resource, March, 1978, 40 pp.
- No.79 T. Tanaka: A Model on Fire Spread in Small Scale Buildings, September, 1978, 76 pp.
- No.80 Y. Aoki: Studies on Probabilistic Spread of Fire, November 1978, 52 pp.
- No.81 F. Saito: Experimental Study of Compartment Fire Using Model Boxes, July, 1979, 50 pp.
- No.82 Y. Matsushima: Random Response of Single-degree-of-freedom System with General Slip Hysteresis, July, 1979, 37 pp.
- No.83 Y. Hasemi: Flashover Criteria of Compartment Fire - Theory on Zero Order Reaction System, August, 1979, 26 pp.
- No.84 T. Tanaka: A Model on Fire Spread in Small Scale Buildings, 2nd Report, March, 1980, 63 pp.
- No.85 Y. Ishiyama: Review and Discussion on Overturning of Bodies by Earthquake Motions, June, 1980, 115 pp.
- No.86 S. Watanabe: Planning History in Japan - A State of the Art Survey - August, 1980, 36 pp.
- No.87 Y. Sugimura: Participation Factor of Horizontal Force Applied to Pile Foundation, March, 1981, 33 pp.
- No.88 Y. Hasemi: Mathematical Basis for Physical Evaluation on Flashover, March, 1981, 41 pp.
- No.89 T. Wakamatsu: A Quantitative Evaluation on Smoke Safety, March, 21 pp.
- No.90 S. Watanabe: Metropolitanism as a Way of Life, March, 1981, 52 pp.
- No.91 M. Hrosawa, T. Goto, M. Yoshimura, H. Hiraishi: Full-Scale Experimental Study on Aseismic Performance of Medium-Rize RC Wall Structure, March, 1981, 28 pp.
- No.92 Y. Yamazaki: Inelastic Torsional Response of Structures Subjected to Earthquake Ground Motions, March, 1981, 102 pp.
- No.93 S. Kose: Study of Accidents Associated with Building Features, March, 1982, 38 pp.
- No.94 S. Okamoto, S. Nakata, Y. Kitagawa, M. Yoshimura, T. Kaminosono: A Progress Report on the Full-Scale Seismic Experiment of a Seven Story Reinforced Concrete Building - Part of the US-Japan Cooperative Program, March, 1982, 92 pp.
- No.95 Y. Hasemi: Characterization of the Intermittent Flaming Region of the Upward Current Above Diffusion Flames, March, 1982, 33 pp.

Address for Communication

BUILDING RESEARCH INSTITUTE

MINISTRY OF CONSTRUCTION

No.1 TACHIHARA, OH-HO-MACHI, TSUKUBA-GUN, IBARAKI-PREF  
JAPAN

2.690  
K33b

ISSN 0453-4972

B R I-Research paper No. 96

# STATISTICAL ANALYSIS OF FIRE SPREAD

THE LIBRARY OF THE

JUN 9 1983

UNIVERSITY OF ILLINOIS  
AT URBANA-CHAMPAIGN

by

Yasaburo MORISHITA

Building Research Institute

Ministry of Construction

May 1982





## FORWARD

This report presents the result of the reseach on the statistical analysis of fire spread phenomenon, which was conducted as the part of continual studies of BRI for 1976 - 1980, entitled "Design System for Fire Safety in buildings".

Concerning fire spread phenomenon, many model fire tests have been carried out so far, besides real fire incidents have also been investigated in detail for many years. Such tests results and investigation reports are now being accumulated as are possible to be statistically analysed by an electric computer.

In this study, by using such data, the effects of various factors on fire spread are statistically analysed and the phenomenon is tryed to be predicted for the given factors.

The result of such statistical studies on fire spread will make the basis for establishing the reasonable design system for fire safety in buildings, together with the phisical or the chemical studies on this field.

I would like to acknowledge with appreciation those who supported on this study.

May, 1982

K.Kamimura, Director General  
Building Research Institute



# STATISTICAL ANALYSIS OF FIRE SPREAD

by

Yasaburo MORISHITA\*

BUILDING RESEARCH INSTITUTE

MINISTRY OF CONSTRUCTION

Tsukuba, Ibaraki, Japan

(Research Paper No.96 May 1982)

## ABSTRACT

In this paper, statistical techniques which can be applied to the estimation of fire spread are introduced, together with their application examples to Occurrence of Flashover in Fire Tests and Development of Real Fire in Dwellings.

These techniques are called "Theory of Quantification", since numerical values are given to the factors expressed in nominal scale so as to estimate fire spread most precisely, based on the assumption of a linear sum model of the factors, where coefficients are given to the factors expressed in interval scale as well. Comparison of the effects of the factors can be achieved by comparing the ranges or the partial correlations calculated by using the given values to the factors.

In the application example of these techniques to Fire Tests Data, the domain where flashover occurs are shown on the two dimensional Euclidian space using linear sum of the factors. Concerning Real Fire Data, the discrimination if a fire develops up to the phase that a room of fire origin is wholly involved is conducted.

The development of such analysis of Fire Test Data or Real Fire Data which are accumulated so far will give more valuable and direct informations to the estimation of fire spread.

---

\* Research Member, Testing & Evaluation Department



## TABLE OF CONTENTS

I. INTRODUCTION	1
II. STATISTICAL TECHNIQUES	2
III. ANALYSIS OF FLASHOVER BY FIRE TEST DATA	6
IV. ANALYSIS OF REAL FIRE SPREAD	11
V. CONCLUDING REMARKS	14
ACKNOWLEDGEMENT	14
LITERATURE	14
APPENDIX I ( MODEL BOX )	15
APPENDIX II ( FACTORS AND CATEGORIES )	16

## I. INTRODUCTION

Fire spread is very complex and manifold phenomenon dominated by many factors including uncertain ones such as natural conditions, fire extinguishment activities, human behaviour, etc. Consequently, in order to analyse and estimate fire spread enoughly, not only deterministic physical approaches but probabilistic or statistical approaches are needed.

Many successful Fire Tests and inquiries of Real Fire Scenes have already conducted. Tokyo Fire Department is now conducting very detailed inquiries of fire scenes including interior linings, structures, ignition sources etc. which are available to analyse fire spread. In Japan, fire reports by Fire Defence Agency, Tokyo Fire Department and some other fire departments are now being accumulated as the data base which can be analysed by electric computers.

When analysing such data concerning fire spread, available statistical techniques should be examined well. Since fire spread has qualitative aspects specified by discrete phase development or occurrence of flashover besides quantitative aspects such as temperature rise, burning rate, flashover time. Similar does the dominate factor, that is, such factors as types of interior linings, structures or kinds of ignition sources are qualitative factors, while, water content of materials, temperature of outside air etc. are quantitative ones. "Theory of Quantification" developed by statistician C. HAYASHI [1] is very useful for analysing the phenomena where qualitative variables and quantitative ones are thus mixed.

After statistical multi-variate techniques including "Theory of quantification" are introduced at the following paragraph, the results of the application to Occurrence of Flashover in Fire Tests and Development of Real Fire in Dwellings are reported.

II. STATISTICAL TECHNIQUES

In statistical terminology, the subject to be analysed or estimated, that is fire spread in this study, is called dependent variable, while, the factors are called independent variables. These variables are either qualitative or quantitative. Qualitative variables have levels given with nominal scale and quantitative variables have values given with interval scale. What kind of multi-variate analysis techniques is available for some subject depends upon the types of dependent variable and independent variables. Table 1 shows the available techniques corresponding to the types of variables. All of these techniques premise linear sum model of factors, and the effect of each factor is estimated by way of maximizing whether the correlation coefficient ( a - c ) or the correlation ratio ( d - f ). Technique (c) covers (a) and (b), and technique (f) covers (d) and (e), so only techniques (c) and (f) are explained below. The other techniques can be led easily as the special cases of these techniques.

Either of the techniques premises the following linear sum model of factors.

Table 1        Statistical Multi-variate Analysis Techniques

<div>Dependent Var. Independent Var.</div>	Interval scale	Nominal Scale
Interval Sale	(a) Multiple Correlation Analysis	(d) Multiple Correlation Ratio Analysis
Nominal Scale	(b) Theory of Quantifica- tion type I	(e) Theory of Quantifica- tion type II
Interval Scale & Nominal Scale are mixed	(c) Theory of Quantifica- tion type I'	(f) Theory of Quantifica- tion type II'

(b),(c),(e),(f) were developed by C.Hayashi



$$(1) \quad \alpha_i = \sum_{j=1}^R \sum_{k=1}^{K_j} \delta_{i(jk)} X_{jk} + \sum_{l=1}^r W_l Z_{li} + C$$

where

$\alpha_i$  : Component Variable on sample  $i$  ( sample score )

$R$  : Number of factors expressed with nominal scale

$K_j$  : Number of categories of factor  $j$

$\delta_{i(jk)} = \begin{cases} 1 & : \text{if sample } i \text{ is classified into category } k \\ & \text{by factor } j \\ 0 & : \text{otherwise} \end{cases}$

$X_{jk}$  : Category Value which is given to category  $k$  of factor  $j$ . This value is estimated by the method explained later.

$r$  : Number of factors expressed in interval scale

$W_l$  : Weight given to factor  $l$  ( interval scale )

$Z_{li}$  : Value of factor  $l$  of sample  $i$

$C$  : Constant

The method to estimate  $X_{jk}$ , and  $W_l$  and  $C$  depends upon the type of the dependent variable.

(i) The case that dependent variable is interval scale. (c)

$X_{jk}$  and  $W_l$  are estimated so that Pearson's product moment correlation coefficient between sample score  $\alpha$  and dependent variable  $y$  may be maximum. The correlation coefficient  $\rho_{y\alpha}$  is expressed as follows.

$$(2) \quad \rho_{y\alpha} = \frac{\frac{1}{n} \sum_{i=1}^n (y_i - \bar{y}) (\alpha_i - \bar{\alpha})}{\sigma_y \cdot \sigma_\alpha}$$

where,  $n$  is the total number of samples.  $\bar{y}, \bar{\alpha}$  are the averages of  $y, \alpha$  and  $\sigma_y, \sigma_\alpha$  are the standard deviations of  $y, \alpha$  respectively.

The condition that  $\rho_{y\alpha}$  is maximum leads to the condition that  $\frac{\partial \rho_{y\alpha}}{\partial X_{uv}} = 0$  ( $u = 1, 2, \dots, R; v = 1, 2, \dots, K_u$ ),  $\frac{\partial \rho_{y\alpha}}{\partial W_l} = 0$  ( $l = 1, 2, \dots, r$ ) are satisfied simultaneously.

These expressions lead to the simultaneous linear equation concerning  $X_{uv}$  and  $W_l$ . This simultaneous linear equation is an arbitrary one as it is, by the fact that whether some sample is

classified into arbitrary one of the categories of each factor or not depends up on the state of classification into other categories. Consequently, this equation is solved generally by adding the following conditions, the number of which is R.

$$(3) \quad \sum_{k=1}^{K_j} X_{jk} n_{jk} = 0 \quad (j = 1, 2, \dots, R)$$

where,  $n_{jk}$  is the number of samples which are classified into category  $k$  by factor  $j$ .

Further, the correlation coefficient is constant even if  $a$  is transformed linearly, so constant value  $C$  and the scale of the solution can be determined arbitrarily. If they are determined as  $\bar{Y} = \bar{a} = C$ , and  $\sigma_a = \rho_{Ya} \cdot \sigma_Y$ , the result of the analysis can be interpreted easier since the solution thus obtained is equal to that by least square method, namely, the solution solved under the condition that the square sum of error term, which is given as the following expression, is minimum.

$$(4) \quad S = \sum_{i=1}^n e_i^2 = \sum_{i=1}^n (y_i - \alpha_i)^2$$

(ii) The case that dependent variable is nominal scale : (f)

This method is a kind of discriminant analysis using the correlation ratio as the criterion of preciseness of discrimination.  $X_{jk}$  and  $W_l$  are estimated so that the correlation ratio may be maximum. The correlation ratio  $\eta^2$  is the ratio of 'between class variance'  $\sigma_b^2$  to the 'total variance'  $\sigma^2$ , which are expressed as follows.

$$(5) \quad \eta^2 = \frac{\sigma_b^2}{\sigma^2}$$

where,

$$\sigma^2 = \frac{1}{n} \sum_{i=1}^n (\alpha_i - \bar{\alpha})^2$$

$$\sigma_b^2 = \sum_{t=1}^{t_m} \frac{n_t}{n} (\bar{\alpha}_t - \bar{\alpha})^2$$

$n$  : Total number of samples

$n_t$  : The number of the samples which is classified into category  $t$  by dependent variable.

$\bar{\alpha}_t$  : The average of sample score  $\alpha$  of the samples belonging to category  $t$ .

$t_m$  : The number of categories of dependent variable

The condition that  $\eta^2$  is maximum leads to the condition that

$$\frac{\partial \eta^2}{\partial X_{uv}} = 0 \quad (u = 1, 2, \dots, R; v = 1, 2, \dots, k_u), \quad \frac{\partial \eta^2}{\partial W_l} = 0$$

( $l = 1, 2, \dots, r$ ) are satisfied simultaneously.

Substituting the expression (5),

$$(6) \quad \frac{\partial \sigma_b^2}{\partial X_{uv}} = \eta^2 \frac{\partial \sigma^2}{\partial X_{uv}} \quad (u = 1, 2, \dots, R; v = 1, 2, \dots, k_u)$$

$$\frac{\partial \sigma_b^2}{\partial W_l} = \eta^2 \frac{\partial \sigma^2}{\partial W_l} \quad (l = 1, 2, \dots, r)$$

These simultaneous equations lead to the eigen value problem after all, where  $\eta^2$  is the eigen value and  $X^t = [ X_{11} \ X_{12} \ \dots \ X_{1k_1} \\ X_{21} \ \dots \ X_{jk} \ \dots \ X_{Rk_R} \ W_1 \ \dots \ W_l \ \dots \ W_r ]$

is the eigen vector.

In order to solve this problem uniquely, besides the condition (3) is necessary to be considered,  $\sigma^2$  and  $C$  are also necessary to be determined appropriately since the correlation ratio is constant even if  $\alpha$  is transformed linearly. Here, the conditions that  $\sigma^2 = \eta^2$  and  $C = 0$  are added.

At this eigen value problem, the spectral factorization of the matrix concerned give the solutions, the number of which is equal to the rank of the matrix, where the eigen vectors are independent with each other. When discriminating the categories of dependent variable, namely, when predicting the phenomenon, better discrimination can be achieved generally by taking up not only the solution which gives the maximum correlation ratio (eigen value) but some other solutions together.

After  $X_{jk}$ ,  $w_l$  and  $C$  were determined, the effect of the factors can be compared with the values of partial correlations between dependent variable and each factor (When calculating the partial correlation,  $\bar{\alpha}_t$  is substituted for the value of dependent variable, if it is nominal scale). The comparison of the effects only among the factors of nominal scale, can be achieved also by the range of category value  $X_{jk}$  within each factor.



By the way, Theory of Quantification type I' (c) is mathematically equal to the multiple correlation analysis using 1-0 dummy variable for the independent variable of nominal scale. However, it would be a remarkable point that the comparison of the effects of qualitative factors with the partial correlations or the ranges is generated by the conception to quantify the qualitative variables, not merely to calculate the partial regression coefficient of 1-0 dummy variable.

### III. Analysis of Flashover by Fire Test Data

Occurrence of Flashover can be analysed by applying Theory of Quantification type I' and type II' introduced at the previous paragraph.

The Fire Test Data analysed here are those done by Dr. F.SAITO, the main purpose of which is to examine the effect of the thickness of plywood on smoke generation. Flashover time is also observed in this test. Such results of the tests are reported at literature [3].

The model box used was 95cm width x 46cm high x 43cm depth in size, and plywood was set on the ceiling and the back and side walls. Cribs were arranged in the corner of the box. Small piece of soft fiber board ( 1cm x 1cm ) dipped with alcohol was used for ignition. The figure of the model box is shown at appendix I.

The tests were designed to examine the effects of the following factors.

1. Rate of Opening Area to Front Area - - - 2 levels

(1) 1/4 (2) 1/2

2. Size of Fuel - - - 3 levels

(1) 8 cribs, the length of which are 6 cm ( 4 layers )

(2) 16 Cribs, the length of which are 14 cm ( 4 layers )

(3) 25 Cribs, the length of which are 17 cm ( 5 layers )

Each Crib has the section 2cm x 2cm.

3. Thickness of Plywood - - - 5 levels

(1) 3.0mm (2) 5.5mm (3) 7.5mm (4) 9.0mm (5) 12.0mm

Rate of water content of Crib and Plywood were also measured,

and they were also taken up as the factors of flashover together with the above three factors.

#### (i) Analysis of Flashover Time

Theory of Quantification type I' can be applied in this case since flashover time, which is dependent variable, is given with interval scale, and the factors, which are independent variables, are given with both nominal scale and interval scale.

The result of the analysis of flashover time is shown at table 2.

Comparing the values of partial correlation, the effects of Size of Fuel is largest among 5 factors, and the effect of Thickness of Plywood is next to it. On the other hand, Rate of Opening Area and Rate of Water Content have little effect. Of course such results are based on the levels of factors taken up.

The category values of Size of Fuel show that the larger is the Size of Fuel, the smaller is the category value. This means that the larger is the fuel, the shorter is flashover time.

Seeing the category value of thickness of Plywood, the value for 3.0mm is particularly small, therefore you can see that flashover time is particularly short in this case. The relation between Thickness of Plywood and category value is not monotonous, the value is maximum in the case of 7.5mm.

Figure 1 shows the relation between observed flashover time and estimated one. The correlation coefficient which indicates the preciseness of the analysis is 0.785.

#### (ii) Analysis including the case that flashover did not occur

Theory of Quantification type II' can be applied in this case by arranging the dependent variables as follows. Namely, flashover time is classified into the following five categories. (1) 199 sec. below (2) 200 - 299 sec. (3) 300 - 399 sec. (4) 400 - 499 sec. (5) 500 sec. above. Further, the category (6) no flashover is added.

As the dependent variable thus arranged is nominal scale, the analysis is done so that above categories may be well discriminated. Table 3 shows the two solutions which give the

Table 2 Result of the analysis of flashovertime by Theory of Quantification type I'

\* AV = 9.4%, SD = 1.7%

\*\* AV = 7.9%, SD = 1.6%

\*\*\* Weight is calculated using standerdised value of Rate of Water Content

$$Z_{zi} = (X_{zi} - AV_z)/SD_z$$

	No. of Sample	Category Value	Range	Partial Corr.
Openings 1/4	30	0.089	0.168	0.063
1/8	34	-0.079		
Crib 6 cm	7	3.897	5.549	0.761
Length 14	36	0.206		
17	21	-1.652		
Thickness 3.0 mm	17	-1.457	2.788	0.573
of 5.5	16	0.292		
Plywood 7.5	11	1.331		
9.0	11	0.155		
12.0	9	0.417		
Rate of Water Content of Crib*	64	0.079 ( Weight )		0.052
Rate of Water Content of Plywood**	64	-0.035 ( Weight )		-0.024

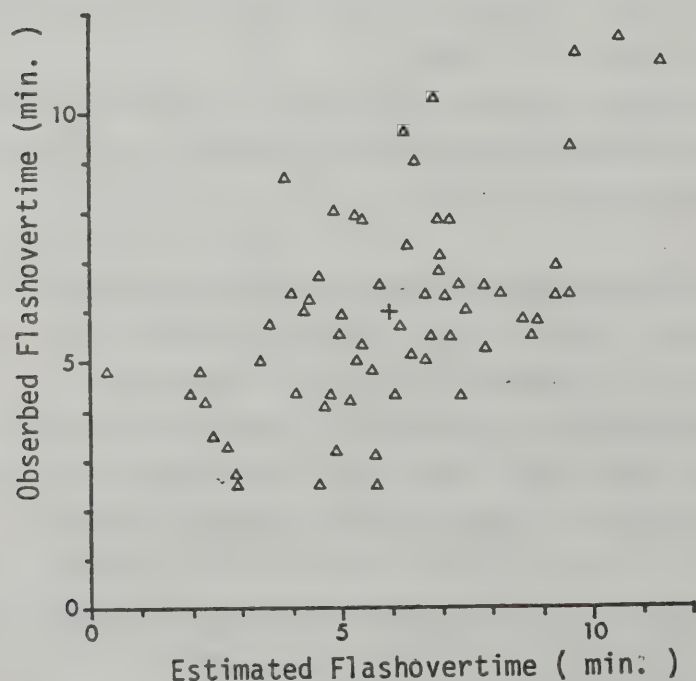


Fig. 1

Relation between Flashover Time and Estimated Value (Correlation Coef. = 0.785 )



largest two correlation ratios ( eigen values ). These two solutions, namely axis I and axis II are independent with each other since they are obtained by spectral factorization of the matrix concerned. The correlation ratios, 0.770 of axis I and 0.357 of axis II are fairly good.

Either the partial correlations and the category values of axis I can be interpreted almost similarly with the results of the analysis of flashover time.

Figure 2 shows the distribution of sample score  $a_i$ . The distribution on the direction of axis I shows that the

Tab.3 Result of Multiple Correlation Ratio Analysis(Quality & Quantity Mixed)

\*AV = 9.4%, SD = 1.7%

\*\*AV = 7.8%, SD = 1.6%

\*\*\* Weight is calculated using standardized value of Rate of Water Content ;  $Z_{ii} = (X_{ii} - AV_i) / SD_i$

AXIS		I			II		
Correlation Ratio		0.770			0.357		
Nominal Scale	No. of Sample	Category Value	Range	Partial Corr.	Category Value	Range	Partial Corr.
Openings							
WxHx1/4	33	-0.022	0.042	0.043	-0.138	0.261	0.157
WxHx1/8	37	0.020			0.123		
Crib Length							
6 cm	13	-1.700	2.390	0.863	-0.382	0.852	0.454
14	36	0.211			0.401		
17	21	0.690			-0.451		
Thickness of Plywood							
3.0 mm	17	0.535	1.036	0.573	-0.543	0.949	0.381
5.5	17	0.002			0.134		
7.5	13	-0.501			-0.020		
9.0	12	-0.064			0.229		
12.0	11	-0.169			0.406		
Water Content of Crib*	70	-0.076 (weight)		-0.136	-0.038 (weight)		-0.041
Water Content of Plywood**	70	0.058 (weight)		0.102	-0.216 (weight)		-0.231

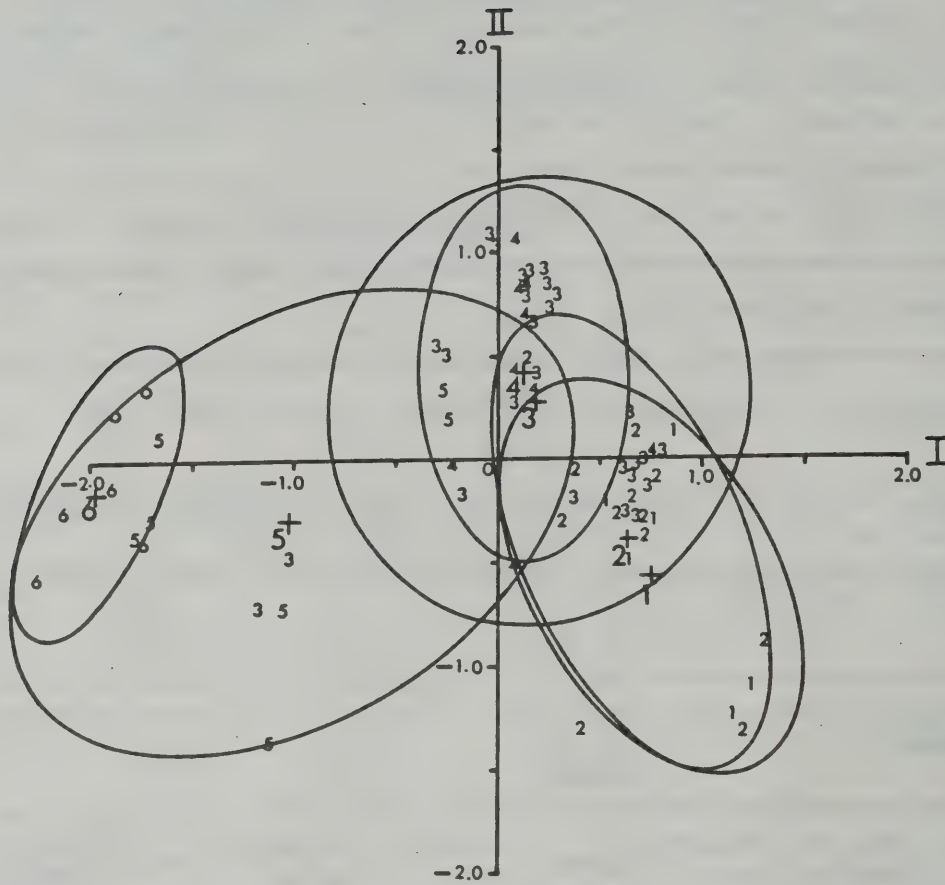


Figure 2 Distribution of Sample Score  $\alpha$

Note: Ellipses show 90% confidence bounds of two dimensional distribution of sample scores based on the assumption of normal distribution.

shorter is the flashover time, the larger is the sample score, and the category (6) no flashover separates remarkably. Axis II shows that the longer is the flashover time, the larger is the sample score except two categories of (5) 500 sec. above and (6) no flashover.

The ellipses in figure 2 show 90% confidence bounds on two dimensional distribution of sample scores based on the assumption of normal distribution. As being expected from this figure, the prediction of flashover time or presence of flashover can be achieved by determining the domains appropriately on the multi-dimensional Euclidian space where sample scores distribute.

#### IV. ANALYSIS OF REAL FIRE SPREAD

Real fire spread is analysed by Theory of Quantification type II in this paragraph.

Real Fire Data used here are residential fire reports inquired by Tokyo Fire Department from 1974 to 1977, the ignition place of which are whether living rooms or kitchens.

The subject to be discriminated is if a fire develops up to the phase that a room of fire origin is wholly involved ( Whole Room Fire Phase ), the statistical index of which is if the burned area of concerned fire exceeds 80% of the floor area of a room of fire origin.

Seven kinds of factors were taken up as independent variables, namely, (1) Ignition Pattern (2) Rate of Combustible Area on Vertical Face (3) Combustibility of Ceiling (4) Rate of Combustible Area on Horizontal Face (5) Openings (  $\Sigma A\sqrt{H}$  ) (6) Structure (7) Extinguishment in the Early Stage of Fire Spread (8) Alert Time to Fire Station. The categories of these factors are explained in detail at appendix II. Though four factors out of these factors are basically expressed in interval scales, they are transformed into qualitative factors by deviding values appropriately. Such transformation is effectual especially if the phenomenon is not linear for the concerned factor.

The result of the analysis by Theory of Quantification type II is shown at Table 4. Comparing the range and the partial correlation, you can see that, for the occurrence of Whole Room Fire, the effect of 'Alert Time to Fire Station' is the highest among the factors, and the effects of Extinguishment in the Early Stage of Fire Spread', 'Ignition Pattern', 'Rate of Combustible Area on Vertical Face', and ' Combustibility of Ceiling' are comparatively high, however, 'Rate of Combustible Area on Horizontal Face' show low effect.

Using the category vlues given as the result of the analysis by Theory of Quantification, the discrimination if a fire develops up to the phase that a room of fire origin is wholly involved can be achieved. Fig.3 shows the distribution of sample scores. From this figure, you can see that Whole Room Fire occurs with the



higher probability as the sample score increases, further it may be also understood that there would be a discriminant point whether Whole Room Fire occurs or not. Based on this distribution of sample scores, the discriminant point  $a_0 = 0.23$  is given under the condition of minimizing the error of discrimination. Using this discriminant point, the rate of success of discrimination is 79%.

Table 4    The result of the analysis of Whole Room Fire Occurrence

FACTOR		CATEGORY	SAMPLE	CATEGORY VALUE		RANGE	PARTIAL CORRELATION
				-0.5	0	0.5	
IGNITION FACTOR	IGNITION PATTERN	1 RANGE+OILES	202	-0.129		0.316	0.187
		2 IMFLAMABLE M., OIL	66	-0.071			
		3 APP.+FIBER, WASTES	85	0.029			
		4 TOBACCO+FIB., WAST.	158	-0.022			
		5 MATCH+FIBER, WAST.	81	0.054			
		6 FURNISHING, FURNIT.	70	0.086			
		7 OTHERS, UNKNOWN	114	0.186			
FIRE SPREAD FACTOR	RATE OF COMBUSTIBLE AREA ON VERTICAL FACE	1 0 - 25 (%)	87	-0.150		0.285	0.147
		2 25 - 50	318	-0.058			
		3 50 - 75	117	0.135			
		4 75 - 100	254	0.062			
	COMBUSTIBILITY OF CEILING	1 NON-COMBUSTIBLE M.	137	-0.116		0.210	0.099
		2 FIRE RETARDANT M.	31	-0.175			
		3 COMBUSTIBLE M.	608	0.035			
	RATE OF COMBUSTIBLE AREA ON HORIZONTAL FACE	1 0 - 75 (%)	46	-0.027		0.028	0.051
		2 75 - 100	730	0.001			
	OPENINGS	1 0 - 2.5 (m <sup>2</sup> )	279	-0.014		0.120	0.038
		2 2.5 - 5.0	288	-0.015			
		3 5.0 - 10.0	179	0.030			
		4 10.0 -	30	0.105			
	STRUCTURE	1 FIRE PROOF STRUCT.	122	-0.093		0.157	0.104
		2 FIRE PROTECTIVE S.	273	-0.046			
		3 WOODEN STRUCTURE	381	0.063			
EXTINGUISHMENT FACTOR	EXTINGUISHMENT IN THE EARLY STAGE OF F.S.	1 BEING DONE	701	-0.033		0.342	0.175
		2 NOT BEING DONE	75	0.309			
	ALERT TIME TO STATION	1 - 3 (MIN.)	440	-0.203		0.497	0.372
		2 3 - 5	218	0.252			
		3 5 -	118	0.293			

Correlation Ratio = 0.30

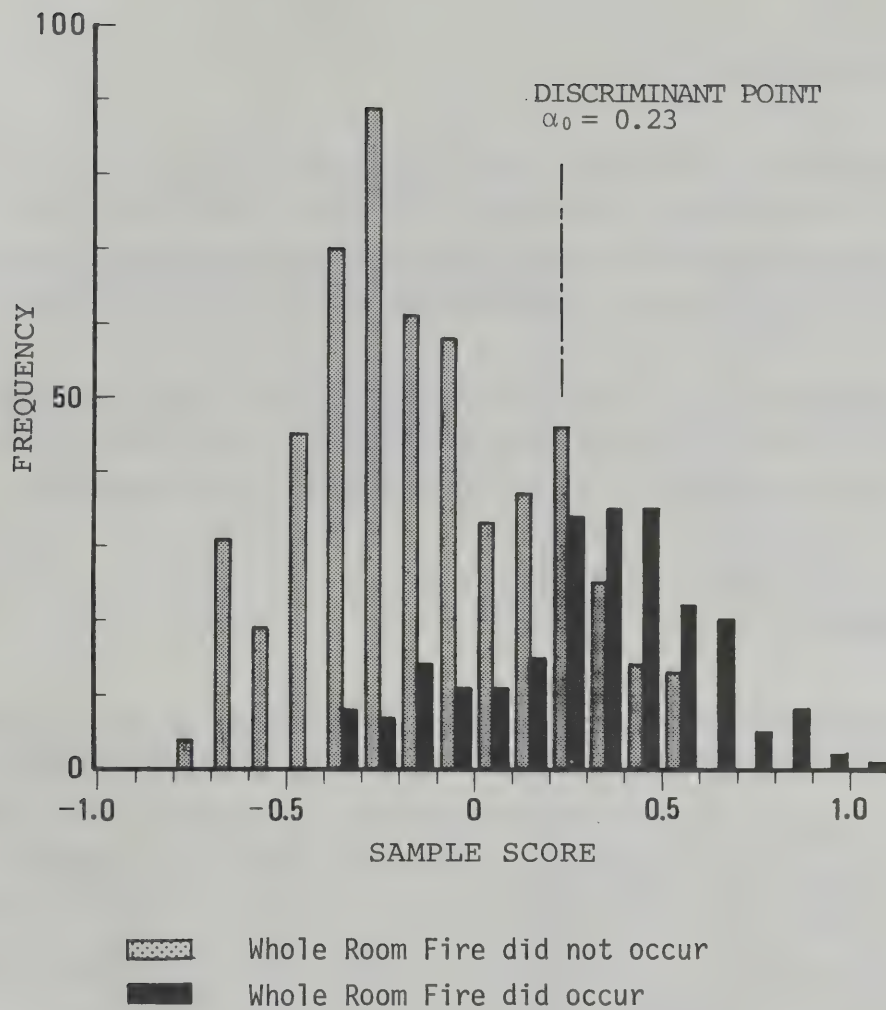


Figure 3 Frequency distribution of sample scores

For example, if 'Ignition Pattern' is '1; range and the likes to oil or fats', 'Rate of Combustible Area on Vertical Face' is '3; 70%', 'Combustibility of Ceiling' is '3; combustible material', 'Rate of Combustible Area on Horizontal Face' is '4; 100%', 'Opening' is '3; 6m  $\frac{5}{2}$  ', 'Structure' is '3; wooden structure', 'Extinguishment in Early Stage of Fire Spread' is '1; being done' and 'Alert Time to Station' is '2; 4 minutes', the sample score comes to be 0.36, and the rate of success of discrimination is 79% when Whole Room Fire is considered to occur.

## V. CONCLUDING REMARKS

It was made out that the multi-variate analysis techniques introduced in this paper is useful for the factor analysis and the estimation of fire spread, the results of which can be easily interpreted in relation to the phenomenon by showing them with a diagram.

The development of such analysis of Fire Test Data and Real Fire Data which were accumulated so far will give more valuable and direct informations to the estimation of fire spread.

## ACKNOWLEDGEMENTS

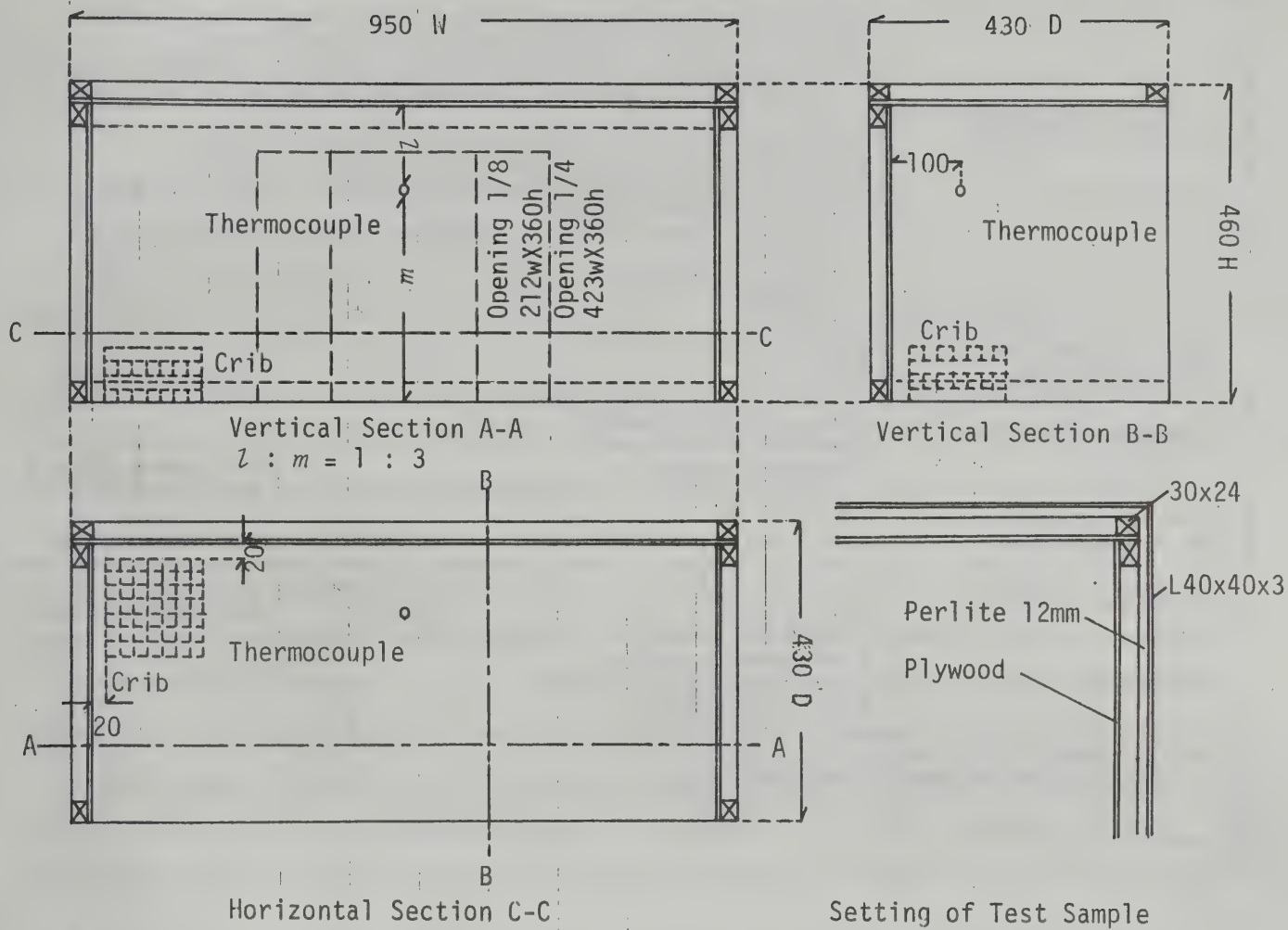
The Fire Test Data analysed here was made by Dr. F.SAITO and his staffs, Mr. M.YOSHIDA et al. They offered thier data willingly and gave helpful suggestions in executing this study. The author would like to express sincere thanks for them.

On the other hand, the Real Fire Data were investigated by Tokyo Fire Department through the project on the Development of the Performance Evaluation System in Dwellings during 1975 - 1977. The author could find a clue of this study through this project. The author would like to express deep thanks for the labour of the investigation by Tokyo Fire Department and for the members of the project who discussed enthusiastically on this study.

## LITERATURE

- [1] C.HAYASHI et al, " Jyoho Shori to Tokei Suri ", Sangyo Tosyo ", 1970
- [2] S.YASUDA et al, " Syakai Tokei Gaku ", Maruzen, 1977
- [3] T.TSUKAMOTO, H.TANAIKE, S.HOSODA, " Kenchiku Zairyo no Hatsunetsusei oyobi Hatsugasusei ni kansuru Kenkyu ", Graduation Thesis of Kanagawa Univercity, 1971





APPENDIX I Model Box

FACTOR		EXPLANATION OF CATEGORY	
IGNITION FACTOR	IGNITION PATTERN	1 Ignition pattern from small kitchen range, range, or water heater to oils and fats (typical ignition pattern at kitchen). 2 Ignition pattern from certain ignition source to inflammable material, oils and fats or explosive substance excluding the pattern stated as 1 3 Ignition pattern from apparatus to fiber goods or wastes. 4 Ignition pattern from tobacco to fiber goods or wastes. 5 Ignition pattern from match, lighter, candle or stick of incense to fiber goods or wastes. 6 Ignition pattern from certain ignition source to furnishings or furnitures. 7 Ignition pattern except above 1 - 6 or the ignition pattern is unknown.	
FIRE SPREAD FACTOR	RATE OF COMBUSTIBLE AREA ON VERTICAL FACE *	1 0 - 25 ( % ) 3 50 - 75	2 25 - 50 4 75 - 100 ( Fire Outbreak Room )
	COMBUSTIBILITY OF CEILING **	1 Non-combustible material 2 Fire retardant material 3 Combustible material	( Fire Outbreak Room )
	RATE OF COMBUSTIBLE AREA ON HORIZONTAL FACE *	1 0 - 75 ( % ) 2 75 - 100	( Fire Outbreak Room )
	OPENINGS ( $\Sigma A\sqrt{H}$ )	1 0 - 2.5 ( m <sup>5/2</sup> ) 3 5.0 - 10.0	2 2.5 - 5.0 4 10.0 - ( Fire Outbreak Room )
	STRUCTURE	1 Fire proof structure 2 Fire protective structure 3 Wooden structure	
EXTINGUISHMENT FACTOR	EXTINGUISHMENT IN THE EARLY STAGE OF FIRE SPREAD***	1 Being done 2 Not being done	
	ALERT TIME TO STATION ****	1 - 3 ( min. ) 3 5 -	2 3 - 5

- \* In the case that there are combustibles such as combustible furnitures, they are projected to the vertical face ( wall ) and the horizontal face ( floor ), and the projected part is regarded as combustible. Next, the projected area and the area of combustible interior finish materials are summed up on the vertical face and the horizontal face, and the rate of the each summed up combustible area to the area of the each face is calculated.
- \*\* The testing method of combustibilities of interior finish materials is decided by the law. The order 1 to 3 corresponds to the order of combustibilities.
- \*\*\* Fire extinguishment activity in the early stage of fire spread ( generally before flashover ) with fire extinguishment equipments such as fire extinguishers.
- \*\*\*\* Elapsed time from the ignition time ( estimated ) to the alert time in fire station.

## APPENDIX II Factors and Categories

# 火災拡大現象の統計解析

森 下 弥 三 郎 \*

リサーチペーパー No. 96

May 1982 建設省建築研究所

火災研究の分野では、今日までに多くの火災実験や火災事例調査がおこなわれ、そうしたデータは、現在、電算機により統計的に解析することが可能な形で蓄積されつつある。

本報告では、模型火災実験および現実の住宅火災事例における火災拡大の過程を、質量混合の数理化理論により解析し、各種要因の効果を比較検討すると共に火災拡大現象の予測を試みたものである。

模型火災実験における火災拡大現象の統計解析に於いては、フラッシュオーバーが発生するまでの時間の長短や、フラッシュオーバーの発生の有無に関して要因分析をおこない、火源の大きさや内装合板の厚さが相対的に大きな効果を有することが分った。さらに、要因分析の際得られた値をもとに現象予測を試み、フラッシュオーバーの発生・非発生の領域を2次元ユークリッド空間上に示した。

住宅火災事例における火災拡大現象の統計解析に於いては、出火室全体が火災に巻きこまれる現象の発生に関して要因分析・判別予測をおこなった。要因分析の結果から、「覚知時間」や「初期消火の有無」、「出火パターン」が壁・天井の燃焼性と共に大きな効果を有していることが明らかとなった。さらに、分析の際得られた値をもとに判別予測を試みた結果、79%の的中率で当該現象の発生の有無を判別可能であることが分った。

現在までに蓄積されている火災実験データや火災事例データを、本報告と同様の方法で解析しておくことは、火災の拡大の予測や評価に対して直接的に有用な情報を提供することになる。







### Research Papers-Recent Issues

- No.72 K. Hayakawa: Study on the Utilization of Space in the Management of Multi-Story Apartments ("Mansions") by Private Enterprises, March, 1977, 24 pp.
- No.73 Y. Kitagawa: Observation System for Underground Earthquake Motions in Japan, March, 1977, 12 pp.
- No.74 K. Imaizumi: Recent Progress in Research and Development on Wood Frame Construction, July, 1977, 51 pp.
- No.75 S. Hattori, Y. Kitagawa, M. Ohtsuka: Regional Coefficients of Earthquakes for Aseismic Designs, August, 1977, 26 pp.
- No.76 Y. Matsushima: Random Response of Single-degree-of-freedom System with Bilinear Hysteresis, September, 1977, 28 pp.
- No.77 A. Baba: Drying Shrinkage Mechanism of Building Materials, March, 1978, 79 pp.
- No.78 K. Hayakawa: The Management of Land as an Environmental Resource, March, 1978, 40 pp.
- No.79 T. Tanaka: A Model on Fire Spread in Small Scale Buildings, September, 1978, 76 pp.
- No.80 Y. Aoki: Studies on Probabilistic Spread of Fire, November 1978, 52 pp.
- No.81 F. Saito: Experimental Study of Compartment Fire Using Model Boxes, July, 1979, 50 pp.
- No.82 Y. Matsushima: Random Response of Single-degree-of-freedom System with General Slip Hysteresis, July, 1979, 37 pp.
- No.83 Y. Hasemi: Flashover Criteria of Compartment Fire — Theory on Zero Order Reaction System —, August, 1979, 26 pp.
- No.84 T. Tanaka: A Model on Fire Spread in Small Scale Buildings, 2nd Report, March, 1980, 63 pp.
- No.85 Y. Ishiyama: Review and Discussion on Overturning of Bodies by Earthquake Motions, June, 1980, 115 pp.
- No.86 S. Watanabe: Planning History in Japan — A State of the Art Survey —, August, 1980, 36 pp.
- No.87 Y. Sugimura: Participation Factor of Horizontal Force Applied to Pile Foundation, March 1981, 33 pp.
- No.88 Y. Hasemi: Mathematical Basis for Physical Evaluation on Flashover, March, 1981, 41 pp.
- No.89 T. Wakamatsu: A Quantitative Evaluation on Smoke Safety, March, 21 pp.
- No.90 S. Watanabe: Metropolitanism as a Way of Life, March, 1981, 52 pp.
- No.91 M. Hirose, T. Goto, M. Yoshimura, H. Hiraishi: Full-Scale Experimental Study on Aseismic Performance of Medium-Rise RC Wall Structure, March, 1981, 28 pp.
- No.92 Y. Yamazaki: Inelastic Torsional Response of Structures Subjected to Earthquake Ground Motions, March, 1981, 102 pp.
- No.93 S. Kose: Study of Accidents Associated with Building Features, March, 1982, 38 pp.
- No.94 S. Okamoto, S. Nakata, Y. Kitagawa, M. Yoshimura, T. Kaminosono: A Progress Report on the Full-scale Seismic Experiment of a Seven Story Reinforced Concrete Building — Part of the US — Japan Cooperative Program, March, 1982, 92 pp.
- No.95 Y. Hasemi: Characterization of the Intermittent Flaming Region of the Upward Current above Diffusion Flames, March, 1982, 33 pp.
- No.96 Y. Morishita: Statistical Analysis of Fire Spread, May, 1982, 17 pp.

Address for Communication

**BUILDING RESEARCH INSTITUTE  
MINISTRY OF CONSTRUCTION**

**No.1 TACHIHARA, OH-HO-MACHI, TSUKUBA-GUN, IBARAKI-PREF**

**JAPAN**



690  
K33b

ISSN 0453-4972

BRI Research paper No. 97

# DETERIORATION MODEL OF POLYMERIC MATERIALS WITH SPECIAL ATTENTION TO AGE AND DETERIORATION DEPTH

THE LIBRARY OF THE

JUN 9 1983

UNIVERSITY OF ILLINOIS  
AT URBANA-CHAMPAIGN

by  
Toshio Fukushima

Building Research Institute  
Ministry of Construction

December 1982



## FOREWORD

This paper reports the result of the research on the dynamical analysis of deterioration processes of polymeric materials, which was conducted as part of continual studies of BRI for 1977-1982, entitled, "Effective Use of Inorganic Polymers for Building Materials".

Recently the importance of durability of building materials and components has been widely appreciated, and the rational evaluation criteria for the progress of deterioration have been pursued in various ways. A lot of phenomenological data have been accumulated. However, there still remain major difficulties to be solved for the analytical methods of deterioration processes.

In this paper, the deterioration process of polymers by the simultaneous action of UV-light and diffusive oxygen is explained theoretically based on an unsteady-state dynamics, taking some experimental data into consideration, and the parabolic law concerning exposure time is derived for a typical path of the progress of deterioration.

The result may be incomplete in some respects, as compared with the whole problems of deterioration, but this paper will be useful as a basis for the evaluation of durability of building materials hereafter.

I would like to express my hope for the development of research on this field and acknowledge with appreciation those who have supported on this study.

December, 1982

K. Kamimura, Director General  
Building Research Institute





# DETERIORATION MODEL OF POLYMERIC MATERIALS

WITH SPECIAL ATTENTION TO AGE AND DETERIORATION DEPTH\*

by

Toshio Fukushima\*\*

BUILDING RESEARCH INSTITUTE

MINISTRY OF CONSTRUCTION

Tsukuba, Ibaraki, Japan

(Research Paper No.97 December 1982)

## ABSTRACT

The deterioration process of polymeric materials by the simultaneous action of UV-light and diffusive oxygen is analyzed theoretically based on an unsteady-state dynamics, taking account of the progress of deterioration inward from surface. It is supposed that the deterioration proceeds photochemically by depolymerization and photooxidation reactions of polymer molecules photoactivated by absorbing UV-light near the absorption band characteristic of polymeric materials. As a result it is shown under some assumptions that the depth of the deteriorated layer increases approximately in proportion to the square root of exposure time.

This  $\sqrt{t}$  law (parabolic law) has previously been observed in the cases of neutralization of concrete and oxidation of metals, but this theory suggests that the parabolic law should also apply to the case of the deterioration of polymeric materials.

Experimentally many polymeric materials show the power law of exposure time ( $t^n$ ;  $n=0.5\sim 1.0$ ). The difference between theory and experiment is considered to be due to the complicated deterioration mechanisms which involve depolymerization and photooxidation.

The reduction in flexural strength over time of polymeric materials is explained by the reduced contribution of the deteriorated surface layer to the strength.

## TABLE OF CONTENTS

I. INTRODUCTION	1
II. OUTLINE OF THE MODEL OF THE DETERIORATION PROCESS	2
III. BASIC DIFFERENTIAL EQUATIONS FOR DYNAMICAL ANALYSIS	4
IV. RESULTS OF DYNAMICAL ANALYSIS	4
V. DISCUSSIONS	5
VI. CONCLUSIONS	8
VII. ACKNOWLEDGEMENTS	8
REFERENCES	9
APPENDIX A	12
APPENDIX B	13
APPENDIX C	15
FIGURE CAPTIONS	17
FIGURES	

---

\*This paper is almost the same as "Deterioration Process of Polymer Materials and Its correlation with Depths from Surface" by the author, presented at the Second International Conference on the Durability of Building Materials and Components, Gaithersburg, U.S.A., September 14-16, 1981, and in submission to Durability of Building Materials.

\*\* Senior Research Member, Materials Department.

## I. INTRODUCTION

Polymeric materials are widely applied in buildings such as paints, adhesives, waterproofings, finishing materials, thermal insulating materials, and solar collector components.

Though they have many attractive properties, they are subject to gradual deterioration when they are used under natural weathering, and they deteriorate rapidly under the simultaneous action of UV-light and diffusive oxygen(say, ozone) in accelerated aging tests.

On the other hand, societal needs for the conservation of natural resources and energy has given increased importance to the concept of durability as performance over time in many fields, especially in building materials, components and/or elements[1-4]. At the same time, in connection with the prediction of lifetimes of buildings, there has been an increasing demand for criteria for evaluating the progress of deterioration and for identifying deterioration mechanisms of building materials. In order to evaluate the performance over time, it would be necessary to consider the change of material properties and the effect of the deteriorated layer on the performance, assuming no change of performance requirements.

The deterioration processes of polymeric materials are very complicated. They show various types of deterioration behavior, depending on the conditions under which they are used, because they are influenced by various extrinsic factors(UV-light, oxygen, water, pollutant gases and freezing-thawing action,etc.) and various intrinsic factors(temperature and humidity conditions, types and compositions of polymers, treatment and maintenance conditions, etc.). Much phenomenological data on the deterioration processes of polymers in buildings has been accumulated. It would be reasonable for us to establish rational selection criteria for the progress of deterioration based on the data. Taking the complexity of the deterioration phenomena into account, however, it may be helpful to try to understand the deterioration mechanisms of polymers under natural weathering theoretically by developing an appropriate model



based on fundamental principles.

This paper deals with the complex deterioration process of polymeric materials by the simultaneous action of UV-light and diffusive oxygen based on an unsteady-state dynamical analysis, paying special attention to the progress of deterioration inward from surface. The aim is to derive the law of the increase of the depth of the deteriorated layer with time, and to consider the reduction in flexural strength as the deterioration advances. It is shown that the degree of deterioration varies continuously with time and depth and that the increase in the depth of the deteriorated layer with time is approximately in accord with the parabolic law [5-6], as is often observed in the cases of neutralization of concrete [7], and oxidation of metals [8].

## II. OUTLINE OF THE MODEL OF THE DETERIORATION PROCESS

The fundamental assumption of the model for dynamical analysis are as follows: 1) Only polymer molecules which are activated into excited states by absorbing the UV-light (photon flux,  $n_0$ ) near the absorption band characteristic of polymeric materials can take part in photochemical reactions (reaction efficiency,  $\eta$ ; molar concentration,  $C^*$ ). 2) Photochemical reactions are i) depolymerization of activated polymer molecules (1st order reaction,  $R_1 = k_1 C^*$ ), ii) photooxidation by the collision of diffusive oxygens (molar concentration,  $C_A$ ; diffusion flux,  $N_A$ ; diffusion coefficient,  $D_A$ ) and activated polymer molecules (2nd order reaction,  $R_2 = k_2 C^* C_A$ ), 3) Deteriorated polymer molecules (molar concentration,  $C_B$ ) do not diffuse and remain in their original positions. 4) The influence of temperatures on the photochemical reactions is included in materials property constants such as rate constants ( $k_1, k_2$ ) and diffusion coefficient ( $D_A$ ) according to the Arrhenius law. 5) Deterioration proceeds inward from the surface and the degree of deterioration varies with exposure time ( $t$ ) and depth below the surface ( $x$ ). As the deterioration advances, deteriorated polymer molecules having IR-active functional groups such as  $-CO$ ,



-OH are created, and the degree of deterioration is reflected in the increase of absorption ( $\alpha$ ) or the decrease of reflection (R) in IR spectra. 6) The deteriorated layers result in a reduction in flexural strength of polymeric materials with the progress of deterioration. Based on the fundamental assumption described above, the following three basic processes are considered.

a) Absorption of UV-light:

Considering the material balance within the infinitesimal plate,  $x \sim x + dx$ , shown in Fig.2, on the assumption that UV-light (wavelength,  $\lambda$ ; photon flux,  $n_0$ ) falls on the polymeric material surface as described in Fig.1, the following differential equations can be obtained (see Appendix A for the derivation of these equations):

$$\partial C^*/\partial t = -(\eta/N_0) \partial n/\partial x - k_1 C^* - k_2 C^* C_A \quad (1)$$

$$\partial n/\partial x = -C_0 \epsilon_\lambda n \quad (2)$$

( $N_0$ , Avogadro's constant;  $C_0$ , initial concentration of undeteriorated polymer molecules;  $\epsilon_\lambda$ , molar absorption coefficient). Equations (1) and (2) lead to equation (3):

$$\partial C^*/\partial t = A C_0 \epsilon_\lambda \exp(-C_0 \epsilon_\lambda x) - k_1 C^* - k_2 C^* C_A \quad (3)$$

$$(A = \eta n_0/N_0)$$

b) Diffusion of Oxygen:

From the material balance of oxygen within the plate shown in Fig.2, and the following equation is obtained:

$$\partial C_A/\partial t = D_A \partial^2 C_A/\partial x^2 - k_2 C^* C_A \quad (4)$$

c) Process of Photochemical Reactions:

Overall reaction rate ( $R=R_1+R_2$ ) is the rate of creation of deteriorated polymer molecules, and it is also equal to the rate of increase of the absorption coefficient in the absorption band of IR-active functional group (say, -CO group, wavelength,  $\lambda'$ ). Consequently,

$$R = k_1 C^* + k_2 C^* C_A = \partial C_B/\partial t = \partial \alpha_{\lambda'}/\partial t \quad (5)$$

Here,

$$k_1 = A_1 \exp(-E_1/kT), \quad k_2 = A_2 \exp(-E_2/kT) \quad (6)$$

$$D_A = D_{A_0} \exp(-E_3/kT) \quad (7)$$

( $T$ , absolute temperature;  $k$ , Boltzman constant;  $E_1, E_2, E_3$ ,

activation energies)

### III. BASIC DIFFERENTIAL EQUATIONS FOR DYNAMICAL ANALYSIS

For the purpose of simplifying the analysis, two assumptions are made, however, the results never fail to have generality. The assumptions are: i) compared with the thickness of the plate of polymeric materials ( $L$ ), the deteriorated depth ( $\delta$ ) can be considered to be small enough for the thickness of the plate to be regarded as virtually infinitely large; ii) in photooxidation reaction ( $R_2 = k_2 C^* C_A$ ), we can consider the reaction to be quasi-1st-order ( $R_2 = k_1' C_A$ ). Taking these considerations into account together with the initial conditions and boundary conditions, basic differential equations for dynamical analysis are summarized as follows:

$$\partial C_A / \partial t = D_A \partial^2 C_A / \partial x^2 - k_1' C_A \quad (8)$$

$$\partial C^* / \partial t = A C_0 \epsilon_\lambda \exp(-C_0 \epsilon_\lambda x) - k_1 C^* - k_1' C_A \quad (9)$$

$$\partial C_B / \partial t = k_1 C^* + k_1' C_A \quad (10)$$

[Initial Conditions]:  $t \leq 0$ ;  $C^* = C_A = C_B = 0$

[Boundary Conditions]: [I]  $t > 0$ ,  $x = 0$ ;  $C_A = C_{A0}$

[II]  $t > 0$ ,  $x \rightarrow +\infty$ ;  $C_A = 0$

[III]  $t > 0$ ,  $x = \delta$ ;  $\partial C_B / \partial x = 0$

### IV. RESULTS OF DYNAMICAL ANALYSIS

Solving the simultaneous differential equations under the given initial conditions and boundary conditions by the Laplace transformation method, analytical solutions (11)-(16) are obtained in the form of dimensionless concentrations (see Appendix B for the derivation of these equations):

$$\phi_A \equiv C_A(x, t) / C_{A0} = (1/2) \{ \exp(-x\sqrt{k_1'/D_A}) \operatorname{erfc}(x/2\sqrt{D_A t} - \sqrt{k_1' t}) + \exp(x\sqrt{k_1'/D_A}) \operatorname{erfc}(x/2\sqrt{D_A t} + \sqrt{k_1' t}) \} \quad (11)$$

$$\phi^* \equiv C^*(x, t) / C_0^* = \{1 - \exp(-k_1 t)\} \cdot \{ \exp(-C_0 \epsilon_\lambda x) - (C_{A0} / C_0^*) k_1' \phi_A \} \quad (12)$$

$$\begin{aligned} \phi_B \equiv C_B(x, t) / C^* = & [k_1 t - \{1 - \exp(k_1 t)\}] \\ & \cdot \{ \exp(-C_0 \epsilon_\lambda x) / k_1 \} + \{ (k_1' - k_1) C_{A0} / C_0^* \} \\ & \cdot \int_0^t \phi_A dt + \{1 - \exp(-k_1 t)\} \cdot (C_{A0} / C_0^*) \phi_A \end{aligned} \quad (13)$$

$$V \equiv \partial_B / \partial t = \{1 - \exp(-k_1 t)\} \cdot \exp(-C_0 \varepsilon_\lambda x) - (C_{A0}/C_0^*) k_1' \exp(-k_1 t) \phi_A \quad (14)$$

Here,

$$C_0^* \equiv C_0 A \varepsilon_\lambda \equiv C_0 \eta n_0 \varepsilon_\lambda / N_0$$

$$\operatorname{erfc} x = 1 - (2/\sqrt{\pi}) \int_0^x \exp(-\xi^2) d\xi \quad (15)$$

Profiles of functions based on calculations by a computer are shown in Fig.3~8.

## V. DISCUSSIONS

The degree of deterioration varies with time and depth, and it is influenced by the photochemical reaction constants ( $k_1$ ,  $k_1'$ ) and diffusion coefficient ( $D_A$ ). In Fig.4, 6, 7, and 8 are shown the changes of the space-distribution of each concentration function with time, and the influence of photooxidation and oxygen diffusion on the distribution of oxygen are shown in Fig.3 and 5, respectively. Deriving the time dependence of surface deterioration, we obtain equation (16):

$$\begin{aligned} \phi_B(0, t) &= [k_1 t - \{1 - \exp(-k_1 t)\}] / k_1 + (C_{A0}/C_0^*) \\ &\quad \cdot [(k_1' - k_1) t + 1 - \exp(-k_1 t)] \\ &\approx k_1' t (C_{A0}/C_0^*) \\ &= k_1 C_{A0} t \end{aligned} \quad (16)$$

This shows that surface deterioration advances approximately in proportion to exposure time, and that the progress of deterioration depends upon the surface oxygen concentration and the rate constant for photooxidation, though it depends, of course, linearly upon the number of photons absorbed, and consequently, upon the intensity of incident UV-light.

That the deterioration proceeds continuously inward from surface with time can be observed in IR absorption spectra and in the change of materials properties. For example, Watanabe et al. [10] have measured IR absorption spectra for sliced samples of outdoor-exposed organic polymer plate of polystyrene (PS) and polyoxymethylene (POM) and other polymers. These experimental data are compared with the theoretical results in Fig.9.a) and 9.b). The fact that the progress of the deterioration is reflected in the change of the IR absorption spectra for the



deteriorated surface layer has been confirmed by the author for inorganic polymers as well [11-12]. Fig.10.a) shows the change of the IR absorption for the hardening of a film of sodium silicate water-glass ( $\text{Na}_2\text{O} \cdot 3.2\text{SiO}_2$ ) for the surface treatment of asbesto-cement board, and Fig. 10.b) for the deterioration of films of sodium silicate water-glass for the surface treatment of steel plate during immersion in 50°C hot water (drying at 120°C). The IR spectra were measured by an infrared spectrophotometer equipped with a micro-computer (HITACHI model 260-50) by the surface reflection-absorption method using a TlCl-TlBr total reflection prism.

In this theory, thermal oxidation is not taken into account directly as an elementary process. But, from the above discussions, we can explain the progress of deterioration of polymeric materials by the chemical attack of penetrative reagents (mainly oxygen) on the activated polymer molecules (mainly by the absorption of UV-light, but possibly also by thermal activation). Eurin [13] has given a valuable review of the degradation of organic polymeric materials, in which he has pointed out the importance of photooxidation and thermal oxidation reactions. Though he ingeniously explained the progress of photochemical degradation, he did not refer to the progress of deterioration inward from surface. The author would like to point out that the deterioration progresses continuously from the surface, and that the evaluation of the degree of deterioration is very important in comparing the durability of building materials.

On the other hand, using the boundary condition [III] i.e.,  $\partial\phi_B/\partial t|_{x=\delta}=0$ , we can obtain approximately the time dependence of the depth of deteriorated layer (see Appendix C for details of the derivation of this equation):

$$\delta = \sqrt{\beta t} \quad \beta \equiv \beta(D_A, k_1, k_1') \quad (17)$$

From this result, it can be shown that the depth of the deteriorated layer increases approximately in proportion to the square root of exposure time. This  $\sqrt{t}$  law (parabolic law) was obtained for the first time for the progress of deterioration



of polymeric materials as the natural derivation based on the unsteady-state dynamical analysis, assuming the simultaneous action of UV-light and diffusive oxygen. Fig.11.a) and b) show the comparison of experimental results with the theory by the least-squares plots. The experimental data are from Kubota et al. [14]. It can be seen that many polymeric materials show the deterioration by the power law of exposure time ( $t^n$ :  $n = 0.5 \sim 1.0$ ). The difference between theory and experiment is considered to be due to deterioration mechanisms which involve depolymerization and photooxidation. If the deterioration is determined by depolymerization, it is expected to proceed linearly with time, and if it is controlled by photooxidation, the progress of deterioration obeys the power law. Usually, the deterioration of polymers occurs by a combination of the two reactions, so that the deterioration of many polymers obeys the power law. To fully understand the deterioration mechanism, it is necessary for us to look at them in more detail. Recently, the author has observed the same parabolic law experimentally in the deterioration by water of water-glass films [11-12].

The parameter  $\beta$  which determines the progress of deterioration is a function of materials property constants ( $D_A, k_1, k_1'$ ), and the progress of deterioration could be evaluated approximately by the parabolic law, if extrinsic factors and these material property constants are clearly quantified. Further, since these constants are functions of temperature as shown in equations (6), (7), the effects of temperature on the progress of deterioration can be considered to be included implicitly in the parabolic law.

Such unsteady-state dynamical analysis should be also applicable to other types of deterioration processes. The author has just applied the same analytical method to the carbonation and neutralization processes of concrete [15-16].

Defining a deterioration progress factor ( $X$ ) as the ratio of the depth of the deteriorated layer to the plate thickness, and considering that deteriorated layers do not contribute to the flexural strength of the plate, the following law for the

reduction in flexural strength with the advance of deterioration can be obtained:

$$X(t) = \delta(t)/L; \quad (0 \leq X \leq 1) \quad (18)$$

$$\begin{aligned} F(t) &= A\{L - \delta(t)\}^2 = AL^2 [1 - \delta(t)/L]^2 \\ &= F_0 \{1 - X(t)\}^2 \end{aligned} \quad (19)$$

where  $A$  is a constant, and  $F$  is the flexural strength of the plates in the initial undeteriorated state. It is assumed, as is often observed experimentally, that the flexural strength is proportional to the second power of the thickness of the plates. According to Watanabe et al. [10], deteriorated layers near the surface of polystyren plates exposed to natural weathering for five years, far from not contributing to the flexural strength, influence the inner undeteriorated layers, and reduce their specific flexural strength. This experimental fact suggests that the deterioration progresses continuously deeper into the polymer plates than is expected. This point must be studied more in detail, and the influence of deterioration on various kinds of mechanical strength such as compressive, tensile and flexural strength, must be considered.

## VI. CONCLUSIONS

The deterioration of polymeric materials by the simultaneous action of UV-light and diffusive oxygen was theoretically analyzed based on an unsteady-state dynamics. The theoretical results are compared with experimental data.

The deterioration of polymeric materials progresses inward from surface, and the degree of deterioration varies with time and depth. The increase in the depth of the deteriorated layer is approximately in accord with the parabolic ( $\sqrt{t}$ ) law.

The deteriorated layer influences the mechanical strength (say, flexural strength), resulting in the reduction in the total strength of polymeric materials.

## VII. ACKNOWLEDGEMENTS

The author would like to express great thanks to Dr. Y. Watanabe, Dr. H. Kubota and their coworkers for their supplying

valuable experimental data about the deterioration of polymeric materials. He also thanks to Mr. T. Nireki, Head of the Durability Division of Materials Department of Building Research Institute for his kind discussion. He would like to express his appreciation for kind help to Dr. S. Fujimatsu, Director and other research members of the Materials Department of Building Research Institute.

#### REFERENCES

- [1] Nireki, T. " Series of durability research, 7th report: Acceleration factor of sunshine carbon arcs ", Proceedings of Annual Symposium of Architectural Institute of Japan, Tokai, October, pp. 225-226, 1985 (in Japanese).
- [2] Nireki, T. " Performance evaluation of vertical external walls: Evaluation of surface finishing materials ", Proceedings of RILEM/ASTM/CIB Symposium, Otaniemi, Finland, August, pp. 197-209, 1977.
- [3] Nireki, T. " An approach to durability studies on the basis of performance concept ", Proceedings of 7th CIB Congress, Edinburgh, United Kingdom, September, pp. 1-6, 1977.
- [4] Shirayama, K., Imaizumi, K. and Nireki, T. " Application of performance concept in Japan ", Proceedings of 7th CIB Congress, Edinburgh, United Kingdom, September, pp. 129-136, 1977.
- [5] Fukushima, T. " Effective use of inorganic polymers for building materials: Deterioration process of polymeric materials and its correlation with depth from surface " Annual report of Building Research Institute, Tsukuba, pp. 136-141, 1978 (in Japanese).
- [6] Fukushima, T. " Deterioration process of polymeric materials and its correlation with depth from surface: Dynamical analysis based on kinetic theory on the complex deterioration by the simultaneous action of UV-light and diffusive oxygen ", Proceedings of Annual Symposium of Architectural Institute of Japan, Kanto, September, pp. 261-262, 1977 (in Japanese).



- [7] Hamada, M. " Neutralization (Carbonation) of concrete and corrosion of reinforcing steel ", Proceedings of 5th International Symposium on the Chemistry of Cement, Tokyo, Japan, December, pp. 343-384, 1969.
- [8] Motto, N. F., Trans. Faraday Soc., 35, p. 1175, 1939; 36, p. 472, 1940.
- [9] Motto, N. F., ibid, 43, p. 429, 1947.
- [10] Watanabe, Y., Kitajima, F. and Hattori, S. " Errosion process on the deterioration of polymeric materials under outdoor and artificially accelerated exposure ", Proceedings of 15th Symposium of Polymer Research Works of Japan Industrial Technology Association, Tokyo, October, pp. 177-184, 1979 (in Japanese).
- [11] Fukushima, T., " Effective use of inorganic polymers for building materials: Hardening processes of cement and water-glass, and the influence of hardening conditions on their durability ", Annual Report of Building Research Institute, Tsukuba, pp. 81-84, 1979 (in Japanese).
- [12] Fukushima, T., " Hardening processes of water-glass inorganic polymer films and the influence of hardening conditions on their durability ", Proceedings of Annual Symposium of Architectural Institute of Japan, Kinki, September, pp. 363-364, 1980 (in Japanese).
- [13] Eurin, Ph. "Degradation process of organic building materials: A short review and some proposals for research ", Durability of Building Materials 1, pp. 161-168, 1982.
- [14] Kubota, H., Suzuki, S., Nishimura, O., Yoshikawa, K. and Shiota, T. " Change of surface behavior of thermoplastics under outdoor and artificially accelerated exposure ", Proceedings of 15th Symposium of Polymer Research Works of Japan Industrial Technology Association, Tokyo, October, pp. 147-163, 1979 (in Japanese).
- [15] Fukushima, T. " Effective use of inorganic polymers for building materials: Dynamical analysis based on chemical kinetics on the neutralization of concrete and on the suppressing effect of water-glass inorganic polymer films ",



Annual Report of Building Research Institute, Tsukuba,  
pp. 53-55, 1980 (in Japanese).

- [16] Fukushima, T. " Consideration based on kinetic theory on the correlation between carbonation and neutralization processes of concrete ", Proceedings of Annual Symposium of Architectural Institute of Japan, Kyushu, September, pp. 405-406, 1981 (in Japanese).

## APPENDIX A: Absorption process of UV-light

Let us consider a polymer plate of thickness  $L$  and the cross section  $S$ , as shown in Fig.1, and take the  $x$ -axis perpendicular to the plate surface.

When UV-light (wavelength,  $\lambda$ ; intensity,  $I_{\lambda_0}$ ) falls on the surface of a plate at an angle  $\theta$ , a part of the light is reflected from the surface at the rate of  $R(\theta, \lambda)$ , and the rest is transmitted into the plate. Consequently the energy flux at the surface for the UV-light transmitted into the plate is given as follows:

$$\Phi_{\lambda_0} = \{1 - R(\theta, \lambda)\} I_{\lambda_0} / S \quad (A1)$$

Representing the energy flux at the depth  $x$  below the surface as  $\Phi_{\lambda}(x)$  and the linear absorption coefficient as  $\kappa_{\lambda}$  the energy absorbed per unit time and unit area within the infinitesimal plate (thickness,  $dx$ ) shown in Fig.2 is:

$$\begin{aligned} - d\Phi_{\lambda} &= \Phi_{\lambda}|_x - \Phi_{\lambda}|_{x+dx} = -(d\Phi_{\lambda}/dx)dx \\ &= \kappa_{\lambda} \Phi_{\lambda}(x) dx \end{aligned} \quad (A2)$$

Consequently, the following equation can be obtained.

$$d\Phi_{\lambda}/dx = -\kappa_{\lambda} \Phi_{\lambda}(x) \quad (A3)$$

$\kappa_{\lambda}$  is usually constant in an undeteriorated transmitting media, but if the deterioration advances, it is considered generally to depend upon the depth from surface ( $x$ ) and time ( $t$ ), i. e.,  $\kappa_{\lambda} \equiv \kappa_{\lambda}(x, t)$ . For convenience, however, it is assumed to be constant throughout this theoretical model.

The linear absorption coefficient ( $\kappa_{\lambda}$ ) can be correlated with a molar absorption coefficient ( $\epsilon_{\lambda}$ ) as follows:

$$\kappa_{\lambda} = C_0 \epsilon_{\lambda} \quad (A4)$$

where  $C_0$  is the initial concentration of undeteriorated polymer molecules.

From equations (A1), (A3), and (A4), the energy flux at a depth  $x$  from the surface ( $\Phi_{\lambda}(x)$ ) is:

$$\Phi_{\lambda}(x) = \Phi_{\lambda_0} \exp(-C_0 \epsilon_{\lambda} x) \quad (A5)$$

Consequently, the photon flux at a depth of  $x$  from the surface  $n(x)$  is obtained, using the Plank constant ( $h$ ), the velocity of light ( $c$ ), and the wavelength of the incident UV-light ( $\lambda$ ), is:

$$n(x) = \Phi_{\lambda}(x) / h(c/\lambda)$$

$$\begin{aligned}
&= (\lambda \Phi_{\lambda_0} / hc) \exp(-C_0 \epsilon_{\lambda} x) \\
&= n_0 \exp(-C_0 \epsilon_{\lambda} x) \\
\partial n / \partial x &= -C_0 \epsilon_{\lambda} n \quad n_0 \equiv \lambda \Phi_{\lambda_0} / hc
\end{aligned} \tag{A6}$$

where  $n_0$  is the photon flux at the surface of the plate.

According to the law of photochemical equivalence, absorbed photons generate as many activated polymer molecules, some of which can participate in photochemical reactions (reaction efficiency,  $\eta$ ), while the rest of which are likely to be thermally or radiately deactivated into the ground state. Consequently, the number of active polymer molecules generated within the infinitesimal plate per unit time is  $\eta \cdot (-\partial n / \partial x) \cdot S dx$ , the mole number being  $(\eta N_0) \cdot (-\partial n / \partial x) \cdot S dx$  ( $N$  : Avogadro's constant).

The accumulation rate of active molecules within the infinitesimal plate is represented as  $(\partial C^* / \partial t) \cdot S dx$  ( $C^*$ , molar concentration of active polymer molecules), and the annihilation rate is  $R \cdot S dx$  ( $R$ , annihilation rate of active polymer molecules and creation rate of deteriorated polymer molecules).

Considering the material balance within the infinitesimal plate, the following equation is derived:

$$(\partial C^* / \partial t) S dx = -(\eta / N_0) \cdot (\partial n / \partial x) S dx - R \cdot S dx$$

so that:

$$(\partial C^* / \partial t) = -(\eta / N_0) \cdot \partial \eta / \partial x - R \tag{A7}$$

## APPENDIX B: Derivation of dimensionless functions

Fundamental differential equations are summarized as follows, together with the initial and boundary conditions:

[DIFFERENTIAL EQUATIONS]

$$\partial C_A / \partial t = D_A \partial^2 C_A / \partial x^2 - k_1 C_A \tag{B1}$$

$$\partial C^* / \partial t = A C_0 \epsilon_{\lambda} \exp(-C_0 \epsilon_{\lambda} x) - k_1 C^* - k_1 C_A \tag{B2}$$

$$\partial C_B / \partial t = k_1 C^* + k_1 C_A \tag{B3}$$

$$[\text{Initial Conditions}]; \quad t \leq 0, \quad x > 0: \quad C_A = C_B = C^* = 0 \tag{B4}$$

$$[\text{Boundary Conditions}]; \quad [\text{I}] \quad t > 0, \quad x = 0, \quad C_A = C_{A_0} \tag{B5}$$

$$[\text{II}] \quad t > 0, \quad x \rightarrow \infty: \quad C_A = 0 \tag{B6}$$

$$[\text{III}] \quad t > 0, \quad x = \delta: \quad \partial C_B / \partial x = 0 \tag{B7}$$

Converting equation (B1) into the form of Laplace

transformation ( $\tilde{C}_A$ , Laplace transformed function of  $C_A$ ;  
 $\tilde{C}_A = \int_0^\infty e^{-st} C_A(x, t) dt$ ),

$$\begin{aligned} s\tilde{C}_A &= D_A d^2 \tilde{C}_A / dx^2 - k_1' \tilde{C}_A \\ d^2 \tilde{C}_A / dx^2 &= (s + k_1') / D_A \end{aligned} \quad (B8)$$

Solving this second order differential equation,

$$\tilde{C}_A(s) = p e^{\omega x} + q e^{-\omega x} \quad (\omega = \sqrt{(s + k_1') / D_A}),$$

p, q: integration constants)

From the boundary conditions (B5), (B6):

$$p + q = C_{A0} / s, \quad p = 0$$

Consequently.

$$\tilde{C}_A(s) = (C_{A0} / s) \exp(-x \sqrt{(s + k_1') / D_A}) \quad (B9)$$

Doing the reversed Laplace transformation, the following analytical solution for the concentration function of oxygen  $C_A(x, t)$  is obtained:

$$\begin{aligned} \{C_A(x, t) / C_{A0}\} &\equiv \phi_A(x, t) \\ &= (1/2) \{ \exp(-x \sqrt{k_1' / D_A}) \cdot \operatorname{erfc}(x / 2 \sqrt{D_A t} - \sqrt{k_1' t}) \\ &\quad + \exp(x \sqrt{k_1' / D_A}) \cdot \operatorname{erfc}(x / 2 \sqrt{D_A t} + \sqrt{k_1' t}) \} \end{aligned} \quad (B10)$$

and the flux function of oxygen  $N_A(x, t)$  is:

$$\begin{aligned} N_A(x, t) &= D_A \partial C_A / \partial x \\ &= (C_{A0} \sqrt{k_1' / D_A}) \phi_A + (C_{A0} / 2) \sqrt{D_A / \pi t} \\ &\quad [ \exp(-x \sqrt{k_1' / D_A}) \cdot \exp\{-(x / 2 \sqrt{D_A t} - \sqrt{k_1' t})^2\} + \\ &\quad \exp(x \sqrt{k_1' / D_A}) \cdot \exp\{-(x / 2 \sqrt{D_A t} + \sqrt{k_1' t})^2\} ] \end{aligned} \quad (B11)$$

From equation (B2), the following Laplace transformed form is derived:

$$s\tilde{C}^* = AC_0 \varepsilon_\lambda \exp(-C_0 \varepsilon_\lambda x) / s - k_1' \tilde{C}^* - k_1' \tilde{C}_A \quad (B12)$$

( $\tilde{C}^*$ , Laplace transforms function of  $C^*$ ;

$$\tilde{C}^* = \int_0^\infty e^{-st} C^*(x, t) dt)$$

Inserting equation (B9) into (B12)

$$\begin{aligned} \tilde{C}^*(s) &= AC_0 \varepsilon_\lambda \exp(-C_0 \varepsilon_\lambda x) / (s(s + k_1')) \\ &\quad - k_1' C_{A0} \exp\{-x \sqrt{(s + k_1') / D_A}\} / (s(s + k_1')) \end{aligned} \quad (B13)$$

By reversed Laplace transformation

$$\begin{aligned} \{C_A^*(x, t) / C_0\} &= \{1 - \exp(-k_1 t)\} / k_1 \\ &\quad \cdot \{A \varepsilon_\lambda \exp(-C_0 \varepsilon_\lambda x) - k_1' (C_{A0} / C_0) \phi_A(x, t)\} \end{aligned}$$

Inserting the equation (B9), (B13) into (B3),



$$\partial/\partial t \{C_B(x, t)/C_0\} = \{1 - \exp(-k_1 t)\} A \varepsilon_\lambda \exp(-C_0 \varepsilon_\lambda x) - k_1' (C_{A0}/C_0) \phi_A(x, t) \cdot \exp(-k_1 t)$$

By integrating concerning times (t),

$$\begin{aligned} \{C_B(x, t)/C_0\} &= [t - \{1 - \exp(-k_1 t)\}]/k_1 \cdot A \varepsilon_\lambda \exp(-C_0 \varepsilon_\lambda x) \\ &+ (k_1' - k_1) \cdot (C_{A0}/C_0) \int_0^t \phi_A dt \\ &+ \{1 - \exp(-k_1 t)\} (C_{A0}/C_0) \phi_A \end{aligned} \quad (B14)$$

Summarizing the analytical results as dimensionless concentration functions, the equations (11), (12), (13), and (14) described in section IV are obtained.

#### APPENDIX C: Derivation of the parabolic law

Let us derive the deterioration depth as a function of exposure time from the boundary condition [III] shown in equation (B7):

$$\begin{aligned} \partial C_B / \partial x|_{x=\delta} &= (-C_0 \varepsilon_\lambda / k_1) \cdot [k_1 t - \{1 - \exp(-k_1 t)\}] \exp(-C_0 \varepsilon_\lambda x) \\ &+ (k_1' - k_1) (C_{A0}/C_0) \cdot \partial / \partial x \{ \int_0^t \phi_A(x, t) dt \} |_{x=\delta} \\ &+ 1 - \exp(-k_1 t) \} (C_{A0}/C_0) \cdot \partial \phi_A / \partial x|_{x=\delta} = 0 \end{aligned} \quad (C1)$$

We can neglect the first term at comparatively short exposure times as  $k_1 \approx 1 - \exp(-k_1 t)$ , so that:

$$\begin{aligned} (k_1' - k_1) \partial / \partial x \{ \int_0^t \phi_A(x, t) dt \} |_{x=\delta} &+ \{1 - \exp(-k_1 t)\} \partial \phi_A / \partial x|_{x=\delta} = 0 \quad (C2) \\ 2 \phi_A / \partial x|_{x=\delta} &= \sqrt{k_1' / D_A} [ \exp(\delta \sqrt{k_1' / D_A}) \operatorname{erfc}(\delta / 2 \sqrt{D_A t} + \sqrt{k_1' t}) \\ &- \exp(-\delta \sqrt{k_1' / D_A}) \operatorname{erfc}(\delta / 2 \sqrt{D_A t} - \sqrt{k_1' t}) ] \\ &+ (1 / \sqrt{\pi D_A t}) [ \exp(\delta \sqrt{k_1' / D_A}) \exp\{-(\delta / 2 \sqrt{D_A t} + \sqrt{k_1' t})^2\} \\ &+ \exp(-\delta \sqrt{k_1' / D_A}) \exp\{-(\delta / 2 \sqrt{D_A t} - \sqrt{k_1' t})^2\} ] \end{aligned} \quad (C3)$$

Making use of the following approximation:

$$\begin{aligned} \operatorname{erfc}(\delta / 2 \sqrt{D_A t} \pm \sqrt{k_1' t}) &\approx 1 - (2 / \sqrt{\pi}) (\delta / 2 \sqrt{D_A t} \pm \sqrt{k_1' t}) \\ \exp\{-(\delta / 2 \sqrt{D_A t} \pm \sqrt{k_1' t})^2\} &\approx 1 - (1/2) (\delta / 2 \sqrt{D_A t} \pm \sqrt{k_1' t}) \\ 1 - \exp(-k_1 t) &\approx k_1 t \end{aligned}$$

$$\begin{aligned} \partial \phi_A / \partial x|_{x=\delta} &\approx \sqrt{k_1' / D_A} \{ (\delta / \sqrt{D_A t}) \sinh(\delta \sqrt{k_1' / D_A}) \\ &+ 2 \sqrt{k_1' t} \cosh(\delta \sqrt{k_1' / D_A}) \\ &+ (1/2 \sqrt{D_A t}) \{ 2 \cosh(\delta \sqrt{k_1' / D_A}) \\ &- (\delta^2 / 4 D_A t) \cosh(\delta \sqrt{k_1' / D_A}) \} \end{aligned}$$

$$\begin{aligned}
& - (\delta \sqrt{k_1'/D_A}) \sinh(\delta \sqrt{k_1'/D_A}) \\
& - k_1 t \cosh(\delta \sqrt{k_1'/D_A}) \\
& \approx \sqrt{k_1'/\pi D_A} \cdot \{ (\delta^2/D_A) \sqrt{k_1' t} + 2\sqrt{k_1' t} \} \\
& + (1/2\sqrt{\pi D_A t}) \{ 2 - (\delta^2/4D_A t) - (k_1'/D_A) \delta^2 - k_1' t \} \\
& = (4k_1' t - 1) (\delta^2/8D_A t \sqrt{\pi D_A t}) + (3k_1' t + 2) / 4D \\
& + (3k_1' t + 2) / 2\sqrt{\pi D_A t} \tag{C4}
\end{aligned}$$

$$\begin{aligned}
\int_0^t \partial \phi_A / \partial x |_{x=\delta} dt & = (4k_1' t + 1) (\delta^2/4D_A \sqrt{\pi D_A t}) \\
& + \sqrt{k_1'/\pi D_A t} (k_1' t + 2) \tag{C5}
\end{aligned}$$

Using the relation:

$$\partial / \partial x \{ \int_0^t \phi_A(x, t) dt \} |_{x=\delta} = \int_0^t (\partial \phi_A / \partial x |_{x=\delta}) dt$$

and inserting equation (C4) and (C5) into (C2), we can obtain the following equations:

$$\begin{aligned}
& (k_1' - k_1) \{ 2\delta^2 t (4k_1' t + 1) + 8D_A t^2 (k_1' t + 1) \} \\
& + k_1 t \{ \delta^2 (4k_1' t - 1) + 4D_A t (3k_1' t + 2) \} = 0 \tag{C6}
\end{aligned}$$

$$\begin{aligned}
\delta^2 & = 4D_A t \{ k_1' (k_1 + 2k_1') t - 2(k_1 - 2k_1') \} / \{ 4k_1' \\
& \quad (k_1 - 2k_1') t + 3k_1 - 2k_1' \} \\
& = 4D_A t [A + B / \{ 4k_1' (k_1 - 2k_1') t + 3k_1 - 2k_1' \}] \tag{C7}
\end{aligned}$$

$$A = (k_1 + 2k_1') / (k_1 - 2k_1') \tag{C8}$$

$$B = 8k_1'^2 / (k_1 - k_1') \tag{C9}$$

As a result:

$$\delta \approx \sqrt{\beta t} \tag{C10}$$

$$\beta \approx D_A (5k_1 + 2k_1') (7k_1 - 2k_1') / (k_1 - 2k_1') (3k_1 - 2k_1') \tag{C11}$$

## FIGURE CAPTIONS

- Fig.1. Incidence of UV-light upon the surface of a polymeric material.
- Fig.2. Material fluxes within an infinitesimal layer of a polymeric plate.
- Fig.3. Influence of photooxidation on the distribution of oxygen.
- Fig.4. Time dependence of the distribution of oxygen.
- Fig.5. Influence of diffusion on the distribution of oxygen.
- Fig.6. Time dependence of the distribution of the activated polymer molecules.
- Fig.7. Profile of the rate of production of deteriorated polymer molecules.
- Fig.8. Time dependence of each concentration function at constant distances from the surface of a polymeric plate.
- Fig.9.a) Change of IR absorption with distance below the surface of polystyrene (PS) polymer exposed outdoors (at Choshi) for three years (from Watanabe et al. [10]).
- Fig.9.b) Change of IR absorption with distance below the surface of polyoxymethylene (POM) polymer exposed outdoors (at Choshi) for five years (from Watanabe et al. [10]).
- Fig.10.a) Hardening of a film of sodium silicate water-glass ( $\text{Na}_2\text{O} \cdot 3.2\text{SiO}_2$ ) for the surface treatment of asbesto-cement board.
- Fig.10.b) Deterioration of films of sodium silicate water-glass for the surface treatment of a steel plate during immersion in 50°C hot water (drying at 120°C).
- Fig.11.a) Least-squares plot using the power law for the depth of the deteriorated layer of polyvinyl chloride (PVC) after various periods of outdoor exposure. Experimental data are from Kubota et al. [14].
- Fig.11.b) Least-squares plot using the power law for the depth of the deteriorated layer of various polymers after various periods of outdoor exposure (at Choshi). Experimental data are from Kubota et al. [14].

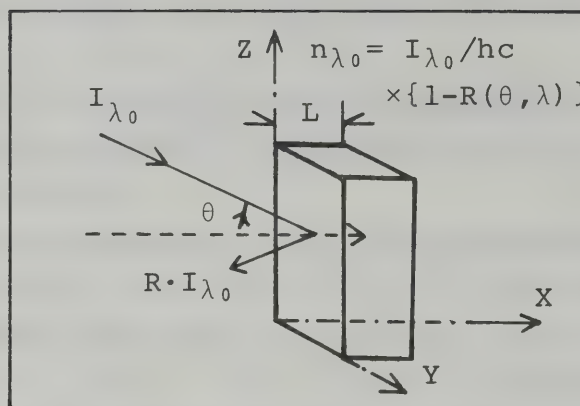


Fig.1.

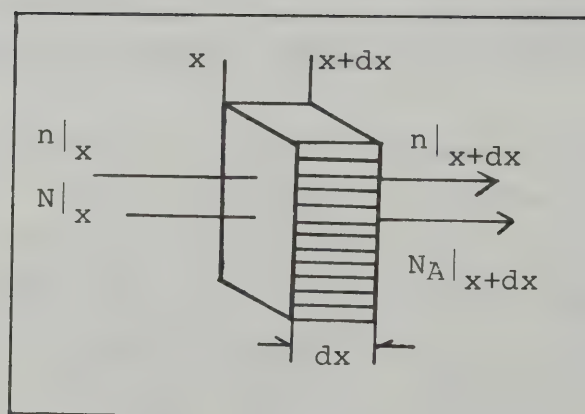


Fig.2.



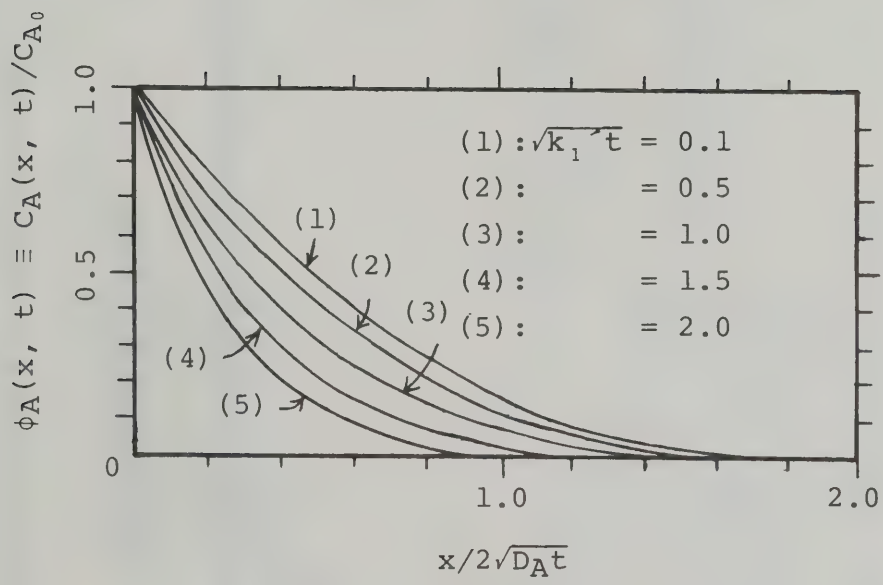


Fig.3.

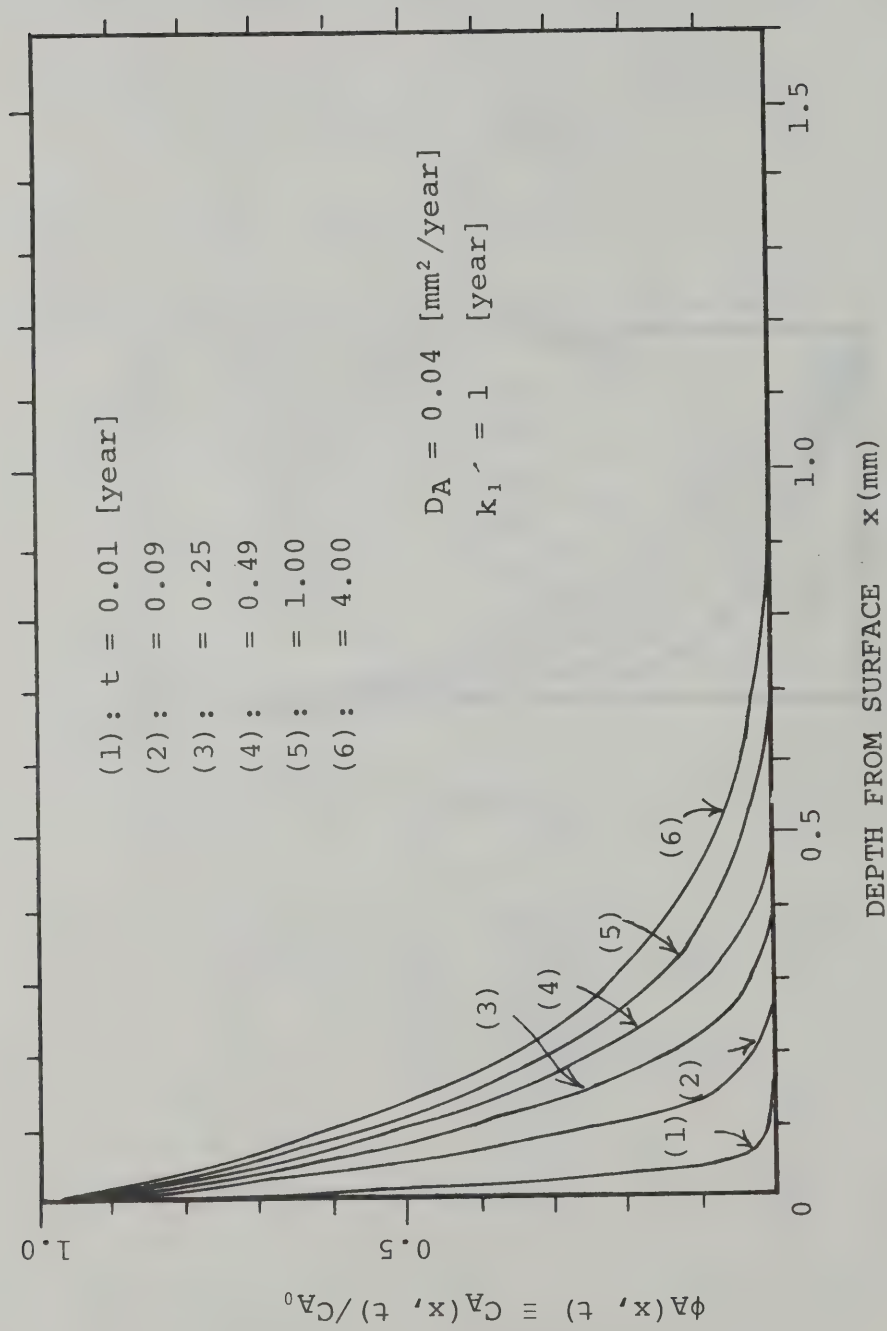


Fig. 4.

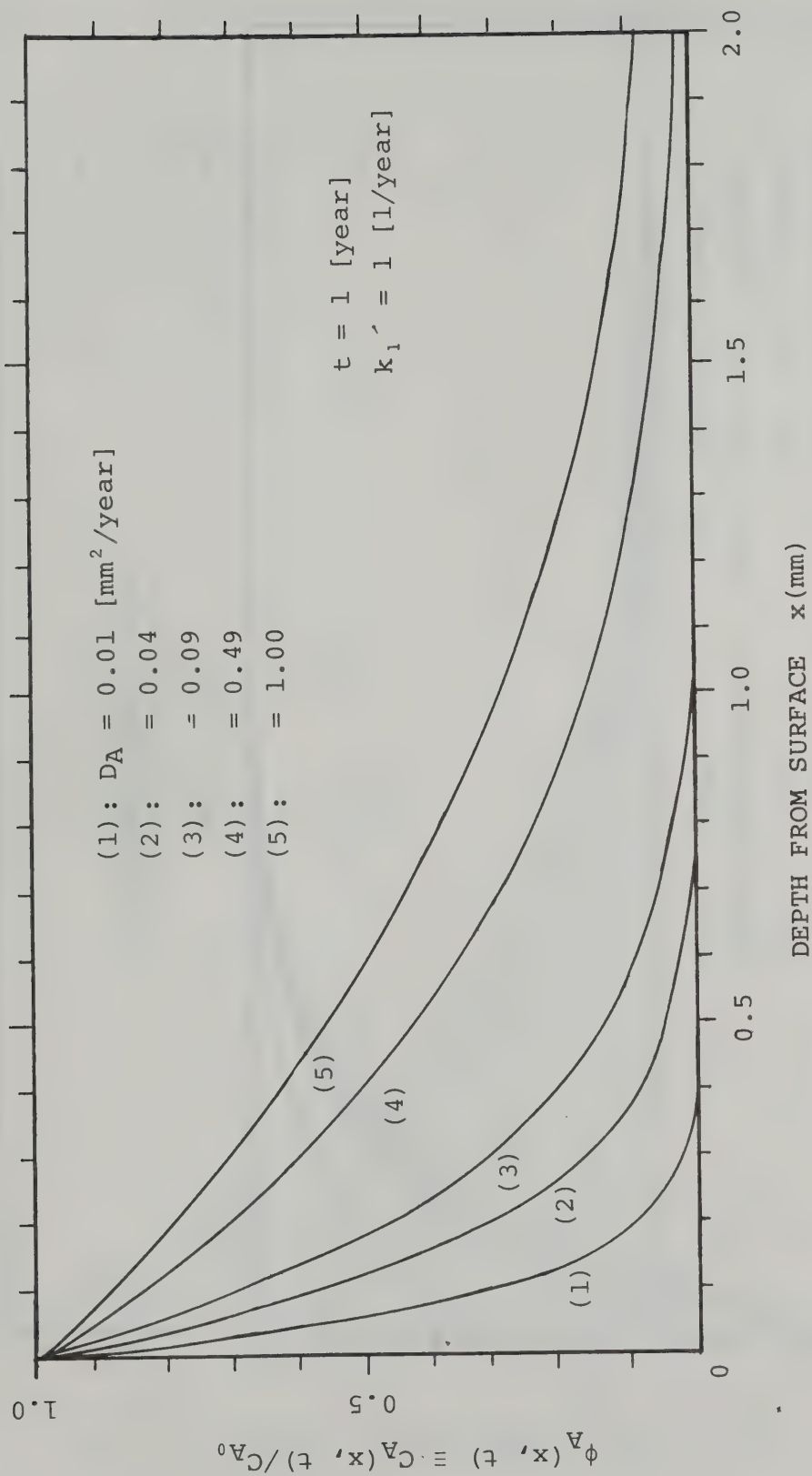


Fig.5.

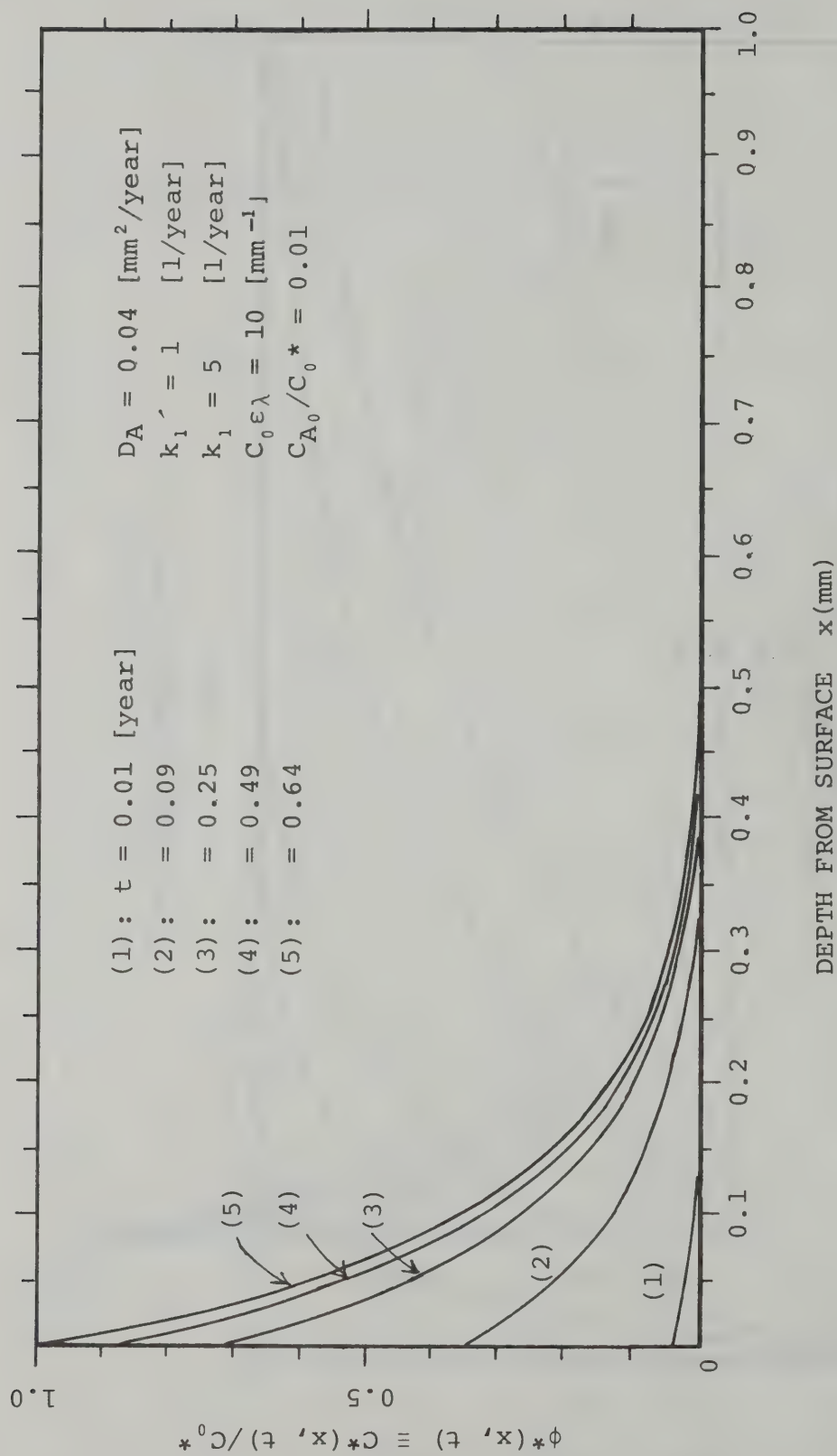


Fig. 6.



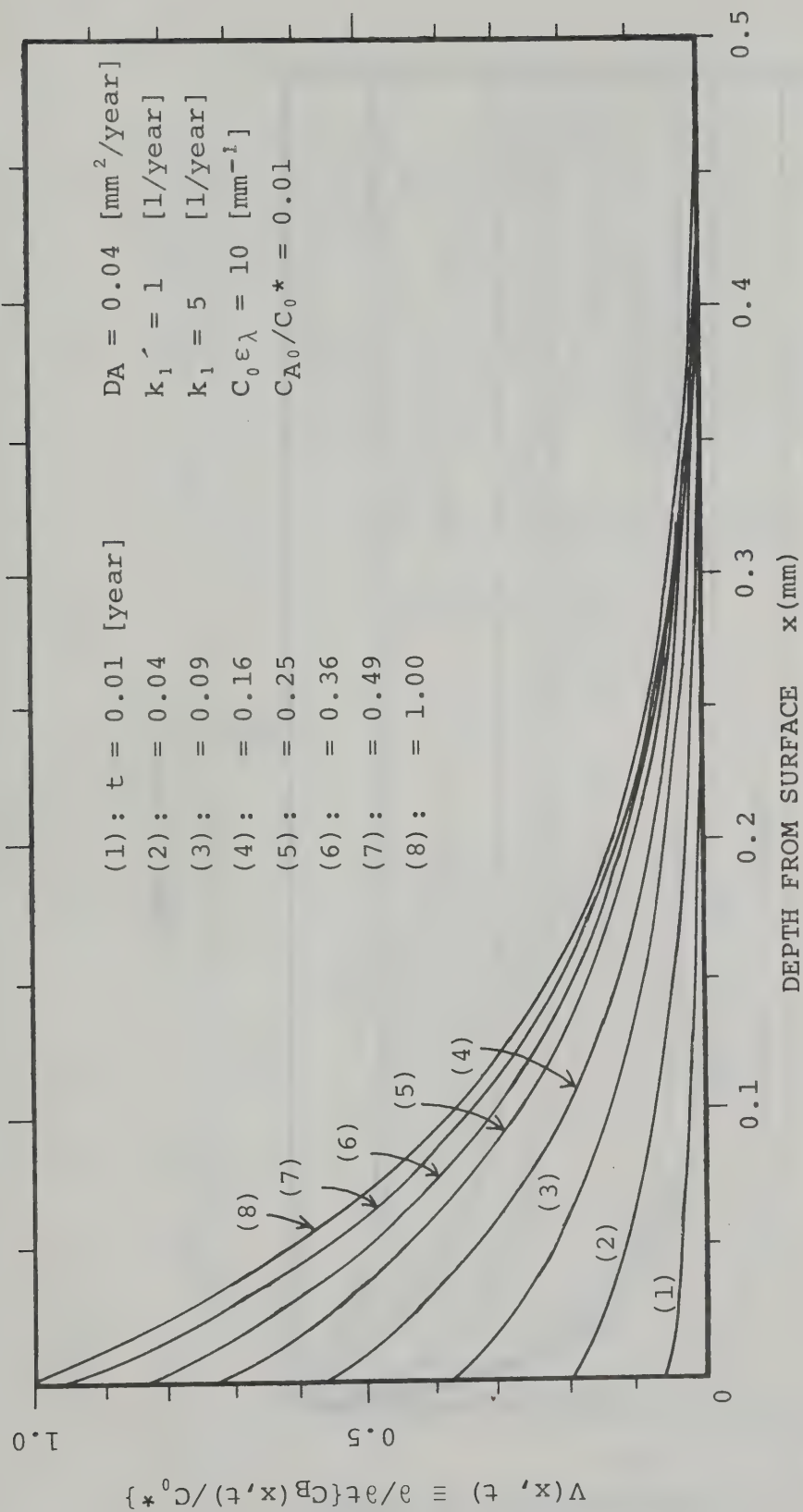


Fig.7.

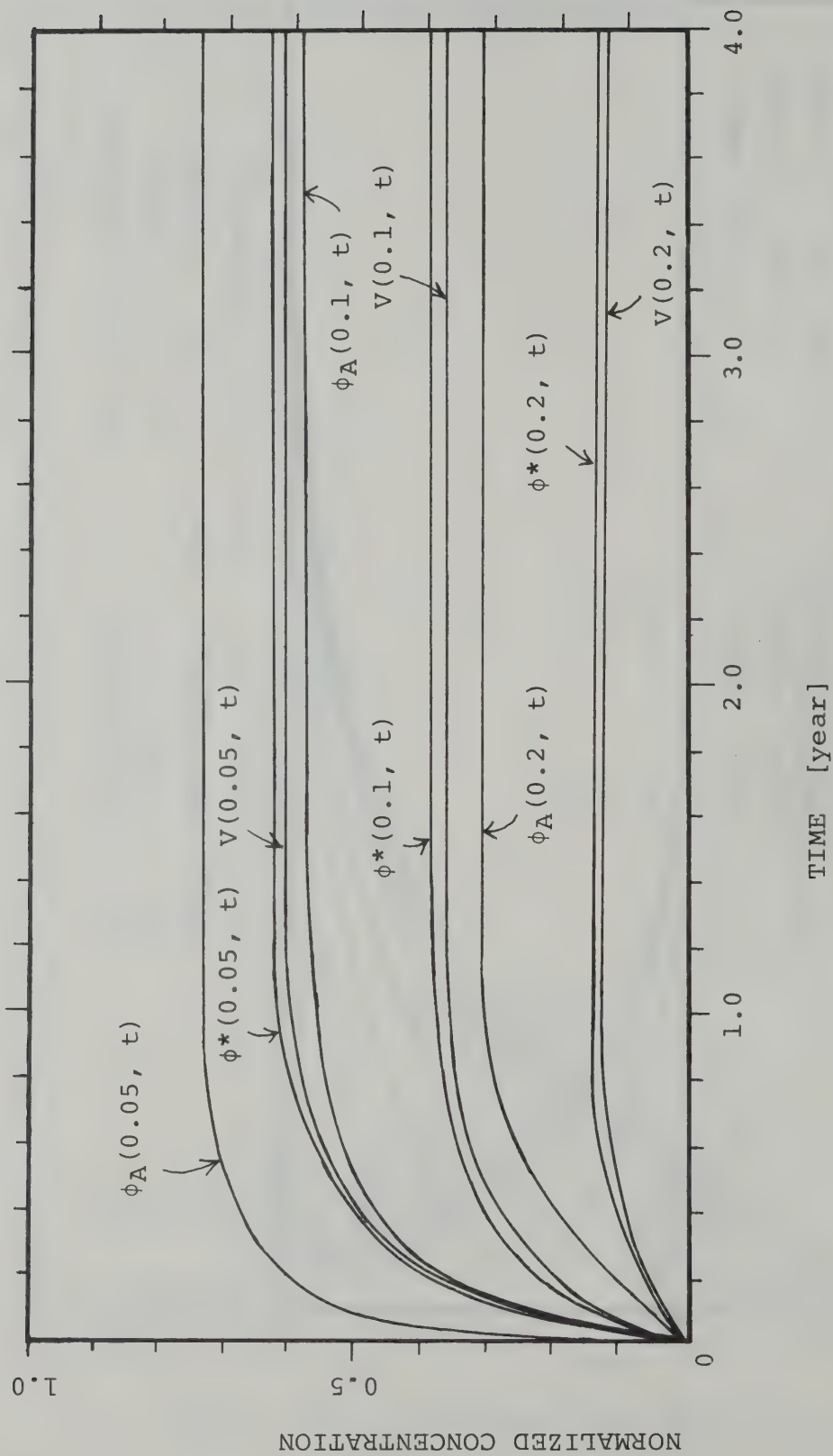


Fig.8.

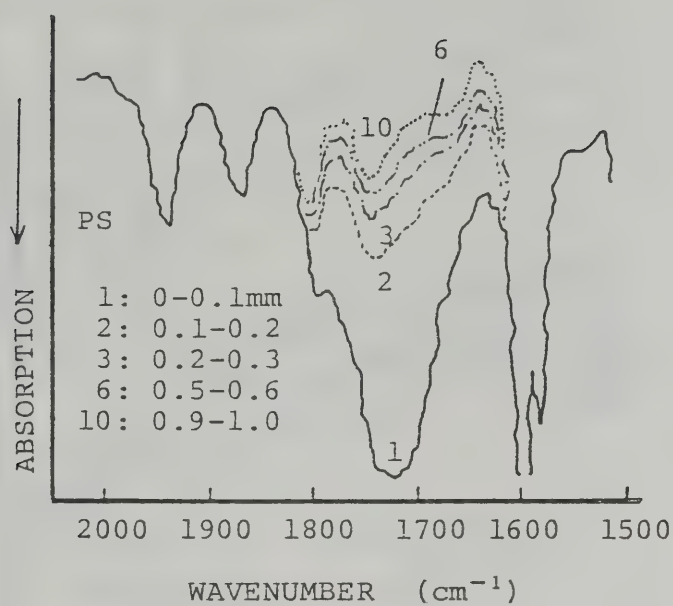


Fig.9a.)

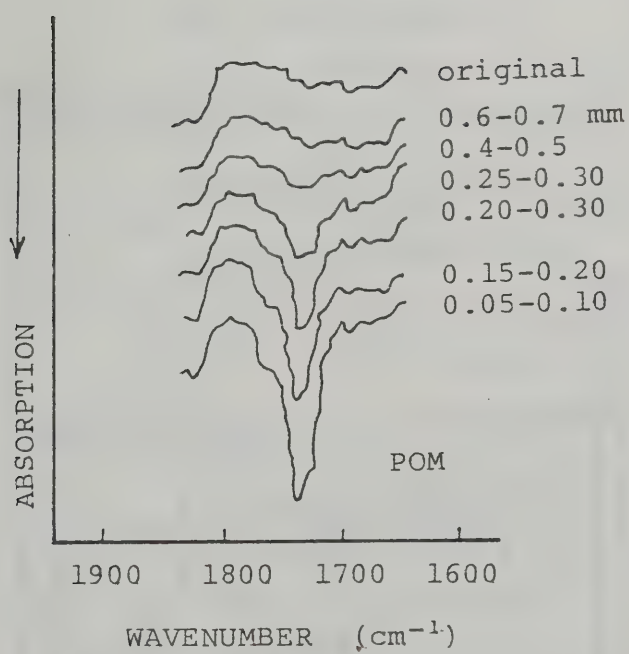


Fig.9b)

Fig.10a)

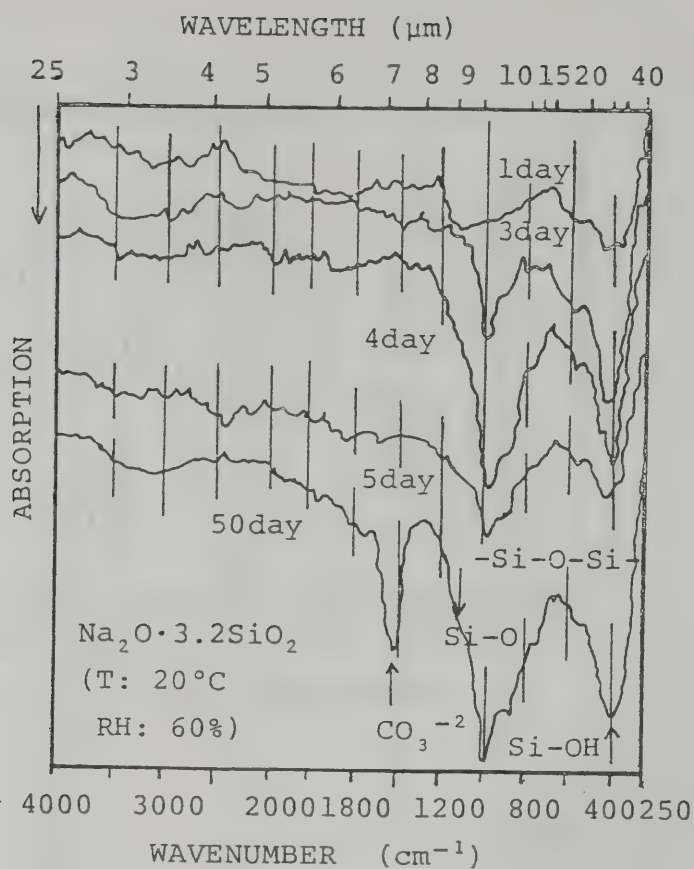
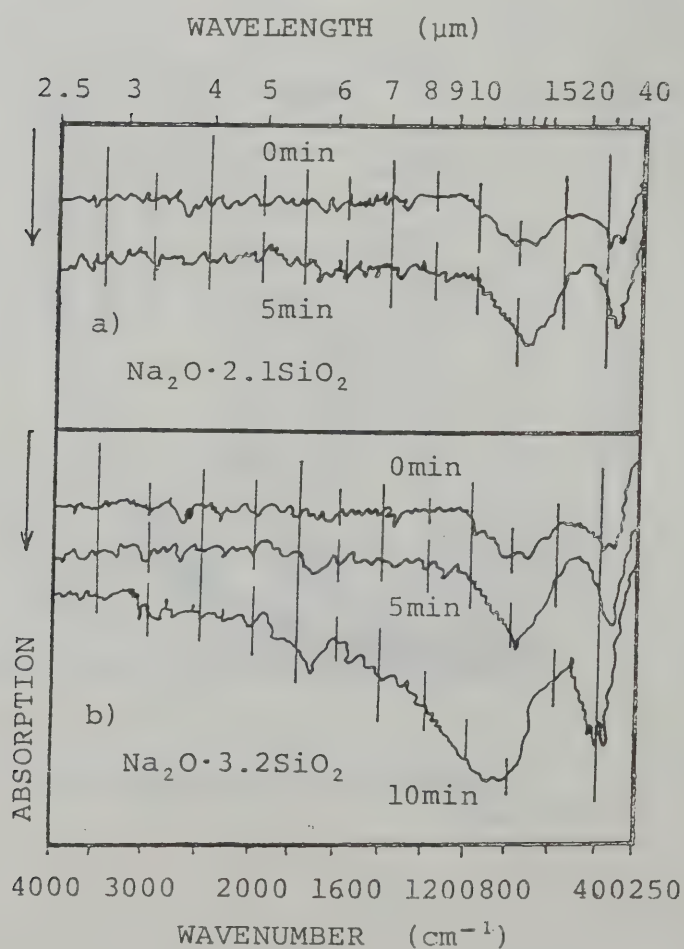


Fig.10b)





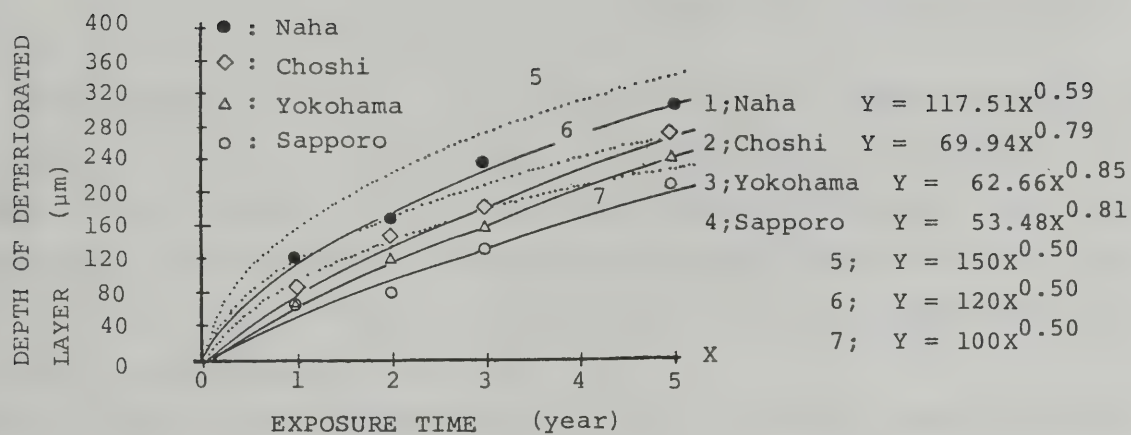


Fig.11a)

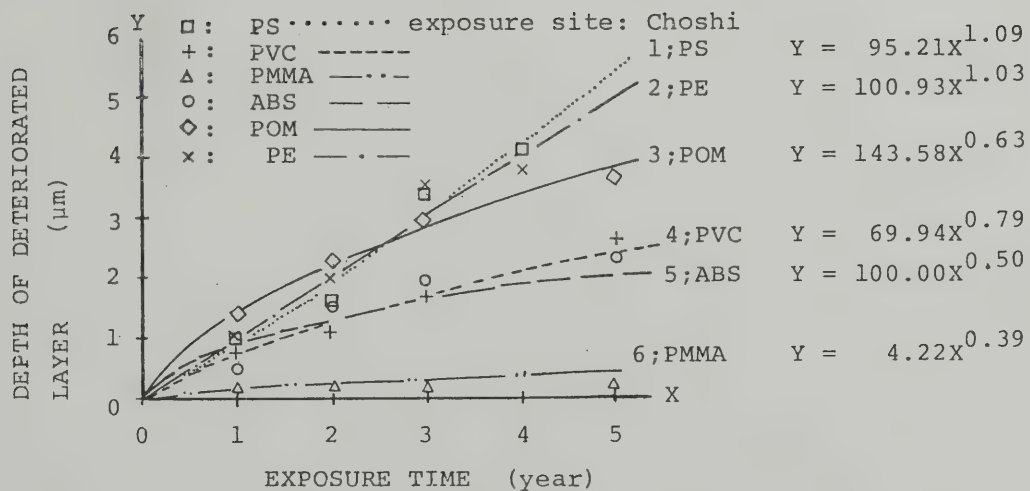


Fig.11b)



# 材令と劣化層深さとに関連した高分子材料の劣化モデル

福 島 敏 夫 \*

リサーチペーパー No.97

December 1982 建設省建築研究所

本研究は、紫外線と拡散性酸素との同時作用による高分子材料の複合劣化過程について、表層部からの劣化進行に関するいくつかの実験データを考慮しながら、非定常速度論解析に基づいて理論的に検討を行ったものである。

近来、省資源・省エネルギーの社会的ニーズの高まりと共に、建築材料・部材の耐久性の重要性が広く認識され、建築物の寿命予測と関連して、建築材料の劣化機構・劣化の経時進行度の合理的な評価の要請が強まりつつある。その評価のために、これまで様々の研究と多くの現象論的データの蓄積が見られる。しかし、劣化の経時進行度の解析方法に関しては、依然として未解決の重要な問題として残されていた。

本研究では、高分子材料の劣化進行は、紫外線吸収により活性化された高分子の解重合反応と表層部からの拡散性酸素との光酸化反応の2つの光化学反応の組み合わせによるものとして解析がなされた。その結果、典型的な高分子材料の劣化進行過程として、暴露時間に関する放物線則が導出された。実験的には、多くの高分子材料は、暴露時間に関するべき乗法則を示すが、その違いは光化学反応の劣化機構の違いにより説明される。曲げ強度の経時的低下も、表面付近の増大で説明される。







## Research Papers-Recent Issues

- No.74 K. Imaizumi: Recent Progress in Research and Development Wood Frame Construction, May, 1977, 61 pp.
- No.75 S. Hattori, Y. Kitagawa, M. Ohtsuka: Regional Coefficients of Earthquakes for Aseismatic Designs, July, 1977, 26 pp.
- No.76 Y. Matsushima: Random Response of Single-degree-of-freedom System with Bilinear Hysteresis, September, 1977, 28 pp.
- No.77 A. Baba: Drying Shrinkage Mechanism of Building Materials, March, 1978, 79 pp.
- No.78 K. Hayakawa: The Management of Land as an Environmental Resource, March, 1978, 40 pp.
- No.79 T. Tanaka: A Model on Fire Spread in Small Scale Buildings, September, 1978, 76 pp.
- No.80 Y. Aoki: Studies on Probabilistic Spread of Fire, November, 1978, 52 pp.
- No.81 F. Saito: Experimental Study of Compartment Fire Using Model Boxes, July, 1979, 50 pp.
- No.82 Y. Matsushima: Random Response of Single-degree-of-freedom System with General Slip Hysteresis, July, 1979, 37 pp.
- No.83 Y. Hasemi: Flashover Criteria of Compartment Fire - Theory on Zero Order Reaction System, August, 1979, 26 pp.
- No.84 T. Tanaka: A Model on Fire Spread in Small Scale Buildings, 2nd Report, March, 1980, 63 pp.
- No.85 Y. Ishiyama: Review and Discussion on Overturning of Bodies by Earthquake Motions, June, 1980, 115 pp.
- No.86 S. Watanabe: Planning History in Japan - A State of the Art Survey - August, 1980, 36 pp.
- No.87 Y. Sugimura: Participation Factor of Horizontal Force Applied to Pile Foundation, March, 1981, 33 pp.
- No.88 Y. Hasemi: Mathematical Basis for Physical Evaluation on Flashover, March, 1981, 41 pp.
- No.89 T. Wakamatsu: A Quantitative Evaluation on Smoke Safety, March, 21 pp.
- No.90 S. Watanabe: Metropolitanism as a Way of Life, March, 1981, 52 pp.
- No.91 M. Hrosawa, T. Goto, M. Yoshimura, H. Hiraishi: Full-Scale Experimental Study on Aseismic Performance of Medium-Rize RC Wall Structure, March, 1981, 28 pp.
- No.92 Y. Yamazaki: Inelastic Torsional Response of Structures Subjected to Earthquake Ground Motions, March, 1981, 102 pp.
- No.93 S. Kose: Study of Accidents Associated with Building Features, March, 1982, 38 pp.
- No.94 S. Okamoto, S. Nakata, Y. Kitagawa, M. Yoshimura, T. Kaminosono: A Progress Report on the Full-Scale Seismic Experiment of a Seven Story Reinforced Concrete Building - Part of the US-Japan Cooperative Program, March, 1982, 92 pp.
- No.95 Y. Hasemi: Characterization of the Intermittent Flaming Region of the Upward Current Above Diffusion Flames, March, 1982, 33 pp.
- No.96 Y. Morishita: Statistical Analysis of Fire Spread, May, 1982, 17 pp.
- No.97 T. Fuhushima: Deterioration Model of Polymeric Materials with Special Attention to Age and Deterioration Depth, December, 1982, 30 pp.

Address for Communication

**BUILDING RESEARCH INSTITUTE  
MINISTRY OF CONSTRUCTION**

No.1 TACHIHARA, OH-HO-MACHI, TSUKUBA-GUN, IBARAKI-PREF

JAPAN

610  
33b

ISSN 0453-4972

B R I Research Paper No. 98

# PLANAR TESTS ON REINFORCED CONCRETE SHEAR WALL ASSEMBLIES

— U.S.-JAPAN COOPERATIVE RESEARCH PROGRAM —

THE LIBRARY OF THE

JUN 19 1983

UNIVERSITY OF ILLINOIS  
AT URBANA-CHAMPAIGN

by

Hisahiro HIRAISHI

Manabu YOSHIMURA

Hiroshi ISOISHI

Shinsuke NAKATA

Building Research Institute

Ministry of Construction

January, 1983





## FOREWORD

This paper presents the experimental results of tests on two half-scale 3-story shear walls with connecting beams, which were conducted as support tests of a full-scale 7-story reinforced concrete building tested in 1980 under the "U.S.-Japan Cooperative Research Program Utilizing Large-Scale Testing Facilities".

The load was applied to the shear walls by operating one horizontal and two vertical jacks during the tests, in order to produce similar stresses in the shear wall as those of the 7-story structure subjected to lateral load.

Detailed measurements were made of horizontal and vertical displacements and of strains of reinforcing bars.

The elastic and inelastic behavior of the shear walls, which includes the effect of connecting beams, is discussed in detail based on test and analytical results.

The shear walls yielded in flexure preceeding shear failure. Thus, these tests are the first in Japan for a flexural type multistory shear wall with large scale.

January, 1983

Katsuro Kamimura  
Director General  
Building Research Institute  
Ministry of Construction



PLANER TESTS ON REINFORCED CONCRETE SHEAR  
WALL ASSEMBLIES

— U.S.-Japan Cooperative Research Program —

by

H. Hiraishi \*1  
M. Yoshimura \*2  
H. Isoishi \*3  
S. Nakata \*4

Building Research Institute, Ministry of Construction.  
Tsukuba, Ibaraki (Research Paper No.98 January 1983)

ABSTRACT

This study was done as support tests for the pseudo-dynamic test of a full-scale seven story reinforced concrete building scheduled for 1980 under the "U.S. - Japan Cooperative Research Program Utilizing Large Scale Testing Facilities".

Tests were made on the shear wall-beam assemblies of the lower three stories of the internal structural frame in the ridge direction of the full-scale seven story building. Test specimens were of two kinds. One was a half-scale test specimen (W1) with reinforcements corresponding to the full-scale design building. The other (W2) was of the same cross-section and shape as W1 but with increased reinforcements and increased strength for the sake of comparison, since the full-scale seven story building has a low base shear at ultimate strength. The boundary beams at each story of the test specimens were connected to each other by tie bars with both pinned ends to prevent vertical displacement, so that bending moments of the boundary beam would decrease wall moment.

The moment distribution applied to the specimen was similar to that of the wall in the seven story buildings under the external forces of inverted triangular distribution. The controlled moment together with the axial force was applied to the test specimen at the top of the third story, by adjusting the load of two jacks installed vertically on each side of the top of the test specimen. Load hysteresis consisted mainly of repetitions to displacement values where considerable plasticization was expected from a preliminary seismic response analysis of the full-scale seven story building.

Detailed measurement was made of the horizontal and vertical displacements at the left and right ends of the respective stories, the stretching forces of the boundary beams in the hinge region, strains in the main and shear reinforcements of the beams and columns, and strains in the vertical and horizontal wall reinforcement.

The test results were as follows:

- i) In both W1 and W2, the load-deflection hysteresis displayed bending-type behavior with a decreasing loss of strength from cycle to cycle at the same displacement level. Final failure was a collapse of the column concrete on the compression side accompanied by a sharp decrease in strength. The rotation angle of the shear wall at the time of rupture was  $1/50$  for W2 and  $1/40$  for W1, but in the case of W1, a stable load-deflection hysteresis was maintained only to  $1/50$ .
- ii) The respective stories produced a nearly identical rotation angle. Particularly in W1, the deformation was mainly, determined by the rotation due to the elongation and shrinkage at the base of the shear wall.
- iii) In both W1 and W2, all the vertical wall reinforcement at the bottom of the wall and the main reinforcements of the tensile side columns yielded before the rotation angle reached to  $1/200$ . The main reinforcement of the boundary beam and the adjacent slab reinforcement also yielded before the rotation angle reached  $1/200$ .
- iv) The test specimens had no beams in the wall, so the shear cracking in the upper and lower stories penetrated the slab and produced continuous cracks throughout the upper and lower stories. However, the absence of beams had little influence on the rigidity and strength.
- v) The shear strength of the test specimens was considerably higher than the maximum flexural strength, so in the pseudo-dynamic test of the full-scale seven story building, the shear wall is not expected to fail in shear.

---

\*1 Chief Researcher, Structure Division, Structural Engineering Department  
\*2 Research Member, Structural Dynamic Division, Structural Engineering Department  
\*3 Assistant Research Member, Construction Techniques Division, Production Department  
\*4 Head, Structure Division, Structural Engineering Department



## TABLE OF CONTENTS

1. PURPOSE	----- ( 1 )
2. TEST SPECIMENS	----- ( 3 )
2.1. Description of Test Specimens	----- ( 3 )
2.2. Mechanical Properties of the Materials	----- ( 4 )
3. EXPERIMENTAL PROCEDURE	----- ( 5 )
3.1. Application of Forces	----- ( 5 )
3.2. Data Measurement	----- ( 7 )
4. TEST RESULTS	----- ( 8 )
4.1. Loading History	----- ( 8 )
4.2. Crack Patterns and Modes of Failure	----- ( 8 )
4.3. Strains in the Reinforcement and Concrete	----- ( 10 )
4.4. Elasto-plastic Behavior	----- ( 12 )
4.5. Elasto-plastic Behavior of Boundary Beams	----- ( 14 )
4.6. Strengths	----- ( 16 )
5. CONCLUSION	----- ( 18 )
ACKNOWLEDGEMENTS	----- ( 20 )

- 
- \*1 Hisahiro Hiraishi: Chief Researcher, Structure Division,  
Structural Engineering Department
  - \*2 Manabu Yoshimura: Research Member, Structural Dynamic Division,  
Structural Engineering Department
  - \*3 Hiroshi Isoishi: Assistant Research Member, Construction  
Techniques Division, Production Department
  - \*4 Shinsuke Nakata: Head, Structure Division, Structural  
Engineering Department



## 1. PURPOSE

This study was carried out as support tests for the pseudo-dynamic test of the full-scale seven story reinforced concrete building, scheduled for 1980 under the "U.S.-Japan Cooperative Research Program Utilizing Large Scale Testing Facilities".

This full-scale seven story building has three spans in the ridge direction and two spans in the transverse direction, and has a shear wall through out all stories at the center of the internal structural plane in the ridge direction (See Figs. 1.1 and 1.2). In such a building, it is generally predicted that the properties of the shear wall will greatly influence the aseismic performance of the building. In fact, in the preliminary analysis of this structure, it was pointed out that the shear wall would carry about 85% of the total horizontal force acting on the first story in the elastic region and bear 60% of the maximum flexural strength of the building. The details of this building were decided basing on discussions between the U.S. and Japan from the structural planning stage. Resultantly, it incorporates various points can not be seen in our country, such as omission of the beams in the shear wall. This full-scale seven story building has a base shear coefficient of about 0.24 (except for the live load as weight) at the maximum flexural strength and is thus designed to resist strong ground motions with ductile behavior. Consequently, the shear wall must have a considerable plastic deformation capacity.

The most important focus of thses tests is on the shear wall and the beams of the lower three stories of the full-scale seven story test building. For this objective, two specimens were made in half- scale. Specimen W1 has reinforcement corresponding to that of the lower three stories of the full-scale seven story building. Specimen W2 has the same cross-section and shape as W1, but it has increased reinforcement and thus a greater strength.

The main objectives of this study are listed below.

i) To obtain load-deflection curves for preliminary analyses of the full-scale seven story building and to analyze the test results, or, more particularly, to confirm the deformation characteristics and the types of failure.

ii) To make clear the vartical displacement and rotation of the shear wall and the effects of the boundary beam and to examine the effects of the transverse beam in the full-scale seven story building.

iii) To examine what effect the absence of the beams in the shear wall is likely to have, and note any problems with the reinforcing method, and more particularly, in the anchoring method of main reinforcing bars in the boundary beams.

It should be noted that as part of the U.S.-Japan Cooperative Research Program, similar test were carried out on the beam-column assemblages, of the full-scale seven story test building.



## 2. TEST SPECIMENS

### 2.1 Description of Test Specimens

The focal point of these tests is on the shear wall-beam assemblies of the lower three stories of the full-scale seven story test building. There were two specimens. One was a one-half scale specimen (W1) with reinforcement corresponding to that of the full-scale building. The other specimen (W2) was of the same cross-section and dimensions as W1 but with increased reinforcement to increase the strength, because the full-scale seven story building has a low base shear at reserve strength.

The length of the boundary beams connected with the shear wall, was one-half of the span, taking the center of the beam of the full-scale building as the inflection point. Further, considering that the behavior of the beams and shear wall, and hence the test results, would be greatly affected by the presence or absence of floor slabs, particularly a shear wall without beams as in the case of the test specimens, floor slabs were provided at each floor with a width as specified in the Building Code Requirements for Reinforced Concrete, Architectural Institute of Japan. This width was effectively equal to that specified in the U.S.A. For accurate evaluation of behavior on the beam-column joint, a cross beam was provided of a length equal to the slab width. The beam provided at the top for applying the force, and the foundation beam for taking the reaction were made as rigid as possible. The both top and bottom main reinforcements of the boundary beams were bent down at the inside of the column. The wall reinforcement and main column reinforcement were lapped at the floors of the second and third stories, respectively. The concrete covering for reinforcement was one-half of the specified value because the test specimens were of one-half scale. Concrete placing was done at the floor surfaces of the foundation, first story, second story and third story.

Drawings of the reinforcement arrangements and a table of the reinforcement for W1 and W2 are shown in Figs. 2.1.1, 2.1.2, respectively and also in Table 2.1.1. The difference in the reinforcement arrangements between W1 and W2 was mainly the amount of main reinforcement for the column, the amount in W2 being 2.5 times that of W1. As for the other reinforcements, i.e. the wall reinforcement, and main and the shear reinforcement of the boundary beam, the arrangement of W2 was from 1.5 to 2.0 times that of W1.

The schedule of work and the testing of the specimens is shown in Table 2.1.2.

## 2.2 Mechanical Properties of the Materials

The concrete was standard, using river sand and river gravel with a design strength of  $F_C = 270\text{kg/cm}^2$ . Three test cylinders were prepared for both the compression and splitting tests from the concrete for the foundation, first story, second story and third story. They were cured indoors until the day of testing under the same conditions as those of the test specimens. Cylinder sizes were  $10\text{cm}\phi \times 20\text{cm}$  for the compression tests and  $15\text{cm}\phi \times 30\text{cm}$  for the splitting tests. As for the reinforcement, deformed bars (SD35) D6, D10 and D13 were used for the main portions of the test specimens and D22 for the main reinforcement of the foundation and loading beam. The test results for the reinforcement and concrete are shown in Tables 2.2.1 and 2.2.2. In Table 2.2.1, the values for the reinforcement are the mean values of three tests of the respective sizes. Stress-strain curves for the reinforcements are shown in Fig. 2.2.1.

### 3. EXPERIMENTAL PROCEDURE

#### 3.1 Application of Force

An inverted triangular distribution was assumed for the distribution of external force on the shear wall of the full-scale seven story building. According to the results of preliminary seismic response analysis of the full-scale seven story building (using as an input seismic wave the NS component at the first floor of the Construction Engineering Department Building at Tohoku University during the Miyagi-Ken Oki Earthquake in 1978, with the maximum acceleration set at  $350\text{cm/sec}^2$ , the ratio between the moment at the top of the third story to that at the base of the wall varies greatly through the response time history. This ratio was approximately within the range from  $1/1.5$  to  $1/4$  when yielding occurred at the base of the shear wall. On the other hand, assuming an inverted triangular distribution of external force and a yield mechanism of the boundary and transverse direction beams, the ratio of the moment in the shear wall at the top of the third story to that at the base of the wall is  $1/2.21$ .

The bending moment diagram when the inverse triangularly distributed external force acts on the one-half scale seven story shear wall assemblies is shown in Fig. 3.1.1. The dashed line represents the bending moment when the external force is assumed to be of a uniform distribution.

The loading apparatus is shown in Figs. 3.1.2 and 3.1.3. The horizontal load was applied as a concentrated load at the top. The boundary beams were connected to each other by tie bars with both pinned ends to constrain their vertical displacement. Two center hole jacks were used to apply the vertical load on the left and right sides of the force transfer beam at the top of the third story. This system allowed the left-and right-vertical loads ( $N_L$  and  $N_R$ ) to vary along with the horizontal load, according to the formulae (1) - (4)

shown below so that:

- a. the axial force in the first story wall would correspond to the axial force of the full-scale seven story shear wall assembly ( $\sigma_0 = 264,000 / (20 \times 500) = 26.4 \text{ kg/cm}^2$ ), and
- b. the moment distribution would correspond to that occurring when an inverted triangularly distributed external force was applied to the full-scale seven story shear wall assembly.

In calculating this moment, it was assumed that the boundary and transverse beams would yield when the base of the shear wall yielded. Before yielding, their loads were assumed to increase linearly with the horizontal load and the effects of their bending moments were taken into account.

Vertical loads of Test Specimen W1 :

$$N_L = 24.6* - 0.356P(t) \quad (1)$$

$$N_R = 25.6* + 0.356P(t) \quad (2)$$

Vertical loads of Test Specimen W2 :

$$N_L = 24.6* - 0.364P(t) \quad (3)$$

$$N_R = 25.6* + 0.364P(t) \quad (4)$$

(\* The difference of 1 ton between  $N_L$  and  $N_R$  is due to the weight of the loading apparatus)

The bending moment diagrams for the test specimens, obtained according to the foregoing loading method, are shown in Fig. 3.1.4. The bending moment diagrams at maximum flexural strength are shown in Fig. 3.1.5 together with those of the half-scale seven story shear walls. Since they agree with each other, this loading method seems well suited to represent the moment distribution of the lower three stories of the seven story shear wall assemblies. Because of limitations in the loading apparatus, for specimen W2, the control of the vertical load was possible only up to 58 tons, which was just short of the yield load.



### 3.2 Data Measurement

The measurement points for strain and displacement, are shown in Figs. 3.2.1 and 3.2.2. The items measured are given below. Figures in parentheses show the gauge number in Figs. 3.2.1 and 3.2.2.

i) Strains in Concrete, steel reinforcement and tie bars were measured with electric resistance wire strain gauges.

a) Strains in the main reinforcing bars of the column, beam, and longitudinal wall reinforcement (1 - 48).

b) Strains in the column hoops, beam stirrups and horizontal wall reinforcement (49 - 68).



c) Strains in the slab reinforcement (69 - 76).

d) Strains on the concrete surface (77 - 109).

e) Strains in the tie bars connecting boundary beams (140 - 157).

ii) Horizontal and vertical displacements were measured by inductance type displacement transducers (110 - 139).

iii) Jack loads were measured by load cells (158, 148 and 149).

The marks  and  represent the displacement transducers provided for measuring rotation angles in the hinge regions at the beam and column ends, respectively. They were positioned at a distance equivalent to their depth, 25cm away from the beam and column ends and the rotation over this distance was measured directly. The measuring jigs for the horizontal and vertical displacements were attached to the transverse beams. The measurement point for vertical displacement was located 10cm away from the column surface.

## 4. TEST RESULTS

### 4.1 Loading History

Figs. 4.1.1 and 4.1.2 show the loading histories recorded for W1 and W2. Tables 4.1.1 and 4.1.2 show the maximum loads and the values of the rotation angle due to horizontal displacement (mean value of the horizontal displacements at the loading side and the opposite side of loading of the shear wall) of the respective stories for each load cycle. Load histeresis consisted mainly of repetitions to displacement values where considerable plasticization was expected from a preliminary seismic response analysis of the full-scale seven story building. Neither W1 nor W2 had any appreciable decrease in the strength during repetitions of the same displacement amplitude before their collapse.

### 4.2 Crack Patterns and Modes of Failure

Flexural cracks were observed at the base of the column for specimen W1 in the first story at a horizontal load of  $Q = 12$  tons ( $\tau = Q/tl = 4.8\text{kg/cm}^2$ ) and 14 tons ( $\tau = 5.6\text{kg/cm}^2$ ) in the positive and negative loading respectively. W2 had a hair crack at the base of column at a positive load of 10 tons ( $\tau = 4\text{kg/cm}^2$ ). The crack became clearly observable at the load of 20 tons ( $\tau = 8\text{kg/cm}^2$ ). At negative loading, the crack appeared at the load of 20 tons. Thereafter, flexural cracks corresponding to the hoop spacing was observed gradually in the upper part of the column. In W1, a flexural crack produced at a position of about  $1.5D$  from the base of the column developed into a shear crack in the wall, under both positive and negative loads of 24 tons ( $\bar{\tau} = 9.6\text{kg/cm}^2$ ). The angles of these cracks were nearly horizontal, probably due to the influence of bending stress, so the cracks should correctly be called flexural shear cracks. W1 also had a slight shear crack at the bottom of the column on the tensile side under a negative load of 20 tons. In W2, a similar shear crack in the wall was produced under a positive load of 16

tons ( $\bar{\tau} = 6.4 \text{ kg/cm}^2$ ) and a negative load of 20 tons ( $\bar{\tau} = 8 \text{ kg/cm}^2$ ). Increased load was accompanied by shear cracking in the wall, while flexural cracks developed upward. A flexural crack occurred in the column at the second story level under a positive load of 28 tons and a negative load of 32 tons for W1, and under a positive and negative load of 32 tons for W2. On the second and third stories, shear cracks in the wall were produced almost simultaneously under a load of 32 to 36 tons ( $\bar{\tau} = 12.8 \sim 14.4 \text{ kg/cm}^2$ ). Thereafter, a flexural crack developed in the column at the third story level. The shear cracks in the walls of the second and third stories were of an angle of about  $30^\circ$ , smaller than the  $45^\circ$  angle of cracks produced by pure shear, but greater than the angle of the shear cracks in the first story.

The foregoing was the phenomena observed before reaching a rotation angle of  $1/400$  of the shear wall, as defined by the following formula:

$$R = \delta_T/h = \delta_T/4750 \text{ mm}$$

where  $R$  = rotation angle of the shear wall;

$\delta_T$  = horizontal displacement of the top of the third story, and

$h$  = height from the top of the third story to column base of the first story.

In the following, the term "rotation angle" means the rotation angle of the shear wall unless otherwise specified.

Up to this point, all of the boundary beams had flexural cracks. After a rotation angle of  $1/400$ , these cracks increased gradually. At a rotation angle of  $1/100$ , clear shear cracks were observed in the first story column of both W1 and W2 and crushing of the concrete was observed at the base of the column and at the compressive bottom sides of the boundary beams. In W1, the concrete of the first story column began to break up significantly due to shear compression at a rotation angle of  $1/50$ , and with three repetitions under  $1/50$ , fracture of the longitudinal wall reinforcement took place. Thereafter, at a rotation angle of  $1/40$ , the majority of the vertical wall



reinforcement and one main reinforcement of the column fractured, and during unloading, the concrete at the base of the column failed in compression. In W2, on the second repetition at a rotation angle of  $1/50$ , the concrete at the base of column failed in compression as in W1. The fact that the rotation angle of W2 at the time of the collapse was smaller than that of W1 may be explained by the higher axial compressive stress of the column on the compression side because of the larger maximum flexural strength.

The test specimens had no beams in the wall so that shear cracks produced in the upper and lower stories penetrated through the slabs to form continuous cracks throughout the upper and lower stories. However, these cracks were of small width and are not considered to have had appreciable effect on the behavior of the shear wall.

Tables 4.2.1 and 4.2.2 list the crack patterns, and Figs. 4.2.1 to 4.2.9 show the cracks after reaching specific rotation angles.

#### 4.3 Strains in the Reinforcement and Concrete

Figures 4.3.1 and 4.3.2 show the yielding patterns of the reinforcement in W1 and W2. The main reinforcements at the base of the column and most of the vertical wall reinforcement yielded before a rotation angle of  $1/400$  and completely yielded by  $1/200$ . Judging from the gauges attached at an interval of 15cm to the anchored portion of the main column reinforcement, the reinforcement yielded at the 15cm from the surface of foundation for W1 and the 30cm for W2, and it seems that a considerable slippage of the reinforcement occurred at ultimate stage. As for the boundary beam, almost all the reinforcement, including the slab reinforcement, yielded before a rotation angle of about  $1/200$ .

As for the shear reinforcement, those at the base of the column yielded after a rotation angle of  $1/200$ . Those at the upper part of the first story column and the bottom of the second story column did not yield and had a strain value of less than  $1000\mu$ . The shear reinforcement at the beam-column



joint on the second floor also did not yield and had a strain value of more than  $1000\mu$ . Concerning horizontal wall reinforcement, it was observed that in W1 only the horizontal reinforcement at the lower part of the wall yielded at a rotation angle of  $1/200$ . In W2, however, horizontal reinforcement on the first story began to yield after a rotation angle of  $1/200$  and, before a rotation angle of  $1/100$  was reached, almost all of the horizontal reinforcements on the first story had yielded. While the structure had no beam in the wall, yielding occurred in some of the vertical and horizontal reinforcement near the corner of the beam-column joint. Summing up the yielding patterns of the reinforcement in both W1 and W2, the main reinforcement of the base of the column and the vertical reinforcement at the base of the wall yielded before a rotation angle of  $1/400$ , the main reinforcement of the boundary beam and the slab reinforcements yielded before a rotation angle of  $1/200$ , and finally, the horizontal wall reinforcements and the hoop of the column only yielded at or beyond the maximum flexural strength.

Figs. 4.3.3 through 4.3.8 show the shearing stress of the wall plate as a function of the horizontal load obtained by wire strain gauges on the concrete surface shown in Fig. 3.2.2. Distribution of stress in the same horizontal plane are shown in Figs. 4.3.9 and 4.3.10 for the respective loads. The dashed line in the drawings shows the stress distribution obtained according to the I-beam primary elemental theory of bending. At the central plane of the wall plate on the first story, the experimental values are in agreement with the values calculated for both central and end parts. For the shearing stress beneath the slabs on the second and third stories, the experimental value at the central part of the wall plate is also in good agreement with the value calculated. However, at both ends, the experimental values are considerably smaller than those calculated. Further, the shearing stress at the loading side varies little with an increasing horizontal load. The value

of the shearing force obtained by integrating the shearing stress distributed on the horizontal plane of the wall agrees relatively well with the value calculated for the central plane of the first story, but for the plane beneath the slab, the value is considerably smaller than the value calculated. Comparing the shearing force acting on the column beneath the slab (obtainable by deducting the shearing force acting on the wall plate from the horizontal shearing force) with the shearing force acting on the column at the central plane of the first story, it may be said that a greater shearing force acts on the column beneath the slab.

#### 4.4 Elastoplastic Behavior

Figs. 4.4.1 through 4.4.6 show the relation of horizontal load  $Q$  to absolute horizontal displacement  $\delta$  of the respective stories of W1 and W2. Figs. 4.4.7 through 4.4.10 show the relation of the horizontal load  $Q$  to the story displacement  $\delta_R$  of the second and third stories. Both W1 and W2 give a stable spindle-shaped loop and have no notable decrease in the strength for load repetitions within a rotation angle of less than  $1/100$ . Further, W1 and W2 have substantially the same rotation angles at the first, second and third stories.

Figs. 4.4.11 and 4.4.12 show the relation of top vertical displacements  $L\delta_v$  of the column of the third and first stories to horizontal load  $Q$  at the loading side for W1, and the similar relation of vertical displacement  $R\delta_v$  to horizontal load  $Q$  at the opposite side of loading for W2. At the top on the tensile side of the third story, both W1 and W2 gave values of a stretch of 5cm or more for a rotation angle of less than  $1/50$ . However, on the compression side, the longitudinal shrinkage was less than 1cm. For both W1 and W2, the vertical displacement of the second floor is not very different to that of the top of the third story, so it may be said that the greater part of the vertical displacement occurs on the first story.

Skeleton-curves for the horizontal and vertical displacements of the respective stories up to a rotation angle of 1/100 are shown together with the analytical results in Figs. 4.4.13 and 4.4.14. For the stress-strain relationship of concrete, the  $\epsilon$ -function proposed by Dr. Umemura was used and a bilinear model with the second gradient taken as 1/200 of the elastic rigidity was used for the stress-strain relationship of the reinforcement. Slippage of the reinforcement at the foundation was not taken into consideration in analysis. The test results for both horizontal and vertical displacements agree well with the analytical results. It may thus be said that W1 produced only flexural deformation and that shearing deformation was negligible. However, in the case of W2, shearing behavior was noted in the first story.

Figs. 4.4.15 through 4.4.20 show the chord rotation  $\theta_i$  obtained from the vertical displacements of the top, third and second floors.

$$\theta_i = (L\delta_{Vi-1} - R\delta_{Vi-1})/\ell_v$$

where  $\theta_i$  = angle of rotation of the floor of the  $i$ -th story;

$L\delta_{Vi-1}$  = vertical displacement at the top of the left side column of the  $(i-1)$  story;

$R\delta_{Vi-1}$  = vertical displacement at the top of the right side column of the  $(i-1)$  story; and

$\ell_v$  = distance between the measurements of vertical displacements.

In the drawing, the dashed line indicates that proper measurements were not obtained because of an insufficient stroke of the displacement transducer. Both W1 and W2 had angles of rotation of substantially the same values and rotation angles due to the horizontal displacements were previously shown in Figs. 4.4.1 through 4.4.6. Figs. 4.4.21 through 4.4.24 show the values of the net horizontal displacement  $\delta_p$ , defined by the following formula, up to a rotation angle of 1/100 for the third and second stories.



$$\delta_{Pi} = \delta_{Ri} - \theta_i h_i$$

where  $\delta_{Pi}$  = net horizontal displacement of i-th story;

$\delta_{Ri}$  = story displacement of i-th story;

$\theta_i$  = angle of rotation of the i-th floor; and

$h_i$  = story height of i-th story.

The net displacement was small enough, and it seems that the second and third stories displayed a rigid behavior.

From the foregoing, it can be seen that deformation of the shear wall of W1 showed bending yielding type behavior governed mainly by the rotation due to elongation and shrinkage of the base of the first story. In the case of W2, it may be said that it showed similar behavior to W1, although a kind of shearing deformation was produced in the first story. In the first story portion of W2, the so called "anisotropic plate characteristic" was seen, where a vertical displacement occurs as a shearing force acts on a wall plate with shear cracks.

#### 4.5 Elastoplastic Behavior of Boundary Beams

Figs. 4.5.1 through 4.5.8 show the relation of shearing force to horizontal load of the boundary beams, calculated in accordance with the following formulae from strains of the wire strain gauges attached to the tie bars connecting boundary beams.

$$\begin{aligned} BQ_1 &= A_S E_S (\epsilon_1 - \epsilon_2) = 7.89 \times 210 \text{ton} \times (\epsilon_1 - \epsilon_2) \\ &= 1657(\epsilon_1 - \epsilon_2) \text{ton} \end{aligned}$$

$$\text{and } BQ_2 = A_S E_S \epsilon_2 = 7.89 \times 210 \text{ton} \times \epsilon_2 = 1657 \epsilon_2 \text{ ton}$$

where  $BQ_1, BQ_2$  = shearing forces of the beams of the first and second stories, respectively;

$A_S$  = cross-sectional area of the tie bar connecting the boundary beams;

$E_S$  = Young's modulus of the tie bar; and

$\epsilon_1, \epsilon_2$  = strains of tie bars at the first and second story, respectively.



The relation of assumed shearing force to horizontal load of the boundary beam for control of the vertical loading jacks provided at the top of the respective test specimens is shown by the broken line in the above mentioned figures. The shearing force produced in the beam while the top side of the beam is under tension is small until the wall begins to yield, but increases sharply after yielding of the wall. The forces measured when tension existed on the bottom side of the beam and during unloading when tension existed on the top side of the beam agrees well with the assumed values. Thus it may be said that the test specimens have developed stresses approximately equal to those assumed (See Fig. 3.1.4).

Figs. 4.5.9 through 4.5.16 show the relations between the shearing force of the boundary beam stated above and the rotation angle of the boundary beam calculated from the vertical displacements of the left and right columns of the shear wall and angles of rotation  $\theta$  as described in paragraph 4.4.

$$RB^{\delta}_i = RB^{\delta}_i = R^{\delta}_{vi} + \theta_i l_B = R^{\delta}_{vi} + 1375\theta_i$$

$$LB^{\delta}_i = L^{\delta}_{vi} - \theta_i l_B = L^{\delta}_{vi} - 1375\theta_i$$

Here,

$RB^{\delta}_i, LB^{\delta}_i$  = displacements of the left and right boundary beams  
on the  $i$ -th floor;

$R^{\delta}_V, L^{\delta}_V$  = left and right vertical displacements on the columns  
of  $i$ -th floor;

$\theta_i$  = angle of rotation of the  $i$ -th floor; and

$l_B$  = clear length of the beam.

Except for the deviation of the loading axis because of an initial stress produced in the beam while attaching the tie bars, the four left and right beams display nearly similar loops for both W1 and W2. The beams are subject to yield at a rotation angle of  $1/200$  and to great deformation thereafter. During tension exist on the bottom side of the beam, rotation angles approximately equal to those of the shear wall are produced, and during

tension exist on the top side of the beam, a rotation angle about two times that of the shear wall is observed. This characteristic presents a remarkable pinching phenomenon as can be seen in the results of the member test on the beam-column assemblages carried out separately to this study.

The test specimens included no transverse beams. However, considering the amount of elongation and shrinkage of the columns on the tensile and compressive sides, it seems sufficient to use the shearing force corresponding to the maximum flexural strength of the beam for calculating the restraining force by the transverse beam located at the tensile column side at maximum flexural strength of the shear wall, and to use the smaller value of the maximum flexural strength of the beam, for bending moment calculations for the transverse beam on the compressive side of the shear wall.

#### 4.6 Strengths

The values for cracking strength and ultimate strength of the test specimens are shown in Table 4.6.1. The analytical results in the table are based on the following formulae.

##### i) Flexural crack moment

$$M_{BC} = 1.8\sqrt{F_C} Z_e + N Z_e/A_e$$

$$Q_{BC} = M_{BC}/(M/Q)$$

##### ii) Shearing force at flexural shear cracking

$$Q_{BSC} = 0.265 \cdot t \cdot D\sqrt{F_C} + M_{BC}/(M/Q - 0.5D)$$

##### iii) Shearing force at shear cracking

$$Q_{SC} = K_{tB} \cdot t \cdot \ell \cdot c\sigma'_t \sqrt{1 + \sigma_o/c\sigma'_t}$$

$$K_{tB} = \frac{1 + 1.05t/B}{1 + 1.77t/B}$$

$$c\sigma'_t = 2.2\sqrt{F_C} - 0.00546F_C^{1.456} P_w^{0.075}$$

##### iv) Shearing force at maximum flexural strength

$$M_{FM} = 0.9ats\sigma_y D + 0.4 ws\sigma_y D + 0.5 ND \{1 - N/(BDF_C)\}$$

$$Q_{FM} = M_{FM}/(M/Q)$$

v) Shearing strength

$$Q_{SM} = \left[ \frac{0.053 P_{te}^{0.23} (F_c + 180)}{M/(Q_d) + 0.12} + 2.7 \sqrt{s_o w y P_{we}} + 0.100 \right] b e_j$$

With respect to the flexural cracking strength, the test results agree well with the analytical results. According to the analysis, both W1 and W2 reach yield strength without producing shear cracks, but according to the test results, shear cracks are produced in all stories. The reason for this difference the test specimens were subject to the influence of bending stress as can be seen from the fact that the angle of the crack is considerably smaller than 45°. According to the tests, these cracks are to be called flexural shear cracks. With respect to the maximum flexural strength, the values agree well with those given by the e-function method. The values obtained by the approximate formula were somewhat lower.

The analytical shearing strength is far beyond the maximum flexural strength in the case of W1. Further, judging from the crack pattern generated in W1, the shear strength seems to be enough stronger than compared with the flexural strength. It may thus be considered that in the pseudo-dynamic tests of the full-scale seven story building, the shear wall is unlikely to be subject to damage by shear.

## 5. CONCLUSIONS

Tests on the shear wall portion of the lower three stories of a seven story building which contains a shear wall were conducted, and the following results were obtained.

i) In both test specimens, W1 and W2, the load-deflection hysteresis of the shear walls showed a behavior of the flexural type with a small loss of strength from cycle to cycle at the same displacement. However, a rapid collapse resulted because the final failure was caused by compressive crushing of the concrete at the base of the column surrounding to the wall. The rotation angle of the shear wall at collapse was  $1/40$  in the case of W1 and  $1/50$  in the case of W2. However, in W1, a stable load-deflection hysteresis was maintained only until a rotation angle of  $1/50$ .

ii) The respective stories produced approximately equal rotation angles. In W1, particularly, the deformation was governed largely by the elongation and shrinkage at the base of the shear wall. Also, in W1, the values of the horizontal and vertical displacements agree well with the analytical values by the e-function method by Dr. Umemura, so that it is considered that the shearing deformation has little effect.

iii) Vertical reinforcements at the base of the wall yielded entirely at a rotation angle of  $1/200$  in both W1 and W2. As for the hoops of the column and the horizontal reinforcements of the wall, at a rotation angle of  $1/200$ , the hoops of the column footing and horizontal reinforcement at the wall footing began to yield for W1. For W2, some of the hoops of the column footing and horizontal reinforcements at the first story wall began to yield at the rotation angle of  $1/200$ , and the majority of these reinforcements yielded after a rotation angle of  $1/100$ .

iv) The boundary beams produced a greater rotation angle than that of the shear wall and yielded generally at the shear wall rotation angle of  $1/200$ .



Slab reinforcements on the second floor yielded almost simultaneously with the main reinforcements of the beam. The beams on the second and third floors produced substantially similar deformations.

v) The measured maximum flexural strength agreed well with the analytical result by the e-function method. The calculated shear strength of the respective test specimens is enough stronger than flexural strength. Thus, it is not expected that the shear wall will be subject to shear failure in the pseudo-dynamic tests of the full-scale seven story building.

vi) As the shear wall had no internal beams, the shear cracks in the upper and lower stories penetrated through the slabs to cause continuous cracks throughout the upper and lower stories. However, absence of the beams had little effect on the rigidity and strength of the wall.

vii) There were no transverse beams in the test specimens. However, from the amount of elongation and shrinkage of the columns at the tensile and compression sides, it seems sufficient for calculating the restraining force by the transverse beam at the maximum flexural strength of the shear wall, to use the shear force at yielding of the beam for the tensile column side, and a value of the shear force somewhat discounted for the compression column side.

## ACKNOWLEDGEMENTS

The valuable advice received from Prof. Hiroyuki Aoyama, University of Tokyo, and the help received from Mr. Tetsuro Goto, Researcher of the Building Research Institute, in carrying out the tests, are most gratefully acknowledged.

### APPENDIX A:

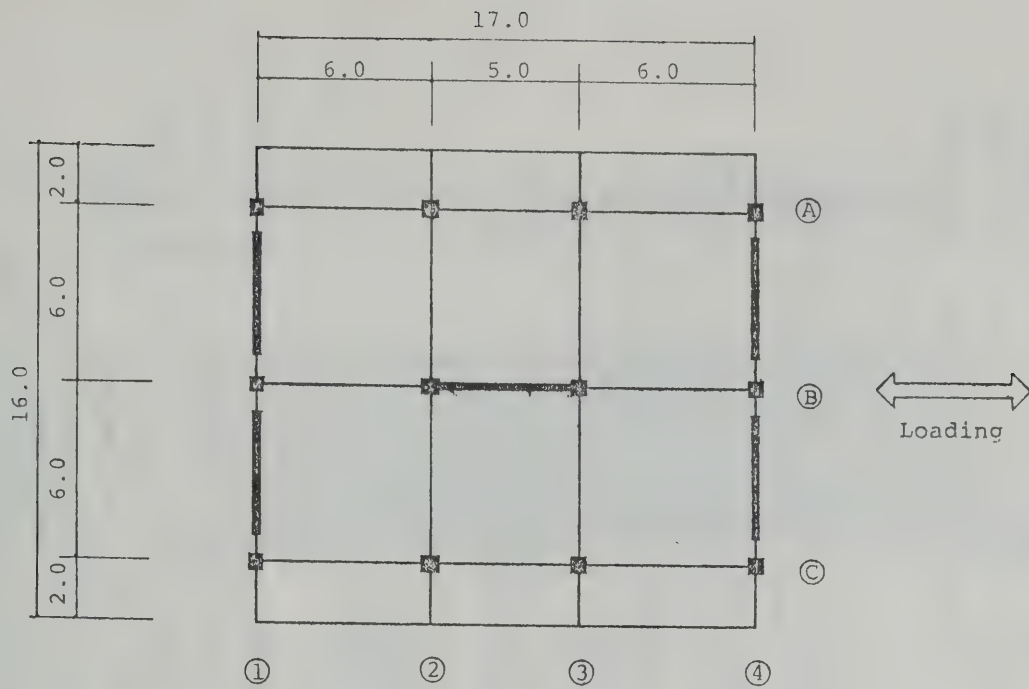
Results of Measurement of Reinforcement and Concrete Strains, Displacements and Loads of W1.

The following load-strain curves and load-displacement curves of the reinforcement and concrete of W1 correspond to Figs. 4.3.1 and 4.3.2 in the text.

### APPENDIX B:

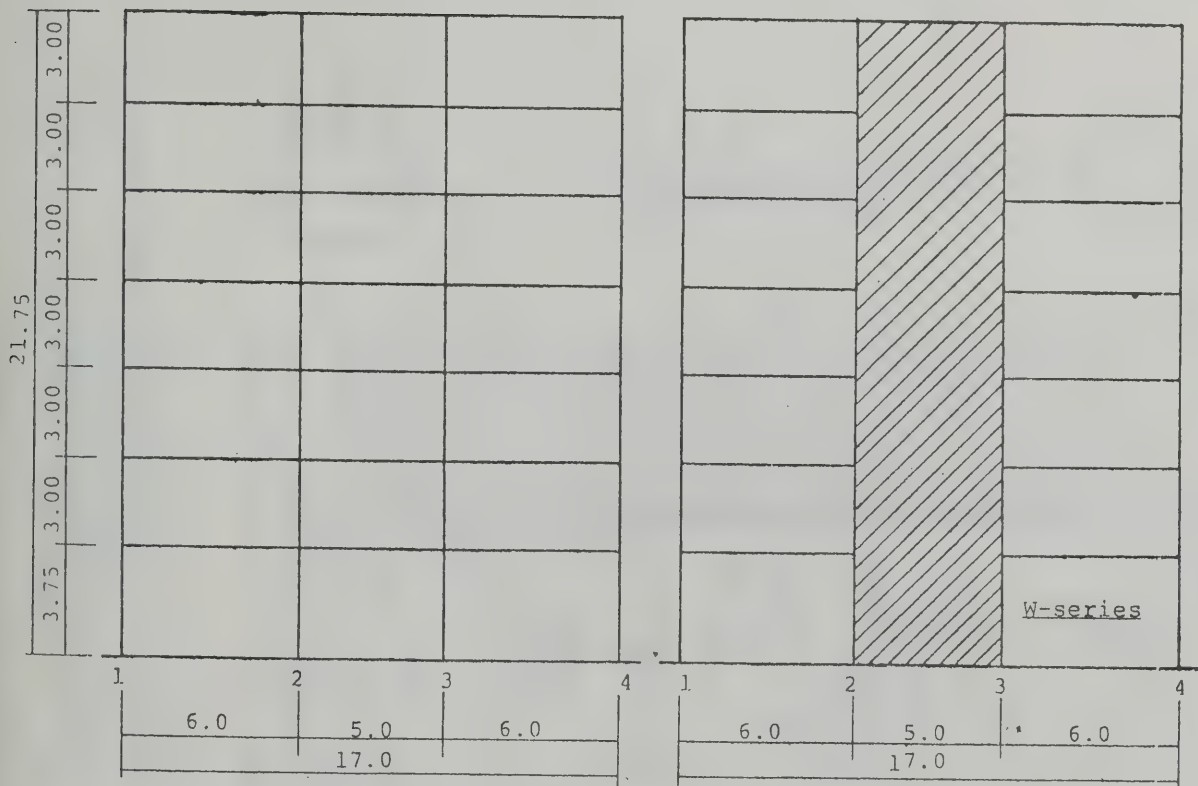
Results of Measurement of Reinforcement and Concrete Strains, Displacements and Loads of W2.

The load-strain curves and load-displacement curves of the reinforcements and concrete of W2 shown in Figs. 4.3.1 and 4.3.2 in the paper are shown.



(a) Plan (unit:m)

Fig. 1.1. : Full-Scale Structure



(b) Elevation : A,C Frame (unit:m) (c) Elevation : B Frame (unit:m)

Fig. 1.2. (Continued) Full-Scale Structure

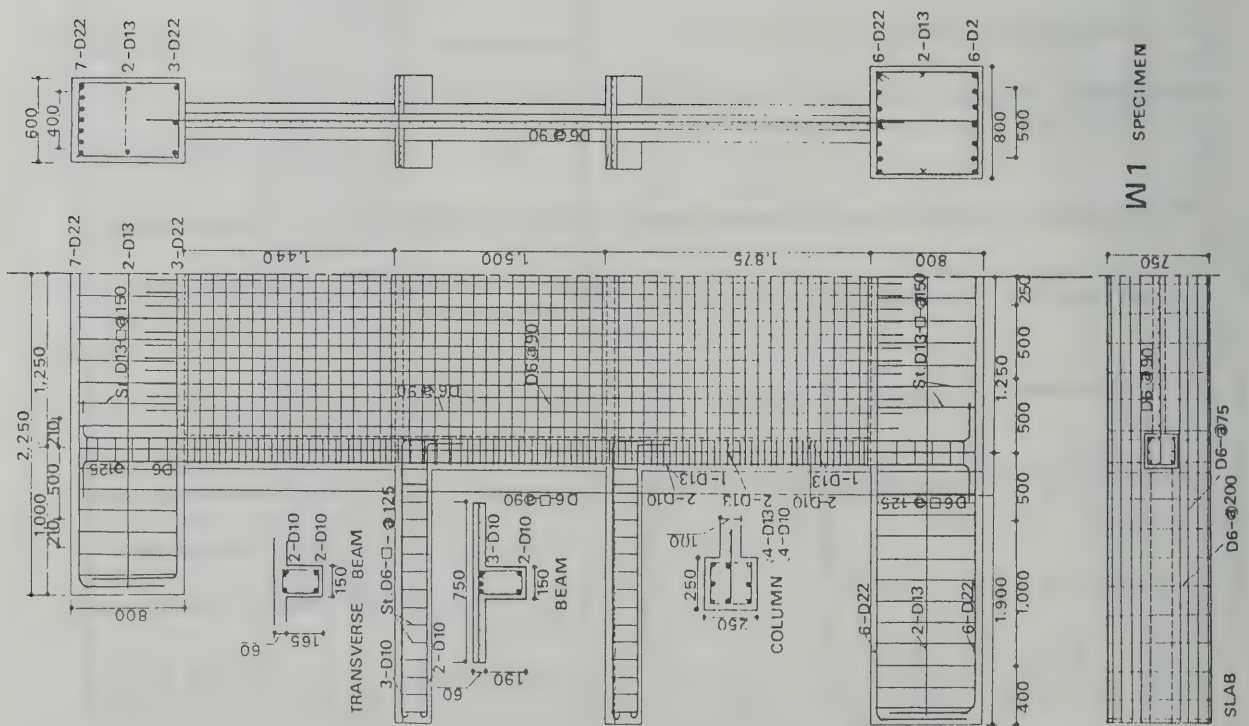
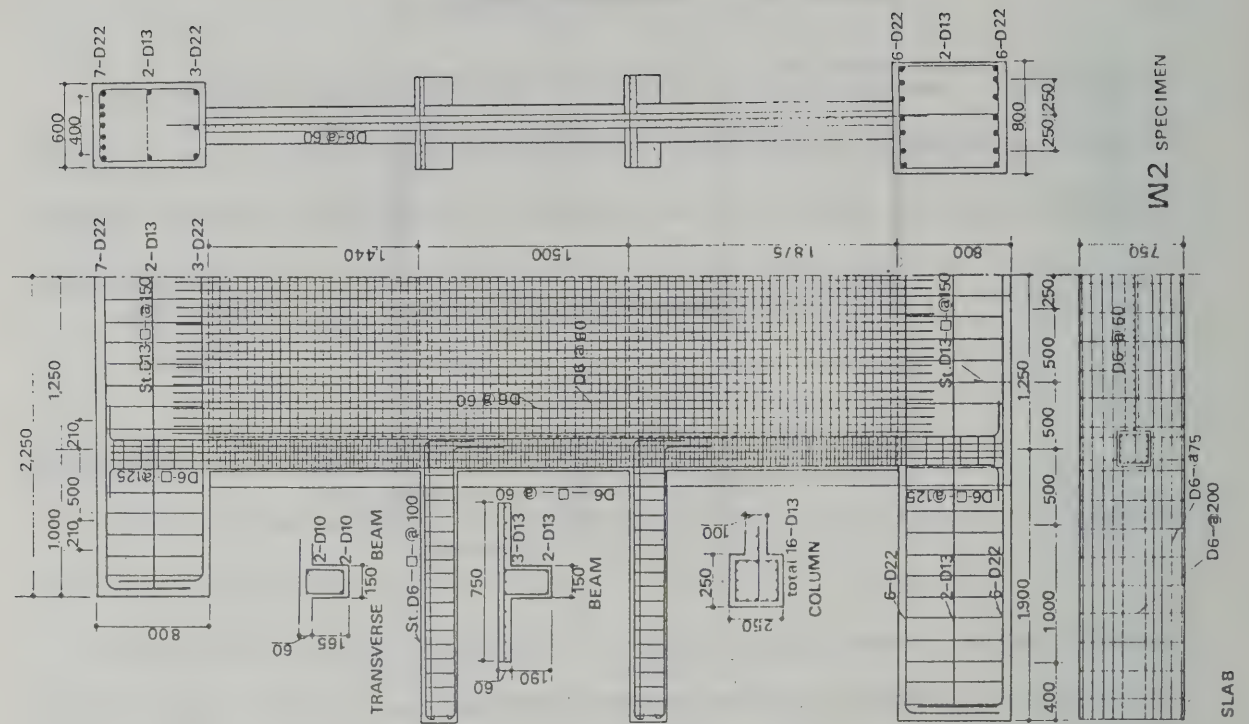




Table 2.1.1.1 Reinforcement of Specimens W1 and W2

Specimen	Column					Wall		Slab	
	a <sub>t</sub> (cm <sup>2</sup> )	a <sub>g</sub> (cm <sup>2</sup> )	p <sub>t</sub> (%)	p <sub>g</sub> (%)	p <sub>s</sub> (%)	p <sub>s</sub> (%)	p <sub>s</sub> (%)	a <sub>s</sub> (cm <sup>2</sup> )	a <sub>s</sub> (cm <sup>2</sup> )
W1	2.7	7.93	0.43	1.27	0.43	0.356		2.56	
W2	6.35	20.32	1.01	3.25	0.64	0.533		2.56	

Specimen	Boundary Beam						Transverse Beam					
	Upper			Bottom			Upper			Bottom		
	a <sub>t</sub> (cm <sup>2</sup> )	p <sub>t</sub> (%)	p <sub>s</sub> (%)	a <sub>t</sub> (cm <sup>2</sup> )	p <sub>t</sub> (%)	p <sub>s</sub> (%)	a <sub>t</sub> (cm <sup>2</sup> )	p <sub>t</sub> (%)	p <sub>s</sub> (%)	a <sub>t</sub> (cm <sup>2</sup> )	p <sub>t</sub> (%)	p <sub>s</sub> (%)
W1	2.14	0.65	0.43	1.43	0.43	0.43	2.14	0.73	0.49	1.43	0.49	0.24
W2	3.81	1.15	0.64	2.54	0.77	0.64	3.81	1.30	0.87	2.54	0.87	0.36

Table 2.1.2 Schedule of Construction Model Work and Tests

Feb. 1	Reinforcement arrangements for the foundation. Molding Work for the foundation. Concrete placing for the foundation.
Feb.12	Reinforcement arrangement for the first story.
Feb.15	Molding work for the first story. Tensile tests of reinforcement to be used.
Feb.18	Concrete placing for the first story.
Feb.21	Reinforcement arrangements for the second story.
Feb.23	Molding work for the second story.
Feb.25	Concrete placing for the second story.
Feb.29	Reinforcement arrangements for the loading part and third story. Molding work for the loading part, third story.
Mar. 1	Concrete placing for the loading part, third story.
Apr. 3-8	W2 loading tests.
Apr.21-28	W1 loading tests.
May. 1	Compression and splitting tests of test cylinders.

Table 2.2.1 Mechanical Behavior of Reinforcing Bar

	$\sigma_y$ (t/cm <sup>2</sup> )	$\sigma_u$ (t/cm <sup>2</sup> )	$\epsilon_y$ (%)	$\epsilon_{st}$ (%)	$\epsilon_u$ (%)	$E_s$ ( 10 <sup>6</sup> kg /cm <sup>2</sup> )
D6	3.77	4.95	0.22		13.78	1.74
D10	3.75	5.32	0.195	2.4	14.39	1.89
D13	4.07	5.81	0.215	1.85	17.50	1.89
D22	3.81	5.96	0.19	1.45	17.95	2.02

$\sigma_y$ = yielding strength                       $\epsilon_y$ = yielding strain

$\sigma_u$ = ultimate tensile strength    $\epsilon_u$ = strain at fracture

$\epsilon_{st}$ = strain at start of strain hardening                       $E_s$ = Young's modulus

Table 2.2.2 Mechanical Behavior of Concrete

	Slump (cm)	F <sub>c</sub> (kg/cm <sup>2</sup> )	F <sub>sp</sub> (kg/cm <sup>2</sup> )	E <sub>c</sub> (kg/cm <sup>2</sup> )	cε <sub>B</sub> (%)	Comment
Foun- dation	17.5	308.3	31.8	————	————	
	19.4		31.5			
			30.0			
1st- story	21.3	322.5	31.8	2.11 x 10 <sup>5</sup>	0.1961	
	18.8	318.7	30.1	2.44 x 10 <sup>5</sup>	0.2212	
		317.8	29.3	2.47 x 10 <sup>5</sup>	0.2068	
			319.7	30.4	2.34 x 10 <sup>5</sup>	0.2080
2nd- story	13.6 13.4	313.4	31.8	2.33 x 10 <sup>5</sup>	0.1841	
		258.6	29.4	2.58 x 10 <sup>5</sup>	0.1394	
		243.0	31.5	3.07 x 10 <sup>5</sup>	0.1150	
		271.7	30.9	2.66 x 10 <sup>5</sup>	0.1462	Mean value
3rd- story	16.1	307.1	30.3	2.25 x 10 <sup>5</sup>	0.2283	
	16.0	277.8	29.0	2.42 x 10 <sup>5</sup>	0.1760	
		292.5	29.7	2.34 x 10 <sup>5</sup>	0.2022	Mean value
* measured 2 times						

F<sub>c</sub> = compressive strength  
E<sub>c</sub> = Young's modulus

F<sub>sp</sub> = splitting tensile strength  
cε<sub>B</sub> = strain at maximum strength



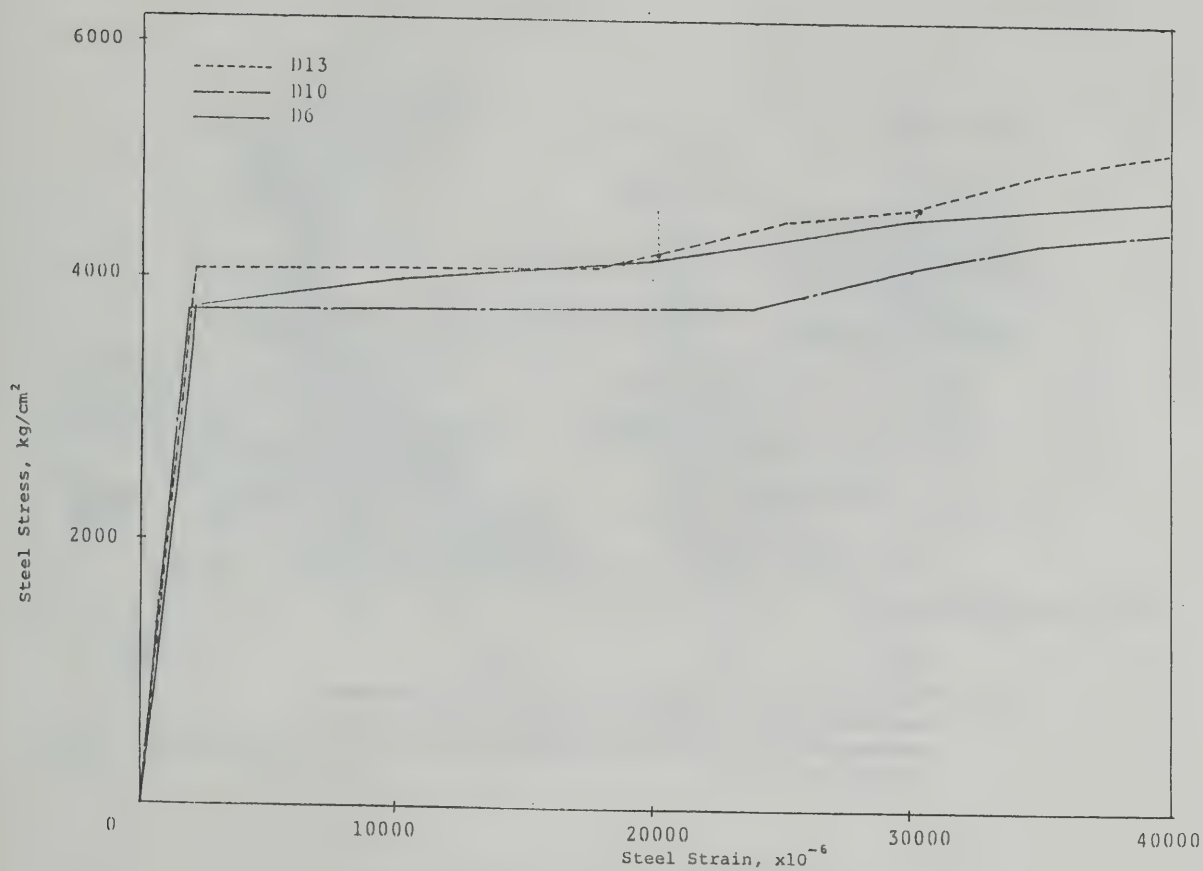


Fig.2.2.1 Stress Strain Relationship of Reinforcing Bars

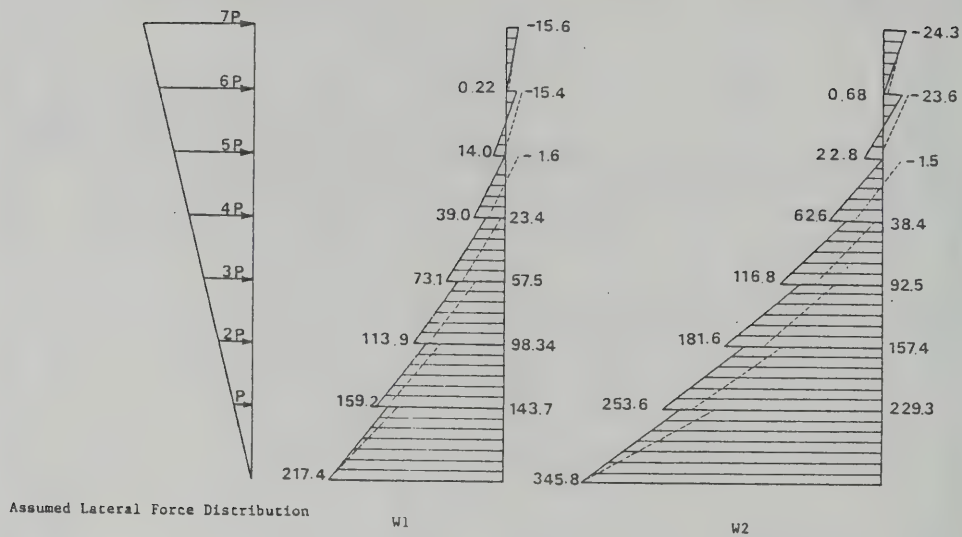


Fig.3.1.1 Bending Moment(t.m) at Yielding of Half-scale Seven-story Shear Walls under Inverted Triangle Lateral Force Distribution, Where Dashed Line Shows the Bending Moment When the Lateral Force is Assumed to Be a Uniform Distribution

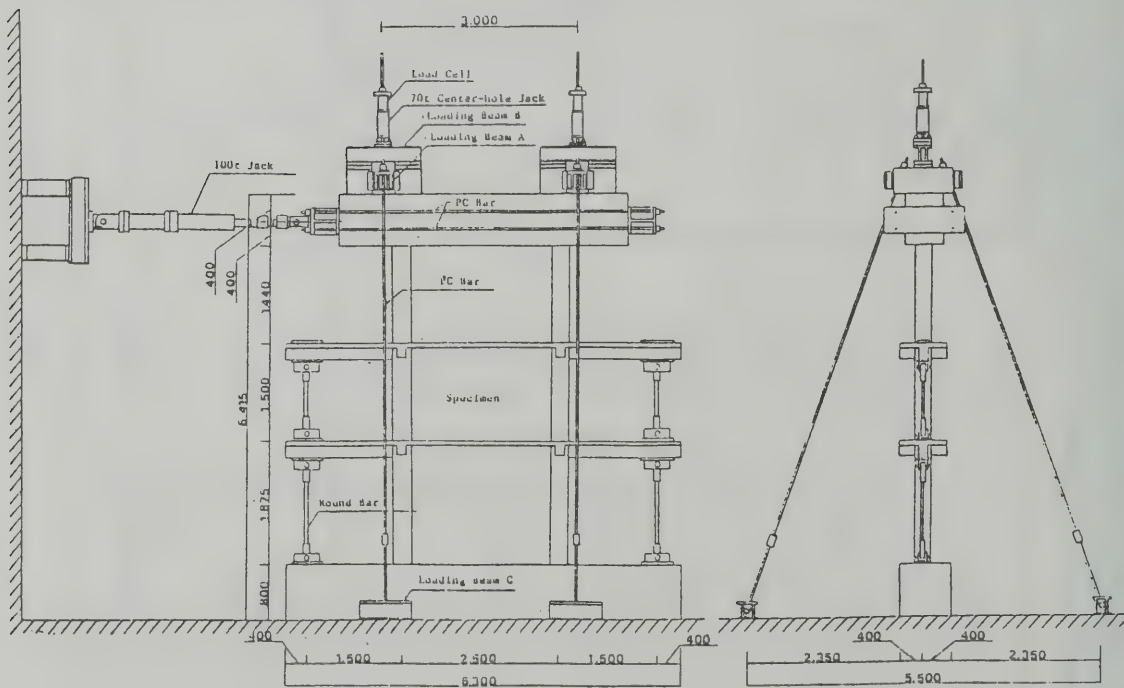


Fig.3.1.2 Test Set-up

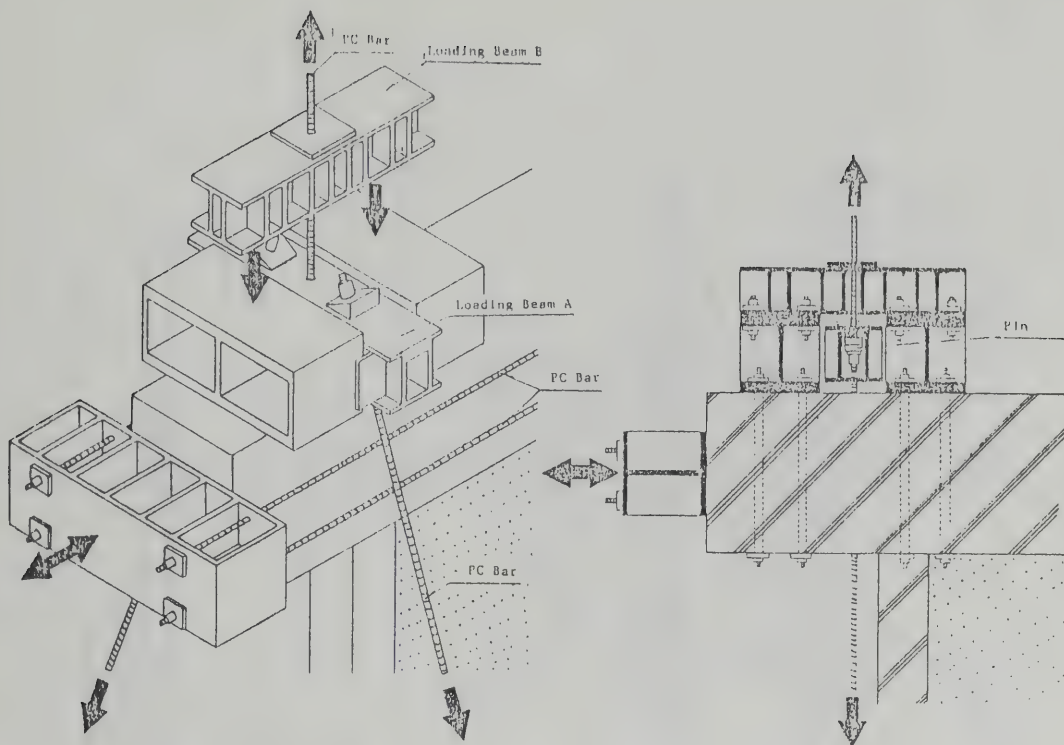


Fig.3.1.3 Detail of Test Set-up

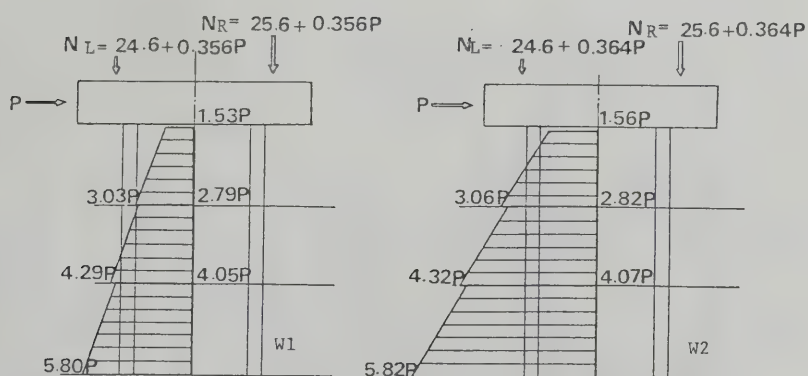


Fig.3.1.4 Bending Moment of the Specimens

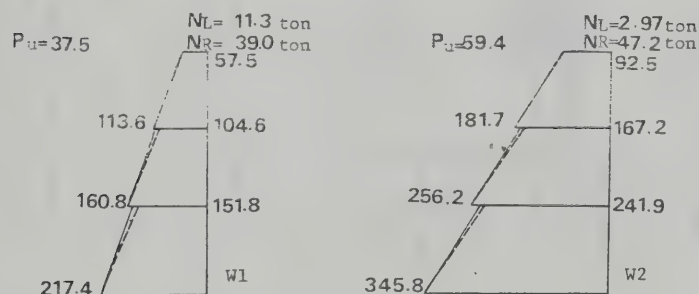
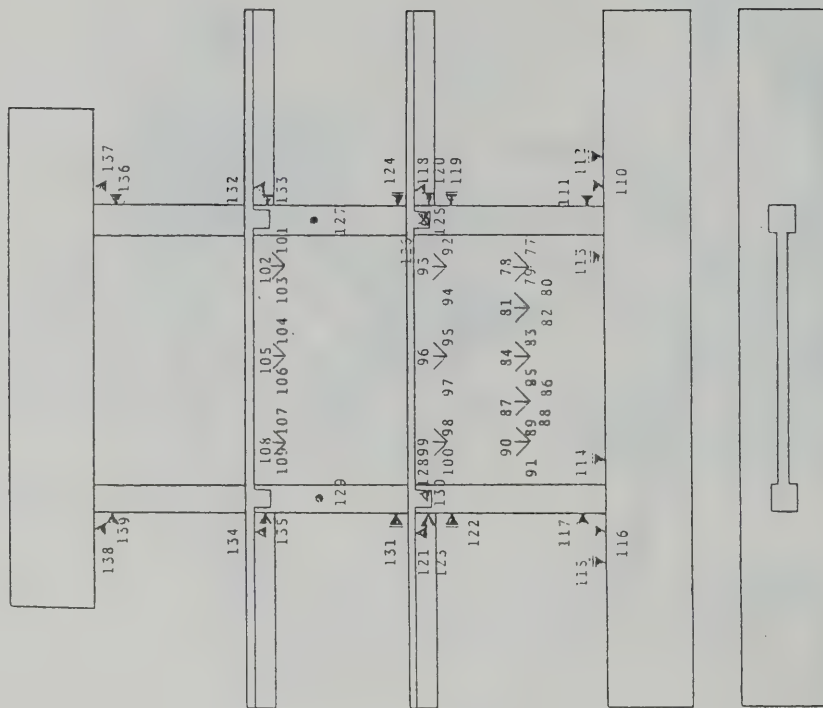
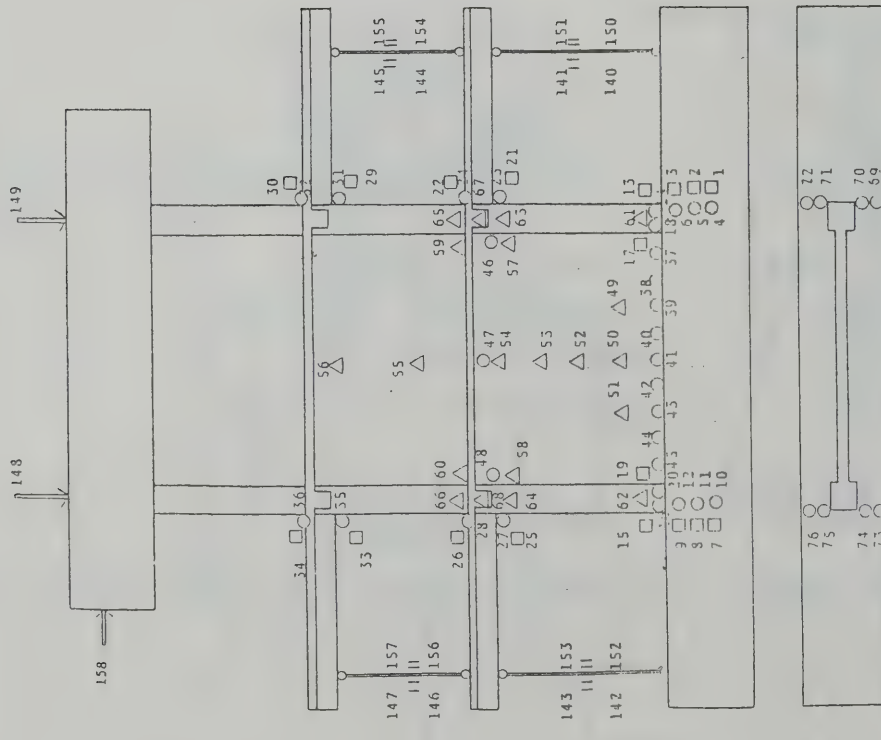


Fig.3.1.5 Bending Moment at Yielding of the Specimens (Unit:t.m)

\* (Dashed lines express these of the half-scale seven-story shear walls.)





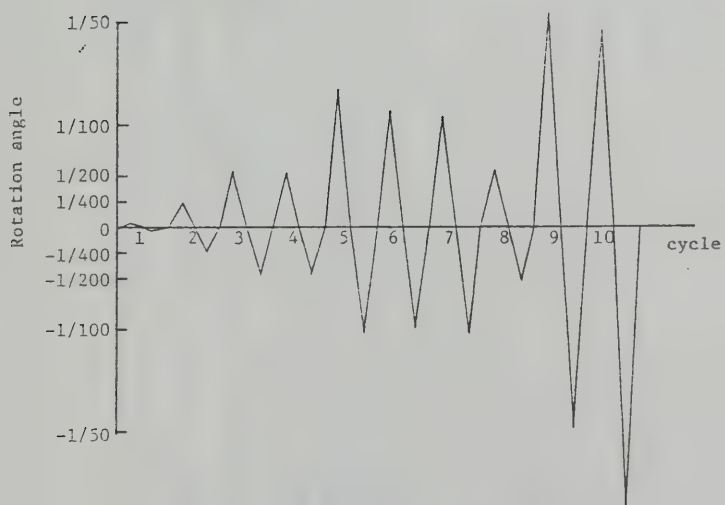
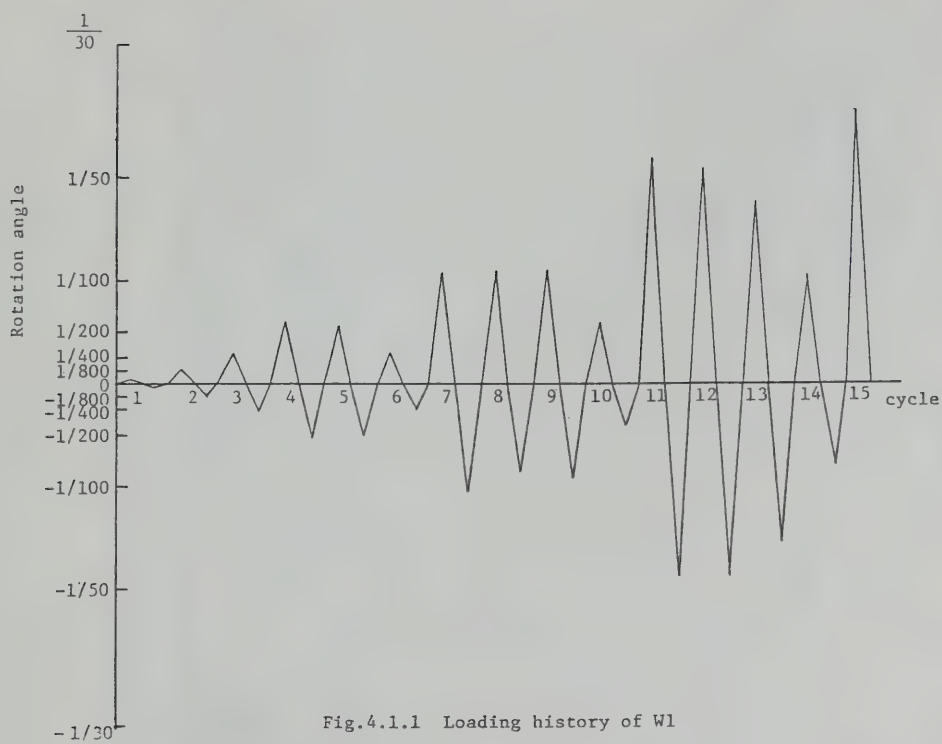


Table 4.1.1.1 Peak load and displacement at each cycle of W1

cycle	Positive loading						Negative loading					
	1st story		2nd story		3rd story		1st story		2nd story		3rd story	
	Load (ton)	dis- place- ment(mm)	Rotation angle-3 ( $\times 10^{-3}$ )	dis- place- ment(mm)	Rotation angle-3 ( $\times 10^{-3}$ )	dis- place- ment(mm)	Load (ton)	dis- place- ment(mm)	Rotation angle-3 ( $\times 10^{-3}$ )	dis- place- ment(mm)	Rotation angle-3 ( $\times 10^{-3}$ )	dis- place- ment(mm)
1	16.45	0.500	0.286	0.733	0.226	1.433	-15.6	-0.283	-0.162	-0.633	-0.195	-1.400
2	28.7	2.250	1.286	3.800	1.169	6.533	-29.25	-1.867	-1.067	-3.900	-1.200	-6.400
3	35.37	4.833	2.762	9.033	2.779	13.200	-35.1	-3.167	-1.810	-6.167	-1.898	-12.200
4	36.95	9.517	5.438	17.533	5.395	26.567	-38.25	-7.750	-4.428	-14.000	-4.308	-25.467
5	36.55	9.550	5.457	17.433	5.364	26.267	-25.4	-7.650	-4.372	-13.700	-4.215	-25.267
6	25.4	5.150	2.943	9.367	2.882	13.333	-22.75	-3.283	-1.876	-5.800	-1.785	-12.433
7	39.15	18.150	10.371	32.700	10.062	49.333	-40.05	-16.783	-9.590	-29.733	-9.149	-50.767
8	37.55	19.067	10.895	34.500	10.615	52.000	-39.8	-13.083	-7.476	-22.933	-7.056	-40.000
9	37.15	19.200	10.971	34.630	10.655	52.133	-39.15	-13.867	-7.924	-24.100	-7.415	-41.933
10	28.1	10.133	5.790	18.133	5.579	26.333	-27.9	-7.900	-4.514	-13.567	-4.174	-25.133
11	39.15	37.933	21.676	62.633	19.272	103.933	-42.65	-32.817	-18.752	-55.367	-17.036	-90.300
12	36.95	37.183	21.247	65.800	20.246	99.467	-39.9	-37.433	-21.390	-55.200	-16.985	-101.233
13	33.35	32.383	18.504	57.000	17.538	84.367	-34.0	-27.500	-15.714	-44.733	-13.764	-73.100
14	23.4	20.750	11.857	35.900	11.046	51.133	-22.65	-13.450	-7.685	-20.433	-6.287	-36.500
15	32.35	50.600	28.914	86.00	26.462	126.600						

Table 4.1.2 Peak load and displacement at each cycle of W2

	Positive loading								Negative loading							
	Load (ton)		1st story		2nd story		3rd story		Load (ton)	1st story		2nd story		3rd story		
			dis- place- ment(mm)	Rotation angle ( $\times 10^{-3}$ )	dis- place- ment(mm)	Rotation angle ( $\times 10^{-3}$ )	dis- place- ment(mm)	Rotation angle ( $\times 10^{-3}$ )		dis- place- ment(mm)	Rotation angle ( $\times 10^{-3}$ )	dis- place- ment(mm)	Rotation angle ( $\times 10^{-3}$ )	dis- place- ment(mm)	Rotation angle ( $\times 10^{-3}$ )	
cycle	1	15.95	0.500	0.286	1.133	0.349	1.267	0.267	-14.95	-0.300	-0.171	-0.633	-0.195	-1.300	-0.273	
	2	47.85	3.750	2.142	7.900	2.431	11.267	2.372	-48.3	-3.317	-1.895	-6.867	-2.113	-11.033	-2.322	
	3	59.9	8.567	4.895	16.600	5.108	24.100	5.073	-62.5	-7.883	-4.504	-15.533	-4.779	-23.333	-4.912	
	4	56.4	8.717	4.981	16.733	5.149	24.067	5.066	-59.75	-8.150	-4.657	-15.867	-4.882	-23.567	-4.961	
	5	66.15	20.650	11.800	42.533	13.087	62.667	13.193	-68.1	-19.650	-11.228	-34.400	-10.585	-48.900	-10.294	
	6	60.75	18.383	10.504	36.867	11.344	54.067	11.382	-63.0	-19.983	-11.418	-33.400	-10.277	-47.033	-9.901	
	7	59.1	17.750	10.142	35.333	10.872	51.567	10.856	-62.0	-21.150	-12.085	-34.567	-10.636	-47.933	-10.091	
	8	36.35	7.750	4.428	15.867	4.882	22.767	4.793	-37.5	-12.733	-7.276	-18.667	-5.744	-24.900	-5.242	
	9	67.3	27.300	15.600	60.100	18.492	97.367	20.498	-72.5	-42.333	-24.190	-70.433	-21.672	-93.433	-19.670	
	10	64.8	24.250	13.850	59.200	18.215	90.700	19.094	-65.0			-101.800	-31.323	-131.767	-27.740	

Table 4.2.1 Crack pattern of W1

	Positive loading			Negative loading		
	Load or Rotation angle	Story	crack pattern	Load or Rotation angle	Story	crack pattern
Wall	24(ton)	1st	shear crack	-24(ton)	1st	shear crack
	34(ton)	2nd	shear crack	-32(ton)	2nd 3rd	shear crack
	36(ton)	3rd	shear crack			
Column	12(ton)	1st	flexure crack	-14(ton)	1st	flexure crack
	28(ton)	2nd	flexure crack	-20(ton)	1st	shear crack
	36(ton)	3rd	shear crack	-32(ton)	2nd 3rd	shear crack
	38(ton)	3rd	flexure crack	//	2nd	flexure crack
	1/100	1st	start of crush of concrete	-1/100	3rd	flexure crack
				-1/40	1st	crush
Beam	28(ton)	2nd 3rd	flexure crack (top)	-10(ton)	2nd	flexure crack (top)
	//	3rd	flexure crack (bottom)	-28(ton)	3rd	flexure crack (top)
	30(ton)	2nd	flexure crack (bottom)	//	2nd 3rd	flexure crack (bottom)



Table 4.2.2 Crack pattern of W2

	Positive loading			Negative loading		
	Load or Rotation angle	Story	crack pattern	Load or Rotation angle	Story	crack pattern
Wall	16(ton)	1st	shear crack	-20(ton)	1st	shear crack
	32(ton)	2nd	shear crack	-32(ton)	2nd	shear crack
	36(ton)	3rd	shear crack	-36(ton)	3rd	shear crack
	1/100	1st	start of crush of concrete	-1/100	1st	start of crush of concrete
Column	20(ton)	1st	flexure crack	-20(ton)	1st	flexure crack
	32(ton)	2nd	flexure crack	-32(ton)	2nd	flexure crack
				-44(ton)	2nd	shear crack
	48(ton)	3rd	flexure crack	-48(ton)	3rd	flexure crack
	1/200	2nd 3rd	shear crack	-1/200	3rd	shear crack
	1/150	1st	shear crack			
	1/100	1st	start of crush of concrete	-1/100	1st	shear crack
				//	1st	start of crush of concrete
				-1/50	1st	crush
Beam	24(ton)	3rd	flexure crack (bottom)	-12(ton)	3rd	flexure crack (bottom)
	28(ton)	2nd	flexure crack (bottom)	-20(ton)	2nd	flexure crack (bottom)
	40(ton)	2nd	flexure crack (top)	-36(ton)	2nd 3rd	flexure crack (top)
	44(ton)	3rd	flexure crack (top)			
	1/100	2nd 3rd	start of crush of concrete (bottom)			
				-1/75	2nd 3rd	start of crush of concrete (bottom)

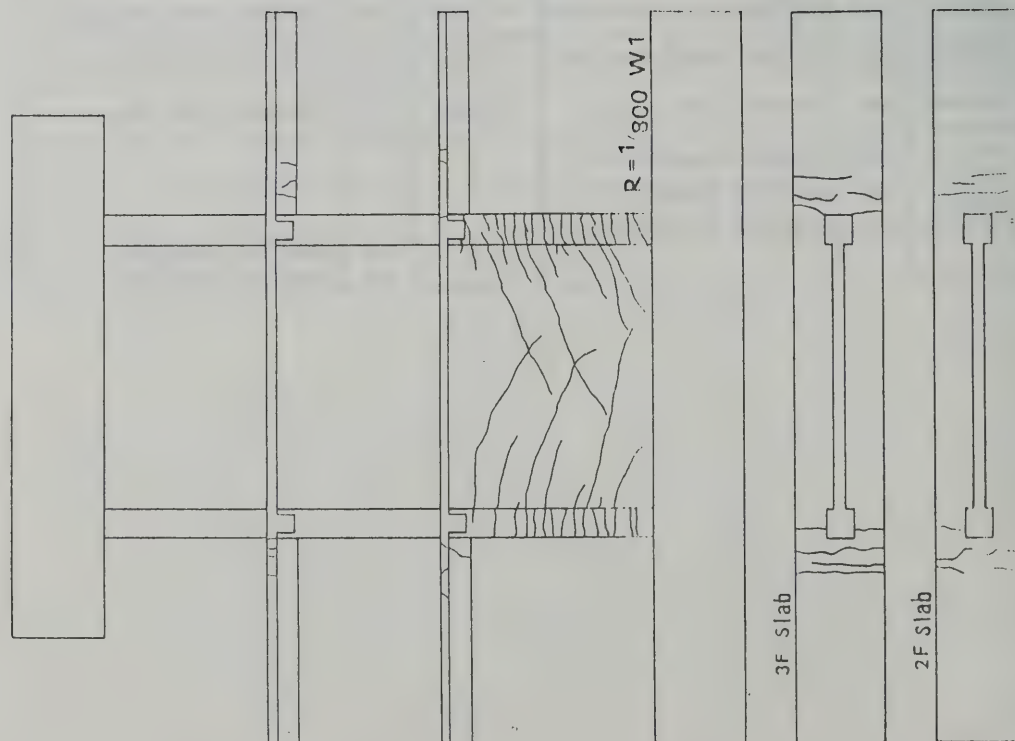


Fig. 4.2.1 Cracks at  $R = 1/800$

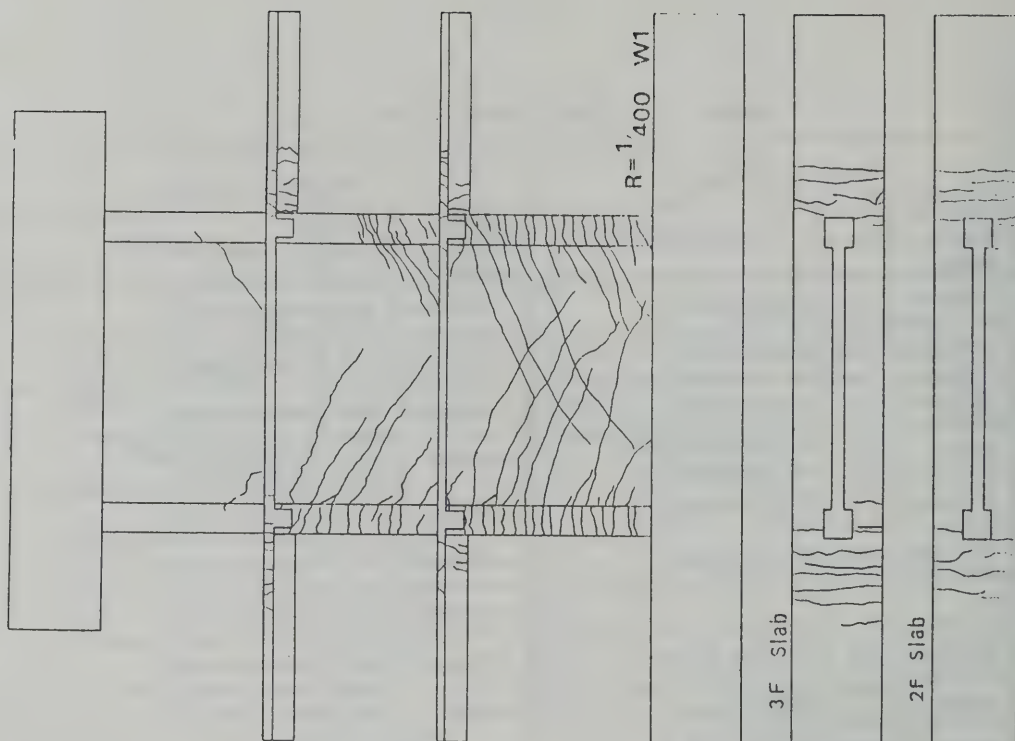


Fig. 4.2.2 Cracks at  $R = 1/400$

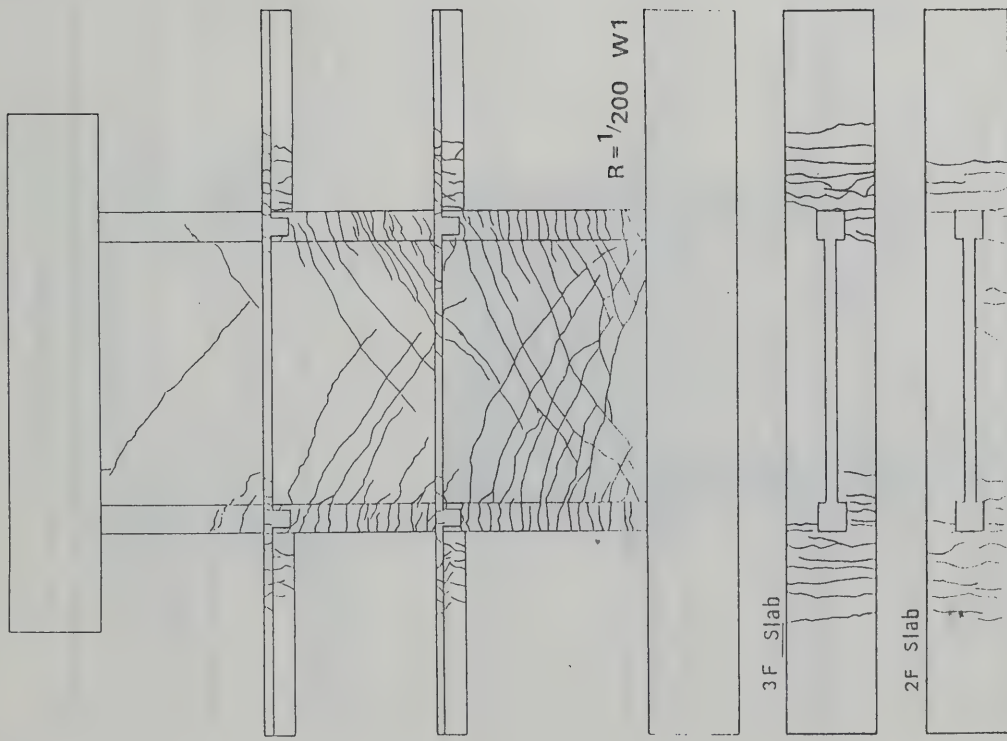


Fig. 4.2.3 Cracks at  $R = 1/200$

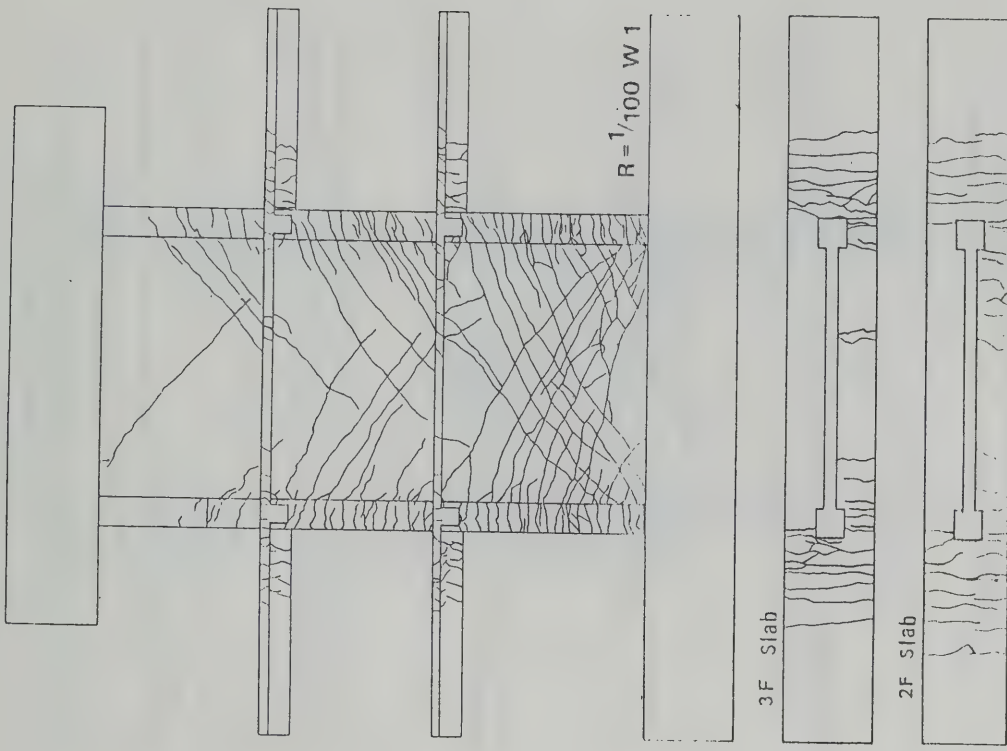


Fig. 4.2.4 Cracks at  $R = 1/100$

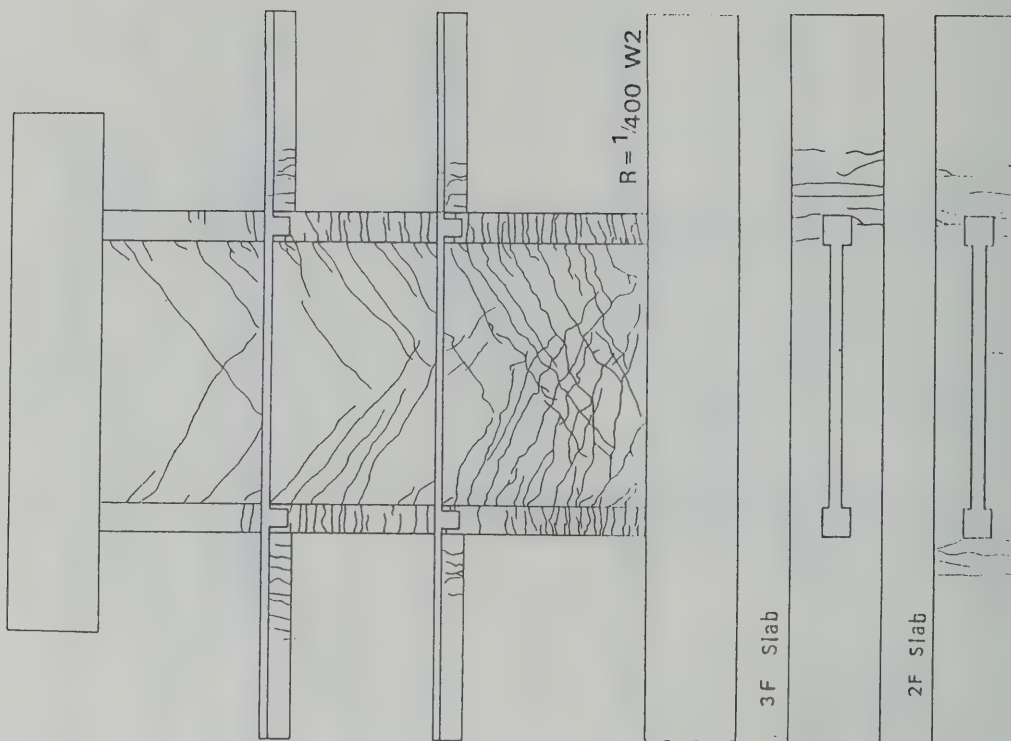


Fig. 4.2.5 Final Cracks

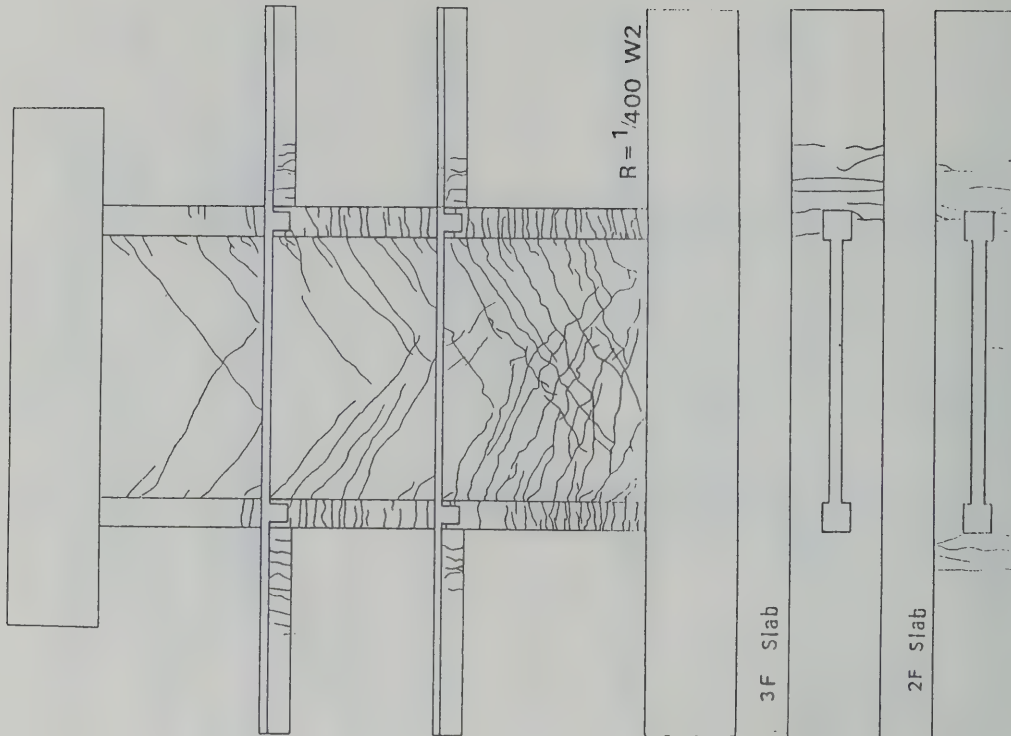
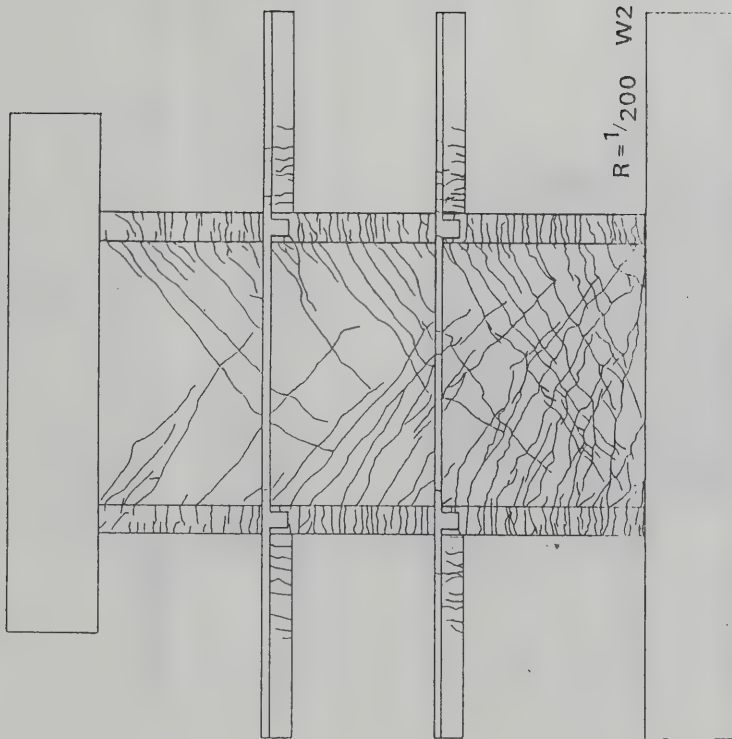
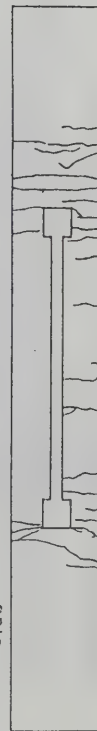


Fig. 4.2.6 Cracks at  $R = 1/400$





3F Slab



2F Slab

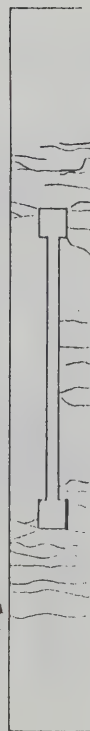
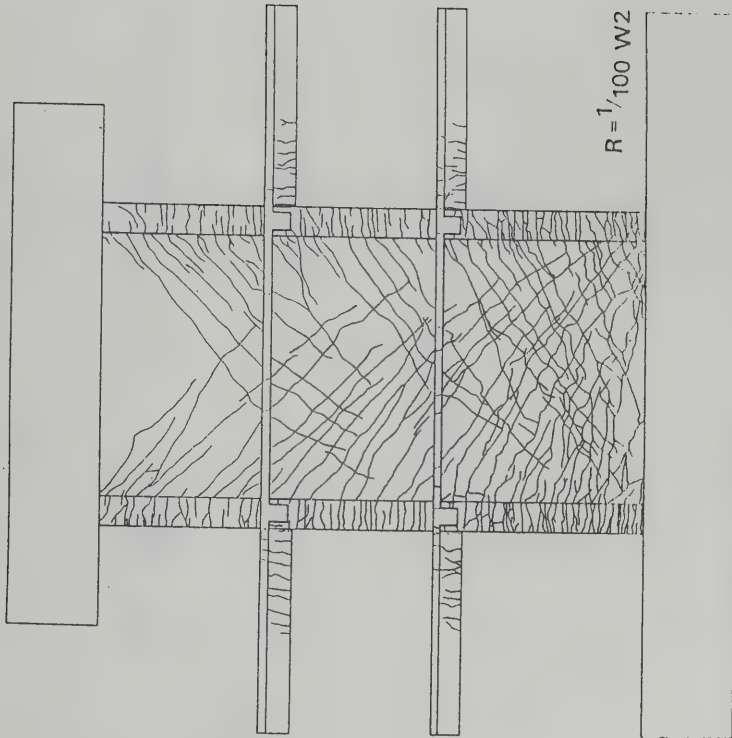
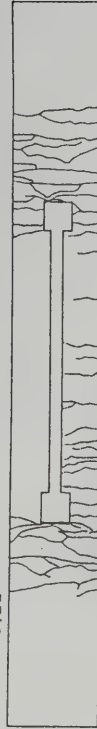


Fig. 4.2.7 Cracks at  $R = 1/200$



3F Slab



2F Slab



Fig. 4.2.8 Cracks at  $R = 1/100$

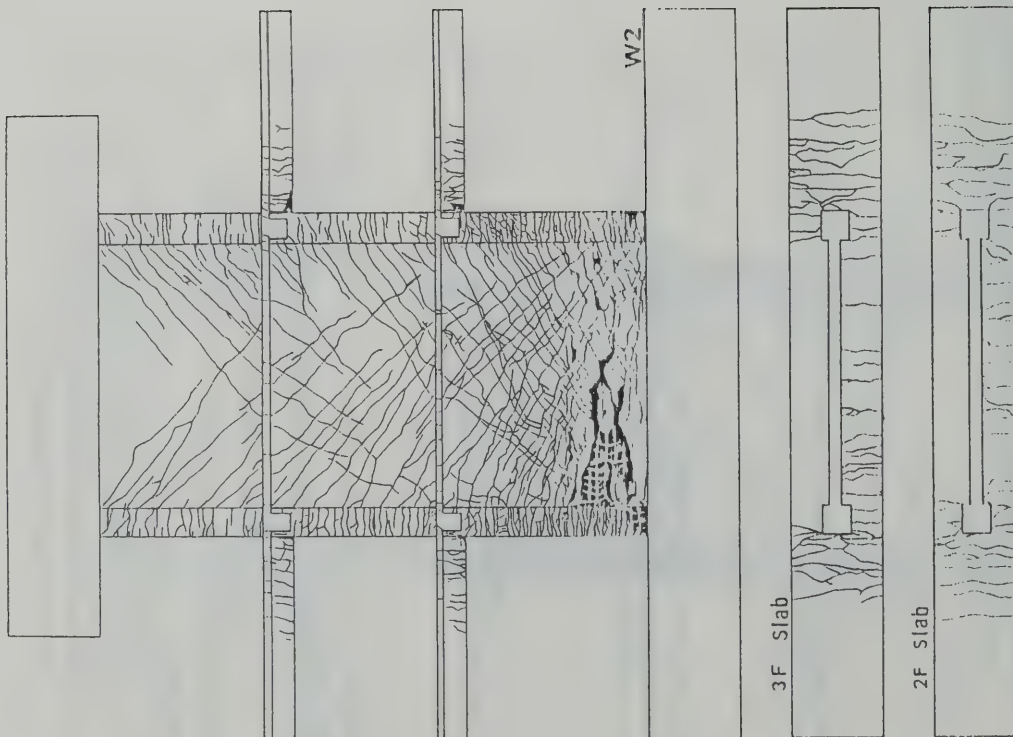
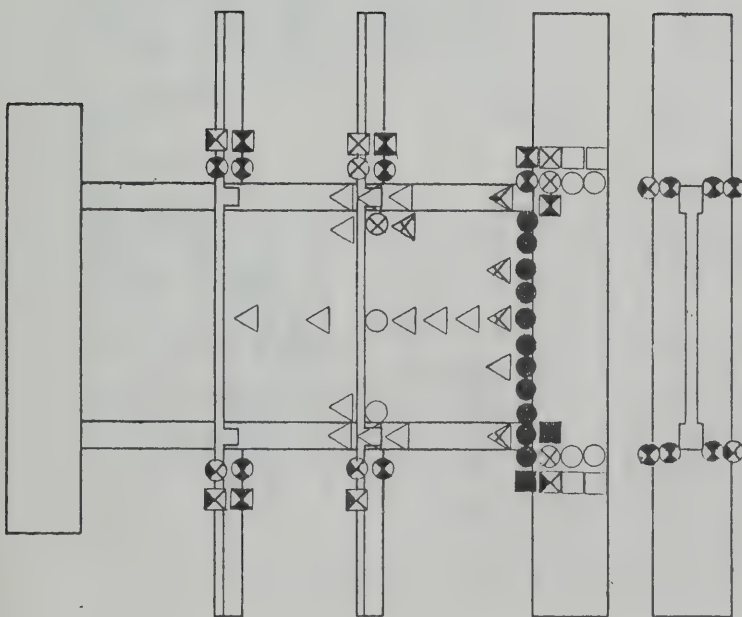


Fig.4.2.3 Final Cracks

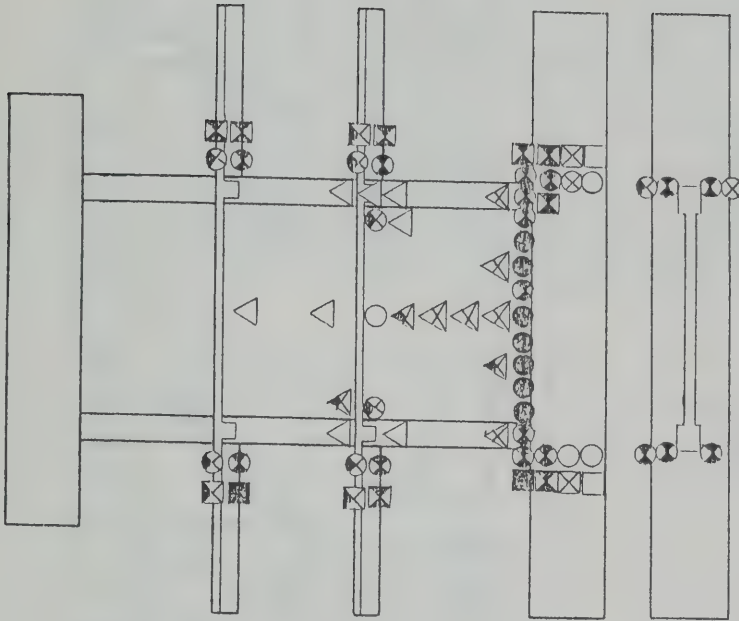


Note: ● ⊗ ○ = main reinforcement in the beam, slab and column, and vertical reinforcement in the wall, which are yielded at  $R=0 \sim 1/400$ ,  $1/400 \sim 1/200$ ,  $1/200 \sim 1/100$ ,  $1/100 \sim 1/50$  and that which did not yield, respectively.

■ ⊗ ⊗ □ = similar reinforcements to those above mentioned, but opposite side.

▲ ▲ ▲ ▲ = hoop and horizontal reinforcement in the wall, which are yielded at  $R=0 \sim 1/400$ ,  $1/400 \sim 1/200$ ,  $1/200 \sim 1/100$ ,  $1/100 \sim 1/50$  and that which did not yield, respectively.

Fig. 4.3.1 Yielding Pattern of Reinforcement of the Specimen W1



Note: ● ⊗ ○ = main reinforcement in the beam, slab and column, and vertical reinforcement in the wall, which are yielded at  $R=0 \sim 1/400$ ,  $1/400 \sim 1/200$ ,  $1/200 \sim 1/100$ ,  $1/100 \sim 1/50$  and not yielded, respectively.

■ ⊗ ⊗ □ = similar reinforcements to those above mentioned, but side is opposite.

▲ ▲ ▲ ▲ = hoop and horizontal reinforcement in the wall, which are yielded at  $R=0 \sim 1/400$ ,  $1/400 \sim 1/200$ ,  $1/200 \sim 1/100$ ,  $1/100 \sim 1/50$  and not yielded, respectively.

Fig. 4.3.2 Yielding Pattern of Reinforcement of the Specimen W2

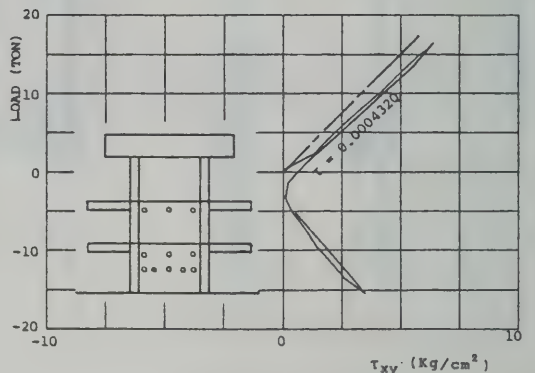
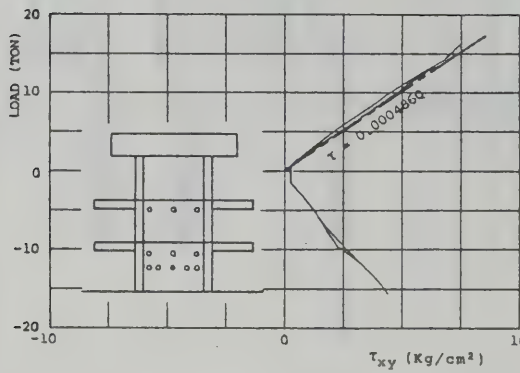
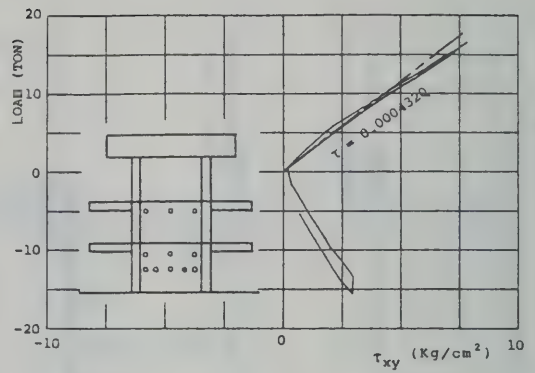
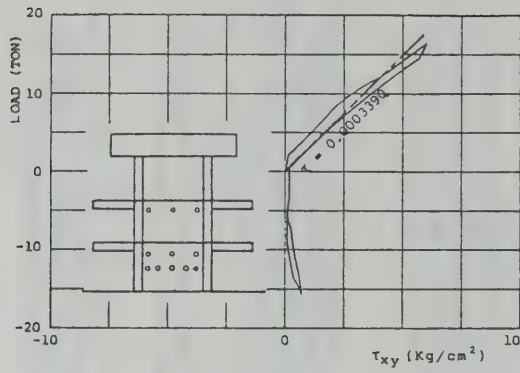


Fig.4.3.3 Lateral load versus shearing stress relationship of wall of W1 (No.1)

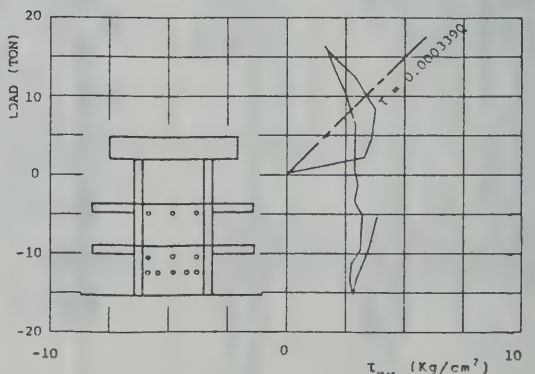
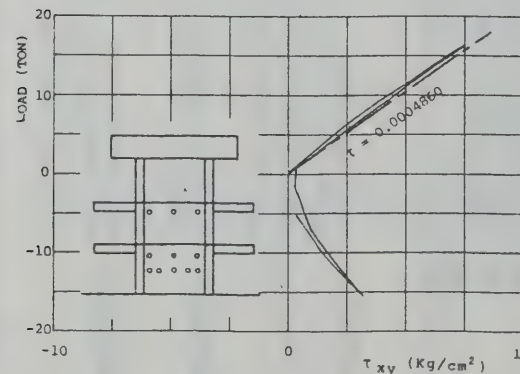
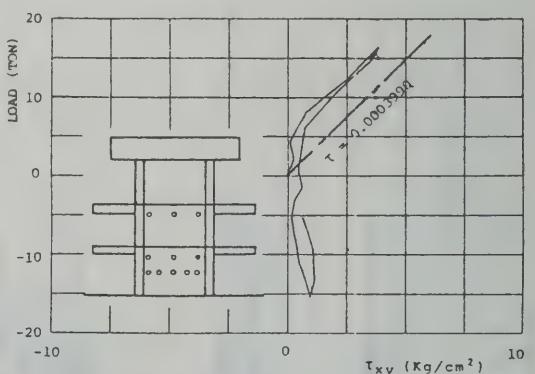
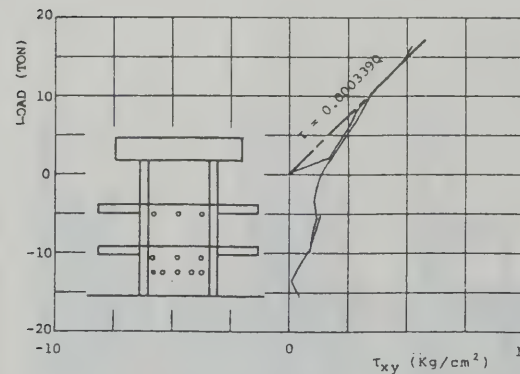


Fig.4.3.4 Lateral load versus shearing stress relationship of wall of W1 (No.2)



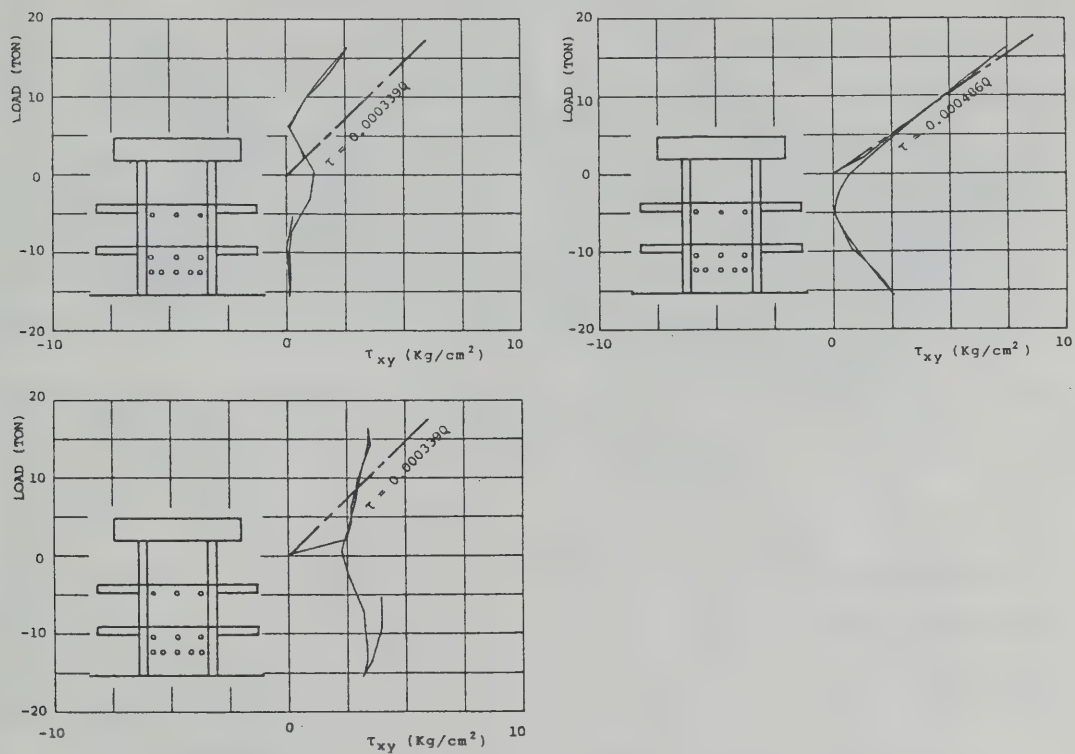


Fig.4.3.5 Lateral load versus shearing stress relationship of wall of W1 (No.3)

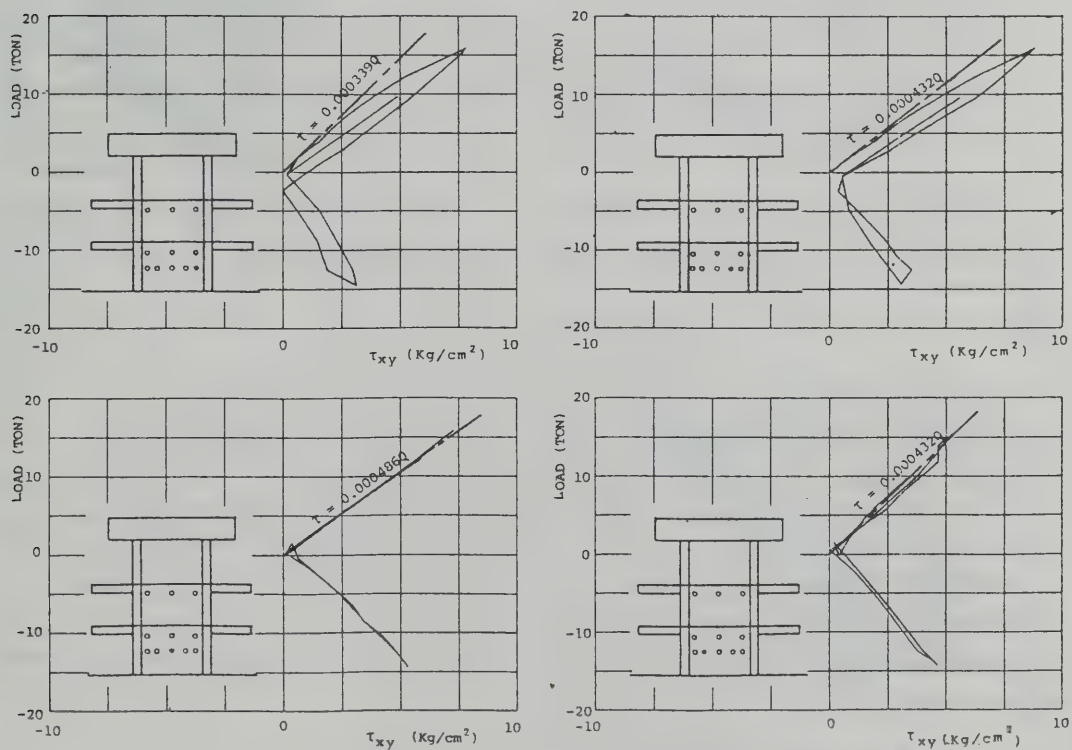


Fig.4.3.6 Lateral load versus shearing stress relationship of wall of W2 (No.1)

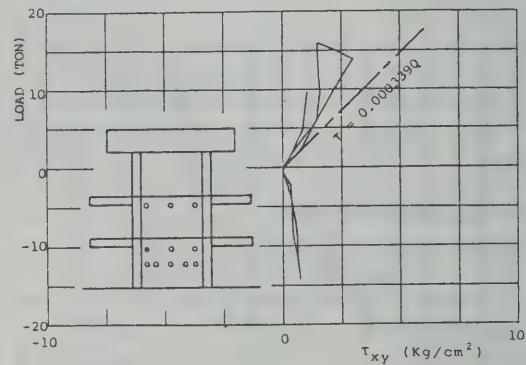
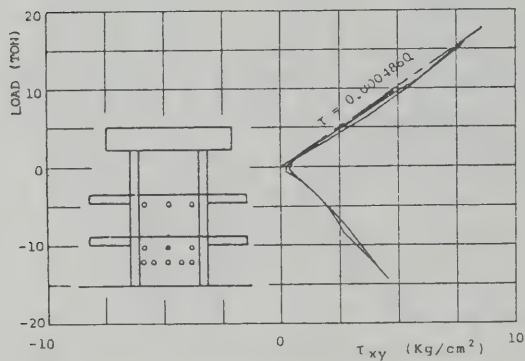
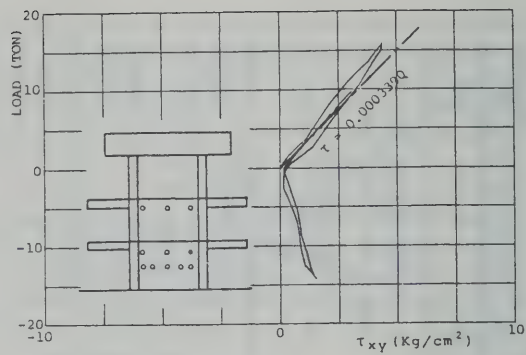
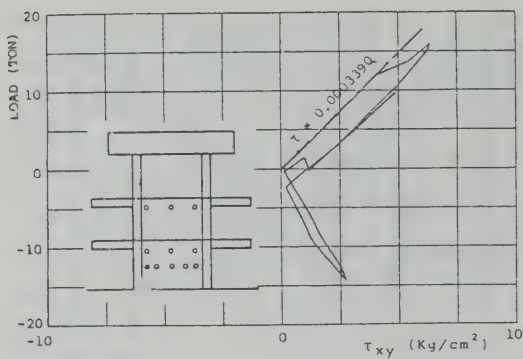


Fig.4.3.7 Lateral load versus shearing stress relationship of wall of W2 (No.2)

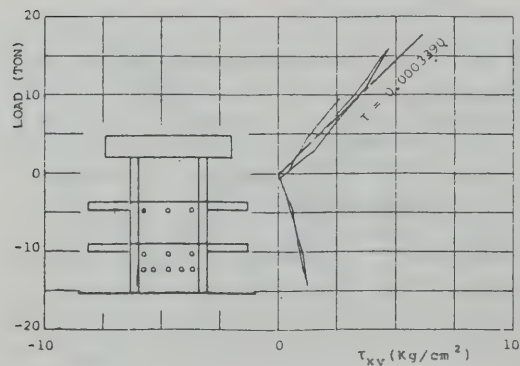
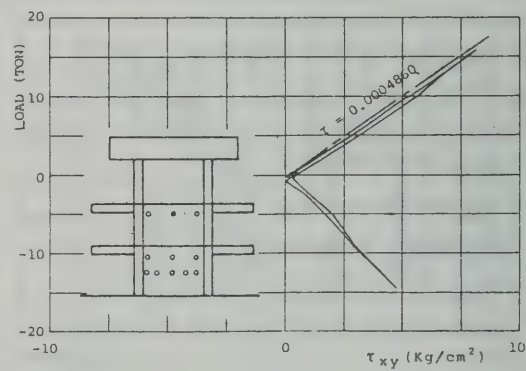
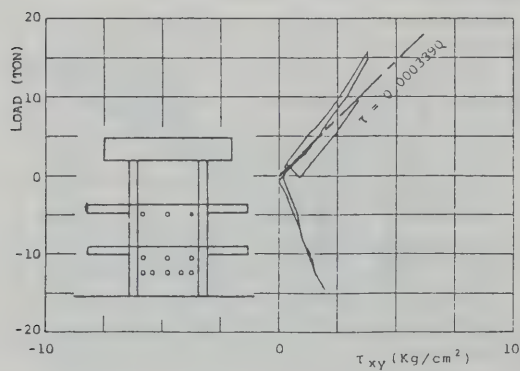


Fig.4.3.8 Lateral load versus shearing stress relationship of wall of W2 (No.3)

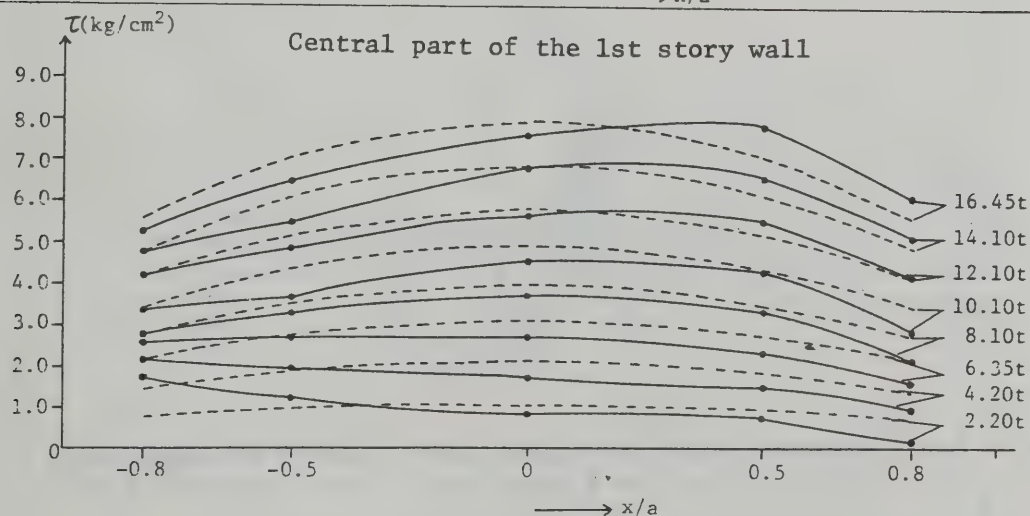
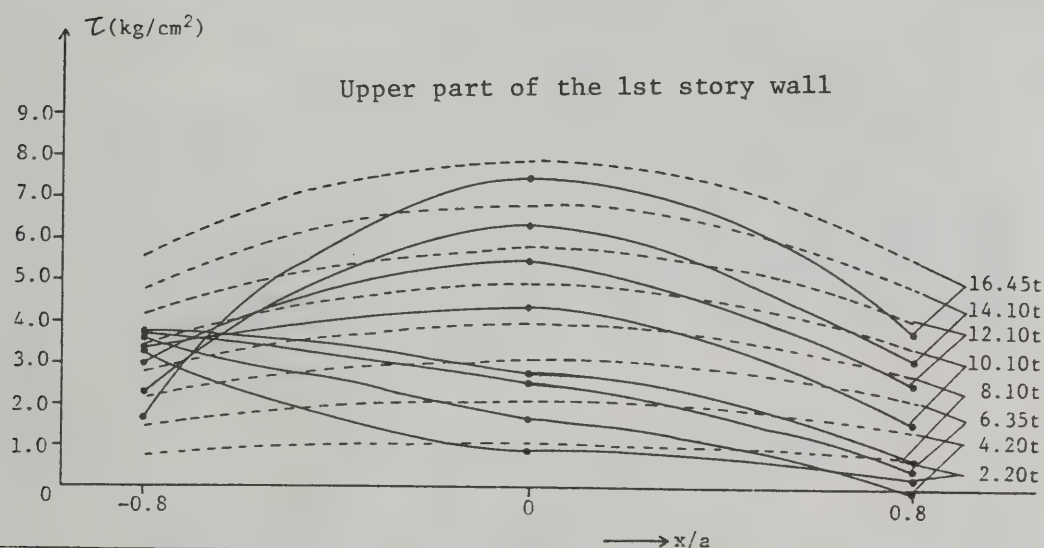
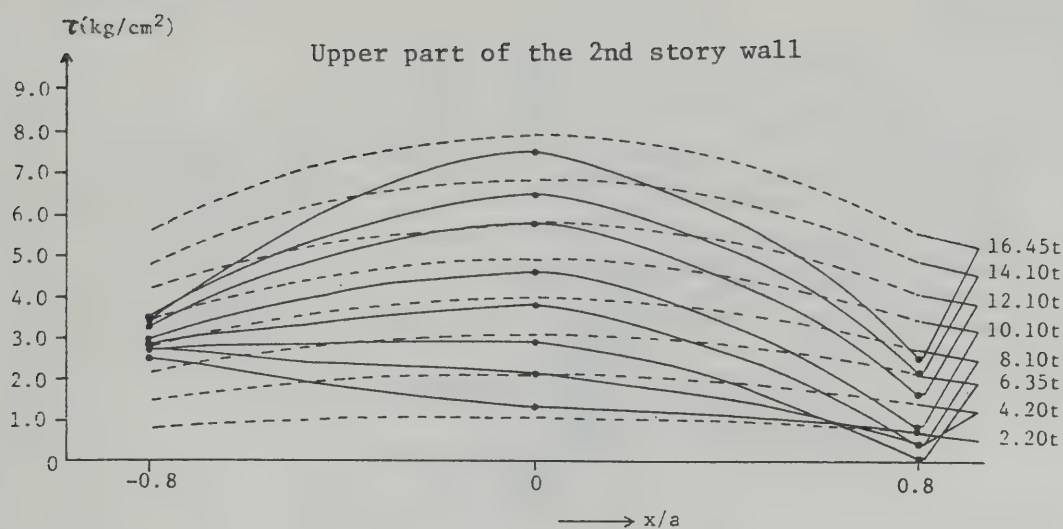
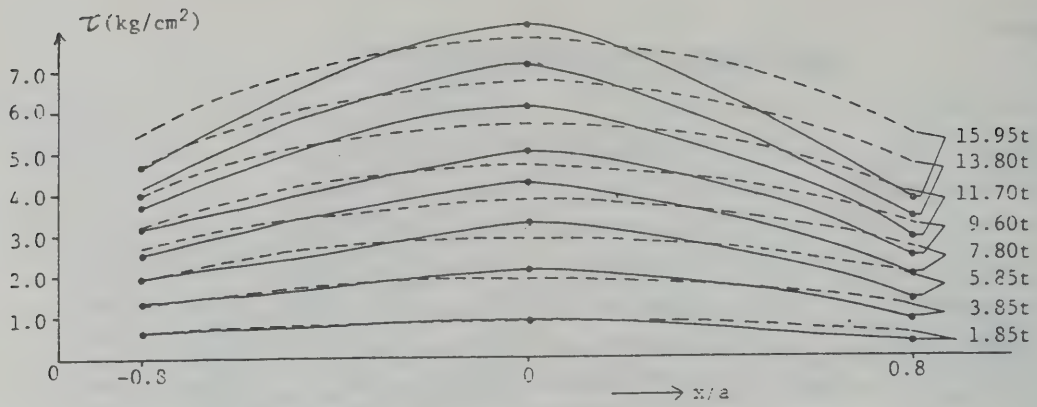


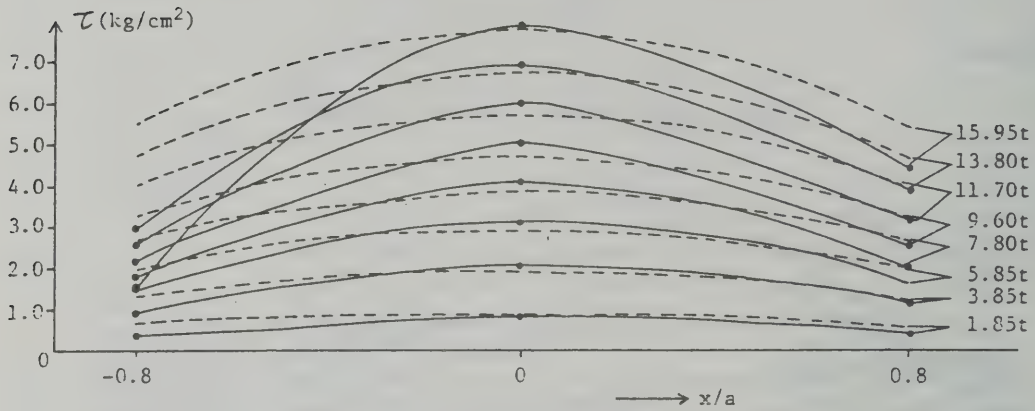
Fig. 4.3.9 Shearing stress distribution of central and upper part of the 1st wall and upper part of the 2nd wall of W1

( note :  $x$  = distance from center of wall  
 $a$  = horizontal half clear length of wall )

### Upper part of the 2nd story wall



### Upper part of the 1st story wall



### Central part of the 1st story wall

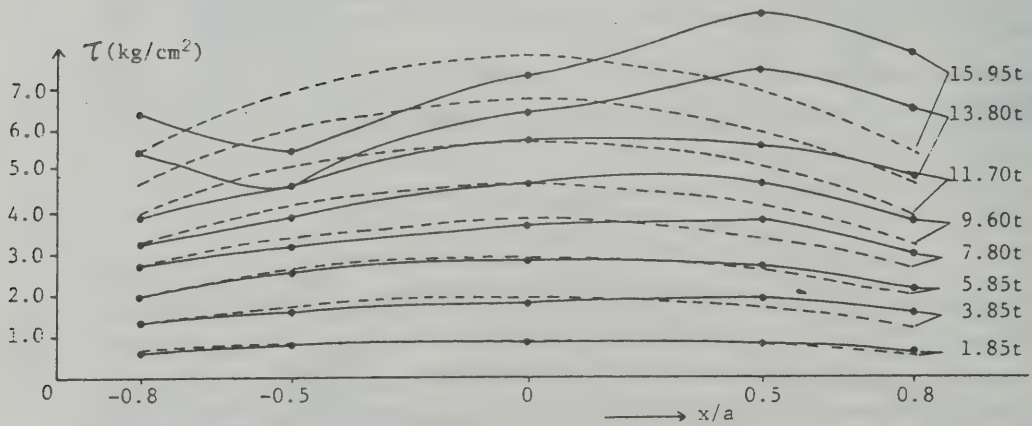


Fig. 4.3.10 Shearing stress distribution of central and upper part of the 1st wall and upper part of the 2nd wall of W2

(note :  $x$  = distance from center of wall  
 $a$  = horizontal half clear length of wall)



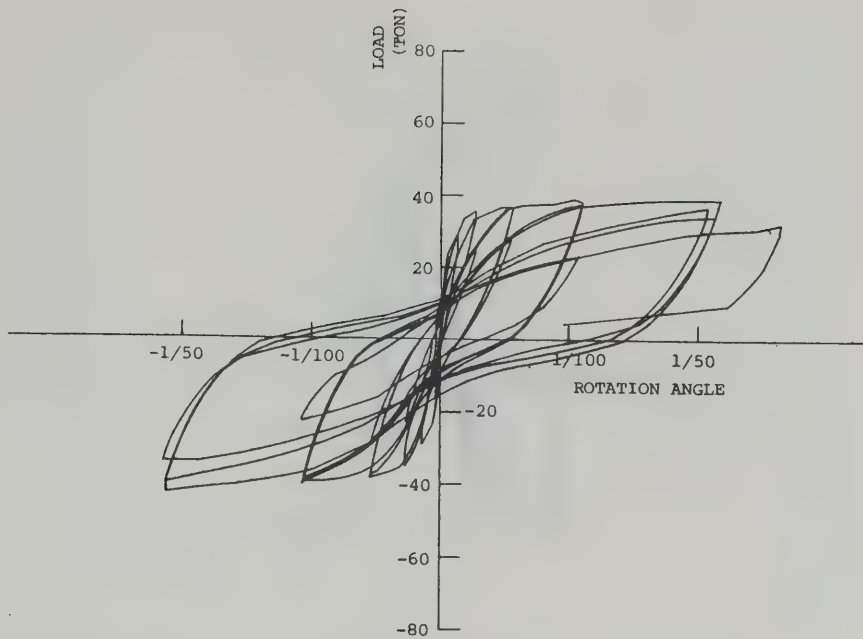


Fig.4.4.1 Lateral load versus top floor deflection relationship of W1

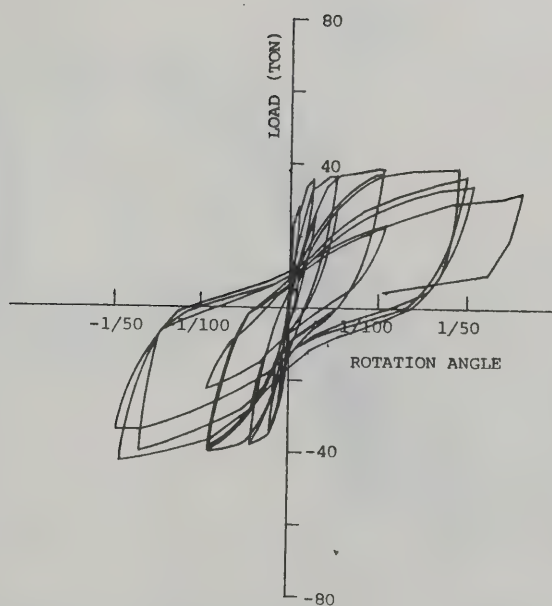


Fig. 4.4.2 Lateral load versus 3rd floor deflection relationship of W1

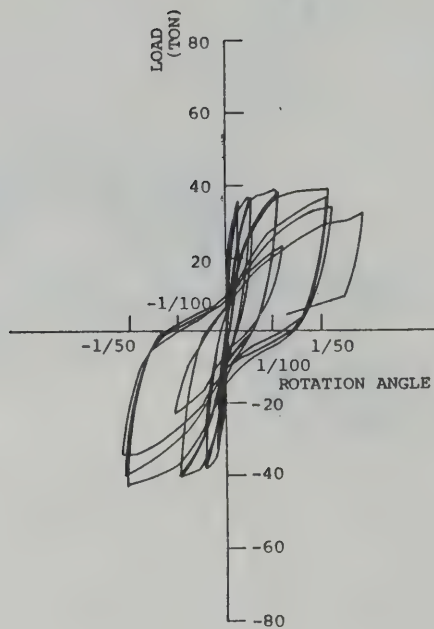


Fig. 4.4.3 Lateral load versus 2nd floor deflection relationship on W1

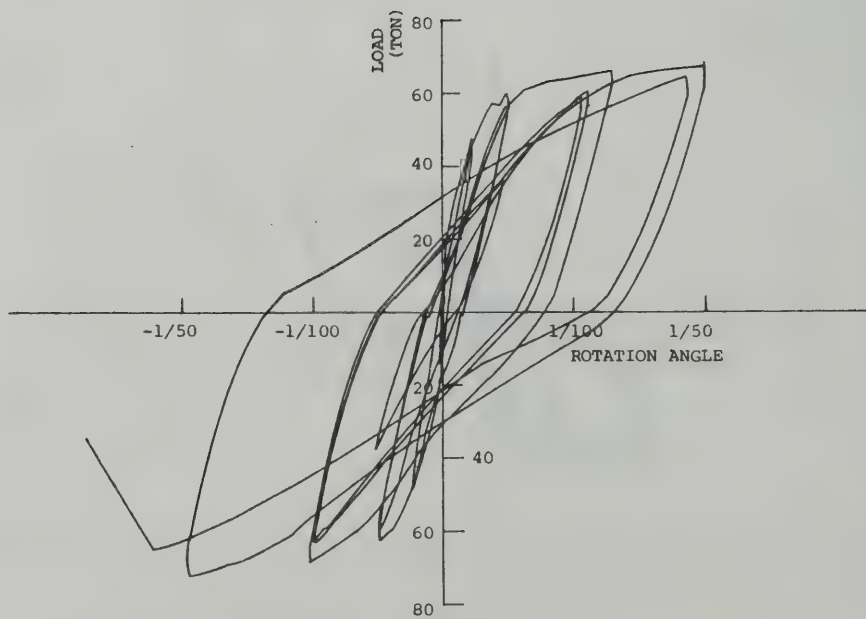


Fig.4.4.4 Lateral load versus top floor deflection relationship of W2

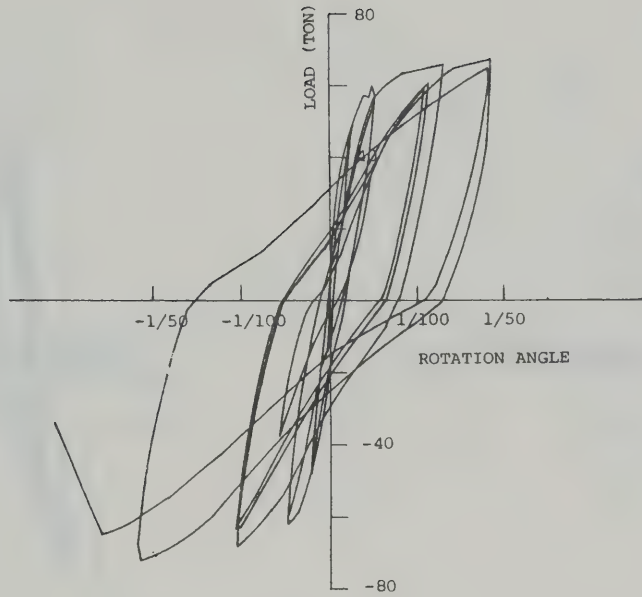


Fig.4.4.5 Lateral load versus 3rd floor deflection relationship of W2

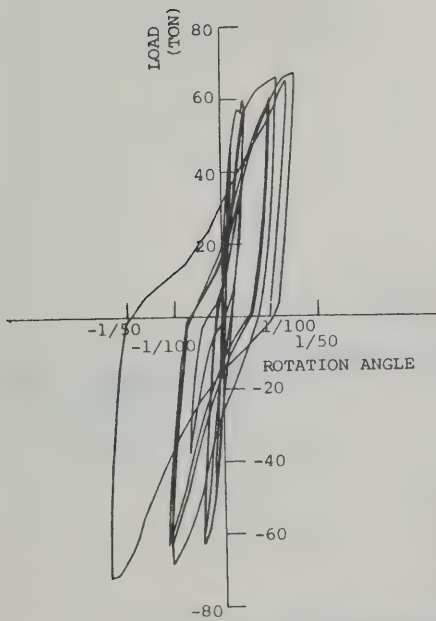


Fig.4.4.6 Lateral load versus 2nd floor deflection relationship of W2

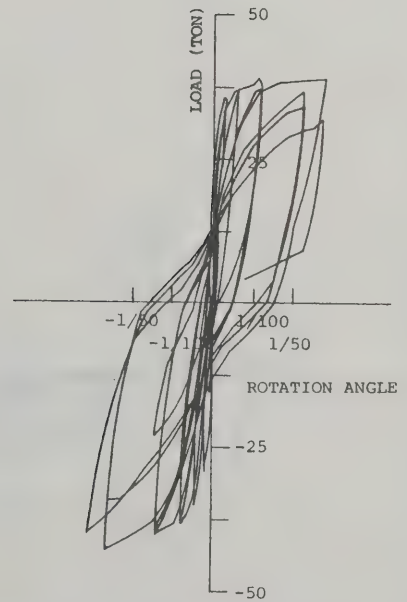


Fig.4.4.7 Lateral load versus relative deflection relationship of 3rd story of W1

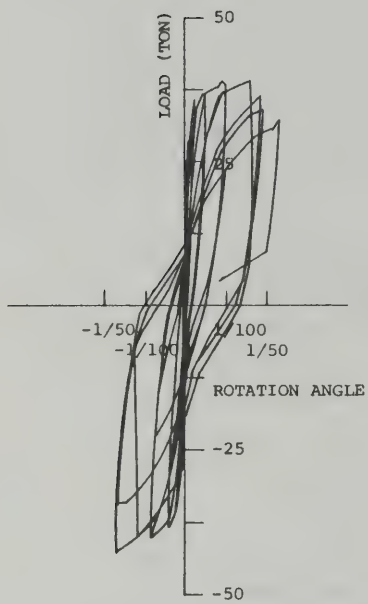


Fig.4.4.8 Lateral load versus relative deflection relationship of 2nd story of W1

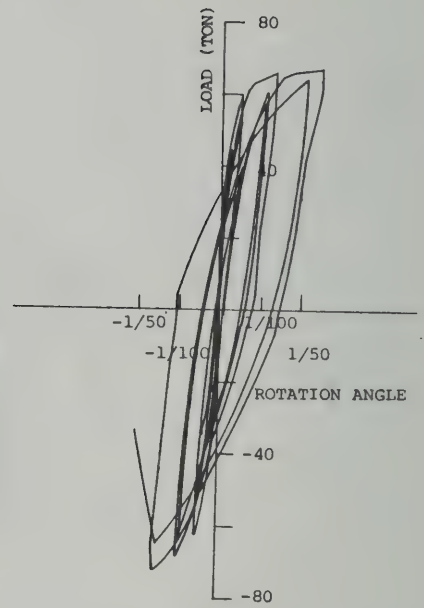


Fig.4.4.9 Lateral load versus relative deflection relationship of 3rd story of W2

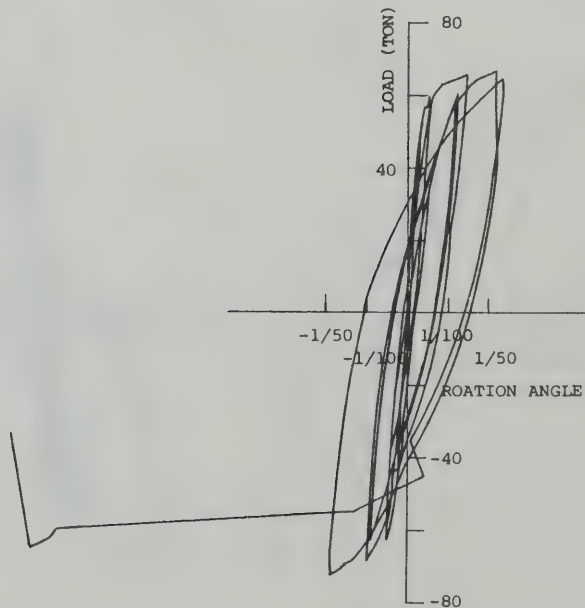


Fig.4.4.10 Lateral load versus relative deflection relationship of 2nd story of W2



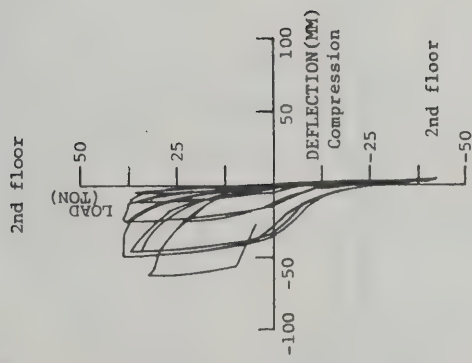
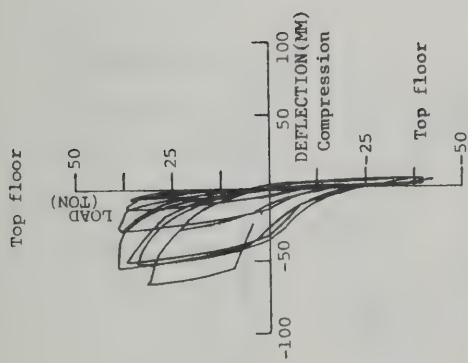


Fig.4.4.11 Lateral load versus vertical displacement relationship of top and 2nd floors at loading side of W1

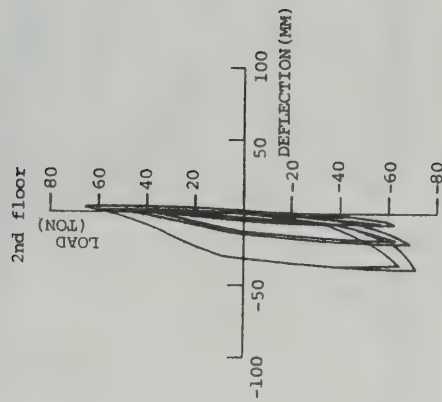
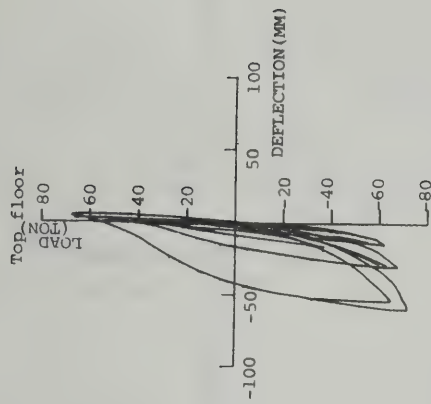


Fig.4.4.12 Lateral load versus vertical displacement relationship of top and 2nd floors at opposite side of loading of W2

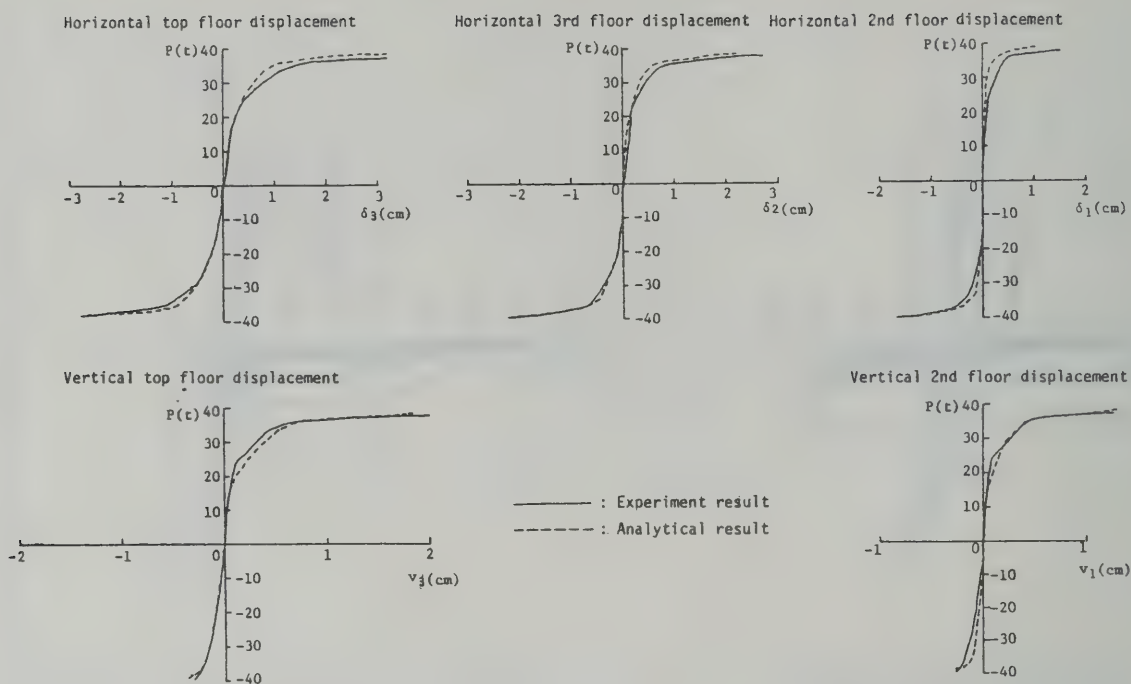


Fig.4.4.13. Comparison of analytical displacements with experimental results of W1

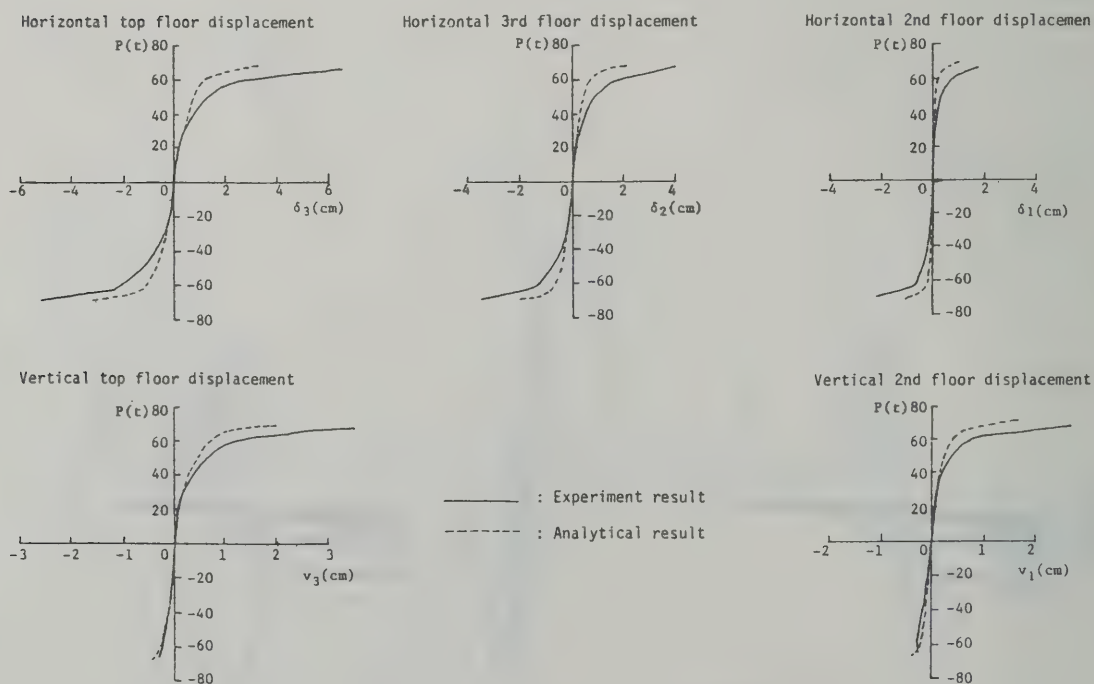


Fig.4.4.14. Comparison of analytical displacements with experimental results of W2

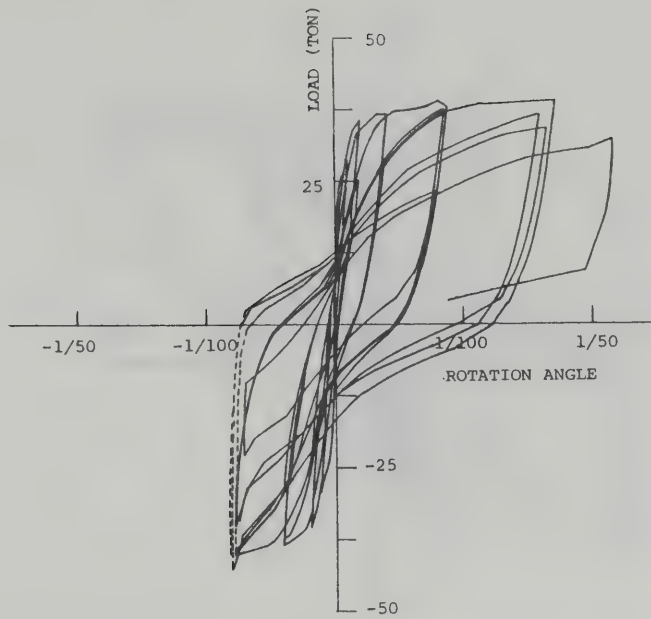


Fig.4.4.15 Lateral load versus chord rotation relationship of 2nd floor of W1 obtained by vertical displacements  $L_{v1}^{\delta}$  and  $R_{v1}^{\delta}$

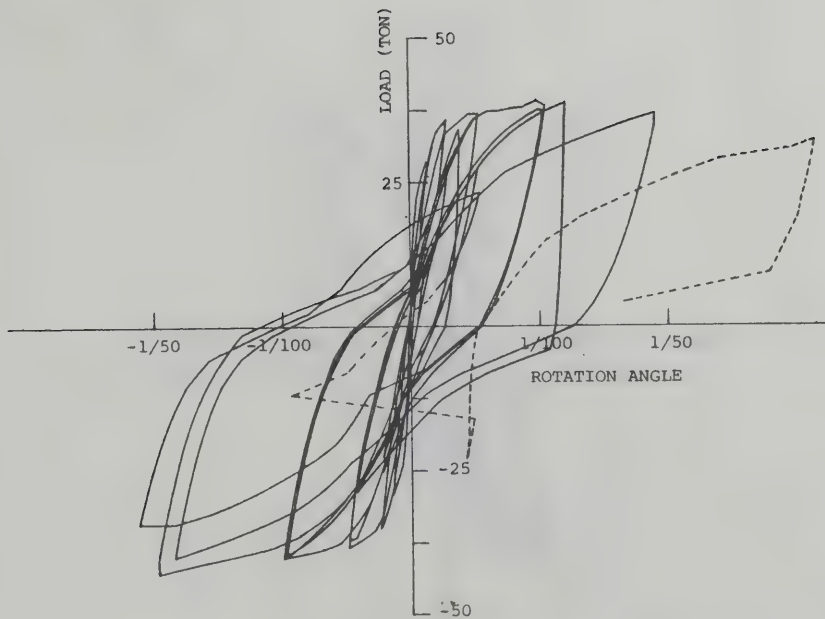


Fig.4.4.16 Lateral load versus chord rotation relationship of 3rd floor of W1 obtained by vertical displacements  $L_{v2}^{\delta}$  and  $R_{v2}^{\delta}$

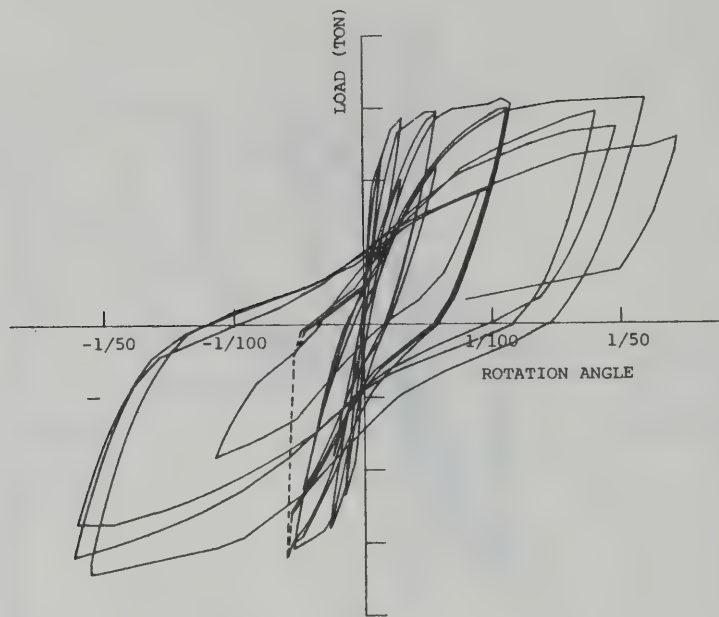


Fig.4.4.17 Laterl load versus chord rotation relationship of top floor of W1 obtained by vertical displacements  $L\delta_{v3}$  and  $R\delta_{v3}$

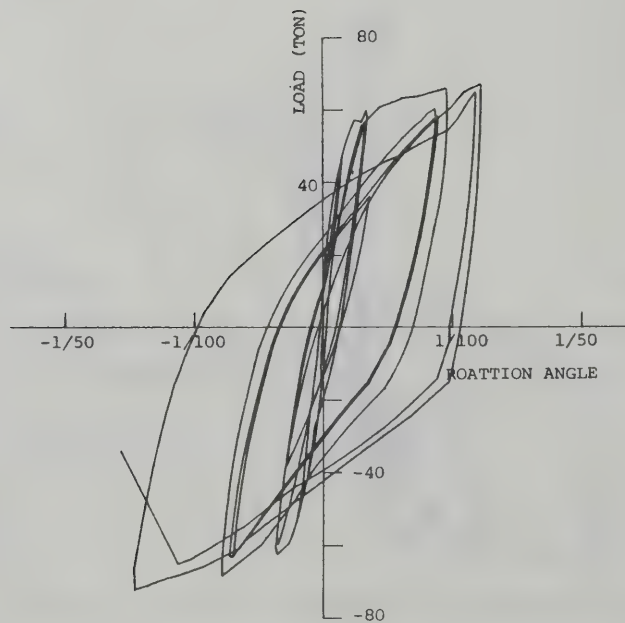


Fig.4.4.18 Laterl load versus chord rotation relationship of 2nd floor of W2 obtained by vertical displacements  $L\delta_{v1}$  and  $R\delta_{v1}$



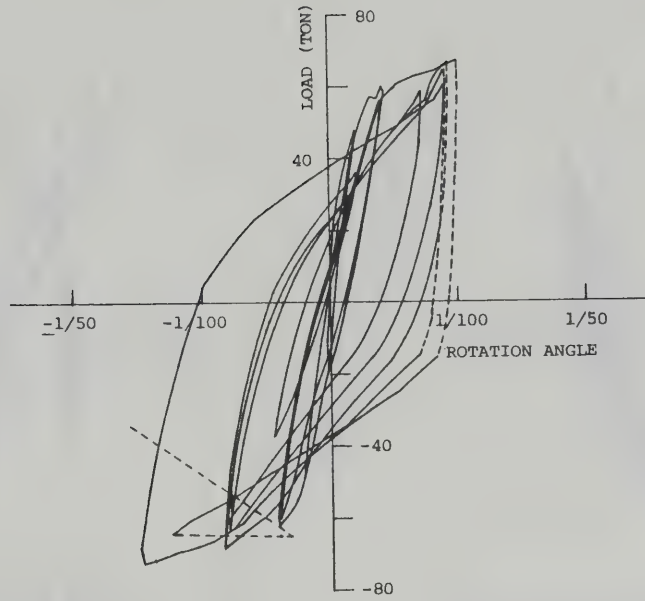


Fig.4.4.19 Lateral load versus chord rotation relationship of 3rd floor of W2 obtained by vertical displacements  $L_{V2}^{\delta}$  and  $R_{V2}^{\delta}$

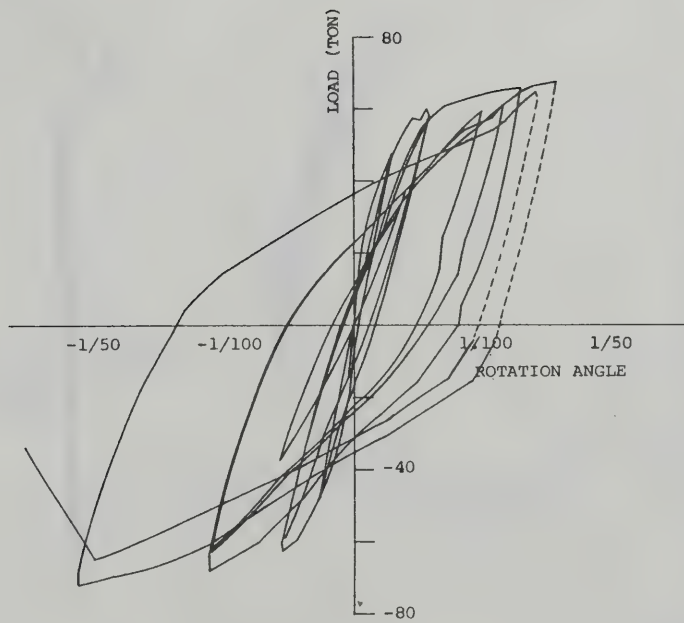


Fig.4.4.20 Lateral load versus chord rotation relationship of top floor of W2 obtained by vertical displacements  $L_{V3}^{\delta}$  and  $R_{V3}^{\delta}$

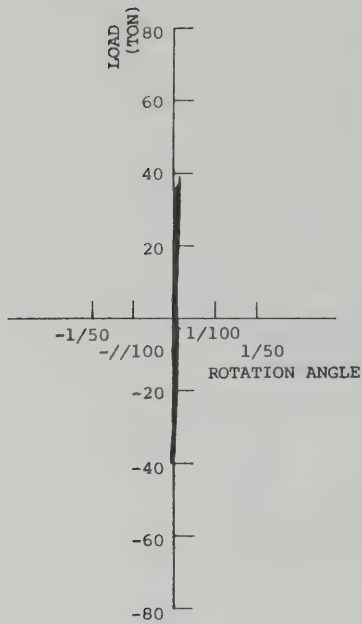


Fig.4.4.21 Lateral load versus tangential drift relationship of 2nd story of W1

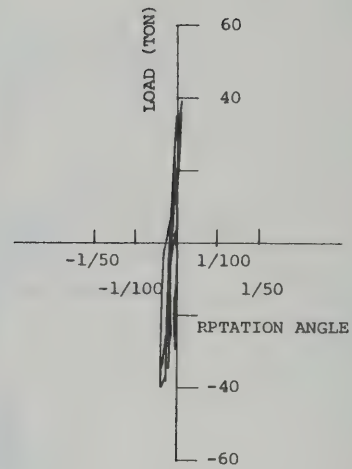


Fig.4.4.22 Lateral load versus rotation angle relationship of the floor of W2 obtained by vertical displacements  $L\delta_{v3}$  and  $R\delta_{v3}$

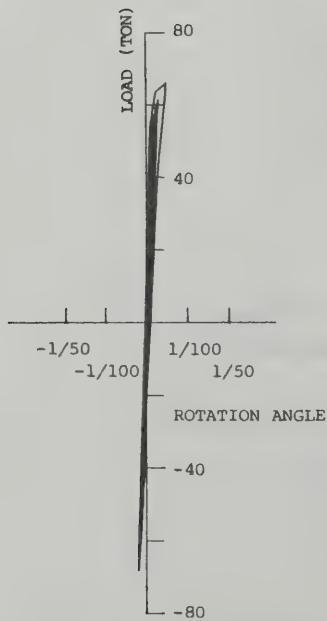


Fig.4.4.23 Lateral load versus tangential drift relationship of 2nd story of W2

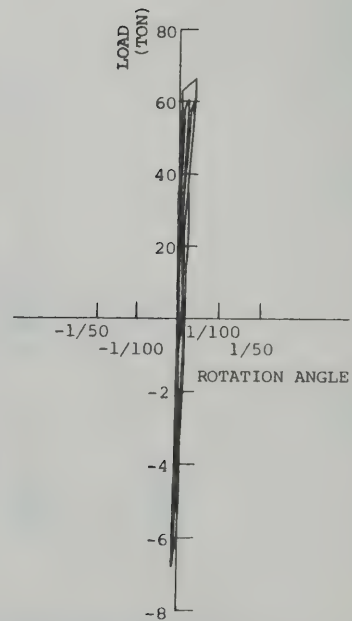


Fig.4.4.24 Lateral load versus tangential drift relationship of 3rd story of W2

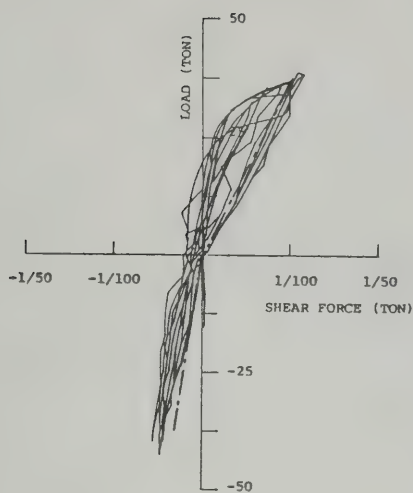


Fig.4.5.1 Lateral load versus shear force relationship of boundary beam of 2nd floor at loading side of W1

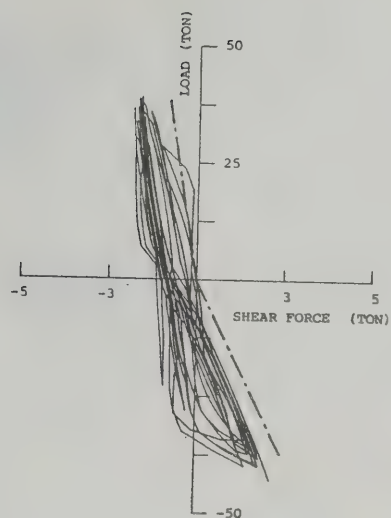


Fig.4.5.2 Lateral load versus shear force relationship of boundary beam of 2nd floor at opposite side of loading of W1

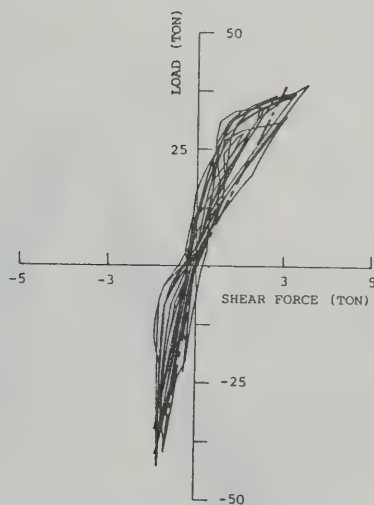


Fig.4.5.3 Lateral load versus shear force relationship of boundary beam of 3rd floor at loading side of W1

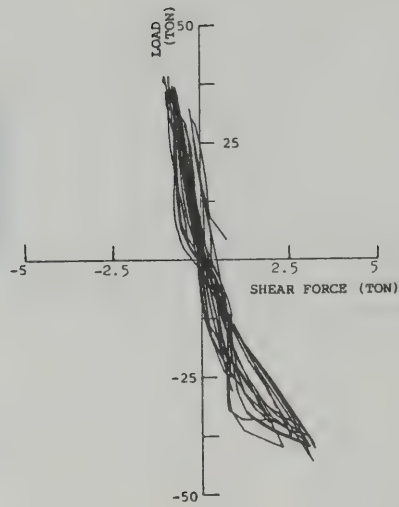


Fig.4.5.4 Lateral load versus shear force relationship of boundary beam of 3rd floor at opposite side of loading of W1

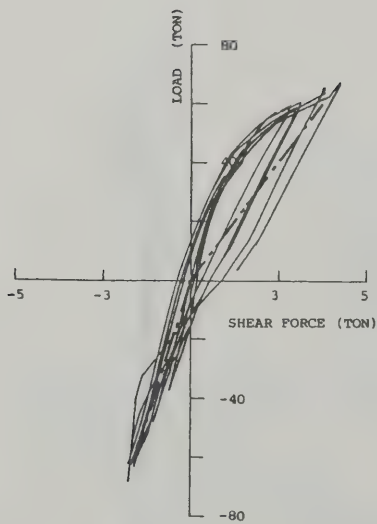


Fig.4.5.5. Lateral load versus shear force relationship of boundary beam of 2nd floor at loading side of W2

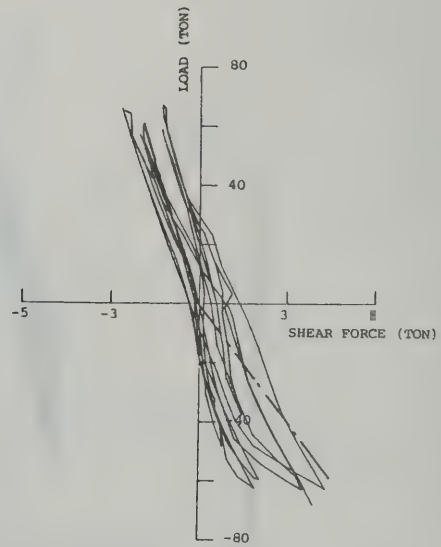


Fig.4.5.6 Lateral load versus shear force relationship of boundary beam of 2nd floor at opposite side of loading of W2



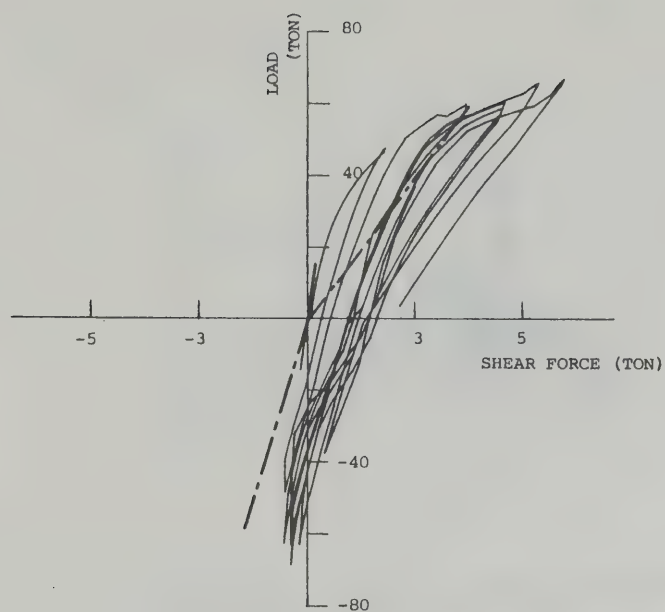


Fig.4.5.7 Lateral load versus shear force relationship of boundary beam of 3rd floor at loading side of W2

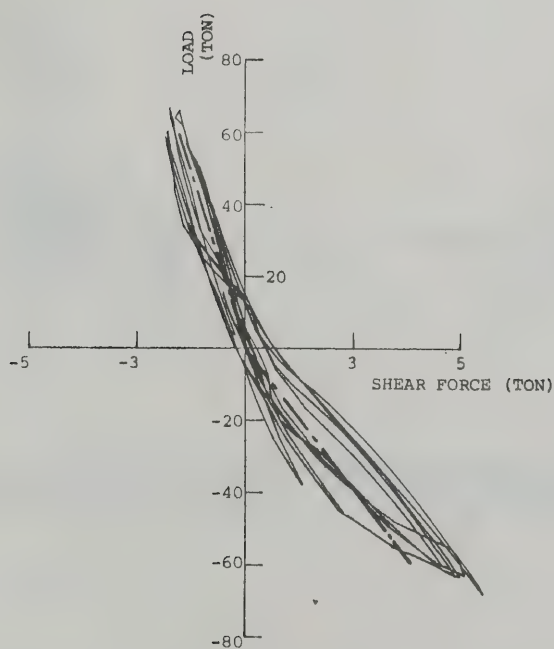


Fig.4.5.8 Lateral load versus shear force relationship of boundary beam of 3rd floor at opposite side of loading of W2

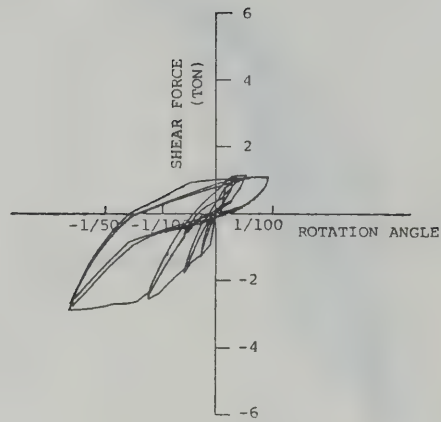


Fig.4.5.9 Shear force versus deflection relationship of boundary beam of 2nd floor at loading side of W1

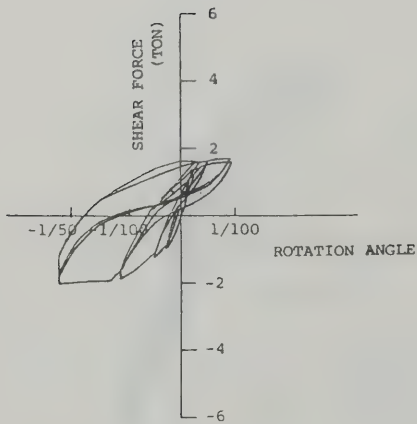


Fig.4.5.10 Shear force versus deflection relationship of boundary beam of 2nd floor at opposite side of loading of W1

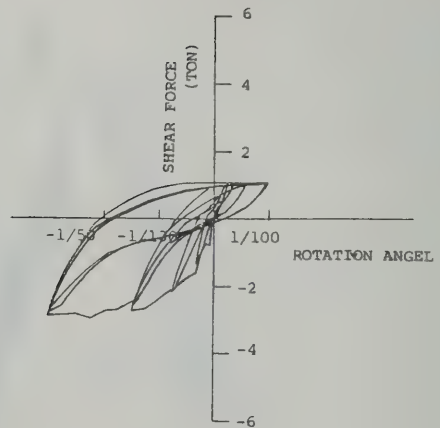


Fig.4.5.11 Shear force versus deflection relationship of boundary beam of 3rd floor at loading side of W1

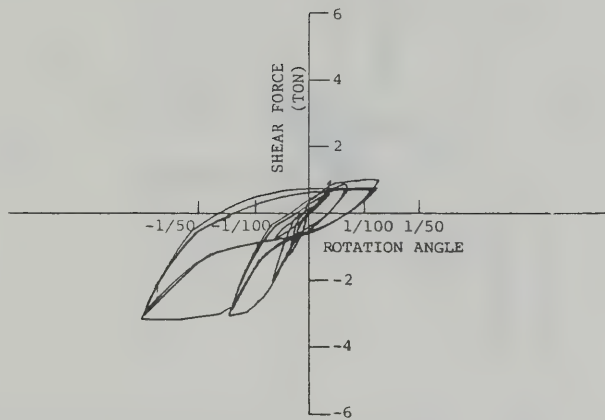


Fig.4.5.12 Shear force versus deflection relationship of boundary beam of 3rd floor at opposite side of loading of W1

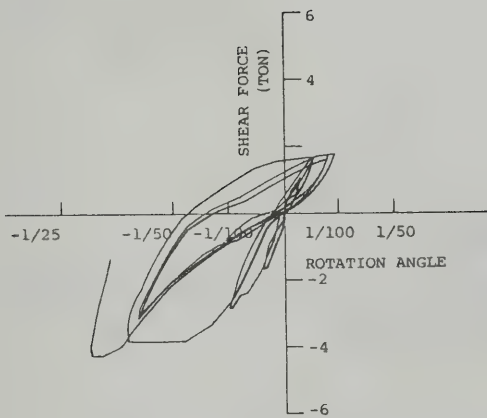


Fig.4.5.13 Shear force versus deflection relationship of boundary beam of 2nd floor at loading side of W2

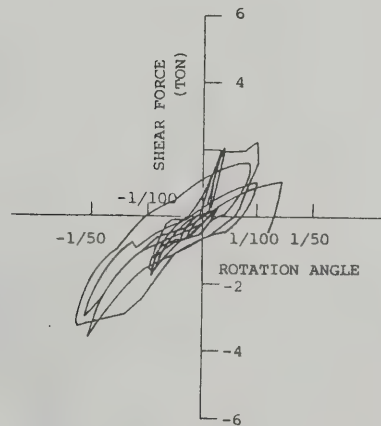


Fig.4.5.14 Shear force versus deflection relationship of boundary beam of 2nd floor at opposite side of loading of W2

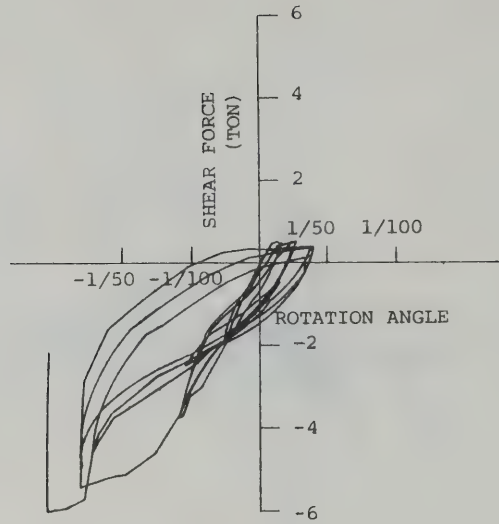


Fig.4.5.15 Shear force versus deflection relationship of boundary beam of 3rd floor at loading side of W2

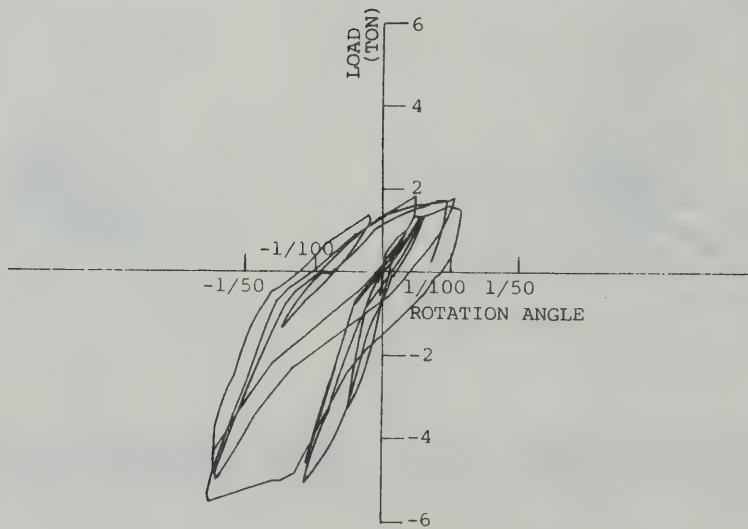


Fig.4.5.16 Shear force versus deflection relationship of boundary beam of 3rd floor at opposite side of loading of W2



Table 4.6.1 Strength

	Specimen	W 1			W 2		
	Floor	1st	2nd	3rd	1st	2nd	3rd
Shear force at first flexure cracking (ton)	Ex(P)	12	28	38	20	32	48
	Ex(N)	-14	-32	—	-20	-32	-48
	Theory	19.27	24.24	34.75	20.94	26.24	37.54
	Ex(P)/Theory	0.623	1.155	1.094	0.955	1.220	1.279
	Ex(N)/Theory	0.726	1.320	—	0.955	1.220	1.279
Shear force at first flexure shear cracking (ton)	Ex(P)	24	34	36	16	32	36
	Ex(N)	-24	-32	-32	-20	-32	-36
	Theory	38.32	47.69	76.09	40.46	50.50	80.64
	Ex(P)/Theory	0.626	0.713	0.473	0.395	0.634	0.446
	Ex(N)/Theory	0.626	0.671	0.421	0.494	0.634	0.446
Shear force at first shear cracking (ton)	Ex	—	—	—	—	—	—
	Theory	67.40	66.46	66.15	64.55	64.36	63.83
Flexure strength (ton)	Ex(P)	37.2	—	—	67.3	—	—
	Ex(N)	-42.7	—	—	-72.5	—	—
	Theory	30.55	—	—	54.55	—	—
	Theory*	38.6	—	—	68.6	—	—
	Ex(P)/Theory	1.218	—	—	1.234	—	—
	Ex(P)/Theory*	0.964	—	—	0.981	—	—
	Ex(N)/Theory	-1.398	—	—	-1.329	—	—
	Ex(N)/Theory*	1.106	—	—	-1.057	—	—
Shear strength (ton)	Ex	—	—	—	—	—	—
	Theory	68.53	74.30	90.23	81.96	89.01	108.55

Ex = experimental result

Ex(P) = experimental result at positive loading

Ex(N) = experimental result at negative loading

Theory = analytical result given by i)~v)

Theory\* = analytical result given by e-function method



# 境界ばりを有する耐震壁の構面実験

(日米共同大型実験研究)

平	石	久	廣 <sup>*1</sup>
芳	村		学 <sup>*2</sup>
五	十	石	浩 <sup>*3</sup>
中	田	慎	介 <sup>*4</sup>

本研究は昭和55年度に予定されている「大型実験施設利用による日米共同耐震研究」における鉄筋コンクリート造実大7層建物仮動的地震加力実験のサポートテストとして行なわれたものである。

実験は実大7層建物の桁行方向の中構面にある連層耐震壁の下部3層の境界ばりを含んだ耐震壁を対象とした。試験体は1/2スケールで、実大7層建物の配筋に対応させた試験体と形状は同じであるが配筋を増し強度を上昇させた試験体の2体である。試験体に設けた境界ばりについては両端をピンとした治具にて上下階の境界ばりを連結し、その鉛直変位を拘束することにより境界ばりによる曲げもどしの影響が表われるようにした。

加力は試験体頂部に設けた水平加力ジャッキ1台と鉛直加力用ジャッキ2台を調整することにより、水平加力時に実大7層建物に生じる応力と等価な応力が生じるようにした。

測定は各階左右の水平、鉛直変位、境界ばりのヒンジ領域の伸縮、はり・柱主筋、せん断補強筋壁横・縦筋のひずみ等について詳細なデータの集収を行った。

試験体は2体とも曲げ降伏し、曲げ降伏後も耐力低下の少い十分粘りのある挙動を示した。なお、本試験体は我が国にはあまり例のない壁内にはりを有してない構造であるがこのはりがなかったことの影響はほとんどみられなかった。

---

* 1	第三研究部	構造研究室主任研究員
* 2	第三研究部	振動研究室研究員
* 3	第四研究部	施工技術研究室研究補助員
* 4	第三研究部	構造研究室長







## Research Papers-Recent Issues

- No.74 K. Imaizumi: Recent Progress in Research and Development Wood Frame Construction, May, 1977, 61 pp.
- No.75 S. Hattori, Y. Kitagawa, M. Ohtsuka: Regional Coefficients of Earthquakes for Aseismatic Designs, July, 1977, 26 pp.
- No.76 Y. Matsushima: Random Response of Single-degree-of-freedom System with Bilinear Hysteresis, September, 1977, 28 pp.
- No.77 A. Baba: Drying Shrinkage Mechanism of Building Materials, March, 1978, 79 pp.
- No.78 K. Hayakawa: The Management of Land as an Environmental Resource, March, 1978, 40 pp.
- No.79 T. Tanaka: A Model on Fire Spread in Small Scale Buildings, September, 1978, 76 pp.
- No.80 Y. Aoki: Studies on Probabilistic Spread of Fire, November 1978, 52 pp.
- No.81 E. Saito: Experimental Study of Compartment Fire Using Model Boxes, July, 1979, 50 pp.
- No.82 Y. Matsushima: Random Response of Single-degree-of-freedom System with General Slip Hysteresis, July, 1979, 37 pp.
- No.83 Y. Hasemi: Flashover Criteria of Compartment Fire - Theory on Zero Order Reaction System - August, 1979, 26 pp.
- No.84 T. Tanaka: A Model on Fire Spread in Small Scale Buildings, 2nd Report, March, 1980, 63 pp.
- No.85 Y. Ishiyama: Review and Discussion on Overturning of Bodies by Earthquake Motions, June, 1980, 115 pp.
- No.86 S. Watanabe: Planning History in Japan - A State of the Art Survey - August, 1980, 36 pp.
- No.87 Y. Sugimura: Participation Factor of Horizontal Force Applied to Pile Foundation, March, 1981, 33 pp.
- No.88 Y. Hasemi: Mathematical Basis for Physical Evaluation on Flashover, March, 1981, 41 pp.
- No.89 T. Wakamatsu: A Quantitative Evaluation on Smoke Safety, March, 21 pp.
- No.90 S. Watanabe: Metropolitanism as a Way of Life, March, 1981, 52 pp.
- No.91 M. Hrosawa, T. Goto, M. Yoshimura, H. Hiraishi: Full-Scale Experimental Study on Aseismic Performance of Medium-Size RC Wall Structure, March, 1981, 28 pp.
- No.92 Y. Yamazaki: Inelastic Torsional Response of Structures Subjected to Earthquake Ground Motions, March, 1981, 102 pp.
- No.93 S. Kose: Study of Accidents Associated with Building Features, March, 1982, 38 pp.
- No.94 S. Okamoto, S. Nakata, Y. Kitagawa, M. Yoshimura, T. Kaminosono: A Progress Report on the Full-Scale Seismic Experiment of a Seven Story Reinforced Concrete Building - Part of the US-Japan Cooperative Program, March, 1982, 92 pp.
- No.95 Y. Hasemi: Characterization of the Intermittent Flaming Region of the Upward Current Above Diffusion Flames, March, 1982, 33 pp.
- No.96 Y. Morishita: Statistical Analysis of Fire Spread, May, 1982, 17 pp.
- No.97 T. Fuhushima: Deterioration Model of Polymeric Materials with Special Attention to Age and Deterioration Depth, December, 1982, 30 pp.
- No.98 H. Hiraishi, M. Yoshimura, H. Isoishi, S. Nakata: Planer Tests on Reinforced Concrete Shear Wall Assemblies. - U.S.-Japan Cooperative Research Program - January, 1983, 63 pp.

Address for Communication

**BUILDING RESEARCH INSTITUTE  
MINISTRY OF CONSTRUCTION**

No.1 TACHIHARA, OH-HO-MACHI, TSUKUBA-GUN, IBARAKI-PREF

JAPAN

Q.690  
K33b

ISSN 0453-4972

B R I Research Paper No. 99

# TESTS OF REINFORCED CONCRETE BEAM-COLUMN ASSEMBLAGES

— U.S.-JAPAN COOPERATIVE RESEARCH PROGRAM —

THE LIBRARY OF THE

JUN 9 1983

UNIVERSITY OF ILLINOIS  
AT URBANA-CHAMPAIGN

by  
Shinsuke Nakata

Building Research Institute  
Ministry of Construction

March 1983





## FORWARD

A U.S.-Japan Cooperative Research Program Utilizing Large Scale Testing Facilities in the United States and Japan was initiated in the summer of 1977.

It was recommended that a full-scale seven-story reinforced concrete building structure representing good current practice be tested.

In the course of designing the full-scale seven-story test structure, difficult choices were encountered due to difference in design codes and practices in the United States and Japan. Differences in the equation for design shear capacity, column tie detailing, and the reinforcement requirements for beam-to-column connections are a few examples.

In order to choose better and economical detailing for the frame parts of the full-scale test structure, half-scale beam-to-column subassemblages were tested using U.S. and Japanese construction practices.

Results from the tests were used to model the stiffness properties of structural members in a nonlinear dynamic analysis, which was used to determine a probable maximum deformation range of the full-scale structure during an earthquake under consideration.

March 1983

Katsuro Kamimura  
Director General  
Building Research Institute  
Ministry of Construction



TESTS OF REINFORCED CONCRETE BEAM-COLUMN ASSEMBLAGES

----- U.S.-JAPAN COOPERATIVE RESEARCH PROGRAM -----

by

Shinsuke Nakata\*

Building Research Institute

Ministry of Construction

Tsukuba, Ibaraki

(Research Paper No. 99)

March 1983

ABSTRACT

One-half scale reinforced concrete test specimens were tested to study the behavior of beam-column subassemblages designed under Japanese and U.S. construction practices. The specimens represented second-floor interior and exterior beam-column assemblies and top-floor exterior beam-column assemblies of a seven-story full-scale test structure.

The placement of beam and column longitudinal reinforcement was the same in all specimens. The amount and arrangement of lateral reinforcement was varied in specimens following the U.S. and Japanese design requirements. More web reinforcement in beams and columns was required by the U.S. design code.

Within a deformation range predicted by a nonlinear earthquake response analysis of the prototype structure, the behavior of the two specimens designed by the two codes was quite similar. Specimens with slab behaved in a manner different from the corresponding specimen without slab.

---

\* Head, Structural Division, Building Research Institute

## ACKNOWLEDGEMENT

This is a part of the U.S.-Japan Cooperative Research Program Utilizing Large Scale Testing Facilities. The members of Japanese academy group for this program are Professor H. Umemura, Shibaura Institute of Technology, Professors B. Kato, H. Aoyama and T. Okada, University of Tokyo, Professor M. Osaki, Chiba University, and Dr. M. Watabe, Building Research Institute, Ministry of Construction.

This particular phase of the research program was supported by the Science Technology Agency, Government of Japan.

The writer wishes to acknowledge the advices received from Professors H. Aoyama and T. Okada and S. Otani of the University of Tokyo, and Dr. M. Watabe of Building Research Institute during the planning stage of the project. The outline of the project was selected by them.

The experimental work was executed by Messrs. T. Kabeyazawa, Research Associate, Y. Kai and S. Kimura, Graduate Students of the University of Tokyo.

The advice and assistance provided by Mr. Y. Hosokawa, Research Associate of the University of Tokyo, during the detail planning and execution stages of the project is gratefully acknowledged. Messrs. T. Ichinose, N. Suzuki and D. Kato, Graduated students of the University of Tokyo, participated in the execution of the tests. Messrs. T. Goto and T. Kawashima of Building Research Institute prepared the instrumentation.



Technical support provided by the Building Construction Cooperative Organization in Ibaraki Prefecture, Tokyo Sokki Kenkyujo Co., and OX Jack Consultant Co. are appreciated.

The final report was prepared by the cooperation of Messrs. T. Kabeyazawa, Y. Kai and S. Kimura under general supervision of Professor S. Otani, University of Tokyo.

---

Shinsuke Nakaea

Head, Structural Division, Building Research Institute



# TABLE OF CONTENTS

	Page
1 INTRODUCTION . . . . .	1
2 TEST SPECIMENS . . . . .	3
2.1 Prototype Full-Scale Test Structure . . . . .	3
2.2 Dimensions of Test Specimens . . . . .	4
2.3 Material Properties of Test Specimens . . . . .	7
3 LOADING . . . . .	8
3.1 Apparatus . . . . .	8
3.2 Program . . . . .	9
4 INSTRUMENTATION . . . . .	11
4.1 Displacement Measurement . . . . .	11
4.2 Strain Measurement . . . . .	16
5 RESULTS OF I-SERIES TEST . . . . .	17
5.1 General Behavior . . . . .	17
5.2 Hysteresis Relation . . . . .	18
5.3 Strain Measurement . . . . .	21
5.4 Measured and Calculated Strengths . . . . .	22
5.5 Summary . . . . .	24
6 RESULTS OF E-SERIES TEST . . . . .	26
6.1 General Behavior . . . . .	26
6.2 Hysteresis Relation . . . . .	28
6.3 Strain Measurement . . . . .	30
6.4 Measured and Calculated Strengths . . . . .	31
6.5 Summary . . . . .	32
7 RESULTS OF T-SERIES TEST . . . . .	33
7.1 General Behavior . . . . .	33
7.2 Hysteresis Relation . . . . .	35
7.3 Strain Measurement . . . . .	36

	Page
7.4 Measured and Calculated Strengths . . . . .	37
8 SUMMARY . . . . .	40
LIST OF REFERENCES . . . . .	43

---

Head, Structural Division, Building Research Institute



## 1 INTRODUCTION

A U.S.-Japan Cooperative Research Program Utilizing Large Scale Testing Facilities in the United States and Japan was initiated in the summer of 1977. The planning group of the program prepared recommendations(1) to improve seismic safety practices through studies and to determine the relationship among full-scale tests, component tests, and analytical studies.

It was recommended(1) that a full-scale seven-story reinforced concrete building structure representing good current practice be tested, and that a series of coordinated experiments associated with the full-scale tests be conducted in Japan and the United States on reinforced concrete joint assemblies, walls, and frames. The results of all associated tests in both countries should be fully correlated with each other and with the results of the tests made in Japan on the full-scale seven-story structure.

In the course of designing the full-scale seven-story test structure, difficult choices were encountered due to difference in design codes and practices in the United States and Japan. Differences in the equation for design shear capacity, column tie detailing, and the reinforcement requirements for beam-to-column connections are a few examples.

In order to choose better and economical detailing for the frame parts of the full-scale test structure, it was recommended that half-scale beam-to-column subassemblages be tested using U.S. and Japanese construction practices.

It was not intended to test the subassemblages beyond

a deformation range expected during the full-scale test. Results from the tests will be used to model the stiffness properties of structural members in a nonlinear dynamic analysis, which is used to determine a probable maximum deformation range of the full-scale structure during an earthquake under consideration.

The test results will also be used to study the correlation between the behavior of half-scale beam-column subassemblies and the behavior of beam-column parts within the full-scale test structure.

## 2 TEST SPECIMENS

### 2.1 Prototype Full-Scale Test Structure

The full-scale seven-story reinforced concrete test structure represents a portion of a building having dimensions common to earthquake resistant construction in the United States and Japan. The lateral load resistance of the structure is provided by interacting structural wall and frames; two moment resisting frames and one structural wall-frame as shown in Fig. 2.1. The structure has three spans in the direction of loading. The structure is symmetric about the center.

Spans are 6m, 5m and 6m, in the direction of loading, and 6m on centers in the transverse direction. Inter-story heights are 3.75m in the first story and 3.0m from the second to the seventh stories. The column dimensions (0.50m x 0.50m) are the same throughout the structure. The beam dimensions (0.30m x 0.50m) are common in the longitudinal direction. The transverse beams have dimensions of 0.30m x 0.45m.

The amount of longitudinal reinforcement is the same in each story and in each span. All columns are reinforced with 8-D22 (No.7) deformed bars (Fig.2.2). Gross reinforcement ratio  $P_g$  is 1.24%. The amount of longitudinal reinforcement is different at beam end and center (Fig.2.2). The beam end is reinforced by 3-D19 (No. 6) deformed bars (reinforcement ratio of 0.65%) at the top, and by 2-D19 (No. 6) deformed bars (reinforcement ratio of 0.43%) at the bottom. The slab reinforcement is the same in each floor (Fig.2.3). The slab is reinforced by D10 (No. 3) deformed bars in double layers.

Additional negative reinforcement (D13, No. 4) is provided perpendicular to beams.

Nominal strength of all reinforcing bars (SD35 in Japan, and Grade 50 in U.S.) is  $3.50 \text{ ton/cm}^2$  (50ksi, or 340MPa). Specified compressive strength of concrete is  $270 \text{ kg/cm}^2$  (4,000psi or 36.5MPa).

The reinforcement details of the full scale structure have not been decided, but will be finalized with the information obtained from the current tests.

## 2.2 Dimensions of Test Specimens

The behavior of the entire structure will be effected by the amount of lateral reinforcement and the method of reinforcement placement. The United States and Japan require different amounts of lateral reinforcement and reinforcement detailing. Therefore, it was desired to study the effect of different reinforcement practices.

Three types of beam-column subassemblies were chosen as test specimens for this purpose;

- (a) interior beam-column assemblies (I-series),
- (b) exterior beam-column assemblies (E-series), and
- (c) exterior beam-top column assemblies (T-series).

These three series of specimens are marked in the elevation diagram in Fig. 2.1.b. The inflection points were assumed to be located at the mid-span of beams and at mid-height of columns. The specimen was taken as the portion bounded by the inflection points.

The dimensions of each test specimen were one-half those of the full-scale structure. However, the amount of



reinforcement was not precisely scaled due to the limitation in available bar sizes. Slab reinforcement in the half-scale specimens was placed in a single layer.

The column and beam sections with longitudinal reinforcement are shown in Fig. 2.4. Although the amount of longitudinal reinforcement at the end and at the center of a beam was not the same in the full-scale structure, the test specimens had uniform longitudinal reinforcement along the beams. Three D10 (No. 3) bars were used at the top (tensile reinforcement ratio of 0.65%), and two D10 (No. 3) bars were placed at the bottom (tensile reinforcement ratio of 0.43%) of a beam section. Four D13 (No. 4) bars were used in the corners and four D10 (No. 3) bars were placed at the middle face of a column section. The gross reinforcement ratio was 1.27 percent.

Three specimens in each series were designed using (a) Japanese design practice with slab, (b) U.S. practice with slab, and (c) Japanese practice without slab. The slab width was chosen to be 75cm on the basis of the effective width of T-beams. The effective width requirements are comparable in the two countries. Dimensions and reinforcement for test specimens are summarized in Table 2.1 and their details are shown in Figs. 2.5 to 2.7.

The major difference in U.S. and Japanese design requirements are the amount and arrangement of lateral reinforcement, and the method of anchoring beam longitudinal reinforcement in the beam-column connection. The amount of beam lateral reinforcement in the specimens was determined

by the minimum requirements in both countries because the expected shear forces in the members were small. It is a Japanese construction practice in the exterior beam-column connection to bend down the beam bottom longitudinal reinforcement and to anchor the reinforcement in the lower column (Figs.2.6 and 2.7) because the concrete is normally cast from a slab face to the next slab face above at a time.

It was decided to use deformed bars for lateral reinforcement. The smallest deformed bar available was D6 (No. 2), and was used in the specimens.

Architectural Institute of Japan Standard (AIJ Standard) for structural Calculation of Reinforced Concrete Structures -1979-(2) requires the amount of beam lateral reinforcement as follows;

- (a) the web reinforcement shall be at least 9-mm diameter plain bars or at least 10-mm diameter deformed bars (D10),
- (b) the web reinforcing bar shall be spaced at not more than one-half the overall beam depth and at not more than 25cm,
- (c) the minimum web reinforcement ratio shall be not less than 0.2 per cent.

therefore, the spacing of beam web reinforcement in Japanese specimens was determined to be 12.5cm, one half the overall depth of the beam section.

The spacing of beam web reinforcement in U.S. specimens was determined as one-fourth of the effective depth of the beam section as specified in ACI standard 318-77(3).

### 2.3 Material Properties

High-early strength concrete was used in the specimens. All specimens were cast outdoors, from the same batch of concrete, in the up-right position. The specimens were left outdoors during the curing period in February, but the temperature never got down below 4°C (39°F).

The average compressive strength of concrete was 340kg/cm<sup>2</sup> (4,900psi or 33MPa), which was 20 per cent higher than the specified strength of 270kg/cm<sup>2</sup> (4,000psi or 26.5MPa). The beam-column subassemblies were tested at 17 to 55 days from concrete casting. The increase in concrete strength was observed to be small during this period.

Reinforcing bars (D6, D10, and D13) were tested in accordance with Japan Industrial Standard, similar to ASTM in U.S. The stress-strain curves of three kinds of reinforcing bars are shown in Fig. 2.8. The yield stresses of D6 (No. 2), D10 (No. 3) and D13 (No. 4) were 3.77ton/cm<sup>2</sup> (54.7ksi or 370MPa), 3.75ton/cm<sup>2</sup> (54.4ksi or 368MPa), and 4.07ton/cm<sup>2</sup> (59.1ksi or 399MPa), respectively. These values were approximately by 5 to 10 per cent higher than the nominal strength of 3.5ton/cm<sup>2</sup> (50.8ksi or 343MPa).

D10 and D13 reinforcing bars showed clear yield plateaus, and D6 bars yielded gradually.

### 3 LOADING

#### 3.1 Apparatus

Varying forced displacements were applied at the free ends of the beams. The loading apparatus for series I (interior), E (exterior) and T (top) beam-column subassembly specimens is shown in Fig. 3.1.

Constant axial load was applied to the column of series I and E specimens, simulating the gravity load corresponding to the working load condition in the full-scale structure. The level of axial stress was  $38.4\text{kg/cm}^2$  (557psi or 3.77MPa) in series I specimens, and  $36.5\text{kg/cm}^2$  (527psi or 3.56MPa) in series E specimens. No constant axial stress was applied in series T specimens, but the column axial stress varied with lateral load.

A 100-ton capacity actuator with  $\pm 30$ -cm stroke was used to apply the constant axial load in the column. The load was measured by a 100-ton load cell. An electrical pump with automatic control was used to apply hydraulic pressure in the 100-ton actuator. The column axial load fluctuated during the experiment by  $\pm 12\%$  from the specified level.

Two 30-ton capacity actuators ( $\pm 30$ -cm stroke) were used to displace the beam free ends of series I specimen. The same actuator was used in a series E or T specimen. Two 30-ton capacity load cells were attached to these actuators.

The existing heavy steel reaction frame was used for the test. The reaction frame is made of 900 x 300 x 16-mm H sections for columns, and 600 x 300 x 12-mm H section for beams. Some extension pipe members were added to the actuator-



load cell assembly to fill the space between the top and bottom beams of the reaction frame.

The top end of the series I and E columns and the free end of the series T beam was supported by a vertical roller. The other ends of all specimens were either supported through a mechanical hinge, or connected to a loading device through a mechanical hinge. The location of mechanical hinges and roller in the specimens corresponded to the assumed location of inflection points in the full-scale structure.

The beam of a series T specimen was subjected to varying amplitude axial load. In an actual structure, the shear force acting in a exterior column must be resisted by the adjacent beam and slab in the form of axial stresses. Therefore, the axial load acting in the beam of a series T specimen was thought justifiable.

### 3.2 Program

Before the tests, the response of the full-scale prototype structure was computed under earthquake motions. One-component model(4), the model which assumed all inelastic deformation to be concentrated at member ends, was used to represent the deformation of reinforced concrete members including the structural wall. The degrading trilinear hysteresis model(5) was used to model the moment-rotation relationship at member ends. The NS component of the 1978 Miyagi-ken Oki earthquake recorded at the Tohoku University Station was used for the analysis.

The response was analyzed:(a) for a medium intensity, and (b) for a major intensity earthquake, by scaling the

acceleration amplitude of the earthquake record. A maximum acceleration of  $200\text{cm/sec}^2$  (0.2g) was chosen for a medium intensity earthquake, and a maximum acceleration of  $450\text{cm/sec}^2$  (0.45g) for a major intensity earthquake.

The maximum beam end rotation in the second floor level was approximately  $1/200$  radian from the medium intensity earthquake, and approximately  $1/100$  radian from the major intensity earthquake. The existing shear wall in B-frame (Fig. 2.1) was effective in reducing the response deformation of the prototype structure. With this information at hand, it was decided to test the specimens causing the beam end rotation up to  $1/50$  radian. It was also decided to apply at least two cycles of load reversals at a given displacement amplitude to study the deterioration in resistance.

The loading program is schematically shown in Fig. 3.2. In a series I specimen, the displacements at both beam ends were moved by the same amplitude, but in the opposite directions. The relation between the beam deformation and story deflection is discussed in Section 4.1.

## 4 INSTRUMENTATION

### 4.1 Displacement Measurement

Two independent reference frames were attached to a test specimen to measure the deformation. Figure 4.1 shows the two reference frames attached to a series I specimen.

The darkened rigid aluminum reference frame A was attached to the sides of a transverse beam immediately adjacent to the column. The column end lateral displacements were measured with respect to the frame A.

The beam end displacements were measured with respect to the shaded rigid aluminum beam B, attached to the top and bottom of the transverse beam immediately adjacent to the column.

One reference frame moved relative to the other during the loading due to the distortion of the beam-column joint panel. The angle change between the two frames approximately represented the shear distortion angle of the beam-column joint panel if the shear distortion was assumed to distribute uniformly within the joint.

The flexural rotation in the critical region of a beam was defined by measuring the longitudinal deformations at the top and the bottom of the beam. A displacement transducer measured the deformation between the column face and a bolt embedded at 10cm from the column face. This measurement included a deformation attributable to the slippage of beam longitudinal bars within the beam-column connection.

The displacements were measured by strain-gauge type transducers, with  $\pm 50$ -mm stroke and  $\frac{1}{100}$  -mm resolution for

column-end displacements, beam-end displacements and beam flexural rotation measurements. The relative movements of the two reference frames were measured by the same type displacement transducers, but with  $\pm 5$ -mm stroke and  $\frac{1}{1000}$  -mm resolution.

The location of displacement transducers is shown in Fig. 4.2 for the three specimens. The usage of the transducers is summarized below. ,

	<u>Specimen I,</u>	<u>Specimen E,</u>	<u>Specimen T</u>
Column Deformation	$\sigma_1, \sigma_2$	$\sigma_1, \sigma_2$	$\sigma_1$
Beam Deformation	$\sigma_3, \sigma_4$	$\sigma_3$	$\sigma_2$
Joint Panel Deformation	$\sigma_5 - \sigma_6$	$\sigma_4 - \sigma_5$	$\sigma_3 - \sigma_4$
Beam End Rotation	$\sigma_7 - \sigma_8, \sigma_9 - \sigma_{10}$	$\sigma_6 - \sigma_7$	$\sigma_5 - \sigma_6$

The displacements measured by the transducers were used to define the member deformations and story deformation. Consider a series I specimen.

Beam-end flexural rotation  $\theta_b$  was defined by the beam longitudinal displacements in the critical region, for example  $\sigma_9$  and  $\sigma_{10}$ , Fig. 4.3,

$$\theta_b = ( \sigma_{10} - \sigma_9 ) / h_b \quad (4.1)$$

in which

$h_b$  : distance between two transducers for displacements  $\sigma_9$  and  $\sigma_{10}$  ;



$\theta_b$  : flexural rotation over a 10-cm gauge length

The shear distortion angle,  $\gamma_p$ , of a beam-column joint panel was defined by the relative displacements of the two reference frames, for example  $\sigma_5$  and  $\sigma_6$  in a series I specimen, as shown in Fig. 4.4,

$$\gamma_p = ( \sigma_5 + \sigma_6 ) / \ell_p \quad (4.2)$$

in which

$\ell_p$  : distance between two displacement transducers  
for displacements  $\sigma_5$  and  $\sigma_6$ .

The measured column-end and beam-end displacements included the displacement contribution from the distortion of the beam-column joint panel. The column-tip displacement,  $\sigma_c$ , measured from the beam top face could be defined as follows, Fig. 4.5,

$$\sigma_c = \sigma_1 + \gamma_p \cdot a \quad (4.3)$$

where

$\sigma_1$  : column-end displacement measured from reference frame A;

$\gamma_p$  : shear distortion angle of beam-column joint panel;

$a$  : one-half of height of beam-column joint panel.

Similarly, the beam-tip displacement,  $\sigma_B$ , measured from the

column side face was defined as follows, Fig. 4.5,

$$\sigma_B = \sigma_2 + \gamma_p \cdot b \quad (4.4)$$

in which

$\sigma_2$  : beam-end displacement measured from reference frame B;

$b$  : one-half of width of beam-column joint panel.

Although the lateral movement at the column tips was prevented during the experiment, the story displacement of the prototype structure could be determined from the displacement measurements of the specimen. In the prototype structure, the inflection points in beams will not appreciably move in the vertical direction. Therefore, if the beam tips were assumed to have stayed horizontal, the story lateral displacement between the two column inflection points can be determined as follows (Fig. 4.6);

$$\begin{aligned} \sigma_{\text{story}} = & \sigma_1 + \sigma_2 + \gamma_p (h_c + a) \\ & + \left\{ \sigma_3 + \sigma_4 + \gamma_p (\ell_b + b) \right\} \times (h_c + a) / (\ell_b + b) \end{aligned} \quad (4.5)$$

in which

$\sigma_1, \sigma_2, \sigma_3$  and  $\sigma_4$  : column and beam tip displacements shown in Fig. 4.2;

$\gamma_p$  : shear distortion angle of beam-column joint panel;

$h_c$  : one-half of column clear height;

$l_b$  : one-half of beam clear span.

Sometimes it is convenient to know a story deformation angle,  $R$ , rather than a relative story displacement. The story deformation angle is defined as the relative story displacement,  $\sigma_{\text{story}}$ , divided by the inter-story height  $h$ .

$$R = \sigma_{\text{story}} / h \quad (4.6)$$

The damage of nonstructural elements in a structure due to earthquake motion is often related to this angle.

Story shear,  $\theta$ , was approximately obtained from the moment equilibrium of the subassembly as given below (Fig. 4.7):

$$\theta = \frac{P_1 + P_2}{2} \times \frac{l}{h} \quad (4.7)$$

where

$P_1, P_2$  : lateral loads applied at beam tips;

$l$  : span length.

The  $P-\Delta$  effect of column axial load on story shear was neglected. The story shear acting in the prototype structure is not exactly the shear given by Fig. 4.7 because Fig. 4.7 does not represent the configuration of the subassembly within the deformed prototype structure.

## 4.2 Strain Measurement

Strain gauges were used to monitor the behavior of longitudinal reinforcement in the beams, columns and slab. The position of strain gauges is shown in Fig. 4.8 for Specimen I-1.

The strains in beam and slab longitudinal reinforcement were measured at the column face. The strains in column reinforcement were measured at beam top and bottom face levels. In addition, the strains in beam longitudinal reinforcement were measured at the center of the beam-column joint panel to examine the deterioration of bond between the reinforcement and concrete in the beam-column joint.

The strain gauges used were high elongation YL-10 (Tokyo Sokki Kenkyujo, TSK) gauges. The gauge length was 10-mm, and the gauge resistance was  $120\ \Omega$ . After the deformation on a reinforcing bar was removed by file, the location for a strain gauge was smoothed by sand paper and cleaned by acetone. A strain gauge was pasted onto the cleaned bar surface by CN adhesive, and was coated with heated wax in two or three layers for water proofing. Furthermore, the gauge was protected by a glass-fibre cloth with P2 adhesive. The two types of adhesive were provided by TSK.

Strain gauges were connected to either of two switch boxes, and to an Automatic Strain Meter TDS-256 (TSK). The strain readings were digitized and punched on a paper tape.



## 5 RESULTS OF I-SERIES TEST

### 5.1 General Behavior

I-Series Specimens (I-1, -2 and -3) were cross-shaped, representing a second-floor interior beam-column subassemblage of the prototype building. Specimens I-1 and I-2 had a slab, and Specimen I-3 did not. Specimen I-1, designed according to Japanese design code (2), had a smaller web reinforcement ratio than Specimen I-2, designed according to U.S. design practice (3), as shown in Table 2.1. The three specimens had the same amount of longitudinal reinforcement. Specimen I-3 had the same web reinforcement ratio as Specimen I-1. The web reinforcement ratio in beams, columns and beam-column connection was varied by the spacing of lateral reinforcement, using the same bar size (D6 or No. 2). Additional sub-ties were placed in Specimen I-2 column to support middle longitudinal reinforcement, increasing substantially the web reinforcement ratio in the columns (Table 2.1).

General behavior of Specimens I-1 and I-2 was similar, but different from that of Specimen I-3.

Figures 5.1 to 5.3 show cracking patterns of these three specimens in the first cycle (story deformation angle  $R = 1/200$ ), in the third cycle ( $R = 1/100$ ), and after test. The story deformation angle is defined in Section 4.1. Tensile yielding of beam reinforcement was observed in the first cycle in all specimens.

Specimens I-1 and I-2 (Figs. 5.1 and 5.2) showed almost identical crack patterns, indicating little effect of the difference in the amount of web reinforcement on the behavior

in this range of deformation.

Flexural cracks were first observed in the beams or slab. Slab cracks developed perpendicular to the beam axis extending over the entire slab width. Diagonal shear cracks in the beam beneath the slab were observed at approximately  $R = 1/200$ , starting from the slab side only. The slab contributed to the flexural capacity when the beam top was in tension, hence the larger shear force was developed to cause shear cracks. However, when the beam bottom was in tension, the slab contribution to the flexural capacity was not large enough to cause shear cracks.

When the deformation increased to approximately  $R = 1/50$ , the cracks developed along the beam-slab boundary line (Figs. 5.1C and 5.2.C ). Wide flexural cracks in the beam lower part concentrated at the column faces. No compressive crushing was observed in these two specimens. Minor flexural cracks were observed in the column at the beam faces.

In the case of Specimen I-3, the shear force in the beams was limited by a relatively low flexural yielding capacity. Therefore, the cracks were all due to bending without compressive crushing. The beams did not develop diagonal shear cracks. No flexural crack was observed in the columns, nor in the beam-column joint panel.

## 5.2 Hysteresis Relationship

The vertical displacements were applied at beam ends of the subassemblage to simulate the lateral load induced in the prototype structure. The magnitude of vertical displacements

( $\delta_B$ ) at both beam tips were the same, but in the opposite directions. The inflection point of the beam in the prototype building were assumed at the mid-span.

Figures 5.4, 5.5 and 5.6 show story shear interstory displacement relationship of Specimens I-1, I-2 and I-3, respectively. The points at which yielding of the beam and slab reinforcement was first observed is also indicated in the figures.

Specimens I-1 and I-2 showed almost identical behavior up to a displacement amplitude of  $R = 1/100$  rad. The two specimens showed conspicuous slip behavior in the fifth cycle ( $R = 1/50$ ) of loading. Strength decay was observed in the repeated cycle at the same large amplitude in these specimens,

Specimen I-1 having a larger strength loss (Figs. 5.4 and 5.5). This slip behavior must be closely related to the wide flexural cracks concentrated in the beam lower portion at the column faces (Fig. 5.7). The subassemblage could not develop resistance until either of the two cracks closed during loading. The smaller slip behavior in Specimen I-2 might be attributable to the extra lateral reinforcement provided in the beam-column connection, rather than to the larger amount of beam or column web reinforcement.

In the earthquake response analysis, the maximum story deformation angle was estimated to be  $R = 1/100$  even from the most severe earthquake motion (Section 3.2). Within this range of deformation, all series I specimens showed fat and stable hysteresis loops. The behavior of the three specimens is judged to be satisfactory.



When the full-scale structure is tested to the capacity of the actuators available at the Building Research Institute, Ministry of Construction, Japan, the  $\pm 50$ -cm stroke capacity of the sixth floor actuators will limit the deformation of the full-scale structure during the experiment. If the displacement is assumed to vary linearly from the base to the sixth floor, the average story deformation angle becomes  $1/37.5$ . If the structure is tested under load reversals at this displacement amplitude, the slip behavior of the subassembly may cause a slip-type hysteresis of the structure.

The second cycle resistance at 6 centimeter displacement (Point B in Fig. 5.4) in Specimen I-1 was lower than the previous maximum resistance (Point A). This was caused by an error in controlling beam ends displacements at point C. The left beam was moved upward by 5.5 cm and the right beam downward by only 2.5 cm. Therefore, the left beam was severely damaged at the point C causing a reduced resistance at point B.

Hysteresis shape of Specimen I-3 was different from those of Specimens I-1 and I-2. Hysteresis loops of Specimen I-3 were fat and stable, and strength decay was not observed. The effect of slab on the hysteresis behavior was significant.

Loading was reversed at small displacement ( $R = 1/400$ ), in the first half and the last half of the third cycle ( $R = 1/100$ ). These small loops are shown in Figs. 5.4, 5.5 and 5.6 with broken lines. These loops were thin and showed slip behavior in Specimens I-1 and I-2.



The overall deflection of the subassembly was composed of contributions from the beam, column and beam-column joint deformations. The beam deformation shared a large portion of the subassembly deformation, particularly after yielding. At  $R = 1/50$ , measured contributions of the beam deformation to the total deformation were 90-92 % in Specimens I-1 and I-2, and 96-98 % in Specimens I-3. Column and joint deformations of Specimen I-3 were small in comparison with the beam, as indicated by no crack observed in column and joint. In the case of Specimens I-1 and I-2, column deformation was larger than that of Specimen I-3 due to the larger force levels.

### 5.3 Strain Measurement

Strain in reinforcement was measured mainly at the critical sections of the beams, columns and slab. The story shear-strain relationship of the six strain gauges shown in Fig. 5.8 is shown in Figs. 5.9 to 5.11 for Specimens I-1, I-2 and I-3, respectively. In the case of Specimens I-1 and I-2, the tensile yielding of beam bottom reinforcement was observed in the first or second cycle of loading (Figs. 5.9 and 5.10). Tensile yielding of beam top reinforcement and slab reinforcement was observed later, in the second or fourth cycle. In the case of Specimen I-3, Fig. 5.11, top and bottom reinforcement yielded during the first or second cycle of loading.

The reinforcement slippage was examined by the strains in beam reinforcement at the center of the beam-column joint. These strains remained in the elastic range, which indicated

that bond failure did not propagate to the center of the beam-column joint (Figs. 5.9 to 5.11).

Common among all I-series specimens, strains in the column reinforcement remained in the elastic region. Strains in column reinforcement in specimens I-1 and I-2 changed their signs due to large moment reversals while in Specimen I-3, strains in column reinforcement remained compressive due to high axial load and lower bending moment reversals.

The distribution of strains in slab reinforcement at the critical section is shown in Figs. 5.12 and 5.13. The strain distribution was relatively uniform prior to the yielding ( $R = 1/200$ ). Once the yielding of a reinforcing bar started, the distribution shape became irregular.

#### 5.4 Measured and Calculated Strengths

Measured and calculated yield and maximum moments at the critical beam section are given in Table 5.1. Measured yield moments were determined when the first yielding of tensile reinforcement (beam or slab) was observed. Measured maximum moment were the largest moment observed during loading.

Yield and maximum moments were calculated in two ways;

(1) Approximate yield moment equations suggested in Commentary of A I J Standard (2)

for beam,

$$M_y = 0.9 a_t \sigma_y d \quad (5.1)$$

and for column,

$$M_y = 0.8 a_t \sigma_y D + 0.5 ND (1 - N/bDF_c) \quad (5.2)$$

where,

- $a_t$  : area of tension reinforcement including slab reinforcement;
- $\sigma_y$  : tensile yield stress of reinforcing steel;
- $d$  : beam effective depth;
- $D$  : column overall depth;
- $N$  : column axial load;
- $b$  : column overall width;
- $F_c$  : compressive strength of concrete.

## (2) Flexural Theory

A linear strain variation across the section was assumed and the stress-strain relationship of the longitudinal steel (including strain hardening) and concrete were considered. Figure 2.8 shows the stress-strain relationships for steel used in computation.

Maximum moments in Table 5.1 were evaluated at the deflection when the maximum moment was observed in test. The deflection was evaluated on the assumption of linear curvature distribution along the beam. Maximum beam-end moment was observed at a relative story displacement of approximate 4 cm ( $R = 1/50$ ), which corresponds to a beam-end curvature of  $1.0 \times 10^{-3}$  (1/cm). Therefore, maximum moments in Table 5.1 were calculated for a curvature of  $1.0 \times 10^{-3}$  (1/cm). Extreme compression fiber strains at this curvature are listed. Table 5.1 shows that calculated values are almost identical to the corresponding test values.

In Specimens I-1 and I-2, measured beam top yield moments are lower than the calculated values;

this is because yielding of all the slab reinforcement occurred slightly after the yielding of the beam reinforcement. In the case of beam bottom tensile yielding, the values of measured yield moments in Specimens I-1 and I-2 were about 30 percent larger than that in Specimen I-3.

## 5.5 Summary

Second-story interior beam-column subassemblages were tested in this series to study the effects of (a) the amount of web reinforcement in beams, columns and beam-column connection, (b) the sub-ties for column middle reinforcement, and (c) the slab.

Within the deformation range predicted by a nonlinear earthquake response analysis, the amount of web reinforcement suggested by the Japanese Code (2) was sufficient. The crack patterns and stiffness characteristics of the subassemblages were not significantly affected by the amount of the web reinforcement used in the study. Slightly better performance of Specimen I-2 was observed in a displacement range where the story deformation angle  $R$  exceeded  $1/50$ , probably because of better confinement in the beam-column connection.

In the specimens tested, the major damage occurred within the beams. The damage of the columns was limited to minor flexural cracks. Therefore, the sub-ties, which gave support to the column middle reinforcing bars, did not affect the behavior of the specimens.

The slab contributed to the resistance of the subassemblage. The yield moments observed in Specimens I-1 and I-2 with a slab



were more than twice that observed in Specimen I-3 without a slab, when the slab was stressed in tension. When the slab was in compression, the yield moments observed in the Specimens with a slab were more than 1.3 times that in the specimen without a slab. Due to the slab contribution to resistance, diagonal shear cracks were observed in the specimens with a slab. Slip-type hysteresis behavior was also noted in the specimens with a slab. especially at large displacement reversals.

## 6 RESULTS OF E-SERIES TEST

### 6.1 General Behavior

E-Series Specimens (E-1, -2 and -3) were of T-shape, representing a second-floor exterior beam-column subassemblage of the prototype full-scale building. Specimens E-1 and E-2 were constructed with a slab, and Specimen E-3 without a slab. The bar size was kept the same in the three Specimens (E-1, 2 and 3). The amount of longitudinal reinforcement in beams and columns was the same in the three specimens. Specimen E-1 was designed in accordance with the Japanese design practice (2), and Specimen E-2 according to the U.S. design practice (3). A major difference in the two Specimens (E-1 and 2) was the amount of lateral reinforcement in beam, columns and beam-column connection as shown in Table 2.1 and Fig. 2.6. The web reinforcement ratio was varied by using different spacing of lateral reinforcement. Additional sub-ties were provided in Specimen E-2 columns to support middle longitudinal reinforcement. The beam longitudinal reinforcement was anchored downward in the beam-column connection of Specimen E-1 as shown in Fig. 2.6.a, following the standard Japanese construction practice. The beam and columns of Specimen E-3 were identical to those of Specimen E-1.

Figures 6.1 to 6.3 show crack patterns of the three specimens:

(a) at a relative-story displacement angle (inter-story displacement divided by inter-story height) of  $R = 1/200$  in the first cycle, (b) at  $R = 1/100$  in the third cycle,

and (c) after test.

Flexural cracks were observed first in all Specimens. No flexural crack was observed in columns, but small vertical cracks were observed above the slab near the beam-column joint in Specimens E-1 and 2. These cracks were not significant.

The behavior of the beams was dominated by flexure. Wider cracks were observed on the slab surface of Specimen E-1 than that of Specimen E-2.

In Specimen E-2 (Fig. 6.2), narrow cracks appeared on the entire slab face in the first cycle. In Specimen E-1 (Fig. 6.1), wide cracks developed near the beam-column joint, and cracks spreaded toward loading point in later loading cycles.

Diagonal shear cracks were observed in the web of beams in Specimens E-1 and E-2 only in one direction, starting from the slab side. These cracks were developed when the slab was in tension, causing the slab longitudinal reinforcement to yield. No diagonal crack was observed in the beam of Specimen E-3 because the flexural capacity of the beam was low.

Cracks observed on the slab surface of Specimens E-1 and E-2 near the joint were perpendicular to the beam longitudinal axis, whereas the cracks near the loading point were in a fanshape pattern with a pivot at the loading point.

A wide flexural crack was observed in the beam lower portion along the column face, in Specimens E-1 and E-2 when the Specimens were displaced by  $R = 1/100$ . The second wide crack appeared approximately 10 cm from the first crack in

the two Specimens at  $R = 1/50$ .

Spalling of the cover concrete occurred at the bottom face of the beam adjacent to the beam-column joint at the final stage of loading in Specimen E-1. No reinforcement bucking was observed.

## 6.2 Hysteresis Relationship

Force-deflection relationship of the specimens is discussed in terms of story shear and inter-story displacement. The method of computing story displacement is described in Section 4.1. Figures 6.4, 5 and 6 show the relations for Specimens E-1, 2 and 3, respectively. The inter-story displacement amplitudes of corresponding loading cycles were not identical in Specimens E-1 and E-2 because the loading control by the beam end displacement was not successful during the two tests.

The amplitudes of story shear in the positive and negative directions were different in Specimens E-1 and E-2, directly reflecting the strength contribution from the slab. When the slab was in tension, the sign of story shear was defined positive. The maximum positive shear was more than 2.5 times the maximum negative shear. The difference was also attributable to the more negative reinforcement in the beam.

The load-deflection relationship of Specimen E-1 was almost identical to that of Specimen E-2 up to a displacement amplitude of approximately 40 mm (story displacement angle of  $R = 1/50$ ). In the second cycle at  $R = 1/50$ , Specimen E-1 showed a larger reduction in resistance at the peak



displacement than Specimen E-2. The resistance of Specimen E-1 at story displacement angle  $R = 1/50$  was 90 per cent of the maximum resistance, whereas the resistance of Specimen E-2 was 96 per cent. The resistance of Specimen E-1 deteriorated further, and became lower than that of Specimen E-2 beyond 40-mm displacement. Larger deterioration of resistance must be attributable to the smaller amount of web reinforcement in the beam and beam-column connection and the method of anchoring the beam longitudinal reinforcement in Specimen E-1. However, the deterioration appeared in a displacement range much larger than the expected maximum earthquake response displacement.

Both Specimens E-1 and E-2 showed a slip-type hysteresis shape in the positive direction (slab in tension) at the story displacement angle greater than  $R = 1/100$ . Up to this displacement, the hysteresis loops were stable.

Specimen E-3 showed a hysteresis loop shape different from Specimens E-1 and E-2; i.e., the hysteresis loop was fat and stable, dominated by flexural behavior. This desirable behavior was obtained because beam shear was limited by low flexural capacity of the beam without the slab contribution.

When the first and repeated cycle hysteresis loops at the same displacement amplitude are compared in Specimens E-1 and E-2, the hysteresis loop in the repeated loading cycle was much thinner than that in the first cycle especially in the positive loading direction (Figs. 6.4 and 5). This reduction in resistance must be attributable to the formation

of wide flexural cracks in the previous cycle. The difference in the hysteresis loops of the first and repeated cycles was much less in Specimen E-3.

The contribution of column and joint-panel deformations to the story displacement was observed to be small. The story displacement was governed by the beam deformation.

### 6.3 Strain Measurement

Strains in the reinforcement were measured at the critical sections of the beam, columns and slab. The location of the gauges on beam reinforcement are shown in Fig. 6.7.

These strains are plotted against story shear, and shown in Figs. 6.8 to 10. The gauge numbers are defined in Fig. 6.7. The strain of beam longitudinal reinforcement at the center of the beam-column connection was also measured to examine the bar slip.

The beam longitudinal reinforcement at the center of the beam-column joint did not yield. This indicates that the bond failure did not propagate to the center of the beam-column joint.

The column reinforcement did not yield because the yield moment of the column was higher than that of the beam.

The distribution of strains in slab reinforcement is shown in Figs. 6.11 and Fig. 6.12 for Specimens E-1 and E-2.

The beam reinforcement was observed to yield first during the test, and then the slab reinforcement adjacent to the beam yielded in the first loading cycle ( $R = 1/200$ ). The yielding of slab reinforcement propagated outward. The

outermost slab reinforcement yielded in the loading cycles at story displacement angles of either  $R = 1/100$  or  $1/50$ .

#### 6.4 Measured and Calculated Strengths

All Specimens were designed to have flexural failure in the beam. Calculated yield and maximum moments at the beam critical section are compared with the observed values in Table 5.1.

Measured yield moments were defined as the moment observed when the yielding of tensile reinforcement (beam or slab) was first reported. Maximum moments were taken as the largest moment attained during all cycles of loading.

(1) Approximate Yield Moment Equations Suggested in Commentary of AIJ Standard (2);

for beam;

$$M_y = 0.9a_t \sigma_y d \quad (6.1)$$

and for column;

$$M_y = 0.8a_t \sigma_y D + 0.5ND(1 - N/bDF_c) \quad (6.2)$$

where

$a_t$  : area of tension reinforcement including slab reinforcement;

$\sigma_y$  : tensile yield stress of reinforcing steel;

$d$  : beam effective depth;

$D$  : column overall depth;

$N$  : column axial load;

$b$  : column overall width;

$F_c$  : compressive strength of concrete.

(2) Computation Based on Flexural Theory.

A linear strain variation across the section was assumed. The stress-strain relationship of the longitudinal steel and concrete were considered in the analysis, as shown in Fig. 2.8.

Equation 6.1 gave the same beam positive yield moment for the three specimens, whereas the flexural theory (Fig. 2.8) calculated the positive yield moment of Specimens E-1 and E-2 approximately 12 per cent greater than that calculated by Eq. 6.1, reflecting the contribution of slab concrete and compressive reinforcement in beam and slab. The positive yield moments observed in Specimens E-1 and E-2 were approximately 30 per cent greater than that calculated by Eq. 6.1.

The calculated beam negative yield moments by the two equations are comparable, and gave good estimate of the observed yield moments of Specimens E-2 and E-3. The observed positive yield moment of Specimen E-1 was approximately 8 per cent lower than that of Specimen E-2.

The flexural theory predicted well the observed positive and negative yield moments of Specimen E-3 without a slab.

The ultimate moment was calculated by the flexural theory at an arbitrarily chosen curvature of 0.001 1/cm. The calculated beam positive ultimate moments were almost identical to the observed maximum moment for the three specimens. The calculated beam negative moments were 6 to 10 per cent lower than the observed values.

## 6.5 Summary

Second-floor exterior beam-column subassemblages were



tested in this series to study the effects of (a) the amount of web reinforcement in beam, columns and beam-column connection, (b) the sub-ties for column middle reinforcement, (c) the method of anchoring beam longitudinal reinforcement in the beam-column connection, and (d) the slab, on the behavior within a practical deformation range. The effects of the amount of web reinforcement and the method of beam longitudinal reinforcement anchoring could not be separately identified in this series of tests.

A nonlinear earthquake response analysis of the prototype structure predicted the maximum story deformation angle to be approximately  $1/100$  radian even from the severe earthquake motion. Within this deformation range, the amount of web reinforcement suggested by the Japanese Code (2) and the method of anchoring the beam longitudinal reinforcement commonly done in Japan was sufficient. Better hysteretic performance was observed from the specimen (I-2) designed using the U.S. practice beyond this deformation range.

No crushing was observed in the critical region of column in any of the three specimen. Therefore, the sub-tie to support middle reinforcing bars of column section was judged to be redundant.

The slab contributed significantly to the resistance of the subassembly, especially when the slab was stressed in tension. The increased resistance caused diagonal cracks in the beam, and wide flexural crack in the lower part of the beam along the column face, causing a slip-type hysteresis loop at large deformation amplitudes.

## 7 RESULTS OF T-SERIES TEST

### 7.1 General Behavior

T-Series Specimens (T-1, 2) represented a top floor exterior column-beam subassembly of the prototype building as shown in Fig. 2.7 (a) and (b). Specimen T-1 was designed according to the Japanese design code (2). Specimen T-2 was designed according to the U.S. design code (3). The U.S. design code (3) requires more web reinforcement (Table 2.1), sub-ties to support column middle reinforcing bars (Fig. 2.7.b), and beam longitudinal reinforcement to be anchored within the beam-column connection (Fig. 2.7.b).

In this series, the beam and column were subjected to changing axial force in proportion to their shear force because of loading system shown in Fig. 3.1(b). The axial load in a beam is not unrealistic because the shear acting in the exterior column must be carried by the connecting beam and slab in the form of axial thrust.

Figures 7.1 and 7.2 show cracking patterns of the two specimens in (a) the first cycle at story deformation angle  $R = 1/200$ , (b) the third cycle  $R = 1/100$ , and (c) the final stage of loading. Crack behavior of the two test specimens was as follows; (a) flexural cracks occurred first in the column and then in the beam, and then (b) inclined shear cracks occurred in beams when the slab was in tension.

When the slab was subjected to tensile stress (negative moment), the number of flexural cracks in the column was larger than that in the beam. Flexural cracks were observed

throughout the height of the column. Wide column cracks appeared near the beam-column connection. Flexural cracks also occurred in the slab. Inclined shear cracks appeared in the beam web immediately below the slab after the third cycle of loading.

A wide flexural crack was observed in the column immediately below the beam-column connection in Specimen T-2. Such a wide crack was not detected in Specimen T-1. This difference may be caused by the method of anchoring the beam reinforcement in the joint; i.e. the beam longitudinal bars were extended beyond the beam-column connection, and crossed the crack in Specimen T-1, reducing the crack width, whereas only the column reinforcement crossed the wide crack in Specimen T-2 (Figs. 7.1 and 2).

When the beam bottom was in tension (positive moment), flexural cracks started from the bottom of the beam. The number of cracks appeared in the column was smaller than in the beam for this case.

General crack patterns of the two specimens were similar at the corresponding loading stage.

## 7.2 Hysteresis Relationship

Figure 7.3 shows story shear - interstory displacement diagrams of the two specimens. Figures 7.4 and 7.5 show beam shear - deflection relationship. The points at which the longitudinal reinforcement in the beam, column and slab was first observed to yield are indicated in the figures.

In Specimen T-1, loading was controlled by the inter-story displacement, while loading of Specimen T-2 was controlled by the beam deflection. Therefore, the loading history of the two specimens was different. The hysteretic behavior of the two specimens could not be compared directly.

The deflection of the column contributed appreciably to the story displacement in the two specimens. This can be noted by the difference in the shapes of the story shear-displacement relationship (Fig. 7.3.a. and b) and of the load-deflection relation of beam (Figs. 7.4 and 7.5).

The lateral load carrying capacity of Specimen T-1 was higher than that of Specimen T-2.

### 7.3 Strain Measurement

Strains in the longitudinal reinforcement was measured at the critical section of the beam, column and slab. The yielding of beam bottom reinforcement was observed in the third cycle of loading ( $R = 1/100$ ) in Specimen T-1, and in the first cycle ( $R = 1/200$ ) in Specimen T-2. The yielding of beam top reinforcement and slab reinforcement was observed in the fourth cycle ( $R = 1/50$ ) in Specimen T-1, whereas the yielding of beam top reinforcement and slab reinforcement was not observed in Specimen T-2. Instead, the column longitudinal reinforcement yielded in the second cycle ( $R = 1/100$ ). The middle longitudinal bar in the column also yielded in Specimen T-2.

The story shear-beam longitudinal bar strain relations (Figs. 7.7 and 7.8) of the two specimens are similar at the



corresponding critical sections.

The story shear-column longitudinal strain relations are shown in Figs. 7.9 and 7.10. The distribution of strains in slab reinforcement is shown in Figs. 7.11 and 7.12.

#### 7.4 Measured and Calculated Strengths

Measured and calculated yield and maximum moments at the critical section of beam and column are given in Table 5.1. Measured yield moments (positive and negative) were determined when the yielding of longitudinal reinforcement (in beam, or column, or slab) was first observed. Measured maximum moments (positive and negative) were the largest moment observed during the test.

Yield and maximum moments were calculated in the two ways:

- (1) Approximate Yield Moment Equation in Commentary of AIJ Standard (2).

Axial force in the beam and column varied proportional to applied load. Therefore, the equation for a column was used for both the beam and column.

$$M_Y = 0.8a_t \sigma_Y D + 0.5 ND (1 - N/bDF_c) \quad (7.1)$$

where

$a_t$  : area of tension reinforcement including slab reinforcement;

$\sigma_Y$  : tensile yield stress of reinforcing steel;

$D$  : overall column (or beam) depth;

$N$  : gross column (or beam) axial load;

$b$  : overall column (or beam) width;

$F_c$  : compressive strength of concrete.

The axial load and bending moment were related in a Specimen,

$$\begin{aligned} M &= 62.5 \text{ N} && \text{for beam} \\ &= 112.5 \text{ N} && \text{for column.} \end{aligned}$$

An iterative method was used to solve for the yield moment and corresponding axial load.

## (2) Computation Based on Flexural Theory

A linear variation of strain across the section was assumed. The stress-strain relations of the steel and concrete were considered in the analysis as shown in Fig. 2.8. Axial loads corresponding to the calculated yield moment (Eq. 7.1) and the observed maximum moment were used in the analysis.

As mentioned in the last section, the yielding was not observed in the beam top reinforcement nor in the slab reinforcement. Instead, the column longitudinal reinforcement yielded when the load was applied downward.

When the slab was in compression, the calculated and yield moments are comparable. A significant difference can be observed between the measured maximum moments of the two specimens in this direction.

When the slab was in tension, a large difference was observed between the yield moments measured in the two tests. This was caused because Specimen T-1 yielded in the beam, whereas Specimen T-2 yielded in the column. The approximate AIJ equation estimated approximately 15 per cent higher value in Specimen T-2. The flexural theory predicted the yield and maximum moments conservatively.

It is considered that such a different hinge mechanism was caused by the different anchoring details for beam reinforcement. In Specimen T-1, the beam reinforcing bars were anchored into the column top. Therefore, it was effective in resisting bending and reducing the crack width at the column top.

## 8 SUMMARY

A full-scale reinforced concrete structure is to be tested as a part of the U.S.-Japan Cooperative Research Program Utilizing Large Scale Testing Facilities in the United States and Japan. In the course of designing the full-scale test structure, difficult choices were encountered due to difference in design codes and construction practices in the United States and Japan.

One-half scale reinforced concrete test specimens were tested to study the behavior of beam-column subassemblages designed under the United States and Japanese construction practices.

The objectives of the investigation is not to decide upon the general betterness of the design codes used in the two countries. But the study was carried out simply to find the minimum sufficiency of design details for a reason of economy within the domain defined by the capacity of testing facilities of the full-scale structure and by the response of the full-scale structure under a probable major earthquake motion.

A nonlinear earthquake response analysis of the full-scale structure was carried out to estimate the maximum deformation under a probable major earthquake motion. The maximum story deformation angle of the structure was calculated to be approximately  $1/100$  radian from an earthquake with the peak ground acceleration of  $0.45g$ . This relatively small displacement amplitude may be attributable to the stiffness of a structural wall in the structure.



The major differences in the United States and Japanese design codes, if applied to this particular structure, are (a) the amount and arrangement of lateral reinforcement, (b) the placement of sub-ties to support the intermediate reinforcement in a column, and (c) the method of anchoring beam longitudinal reinforcement in the beam-column connection. The amount of lateral reinforcement in the specimens was determined by the minimum requirements in the two codes, because the expected shear forces in the members were small. In this case, the U.S. design code (3) required larger amount of web reinforcement in the beam, column and beam-column connection, and also required the sub-ties in the column.

It is a Japanese construction practice in the exterior beam-column connection to bend down the beam bottom longitudinal reinforcement and to anchor the reinforcement in the lower column because the concrete is normally cast from a slab face to the next slab face above at a time.

Three types of beam-column subassemblies were chosen to study the difference in the behavior of Specimens designed by the requirements of the two codes;

- (a) second-floor interior beam-column subassemblies,
- (b) second-floor exterior beam-column subassemblies, and
- (c) top-floor exterior beam-column subassemblies.

The effect of slab on the behavior of the subassemblies was also studied.

Within the deformation range predicted by a nonlinear earthquake response analysis, the larger amount of web reinforcement and the placement of sub-ties in a column

required by the United States design code did not improve the performance of the specimen because the deformation was not large enough to cause wide shear cracks, nor to cause the crushing of concrete in beams and columns, nor to cause the buckling of column reinforcement. Therefore, the minimum requirements suggested by the Japanese design code (2) were judged to be sufficient.

Slightly better performance was observed from the specimens designed under the United States design code in a displacement range where the story deformation angle exceeded  $1/50$ .

The slab contributed significantly to the resistance of the subassemblage, especially when the slab was stressed in tension. The increased resistance caused diagonal shear cracks in the beam, and a wide flexural crack in the lower part of the beam along the column face, causing a slip-type hysteresis loop at a story deformation angle greater than  $1/100$ .

## LIST OF REFERENCES

- (1) U.S.-Japan Planning Group, "Recommendations for a U.S.-Japan Cooperative Research Program Utilizing Large-Scale Testing Facilities", Report No.UCB/EERC-79/26, Earthquake Engineering Research Center, University of California, Berkeley, September 1979.
- (2) ———, "Architectural Institute of Japan Standard for Structural Calculation of Reinforced Concrete Structures -1979- (In Japanese)", Architectural Institute of Japan, 1979.
- (3) ———, "Building Code Requirements for Reinforced Concrete (ACI 318-77)", American Concrete Institute, 1977.
- (4) Giberson, M.F., "The Response of Nonlinear Multi-Story Structures Subjected to Earthquake Excitation", Earthquake Engineering Research Laboratory, California Institute of Technology, Pasadena, California, 1967.
- (5) Fukada, Y., "Study on the Restoring Force Characteristics of Reinforced Concrete Buildings (in Japanese)", Proceedings, Kanto District Symposium, Architectural Institute of Japan, Tokyo, No.40, 1969.

Table 2.1. Summary of Specimens

Specimen	Slab *	Design Code	Lateral Reinforcement Ratio	
			Column (%)	beam (%)
I-1	O	Japan	0.290	0.238
I-2	O	U.S.A	1.310	0.430
I-3	X	Japan	0.290	0.238
E-1	O	Japan	0.290	0.238
E-2	O	U.S.A	1.310	0.430
E-3	X	Japan	0.290	0.238
T-1	O	Japan	0.290	0.238
T-2	O	U.S.A	1.310	0.430

O; with floor slab

X; without floor slab



Table 5.1. Measured and Calculated , Yield and Maximum Moments

Specimen	Measured				Calculated					
	Yield Moment		Max. Moment		Approximate		Flexural Theory			
					Yield Moment (A.I.J.)		Yield Moment		Max. Moment at $\phi=1 \times 10^{-4} / \text{cm}$	
	T.T.	B.T.	T.T.	B.T.	T.T.	B.T.	T.T.	B.T.	T.T.	B.T.
I-1 L	354	141	377	158	349	106	342	119	367	158
	313	129								
I-2 L	309	137	376	167					$c^{\epsilon}c$	$c^{\epsilon}c$
	324	-								
I-3	152	107	192	141	158	106	157	111	171	129
	155	107								
E-1	317	136	390	158	349	106	342	119	367	158
E-2	344	137	393	150						
E-3	161	111	189	131	158	106	157	111	171	129
T-1	420	105	421	112	433	106	397	103	415	140
T-2	307	113	395	155			297		379	

Unit in ton-cm

T.T. : Beam Top in Tension

B.T. : Beam Bottom in Tension

$c^{\epsilon}c$  : Strain at Extreme Compressive Fiber

$\phi$  : Curvature

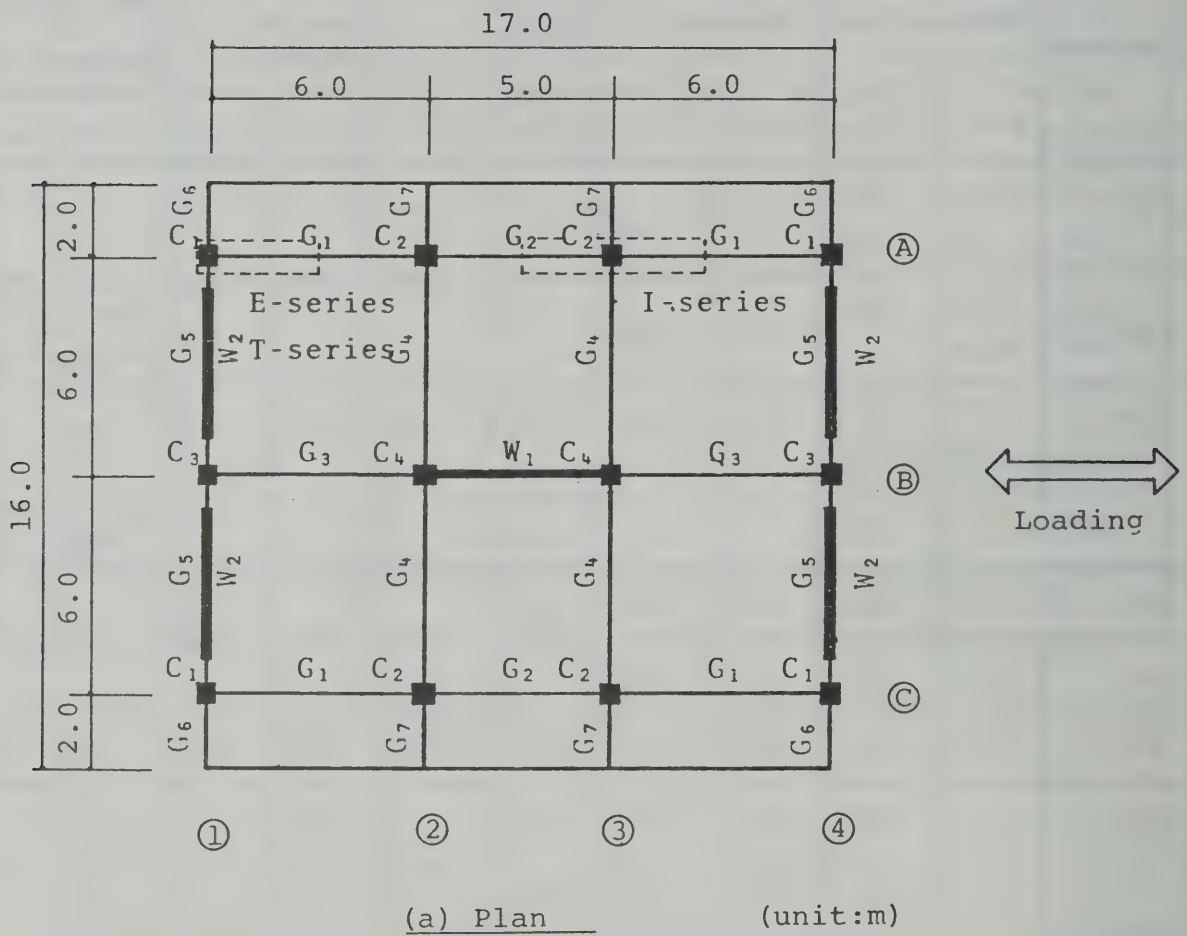


Fig. 2.1. : Full-Scale Structure



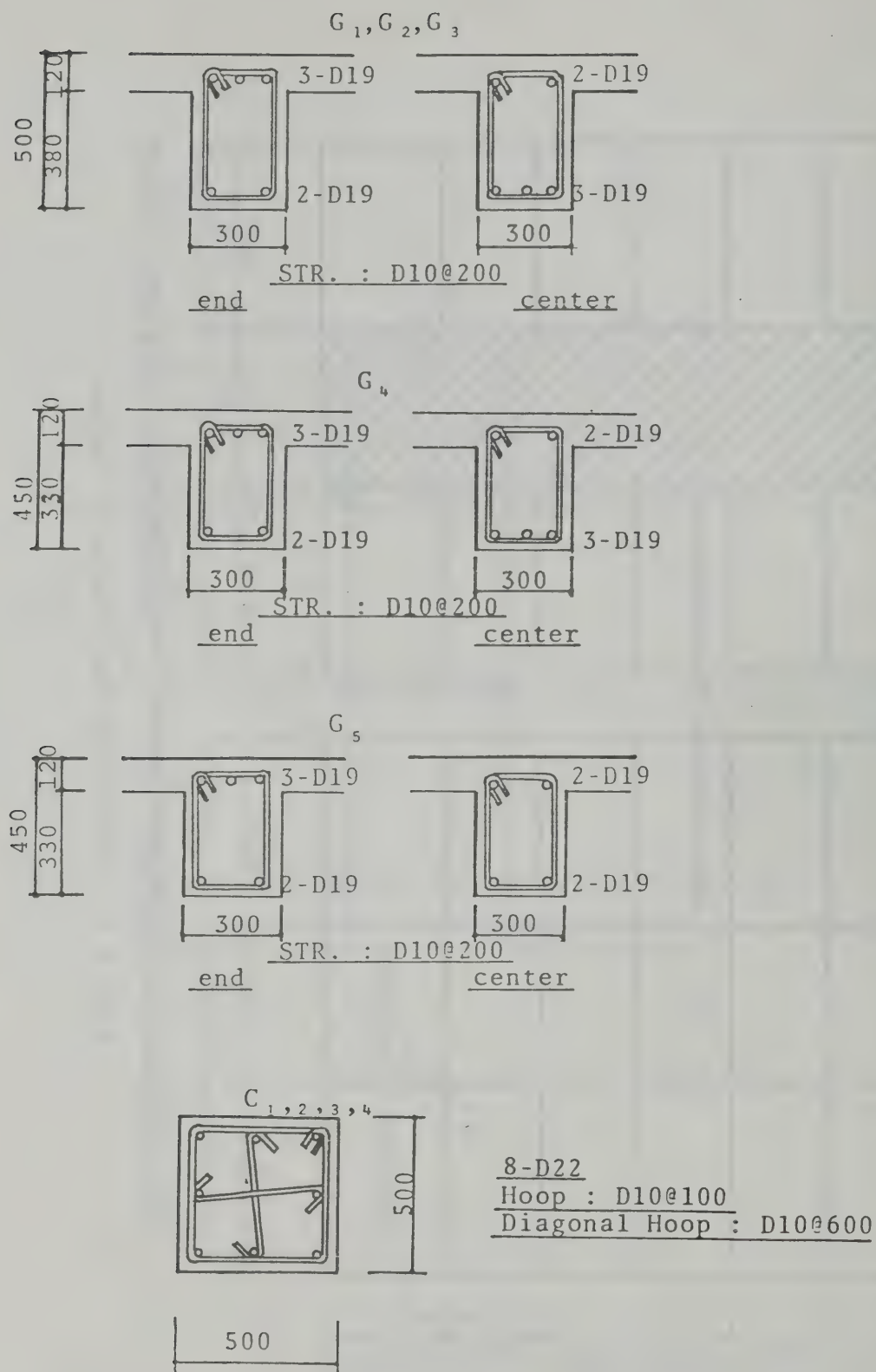


Fig.2.2. : Longitudinal Reinforcement in  
Full-Scale Structure



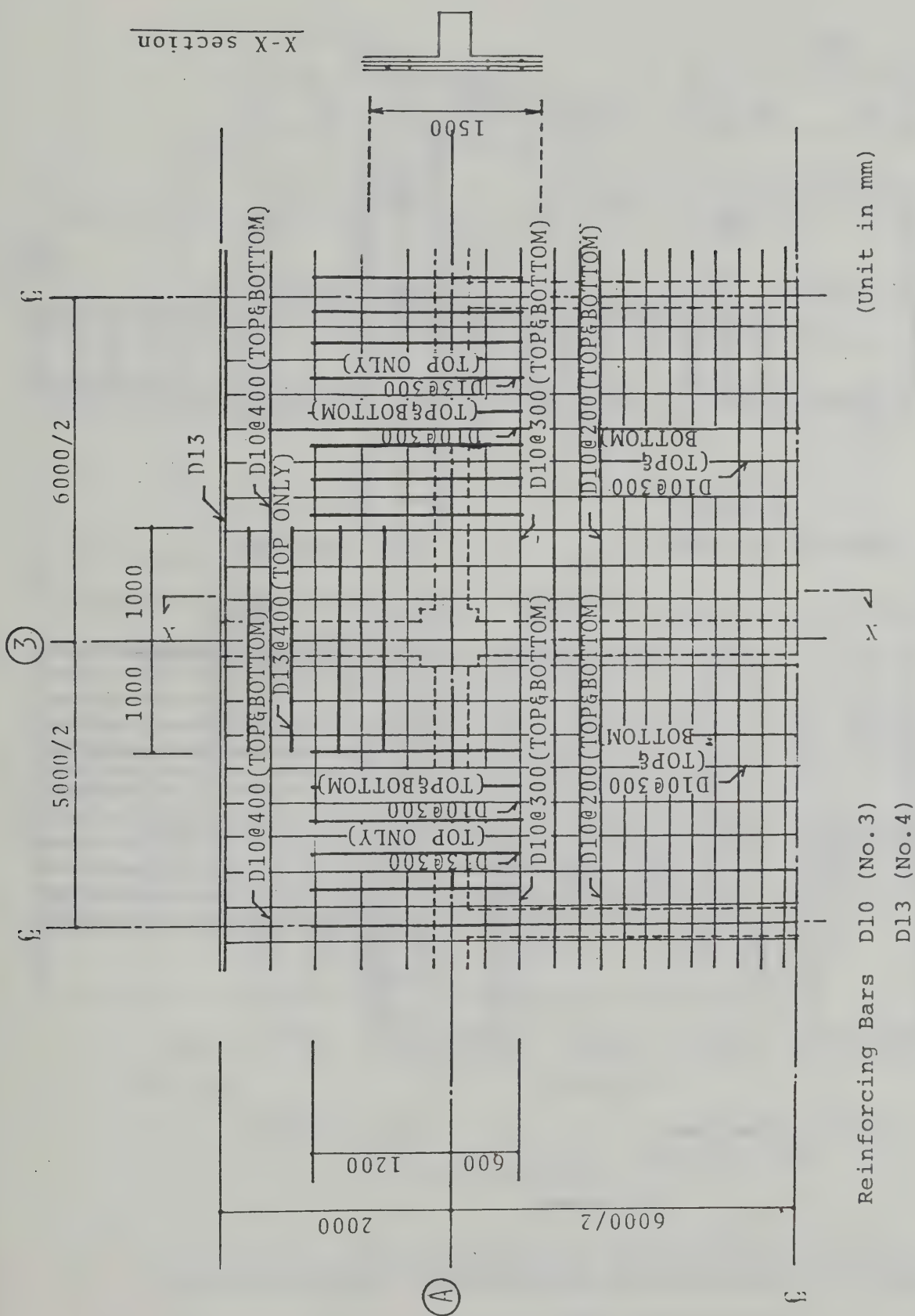
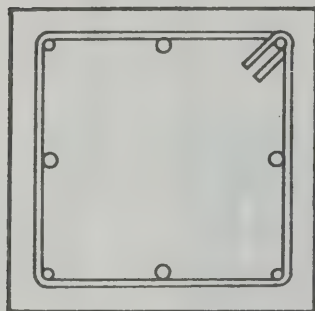
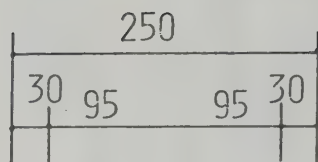


Fig. 2.3. : Details of Slab Reinforcement



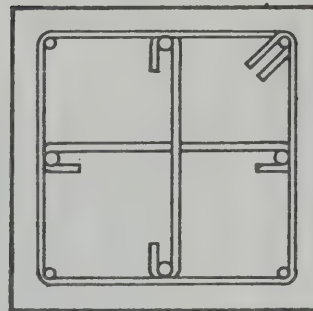
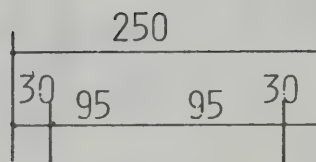
2-D10,1-D13

2-D13

2-D10,1-D13

Pt=0.43%  
Pg=1.27%

Japanese Specimen



2-D10,1-D13

2-D13

2-D10,1-D13

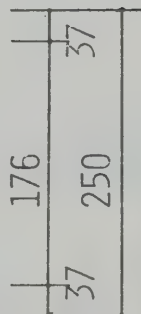
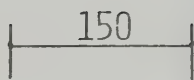
Pt=0.43%  
Pg=1.27%

U.S. Specimen

(a) Column

Pt : Tensile Reinforcement  
Ratio

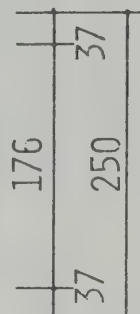
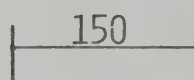
Pg : Gross Reinforcement  
Ratio



3-D10  
Pt=0.65%

2-D10  
Pt=0.43%

Japanese Specimen



3-D10  
Pt=0.65%

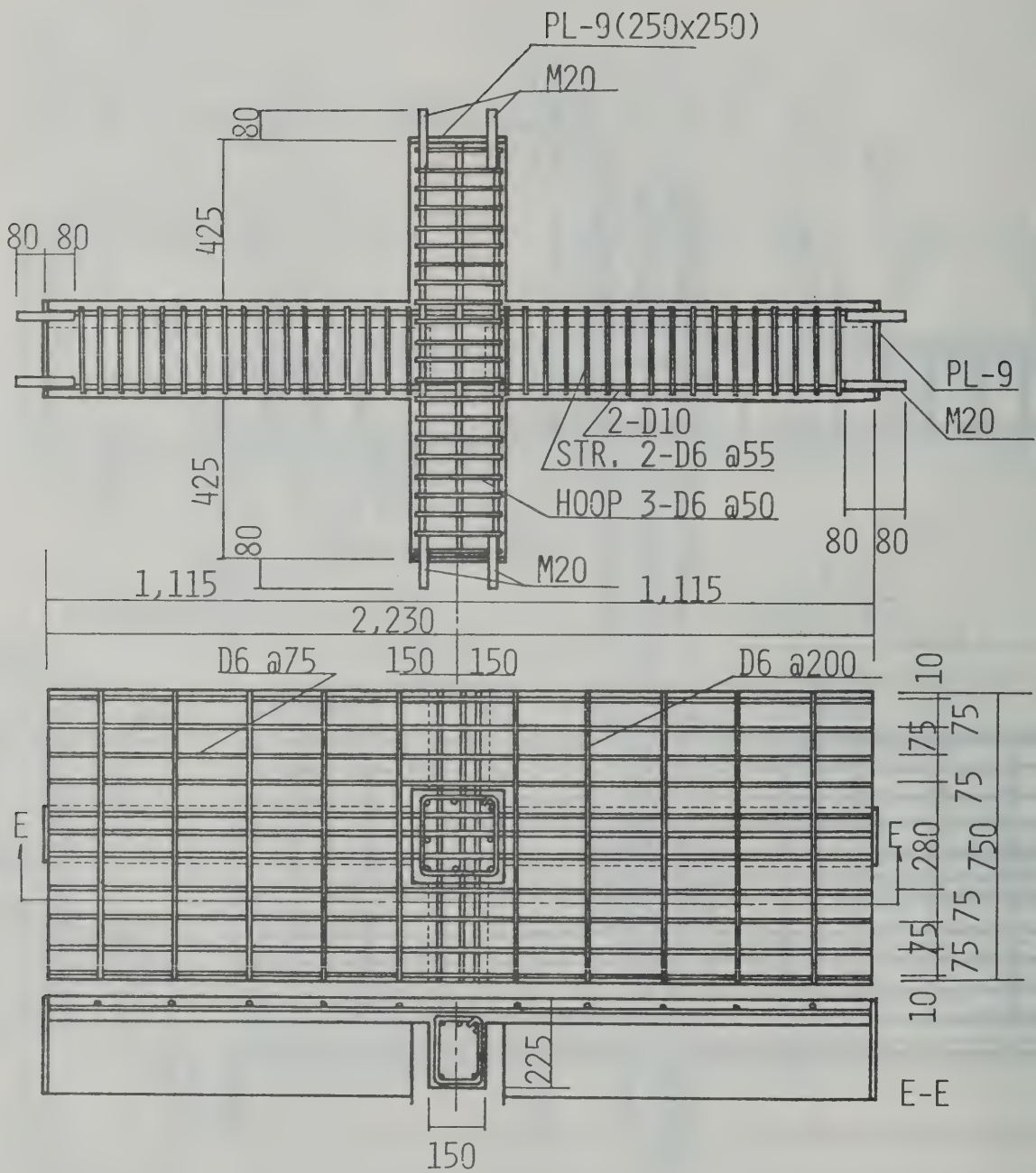
2-D10  
Pt=0.43%

U.S. Specimen

(b) Beam

Fig.2.4. : Longitudinal Reinforcement in Beam-Column  
Subassembly Test



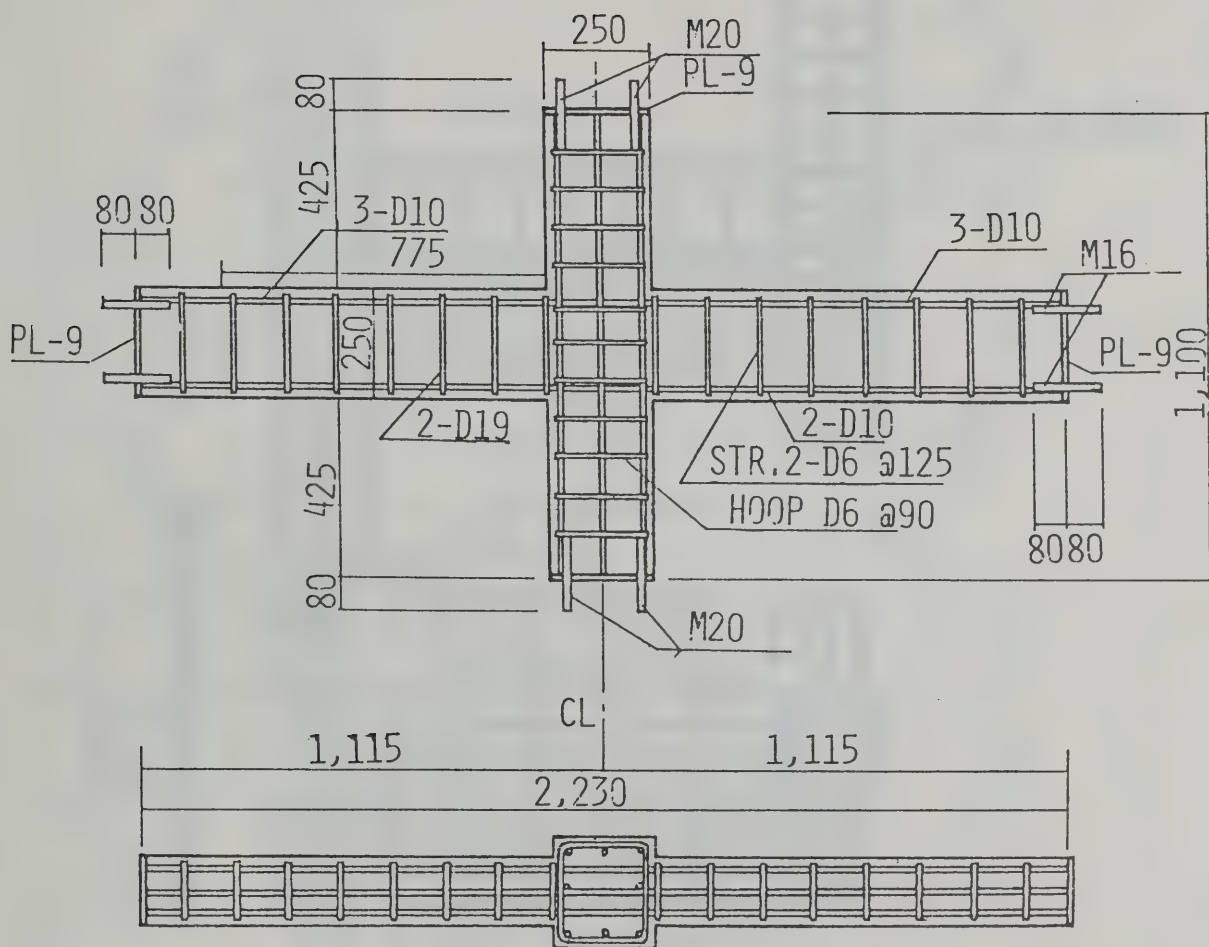


(Unit in mm)

(b) Specimen I-2

Fig.2.5. (Continued): Details of I-Series Test Specimens

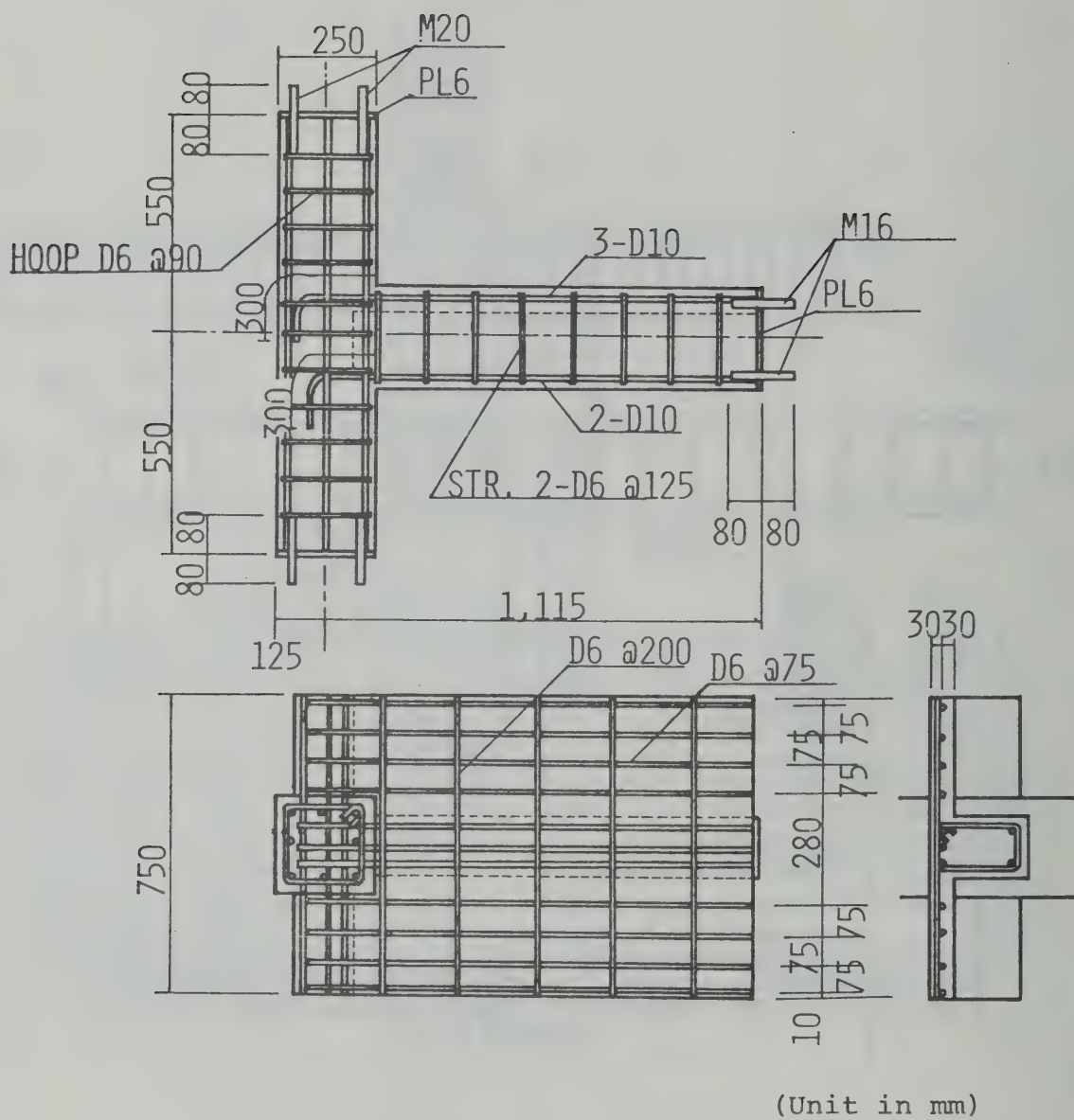




(Unit in mm)

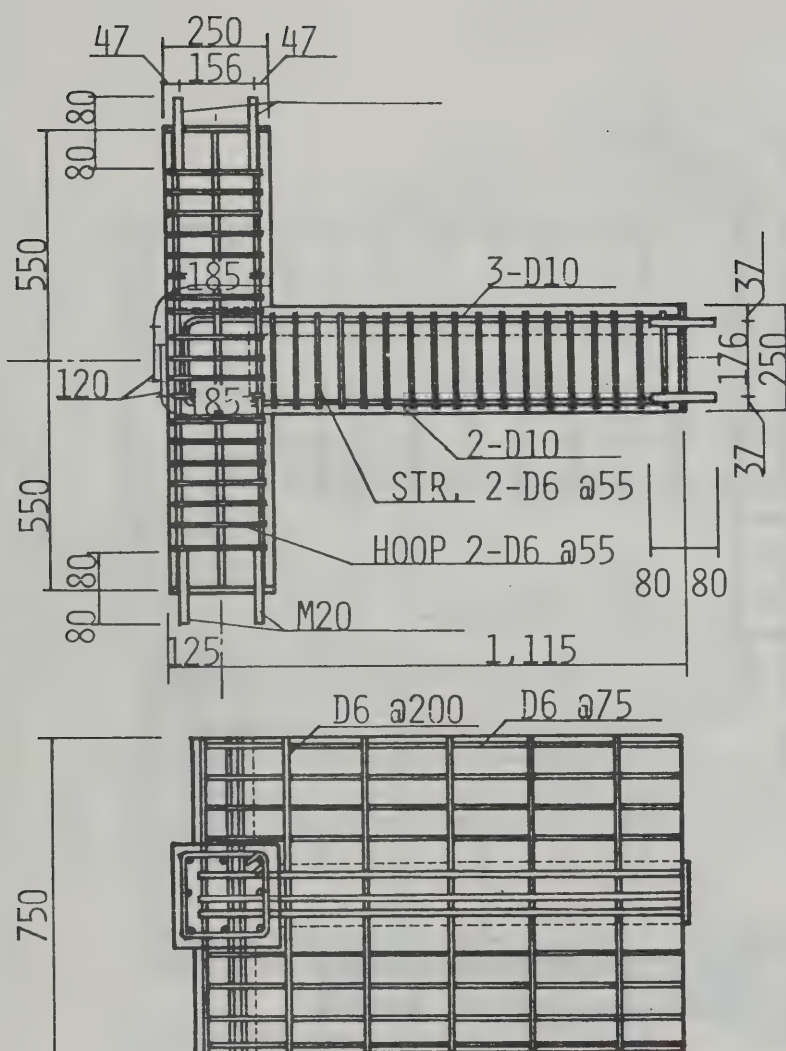
(c) Specimen I-3

Fig.2.5.(Continued): Details of I-Series Test Specimens



(a) Specimen E-1

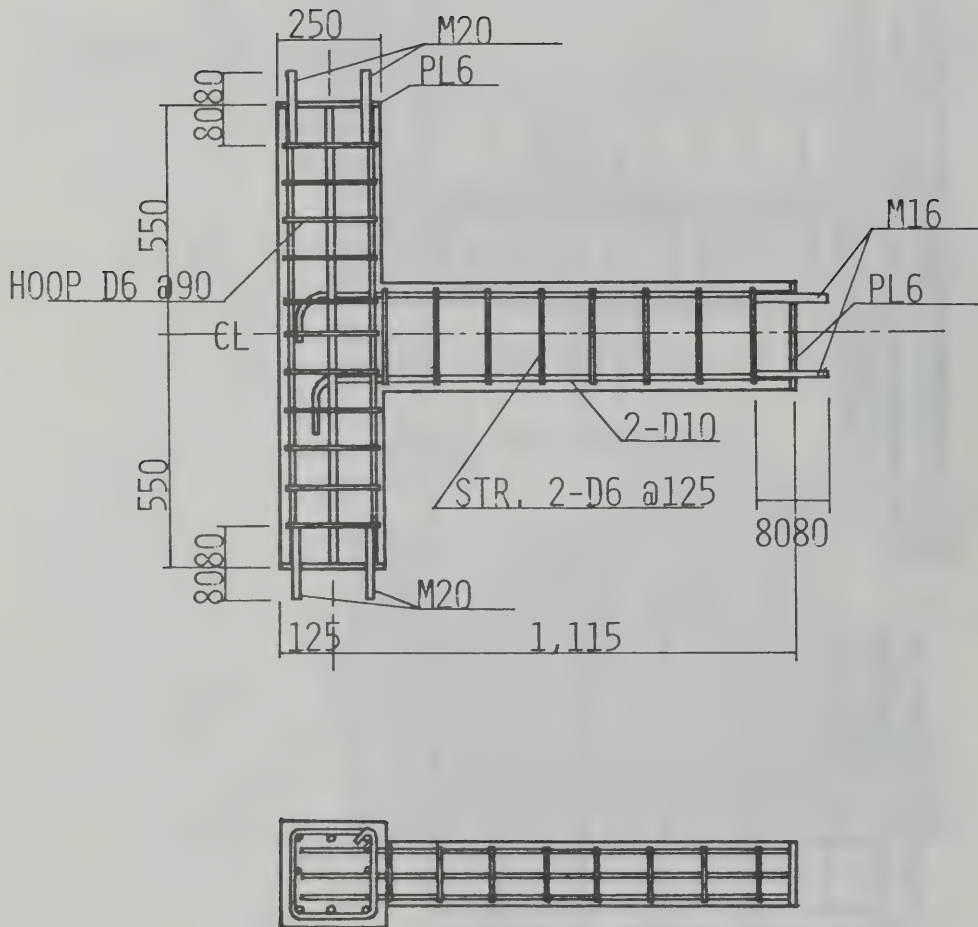
Fig.2.6. : Details of E-Series Test Specimens



(Unit in mm)

(b) Specimen E-2

Fig.2.6.(Continued): Details of E-Series Test Specimens

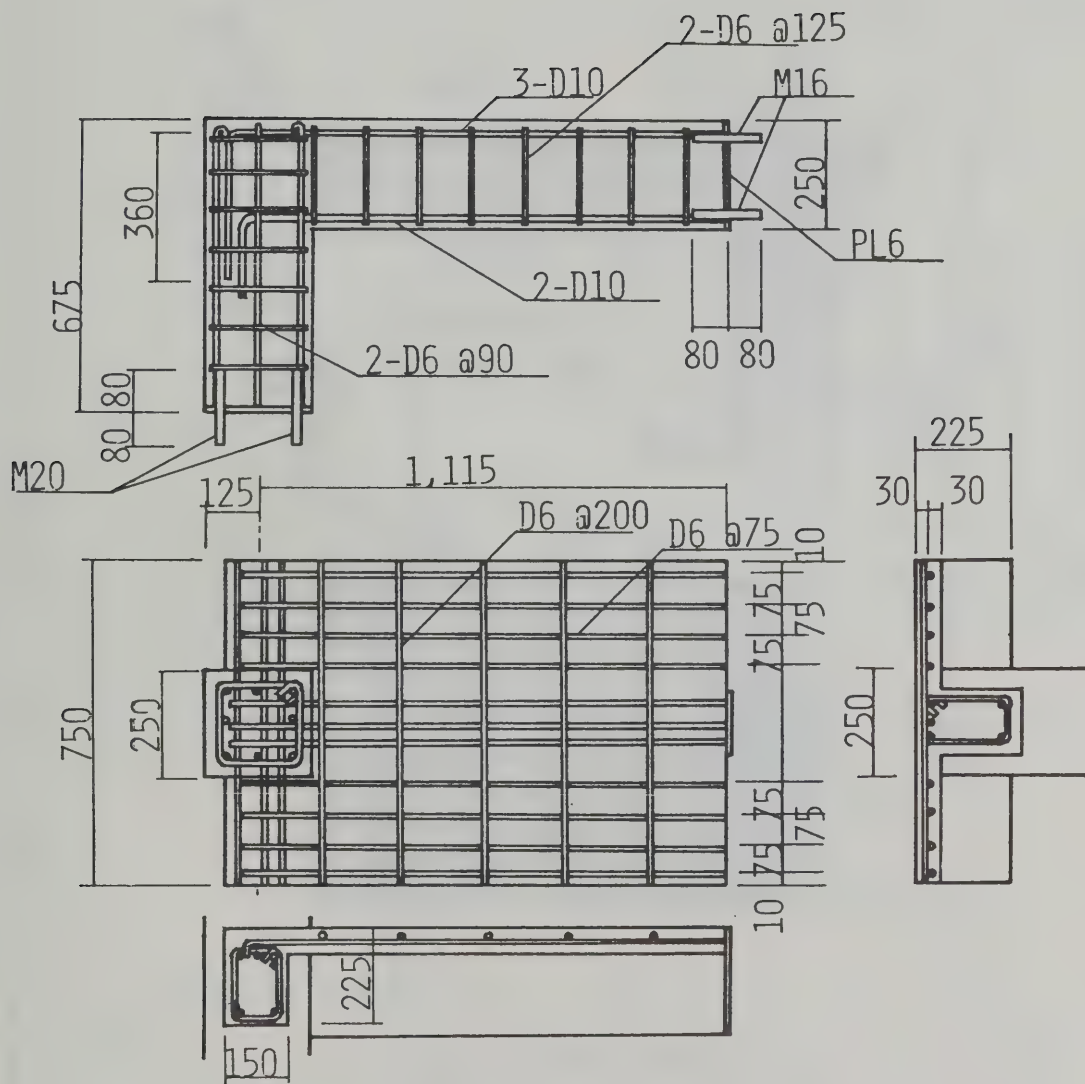


(Unit in mm)

(c) Specimen E-3

Fig.2.6.(Continued): Details of E-Series Test Specimens

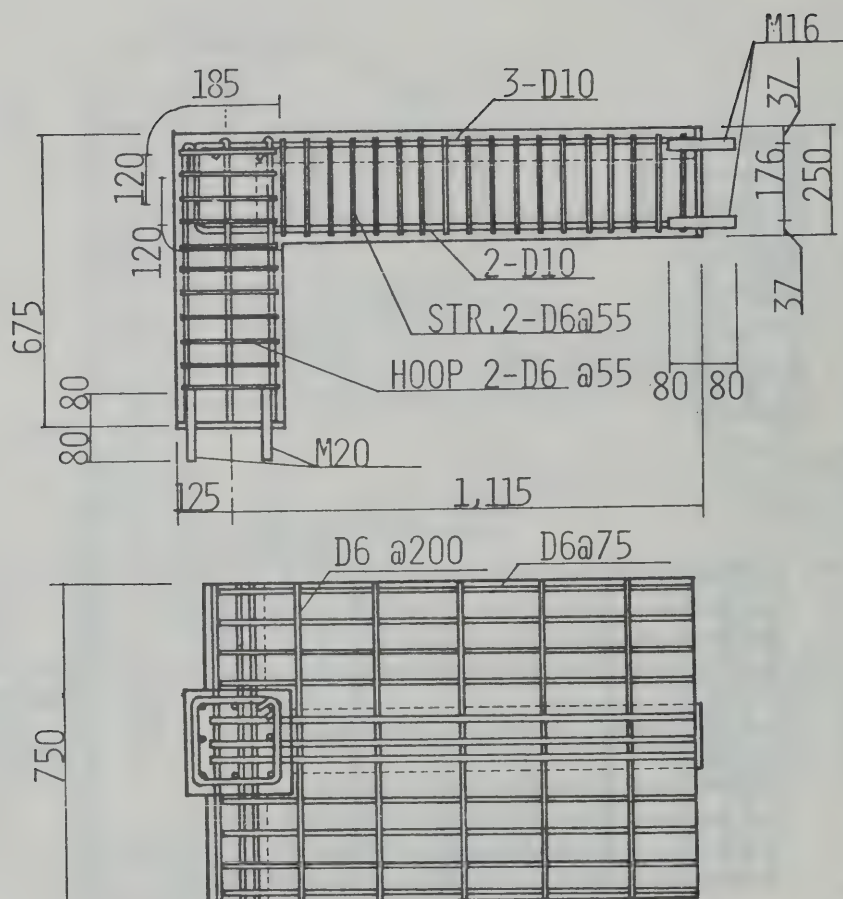




(a) Specimen T-1

(Unit in mm)

Fig.2.7. : Details of T-Series Test Specimens



(Unit in mm)

(b) Specimen T-2

Fig.2.7.(Continued): Details of T-Series Specimens

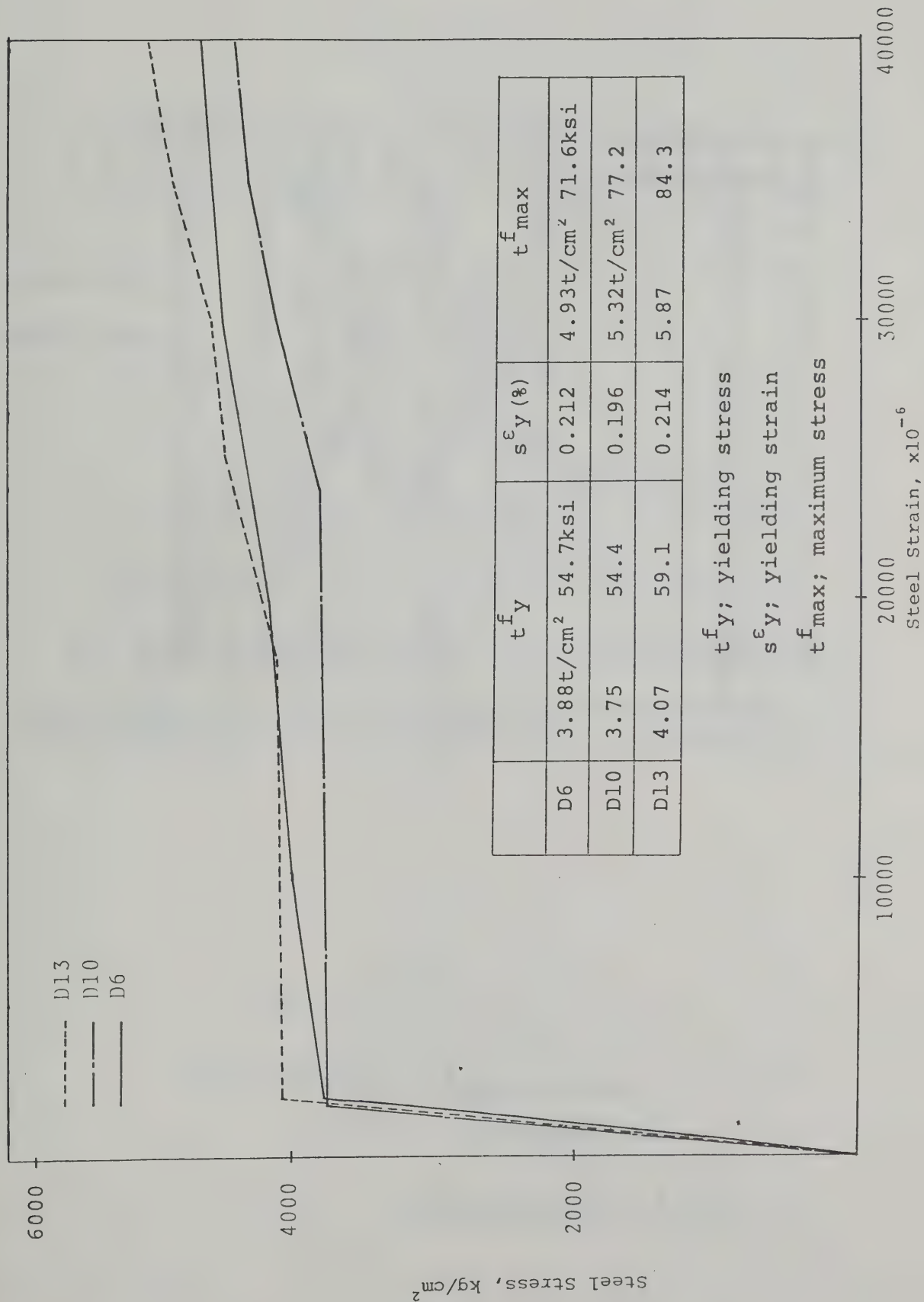
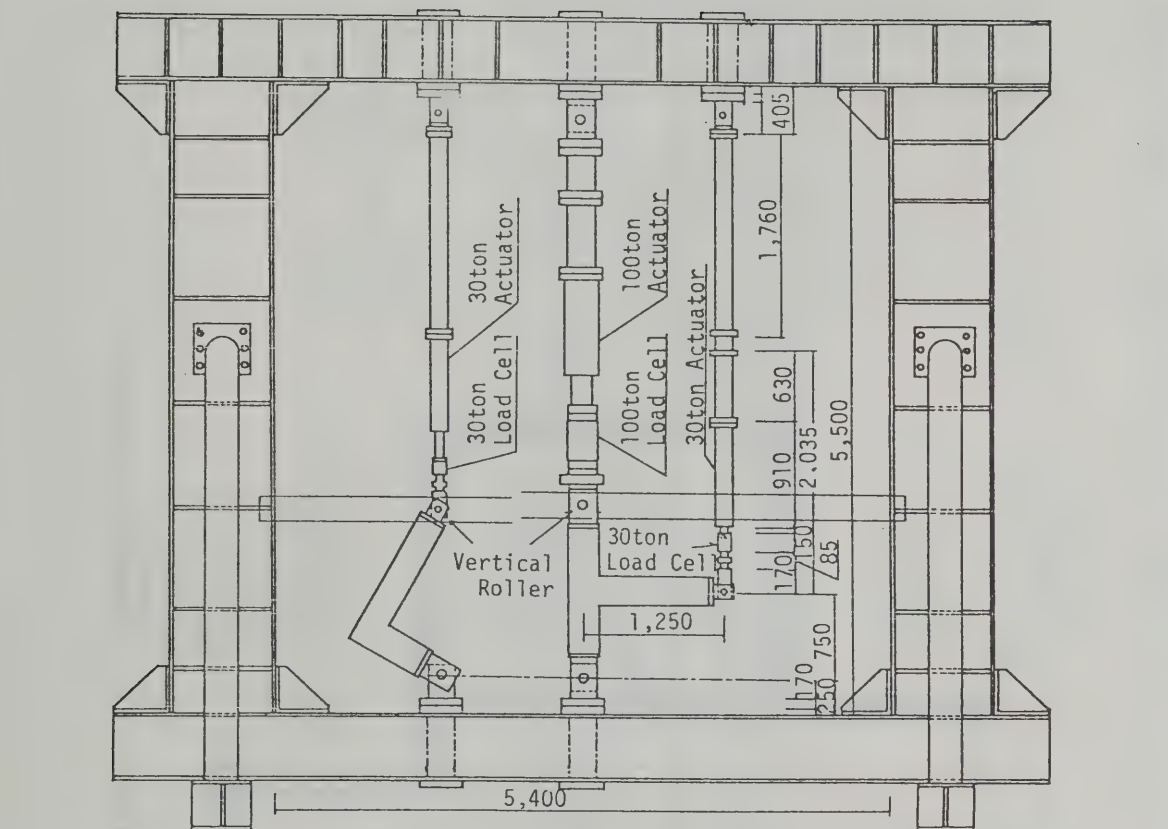


Fig.2.8. Stress-Strain Relationship of Reinforcing Bars







(b) E and T Series Test

Fig.3.1.(Continued): Loading Apparatus

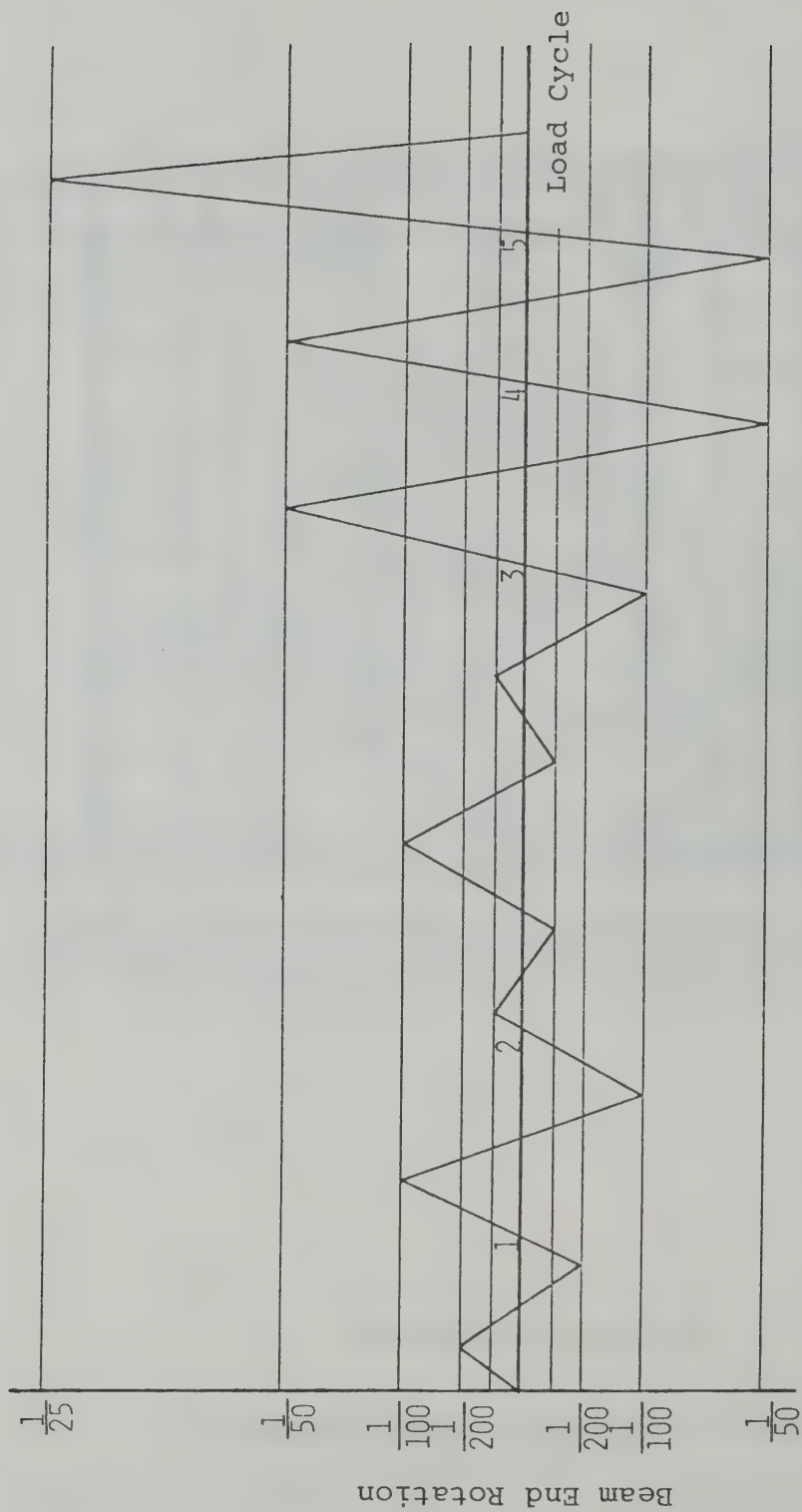


Fig.3.2.2. : Loading Program

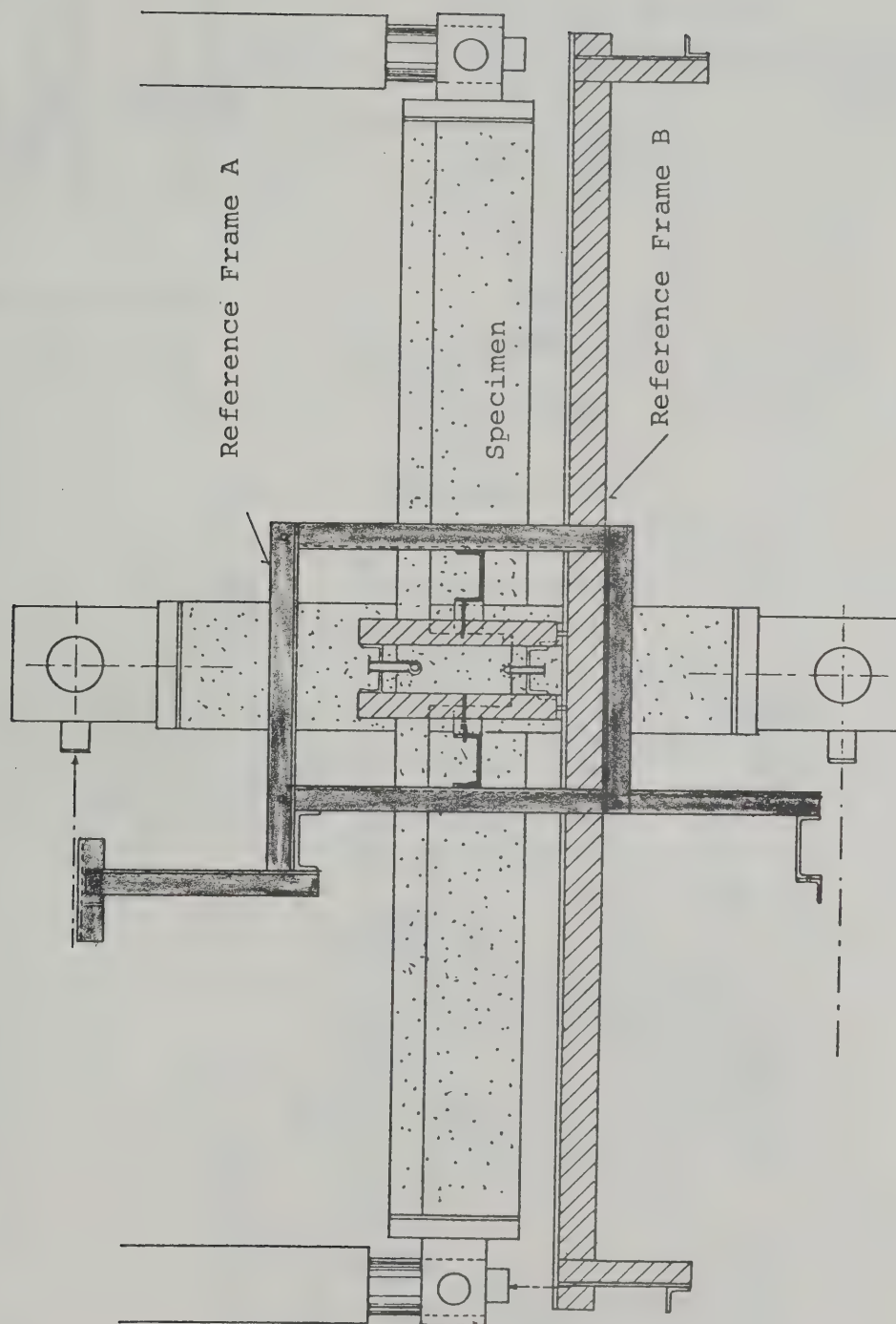


Fig.4.1. : Reference Frames for Displacement Measurements

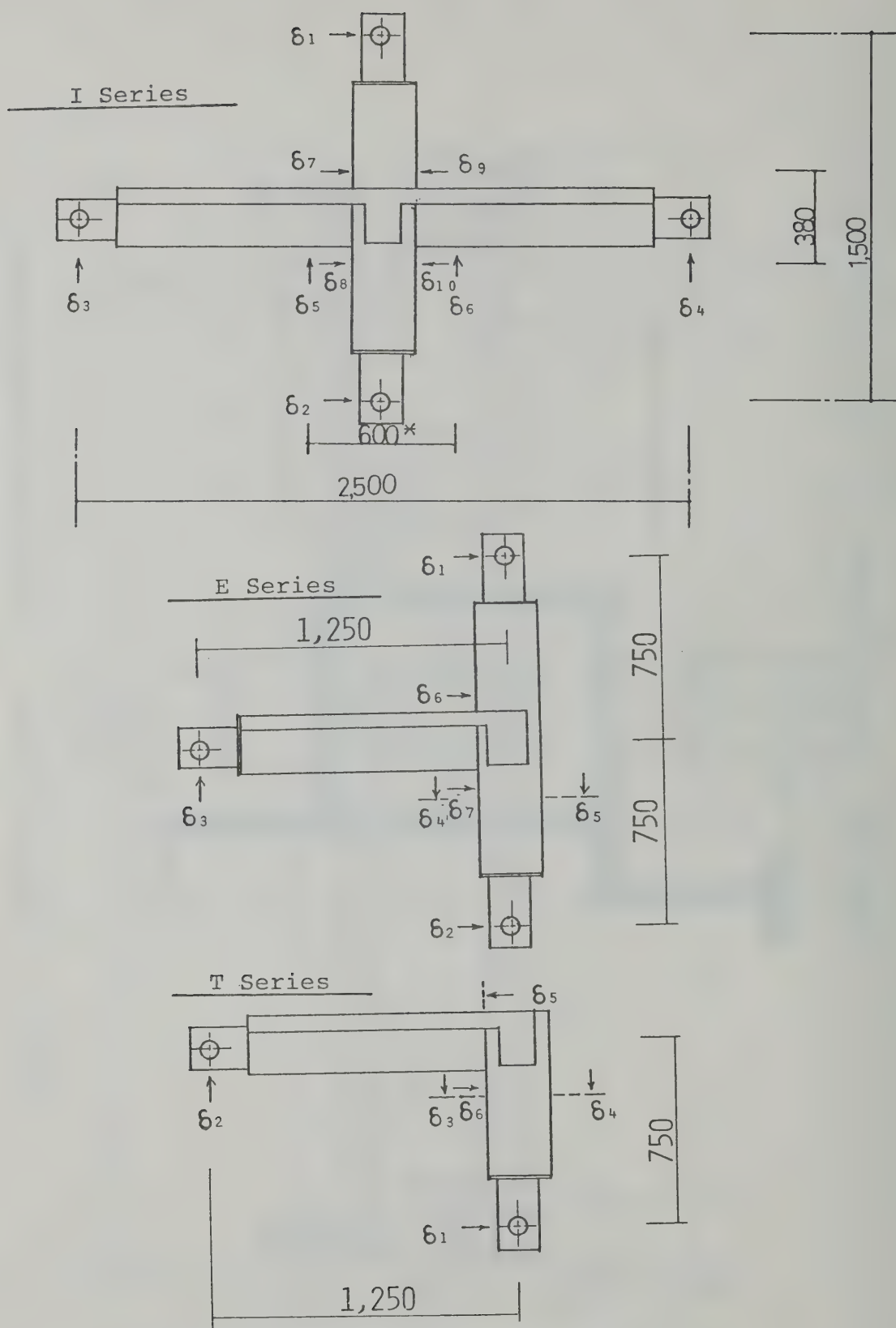
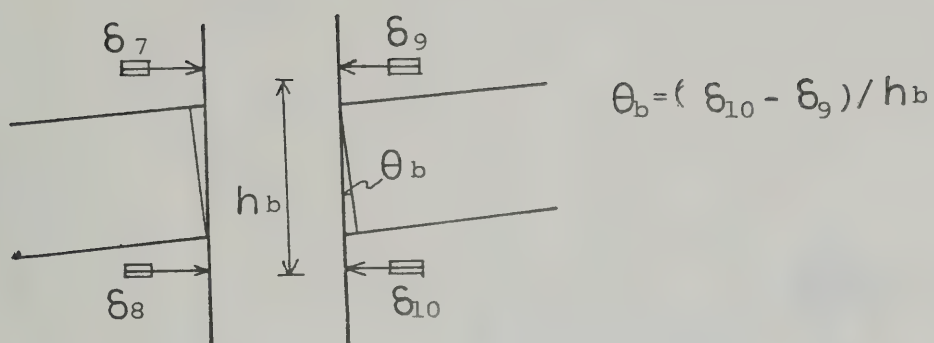


Fig.4.2. : Location of Displacement Gauges





Series I specimen

Fig.4.3. : Determination of Beam-End Rotation

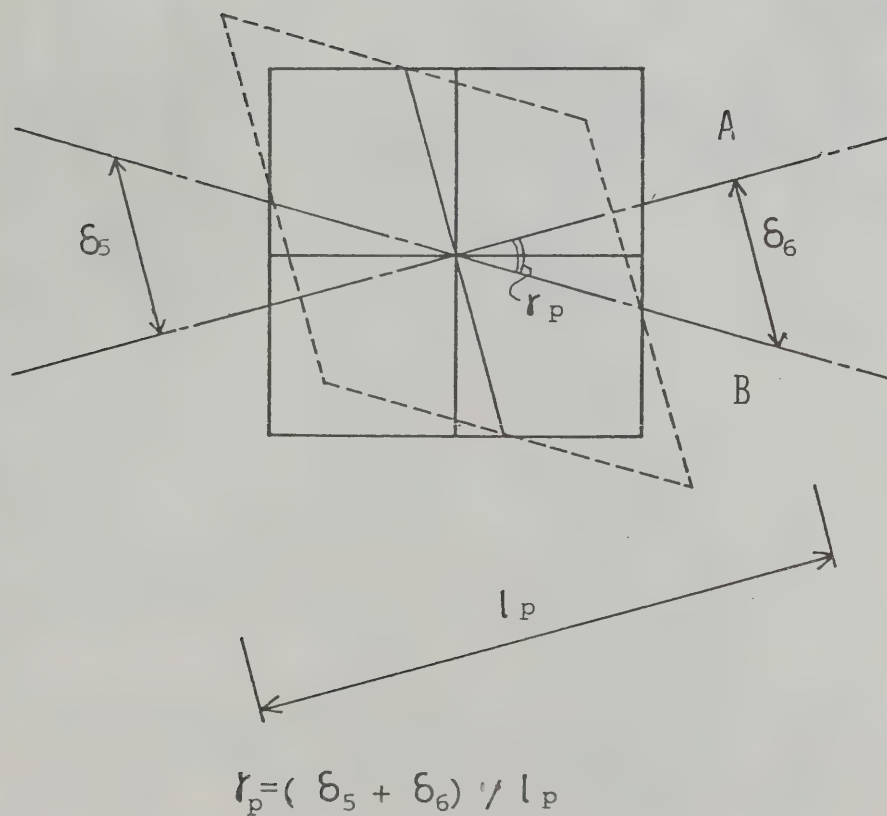


Fig.4.4. : Determination of Shear Distortion Angle of Beam-Column Joint Panel

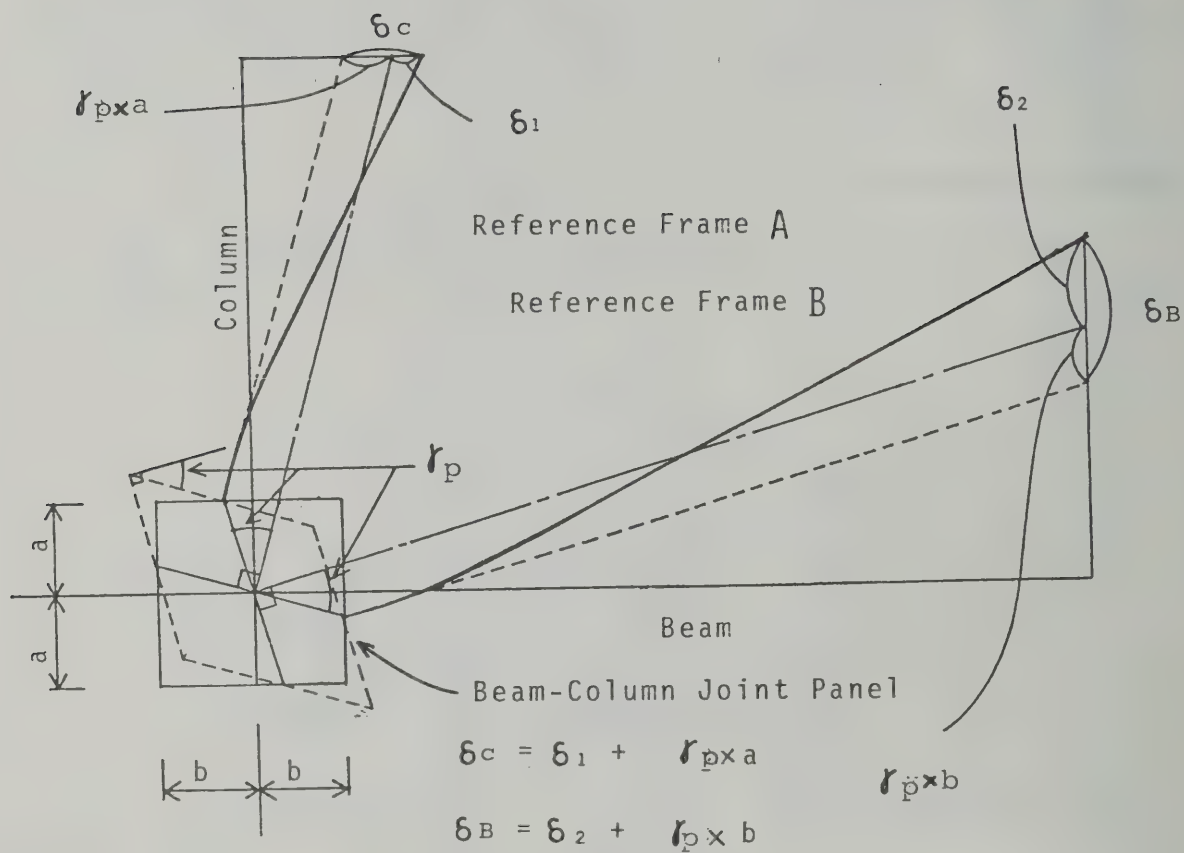
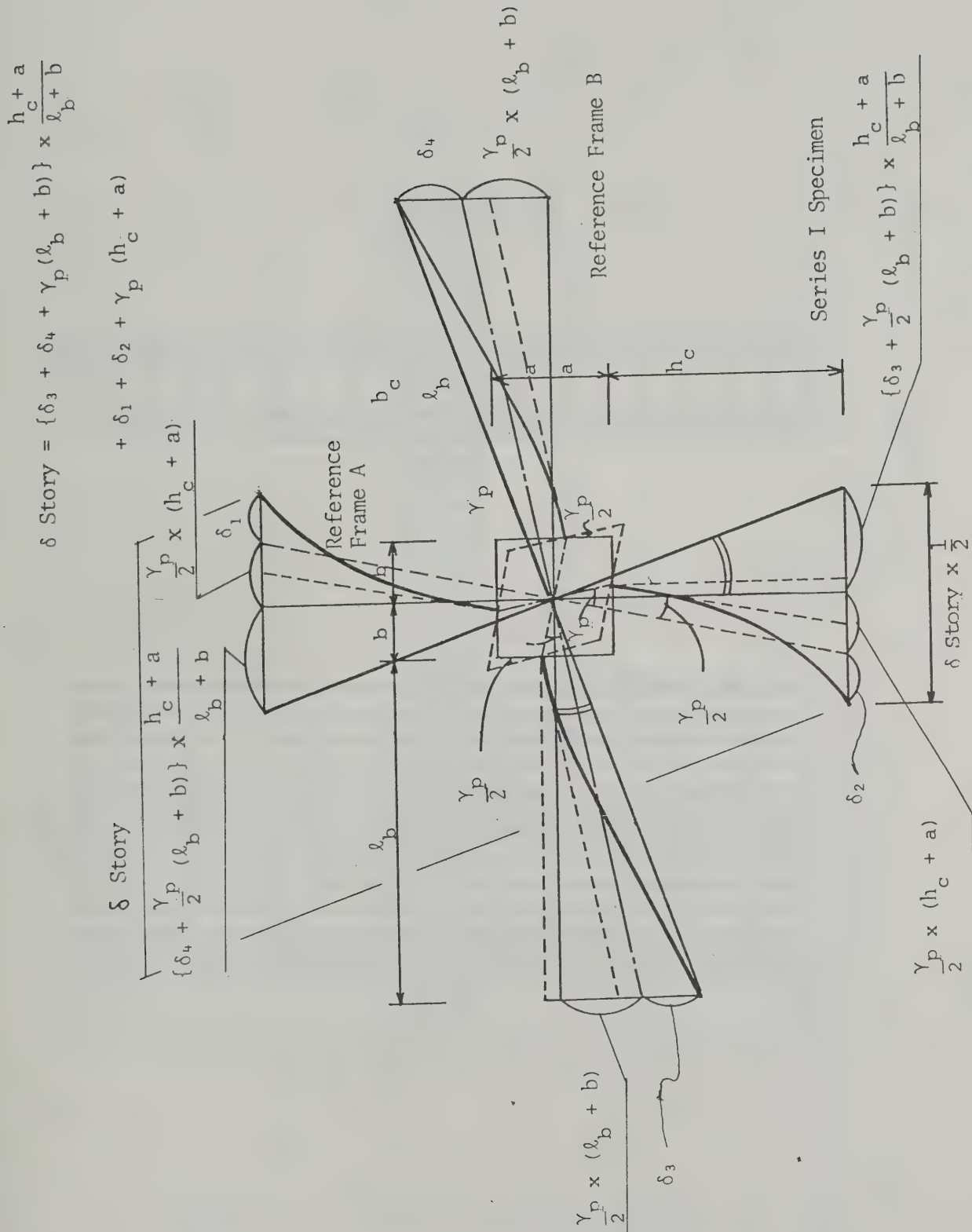


Fig.4.5. : Column and Beam Deformation Measured from Face of Beam-Column Joint Panel



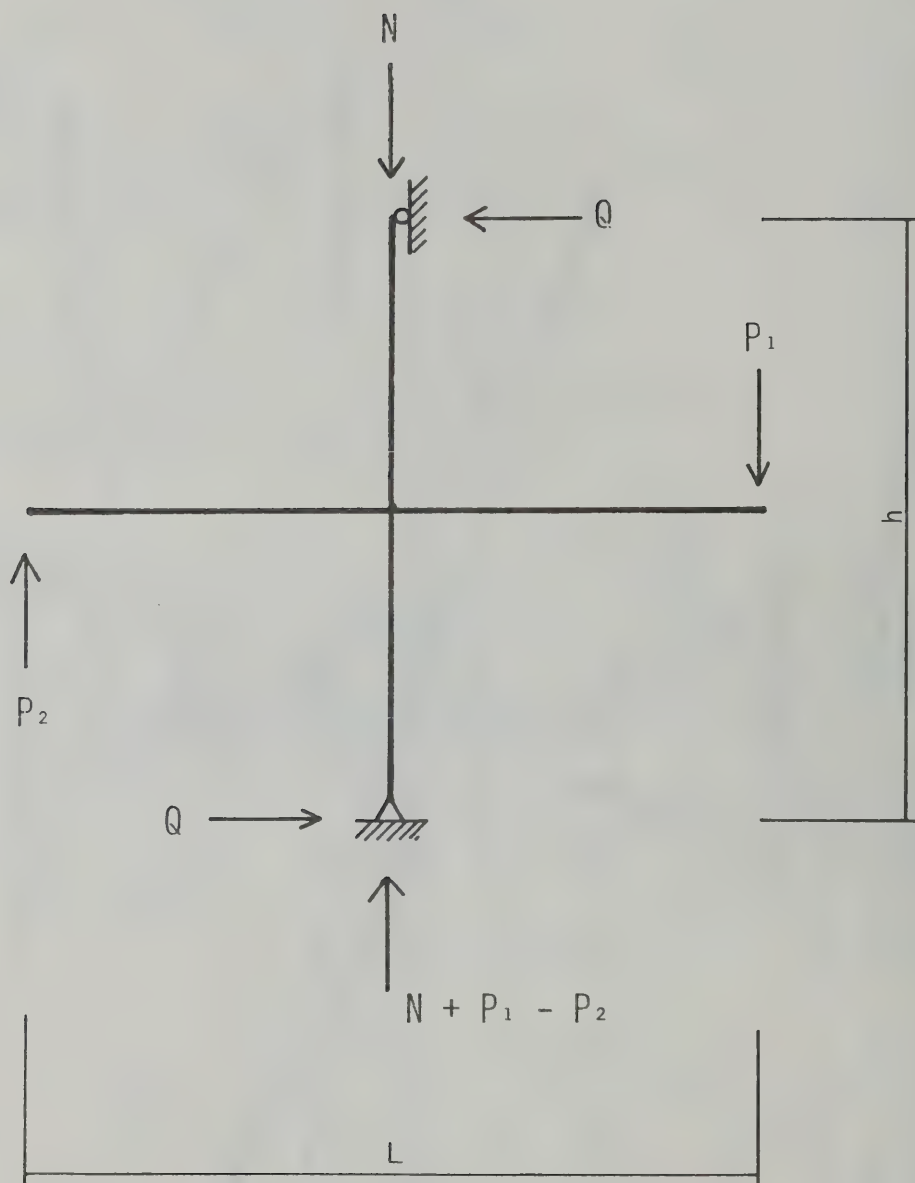


Fig.4.7. : Determination of Story Shear



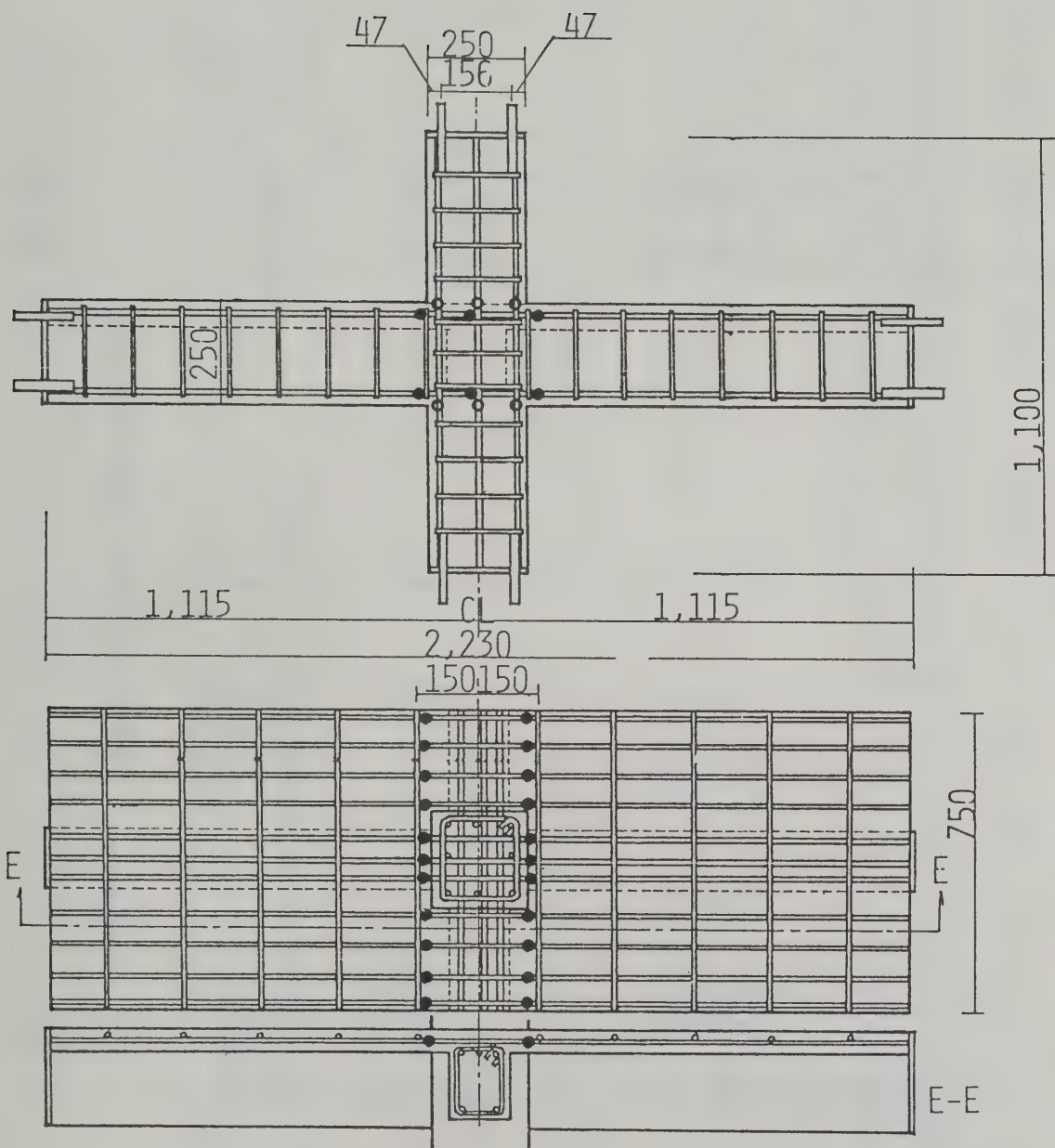
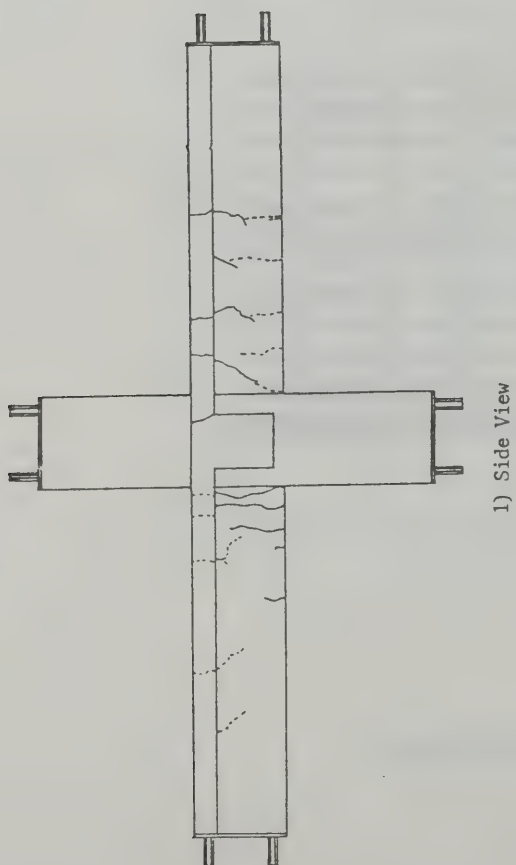
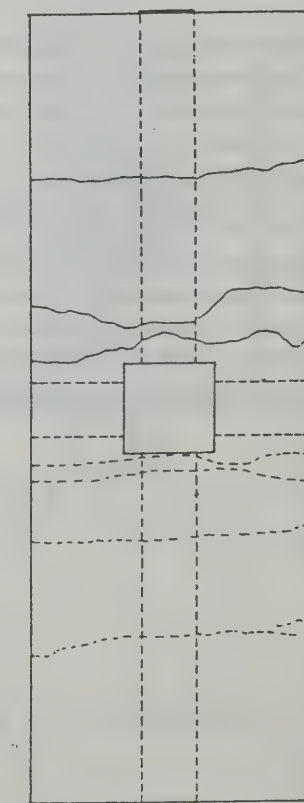


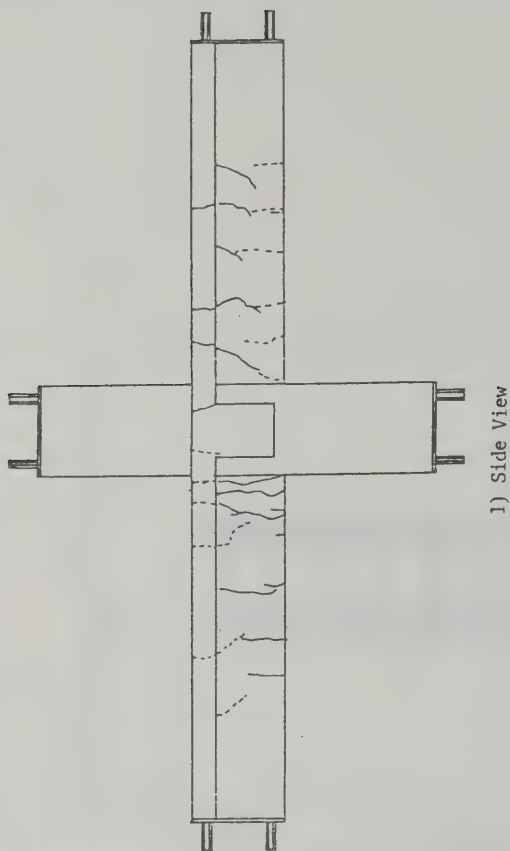
Fig.4.8. : Location of Strain Gauges



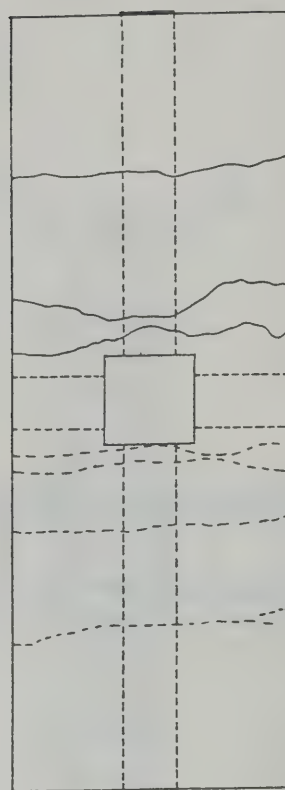
1) Side View



2) Plan View  
a) R=1/200



1) Side View



2) Plan View  
b) R=1/100

Fig.5.1.1. : Crack Pattern (Specimen I-1)

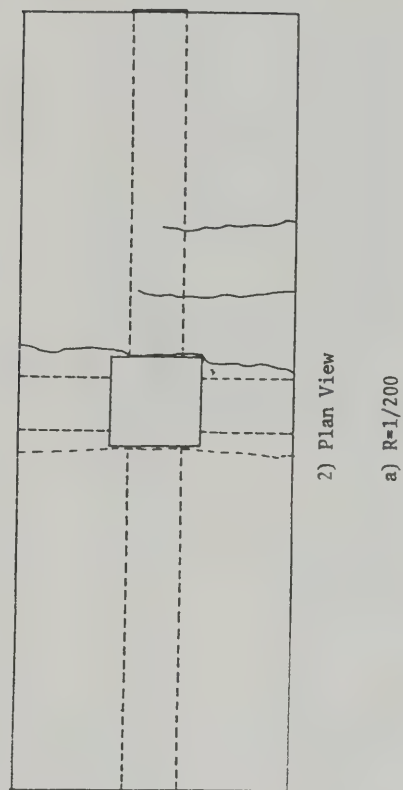
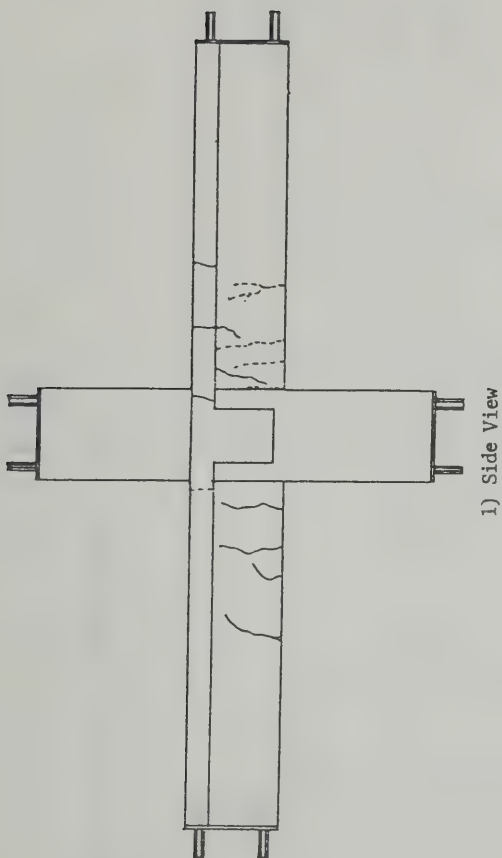
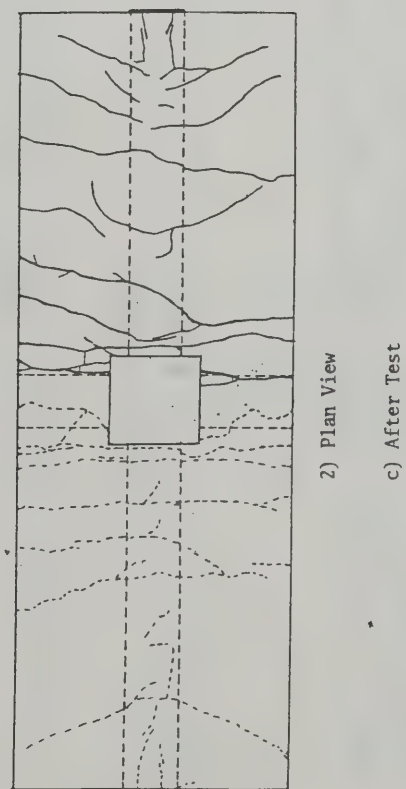
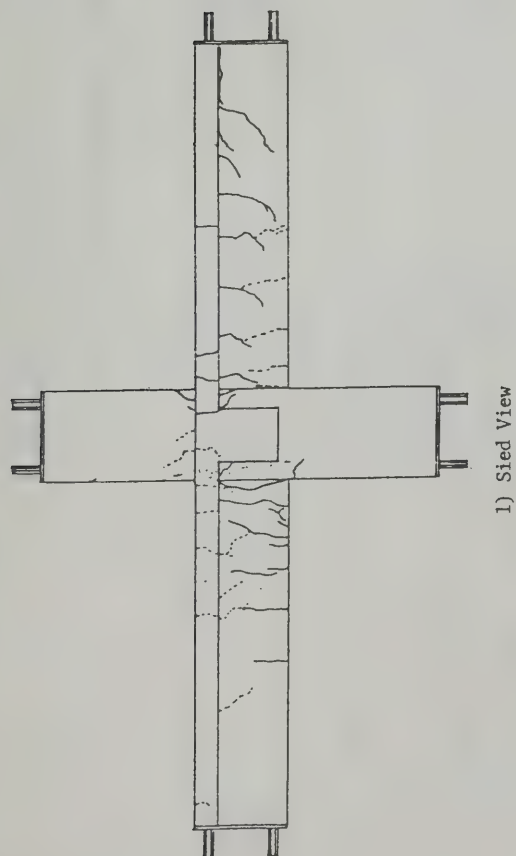
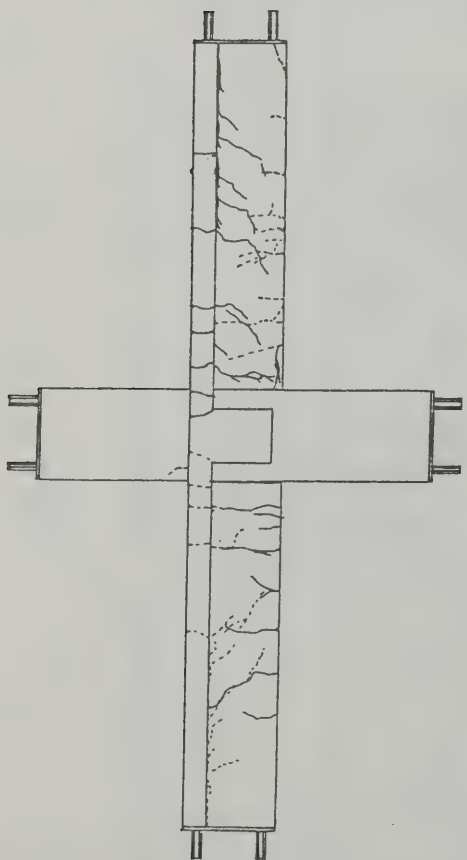
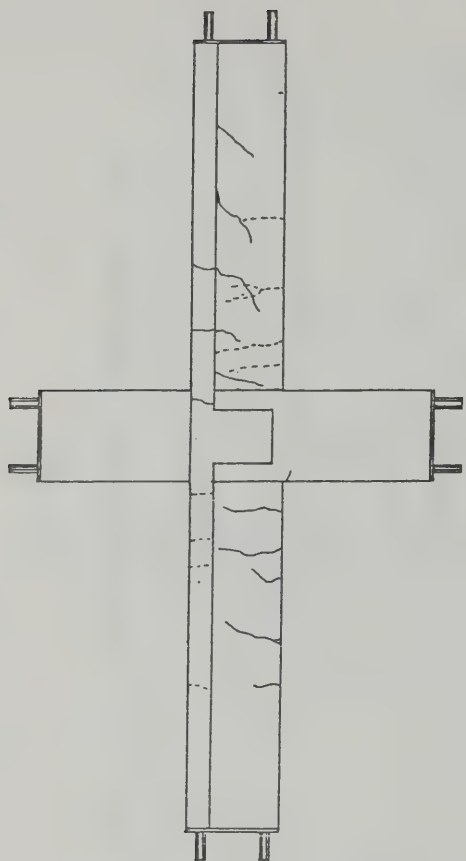


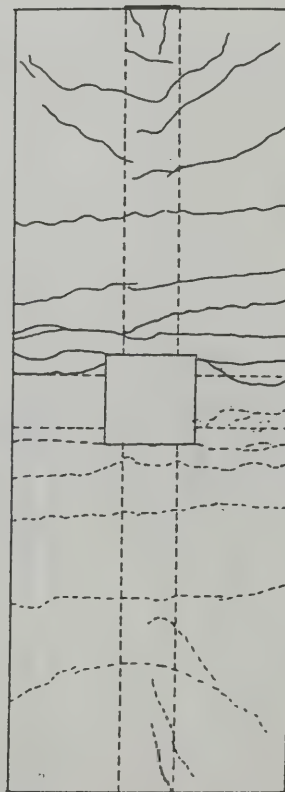
Fig.5.1.(Continued): Crack Pattern (Specimen I-1)      Fig.5.2. : Crack Pattern (Specimen I-2)



1) Side View

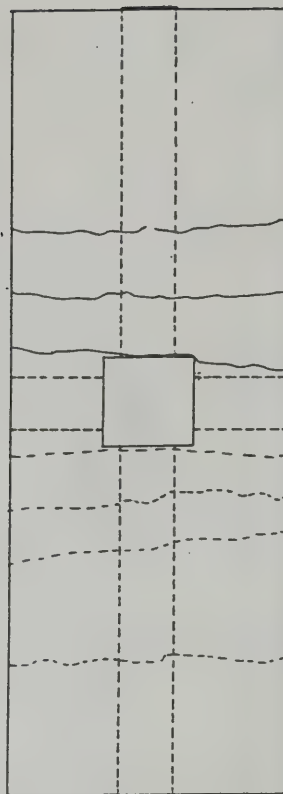


1) Side View



2) Plan View

c) After Test



2) Plan View

b)  $R=1/100$

Fig.5.2. (Continued): Crack Pattern (Specimen I-2)



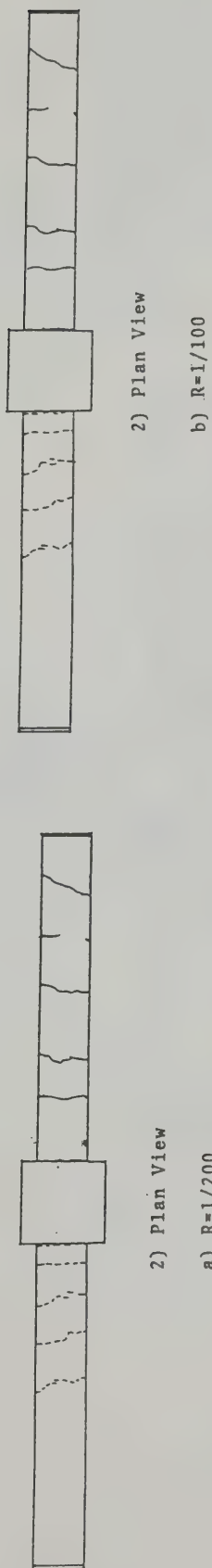
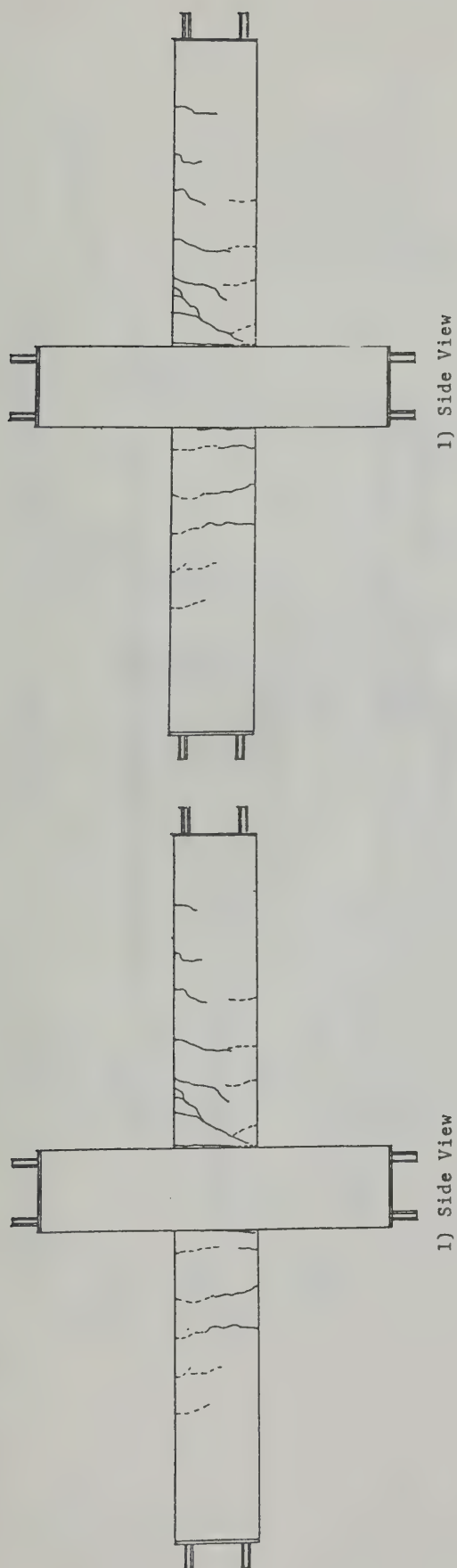
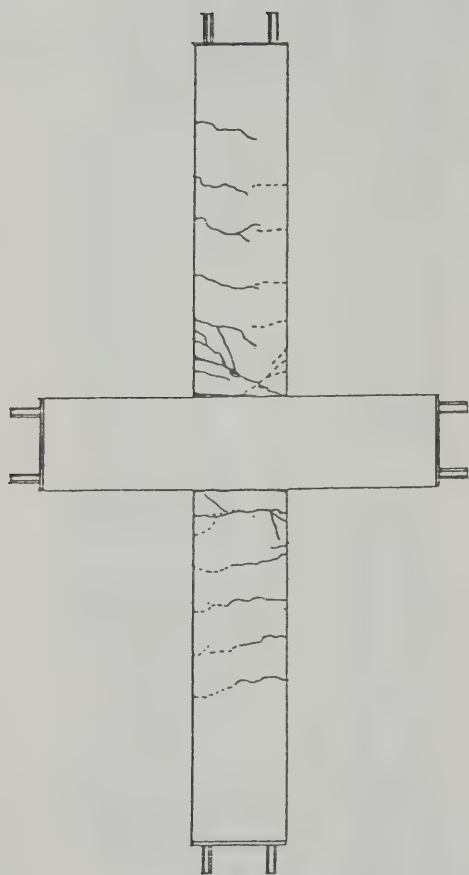


Fig.5.3. : Crack Pattern (Specimen I-3)



1) Side View



2) Plan View

c) After Test

Fig.5.3.3.(Continued): Crack Pattern (Specimen I-3)

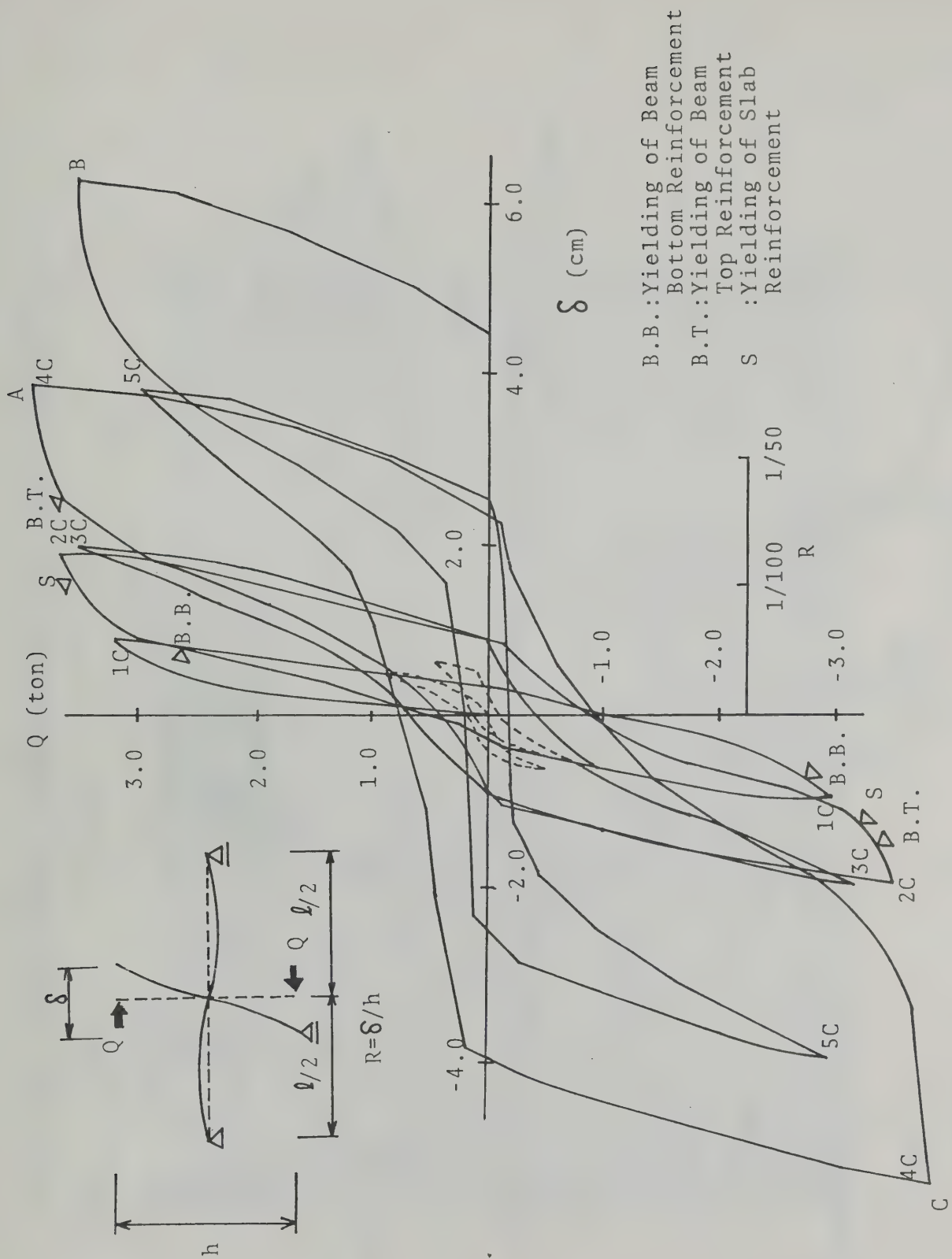


Fig. 5.4. : Story Shear - Displacement Relationship (Specimen I-1)

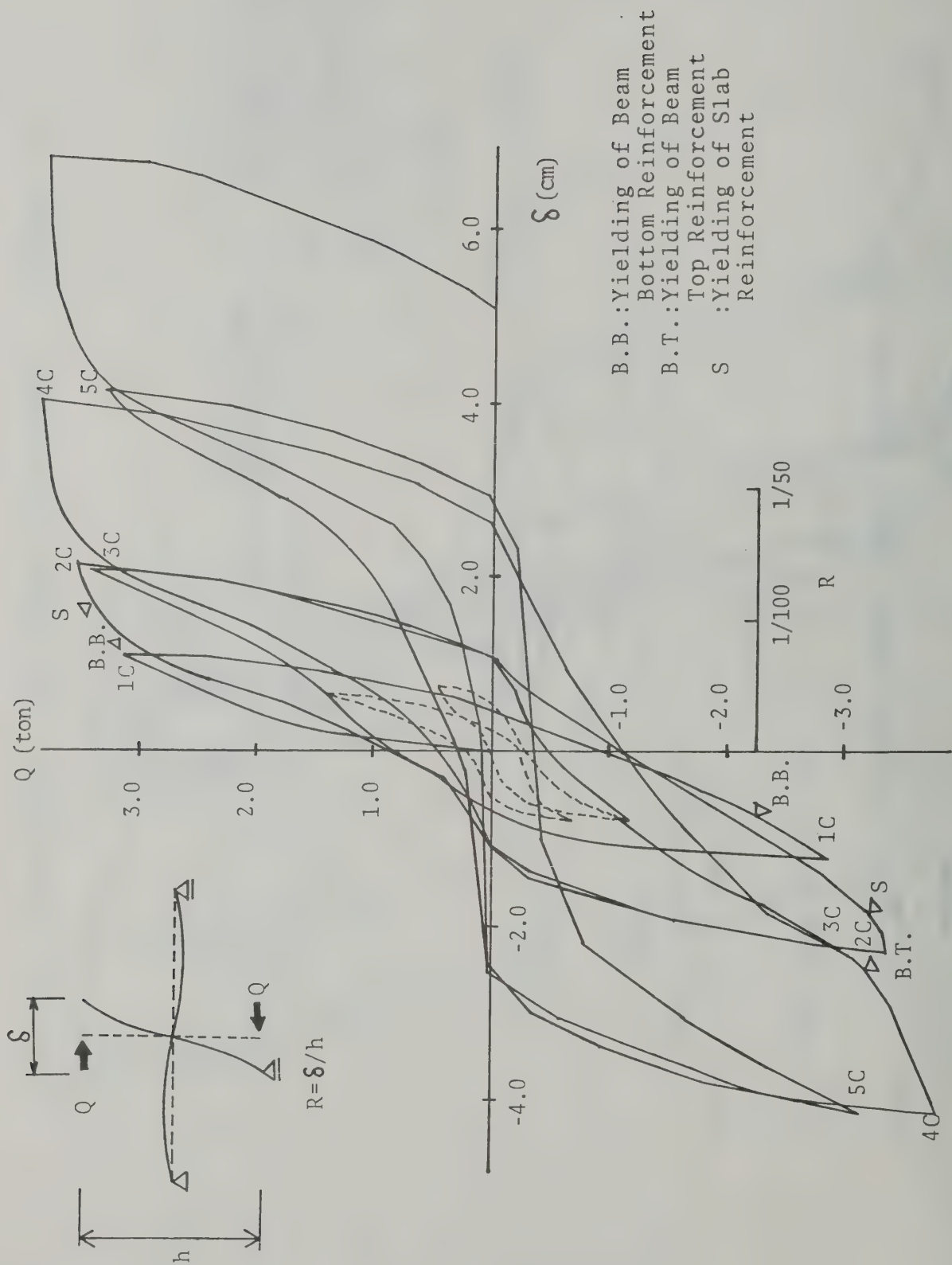
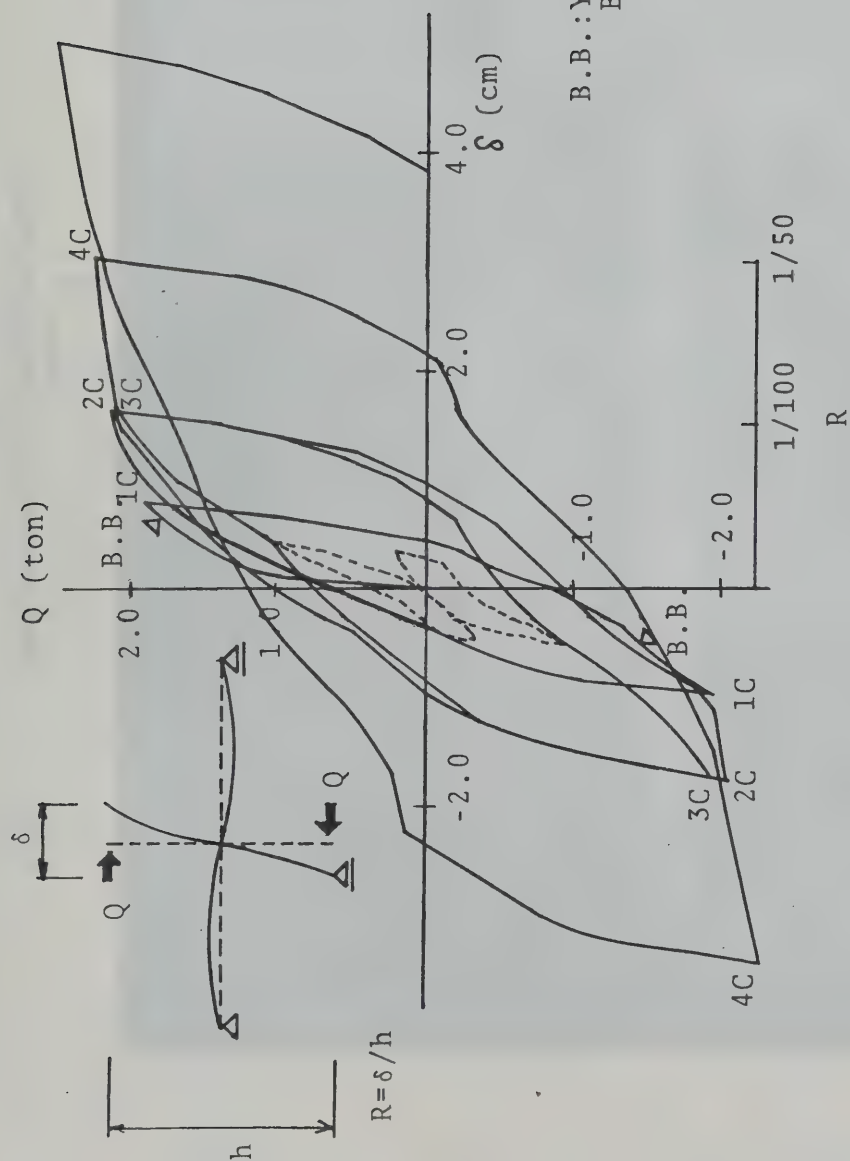


Fig. 5.5. : Story Shear - Displacement Relationship (Specimen I-2)





B.B.:Yielding of Beam  
Bottom Reinforcement

Fig. 5.6. : Story Shear - Displacement Relationship (Specimen I-3)

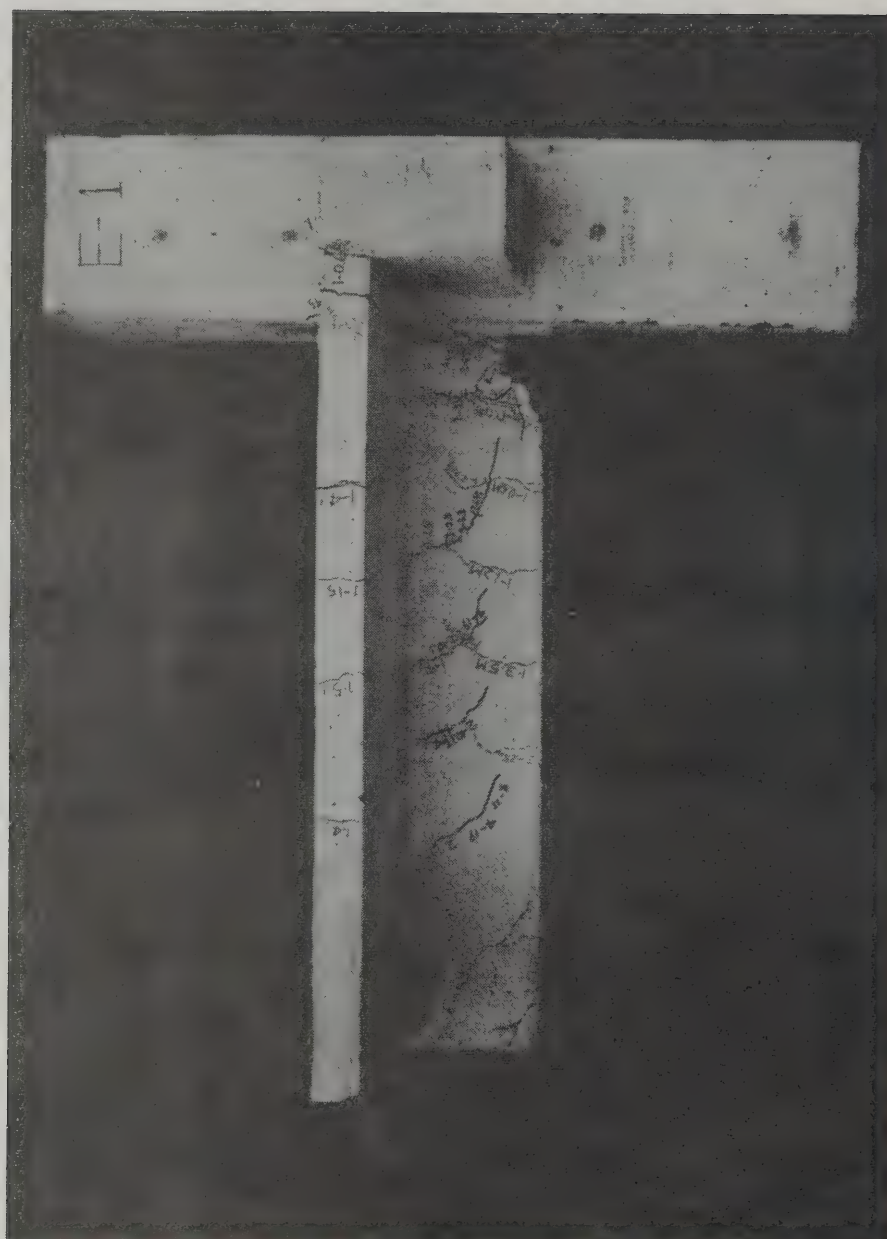


Fig.5.7. : Photograph of Crack Pattern

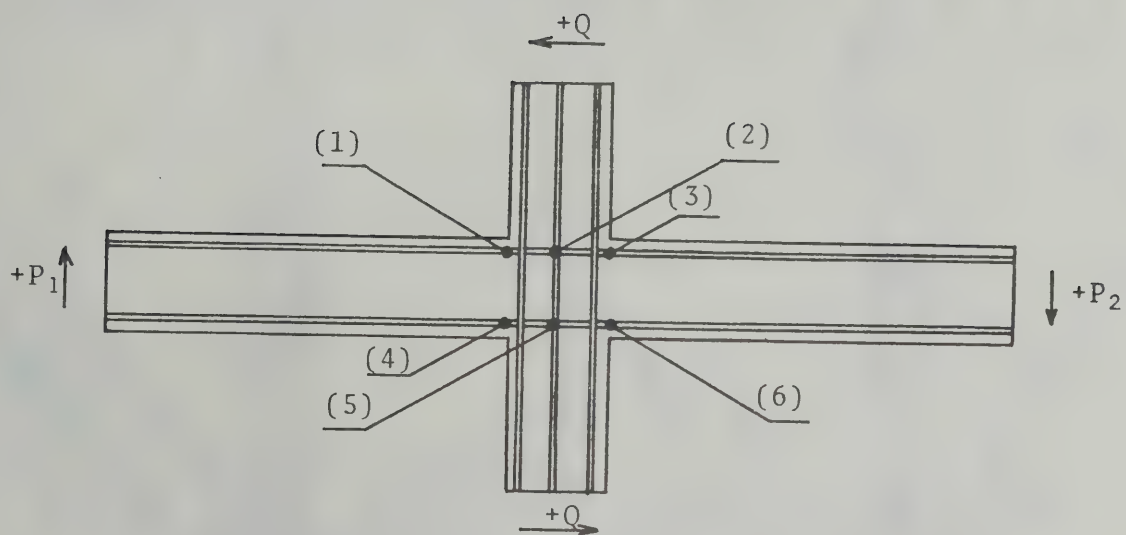
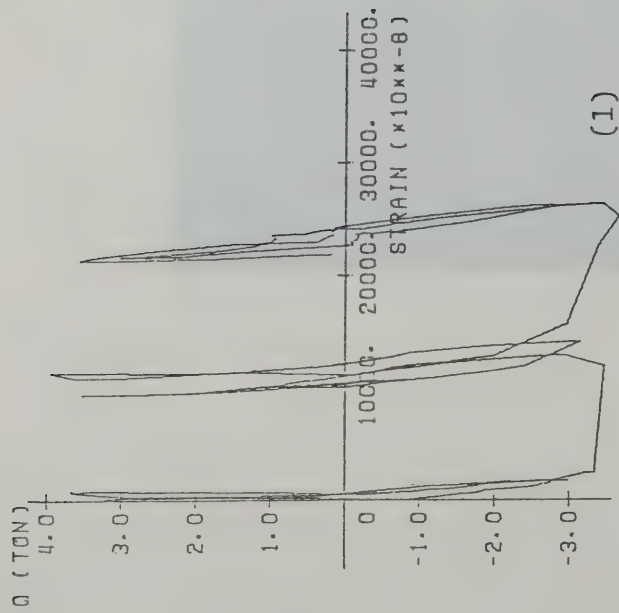
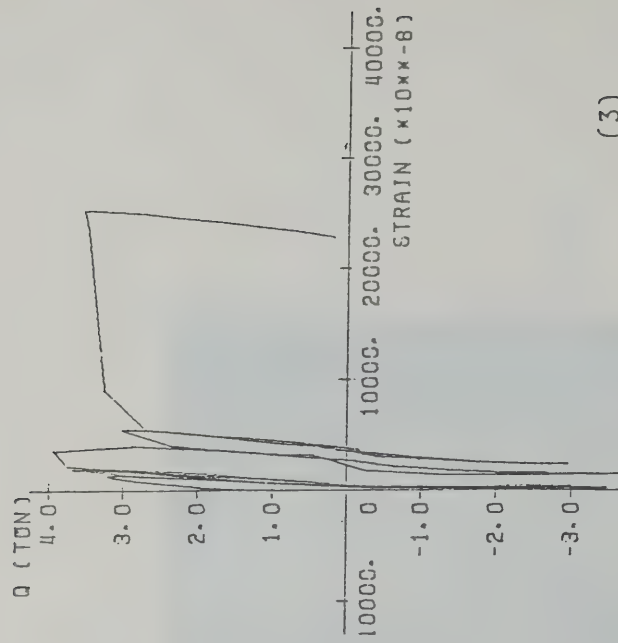


Fig.5.8. : Gauge Numbers in Beam Longitudinal Bars  
(I-Series Specimens)

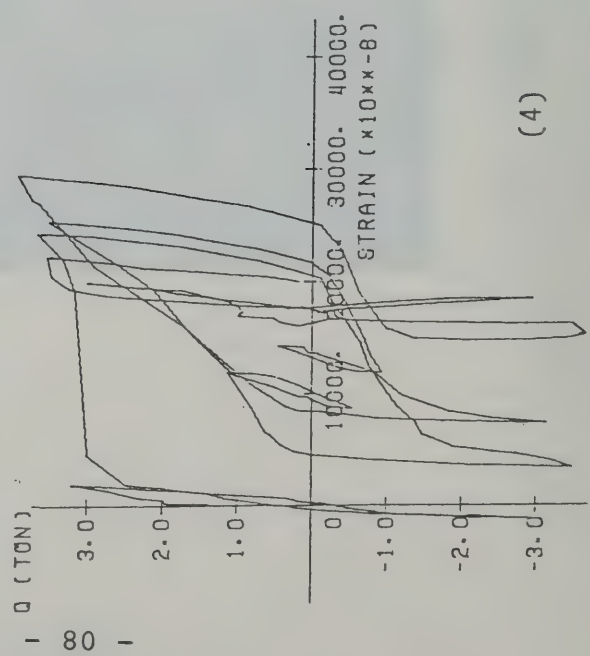


(2) not recorded

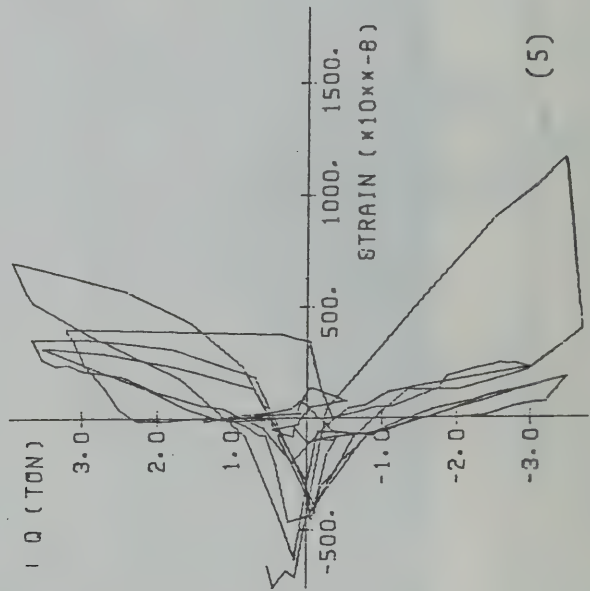


(1)

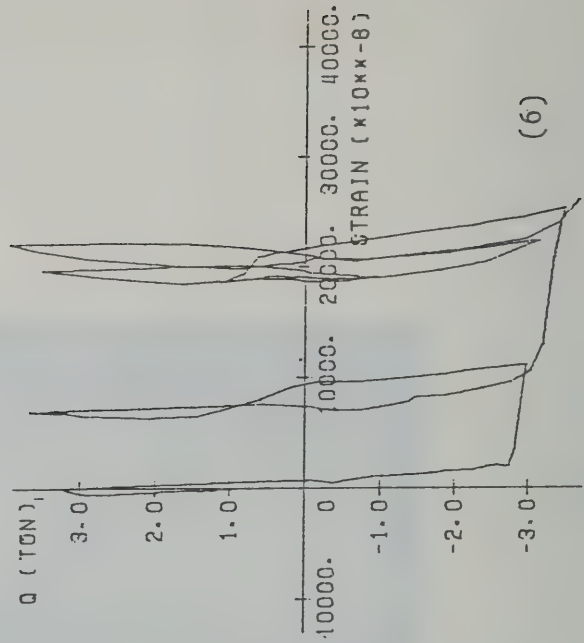
(3)



(4)



(5)



(6)

Fig. 5.9. : Story Shear - Beam Longitudinal Bar Strain Relationship (Specimen I-1)



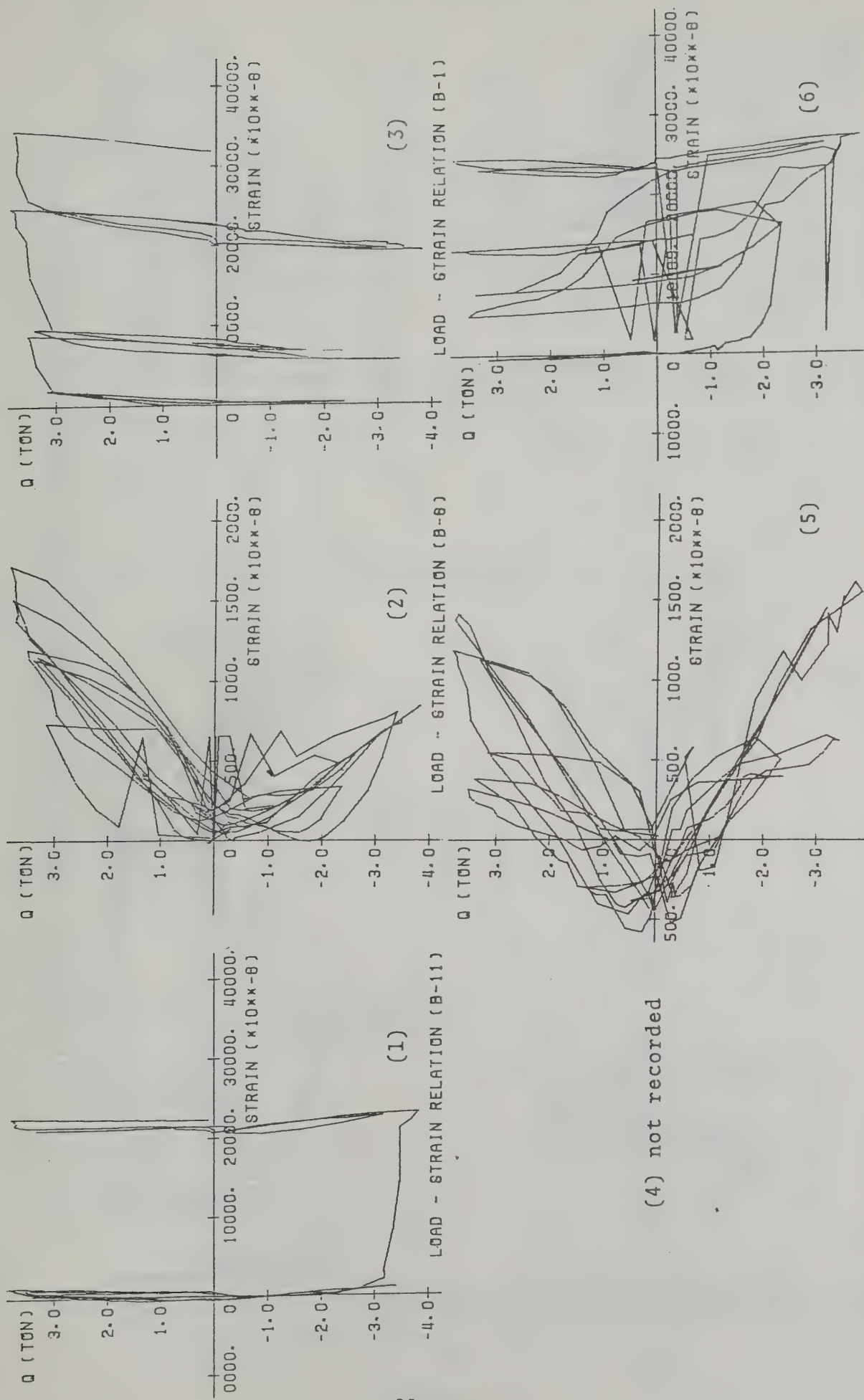


Fig. 5.10. : Story Shear - Beam Longitudinal Bar Strain Relationship (Specimen I-2)

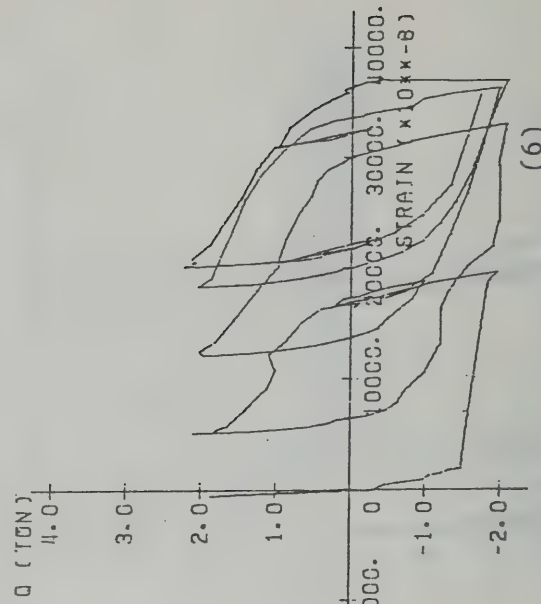
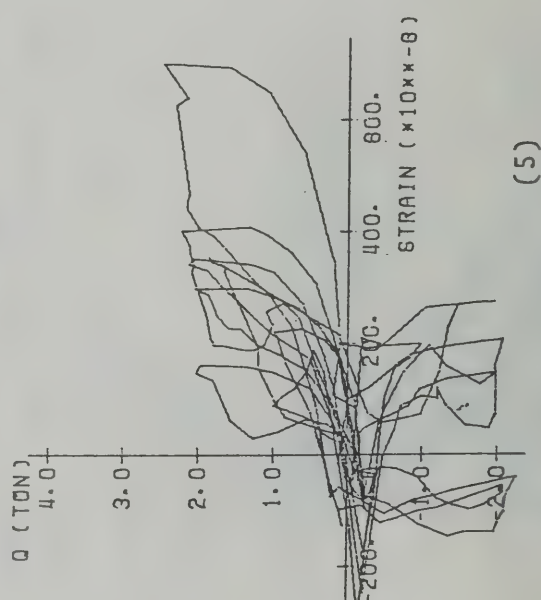
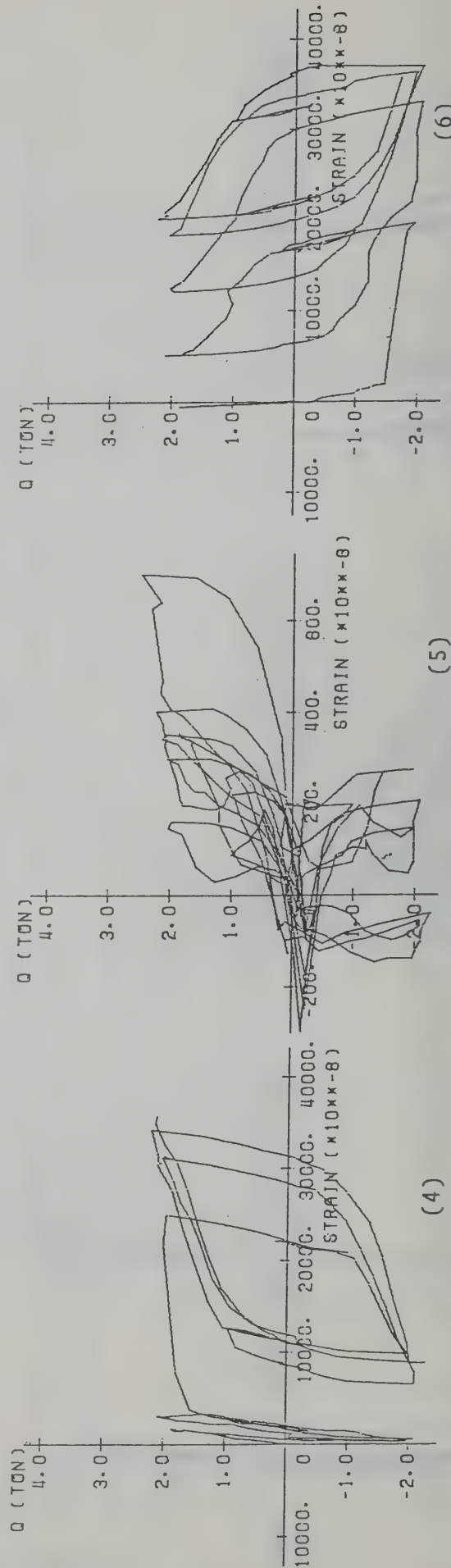
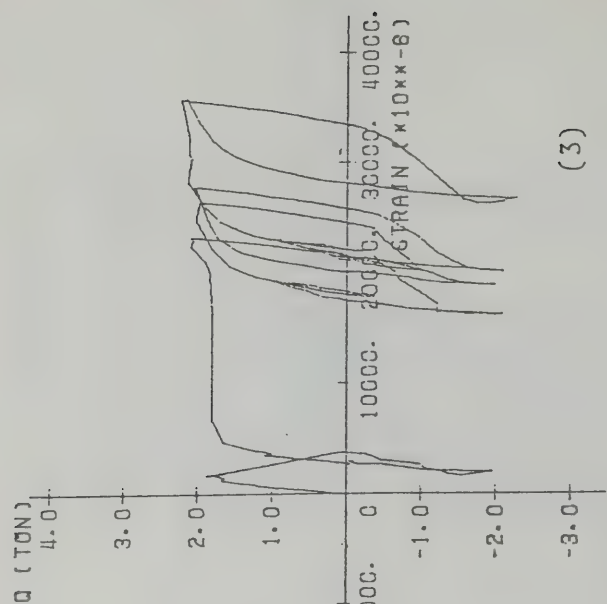
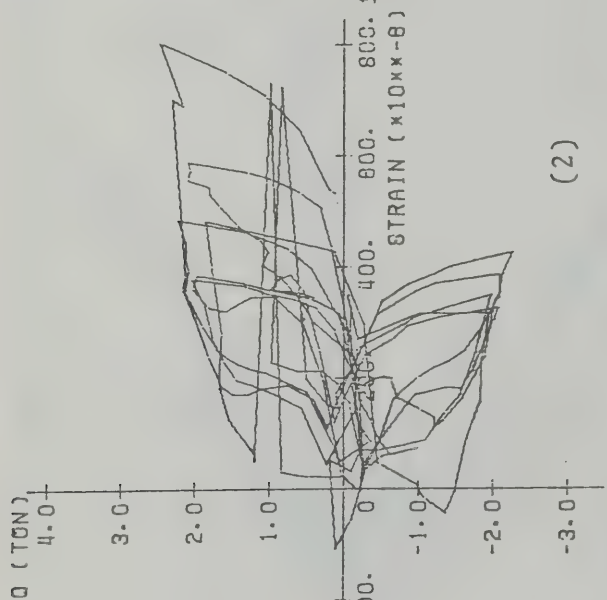
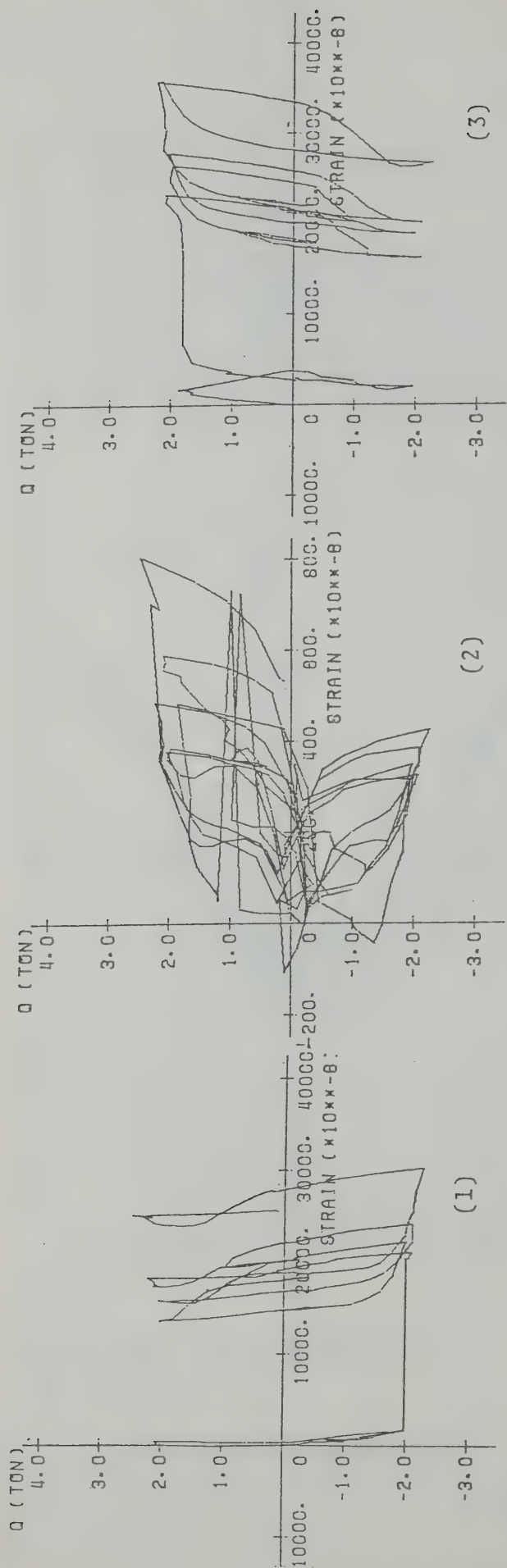


Fig. 5.11. : Story Shear - Beam Longitudinal Bar Strain Relationship (Specimen I-3)

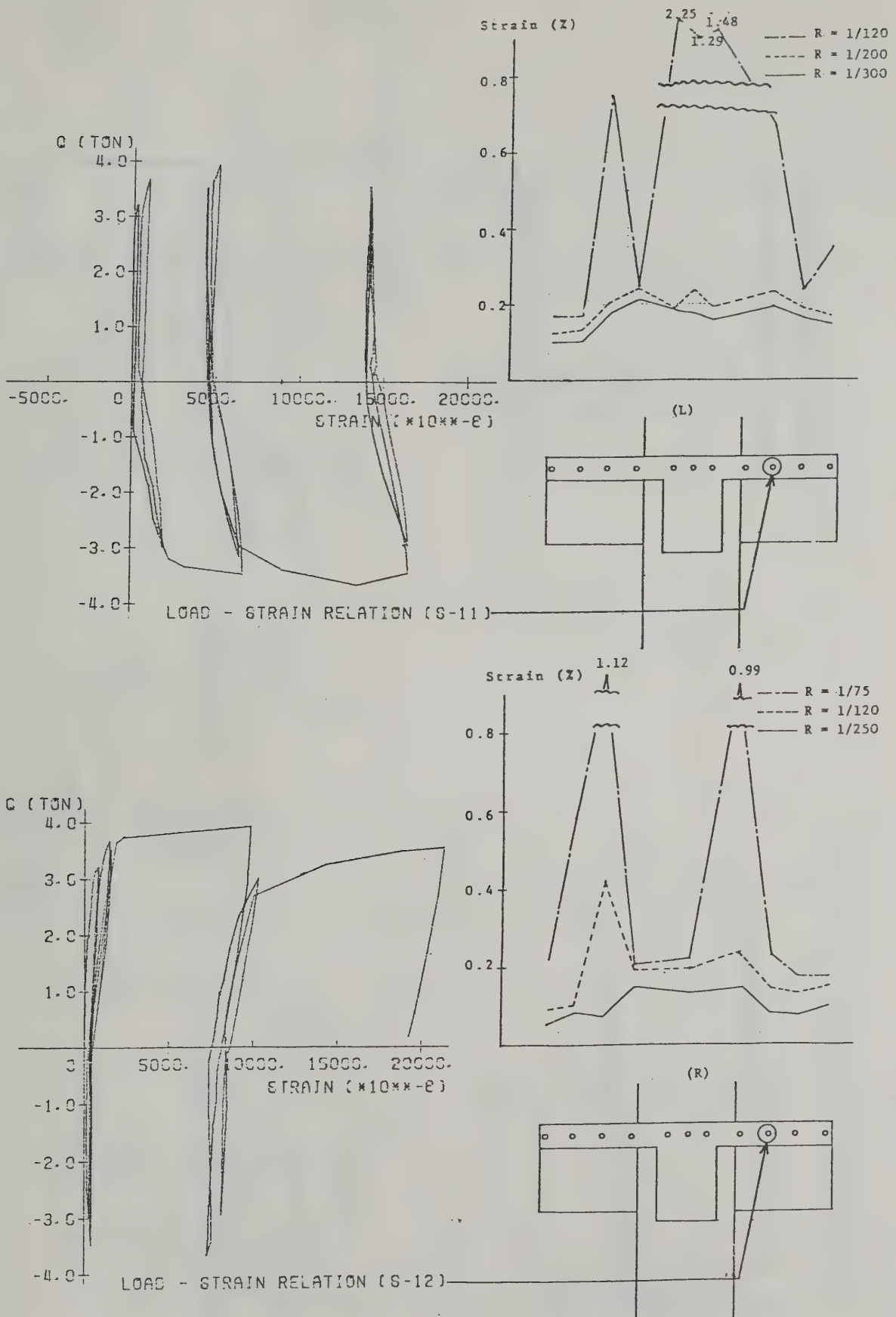


Fig. 5.12. : Strain Distribution in Slab Reinforcement  
(Specimen I-1)

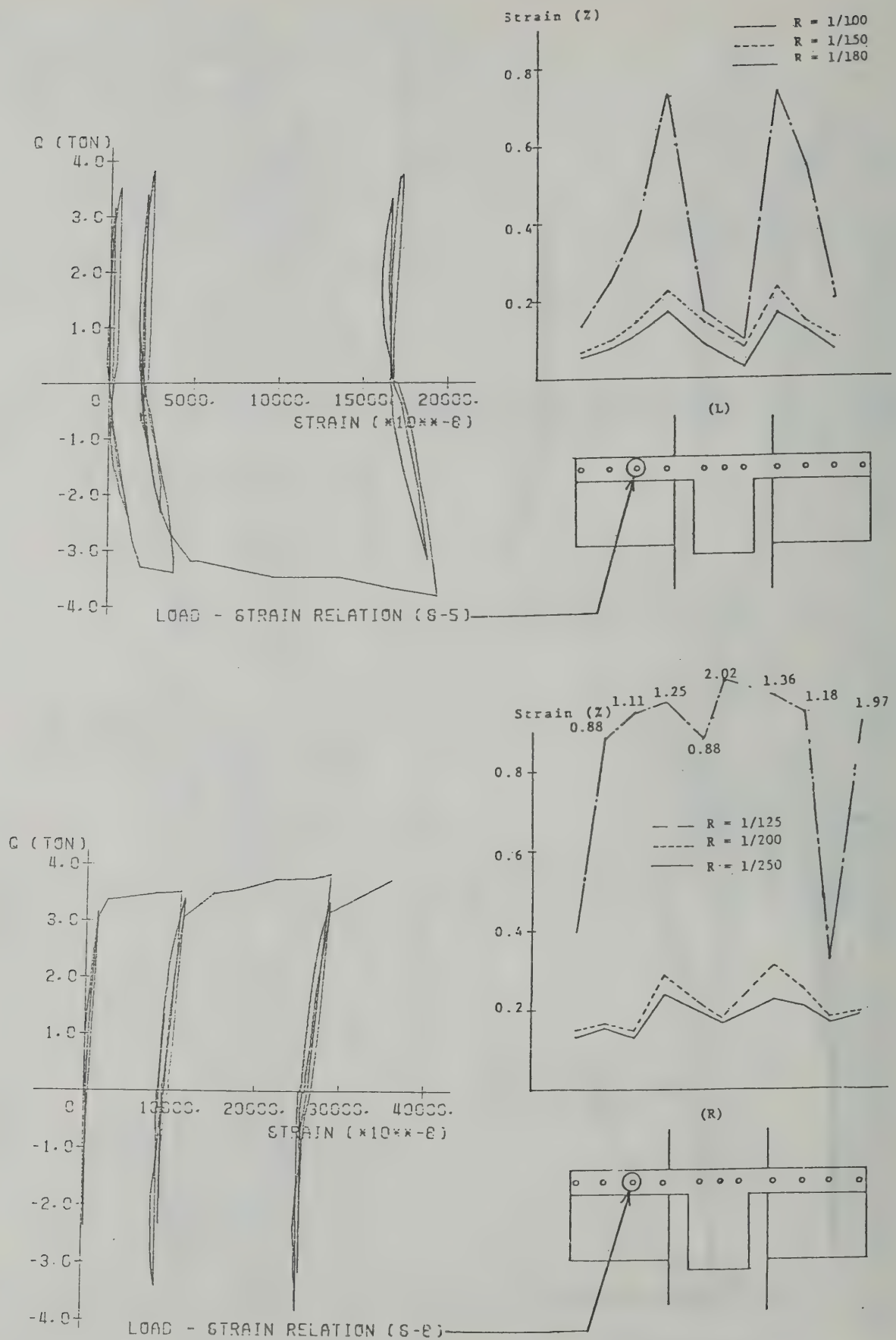
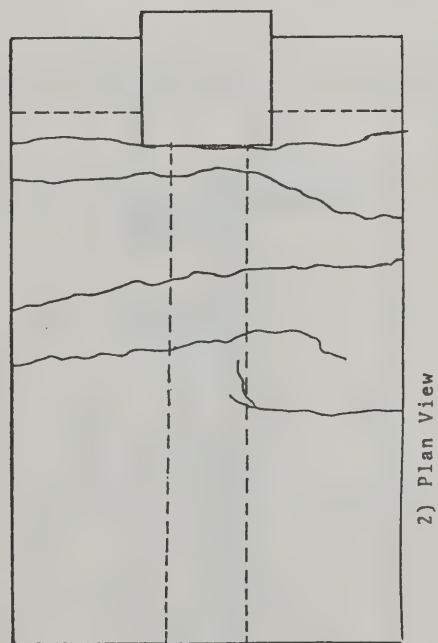
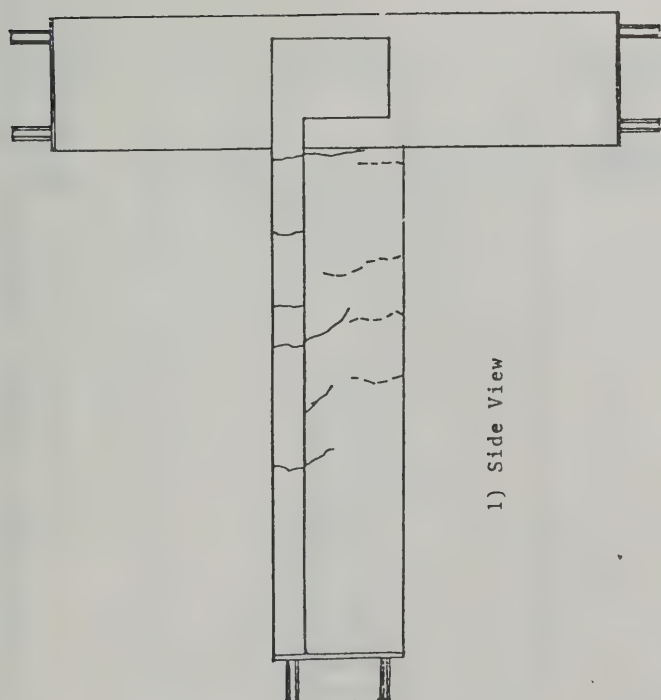
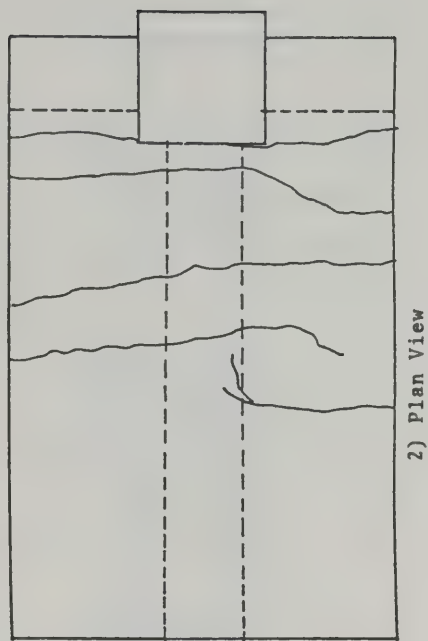
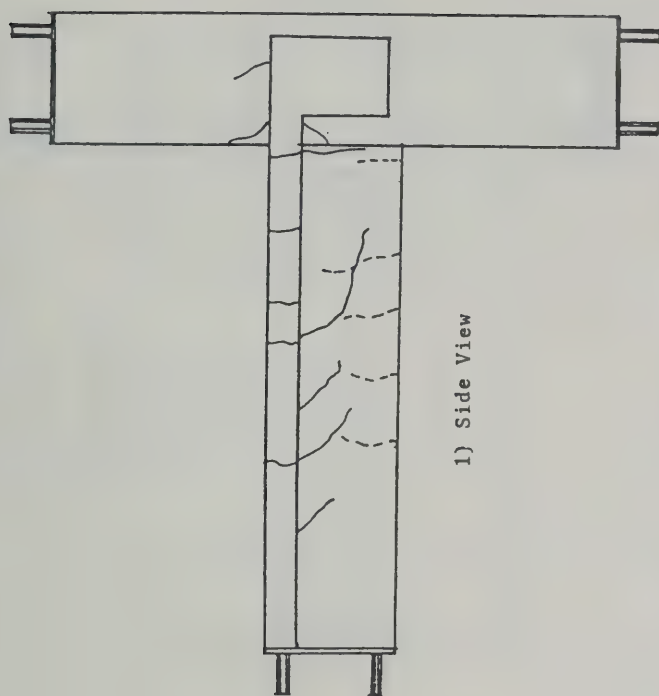


Fig. 5.13. : Strain Distribution in Slab Reinforcement (Specimen I-2)



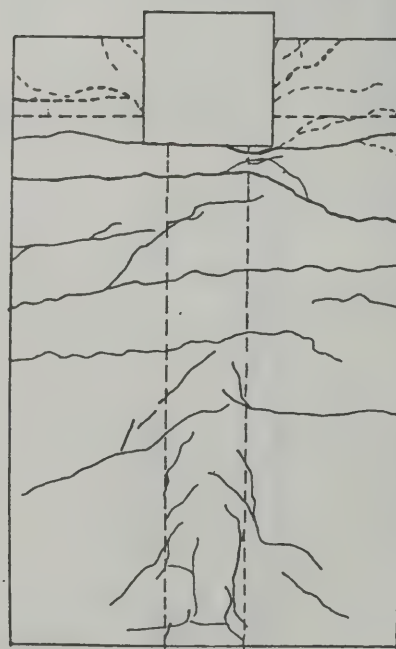
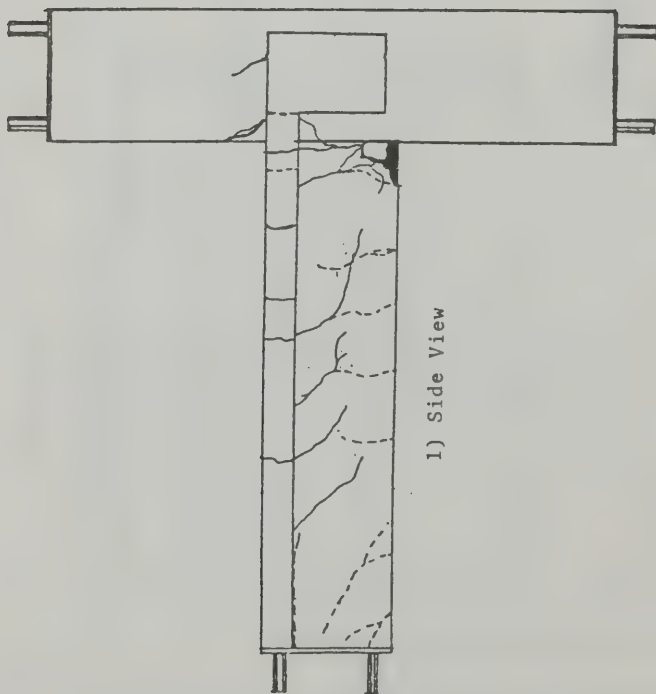


a) R=1/200



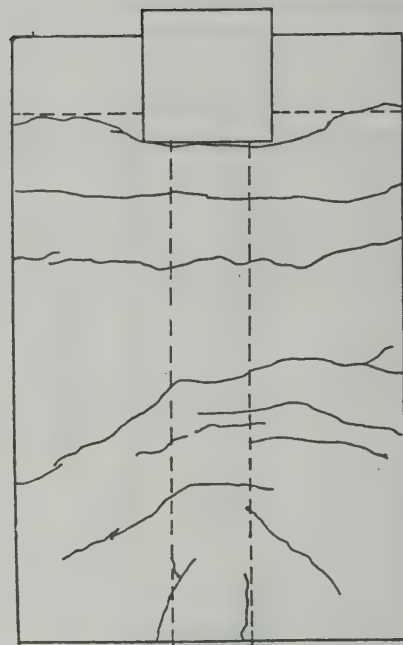
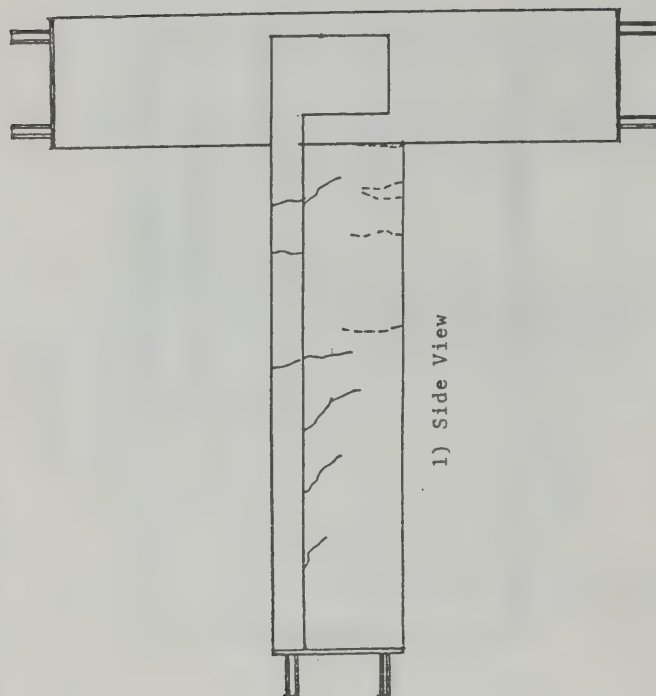
b) R=1/100

Fig.6.1.1. : Crack Pattern (Specimen E-1)



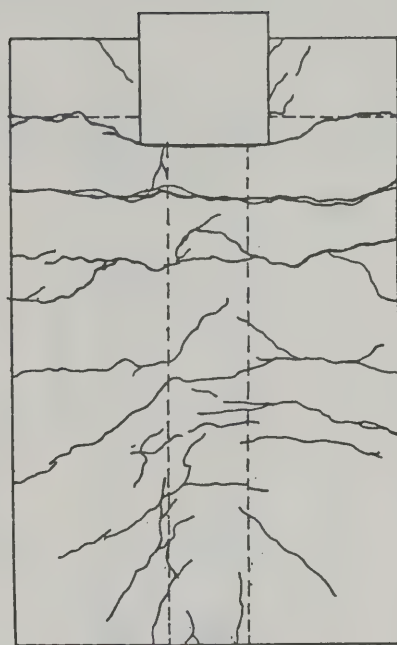
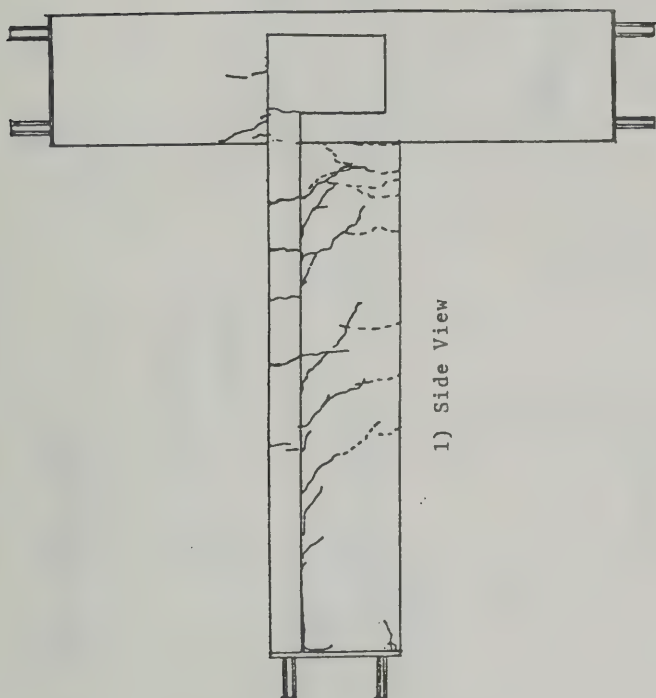
c) After Test

Fig.6.1.(Continued): Crack Pattern (Specimen E-1)

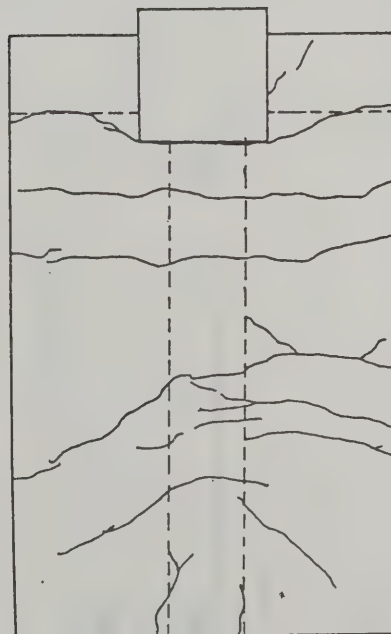
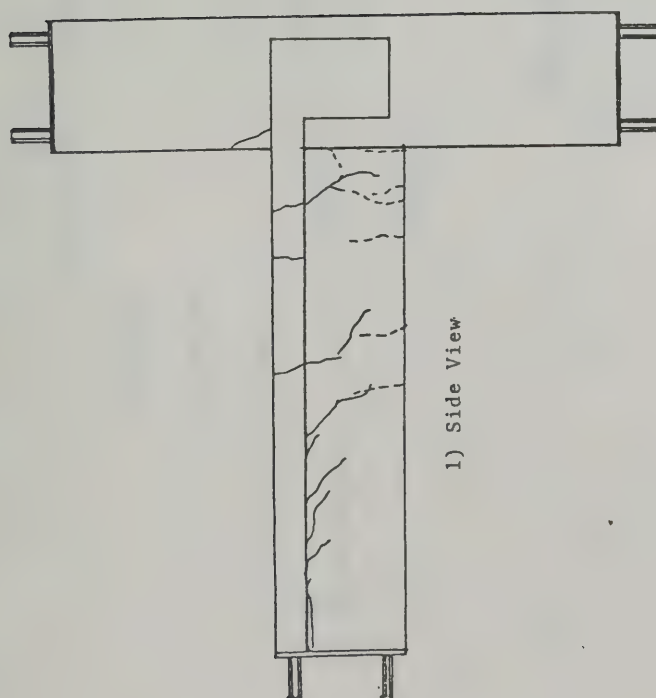


a) R=1/200

Fig.6.2.: Crack Pattern (Specimen E-2)

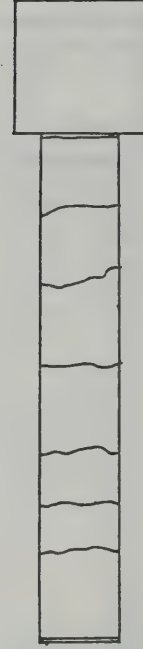
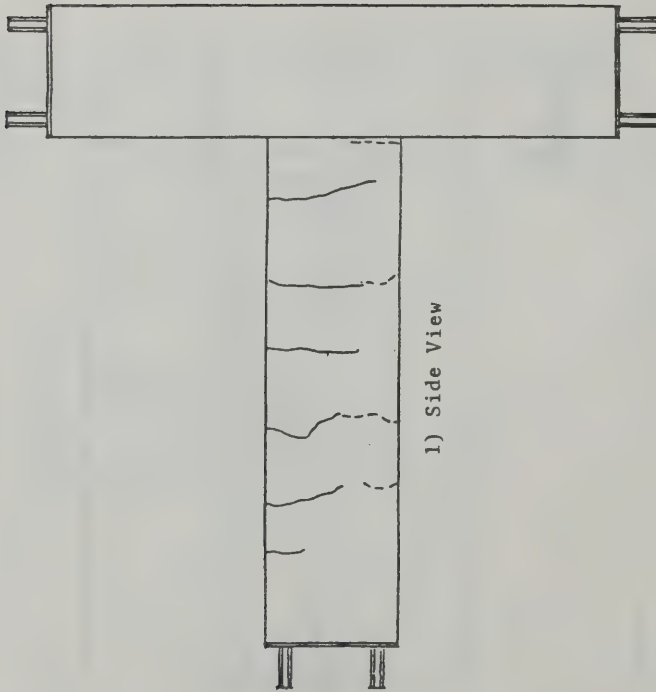
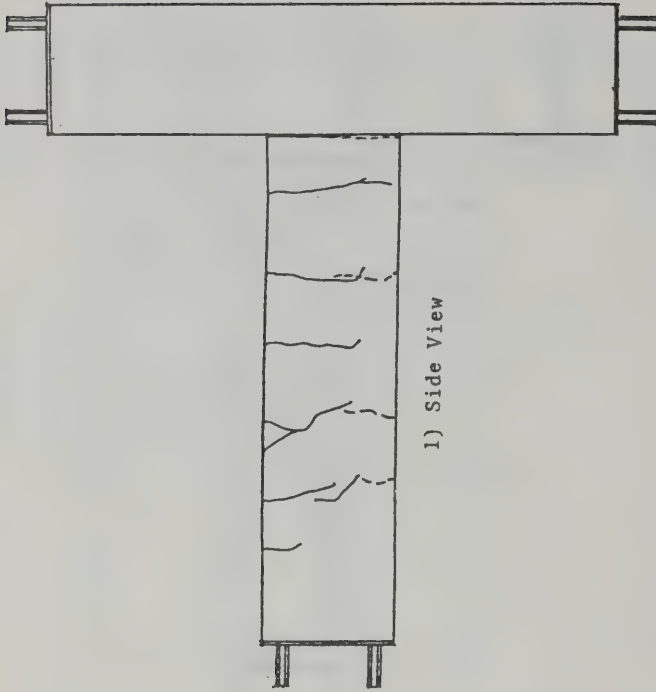


c) After Test

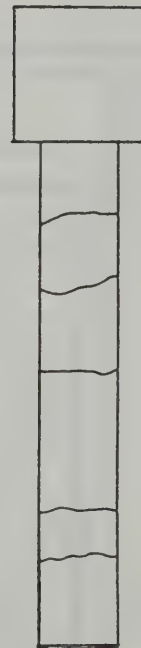


b) R=1/100

Fig.6.2.2.(Continued): Crack Pattern (Specimen E-2)



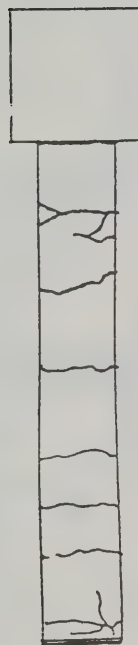
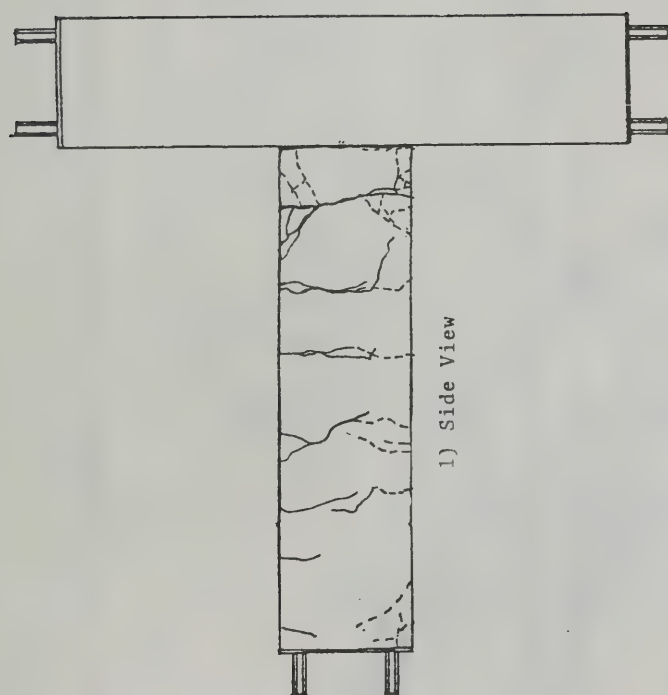
2) Plan View  
b) R=1/100



2) Plan View  
a) R=1/200

Fig.6.6.3. : Crack Pattern (Specimen E-3)





c) After Test

Fig.6.6.3.(Continued): Crack Pattern (Specimen E-3)

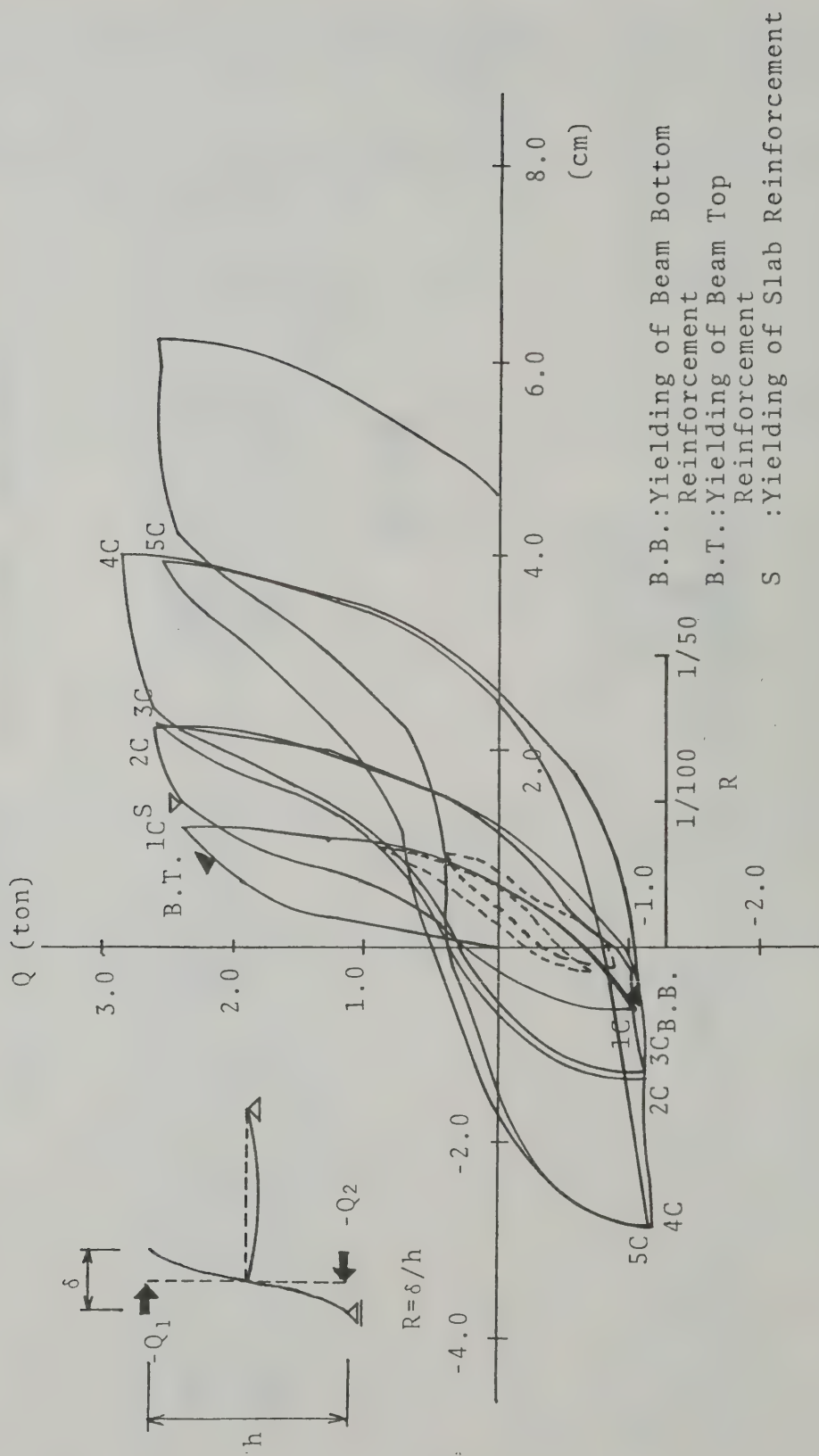


Fig. 6.4. : Story Shear - Displacement Relationship (Specimen E-1)

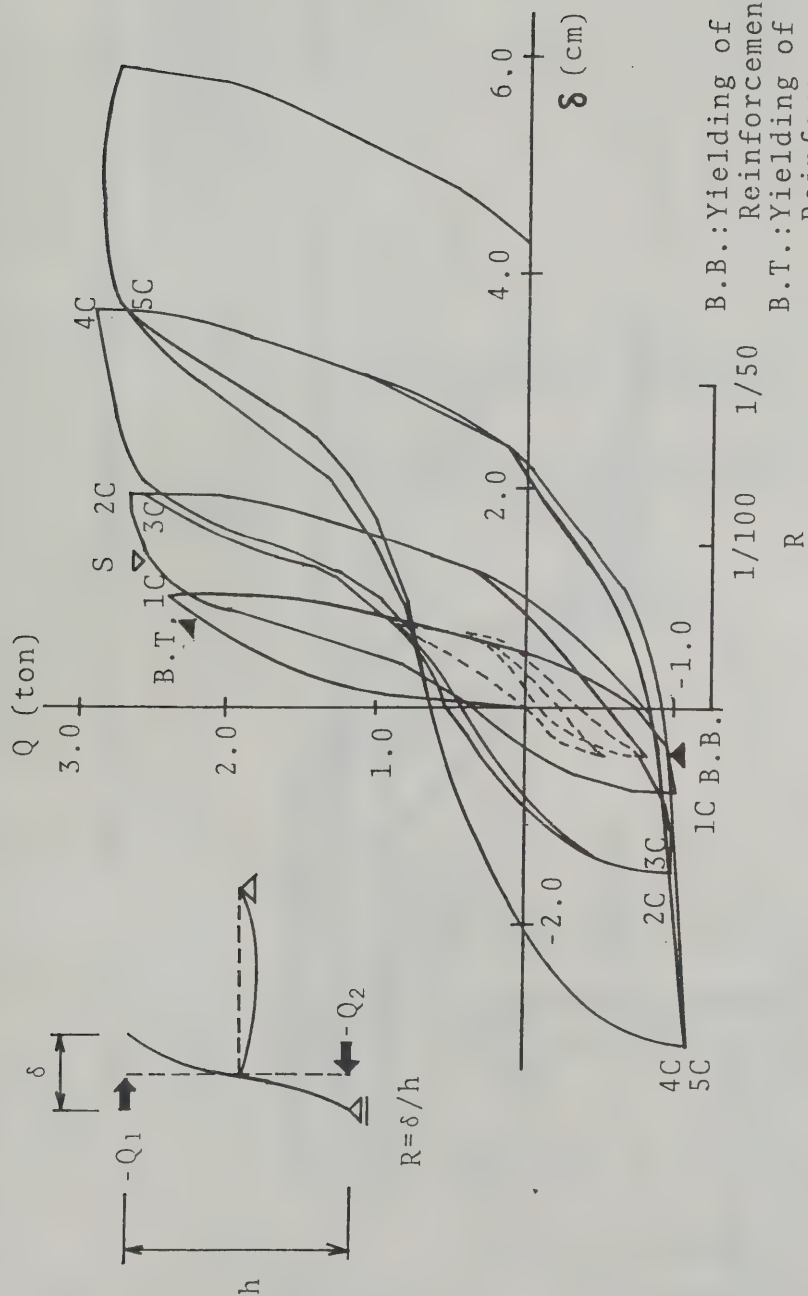


Fig. 6.5. : Story Shear - Displacement Relationship (Specimen E-2)

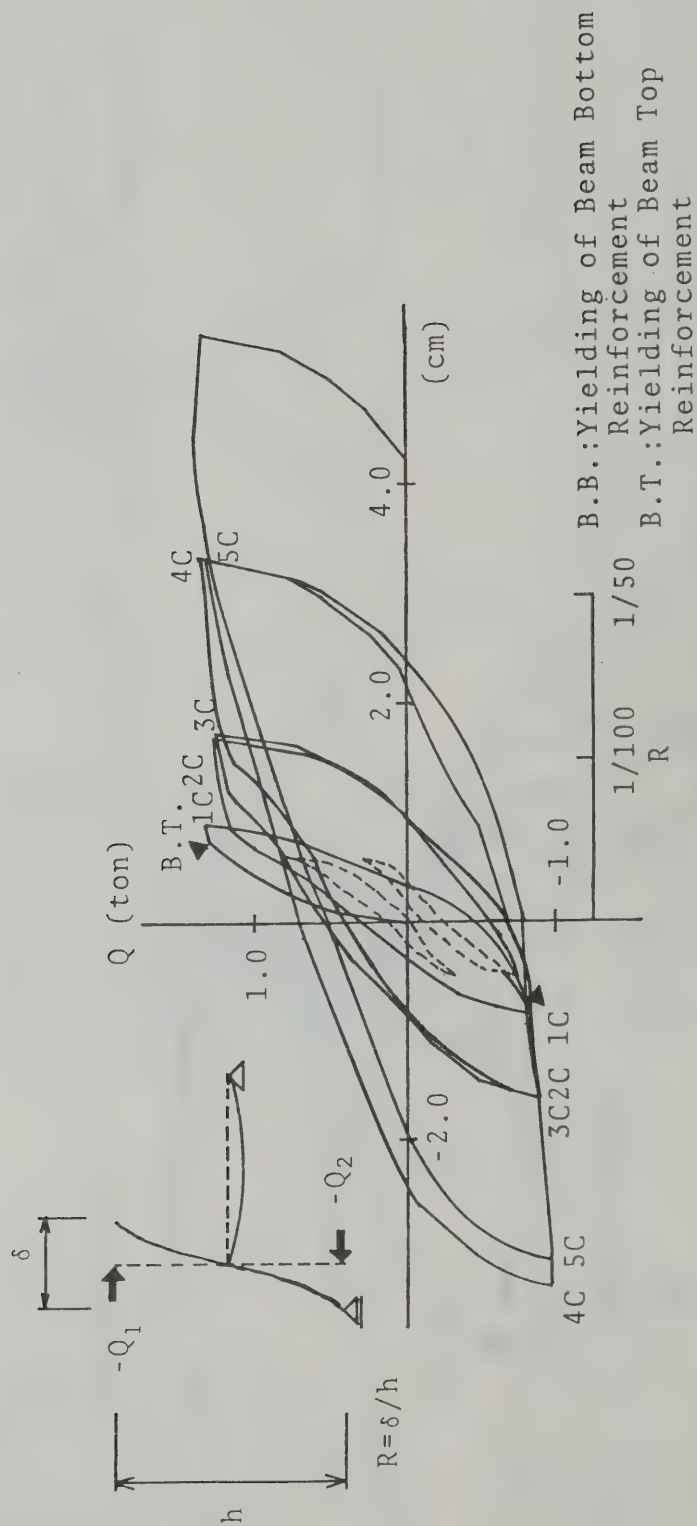


Fig. 6.6. : Story Shear - Displacement Relationship (Specimen E-3)



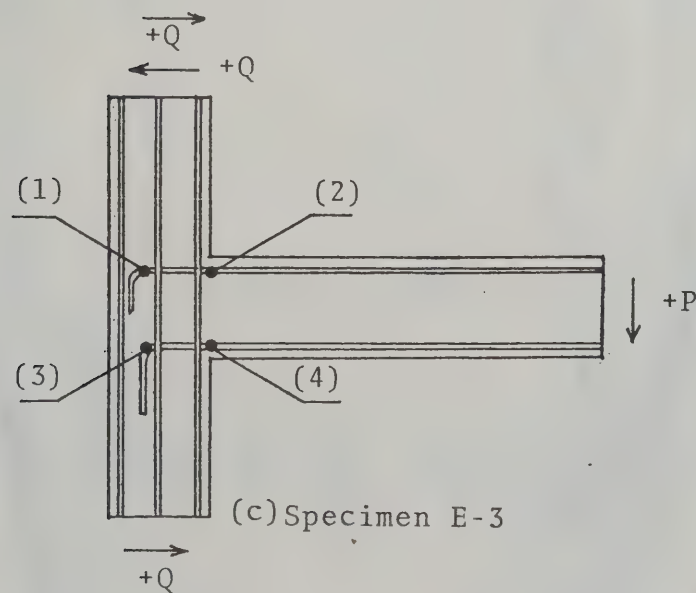
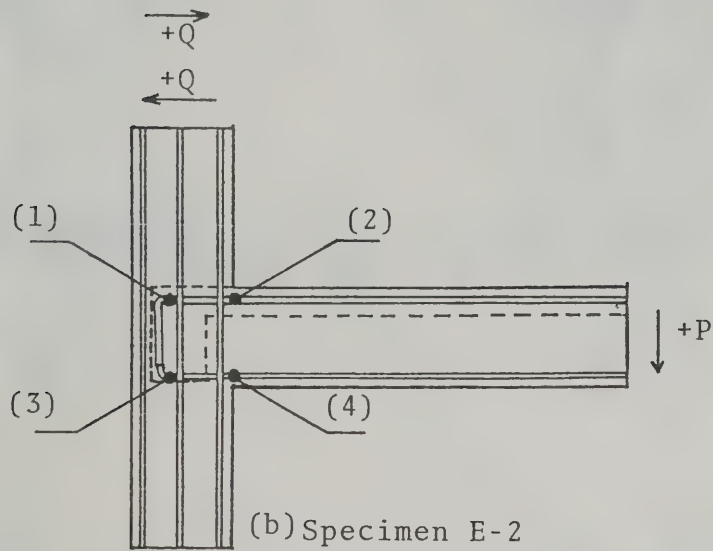
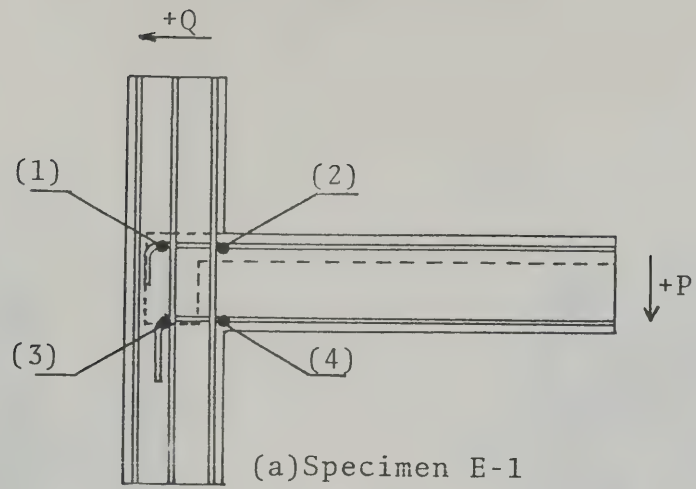


Fig. 6.7. : Gauge Numbers in Beam Longitudinal Bars  
(E-Series Specimens)

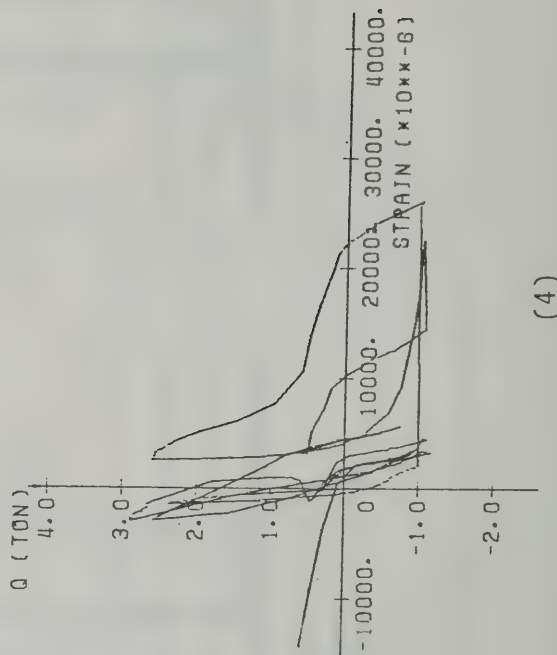
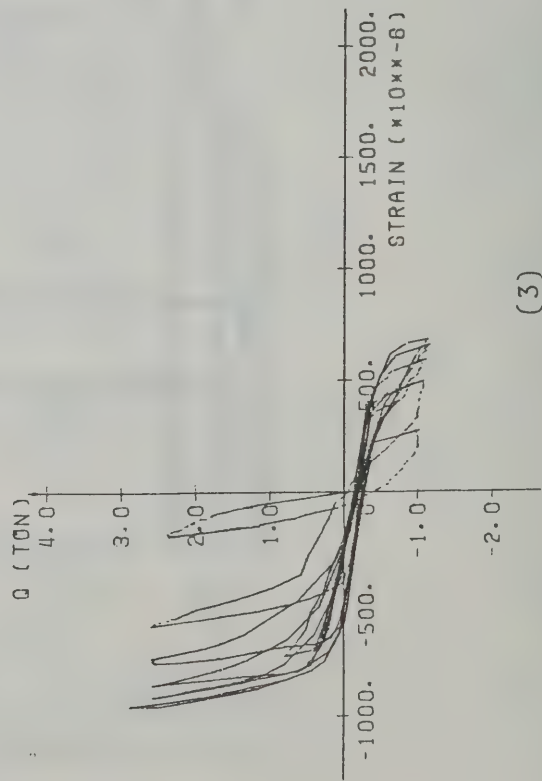
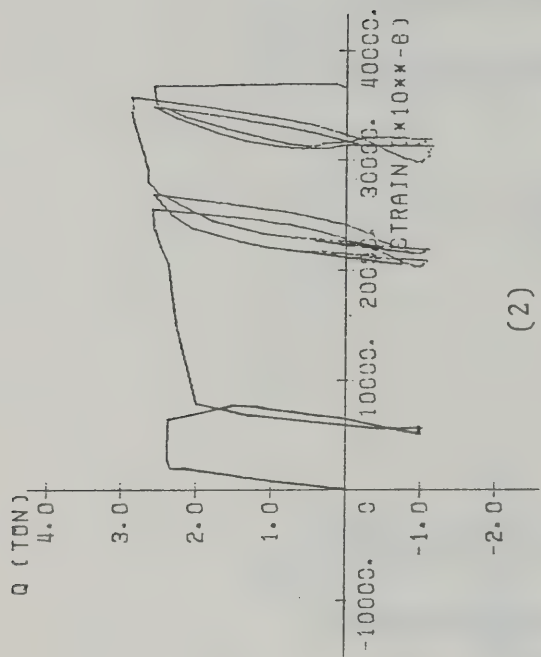
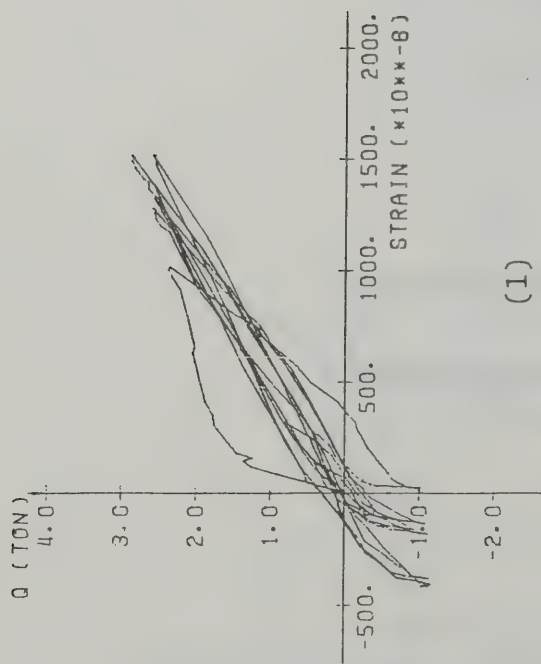


Fig. 6.8. : Story Shear - Beam Longitudinal Bar Strain Relationship (Specimen E-1)

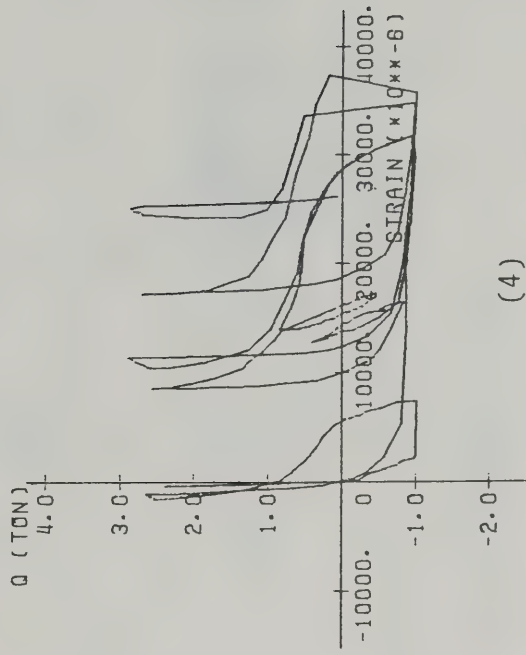
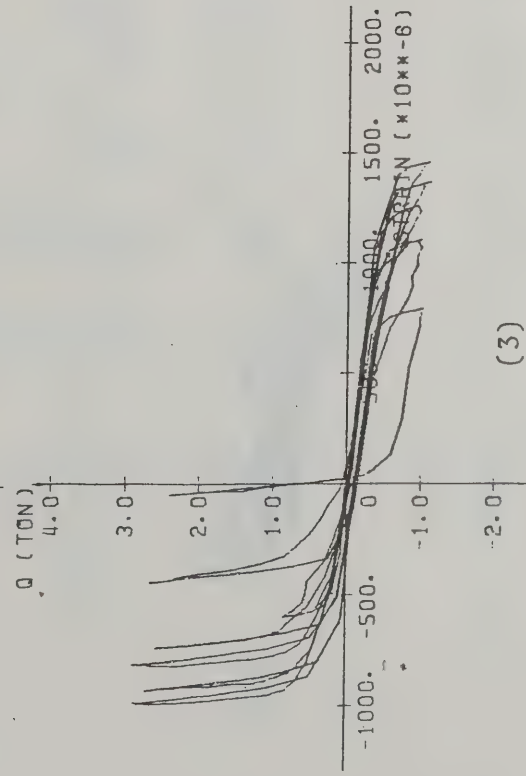
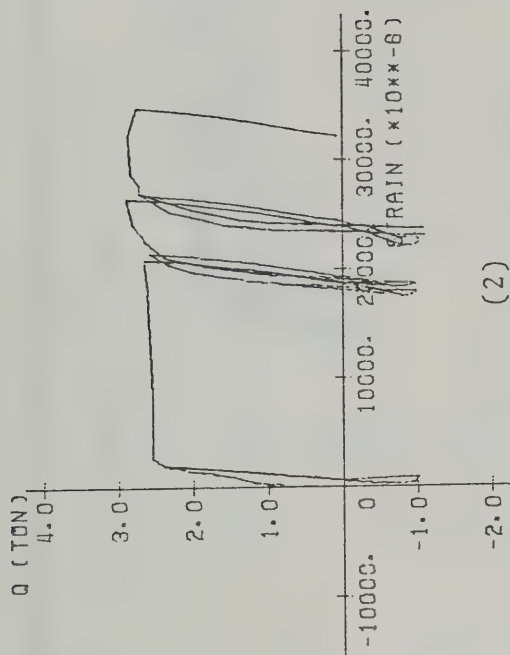
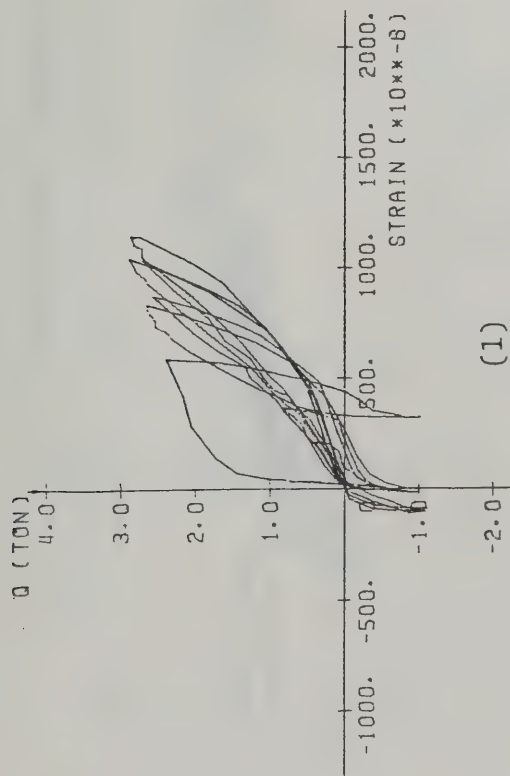


Fig. 6.9. : Story shear - Beam Longitudinal Bar Strain Relationship (Specimen E-2)

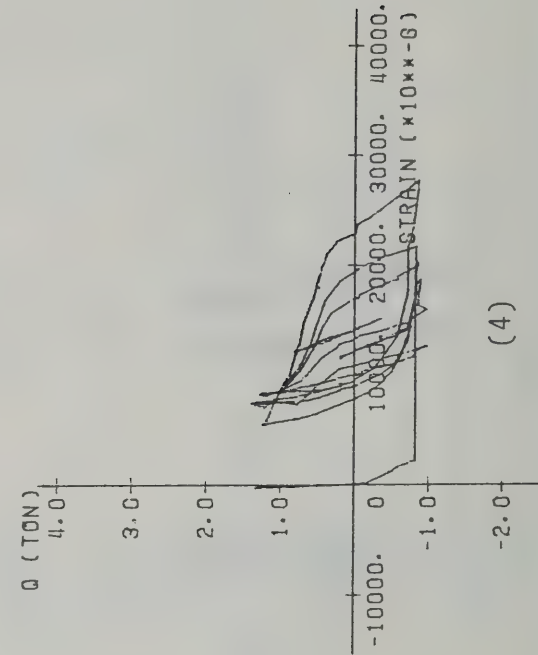
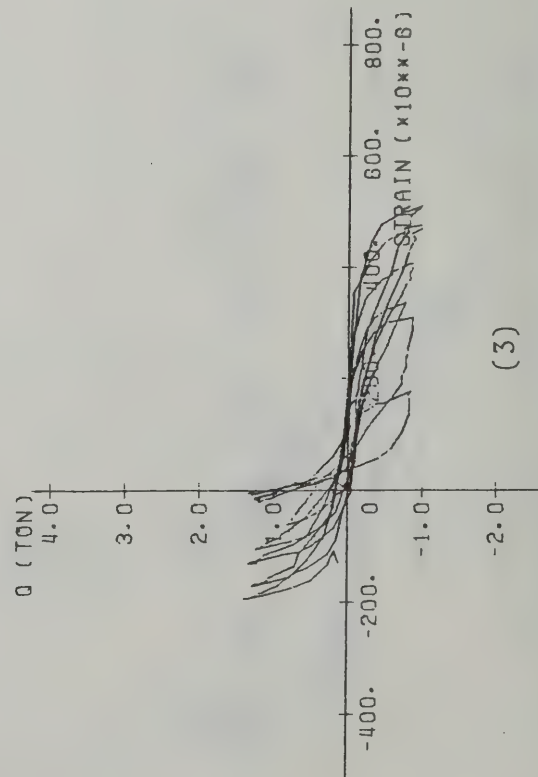
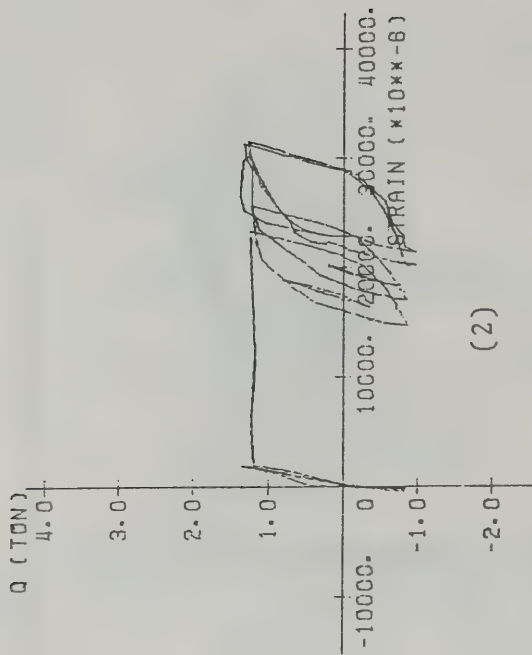
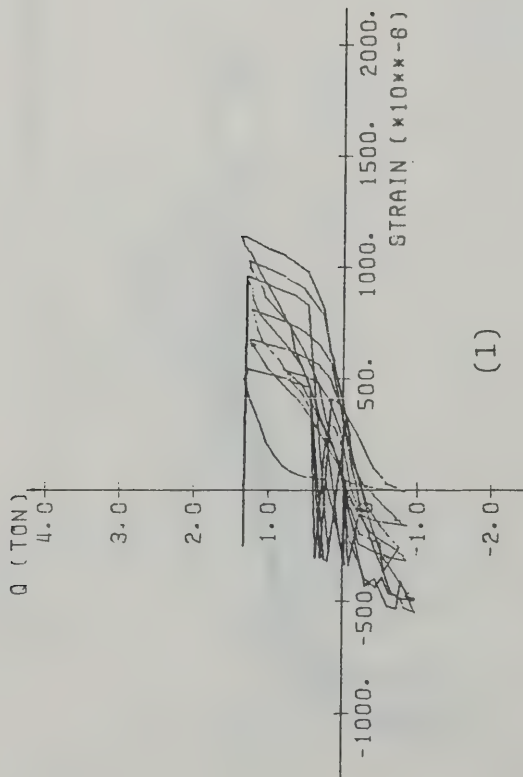


Fig. 6.10. : Story Shear - Beam Longitudinal Bar Strain Relationship (Specimen E-3)



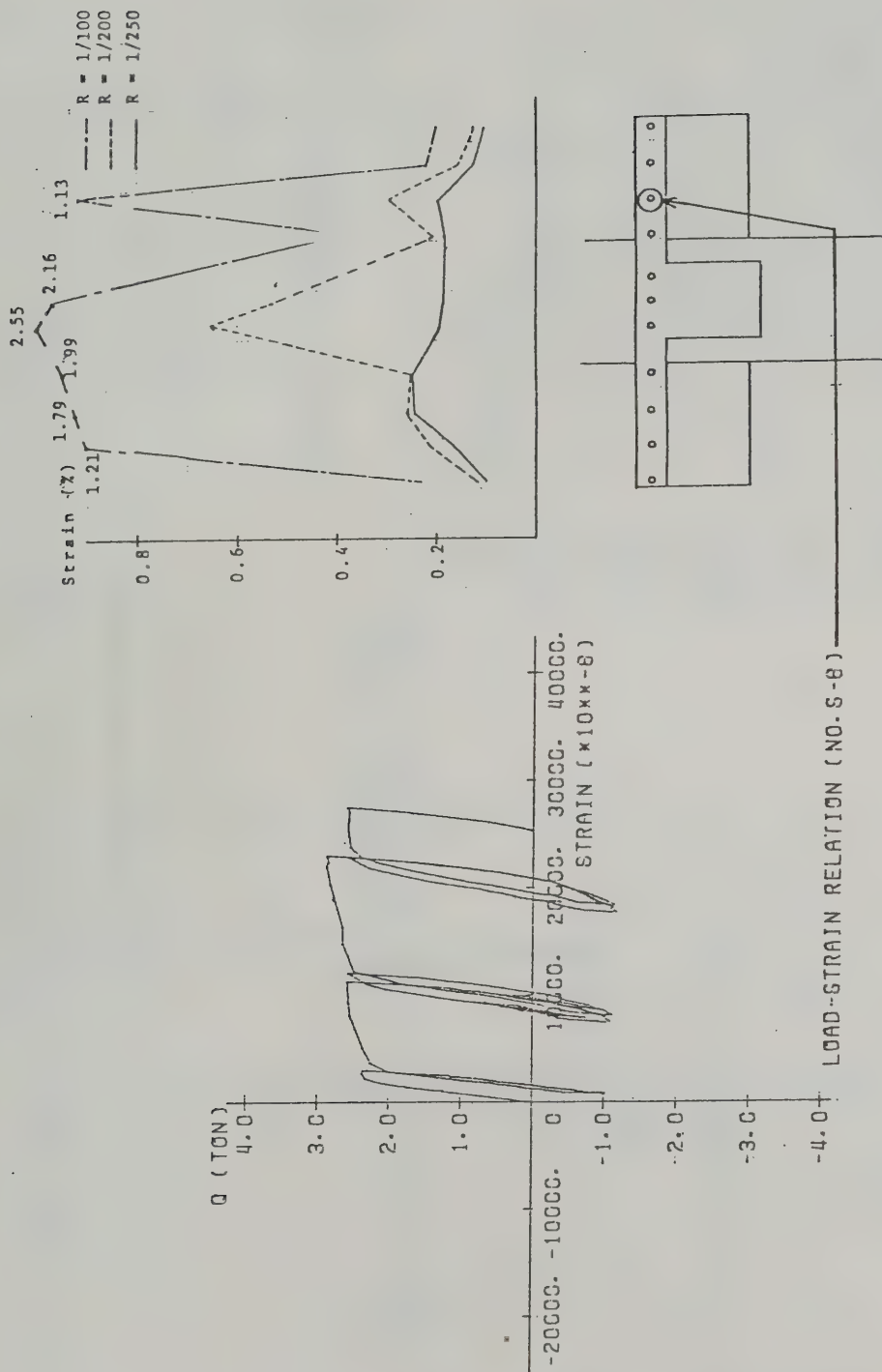


Fig. 6.11. : Strain Distribution in Slab Reinforcement  
(Specimen E-1)

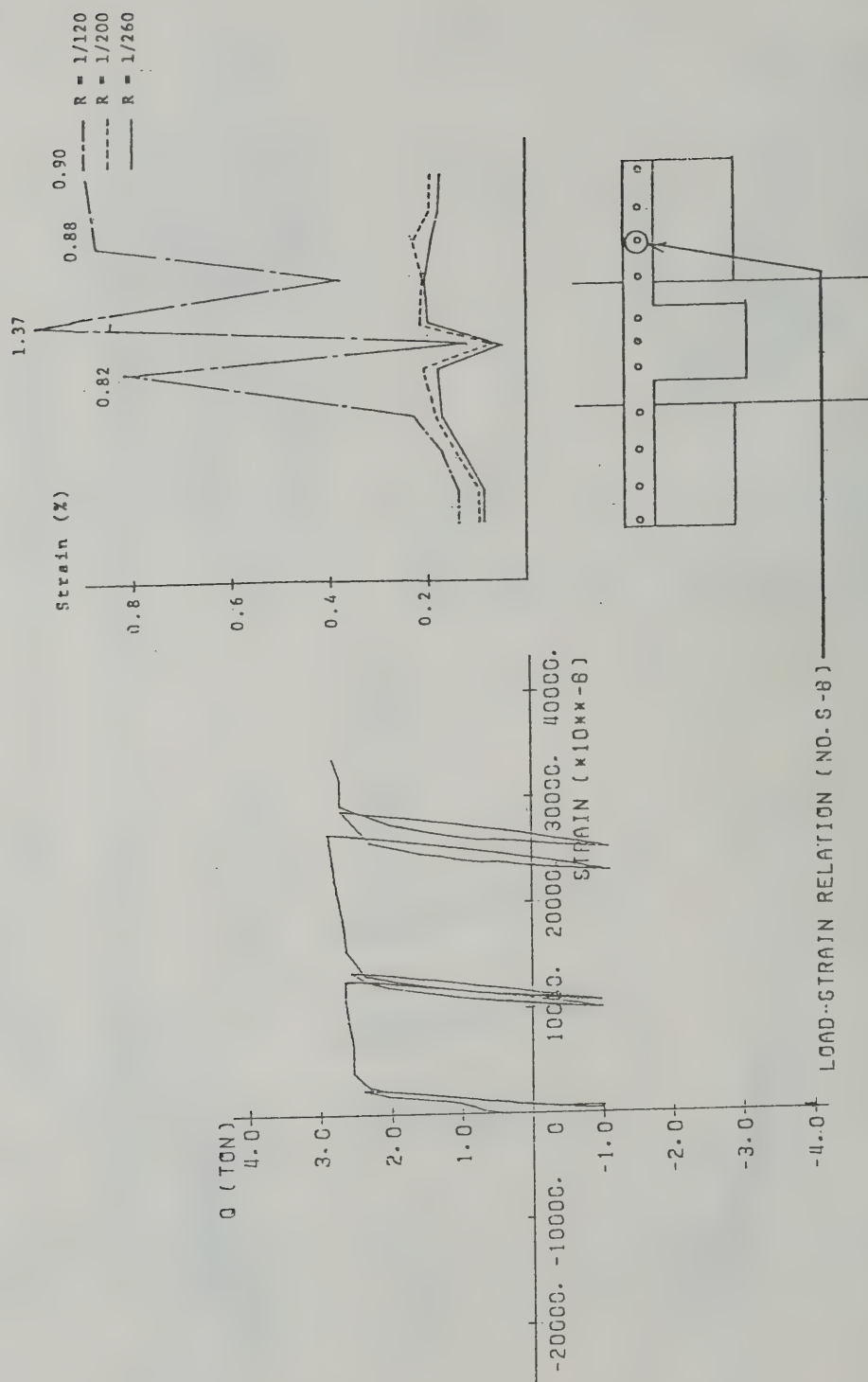
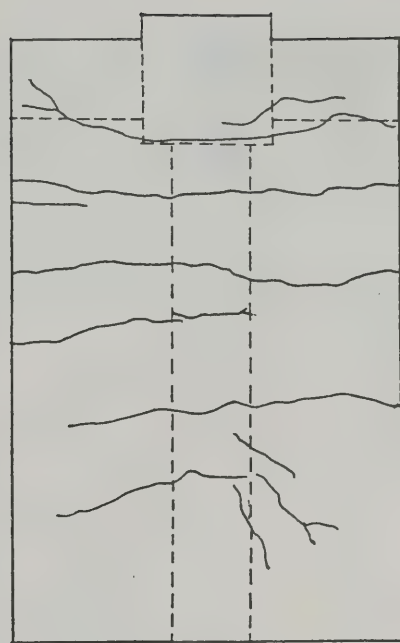
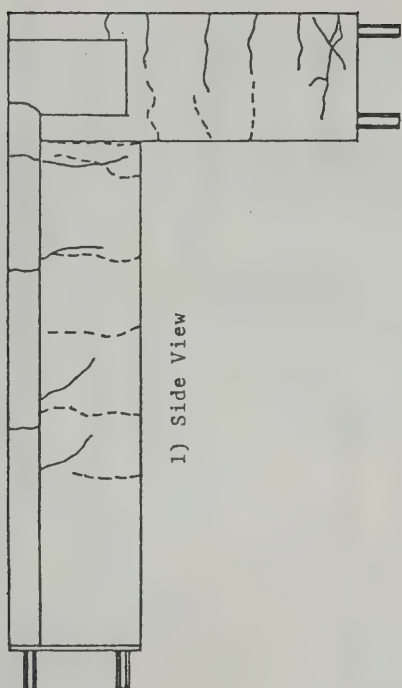
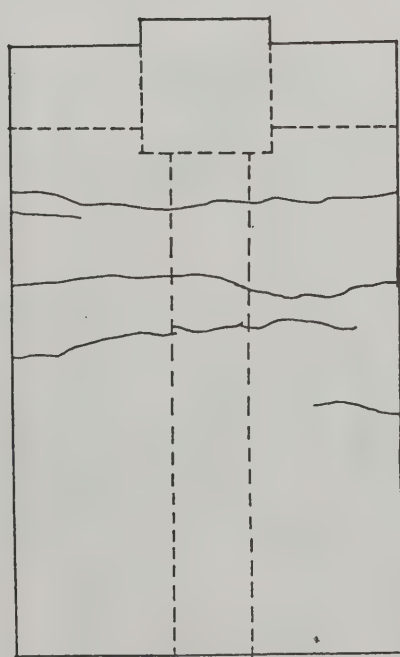
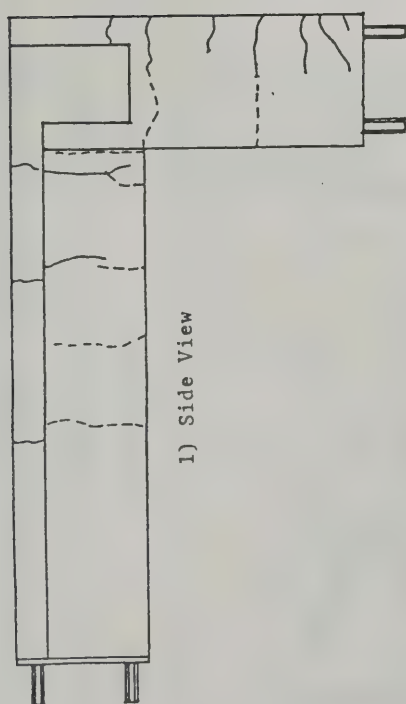


Fig. 6.12. : Strain Distribution in Slab Reinforcement  
(Specimen E-2)



2) Plan View

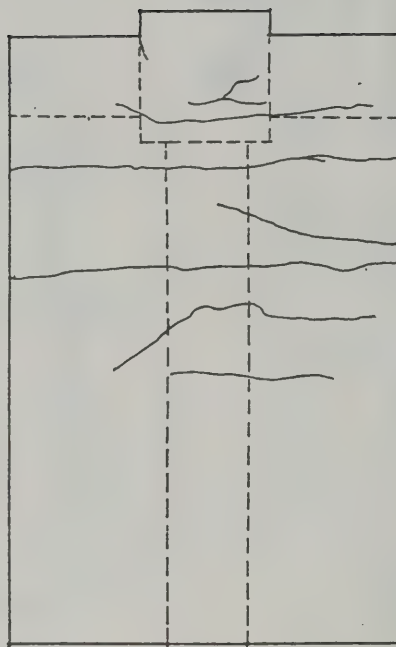
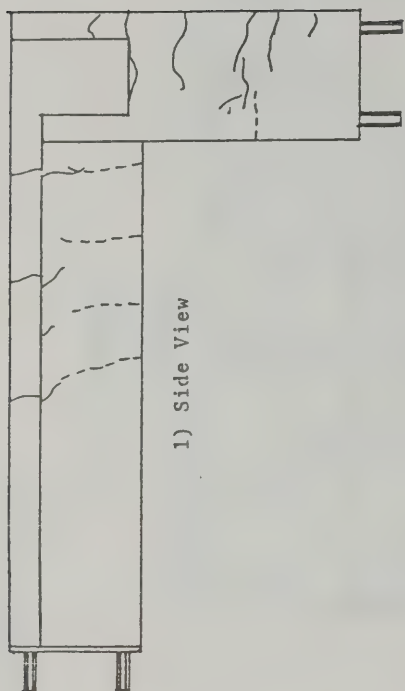
b)  $R=1/100$



2) Plan View

a)  $R=1/200$

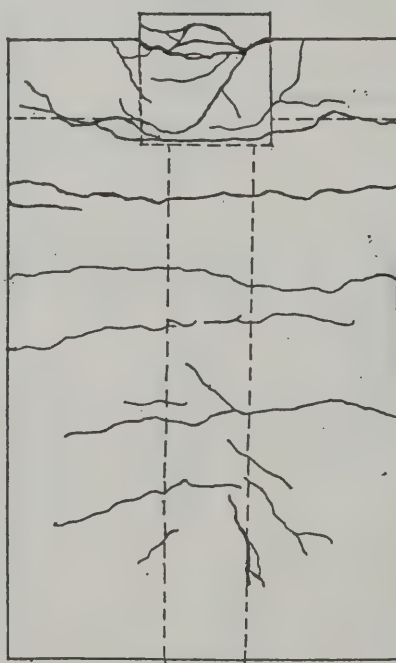
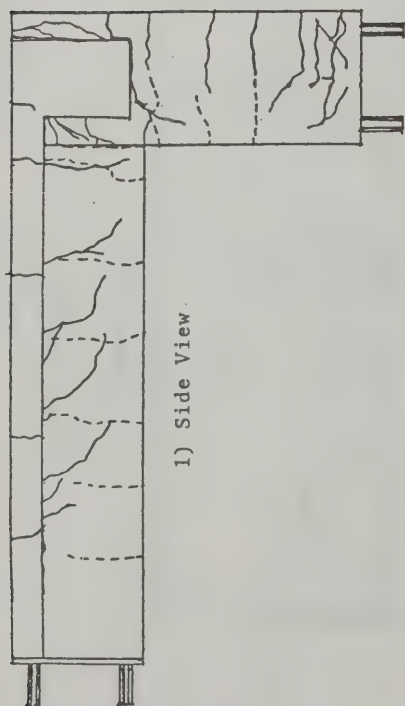
Fig.7.1.1. : Crack Pattern (Specimen T-1)



2) Plan View

a)  $R=1/200$

Fig.7.2. : Crack Pattern (Specimen T-2)

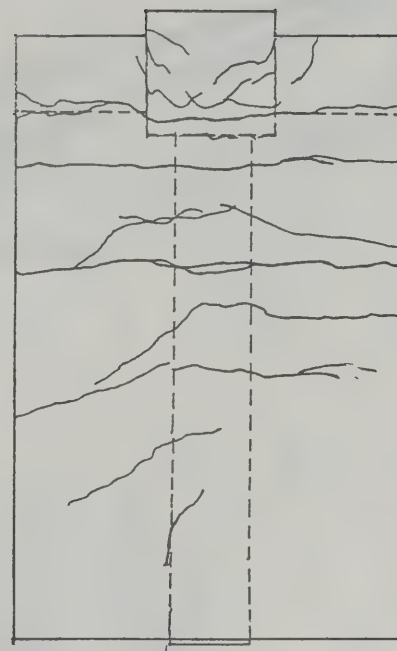
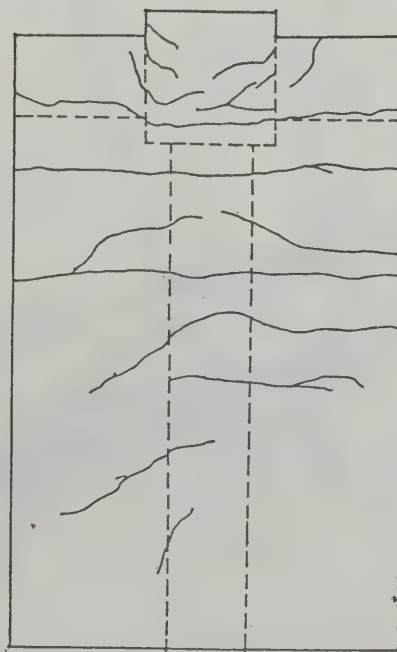
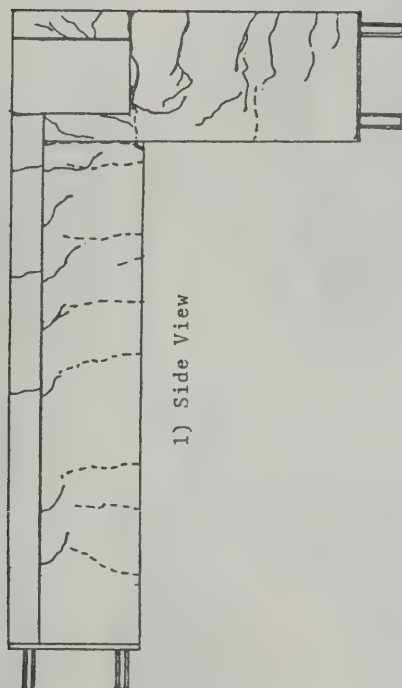
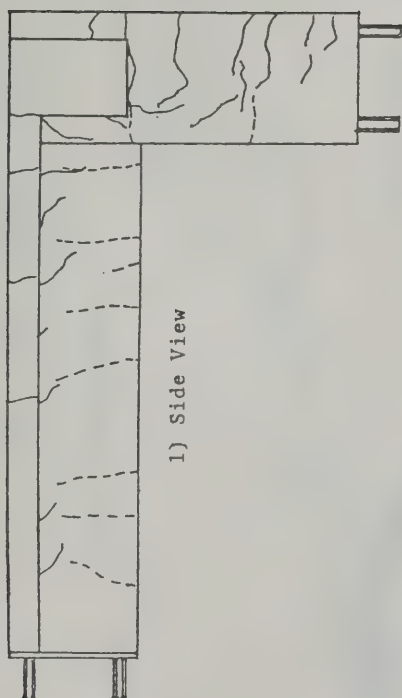


2) Plan View

c) After Test

Fig.7.1.(Continued): Crack Pattern (Specimen T-1)

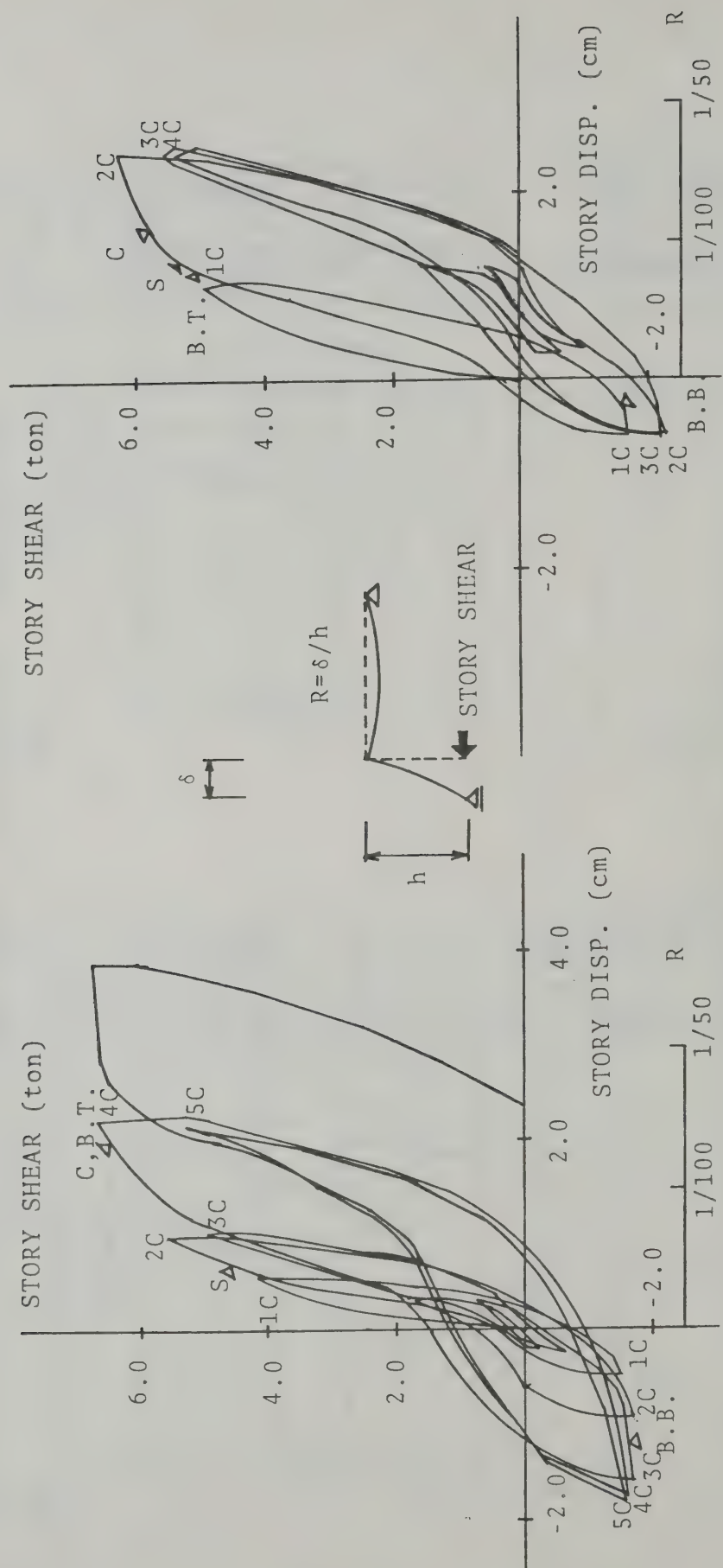




b) R=1/100

c) After Test

Fig.7.2. (Continued): Crack Pattern (Specimen T-2)



(a) Specimen T-1

(b) Specimen T-2

Fig. 7.3. : Story Shear - Displacement Relationship (T-Series Test)

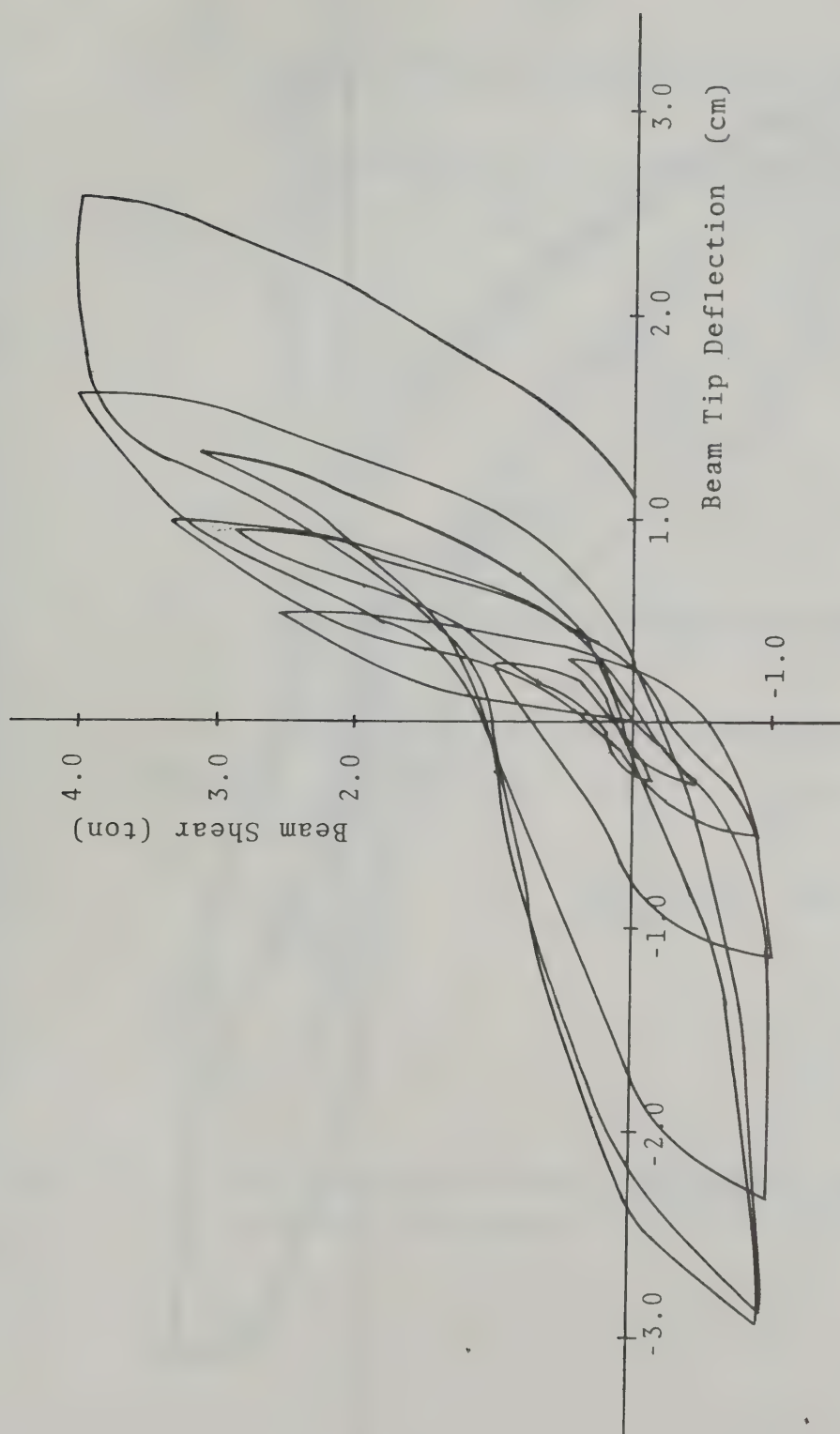


Fig. 7.4. : Load - Deflection Relation of Beam (Specimen T-1)

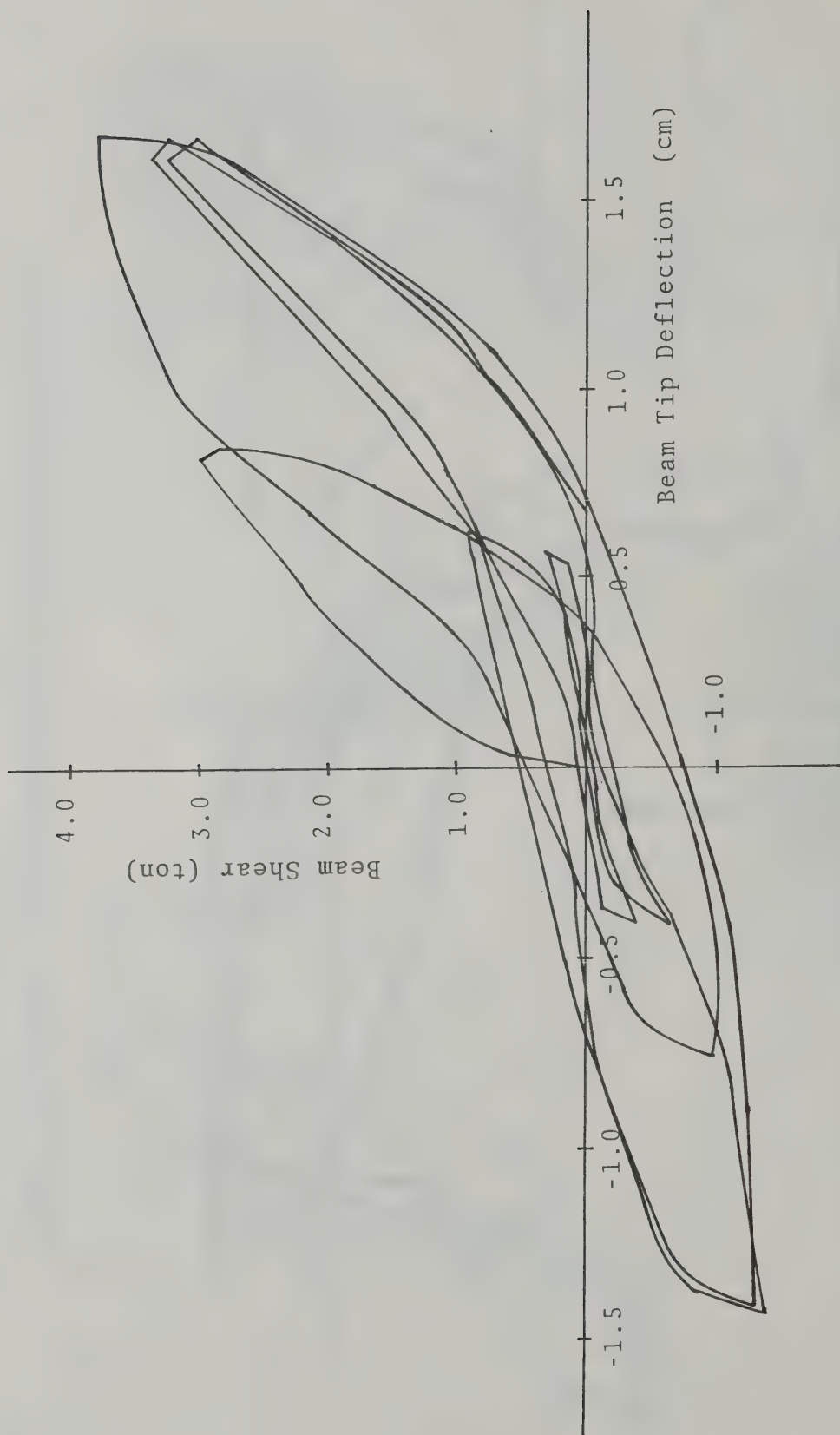


Fig. 7.5. : Load - Deflection Relation of Beam (Specimen T-2)

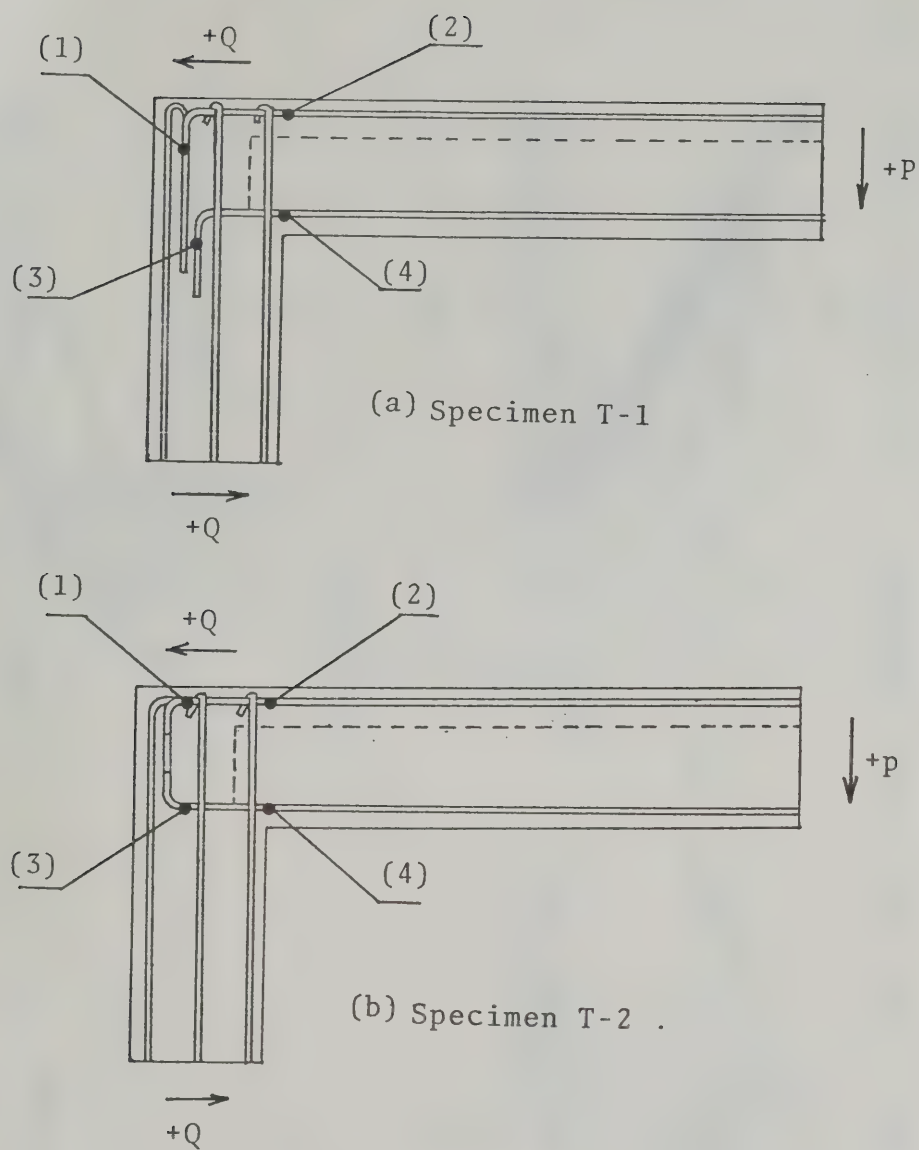
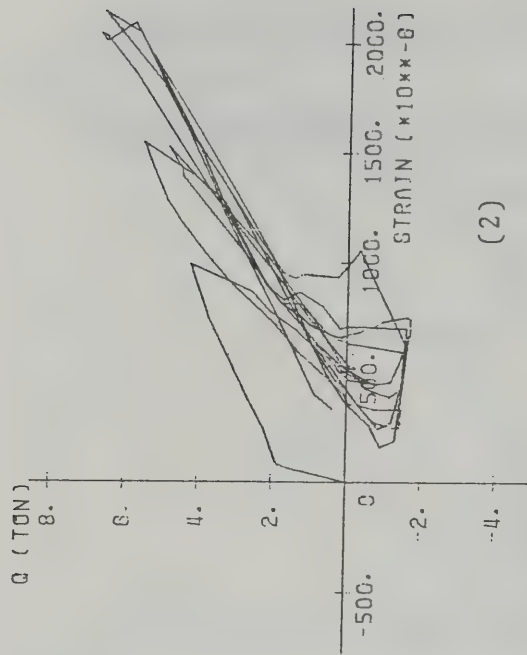
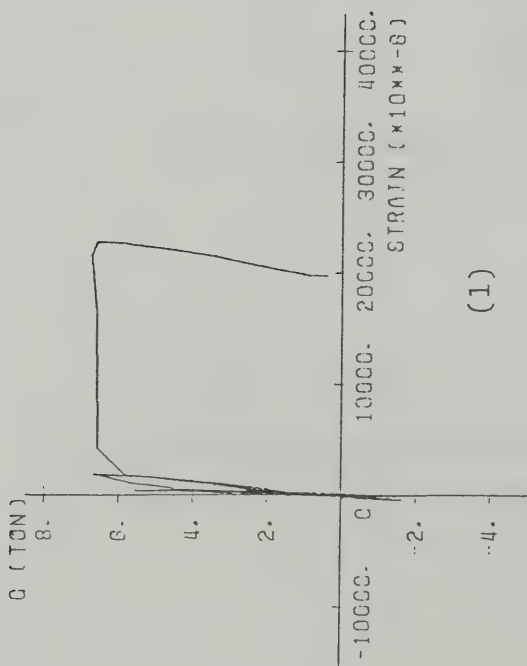


Fig. 7.6. : Gauge Numbers in Beam Longitudinal Bars  
(T-Series Specimens)





(3) not recorded

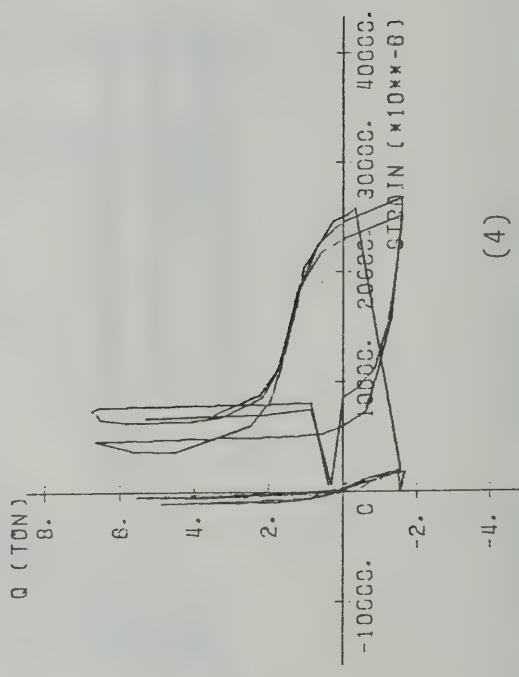
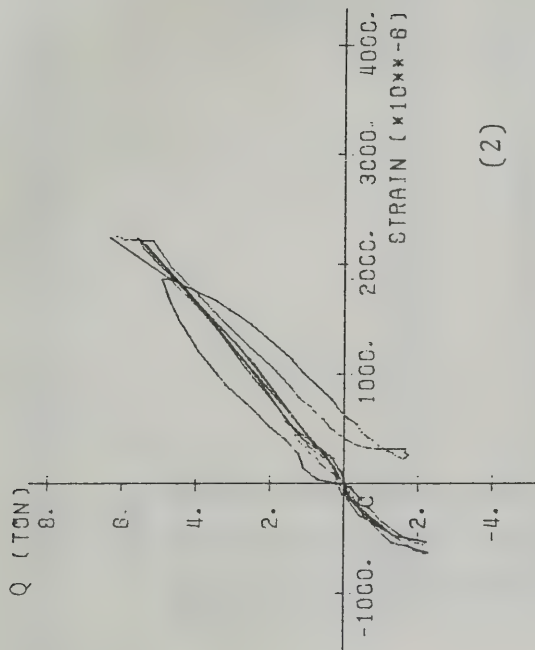
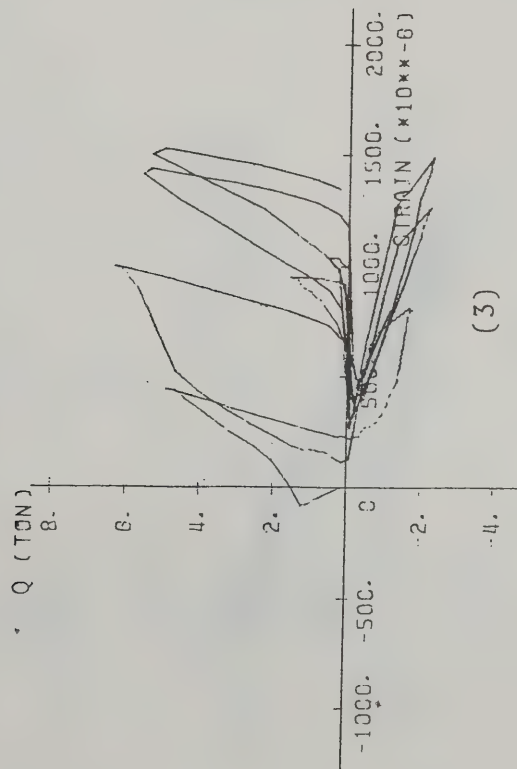


Fig. 7.7. : Story Shear - Beam Longitudinal Bar Strain Relationship (Specimen T-1)

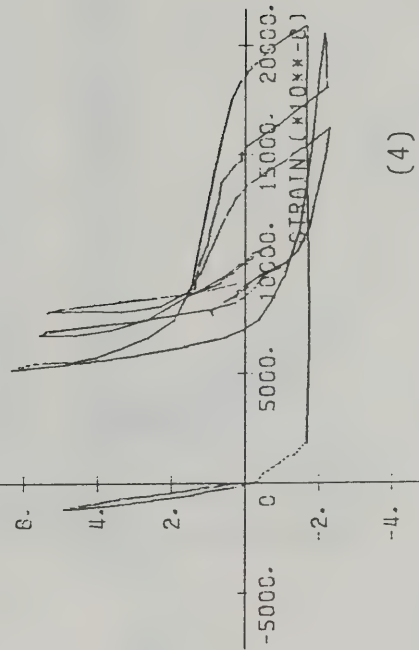
(1) not recorded



(2)

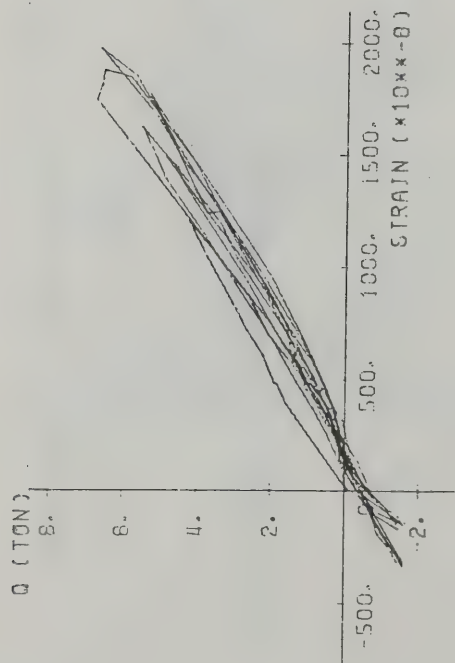


(3)

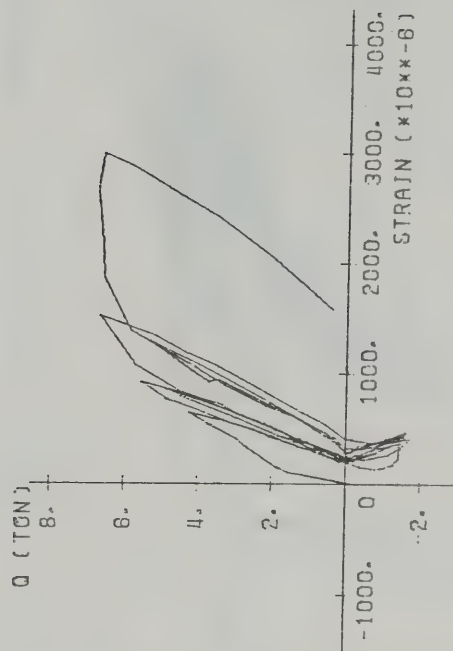


(4)

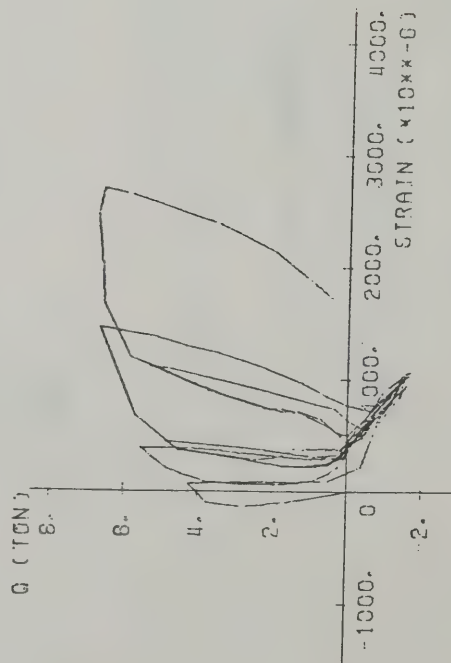
Fig. 7.8. ; Story Shear - Beam Longitudinal Bar Strain Relationship (Specimen T-2)



(a)



(b)



(c)

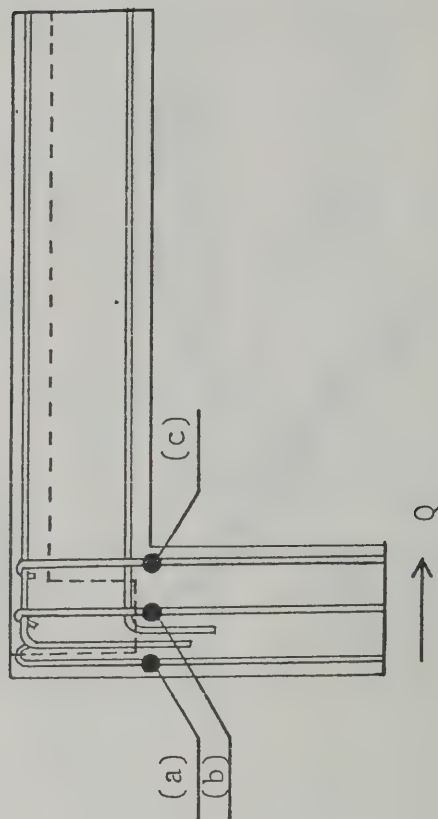
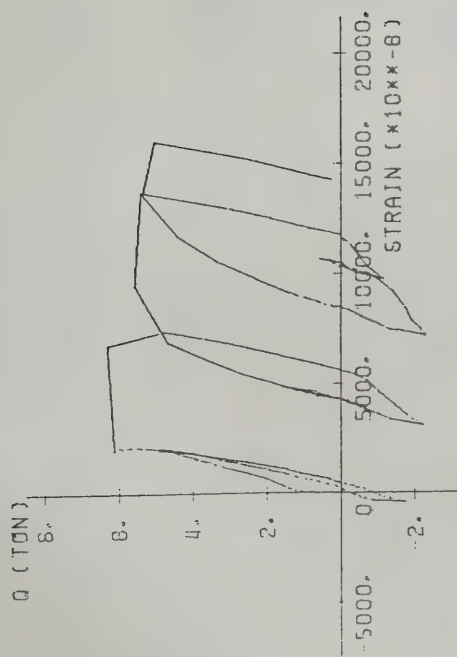
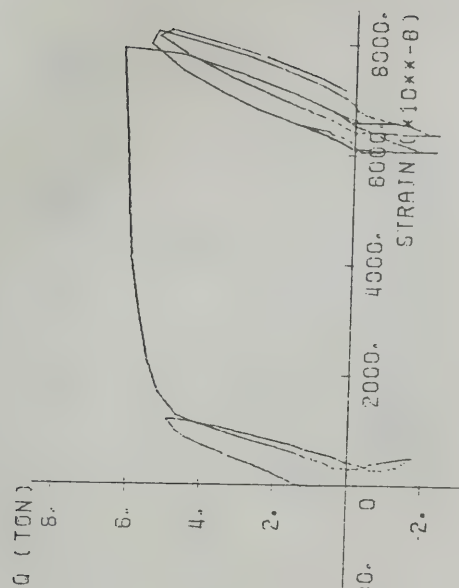


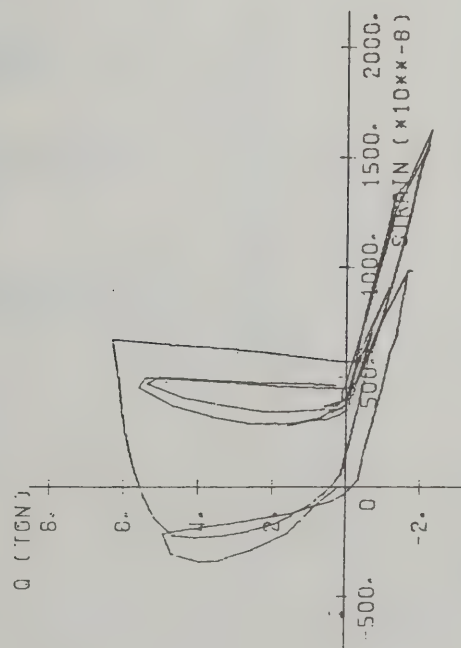
Fig. 7.9. : Story Shear - Column Reinforcement Strain Relation (Specimen T-1)



(a)



(b)



(c)

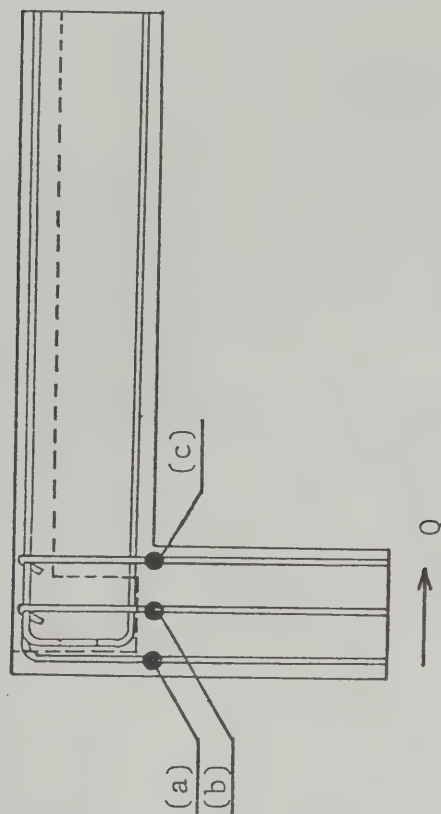


Fig. 7.10. : Story Shear - Column Reinforcement Strain Relation (Specimen T-2)

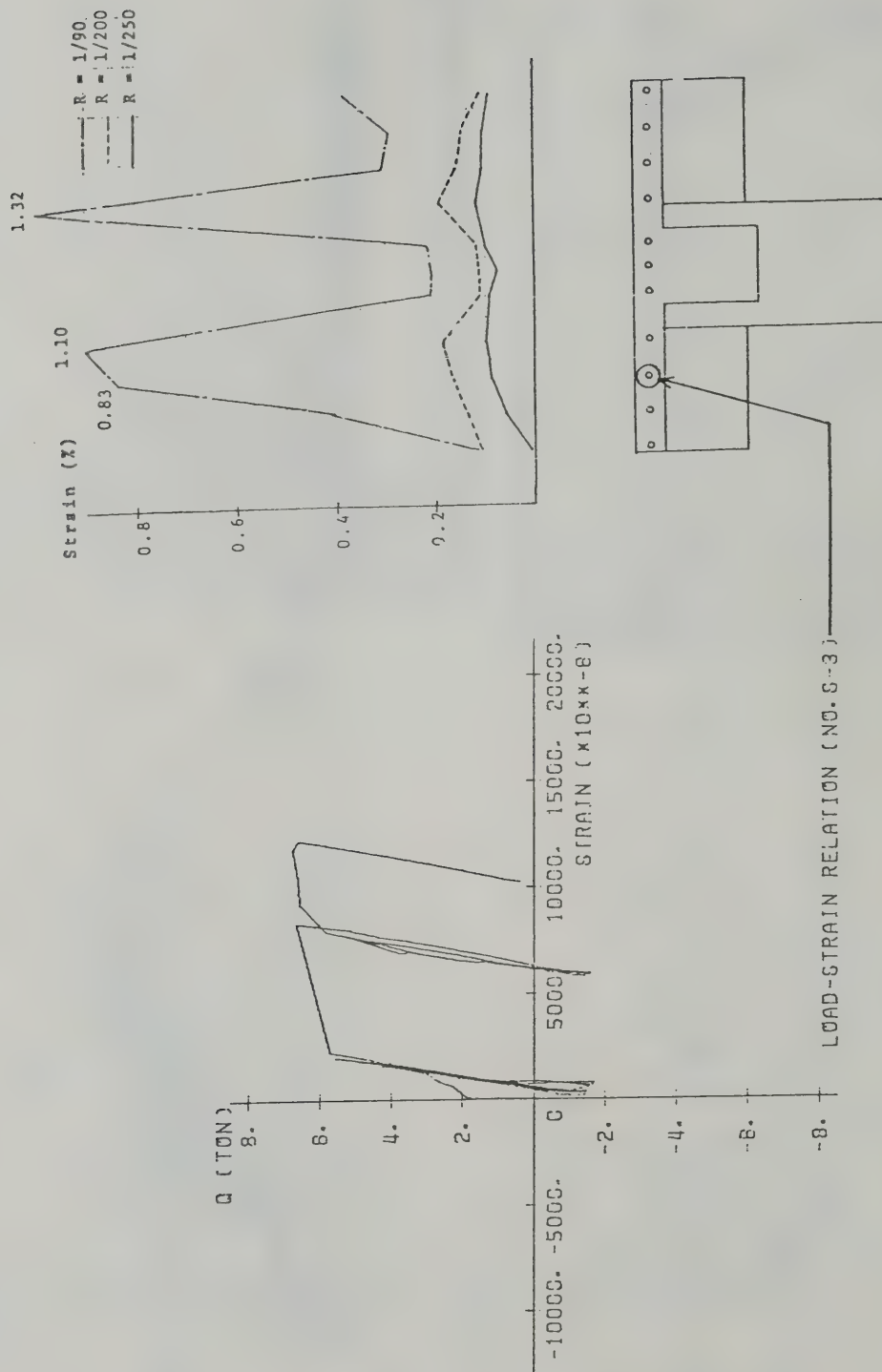


Fig. 7.11. : Strain Distribution of Slab Reinforcement (Specimen T-1)



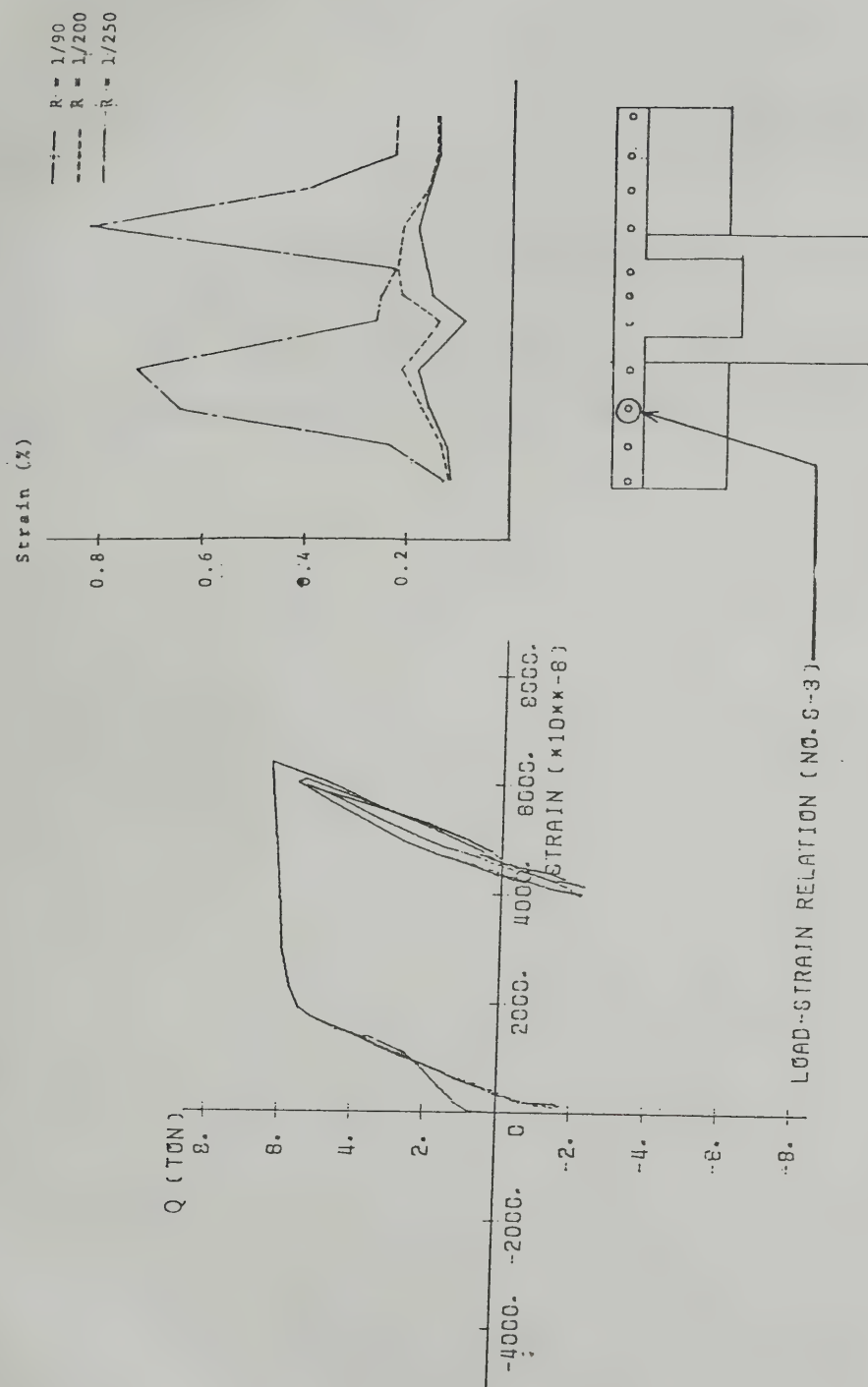


Fig. 7.12. : Strain Distribution of Slab Reinforcement (Specimen T-2)



# R C実大7層建物の地震応力下の復元力特性

## — はり・柱接合部分 —

中 田 慎 介\*

BRI Research Paper No.99

March 1983 建築省建築研究所

本研究は日米共同による耐震実験研究の一環として、建物を構成するはり・柱接合部部分の静加力実験を行ない、実際の構成部材の復元力特性を知ることが目的としている。

実験は、スラブの有無・下層の内柱Bび外柱・最上層の外柱といった異なる条件の試験体8体を使用して行なわれ、その結果としてはりの復元力特性及び強度に対するスラブの影響及びこれらの部材が十分なじん性を有していることなどが明らかとなった。







## Research Papers-Recent Issues

- No.76 Y. Matsushima: Random Response of Single-degree-of-freedom System with Bilinear Hysteresis, September, 1977, 28 pp.
- No.77 A. Baba: Drying Shrinkage Mechanism of Building Materials, March, 1978, 79 pp.
- No.78 K. Hayakawa: The Management of Land as an Environmental Resource, March, 1978, 40 pp.
- No.79 T. Tanaka: A Model on Fire Spread in Small Scale Buildings, September, 1978, 76 pp.
- No.80 Y. Aoki: Studies on Probabilistic Spread of Fire, November 1978, 52 pp.
- No.81 F. Saito: Experimental Study of Compartment Fire Using Model Boxes, July, 1979, 50 pp.
- No.82 Y. Matsushima: Random Response of Single-degree-of-freedom System with General Slip Hysteresis, July, 1979, 37 pp.
- No.83 Y. Hasemi: Flashover Criteria of Compartment Fire - Theory on Zero Order Reaction System -, August, 1979, 26 pp.
- No.84 T. Tanaka: A Model on Fire Spread in Small Scale Buildings, 2nd Report, March, 1980, 63 pp.
- No.85 Y. Ishiyama: Review and Discussion on Overturning of Bodies by Earthquake Motions, June, 1980, 115 pp.
- No.86 S. Watanabe: Planning History in Japan - A State of the Art Survey -. August, 1980, 36 pp.
- No.87 Y. Sugimura: Participation Factor of Horizontal Force Applied to Pile Foundation, March, 1981, 33 pp.
- No.88 Y. Hasemi: Mathematical Basis for Physical Evaluation on Flashover, March, 1981, 41 pp.
- No.89 T. Wakamatsu: A Quantitative Evaluation on Smoke Safety, March, 21 pp.
- No.90 S. Watanabe: Metropolitanism as a Way of Life, March, 1981, 52 pp.
- No.91 M. Hrosawa, T. Goto, M. Yoshimura, H. Hiraishi: Full-Scale Experimental Study on Aseismic Performance of Medium-Rize RC Wall Structure. March, 1981, 28 pp.
- No.92 Y. Yamazaki: Inelastic Torsional Response of Structures Subjected to Earthquake Ground Motions. March, 1981, 102 pp.
- No.93 S. Kose: Study of Accidents Associated with Building Features. March, 1982, 38 pp.
- No.94 S. Okamoto, S. Nakata, Y. Kitagawa, M. Yoshimura, T. Kaminosono: A Progress Report on the Full-Scale Seismic Experiment of a Seven Story Reinforced Concrete Building - Part of the US-Japan Cooperative Program, March, 1982, 92 pp.
- No.95 Y. Hasemi: Characterization of the Intermittent Flaming Region of the Upward Current Above Diffusion Flames, March, 1982, 33 pp.
- No.96 Y. Morishita: Statistical Analysis of Fire Spread. May, 1982, 17 pp.
- No.97 T. Fuhushima: Deterioration Model of Polymeric Materials with Special Attention to Age and Deterioration Depth. December, 1982, 30 pp.
- No.98 H. Hiraishi, M. Yoshimura, H. Isoishi, S. Nakata: Planer Tests on Reinforced Concrete Shear Wall Assemblies. -U.S.-Japan Cooperative Research Program-. January, 1983, 63 pp.
- No.99 S. Nakata: Tests of Reinforced Concrete Beam-Column Assemblages -U.S.-Japan Cooperative Research Program-. March, 1983, 111 pp.

Address for Communication

**BUILDING RESEARCH INSTITUTE  
MINISTRY OF CONSTRUCTION**

No.1 TACHIHARA, OH-HO-MACHI, TSUKUBA-GUN, IBARAKI-PREF  
JAPAN

# ASSESSMENT OF AN URBAN SAFETY EVALUATION FUNCTION

by  
Yoshitsugu Aoki

Building Research Institute  
Ministry of Construction

May 1983

THE LIBRARY

UNIVERSITY OF CALIFORNIA  
AT LOS ANGELES



## FOREWORD

BRI Research Papers are published in English by the Building Research Institute and distributed to major research organizations and libraries throughout the world. I consider that the introduction of BRI research results to building researchers and engineers throughout the world is one of our roles for international research cooperation. Therefore, it gives me great pleasure to announce that the Research Paper No.100 has just been published.

BRI is the only national organization of the Japanese Government concentrated upon housing, planning and the building science along the following five goals:

1. The prevention of disasters,
2. The improvement of the living environment,
3. The rational organization of building production and the development of new building techniques,
4. The effective use of energy and resources,
5. The promotion of international research cooperation.

Since 1960 when the BRI Research Paper No.1 was published, the main research results achieved by the Building Research Institute have been introduced through these publications.

Our research approach is extending from "how to build good buildings" to "what are good buildings". In this point of view, this Research Paper No.100; "ASSESSMENT OF AN URBAN SAFETY EVALUATION FUNCTION" by Dr. Yoshitsugu Aoki is a new type of research which belongs to the latter approach. This study surveys what safety level in an urban inhabitants could expect using a skillful mathematical technique called urban safety evaluation function.

When we think of buildings or urban environment from the stand point of safety, we must consider a kind of balance, which is safe and not too safe. The excessive safe design of building takes too much cost and sometimes loses the architectural function. These excesses could alternatively be put towards improving the other items for total our living environment. Thus, I consider, the safety evaluation function

proposed by Dr. Aoki in this short paper would be a very important criterion for evaluating a well-balanced approach for buildings.

Katsurou Kamimura  
Director General  
Building Research Institute

April 14 1983



# ASSESSMENT OF AN URBAN SAFETY EVALUATION FUNCTION

Yoshitsugu Aoki

## Synopsis

The aim of this paper is to make clear the concept of safety evaluation of urban area and to identify an urban safety evaluation function.

Firstly, the concepts on the urban safety level are analyzed. The definitions on a loss vector, a frequency function, a safety evaluation function, and a safety level are given.

Secondly, the formula on the relationship between the safety evaluation function and the preference of individuals are obtained

Furthermore, the safety evaluation function are estimated through the survey of preference. By the criterion AIC, the most reasonable safety evaluation function is a first-order threshold type function.

---

Dr. of Engineering. Deputy Head, Planning and Information Department,  
Building Research Institute.

## Contents

### 1. INTRODUCTION

### 2. PROBLEM FORMULATION

- 2.1. Definition of Urban Safety Level and Safety Evaluation Function
- 2.2. Relation between Safety Evaluation Function and Preference of an Individual

### 3. CASE STUDY

- 3.1. Survey of Safety Preference
- 3.2. Estimation of Polynomial Type Evaluation Function
- 3.3. Optimal Order of the Polynomial Type Evaluation Function
- 3.4. Threshold Type Evaluation Function

### 4. CONCLUSION

## List of Tables and Figures

- Table 1. Data presented in Safety Preference Survey.
- Table 2. Ordering Relation Matrix for Safety Preference Survey.
- Table 3. Estimated Polynomial Type Safety Evaluation Function.
- Table 4. Values of Akaike's Information Criterion for Polynomial Type Models.
- Table 5. Estimated Threshold Type Safety Evaluation Function.
- Table 6. Values of Akaike's Information Criterion for Threshold Type Models.
- Figure 1. Polynomial Type Safety Evaluation Function.
- Figure 2. Threshold Type Safety Evaluation Function.



## 1. INTRODUCTION

Safety is one of the most important factors in a modern high-density urban environment, and one which might be improved by urban planning or government policy. However, the concept of urban safety is not easily understood or measured with sufficient confidence.<sup>(1)</sup> It is difficult to express numerically the total urban safety level.

If we could express urban safety as a function of physical characteristics, and improve those characteristics in the actual planning process, we can formulate the urban safety planning problem as an optimization problem. We should expect to obtain useful information from the result of this optimization procedure.

Generally, the urban safety level is expressed as a function of life loss, property loss, and service loss in an urban area. Research on estimation of typical losses is frequently performed. With the results of loss assessment studies, we could obtain an actual urban safety function, for use in the decision and planning process of urban development and renewal. However, this would be possible only if we could define and estimate a function which evaluate the above losses numerically and synthetically.

## 2. PROBLEM FORMULATION

### 2.1. Definition of Urban Safety Level and Safety Evaluation Function

In the usual case, safety level is expressed either as a loss or as a potential risk of loss. That is, there are two types of safety concepts in our perception, as follows;

$$A) \text{ safety level} = -(\text{loss})$$

or

$$B) \text{ safety level} = -(\text{possibility}) \times (\text{loss}).$$



The distinction between these two types of concepts is important in safety analyses, but is not clearly distinguished in our perception. Furthermore, the above loss is a kind of vector which includes components for life, property and service loss. Then, in our perception, there is a mapping from a loss vector to a scalar value.

In order to formulate the above concepts, some definitions are needed.

(Def.1) Loss vector:  $x = (x_1, x_2, \dots, x_n) \in L$ ,

(Def.2) Frequency function:  $f(x), f:L \rightarrow [0,1]$ ,

(Def.3) Safety evaluation function:  $g(x), g:L \rightarrow R$

(Def.4) Safety level:  $s = \int_L f(x) \cdot g(x) dx$ .

Note that the frequency function is defined for each urban area and each hazard type. Therefore the safety level is determined for each urban area.

The safety level for each urban area could be calculated using the given frequency function of that area if we have available the safety evaluation function. Thus, our main objective is to obtain the safety evaluation function.

The safety evaluation function might satisfy the following condition because our results ought to be effective at decisions in an actual planning;

(C.1) The safety level of an urban area  $k$  is greater than that of area  $k'$  if and only if area  $k$  is preferable more than area  $k'$  from a viewpoint of safety.

However, it is possible that preference for an urban area from a viewpoint of safety is different for each individual. That is, the safety evaluation function varies with each individual. Then, we must define a (social) safety evaluation function  $g$  (unsubscripted), where each individual  $i$  has a safety evaluation function  $g_i$ .

(Def.5) (Social) Safety evaluation function  $g(x) = E_i(g_i(x))$ .

(C.1') The safety level of an urban area  $k$  calculated with safety evaluation function of individual  $i$ :  $g_i$ , is greater than one of area  $k'$  if and only if area  $k$  is more preferable than area  $k'$  from a viewpoint of safety for individual  $i$ .

## 2.2. Relation between Safety Evaluation Function and Preference of an Individual

The safety evaluation function  $g(x)$  can be expressed in the following way according to Def.5;

$$g_i(x) = g(x) + e_i, \dots\dots\dots (1)$$

$$E(e_i) = 0. \dots\dots\dots (2)$$

Furthermore, the safety level of urban area  $k$  evaluated by individual  $i$  is expressed as;

$$\begin{aligned} s_k^i &= \int f_k(x) \cdot g_i(x) \, dx, \\ &= \int_L f_k(x) \cdot g(x) \, dx + \int f_k(x) \cdot e_i \, dx. \dots\dots\dots (3) \end{aligned}$$

The variable  $e_i$  expresses a kind of personal feeling for safety, and it is probable that this variable is independent from the frequency function of any urban area. In this case, the safety level of urban area  $k$  evaluated by individual  $i$  can be expressed as follows;

$$s_k^i = s_k + e_i. \dots\dots\dots (4)$$

where  $s_k$  denotes the safety level of area  $k$  defined by;

$$s_k = \int_L f_k(x) \cdot g(x) \, dx. \dots\dots\dots (5)$$

On the other hand, the preference for urban area  $k$  over area  $k'$   $P_{kk'}$ , from a viewpoint of individual safety, becomes a random variable under the condition that the number of individuals is sufficiently large. That is;

$$P_{kk'} = \text{Prob}(s_k^i > s_{k'}^i). \dots\dots\dots (6)$$

Note that the variable  $e_i$  is a random variable in this case.

In the case such that we can assume the distribution of random variable  $e_i$  to be normal, we obtain the following equation.

$$P_{kk'} = \Phi((s_k - s_{k'})/\sigma). \dots\dots\dots (7)$$

where  $\sigma$  is the standard deviation of random variable  $e_i$ , and  $\Phi$  denotes the standard normal distribution function. This equation and Eq.(5) show the relation between the social safety function and the preference of individuals.

In order to define a numerical value for safety level, we can define an origin  $x_0$  and a safety level scale in the following way.

$$g(x_0) = 0, \dots\dots\dots (8)$$

$$\sigma = 1. \dots\dots\dots (9)$$

Equation (7) above can be written in the following way with the inverse function of the standard normal distribution function.

$$s_k - s_{k'} = \Phi^{-1}(P_{kk'}). \dots\dots\dots (10)$$

By the least square method, we can estimate the safety evaluation function that minimizes a following value, if we could obtain the data  $P_{kk'}$ , by minimizing  $Q$  given as

$$Q = \sum_{\substack{k, k' \\ k > k'}} [s_k - s_{k'} - \Phi^{-1}(P_{kk'})]^2. \dots\dots\dots (11)$$

3. CASE STUDY

In this section, we shall examine the safety evaluation function in the case that the loss vector has only one component; life loss.

3.1. Survey of Safety Preference

In order to obtain the data for the ratio  $P_{kk'}$ , we have designed a preference survey. The data about life loss by accidents for 6 urban areas, as shown in Table 1, have been presented to 90 individuals who have lived in a downtown area of Tokyo city. We asked them for their safety preference above 6 areas. A safety preference ordering for 6 areas was obtained from each individual. From these answers, the ratio  $P_{kk'}$  was calculated as Table 2.

On the other hand, the frequency function of life loss for each urban area can be constructed consistent with the data presented to individuals as shown in Table 1.

3.2. Estimation of Polynomial Type Safety Evaluation Function

When we assume that the type of safety evaluation function is polynomial;

$$g(x) = \sum_{i=1}^m a_i x^i, \dots\dots\dots (12)$$

we have a following result from Eq.(5);

$$s_k = \sum_{i=1}^m a_i \int_L x^i \cdot f_k(x) \, dx, \dots\dots\dots (13)$$

where the integral represents the i-th moment of loss. ( It remains for the analyst to choose the order of the function which yields the best results. )

The condition of the least square estimation, i.e., the condition to minimize Q defined by Eq.(11) is;

$$\frac{\partial Q}{\partial a_i} = 0 \text{ for } i = 1 \sim m. \dots\dots\dots (14)$$

Table 1. Data Presented in Safety Preference Survey

Life Loss per Year

Year	Urban Areas					
	A	B	C	D	E	F
1970	10	10	9	8	5	4
1971	12	13	10	11	7	7
1972	8	6	7	5	3	1
1973	13	16	10	12	8	9
1974	11	9	8	7	5	3
1975	14	20	11	16	10	15
1976	7	4	6	3	2	1
1977	9	7	7	6	4	2
1978	10	8	8	6	4	3
1979	11	12	9	9	6	6



Table 2. Ordering Relation Matrix for Safety Preference Survey

The value of  $P_{kk'}$

Urban Area Code		1	2	3	4	5	6
and							
Name of Area		A	B	C	D	E	F
1	A	-					
2	B	0.22	-				
3	C	0.94	0.99	-			
4	D	0.58	0.99	0.37	-		
5	E	0.85	0.99	0.69	0.99	-	
6	F	0.64	0.97	0.49	0.79	0.39	-

or

$$\sum_{k,k'} \{ [\Phi^{-1}(P_{kk'}) - \sum_{i=1}^m a_i \{ \int_L x^i f_k(x) dx - \int_L x^i f_{k'}(x) dx \} ] \times [ \int_L x^i f_k(x) dx - \int_L x^i f_{k'}(x) dx ] \} = 0. \quad (15)$$

This set of equations is a m-th order linear equation system for unknown parameter  $a_i$ , and it should be solved easily.

The results using orders 1, 2, 3 and 4 are shown in Table 3 and Fig.1. These results will be discussed in a succeeding section.

### 3.3. Optimal Order of the Polynomial Type Safety Evaluation Function

It remains to determine what order is the best for the polynomial type safety evaluation function in the results above. Dr. Akaike<sup>(2)</sup> proposed a criterion for such a problem, named AIC or Akaike's Information Criterion.

According to his theory, the best model would have the lowest value of AIC, defined by the following formula.

$$AIC = -2 \ln(\text{maximum likelihood of model for given data}) + 2 (\text{number of parameters in model}). \quad \dots\dots\dots (16)$$

In our case, the polynomial type safety evaluation function has m parameters and the likelihood of the model for the preference data  $P_{kk'}$  can be written as follows;

$$L = \sum_{k,k'} \left[ \frac{1}{\sqrt{2\pi} \rho} \exp \left[ -\frac{\{ \Phi^{-1}(P_{kk'}) - (s_k - s_{k'}) \}^2}{2\rho^2} \right] \right], \quad (17)$$

in which n is the number of summations in Eq.(15). In our safety preference survey, the number of urban areas evaluated by individuals is 6. Therefore,

Table 3. Estimated Polynomial Type Safety Evaluation Function

Model Code	Order of Model	Estimated Model
1	1	$g(x) = -0.03150x$
2	2	$g(x) = 0.05799x - 0.00571x^2$
3	3	$g(x) = 0.01252x + 0.00003x^2 - 0.00020x^3$
4	4	$g(x) = -0.07173x + 0.01787x^2 - 0.00161x^3 + 0.00004x^4$

Table 4. Values of Akaike's Infomation Criterion for Polynomial Type Models

Model Code	AIC for Each Model
1	0.91
2	-16.44
3	-15.66
4	-13.99

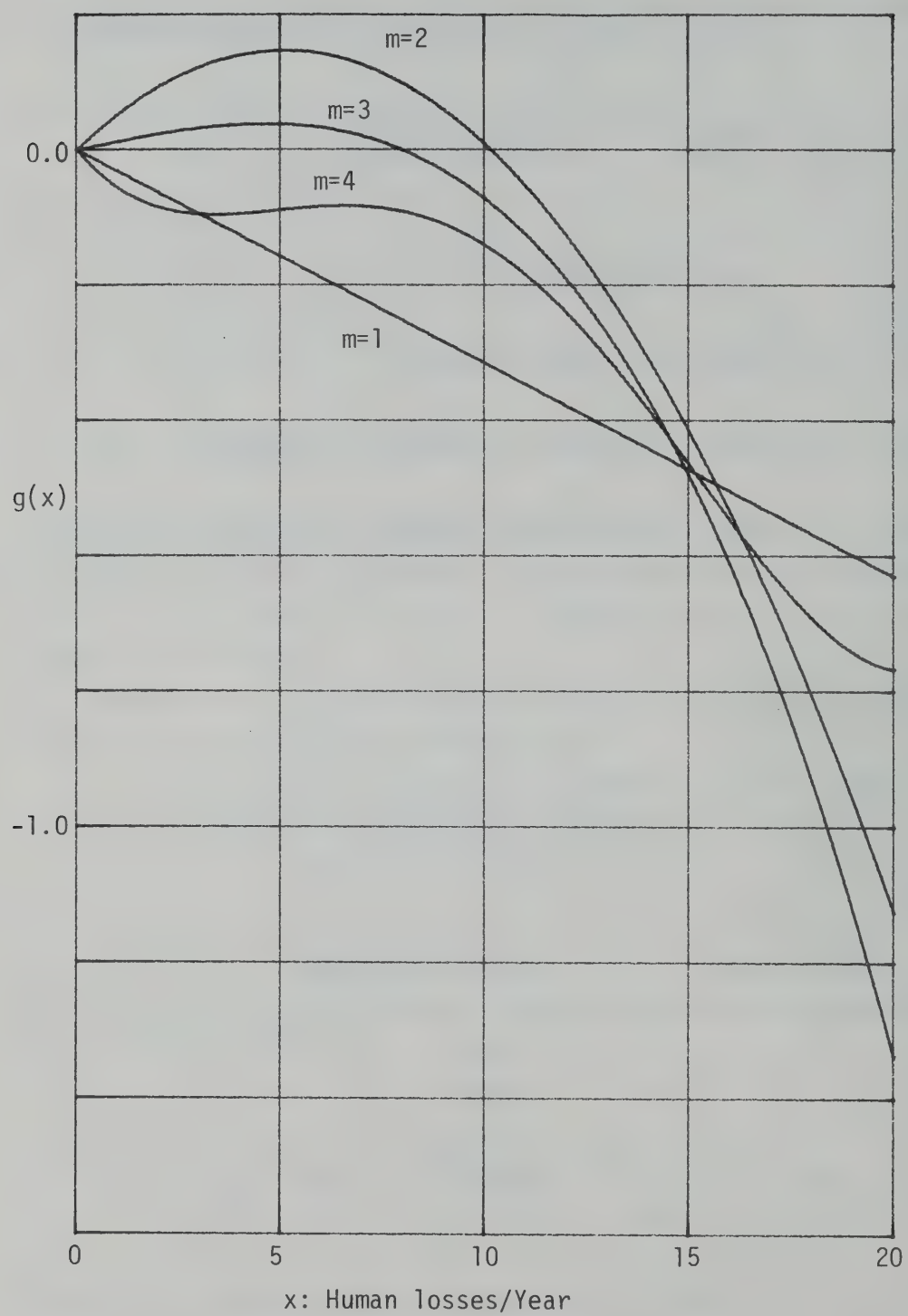


Fig.1. Polynomial type safety evaluation function

$$n = 5 + 4 + 3 + 2 + 1 = 15. \dots\dots\dots (18)$$

The maximum likelihood  $\hat{\Gamma}$  must satisfy the condition;

$$\frac{\partial}{\partial \rho} \hat{\Gamma} = 0, \text{ or } \frac{\partial}{\partial \rho} [ \ln \hat{\Gamma} ] = 0. \dots\dots\dots (19)$$

From this condition and Eq.(17),

$$\rho = Q, \dots\dots\dots (20)$$

and

$$\ln \hat{\Gamma} = -n \cdot \ln[\sqrt{2\pi}] - n \cdot \ln[\rho] - \frac{nQ}{2\rho^2} . \dots\dots\dots (21)$$

Therefore, Akaike's information criterion AIC for our polynomial type model of safety evaluation function is calculated as follows;

$$AIC = n \ln(Q) + 2m + C, \dots\dots\dots (22)$$

where C is constant.

The value of AIC for the above estimated polynomial type models of safety evaluation function are shown in Table 4. According to AIC, the second order model is the best among the polynomial type models.

However, this safety evaluation function is not monotonous as seen in Fig.1. That is, this function increases in a range in which the loss is small. It implies the strange result that more loss is preferable in that part of the range. To avoid this strange conclusion, another type of model for the safety evaluation function is needed.

### 3.4. Threshold Type Safety Evaluation Function

Instead of the polynomial type of safety evaluation function, consider the following threshold type model of safety evaluation function;



$$g(x) = \sum_{i=1}^m a_i (h(x, \theta))^i, \quad \dots\dots\dots (23)$$

where

$$\begin{aligned} h(x, \theta) &= x - \theta \text{ if } x \geq \theta, \\ &= 0 \quad \text{if } x < \theta. \quad \dots\dots\dots (24) \end{aligned}$$

In this case, the safety level can be written as;

$$s_k = \sum_{i=1}^m [ a_i \int_L f_k(x) \cdot (h(x, \theta))^i dx ], \quad \dots\dots\dots (25)$$

and the condition to minimize Q is;

$$\begin{aligned} \sum_{k, k'} [ [ \Phi^{-1}(P_{kk'}) - \sum_{i=1}^m a_i ( \int h^i(x, \theta) f_k(x) dx - \int h^i(x, \theta) f_{k'}(x) dx ) ] \\ \times [ \int h^i(x, \theta) f_k(x) dx - \int h^i(x, \theta) f_{k'}(x) dx ] ] = 0. \quad (26) \end{aligned}$$

We can solve the above equation system numerically and estimate the threshold type safety evaluation function for each order  $m = 1, 2, 3$ , and 4 as reported in Table 5 and Fig. 2.

The threshold type models have a new parameter  $\theta$  in addition to parameters  $a_i$ . Akaike's information criterion is;

$$AIC = n \ln(Q) + 2m + 2 + C. \quad \dots\dots\dots (27)$$

The value of AIC for each threshold type model of safety evaluation function is calculated by the above equation and the results are shown in Table 6.

According to AIC, we can conclude that the best model among the threshold type models is;

$$g(x) = -0.10987 h(x, 9.6), \quad \dots\dots\dots (28)$$

where

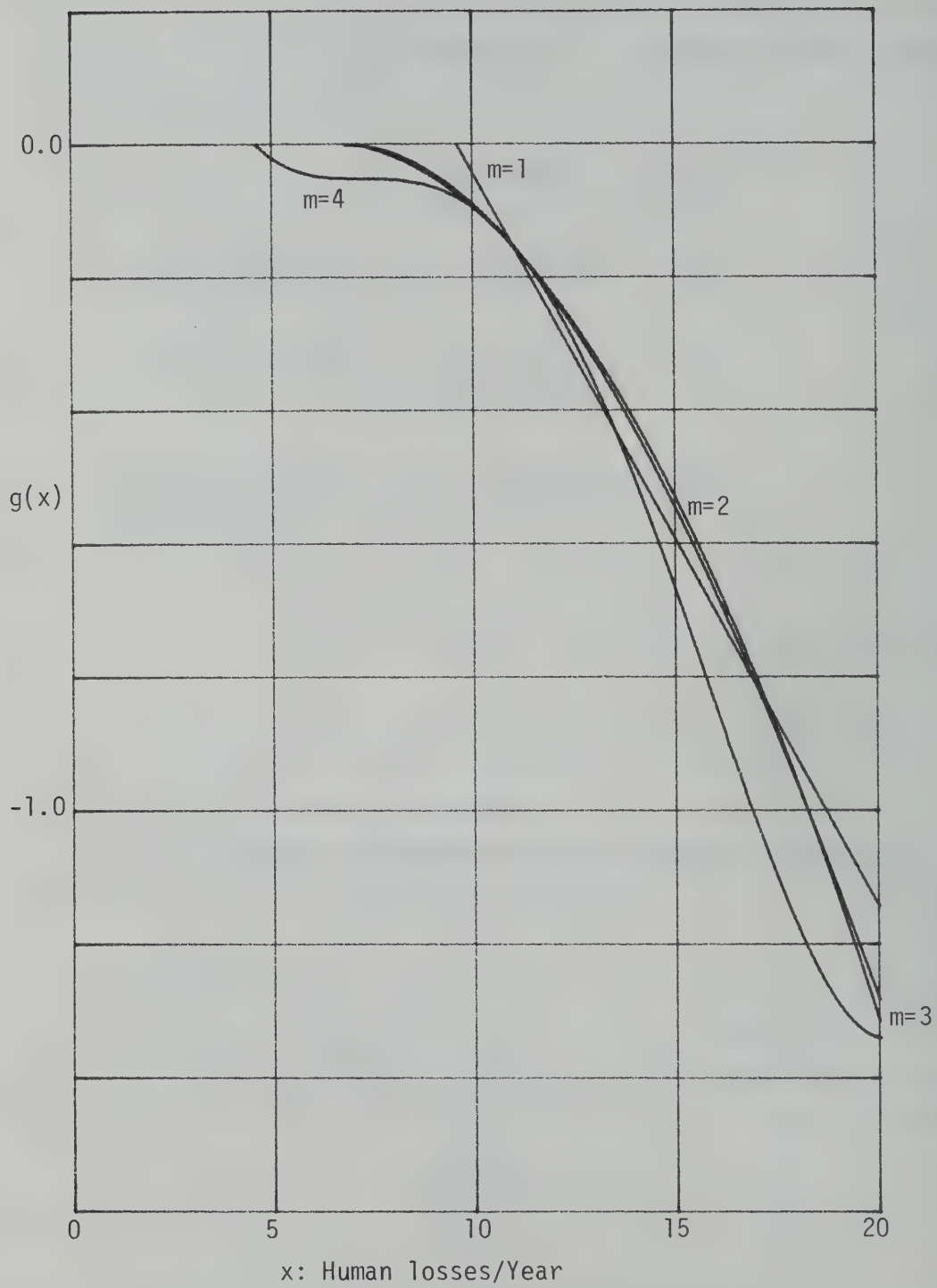
Table 5. Estimated Threshold Type Safety Evaluation Function

Model Code	Order of Model	Estimated Model
5	1	$g(x) = -0.1099h(x, 9.6)$
6	2	$g(x) = -0.01245h(x, 7.1) - 0.00693h^2(x, 7.1)$
7	3	$g(x) = 0.00057h(x, 6.8) - 0.00951h^2(x, 6.8) + 0.00016h^3(x, 6.8)$
8	4	$g(x) = -0.06049h(x, 4.6) + 0.02483h^2(x, 4.6) - 0.00388h^3(x, 4.6) + 0.00014h^4(x, 4.6)$

where  $h(x, \theta) = x - \theta$  for  $x \geq \theta$ ,  $h(x, \theta) = 0$  for  $x < \theta$ .

Table 6. Values of Akaike's Information Criterion for Threshold Type Models

Model Code	AIC for Each Model
5	-16.83
6	-15.83
7	-13.88
8	-12.48



F.g.2. Threshold type safety evaluation function

$$\begin{aligned} h(x, 9.6) &= x - 9.6 && \text{if } x \geq 9.6 \\ &= 0 && \text{if } x < 9.6. \end{aligned} \quad \dots\dots\dots (29)$$

This threshold type model of the safety evaluation function is better than any polynomial type model from a viewpoint of Akaike's theory. Moreover, this function is monotonously non-increasing. This property of the safety evaluation function does not contradict our feeling that more loss is more dangerous.

#### 4. CONCLUSION

We obtained an equation (7) that shows a relation between the safety preference for an urban area and the safety level defined by (Def.4) and Eq.(5). In the case where the loss vector has only one component: human loss, the safety evaluation function is obtained as a threshold type function presented by Eq.(28) and Eq.(29) from the case study safety preference survey. By this result, it is possible to consider that there is a threshold such that any losses perceived as negligible.

The safety level of any urban,  $s_k$ , can be calculated with the safety evaluation function. For example, if we use the safety evaluation function which is estimated in the case study, we can show the safety level  $s_k$  as follows when we can obtain the frequency function of loss  $x$ ,  $f_k(x)$ , for the urban area  $k$ ;

$$s_k = -0.1099 \int_{x \geq 9.6} f_k(x) \cdot (x - 9.6) dx. \quad \dots\dots\dots (30)$$

These results show the possibility of obtaining the safety evaluation function for the case where the loss vector has multi-components, permitting us to assess the safety level of an urban area synthetically. Further research on this possibility is needed in order to develop safety planning methods for modern urban areas.

## ACKNOWLEDGEMENT

This study owes very much to kind advices from research members of the Building Research Institute and faculties of the Department of Civil Engineering, Carnegie-Mellon University.

The author is deeply indebted to Prof. I. J. Oppenheim. I appreciates Mrs. H. Pusty to help making the draft of this paper.

## REFERENCES

1. Aoki, Y. "Concepts and Methods on Optimization of Fire Safety Planning", CIB Symposium:Systems Approach to Fire Safety in Buildings.
2. Akaike, H. "Information Theory and an Extension of the Maximum Likelihood Principle", Research Memo. No.46, The Institute of Statistical Mathematics.



# 安全評価関数の推定

青 木 義 次\*

BRI Research Paper No. 100

建設省建築研究所

近年、都市防災の必要性が強調され、防災対策に関する研究が進められており、より効果的な対策の実施が期待されている。また、具体的な防災対策の立案にあたっては、どのような安全レベルを目標とするかが基本的問題となるが、そのためには想定される被害の減少をどのように評価するかという評価方法が確立していることが望ましい。

本研究では、都市の安全レベルを評価する方法を提案し、さらにこの方法の中核となる安全評価関数の推定手法を開発している。

第1章では、研究の目的・問題点を示した。

第2章で、安全評価にかかわる各種概念を整理し数学的定義を与え、さらに相互の数理的關係を導出し安全評価関数の推定手法を開発した。

第3章では、住民アンケート調査を実施し、このデータから統計学的にもっとも望ましい安全評価関数を具体的に推定した。

第3章で、本研究から得られた結果をまとめている。





## Research Papers-Recent Issues

- No.76 Y. Matsushima: Random Response of Single-degree-of-freedom System with Bilinear Hysteresis, September, 1977, 28 pp.
- No.77 A. Baba: Drying Shrinkage Mechanism of Building Materials, March, 1978, 79 pp.
- No.78 K. Hayakawa: The Management of Land as an Environmental Resource, March, 1978, 40 pp.
- No.79 T. Tanaka: A Model on Fire Spread in Small Scale Buildings, September, 1978, 76 pp.
- No.80 Y. Aoki: Studies on Probabilistic Spread of Fire, November 1978, 52 pp.
- No.81 F. Saito: Experimental Study of Compartment Fire Using Model Boxes, July, 1979, 50 pp.
- No.82 Y. Matsushima: Random Response of Single-degree-of-freedom System with General Slip Hysteresis, July, 1979, 37 pp.
- No.83 Y. Hasemi: Flashover Criteria of Compartment Fire - Theory on Zero Order Reaction System -, August, 1979, 26 pp.
- No.84 T. Tanaka: A Model on Fire Spread in Small Scale Buildings, 2nd Report, March, 1980, 63 pp.
- No.85 Y. Ishiyama: Review and Discussion on Overturning of Bodies by Earthquake Motions, June, 1980, 115 pp.
- No.86 S. Watanabe: Planning History in Japan - A State of the Art Survey -, August, 1980, 36 pp.
- No.87 Y. Sugimura: Participation Factor of Horizontal Force Applied to Pile Foundation, March, 1981, 33 pp.
- No.88 Y. Hasemi: Mathematical Basis for Physical Evaluation on Flashover, March, 1981, 41 pp.
- No.89 T. Wakamatsu: A Quantitative Evaluation of Smoke Safety, March, 21 pp.
- No.90 S. Watanabe: Metropolitanism as a Way of Life, March, 1981, 52 pp.
- No.91 M. Hirose, T. Goto, M. Yoshimura, H. Hiraishi: Full-Scale Experimental Study on Aseismic Performance of Medium-Rise RC Wall Structure, March, 1981, 28 pp.
- No.92 Y. Yamazaki: Inelastic Torsional Response of Structures Subjected to Earthquake Ground Motions, March, 1981, 102 pp.
- No.93 S. Kose: Study of Accidents Associated with Building Feature, March, 1982, 38 pp.
- No.94 S. Okamoto, S. Nakata, Y. Kitagawa, M. Yoshimura, T. Kaminosono: A Progress Report on the Full-Scale Seismic Experiment of a Seven Story Reinforced Concrete Building - Part of the US-Japan Cooperative Program, March, 1982, 92 pp.
- No.95 Y. Hasemi: Characterization of the Intermittent Flaming Region of the Upward Current Above Diffusion Flames, March, 1982, 33 pp.
- No.96 Y. Morishita: Statistical Analysis of Fire Spread, May, 1982, 17 pp.
- No.97 T. Fukushima: Deterioration Model of Polymeric Materials with Special Attention to Age and Deterioration Depth, December, 1982, 30 pp.
- No.98 H. Hiraishi, M. Yoshimura, H. Isoishi, S. Nakata: Planer Tests on Reinforced Concrete Shear Wall Assemblies. - U.S.-Japan Cooperative Research Program-, January, 1983, 63 pp.
- No.99 S. Nakata: Tests of Reinforced Concrete Beam-Column Assemblages -U.S.-Japan Cooperative Research Program-, March, 1983, 111 pp.
- No.100 Y. Aoki: Assessment of an Urban Safety Evaluation Function, March, 1983, 16 pp.

Address for Communication

**BUILDING RESEARCH INSTITUTE  
MINISTRY OF CONSTRUCTION**

No.1 TACHIYAMA, OH-HO-MACHI, TSUKUBA-GUN, IBARAKI-PREF  
JAPAN

690  
33b

ISSN 0453-4972

BRI Research Paper No.101

# TECHNIQUES FOR LARGE SCALE TESTING AT BRI LARGE SCALE STRUCTURE TEST LABORATORY

by

Shin Okamoto

Takashi Kaminosono

Masayoshi Nakashima

and

Hiroto Kato

Building Research Institute

Ministry of Construction

May 1983

THE LIBRARY

UNIVERSITY OF  
AT THE





## FOREWORD

Progress of research on the behavior of building structures is remarkable; member and subassemblage tests have provided detailed information on the behavior of individual building components. Analytical study, such as computer simulation, has also enabled us to examine the complicated behavior of building structures. While these findings have been incorporated into our design practices, one problem remains as to how the results should be interpreted in view of the real behavior of structures. To assess the suitability of our engineering judgements, there is an increasing demand to test building structures on a large scale.

Building Research Institute set up in 1978 a new test laboratory for large scale testing of building structures, and subsequently has developed new systems that facilitate such large scale testing. This paper is the first issue of a series of reports in which we plan to introduce the details of the test facilities and systems in this laboratory. This first paper depicts an overview of the test laboratory, loading and measuring techniques, and computer controlled test system.

We wish readers' critical comments on the content of this paper.

Katsuro Kamimura  
Director General  
Building Research Institute  
Ministry of Construction



TECHNIQUES FOR LARGE SCALE TESTING  
AT BRI LARGE SCALE STRUCTURE TEST LABORATORY

by  
Shin Okamoto<sup>1</sup>  
Takashi Kaminosono<sup>2</sup>  
Masayoshi Nakashima<sup>2</sup>  
and  
Hiroto Kato<sup>3</sup>

Building Research Institute, Ministry of Construction  
Tsukuba, Ibaraki JAPAN

ABSTRACT

Study on the behavior of building structures has greatly been progressed. Tests of structural members and assemblies and scale models of buildings have been conducted extensively all over the world. Numerical techniques for analysis of structures have also been developed a great deal thanks to innovation of digital computers. While many findings obtained from these studies have been reflected to various design practices, one problem remains as to how effectively they have been interpreted. Many engineering judgements are needed to incorporate member and assembly test data into structural design. Assumptions and simplifications are inevitably employed in numerical analysis. In order to evaluate the validity of these judgements and assumptions and to examine ultimately the overall behavior of building structures, one needs to execute tests of building structures on a large scale.

This paper introduces the structural test laboratory at the Building Research Institute, Ministry of Construction, Tsukuba, Japan. The laboratory has various facilities specially designed for large scale testing. They include the large test floor, loading system, data processing system and computer supervised testing system.

- 
1. Director, Production Department
  2. Research Engineer, Production Department
  3. Assistant Research Engineer, Production Department

The laboratory has an open space of 30 meters by 60 meters in plan and 40 meters in height. In the middle of the laboratory, a 25 meter high wall is built to provide reaction to horizontally installed actuators with which earthquake forces are to be simulated. The capacity of the wall is 40 MN and 720 MN x m in allowable shear and bending moment. Either of two test floors, one on each side of the wall, can accommodate a building specimen of as much as 300 m<sup>2</sup> floor area and 25 meter height.

Servo-controlled actuators are prepared for load application, having capacity of  $\pm 1000$  kN in force and  $\pm 1000$  mm in stroke. The needed power is provided by hydraulic pressure, and the actuators are controlled by electronic servo-controllers.

Various types of displacement transducers (DLT's) are provided for the measurement of large displacements. Specially designed digital type DLT's are unique. They are magnetic response type and can measure displacements up to  $\pm 1000$  mm with accuracy of 0.01 mm. Signals of these DLT's are completely noise free.

For systematic loading, data processing, and safety check, two computers are introduced. One serves for servo-control. During the test, the computer keeps supervising the motion of actuators for accurate command control and for safety check. The other computer, on line with data acquisition units, is used for data processing. This computer is linked to the servo-control computer. Commands for servo-controllers can then be created in this data processing computer and sent to the servo-control computer.

These two computers, servo-controllers, actuators, measuring instruments, and data acquisition units constitute one closed loop test system. This closed loop system, involving minimized manual operation, enables us to perform a new test method developed for simulation of building response under earthquake motions, referred to as the pseudo-dynamic (PSD) test method. This paper also introduces large scale tests conducted at the laboratory by means of this new method.



## TABLE OF CONTENTS

	ABSTRACT.....	i
I	INTRODUCTION.....	1
II	LABORATORY FOR LARGE SCALE TESTING.....	3
III	LOADING SYSTEM.....	4
IV	MEASURING TECHNIQUES.....	6
V	COMPUTER ON-LINE TESTING SYSTEM.....	7
VI	PSEUDO-DYNAMIC TESTING METHOD.....	9
VII	LARGE SCALE TESTS CONDUCTED AT LABORATORY.....	12
VIII	CONCLUDING REMARKS.....	13
	NOTATION.....	14
	TABLES.....	15
	FIGURES.....	19
	REFERENCES.....	37



## I INTRODUCTION

Research on building structures has been progressed for decades, and many findings obtained from works associated with the behavior of various types of structures have effectively been incorporated into design practices. Two approaches are common in those research works. Experimental work is the first approach, where scaled models of structural members, subassemblages, and frames are tested with various loading and support conditions, and these results are correlated with the behavior of real building structures. The other is the analytical approach. This approach ranges from purely mathematical formulation of physical phenomena (belonging to the applied mechanics) to numerical analyses using large size digital computers.

In these days, experiments have been facilitated a great deal thanks to the innovation of technologies of various kinds. Load applying actuators have been upgraded in both capacity and accuracy. Dynamic servo-controlled actuators are now available in many structural laboratories. Very fine measuring instruments make it possible to monitor displacements, rotations, and strains of test structures with great accuracy. The actuator control, and storing and reducing data have also been advanced by means of digital computers. The progress of analytical study is also remarkable. Specifically, work that utilizes large size digital computers has proven its great capability. Iterative solution techniques enable to solve various non-linear problems. The finite element method is one of those powerful techniques.

With all of these sophistications in experiment and analysis, there is one thing still lacking before making final judgement on the evaluation of the behavior of real building structures. That is the test of building structures as building structures. Component tests provide useful information on the individual characteristics of these members, but by these tests, little can be known with respect to the overall behavior of building structures in which many members are combined. Structural integrity, in other words, the effect of member connections on the overall behavior, is after all difficult to predict by the member tests. The subassemblage test is a useful approach to

investigate closely the behavior of a building structure as a unit. There is still one problem; when selecting an subassemblage, we must assign some artificial boundary conditions in the subassemblage. In a real structure, the part that is extracted as a subassemblage is supported by other members and subassemblages. In many occasions, it is difficult to perfectly simulate those boundary conditions. The ultimate validity of the adopted (or assumed) boundary conditions can only be checked by comparing with the behavior of the real structure. Structural tests of scaled models are often employed in order to evaluate the overall behavior of building structures. Tests of scaled models always accompany one problem as to how individual constituents of real structures are to be scaled down. For example, in reinforced concrete structural models, the size of aggregates and reinforcing bars cannot be scaled down correctly once the scale ratio is lowered to a certain level.

Numerical analysis such as the finite element analysis is a very powerful tool to study the overall behavior of building structures, and, as a matter of fact, many practical design provisions, suggestions, and recommendations have been made on the basis of these analytical results. Nevertheless, we must be reminded that assumptions of various levels - stress-strain level, moment-curvature level, end force-end displacement level, or story level - are inevitably involved in these analyses. These assumptions can first be verified when the analytical results are compared with the behavior of real structures.

All of those statements suggest a need of executing tests of full (or at least large) scale building structures. It does not indicate, however, that we need to test large scale structures all the time. Such tests are very costly, and therefore need only to be done on a timely basis when final confirmation is required.

The Building Research Institute of Ministry of Construction constructed in 1978 a laboratory for tests of large scale building structures, and subsequently has developed various systems that facilitate such testing. In addition to conventional test equipment, special facilities are indispensable for large scale tests; first, we need a large open space to accommodate a large scale building specimen.



Actuators that apply forces and deflections which are commensurate with the capacity of the test building are required. Not only accuracy but large capacity in stroke is also required for some measuring instruments. Since we deal with a large scale specimen, many displacement, rotation, and strain signals must effectively be read, stored, and reduced into meaningful forms.

This paper reports on this large scale structural laboratory and the outline of the techniques developed for large scale testing. A number of large scale tests performed in this laboratory are also described.

## II LABORATORY FOR LARGE SCALE TESTING

In order to execute large scale tests, first we need a good environment for the testing. The test laboratory shelters a space which is about 30 meters by 60 meters in plan and 40 meters in height (Fig. 1). Figures 2 and 3 show the overall dimension of the test laboratory. In most tests, specimens must be rigidly supported on the test floor. The test floor, therefore, is designed so that it is strong as well as stiff enough to sustain securely the forces applied through the specimens. The test floor, made of prestressed concrete, has a dimension of 44.6 meters by 20 meters in plan and 6.6 meters in thickness and is able to sustain  $1.0 \text{ MN/m}^2$  of bearing force and  $720 \text{ MN} \times \text{m}$  of bending moment (Fig. 4).

To simulate wind or earthquake forces applied to a specimen, it is often needed to install load applying actuators in a horizontal direction. For this purpose, a wall, referred to as reaction wall, is arranged in the middle of the test floor (Fig. 5). The wall is 20 meters by 25 meters in surface dimension and 6.6 meter thick. The wall is also made of prestressed concrete, having an allowable capacity of 40 MN and  $720 \text{ MN} \times \text{m}$  in shear and bending moment respectively. Having the wall placed in the middle of the floor, the test floor is essentially divided into two areas (Floors A and B in Fig. 2). These floors are respectively 20 meters by 24.6 meters, and 15.4 meters by 20 meters in plan dimension. Therefore, the larger test floor (Floor A)



can easily accommodate a building that is as much as  $300 \text{ m}^2$  in floor area and 25 meters (approximately eight story equivalent) in height. Since the test floor is divided into two areas, it is possible to execute many tests simultaneously.

Test specimens, load applying actuators, and other test setups must be securely tightened to the test floor as well as the reaction wall. For this tightening, the floor and wall have holes that are 100 mm in diameter and spaced at every 500 mm pitch in both directions (Fig. 6). Some holes penetrate through the thickness of the floor or wall, whereas the other holes are threaded and stop at one meter in depth. By using specially designed prestressing steel rods, specimens, actuators, and setups can be clamped to the floor or wall.

To make facilitated connecting cables extending from various measuring instruments to data acquisition units in the measuring room (Fig. 3), permanent cables are embedded throughout in the floor and wall. These cables extend from the data acquisition units and terminates at cable relaying boxes, called "Junction Boxes", that are installed at strategic locations in the floor and wall. Cables extending from measuring instruments then can readily be connected to junction boxes in the vicinity of the test area, and the signals are sent forward to the data acquisition units.

### III LOADING SYSTEM

For large scale testing, load applying actuators must have capacity sufficient to provide large force to a test specimen and at the same time to follow the specimen's deflection. The most suitable power element to generate such large force is hydraulic. All of the actuators for the large scale testing then are controlled by an electro-hydraulic servo-control system.

Two types of actuators are available in the laboratory. The first type of actuators, designated as JB type, has a capacity of  $\pm 1.0 \text{ MN}$  in maximum applying force and  $\pm 1000 \text{ mm}$  or  $\pm 500 \text{ mm}$  in full stroke (Fig. 7). In each of these JB type actuators, one load cell and one inductive type displacement transducer (DLT) are attached. Signals from the load cell

or DLT are first sent to one of the junction boxes and further to the data acquisition unit, or to the servo-control unit if those signals are to be used for test control. The maximum piston velocity of these actuators are 2 mm/sec., and, therefore, they are primarily used for quasi-static loading tests.

Another type of actuator, designated as JA type, is able to run to  $\pm 300$  mm with as much as 350 mm/sec. in piston velocity and primarily used for vibration and fatigue tests (Fig. 8). The maximum force that could be applied by this actuator ranges from  $\pm 500$  kN to  $\pm 750$  kN in accordance with the piston velocity of from 350 mm/sec. down to the quasi-static level. One load cell, two DLT's, and one accelerometer are installed in this actuator. One of the DLT's covers the full range ( $\pm 300$  mm), while the other measures within a range of  $\pm 60$  mm but with higher accuracy. As in JB type actuators, signals of the load cell, DLT's, and accelerometer in this actuator are sent to the data acquisition unit and to the servo-control unit. A function generator is prepared for this actuator. The generator can provide sinusoidal, square, ramp, sawtooth functions with a frequency range of between 0.01 to 10,000 Hz.

The actuators have a swivel base and swivel head to provide freedom at both ends of the actuators. The type, number, and capacity of these actuators are tabulated in Table 1.

Hydraulic power units provide the needed power for the actuators. Six pairs of oil reservoir and hydraulic pump are installed at the basement of the laboratory (Fig. 9). Each of the pumps is capable of delivering  $0.3 \text{ m}^3/\text{min.}$  of oil at a pressure of  $21 \text{ MN/m}^2$ .

The motion of an actuator piston is controlled by the hydraulic servo-control system. The system consists of a feedback selector panel, input module, servo controller, and servo-valve. This system together with the actuator forms a closed-loop. Input, given as either displacement or load, is applied to the input module manually or from various external sources such as the function generator, magnetic type reader, or computer that are on-line with the servo-control system. (The computer on-line testing system will be discussed in detail in a later section.) An input signal, either displacement or load increment,

is converted to a voltage change in the servo-controller (Fig. 10) (the full range corresponds to  $\pm 10$  volt). This electrical command signal is then converted by means of the servo-valve to a regulated flow of high pressure hydraulic fluid.

#### IV MEASURING TECHNIQUES

In a quasi-static structural test, displacement and rotation measurement is of the most importance to evaluate the structural behavior of the test specimen. Various types of displacement transducers (DLT's) are prepared in the test laboratory. A number of DLT's that can read small to medium displacements (a range up to about  $\pm 100$  mm) are available. They are either strain gage type or inductive type. In addition to those DLT's, DLT's that can measure large displacements are inevitable for large scale testing. For this purpose, two types of large range DLT's are provided in the laboratory. The first type of DLT's is inductive type and has a capacity of either  $\pm 200$  mm,  $\pm 300$  mm, or  $\pm 500$  mm in full stroke (Fig. 11). The second is digital type with a full stroke of either  $\pm 500$  mm or  $\pm 1000$  mm (Fig. 12). In each of these digital type DLT's, plus and minus magnetic elements are coated alternately at a pitch of 0.01 mm along its length. A cursor of the DLT shifts in accordance with the movement of a measuring point, and the displacement is measured by counting the number of magnetic elements that are passed by the cursor. These DLT's are digital type and free from any noise signals, which are often generated in analog type DLT's that need amplifiers. The detailed description of the DLT's, including the available number, stroke capacity, and sensitivity, are shown in Table 2.

DLT and strain gage signals are first transmitted to scanning boxes set on the test floor. Cables extending from those scanning boxes are to be connected to junction boxes (described in the previous section). The signals, scanned with 0.1 sec. per channel, are then sent forward to the static data acquisition unit in the measuring room (Fig. 13). At the present time, a total of 700 channels can be connected to those scanning boxes (seven boxes with each box having 100 channels).



In the data acquisition unit, analog signals are amplified and converted to digital values by an A/D converter. Those digitized data are stored in a cartridge disk of a data processing computer which is connected to the unit. Data reduction can be done with the computer, or alternatively, those data can be sent to a larger computer in the computer center for more refined data reduction.

All of inductive type DLT's and many of strain gage type DLT's can also be used for measurement of dynamic tests. Signals of DLT's and accelerometers recorded in a dynamic test are assembled to bridge boxes on the test floor and sent forward to the interface of a dynamic measuring unit in the measuring room. Then the signals are scanned by a multiplexer in this unit with a speed of 0.000050 sec. per channel and digitized by an A/D converter. Those digitized data are stored in a cartridge disk as for the measurement in static tests. Analog signals can also be recorded directly in magnetic tapes before passing the A/D converter. Table 3 provides details on the capacity of the data acquisition units.

Since the test control room is away from the test floors, and furthermore it is very difficult to keep tracking all local behaviors of a large scale test structure, many portable TV cameras are provided in the laboratory for the purpose of monitoring those local behaviors. These cameras can be mounted at strategic positions so that critical locations of the structure are to be continuously monitored. Pictures sent from those cameras can be displayed in color displays in the measuring room (Fig. 14). Those pictures can also be recorded in video tape recorders if it is found necessary.

## V COMPUTER ON-LINE TESTING SYSTEM

When a test specimen is large, the level of applying force becomes proportionally high. Many load, displacement, and strain data also need to be acquired during the test. More importantly, it should be noted that malfunction in testing may cause a disaster since the specimen no longer is a miniature. Under these conditions in large scale testing, an unified control of loading and data processing as well as continuous

safety check are very critical. To achieve effective execution of large scale tests, the overall testing has been designed to be computer controlled, named the computer on-line testing. This computer on-line testing system (Fig. 15) comprises one servo-controller control computer, servo-controllers, servo-controlled actuators, data acquisition units, and one data processing computer. All of them, linked together, constitutes one closed loop as shown in Fig. 11. The servo-controllers, actuators, and data acquisition units have already been described in the previous sections.

The servo-controller control computer, as the name explains what it is, controls the servo-controllers of actuators. The loop of test control - control by actuator loads, by actuator displacements, or by external measuring instruments - can be selected by this computer. The piston velocity of actuators can also be set up from this computer. If two or more actuators are used in one test, the piston velocity of each actuator can be adjusted so that all actuators would reach their specified command values simultaneously. Accuracy of the attained command values (command displacements, loads, or external signals) relative to the specified command values is continuously checked by this computer. First, allowable error bounds are set up. The computer then keeps monitoring the control command values as to whether the measured values are within the specified error bounds. When all values fall within these bounds, the actuators stop their motion, and the computer starts a stability check. The computer scans the command values at a specified time interval (of an order of 0.00005 sec.) and repeats the scanning for a certain period (say, for one second). If those values constantly are within the error bounds, the computer presumes that the specified values are all achieved and sends a message to the data acquisition units, for starting measuring. If the values exceed the bounds during the scanning, the stability is assumed not to be achieved, and the computer gives a pause signal to the servo-controllers. Several options are prepared in this situation; the stability check may be repeated again, the error bounds may be enlarged, or the test may be continued as if the stability check were cleared.

The computer keeps monitoring the signals of actuator loads and



displacements in order to ensure the safety of the test. When one of them exceeds its predetermined (upper or lower) limit, a command is given to stop the loading. The computer also monitors the hydraulic pressure of oil, the currents and voltages of the servo-control interfaces, servo-valves and others. Upon detecting an abnormal signal, the computer gives a pause signal to the servo-controllers.

The data processing computer are on-line with on one side the data acquisition units and on the other the servo-controller control computer. This data processing computer is composed of its main body, one system typewriter, one card reader, one line printer, one X-Y plotter, and one graphic display. The computer receives from the data acquisition units key data, which are selected by a fortran computer program made by a test operator. Data reduction is performed according to the fortran program, and the reduced data can be output on the output devices. The displayed pictures can be copied in hard sheets if requested. Sometimes, the test (loading) program may not be predetermined; in other words, command signals are to be determined on the basis of data acquired in previous steps of the test. This computer is capable of executing such post-determined program test. The computer receives data needed for computing the next command signals, executes a fortran program that is to compute the signals, and send the signals to the servo-controller control computer. A flow chart of this computer supervised closed loop testing system is given in Fig. 16.

## VI PSEUDO-DYNAMIC TESTING METHOD

The Pseudo-Dynamic (PSD) testing method is a technique to simulate the earthquake behavior of structures and was originally proposed by Tanaka et al. (Ref. 1). The basic concept of this method is to solve equations of motions of a structure by means of the direct integration technique. This method, however, is not a pure numerical analysis but a combined simulation technique of experiment and numerical analysis. To explain this method, let us consider an example shown in Fig. 17. First, the test structure is set on a test floor, and actuators are installed at appropriate positions (Fig. 17 (a)). The test structure

then is assumed to be a discrete mass system (Fig. 17 (b)). The equations of motion of the system can be written in a matrix form as:

$$[M]\{\ddot{x}_n\} + [C]\{\dot{x}_n\} + \{f_n\} = -[M]_0\ddot{x}_n \text{ ----- Eq. 1}$$

Where  $\{\ddot{x}_n\}$ ,  $\{\dot{x}_n\}$ , and  $\{x_n\}$  respectively indicate the acceleration, velocity, and displacement vector of the discrete system at the n-th step.  $[M]$  and  $[C]$  are the mass and viscous damping matrix.  $\{f_n\}$  denotes the restoring force vector of the system at the n-th step.

Various integration techniques have been developed to solve the equations of motion for linear and nonlinear structures. The techniques are divided primarily into two groups. The first group, referred to as the implicit solution technique, includes the techniques such as the Houbolt method, the Newmark method, and the Wilson method. The second group, referred to as the explicit solution technique, includes the central difference method, the two-cycle iteration with the trapezoidal rule, and the Runge-Kutta method. Among those techniques, the central difference technique is used to solve the equations in the PSD testing method. In the central difference technique, the acceleration and velocity vectors at the n-th step are expressed in terms of the displacements at the (n-1)-th, n-th and (n+1)-th steps as:

$$\{\ddot{x}_n\} = \frac{\{x_{n+1}\} - 2\{x_n\} + \{x_{n-1}\}}{\Delta t^2} \text{ ----- Eq. 2}$$

$$\{\dot{x}_n\} = \frac{\{x_{n+1}\} - \{x_{n-1}\}}{2 \Delta t} \text{ ----- Eq. 3}$$

By substituting the above two equations into the equations of motion (Eq. 1), and solving for the displacement vector at the (n+1)-th step, we can obtain the following relationship:

$$\begin{aligned} \{x_{n+1}\} = & \left[ [M] + \frac{\Delta t}{2} [C] \right]^{-1} [2[M]\{x_n\} + \left( \frac{\Delta t}{2} [C] - [M] \right) \{x_{n-1}\} \\ & + (\Delta t)^2 \{f_n\} - [M](\Delta t)^2_0 \ddot{x}_n] \text{ ---- Eq. 4} \end{aligned}$$

That is, the displacement vector at the (n+1)-th step can be derived from the displacement vectors at the (n-1)-th and n-th steps, the ground acceleration at the n-th step, and the restoring force vector at the n-th step. The PSD test procedure of the structure shown in Fig. 17 can be described as follows:

Suppose the test specimen is in the  $n$ -th step, the  $n$ -th step ground acceleration  $\ddot{X}_n$ , the displacements at the  $(n-1)$ -th and  $n$ -th steps  $\{X_{n-1}\}$  and  $\{X_n\}$ , and the restoring forces (measured from actuator load cells)  $\{f_n\}$ , are all known. Substituting these values into the equations of motion (Eq. 4), we can solve the displacements at the  $(n+1)$ -th step  $\{X_{n+1}\}$ . Next, the specimen is loaded quasi-statically to the calculated displacements by the actuators. When the displacements are attained, the restoring forces  $\{f_{n+1}\}$ , are measured by the actuator load cells. The test is advanced by repeating this procedure. A flow diagram of the test is also shown in Fig. 18

Some good reasons to employ the central difference technique can be drawn in view of the above formulation and procedure. First, in this technique, no iterative process is required even in the inelastic range. It should be noted that, in an implicit technique, iteration is inevitable in the inelastic range because the equations of motion are to be formulated for the  $(n+1)$ -th step rather than for the  $n$ -th step. Such iteration is not suitable for the PSD method. Second, as seen from Eq. 4, the computation does not involve any matrix calculation if the mass and viscous damping matrices are diagonal, which we generally adopt in PSD tests. As a result, the time and storage space required for computation is reduced significantly. According to previous studies (Refs. 2 and 3), the central difference technique is stable and reasonably accurate as long as the time interval for the calculation is small. The stability condition is given as (Ref. 3):

$$\Delta t \leq \frac{1}{\pi} T_{\min} \text{ ----- Eq. 5}$$

Where  $\Delta t$  is the time interval, and  $T_{\min}$  is the smallest natural period of the mass system representing the test structure. Further, use of one-sixth of the above time interval is recommended to guarantee sufficient accuracy.

The most prominent advantage of this method over numerical analysis is that no assumption is required for the stiffness (restoring force) characteristics of the structure. The PSD method, therefore, is very powerful when analyzing dynamic behavior of inelastic systems. A second



benefit of this method is that it is possible to keep tracking the local behavior and damage propagation of the test structure since the test structure is loaded quasi-statically. This statement can readily be understood if the test is compared with a shaking table test, in which the testing time is very short (of an order of 10 to 30 seconds). In the PSD test, selection of the viscous damping matrix  $[C]$ , however, is debatable as in numerical analysis. Idealization needs to be made such that  $[C]$  be proportional to the initial stiffness matrix, to the mass matrix or to the combination of the two. Such idealization can be a disadvantage if compared with shaking table tests. It may be cited, however, that miniature model structures used in a majority of shaking table tests are also poor in simulating the damping characteristics of their prototypes.

To execute a PSD test, the restoring forces of the test structure must be measured, and are to be sent to a computer which calculates the equations of motion. Then, the calculated displacement increments for the next step must be applied to the test structure. It is clear that the computer supervised closed loop test system described in the previous section can control the execution of the PSD test systematically. Furthermore, it should be emphasized that the earthquake behavior of a structure which is too large to be tested on a shaking table can directly be simulated with this PSD method, for the laboratory of the Building Research Institute can serve for a large scale test structure. To the authors' best knowledge, the world largest shaking table, a counterpart of this laboratory with the PSD test method, is 15 meters by 15 meters in table dimension and can carry at most 10 MN of weight. From these numbers, we can notice a sizable difference in the allowable maximum scale of test structures between the shaking table test and the PSD test.

## VII LARGE SCALE TESTS CONDUCTED AT LABORATORY

Table 4 lists large scale structural tests conducted at the laboratory from 1978 through 1982. As seen from the third rightmost column of the table (Objectives), a majority of the tests was made to

investigate the earthquake behavior of various types of building structures.

### VIII CONCLUDING REMARKS

This paper has introduced various facilities specially designed for the large scale testing at the Building Research Institute of Ministry of Construction. We demonstrated distinguished features of those facilities particularly those closely associated with the performance of large scale tests. For effective and systematic control of loading, data processing, and safety monitoring during the test, a computer supervised closed loop system has been devised and explained in detail in this paper. We believe that this large scale testing system has high potential for research of various aspects of structures. Some of the research projects being planned are as follows:

1. Study on the behavior of high-rise buildings: There have been very few experimental works to have investigated the wind and earthquake resistance mechanism of high-rise buildings. Since the laboratory has a space that can accommodate a specimen of as high as 25 meters, a test specimen can rise to 25 story high if one third of scale ratio is adopted.
2. Study on the behavior of three-dimensional buildings: In a building that has a slender rectangular plan shape; that is, has many spans in one horizontal direction relative to the other direction (like an apartment building), the distribution of earthquake force to each force resisting component is very complex particularly if the force is applied beyond the elastic limit of the building. With one third of scale ratio, a building model that has as many as ten spans can be tested in this laboratory.
3. Study of soil structure interaction: Behavior of foundations, footings and piles is still very difficult to evaluate because of the complexity of soil properties and the interaction between the super structure and the soil. Considering that soils are difficult to scale down properly, a full scale test can be performed on the laboratory test floor of 400 m<sup>2</sup>.



## NOTATION

The following symbols are used in this paper.

$[C]$	: Viscous damping matrix
$\{f_n\}$	: Restoring force vector at the $n$ -th step
$[M]$	: Mass matrix
$\{\ddot{x}_n\}$	: Acceleration vector at the $n$ -th step
$\{\dot{x}_n\}$	: Velocity vector at the $n$ -th step
$\{x_n\}$	: Relative displacement vector at the $n$ -th step
${}_0\ddot{x}_n$	: Ground acceleration at the $n$ -th step
$T_{\min}$	: Smallest natural period of discrete mass system
$\Delta t$	: Time interval for direct integration

Table 1 Capacity of Actuators

ACTUATORS

Type	Number of Actuators	Maximum Force (kN)	Maximum Stroke (mm)	Maximum Ram Velocity (mm/sec.)	Load Cell Capacity (kN)	LVDT Capacity (mm)
Static (JB)	6	<u>+1000</u>	<u>+500</u>	2.0	<u>+1000</u>	<u>+500</u>
	2		<u>+1000</u>			<u>+1000</u>
Dynamic (JA)	1	<u>+500</u> (dynamic) <u>+750</u> (static)	<u>+300</u>	350.0	<u>+750</u>	<u>+300</u> (type I) <u>+60</u> (type II)

Table 2 Capacity of Displacement Transducers

DISPLACEMENT TRANSDUCERS (DLT)

Type	Number of DLT	Full Stroke (mm)	Sensitivity
Strain Gage	6	+300	0.1 mm
	40	+200	
	20	+100	0.01 mm
	150	+50	
Inductive	20	+12.5	0.002 mm
	20	+500	
	2	+300	
	2	+200	0.5 percent of full range
	4	+100	
	2	+50	
Digital	3	+1000	0.01 mm
	5	+500	
	3	+50	0.001 mm
	2	+25	
	2	+12.5	
	1	+5.0	

Table 3 Capacity of Data Acquisition Units

DATA ACQUISITION SYSTEM

1. Static Strain Data Acquisition System	
Number of channels:	700
Number of scanning boxes:	3
Number of strain measuring units:	2
Scanning time:	0.1 sec./channel
Measuring range:	$\pm 30,000 \times 10^{-6} \mu$
2. Dynamic Strain Data Acquisition System	
a. for digitized data	
Number of channels:	30
Number of bridge boxes:	3
Number of signal conditioners:	30
Number of low path filters:	30
Scanning time:	50 $\mu$ sec./channel
Measuring range:	$\pm 30,000 \times 10^{-6} \mu$
Maximum frequency measurement:	5,000 Hz
b. for analog data	
Number of data recorders:	14

Table 4 Large Scale Tests Conducted at Laboratory

	Type of Structure	Specimen Plan Area (m <sup>2</sup> )	Specimen Height (m)	Scale Ratio	Type of Loading	Objectives	Test Period	Ref. #
1	Subassemblage of 3D Truss System	72	4.5	full	Static Vert. Load	Ultimate Capacity of Space Frame	Sept. 1978 to Jan. 1979	4
2	RC Prefabricated Building	68.5	7.55 (3 story)	full	Static Hori. Load	Seismic Behavior of RC Prefabricated Building	Aug. 1978 to Feb. 1979	5
3	2 Story Steel Braced Frame	7.5	5.0 (2 story)	1/3	Earthquake Load	Evaluation of PSD Test Technique	April 1979 to Sept. 1979	6
4	RC Prefabricated Panel Building	170.5	15.15 (5 story)	full	Static Hori. Load	Seismic Behavior of RC Prefabricated Panel Building	June 1979 to March 1980	7
5	Subassemblage of RC Coupled Shear-Wall	34.7	6.42 (4 story)	1/2	Static Hori. Load	Seismic Behavior of RC Coupled Shear-Wall	Dec. 1979 to March 1980	8
6	2 Story RC Planar Frame	12.0	6.75 (2 story)	2/3	Earthquake Load	Seismic Behavior of RC Frame	Oct. 1979 to Feb. 1980	9
7	2 Story RC Frame	3.0	3.9 (2 story)	1/2	Earthquake Load	Evaluation of PSD Test Technique	July 1980 to Aug. 1980	10
8	4 Story RC Frame	21.0	8.23 (4 story)	2/3	Earthquake Load	Evaluation of PSD Test Technique	Dec. 1980 to June 1980	11
9	7 Story RC Building	272.0	23.0 (7 story)	full	Earthquake Load	Seismic Behavior of RC Building with Shearwall	Sept. 1980 to Jan. 1982	12
10	Subassemblage of Steel Frame with K-Braces	26.3	5.6 (3 story)	1/2	Static Hori. Load	Seismic Behavior of K-Braces in Steel Frame	April 1982 to Nov. 1982	13
11	2 Story Prestressed Concrete Frame	7.8	3.5 (2 story)	1/3	Static Hori. Load	Seismic Behavior of Prestressed Concrete Frame	April 1982 to Aug. 1982	14
12	5 Story Steel Braced Frame	2.0	5.0 (5 story)	1/3	Earthquake Load	Evaluation of PSD Test Technique	May 1982 to Nov. 1982	15



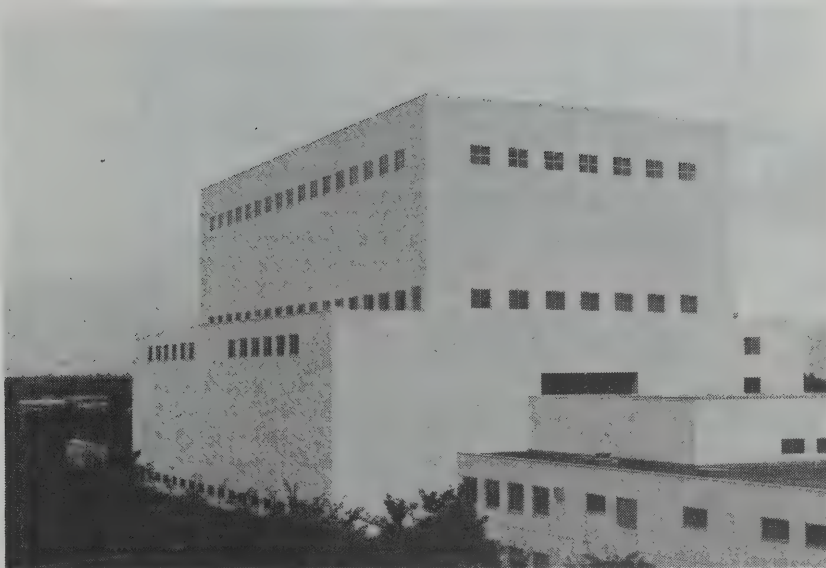


Fig. 1 Large Scale Test Laboratory of Building Research  
Institute, Ministry of Construction

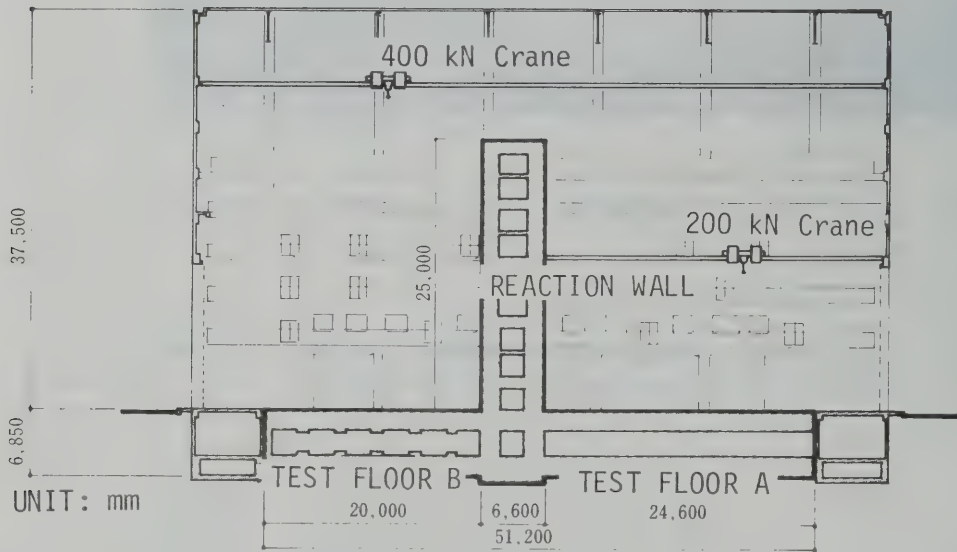
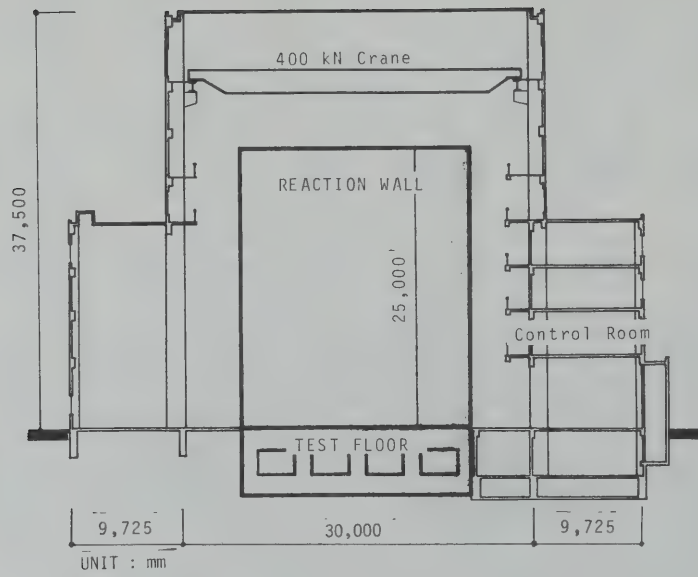


Fig. 2 Elevation of Laboratory

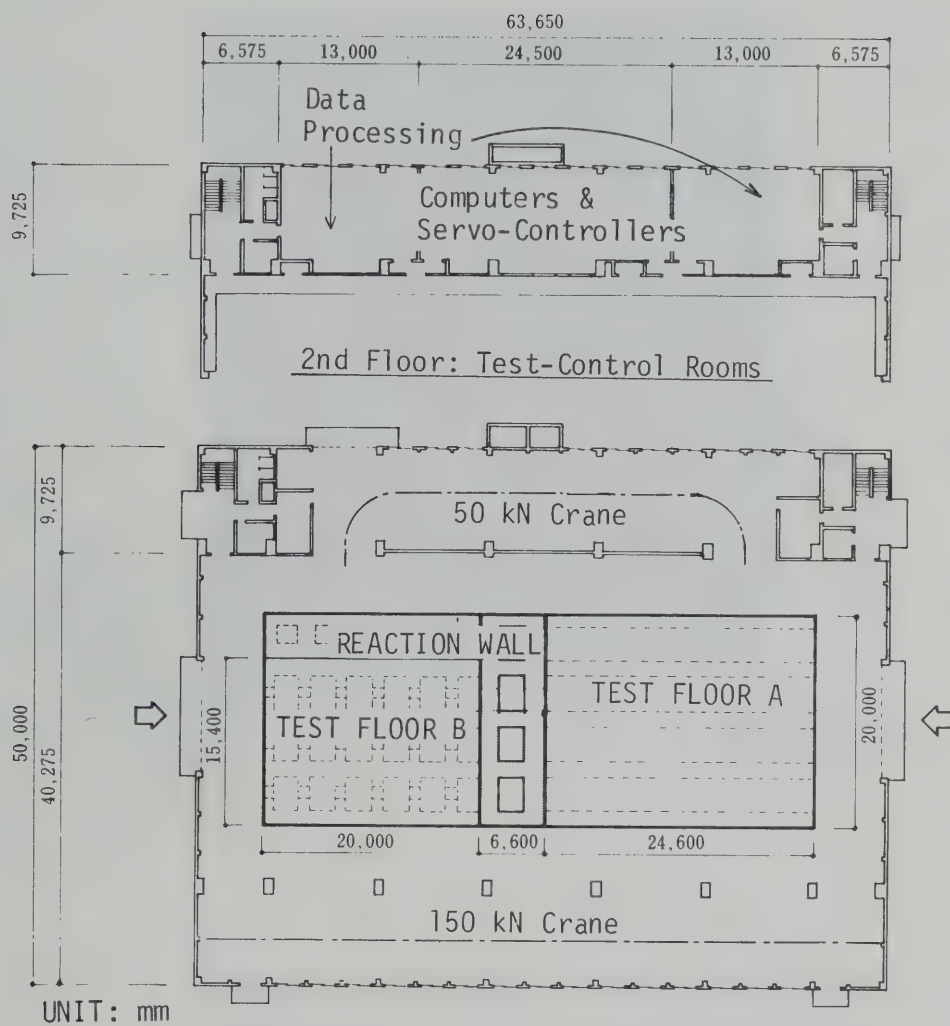


Fig. 3 Plan of Laboratory

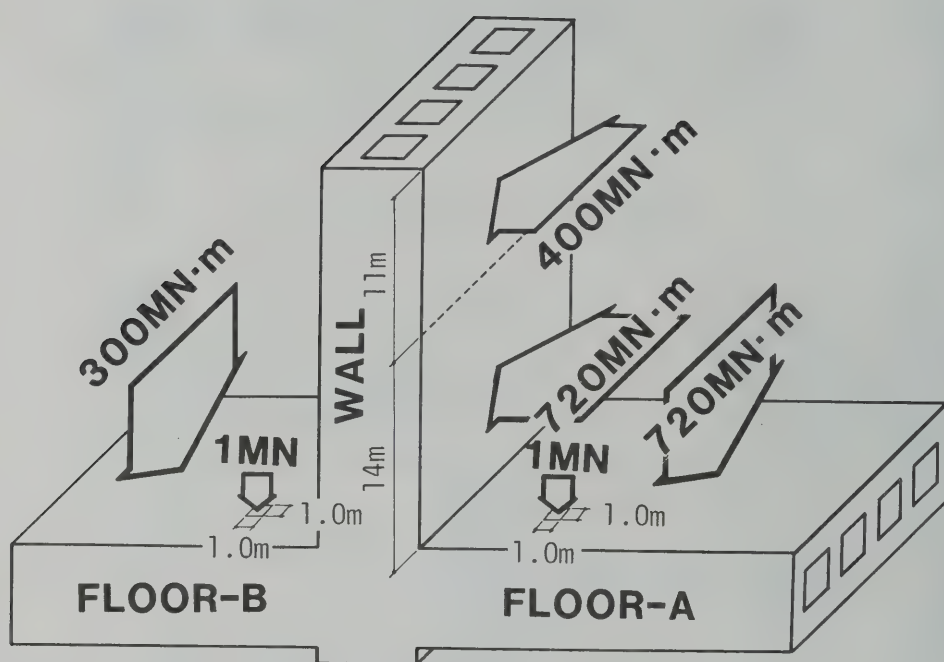


Fig. 4 Floor and Wall Load Carrying Capacity

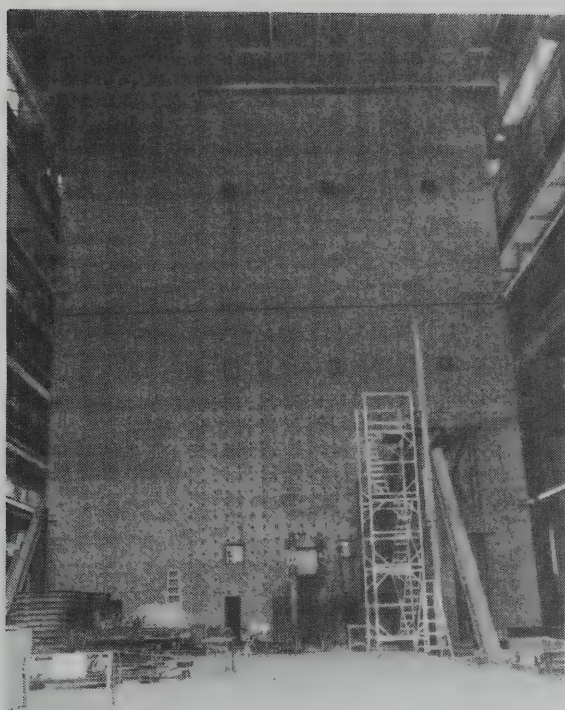
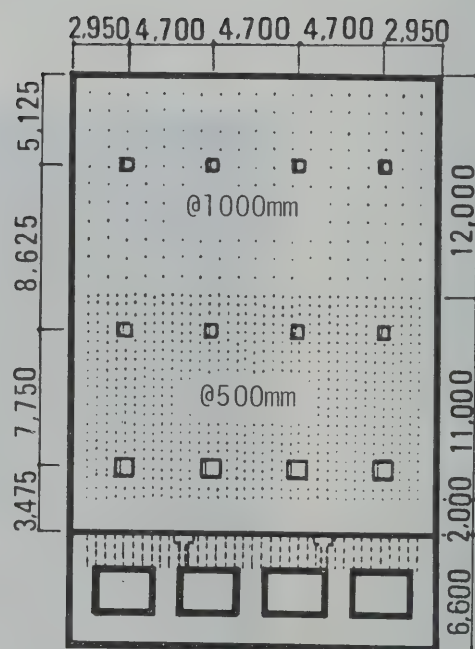
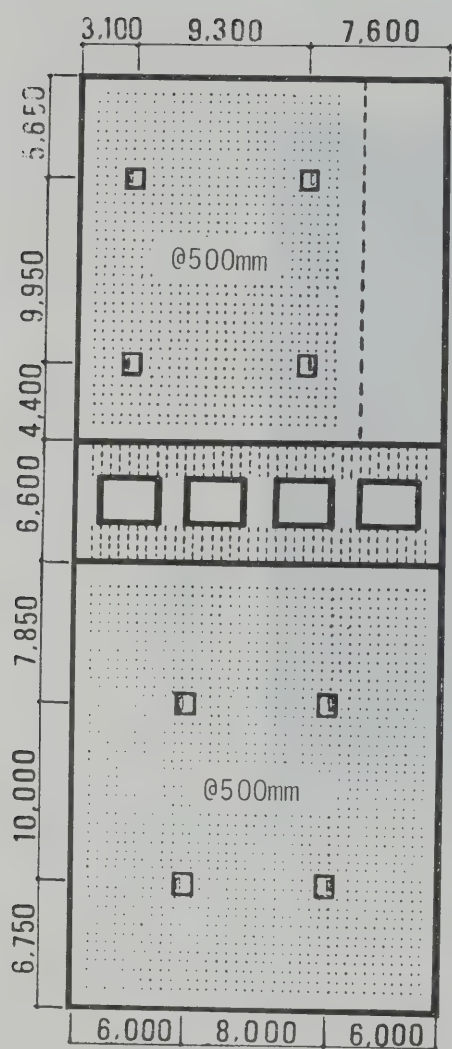


Fig. 5 Reaction Wall (25m x 20m x 6.6m)





□ Port block for Actuators

• Anchor hole

(Unit : mm)

Fig. 6 Dimension of Test Floor and Reaction Wall

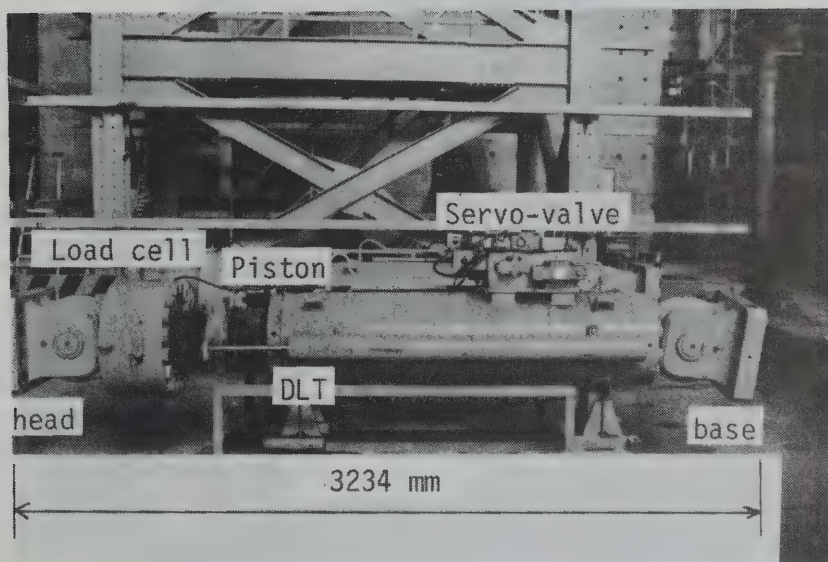


Fig. 7 JB Type Actuator (for Static Loading)

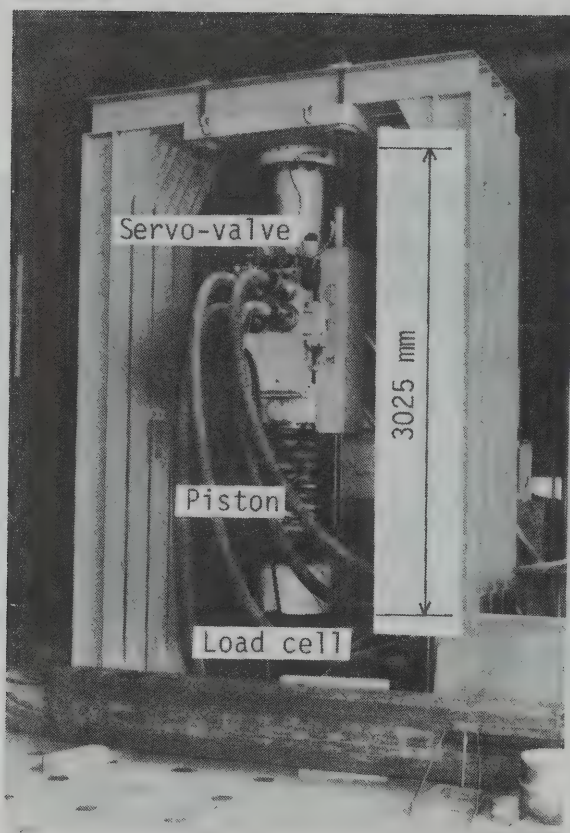


Fig. 8 JA Type Actuator (for Dynamic Loading)

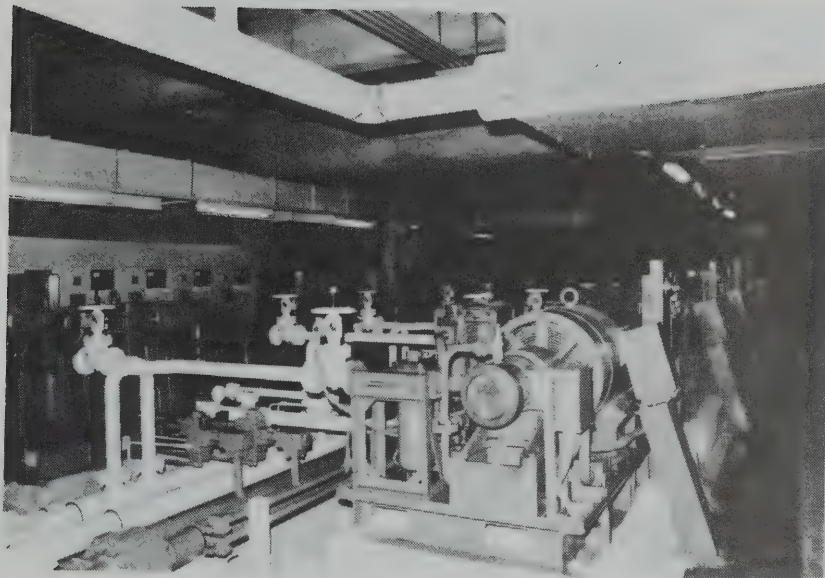


Fig. 9 Hydraulic Pump Unit at the Basement of Laboratory

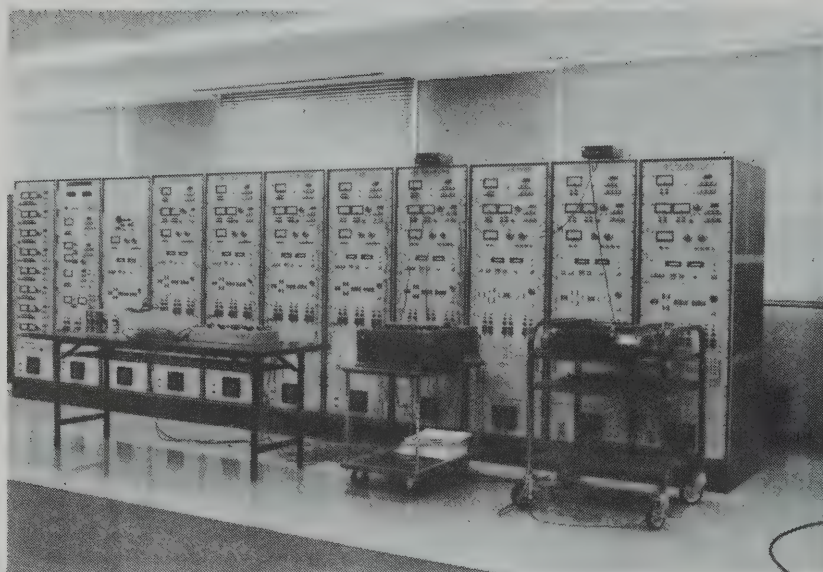


Fig. 10 Servo - Controllers in Control Room



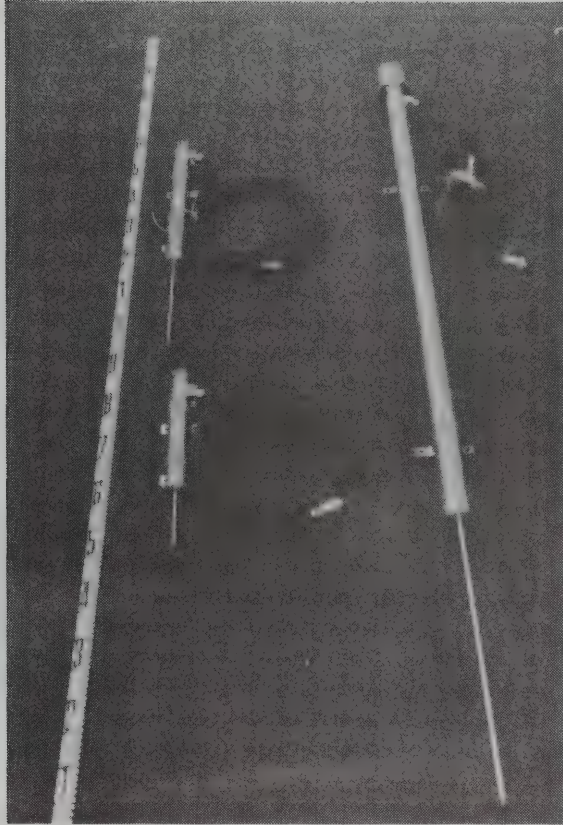


Fig. 11 Analog Type Displacement Transducers

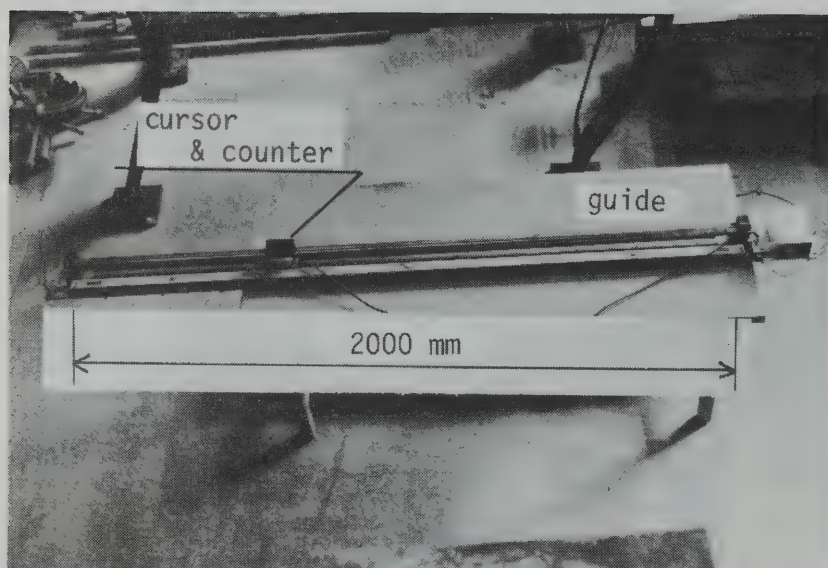


Fig. 12 Digital Type Displacement Transducer

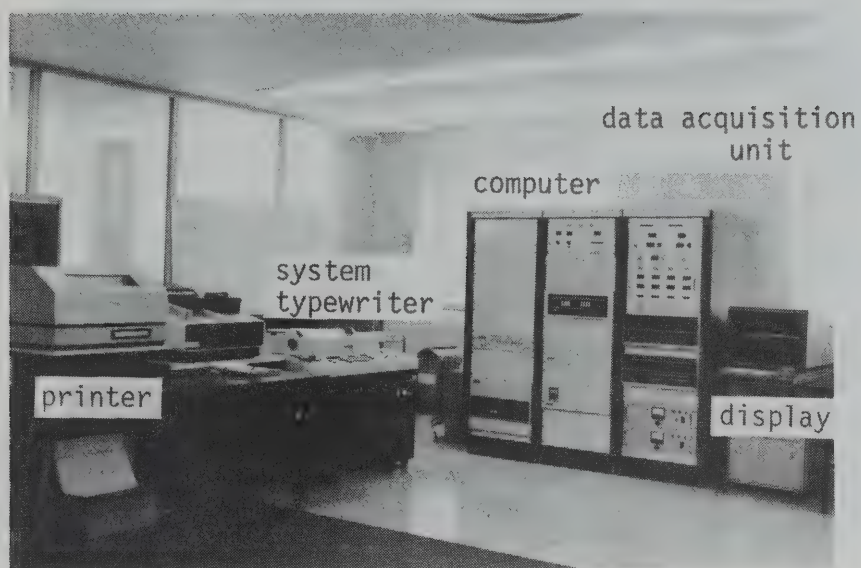


Fig. 13 Data Processing System

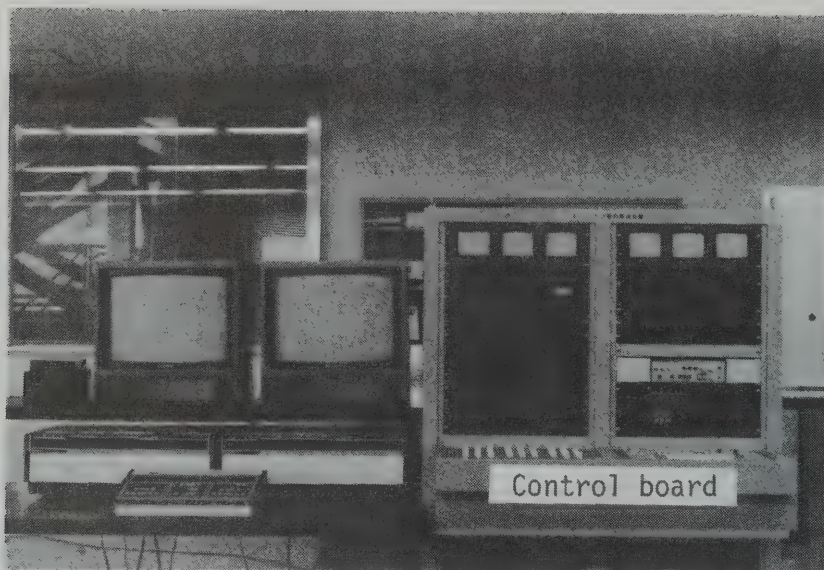


Fig. 14 Test Monitoring Unit (Displays and Video Recorders)



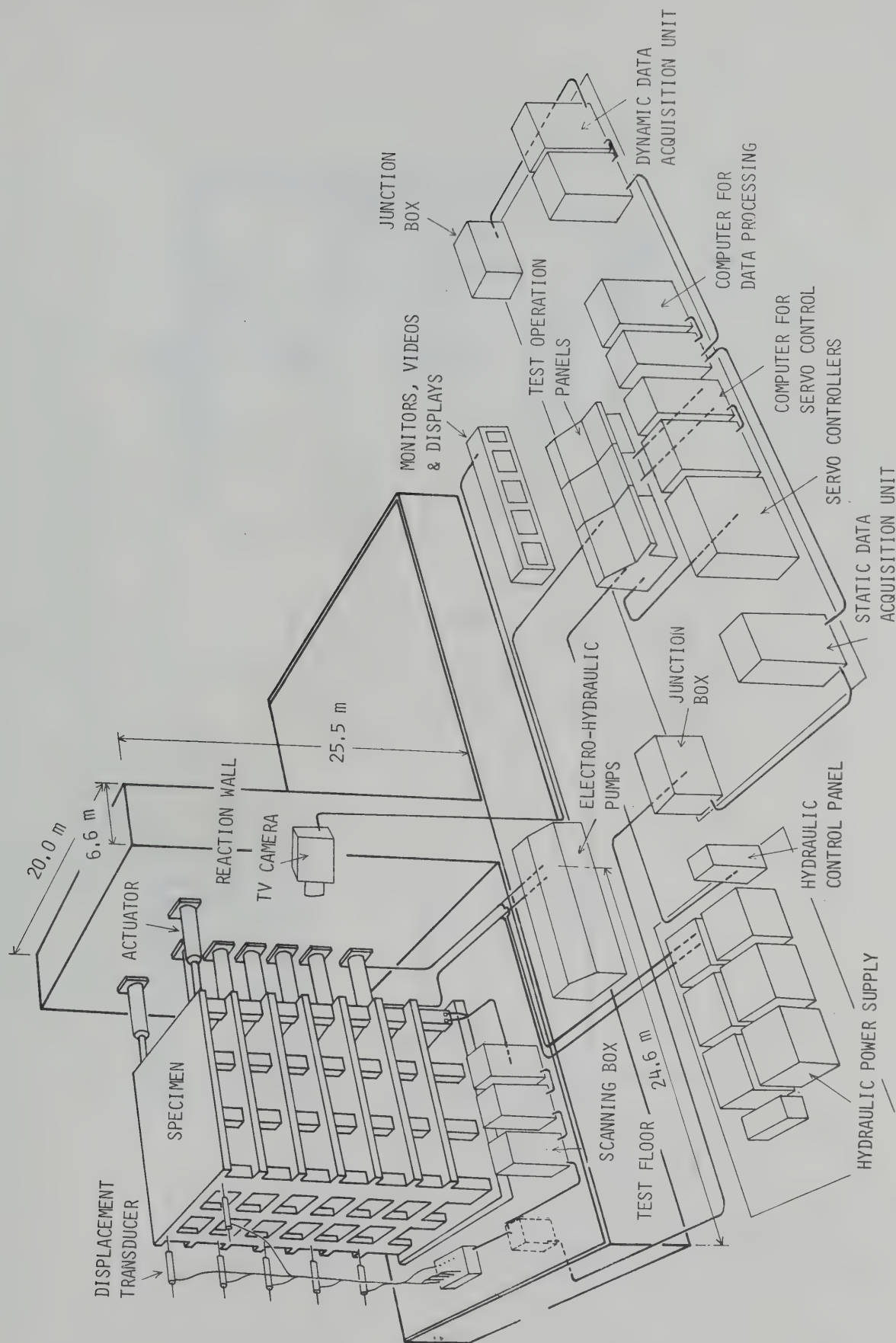


Fig. 15 Computer Supervised Closed Loop Testing System



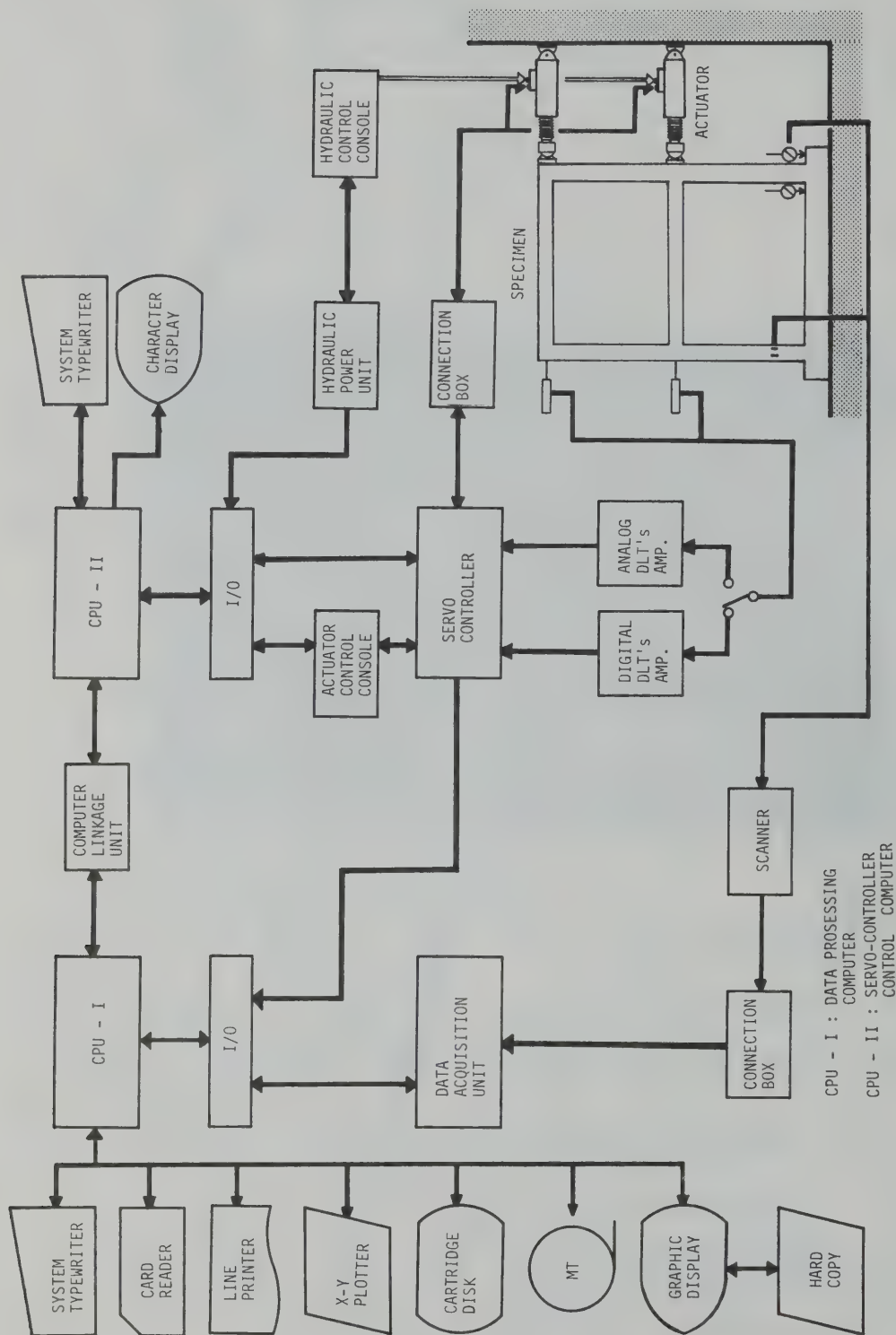


Fig. 16 Flow Diagram of Computer On-Line Testing

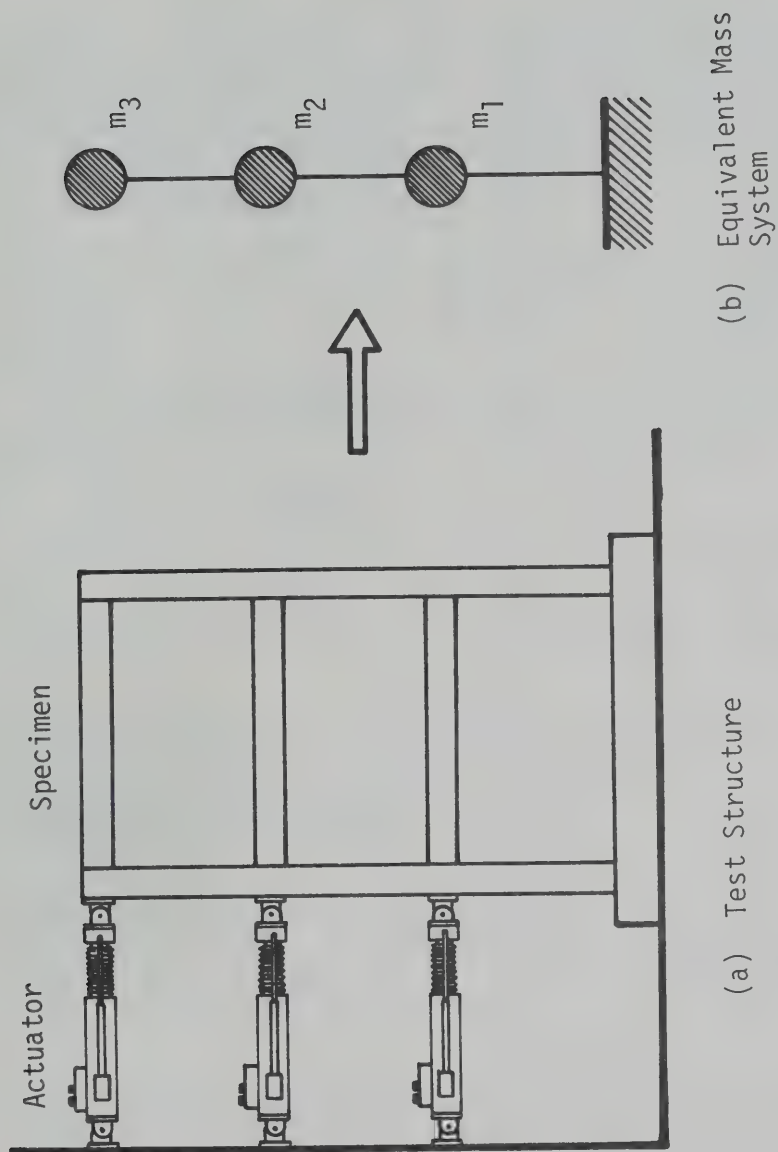


Fig. 17 Representation of Pseudo - Dynamic Testing

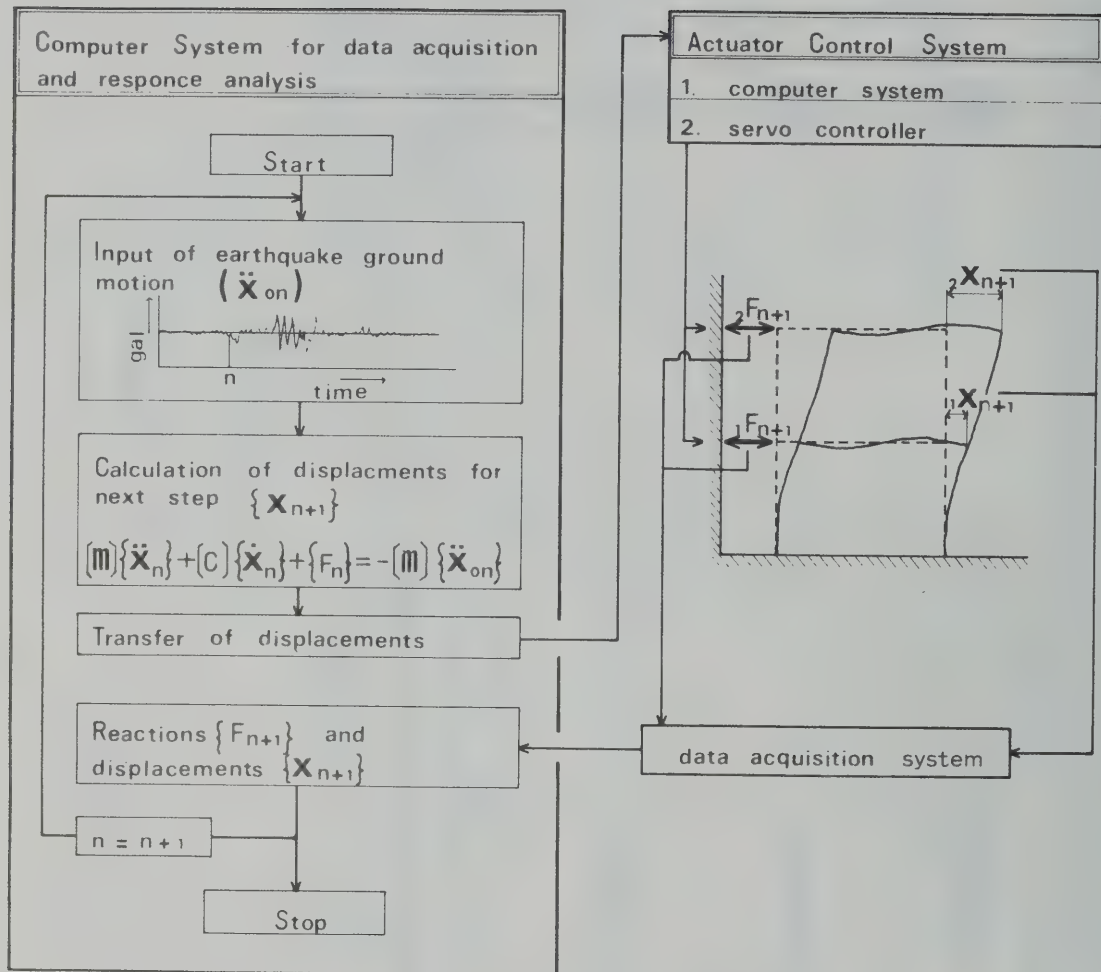


Fig. 18 Flow Diagram of Pseudo - Dynamic Test Operation

## REFERENCES

1. Tanaka H., "A Computer-Actuator On-Line System for Non-Linear Earthquake Response Analysis of Structures," Seisan Kenkyu, Institute of Industrial Science, The University of Tokyo, Vol. 27, No. 12, December 1975, pp.15-19. (in Japanese)
2. Bathe, K. J. and Wilson E. L., "Numerical Methods in Finite Element Analysis," Prentice-Hall Inc., Englewood Cliffs, New Jersey, 1976.
3. Leech, J. W., Hsu, P. T. and Mack, E. W., "Stability of a Finite Difference Method for Solving Matrix Equations," AIAA Journal, Vol. 3, No. 11, November 1965, pp.2172-2173.
4. Kimura, M., "An Experiment of a Space Truss Structure under Cyclic Horizontal Loading," Annual Transactions of Architectural Institute of Japan, September 1979, pp.953-954. (in Japanese)
5. Nakata, S., Okamoto, S. and Kaminosono, T., "Full Scale Earthquake Loading Test on Precast Wall Frame Housing," Annual Transactions of Architectural Institute of Japan, September 1979, pp.1449-1450. (in Japanese)
6. Okamoto, S., Kubota, T., Yamanouchi, H., Hiraishi, H., Kaminosono, T. and Kato, H., "Empirical Seismic Analysis on a Full-Scale Model Using Pseudo-Dynamic Test Method," Annual Transactions of Architectural Institute of Japan, September 1980, pp.697-700. (in Japanese)
7. Hirose, M., Goto, T., Yoshimura, M. and Hiraishi, H., "Full-Scale Experimental Study on Aseismic Performance of Medium-Rise RC Wall Structure," Research Paper of the Building Research Institute, Ministry of Construction, March 1981.
8. Hiraishi, H., Isoishi, H., Yoshimura, M. and Nakata, S., "US-Japan Cooperative Research Program Utilizing Large Scale Testing Facilities, Part 4 - Joint Assembly Tests, Shear Wall - Beam," Annual Transactions of Architectural Institute of Japan, September 1980, pp.1661-1662. (in Japanese)
9. Kubota, T., Okamoto, S. and Kaminosono, T., "Empirical Seismic Analysis on a Full-Scale Model Using Pseudo-Dynamic Method, Part 4 - Test on a Reinforced Concrete 2-Story Full-Scale Model," Annual Transactions of Architectural Institute of Japan, September 1980, pp.701-702. (in Japanese)
10. Kaminosono, T., Kubota, T., Kato, H. and Isoishi, H., "Correlation Study Between Shaking Table Tests and Pseudo-Dynamic Test by Half Scale R.C. Models, Part 3 - Dynamic Tests," Annual Transactions of Architectural Institute of Japan, September 1981, pp.883-884. (in Japanese)
11. Unpublished.

12. Okamoto, S., Nakata, S., Kitagawa, Y., Yoshimura, M. and Kaminosono, T., "A Progress Report on the Full-Scale Seismic Experiment of a Seven Story Reinforced Concrete Building - Part of the US-Japan Cooperative Program," Research Paper of the Building Research Institute, Ministry of Construction, March 1982.
13. to be published soon.
14. to be published soon.
15. to be published soon.



# 建築研究所実大構造物実験棟における大型実験手法の開発

岡	本		伸 <sup>*1</sup>
上	之	蘭	隆志 <sup>*2</sup>
中	島	正	愛 <sup>*2</sup>
加	藤	博	人 <sup>*3</sup>

BRI Research Paper No.101

建設省建築研究所

近年、建築構造物の挙動に関する研究は目覚しく、事実建築部材の実験や縮小モデルによる構造実験は世界中で実施され、また電子計算機の発達と相俟って構造解析も数多く行なわれている。これら実験や解析の結果は種々の設計規準に採り入れられているが個々の結果が全体の設計体系に正しく組み込まれているかについては議論の余地がある。例えばある部材実験の結果を全体設計に反映させるためには材端条件の取り扱いなど多くの工学的判断が必要であり、また構造解析に際しては種々の仮定が予め設定されなければならない。これら判断や仮定の妥当性を検証し、全体としての構造物の挙動を正しく評価するためには、適宜建築構造物を実際に近い規模で実験することが望ましい。

本論では昭和53年に完成した建築研究所実大構造物実験棟の概要を報告する。本実験棟では、大型構造物を効率よく実験するために、数々の装置を導入した新しい実験手法を開発している。その内本論では(1)実験棟の規模、反力壁の容量、可能な試験体規模、(2)サーボ制御による加力ジャッキの容量と作動機構、(3)計測システムと大型実験用計測装置、(4)電子計算機によるオンライン実験制御システムについて詳述する。また最後に昭和57年11月までに本実験棟で実施された大型実験の概要を紹介する。

..

..

\* 1 第四研究部長  
\* 2 第四研究部住宅建設研究室研究員  
\* 3 第四研究部住宅建設研究室研究補助員





## Research Papers-Recent Issues

- No.76 Y. Matsushima: Random Response of Single-degree-of-freedom System with Bilinear Hysteresis, September, 1977, 28 pp.
- No.77 A. Baba: Drying Shrinkage Mechanism of Building Materials, March, 1978, 79 pp.
- No.78 K. Hayakawa: The Management of Land as an Environmental Resource, March, 1978, 40 pp.
- No.79 T. Tanaka: A Model on Fire Spread in Small Scale Buildings, September, 1978, 76 pp.
- No.80 Y. Aoki: Studies on Probabilistic Spread of Fire, November 1978, 52 pp.
- No.81 F. Saito: Experimental Study of Compartment Fire Using Model Boxes, July, 1979, 50 pp.
- No.82 Y. Matsushima: Random Response of Single-degree-of-freedom System with General Slip Hysteresis, July, 1979, 37 pp.
- No.83 Y. Hasemi: Flashover Criteria of Compartment Fire - Theory on Zero Order Reaction System -, August, 1979, 26 pp.
- No.84 T. Tanaka: A Model on Fire Spread in Small Scale Buildings, 2nd Report, March, 1980, 63 pp.
- No.85 Y. Ishiyama: Review and Discussion on Overturning of Bodies by Earthquake Motions, June, 1980, 115 pp.
- No.86 S. Watanabe: Planning History in Japan - A State of the Art Survey -. August, 1980, 36 pp.
- No.87 Y. Sugimura: Participation Factor of Horizontal Force Applied to Pile Foundation, March, 1981, 33 pp.
- No.88 Y. Hasemi: Mathematical Basis for Physical Evaluation on Flashover, March, 1981, 41 pp.
- No.89 T. Wakamatsu: A Quantitative Evaluation of Smoke Safety, March, 21 pp.
- No.90 S. Watanabe: Metropolitanism as a Way of Life, March, 1981, 52 pp.
- No.91 M. Hirose, T. Goto, M. Yoshimura, H. Hiraishi: Full-Scale Experimental Study on Aseismic Performance of Medium-Rise RC Wall Structure. March, 1981, 28 pp.
- No.92 Y. Yamazaki: Inelastic Torsional Response of Structures Subjected to Earthquake Ground Motions. March, 1981, 102 pp.
- No.93 S. Kose: Study of Accidents Associated with Building Feature. March, 1982, 38 pp.
- No.94 S. Okamoto, S. Nakata, Y. Kitagawa, M. Yoshimura, T. Kaminosono: A Progress Report on the Full-Scale Seismic Experiment of a Seven Story Reinforced Concrete Building - Part of the US-Japan Cooperative Program, March, 1982, 92 pp.
- No.95 Y. Hasemi: Characterization of the Intermittent Flaming Region of the Upward Current Above Diffusion Flames. March, 1982, 33 pp.
- No.96 Y. Morishita: Statistical Analysis of Fire Spread. May, 1982, 17 pp.
- No.97 T. Fukushima: Deterioration Model of Polymeric Materials with Special Attention to Age and Deterioration Depth. December, 1982, 30 pp.
- No.98 H. Hiraishi, M. Yoshimura, H. Isoishi, S. Nakata: Planer Tests on Reinforced Concrete Shear Wall Assemblies - U.S.-Japan Cooperative Research Program-, January, 1983, 63 pp.
- No.99 S. Nakata: Tests of Reinforced Concrete Beam-Column Assemblages -U.S.-Japan Cooperative Research Program-, March, 1983, 111 pp.
- No.100 Y. Aoki: Assessment of an Urban Safety Evaluation Function. March, 1983, 16 pp.
- No.101 S. Okamoto, T. Kaminosono, M. Nakashima, H. Kato: Techniques for Large Scale Testing at BRI Large Scale Structure Test Laboratory. March, 1983, 38 pp.

Address for Communication

BUILDING RESEARCH INSTITUTE  
MINISTRY OF CONSTRUCTION

No.1 TACHIHARA, OH-HO-MACHI, TSUKUBA-GUN, IBARAKI-PREF

JAPAN

Q.690  
K336

ISSN 0453-4972

BRI Research Paper No.102

# DEVELOPMENT OF PROCEDURE FOR CALCULATING ROOM AIR TEMPERATURES INCLUDING EFFECT OF NATURAL VENTILATION

by  
Yuzo Sakamoto

Building Research Institute

Ministry of Construction

October 1983

THE LIBRARY

UNIVERSITY OF  
TAT 112





## FOREWORD

This paper describes the result of the research on the calculation procedure for room air temperatures including effect of natural ventilation. This research had been made as part of a development project conducted by the Ministry of Construction for 1977-1981, entitled, "Development of Total Energy Conservation System for Dwellings".

In Japan, energy conservation for dwellings is one of the major national problems. The method of estimating heating and cooling loads in a dwelling house can be regarded as one of useful fundamental tools for this problem.

In this paper, taking account of the structure and the use of dwelling houses in Japan, the procedure for calculating room air temperatures is formulated where natural ventilation takes place. Validity of this procedure has been checked by comparing the calculated temperatures with the observed ones.

The computer program of heat loads made according to this calculation procedure was named BRIMAP and has been used to develop a design system and a simplified evaluation system for energy conservation in dwellings. I would like to express my hope for the development of research on this field and acknowledge with appreciation those who have supported on this study.

October, 1983

K. Kamimura, Director General  
Building Research Institute



DEVELOPMENT OF PROCEDURE FOR CALCULATING ROOM AIR TEMPERATURES  
INCLUDING EFFECT OF NATURAL VENTILATION \*

by

Yuzo SAKAMOTO \*\*

BUILDING RESEARCH INSTITUTE

MINISTRY OF CONSTRUCTION

Tsukuba, Ibaraki, Japan

ABSTRACT

Natural ventilation has an important effect on thermal behavior of a dwelling house in Japan. A calculation procedure was developed to predict the room air temperature and the heat load of Japanese housing. It includes the process to calculate natural ventilation precisely and quickly. The room air temperatures of two experiment houses were predicted by this procedure. The prediction was compared with the observation to evaluate the accuracy and the validity of this procedure. The agreement between both is good and satisfactory.

---

\* This paper was reproduced from the manuscript prepared for the Fourth International Symposium on the Use of Computers for Environmental Engineering Related to Buildings, 1983, Tokyo.

\*\* Chief Research Member, Building Services Division





## CONTENTS

1. INTRODUCTION	1
2. MATHEMATICAL PROCEDURE	2
2-1 PROCEDURE FOR CALCULATING ROOM AIR TEMPERATURES OR HEAT LOADS	2
(1) Room Heat Balance Equation	2
(2) Thermal Interaction with the Ground	4
(3) System of Equations of Room Heat Balance and its Solution	5
2-2 PROCEDURE FOR CALCULATING NATURAL VENTILATION	7
(1) Development of a New Approximate Procedure	7
(2) Net Volume Flow of Air	7
(3) System of Equations of Ventilation Network and its Solution	8
(4) Calculation of Volume Flow Rate of Air	11
3. VALUATION OF DEVELOPED PROCEDURE	13
(1) Purpose and Process	13
(2) Results	16
4. CONCLUSIONS	18
ACKNOWLEDGEMENTS	19
REFERENCES	19



## 1. INTRODUCTION

Generally speaking, the dwelling house of Japan is air-conditioned partially and intermittently. It is very rare that rooms are air-conditioned all day long. Air-conditioning is usually performed only in the room used. Furthermore, natural ventilation (including infiltration in this paper) has an important effect on thermal behavior of Japanese housing. The typical example is seen for a wooden house built by the conventional construction method of Japan. Namely, because its walls, floors, windows, and other components have many cracks, the heat loss by infiltration is considerable. In addition, windows and doors are opened during cool summer nights, even if an air condition system is installed. This paper describes a calculation procedure developed to predict room air temperatures or room heat loads in the dwelling house of Japan, which has the features mentioned above. The actual examples of prediction by this procedure are shown and compared with the observation to check accuracy and validity.

Air temperatures or heat loads of multi-room houses can be calculated by solving the system of equations of room heat balance. It is possible to formulate the multi-room problem using the response factor method<sup>1)</sup>. This formulation and its solution have been presented by Eguchi<sup>2)</sup>. The calculation procedure developed in this work is based on the same formulation as his, but includes the precise calculation process for natural ventilation and for thermal interaction with the ground on new assumptions and approximations.

This calculation procedure emphasizes the importance of natural ventilation in the calculation of thermal behavior in dwelling houses. Natural ventilation has tended to be assumed as a steady quantity in these problems. However, in this procedure, it is treated as unsteady and the precise calculation is performed for its effect. Volume flow rate of air by natural ventilation is calculated by solving the system of equations of the ventilation network constituted on the basis of the crack method. An approximate method is adopted to solve this system of equations quickly.

## 2. MATHEMATICAL PROCEDURE

### 2-1 PROCEDURE FOR CALCULATING ROOM AIR TEMPERATURES OR HEAT LOADS

#### (1) Room Heat Balance Equation

Various heat transfer processes take place inside a room. If the heat exchanges by radiation among the surfaces enclosing the room can be neglected, the heat gain or loss of room air can be divided into five types as shown in Fig.1. When the number of the present room is "i", these types are described as follows:

$Q_{ij}$  = net heat gain by transmission through components located between i and j, such as wall and a floor

$H_{ij}$  = net heat gain by ventilation and infiltration between i and j

$G_i$  = net heat loss by transmission to the component fixed on the ground

$S_i$  = net heat loss by storage of heavy objects, such as furniture and a column

$E_i$  = heat gain by convection from appliances, human bodies, and so forth.

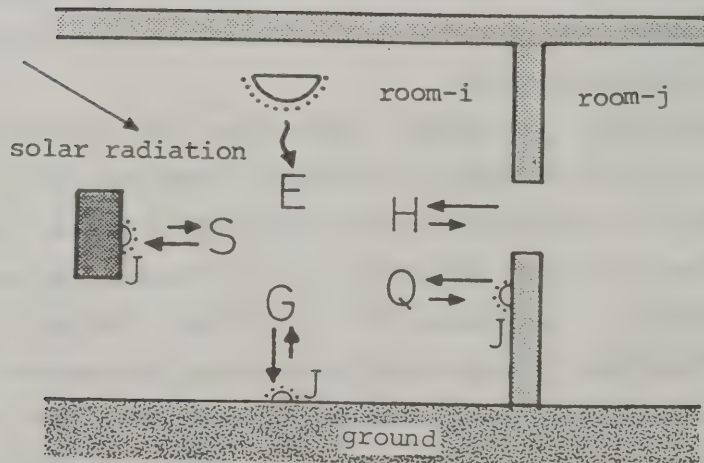


Fig.1 Five Types of Heat Gain or Loss in a Room

A heat balance equation for air of i is given by,

$$C_i (\theta_i^n - \theta_i^{n-1}) / \Delta t = \sum_{j=1}^M (Q_{ij}^n + H_{ij}^n) - G_i^n - S_i^n + E_i^n \quad (1)$$

Where

$\theta_i$  = air temperature of i

$C_i$  = heat storage capacity of air volume of i

M = number of rooms including outdoor spaces, and the superscript n indicates time  $n\Delta t$  ( $\Delta t$  is time increment).

The net heat gain by ventilation and infiltration is represented,

$$H_{ij}^n = c\gamma (V_{ij}^n \theta_j^n - V_{ji}^n \theta_i^n) \quad (2)$$

where

$V_{ij}$  = volume flow rate from j into i by ventilation and infiltration

$c\gamma$  = heat storage capacity of air per unit volume.

According to the response factor method,

$$Q_{ij}^n = \sum_k A_{ijk} \left[ \sum_{m=0}^{\infty} \{ Y_{ijk}^m (\theta_j^{n-m} + J_j^{n-m}/\alpha) - Z_{ijk}^m (\theta_i^{n-m} + J_i^{n-m}/\alpha) \} + J_i^n \right] \quad (3)$$

$$S_i^n = \sum_k AI_{ik} \left\{ \sum_{m=0}^{\infty} (ZI_{ik}^m - YI_{ik}^m) (\theta_i^{n-m} + J_i^{n-m}/\alpha) - J_i^n \right\} \quad (4)$$

where

$A_{ijk}$  = area of a component k between i and j

$Y_{ijk}$  and  $Z_{ijk}$  = thermal response factors of this component

$AI_{ik}$  = surface area of a heavy object k inside i

$YI_{ik}$  and  $ZI_{ik}$  = thermal response factors of this object

$J_i$  = mean radiation absorbed on the surfaces of components and objects inside i

$\alpha$  = overall surface conductance.

If the heat storage capacity of the component is negligible,

$$Y_{ijk}^0 = Z_{ijk}^0 = K_{ijk}$$

$$Y_{ijk}^m = Z_{ijk}^m = 0, \text{ for } m \geq 1$$



where  $K_{ijk}$  is the total heat transmission coefficient of the component. Notice here that  $J_i$  includes solar radiation and radiant energy from appliances and others, but that long wave radiation emitted from the surfaces enclosing  $i$  and the objects inside  $i$  is not included. The solar radiation incident on the arbitrary surface of the outside component can be calculated from normal direct radiation and sky radiation, both of which are regarded as input meteorological data. Direct solar gain in a room is calculated from the solar radiation calculated above by taking account of the shading effects of window glass and shades. If the room  $i$  is an outdoor space,  $J_i$  also includes the contribution of nocturnal radiation, which is treated as input data. The nocturnal radiation can be evaluated from cloud amount and atmospheric vapor pressure according to Yamamoto's empirical formula<sup>3)</sup>, if the observed one is not available. Thus the same radiation data is input in this procedure as in the program of HASP<sup>4)</sup> developed by the Society of Heating, Air-Conditioning and Sanitary Engineers of Japan.

## (2) Thermal Interaction with the Ground

The net heat loss by transmission to the component fixed on the ground can be assumed as follows.

If daily fluctuations are neglected, natural soil temperature can be approximated by,

$$\theta G(z, t) = \theta A \cdot \exp(-\beta z) \cdot \cos(2\pi t/T_0 - \beta z - \phi) + \theta M \quad (5)$$

where

$\theta G$  = natural soil temperature

$\theta A$  = annual amplitude of  $\theta G$  at  $z=0$

$\theta M$  = annual mean of  $\theta G$

$z$  = depth from the ground surface

$t$  = time

$$\beta = \sqrt{\pi/(aT_0)}$$

$T_0$  = period of  $\theta G$  = a year

$a$  = thermometric conductivity of soil

$\phi$  = phase difference.

If it is assumed that the temperature under the building is equal to  $\theta G$  below  $z=d$ ,  $G_i$  is given as:

$$G_i^n = \zeta_i \{ ZG_i^0 (\theta_i^n - \theta S^n) - J_i^n + q_i^n + \sum_{m=1}^{\infty} ZG_i^m \theta E_i^{n-m} \} \quad (6)$$

where

$$\zeta_i = \alpha AG_i / (ZG_i^0 + \alpha)$$

$$\theta S^n = \theta G(0, n\Delta t)$$

$$q_i^n = \lambda_i \sqrt{\pi/a_i T_0} \cdot \theta A \cdot \cos(2\pi n\Delta t/T_0 - \phi + \pi/4)$$

$$\theta E_i^n = \theta_i^n - \theta S^n - G_i^n / (\alpha AG_i)$$

$AG_i$  = surface area of the component fixed on the ground inside  $i$

$ZG_i$  = thermal response factor of this component  
(but surface boundary layer is excluded and component's thickness is  $d$ )

$\lambda_i$  = mean thermal conductivity of this component

$a_i$  = mean thermometric conductivity of this component.

### (3) System of Equations of Room Heat Balance and its Solution

Substitution of equation (2), (3), (4), and (6) in equation (1) and collection of the unknown air temperatures on the left-hand side give:

$$\sum_{j=1}^N \xi_{ij}^n \theta_j^n = \eta_i^n \quad (7)$$

where

$$\xi_{ij}^n = -(\sum_k A_{ijk} Y_{ijk}^0 + c V_{ij}^n), \text{ for } i \neq j$$

$$\xi_{ii}^n = C_i / \Delta t + \sum_{j=1}^M (\sum_k A_{ijk} Z_{ijk}^0 + c V_{ji}^n) + \zeta_i ZG_i^0 + \sum_k A I_{ik} (Z I_{ik}^0 - Y I_{ik}^0)$$

$$\eta_i^n = \sum_{j=1}^M \sum_k A_{ijk} \{ \sum_{m=1}^{\infty} Y_{ijk}^m (\theta_j^{n-m} + J_j^{n-m}/\alpha) + Y_{ijk}^0 J_j^n / \alpha \} + \zeta_i (ZG_i^0 \theta S^n + J_i^n - q_i^n - \sum_{m=1}^{\infty} ZG_i^m \theta E_i^{n-m})$$

$$- \sum_k A I_{ik} \{ \sum_{m=1}^{\infty} (Z I_{ik}^m - Y I_{ik}^m) (\theta_i^{n-m} + J_i^{n-m}/\alpha)$$

$$+ (Z I_{ik}^0 - Y I_{ik}^0) J_i^n / \alpha - J_i^n \} - \sum_{j=n+1}^M \xi_{ij}^n \theta_j^n + C_i \theta_i^{n-1} / \Delta t + E_i^n$$

$N$  = number of indoor rooms (indoor rooms are numbered from 1 to  $N$ ).

Because  $\xi_{ij}^n$  is square matrix of order  $N$ , equation (7) forms a system of linear equations in which the unknowns are the indoor air temperatures and can be solved by the successive over-relaxation method<sup>5)</sup>. The solution of equation (7) is natural temperature without air conditioning. On the other hand, if some rooms are air-conditioned, their sensible heat loads can be calculated as the residuals defined in the successive over-relaxation method while regarding their air temperatures as known.

## 2-2 PROCEDURE FOR CALCULATING NATURAL VENTILATION

### (1) Development of a new Approximate Procedure

Natural ventilation (including infiltration) arises as a result of pressure differences generated across openings and cracks by the action of external wind and by buoyancy due to air temperature differences. However, the relationship between air flow rate by ventilation and pressure difference is nonlinear for an opening or a crack. Therefore, it will take much computer time to calculate the amount of natural ventilation in each room hour by hour, if the system of equations of ventilation remains nonlinear. In this paper, a new approximate computer procedure for solving the system of equations of ventilation is developed and applied to the calculation of natural ventilation. It is expected that this procedure has an appropriate accuracy and an acceptable computer time for the practical computation of air-conditioning loads.

### (2) Net Volume Flow of Air

In the notation of this section, attention must be paid to the omission of the superscript indicating the time point. Applying the crack method, the net volume flow rate  $v_{ijk}$  of air through an opening or a crack "k" located between i and j is approximately represented by,

$$v_{ijk} = \sigma_{ijk} \omega_{ijk} |\omega_{ijk}|^{n_{ijk}-1} \quad (8)$$

where the expressions of  $\sigma_{ijk}$ ,  $\omega_{ijk}$  and  $n_{ijk}$  are given in Table 1. The expression of a crack or an opening is introduced by the following approximation:

$$\begin{aligned} v_{ijk} &= \int_{z_{ijk}}^{z_{ijk}+L_{ijk}} \left\{ \frac{\sigma_{ijk}}{L_{ijk}} (\Delta P_{ij} - gz\Delta\rho_{ij}) \times |\Delta P_{ij} - gz\Delta\rho_{ij}|^{n_{ijk}-1} \right\} dz \\ &\approx \sigma_{ijk} \{ \Delta P_{ij} - gz\Delta\rho_{ij} (z_{ijk} + L_{ijk}/2) \} \\ &\quad \times |\Delta P_{ij} - g\Delta\rho_{ij} (z_{ijk} + L_{ijk}/2)|^{n_{ijk}-1} \end{aligned}$$

Though equation (8) is nonlinear in the relationship between  $v_{ijk}$  and  $\omega_{ijk}$ , it can be approximated by applying several linear relationships:

$$v_{ijk} = \sigma_{ijk}(m_{ijk}\omega_{ijk} + h_{ijk}) \quad (9)$$

where  $m_{ijk}$  and  $h_{ijk}$  have several values different in the range of  $\omega_{ijk}$  and for the value of  $n_{ijk}$  respectively. Here the term "range" means a range within which one of several linear relationships expressed by equation (9) is applied, and the number of ranges is equal to that of the relationships. Five linear relationships were applied to equation (8) for a value of  $n_{ijk}$  in the actual computer program.

### (3) System of Equations of Ventilation Network and its Solution

The balance equations of room air volume is described for the room "i" as follows:

$$\sum_{j=1}^M \sum_k v_{ijk} = 0 \quad (10)$$

Substitution of equation (9) in equation (10) and reference to the expression for  $\omega_{ijk}$  in Table 1 lead to the system of equations of the natural ventilation network in which pressures are unknown,

$$\sum_{j=1}^N \lambda_{ij} P_j = \mu_i \quad (11)$$

where

$$\lambda_{ij} = -v_{ij}, \text{ for } i \neq j$$

$$\lambda_{ii} = \sum_{j=1}^M v_{ij}$$

$$\mu_i = \sum_{j=1}^M \left( \sum_k \sigma_{ijk} h_{ijk} - g \Delta \rho_{ij} \sum_k \sigma_{ijk} \delta_{ijk} m_{ijk} \right) + \sum_{j=N+1}^M v_{ij} P_j$$

$$v_{ij} = \sum_k \sigma_{ijk} m_{ijk}$$

$$\delta_{ijk} = z_{ijk} \text{ or } z_{ijk} + L_{ijk}/2$$



Table 1 Expressions of  $\sigma_{ijk}$ ,  $\omega_{ijk}$ , and  $n_{ijk}$

	$\sigma_{ijk}$	$\omega_{ijk}$	$n_{ijk}$
horizontal crack	$a_{ijk} L_{ijk}$	$\Delta P_{ij} - g \Delta \rho_{ij} z_{ijk}$	$\frac{2}{3}$
vertical crack	$a_{ijk} L_{ijk}$	$\Delta P_{ij} - g \Delta \rho_{ij} (z_{ijk} + \frac{L_{ijk}}{2})$	$\frac{2}{3}$
opening	$\sqrt{\frac{2}{\rho_0}} \alpha_{ijk} S_{ijk}$	$\Delta P_{ij} - g \Delta \rho_{ij} (z_{ijk} + \frac{L_{ijk}}{2})$	$\frac{1}{2}$

#### Definition of Terms

$a_{ijk}$  = infiltration constant per unit length of crack

$g$  = gravitational constant

$L_{ijk}$  = length of crack or opening (any opening is assumed to be rectangular)

$n_{ijk}$  = flow exponent of crack or opening

$P_i$  = static pressure on the ground level

$S_{ijk}$  = area of opening

$z_{ijk}$  = height of crack or opening

$\alpha_{ijk}$  = discharge coefficient of opening

$\Delta P_{ij} = P_j - P_i$

$\Delta \rho_{ij}$  = air density difference between i and j  
 $\approx \rho_0 (\theta_i^{n-1} - \theta_j^{n-1}) / 353^*$

$\rho_0$  = mean air density (constant)

---

\* This assumption is not elaborate, but is inevitable to make calculation procedure as simple as possible.

The pressures of outdoor spaces ( $i=N+1 \sim M$ ) are taken as the boundary conditions and are given by,

$$P_i = CD_i \rho_0 U^2 / 2 \quad (12)$$

where

$CD_i$  = wind pressure coefficient

$U$  = wind velocity at the roof of building.

The wind pressure coefficients are evaluated from an empirical function which depends on an angle between wind direction and normal of outside surface. This function, which is shown in Fig.2, was formulated on the basis of Sekine's experimental data<sup>6)</sup>.

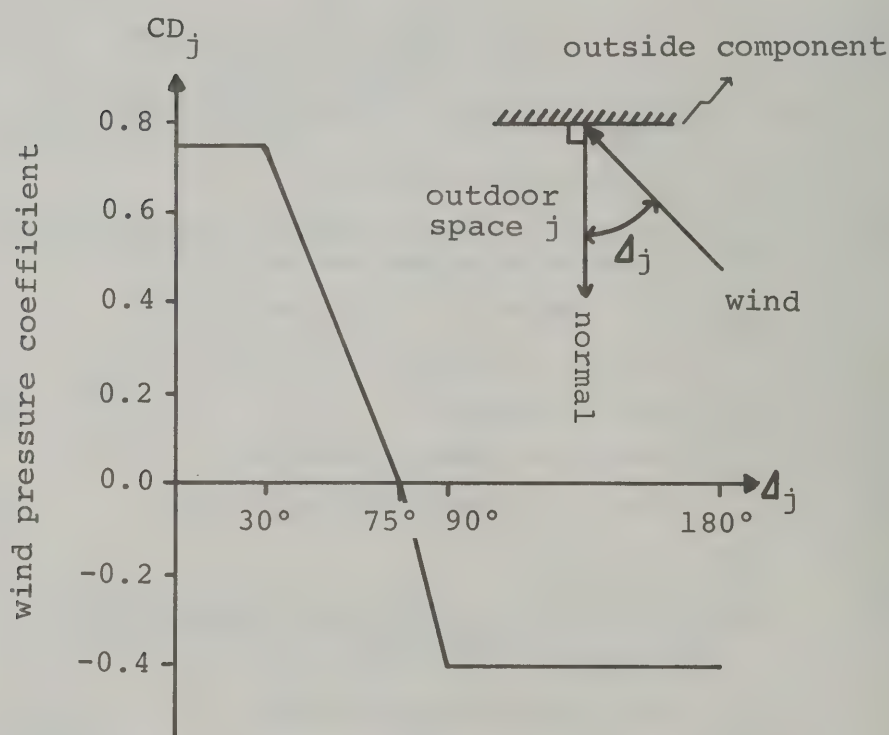


Fig.2 Wind Pressure Coefficient Adopted in Calculation of Natural Ventilaion

Equation (11) can be solved by the Choleski method<sup>7)</sup> because the matrix  $\lambda_{ij}$  is symmetric. The solved pressures are substituted into the expression of  $\omega_{ijk}$ , which results in new values of  $\omega_{ijk}$ . The ranges re-defined by the new values of  $\omega_{ijk}$  have to be compared individually with the former values. Disagreement between the former ranges and re-defined ones requires the re-solving equation (11), whose coefficient matrix and constant vector are re-calculated. Thus this process must be iterated until the agreements between both ranges are completely reached. In this way the final solution of pressures can be attained.

#### (4) Calculation of Volume Flow Rate of Air

The volume flow rate from j to i is given by,

$$V_{ij} = \sum_k u_{ijk} \quad (13)$$

where  $u_{ijk}$  is volume flow rate which goes across k into i. Applying the final pressure solution,  $u_{ijk}$  can be calculated in the following four cases restricted by two factors:

$$\phi_{ijk} = g\Delta\rho_{ij}z_{ijk}$$

$$\psi_{ijk} = g\Delta\rho_{ij}(z_{ijk} + L_{ijk})$$

$$1) [\Delta\rho_{ij} \leq 0 \text{ and } \Delta P_{ij} \geq \phi_{ijk}] \text{ or } [\Delta\rho_{ij} \geq 0 \text{ and } \Delta P_{ij} \geq \psi_{ijk}]$$

$$u_{ijk} = \sigma_{ijk}(m_{ijk}\omega_{ijk} + h_{ijk})$$

$$2) [\Delta\rho_{ij} < 0 \text{ and } \psi_{ijk} < \Delta P_{ij} < \phi_{ijk}]$$

$$u_{ijk} = - \frac{\sigma_{ijk}}{(n_{ijk} + 1)g\Delta\rho_{ij}L_{ijk}} (\Delta P_{ij} - \psi_{ijk})^{n_{ijk}+1}$$

$$3) [\Delta\rho_{ij} \leq 0 \text{ and } \Delta P_{ij} \leq \psi_{ijk}] \text{ or } [\Delta\rho_{ij} \geq 0 \text{ and } \Delta P_{ij} \leq \phi_{ijk}]$$

$$u_{ijk} = 0$$

$$4) [\Delta\rho_{ij} > 0 \text{ and } \phi_{ijk} < \Delta P_{ij} < \psi_{ijk}]$$

$$u_{ijk} = \frac{\sigma_{ijk}}{(n_{ijk} + 1)g\Delta\rho_{ij}L_{ijk}} (\Delta P_{ij} - \phi_{ijk})^{n_{ijk}+1}$$

As soon as  $V_{ij}$  is calculated, the volume flow rate from i to j is obtained by,

$$V_{ji} = V_{ij} - \sum_k V_{ijk} \quad (14)$$

Thus the volume flow rates calculated by this procedure are applied to the room heat balance equations.

### 3. VALUATION OF DEVELOPED PROCEDURE

#### (1) Purpose and Process

It is necessary to valuate the accuracy and the validity of this calculation procedure by an appropriate process, because it includes many physical assumptions and many mathematical approximations. In this paper the valuation was attempted by comparing the prediction by this procedure with the observation in actual dwelling houses. This valuation process seems to be most reliable to valuate general accuracy and validity easily. In fact, room air temperature was adopted as a comparable quantity for the valuation. It is the main reason for this adoption that room air temperatures can be measured more easily and more accurately than room heat loads.

The calculation procedure was coded with Fortran language, and the abbreviated name of BRIMAP\* was applied to this computer program. The observation on room air temperature was made in two different types of dwelling house. Both are experiment houses and were built using the conventional construction method of Japan. One is a house without thermal insulation, which is called by the name of House-A. The other is a well insulated house named House-B. However, both have the same features except

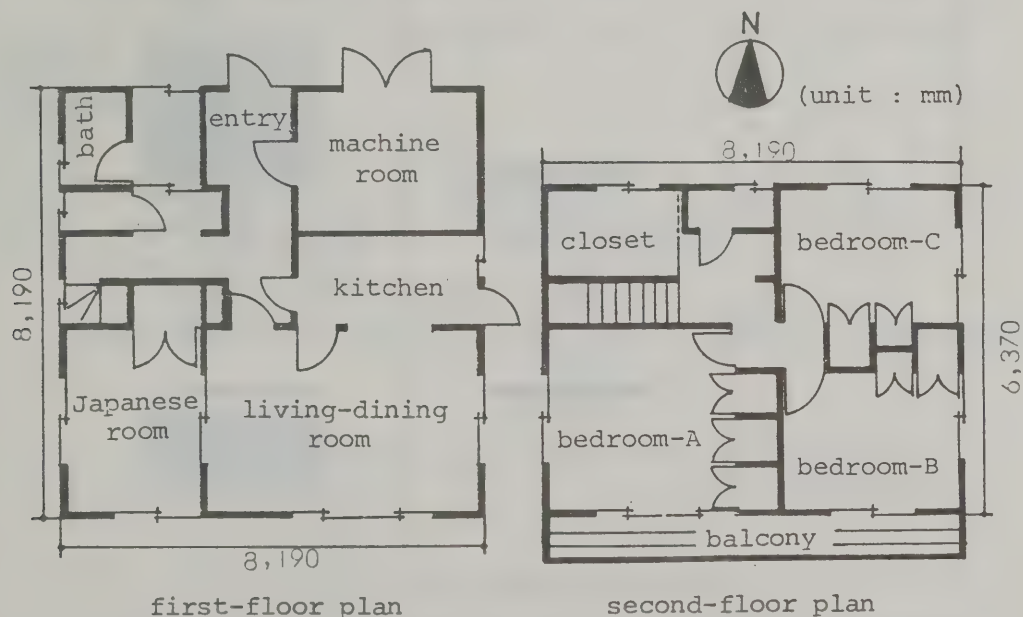


Fig.3 Plan of House-A and House-B

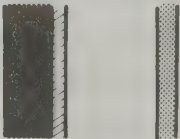
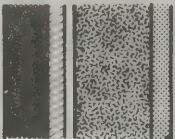

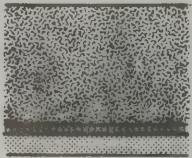

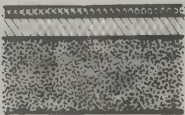
\* Building Research Institute/Multi-Room Air-Conditioning Load Program



for the insulation of the outside wall, the floor, and the ceiling and the material of the window frame. In addition, both were built adjacently on the same site of BRI at Tsukuba, Japan. The plan of both houses is shown in Fig.3, and the differences between both are listed in Table 2. The

Table 2 Difference of Component Specification between House-A and House-B

(unit of thickness is mm)

component	House-A	House-B
outside wall	 <div>room</div> <div>mortal 30 wooden board 8 air space plaster board 12</div>	 <div>room</div> <div>mortal 30 wooden board 8 air space glass wool 50 plaster board 12</div>
2F ceiling	 <div>room</div> <div>wooden board 5 insulation board 12</div>	 <div>room</div> <div>glass wool 100 wooden board 5 insulation board 12</div>
1F-floor	 <div>room</div> <div>carpet 4 wooden board 12</div>	 <div>carpet 4 wooden board 12 glass wool 50</div>
window	single pane with wooden frame	single pane with aluminium frame

observations were taken under the two kinds of living conditions simulating an actual living pattern. One was to heat some rooms intermittently with fan-heaters. The other condition was to open and close doors, windows, and curtains. Both conditions were common to both houses. The time schedules for both conditions are illustrated in Fig.4, which is accompanied with the meteorological condition observed in the vicinity of both houses. The meteorological condition consists of atmospheric temperature, direct solar radiation, sky solar radiation, and wind vector. These conditions of living and weather were input for the prediction. The minimum unit of time was half an hour in both observation and prediction.

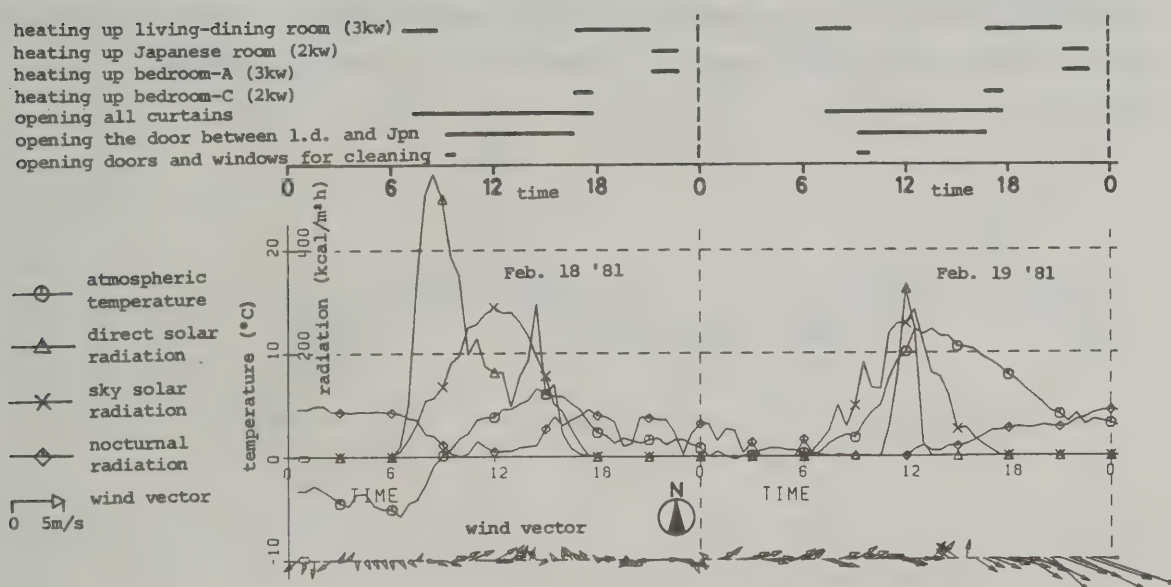
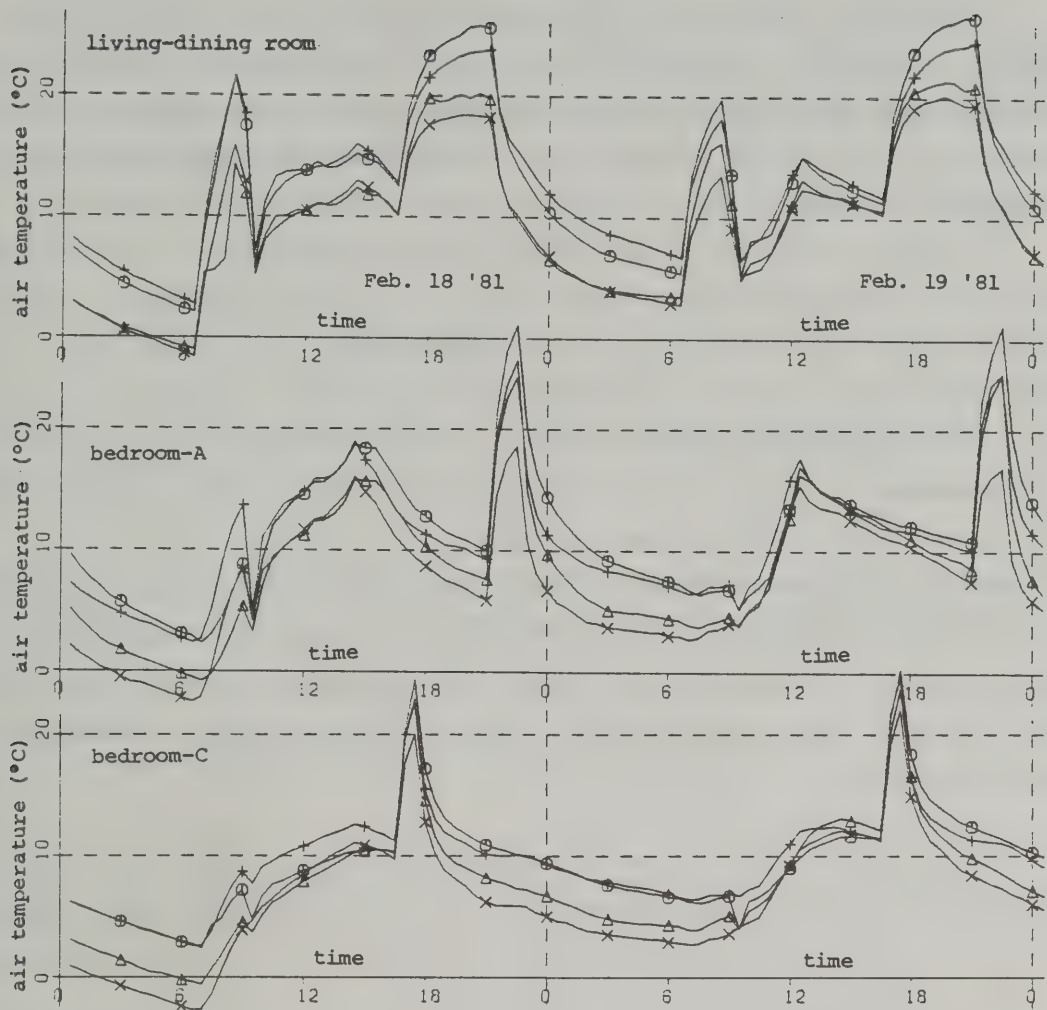


Fig.4 Living and Meteorological Conditions in the Observation and the Prediction

## (2) Results

Fig.5 represents the comparisons between prediction and observation in some room air temperatures of both houses. The observed room air temperatures in this figure are the temperatures which were defined by averaging the profile formed of the temperatures observed with seven thermocouples lined vertically.

An agreement between the prediction and the observation is fairly good and seems to be satisfactory for the practical calculation of air conditioning loads. The difference between House-A and House-B is well simulated. This difference is brought about by the insulation with glass wool. The sudden descents of temperature at 9:30 a.m. every day, which were caused by opening most windows and most doors for cleaning, are also simulated suitably. However, considerable disagreements between the prediction and the observation are found here and there, where the room was heated. These disagreements are considered to be caused by ignoring the heat exchange by long wave radiation among the room surfaces and the vertical distribution of room air temperature in the calculation procedure.



—X— prediction for House-A      —Δ— observation in House-A  
 —+— prediction for House-B      —⊕— observation in House-B

Fig.5 Comparison of Room Air Temperatures between the Prediction and the Observation



#### 4. CONCLUSIONS

This paper presented a calculation procedure for the multi-room problem including the effect of natural ventilation. The calculation procedure for natural ventilation is a new approximate procedure developed according to the crack method. The calculation procedure for multi-room temperatures or heat loads is based on the response factor method.

In order to evaluate the accuracy and the validity of this procedure, the room air temperatures predicted by it were compared with those observed. Generally speaking, an agreement between the prediction and the observation was good and acceptable for practical calculation. However, there were some disagreements in the period of heating the rooms. These disagreements suggest that it is necessary for more accurate simulation to develop the calculation procedure including the effect of the heat exchange by long wave radiation and the vertical temperature distribution in a room. Nevertheless, this calculation procedure is considerably valid and available for seasonal heat loads. The computer program BRIMAP has been utilized for designing and evaluating the energy conservation in houses of Japan.



#### ACKNOWLEDGEMENTS

The author would like to thank his colleagues at Building Research Institute, in particular Mr K. Eguchi and Mr H. Osawa, for their valuable contributions to the paper described.

#### REFERENCES

- 1) Mitalas, G.P. and Stephenson, D.G., Room Thermal Response Factors, 1967, ASHRAEA Trans., Vol.73, Part 1.
- 2) Eguchi, K., Heating and Cooling Load Calculations by Means of Periodic Window Function, 1971, Use of Computers for Environmental Engineering Related to Buildings, NBS.
- 3) Yamamoto, G., Atmospheric Radiation, 1954, Iwanami.
- 4) Matsuo, Y., Dynamic Calculation Method of Heat Loads, 1977-1978, Heating, Air-Conditioning and Sanitary Engineering, from Vol.51 No.10 to Vol.52 No.3.
- 5) Smith, G.D., Numerical Solution of Partial Differential Equations, 1965, Oxford University Press.
- 6) Sekine, T. and Katsuta, C., Effect of Wind on Ventilation by Openings of Building, 1962, Heating, Air-Conditioning and Sanitary Engineering, Vol.36, No.4.
- 7) Togawa, H., Numerical Calculation of Differential Equations, 1973, Ohm-Sha.



# 自然換気を考慮した多数室室温計算法の開発

坂 本 雄 三\*

リサーチペーパーNo.102

1983年10月 建設省建築研究所

日本の住宅では、窓を開放して通気・換気を行うことがごく一般的であることや、建物の気密性が悪いことなどが原因で、その熱環境を論ずる際自然換気の効果は非常に大きい要素と考えられる。建物の熱負荷や室温変動に関する従来の計算体系の中では、自然換気量は理論的な計算が煩雑なため、ともすれば安易な方法で与えられる傾向が強かった。そこで、建物全体の換気経路を考慮した自然換気の近似解法を考案し、それを従来の多数室室温計算の体系の中に組みこみ、日本の住宅のように自然換気が重要であり、尚且つ、部分・間歇暖冷房を行うような建物に対しても比較的短時間で精度のよい室温シミュレーションが行える計算法を開発した。

開発された計算法はフォートラン言語で電算プログラム化され、BRIMAPという名称が冠せられた。2棟の実験住宅における室温について、当プログラムによる計算結果と実測結果とが比較・照合された。その結果、計算値は比較的良好に実測値と一致しており、計算法の妥当性とプログラムの実用性が確かめられた。当プログラムは既に省エネルギー住宅の評価や設計法の開発のために使用されており、今後とも種々の目的で利用されるものと思われる。







## Research Papers-Recent Issues

- No.77 A. Baba: Drying Shrinkage Mechanism of Building Materials, March, 1978, 79 pp.
- No.78 K. Hayakawa: The Management of Land as an Environmental Resource, March, 1978, 40 pp.
- No.79 T. Tanaka: A Model on Fire Spread in Small Scale Buildings, September, 1978, 76 pp.
- No.80 Y. Aoki: Studies on Probabilistic Spread of Fire, November 1978, 52 pp.
- No.81 F. Saito: Experimental Study of Compartment Fire Using Model Boxes, July, 1979, 50 pp.
- No.82 Y. Matsushima: Random Response of Single-degree-of-freedom System with General Slip Hysteresis, July, 1979, 37 pp.
- No.83 Y. Hasemi: Flashover Criteria of Compartment Fire - Theory on Zero Order Reaction System -, August, 1979, 26 pp.
- No.84 T. Tanaka: A Model on Fire Spread in Small Scale Buildings, 2nd Report, March, 1980, 63 pp.
- No.85 Y. Ishiyama: Review and Discussion on Overturning of Bodies by Earthquake Motions, June, 1980, 115 pp.
- No.86 S. Watanabe: Planning History in Japan-A State of the Art Survey -. August, 1980, 36 pp.
- No.87 Y. Sugimura: Participation Factor of Horizontal Force Applied to Pile Foundation, March, 1981, 33 pp.
- No.88 Y. Hasemi: Mathematical Basis for Physical Evaluation on Flashover, March, 1981, 41 pp.
- No.89 T. Wakamatsu: A Quantitative Evaluation of Smoke Safety, March, 21 pp.
- No.90 S. Watanabe: Metropolitanism as a Way of Life, March, 1981, 52 pp.
- No.91 M. Hirose, T. Goto, M. Yoshimura, H. Hiraishi: Full-Scale Experimental Study on Aseismic Performance of Medium-Rise RC Wall Structure. March, 1981, 28 pp.
- No.92 Y. Yamazaki: Inelastic Torsional Response of Structures Subjected to Earthquake Ground Motions. March, 1981, 102 pp.
- No.93 S. Kose: Study of Accidents Associated with Building Feature. March, 1982, 38 pp.
- No.94 S. Okamoto, S. Nakata, Y. Kitagawa, M. Yoshimura, T. Kaminosono: A Progress Report on the Full-Scale Seismic Experiment of a Seven Story Reinforced Concrete Building - Part of the US-Japan Cooperative Program, March, 1982, 92 pp.
- No.95 Y. Hasemi: Characterization of the Intermittent Flaming Region of the Upward Current Above Diffusion Flames. March, 1982, 33 pp.
- No.96 Y. Morishita: Statistical Analysis of Fire Spread. May, 1982, 17 pp.
- No.97 T. Fukushima: Deterioration Model of Polymeric Materials with Special Attention to Age and Deterioration Depth. December, 1982, 30 pp.
- No.98 H. Hiraishi, M. Yoshimura, H. Isoishi, S. Nakata: Planer Tests on Reinforced Concrete Shear Wall Assemblies. - U.S.-Japan Cooperative Research Program-, January, 1983, 63 pp.
- No.99 S. Nakata: Tests of Reinforced Concrete Beam-Column Assemblages -U.S.-Japan Cooperative Research Program-, March, 1983, 111 pp.
- No.100 Y. Aoki: Assessment of an Urban Safety Evaluation Function. March, 1983, 16 pp.
- No.101 S. Okamoto, T. Kaminosono, M. Nakashima, H. Kato: Techniques for Large Scale Testing at BRI Large Scale Structure Test Laboratory. March, 1983, 38 pp.
- No.102 Y. Sakamoto: Development of Procedure for Calculating Room Air Temperatures Including Effect of Natural Ventilation. October, 1983, 19pp.

Address for Communication

BUILDING RESEARCH INSTITUTE  
MINISTRY OF CONSTRUCTION

No.1 TACHI HARA, OH-HO-MACHI, TSUKUBA-GUN, IBARAKI-PREF.  
JAPAN











UNIVERSITY OF ILLINOIS-URBANA



3 0112 081487230